AN INNOVATIVE SENSING APPROACH USING CARBON NANOTUBE-BASED COMPOSITES FOR STRUCTURAL HEALTH MONITORING OF CONCRETE STRUCTURES

by

Hongbo Dai

A dissertation submitted to the Faculty of the University of Delaware in partial fulfillment of the requirements for the degree of Doctor of Philosophy in Civil Engineering

Fall 2017

AN INNOVATIVE SENSING APPROACH USING CARBON NANOTUBE-BASED COMPOSITES FOR STRUCTURAL HEALTH MONITORING OF CONCRETE STRUCTURES

by

Hongbo Dai

Approved: _____
Sue McNeil, Ph.D.
Chair of the Department of Civil and Environmental Engineering

Approved: _____
Babatunde A. Ogunnaike, Ph.D.
Dean of the College of Engineering

Approved: _____
Ann L. Ardis, Ph.D.
Senior Vice Provost for Graduate and Professional Education

I certify that I have read this dissertation and that in my opinion it meets the academic and professional standard required by the University as a dissertation for the degree of Doctor of Philosophy.

Signed: _____

Thomas Schumacher, Ph.D.
Co-Advisor in charge of dissertation

I certify that I have read this dissertation and that in my opinion it meets the academic and professional standard required by the University as a dissertation for the degree of Doctor of Philosophy.

Signed: _____

Erik T. Thostenson, Ph.D.
Co-Advisor in charge of dissertation

I certify that I have read this dissertation and that in my opinion it meets the academic and professional standard required by the University as a dissertation for the degree of Doctor of Philosophy.

Signed: _____

Michael J. Chajes, Ph.D.
Member of dissertation committee

I certify that I have read this dissertation and that in my opinion it meets the academic and professional standard required by the University as a dissertation for the degree of Doctor of Philosophy.

Signed: _____

Jennifer Righman McConnell, Ph.D.
Member of dissertation committee

ACKNOWLEDGMENTS

First and foremost, I would like to sincerely acknowledge my adviser Professor Thomas Schumacher and co-adviser Professor Erik T. Thostenson for their constant guidance, support, and insightful advices during the entire journey of my doctoral study. Their professional mentoring and warm encouragement have motivated me to successfully complete this doctoral research. I am truly blessed to have had such excellent advisors! I would also like to express my sincere thanks to Professor Michael J. Chajes and Professor Jennifer Righman McConnell for serving on the dissertation committee.

I also gratefully thank all the faculty, laboratory technicians and staff of the Center for Composite Materials (CCM) and Civil Engineering Structures Laboratory at University of Delaware for providing me knowledgeable advices and generous support whenever I have requested them for.

In addition, I would like to greatly appreciate the funding support of this collaborative research effort by the National Science Foundation, CMMI Division, Award # 1234830 (Dr. Kishor Methta, Program Director).

Last but not the least, I would like to express my deep gratitude and great thanks to my loving family, my colleagues and my friends for their heartful encouragement and support throughout my graduate education.

TABLE OF CONTENTS

LIST OF TABLES

LIST OF FIGURES

ABSTRACT

Over the time, the integrity and reliability of civil infrastructures are threatened by overloading, fatigue, impact damage, and structural deterioration. Structural health monitoring (SHM) is therefore becoming a viable tool to collect real-time quantitative data from in-service structures concerning structural condition and performance. Being capable of continuously monitoring critical components, SHM systems can instantaneously identify damage, guide necessary repairs, and may ultimately help prevent catastrophic failure. As the core of SHM, the capability, accuracy and reliability of the applied sensing system govern the overall success of the implementation of SHM. To date, conventional sensors such as strain gages, accelerometers, and displacement gages have been widely employed in SHM systems for attaining global or/and local responses of a structure. However, these point-type sensors still suffer from limitations and challenges, which indeed have inspired the development of next-generation sensing methodologies for SHM. Recent advances in nanotechnology offer a variety of self-sensing nanocomposites with integrated nanoscale, noninvasive, electrically percolating networks providing exceptional sensitivity to sense changes in strain as well as the formation and propagation of micro- and macro-damage. By appropriately integrating nanocomposites with distributed sensing schemes, an extensive nerve-like sensing system with enhanced detection capabilities and spatial sensitivity of strain and growing damage can be established for SHM of civil infrastructures.

The research work presented in this dissertation advances the state of the art by introducing an innovative carbon nanotube (CNT)-based nonwoven composite sensor that can be tailored for strain and damage sensing properties and potentially offers a reliable and cost-effective sensing option for SHM. First, a readily scalable two-step process for manufacturing nanocomposites was developed. Specifically, a thin, lightweight and inexpensive nonwoven fabric was selected as the CNT carrier and nanotubes were deposited following a dip-coating procedure. Second, the microstructure, mechanical, and electrical properties of the proposed CNT-based composite sensor were investigated. Its electrical double percolation was observed for the first time and its self-sensing capability, and strain sensitivity was validated and characterized using coupon-level experiments. The sensors were found to be repeatable and respond linearly up to 0.4% strain with achievable elastic strain gage factors of 1.9 and 4.0 in the longitudinal and transverse direction, respectively. Third, the established composite sensors were further integrated with a difference imaging-based electrical impedance tomography (EIT) sensing scheme to offer a true two-dimensional damage sensing methodology, from which damage location, size, and severity can be estimated. This represents a significant extension to the commonly applied direct current (DC)-based point sensing scheme. Next, a systematic characterization of the thermoresistive behavior in these CNT-based nanocomposites and multiscale composites was performed under thermal cycling between 25 to 145 °C. A dynamic dominance for a double-crossover-shaped temperature dependence of their resistances was observed and methodically investigated. Finally, a hybrid composite system was applied on two large-scale reinforced concrete laboratory beams (12 in × 24 in × 16 ft), in which the CNT-modified nonwoven sensing sheet for

SHM is integrated with a glass fiber reinforcement to create a combined strengthening and sensing solution. The 14-ft-long nanocomposite sensor was interrogated using a multiplexing approach with multiple electrodes to spatially estimate the damage locations. To date, this is the largest CNT-based composite sensor ever tested.

The findings from this dissertation research have made important scholarly contributions to the fundamental understanding of the sensing networks of the innovative CNT-based nonwoven composites. Important broader impacts have also been made by promoting applications of using CNT-based sensing composites as strain/damage sensors for SHM. The presented methodology has remarkable potential to revolutionize the fields of SHM and structural engineering.

Chapter 1

INTRODUCTION

1.1 Motivation and Background

Civil infrastructure, a universal group of basic structures including bridges, buildings, dams, tunnels, pipelines, and many others, supports the operation of a society and facilitates economic and civilized development of many regions in the world. If structural deficiencies and malfunctions are unable to be detected and repaired in time, simply ignoring the structures with poor integrity can ultimately lead to tragic consequences such as loss of human lives [1-4]. Structural health monitoring (SHM) can be a viable solution to maintain integrity and reliability of structures. SHM is a recently developed technology that collects and analyzes the measurements from sensors attached to in-service structures in real-time. The collected data are used to assess structural performance under ambient loads and to detect and characterize structural damage. The ultimate goal is to help owners, builders, and designer of structures in rational decision-making on maintenance strategies [5,6]. As SHM systems continuously monitor the health of a structure, the cost of unnecessary inspections can be minimized. Meanwhile, the instantaneously collected real-time information from SHM system can guide inspection intervals and maintenance interventions.

It is obvious that the nation's transportation infrastructure network continues to age. According to the 2017 ASCE report card [7], the overall rating for safety of the bridges in the United States is C+ and 9.1% of the nation's bridges (that is nearly

56,000 bridges) are rated as structurally deficient. Specifically, steel, reinforced and prestressed concrete bridges represent a large portion and crucial components of the transportation network. Due to the deficiencies in the bridge codes at the time when the bridges were built as well as increasing truck weights and frequencies, many bridges have been put under load restrictions or must be renovated before reaching their intended service life. SHM as a technique to help prevent and mitigate the progress of structural damage, is now more and more recognized and accepted in the civil engineering community.

As the fundamental and critical component in SHM systems, sensors govern the overall success of the implementation of SHM. For example, visual inspection (i.e., an active nondestructive testing (NDT) method), basing on human senses and simple equipment, is a common and dominant SHM approach at present [8,9], however, the possibility of undetected damage evolution to critical levels without immediate recognition is always a serious cause for concern. As another example, deployable sensing systems consisting of conventional sensors such as strain gages, accelerometers, displacement gages etc. have been traditionally employed in SHM systems [5,6]. The pros and cons of the commonly employed SHM sensors are listed in Table 1.1. Generally, these point-type sensors can only cover a finite number of discrete points and the selection of critical areas for monitoring remains subject to the owner's expertise and experience [5,6]. In particular, concrete is a heterogeneous material and therefore concrete structures have complex local strain fields and nonlinear strain distribution along the gage length [10-12]. To get a global view of a concrete structure's health condition, one practical solution is to apply a distributed sensor capable of capturing the response of the entire structure to continuously

monitor critical components that show distress [13]. Some experimental work has been performed on using distributed sensors for SHM, such as continuous networks of fiber optic sensors for one-dimensional strain field monitoring of concrete structures [14-16], two-dimensional networks of piezoelectric sensors for spatial damage detection [17-19], and laser sensors for assessing loading conditions [20,21] of concrete and composite members. Finally, three-dimensional networks of acoustic emission sensors have been used for monitoring cracking in concrete structures [22-25].

Table 1.1: Typical Sensors for SHM Systems.

Sensor Type	Advantages	Drawbacks/Challenges
Foil/Demountable Strain Gages [5,26,27]	Easy to install, accurate, available in many sizes, well-established	Heavy wiring needed, quasi-point measurement, very sensitive to local strain but only if at or nearby location of damage
Accelerometers [28,29]	Easy to install, accurate, sensitive to dynamic response	Point measurement, global, indirectly correlating to structural performance, low sensitivity to local damage
Displacement Gages [30,31]	Easy to install, accurate, good linearity within the elastic range of the sensor and structure	Point measurement, global, indirectly correlating to structural health, low sensitivity to local damage
Acoustic Emission Sensors [24,25]	Passive (no need for external stimulus), volumetric coverage, real-time damage detection	Network with large number of sensors needed for locating damage, difficult to apply, susceptible to ambient noise
Ultrasonic Sensors [32-34]	Sensitive for locating voids and discontinuities in concrete, relatively high resolution	Point measurement, must knowing the approximate location of damage in advance, difficult interpretation of outputs
Fiber-Optic Sensors [35-38]	Capable of distributed sensing, no need for electrical powder, quantitative	Susceptible to temperature changes, extremely small sensing area (fiber diameter in micron-lever), moderated sensitivity for local strain

1.2 Carbon Nanotube-Based Nanocomposites and Multiscale Composites

Carbon nanotubes (CNTs) exhibit remarkable mechanical, electrical and thermal properties [39,40]. Over the past two decades, CNT-based nanocomposites have drawn considerable attention and are still extensively investigated due to their excellent properties and significant industrial applications [41]. With their exceptionally high aspect ratio and small size, CNTs are commonly introduced into polymers at a small concentration and then utilized as passive reinforcement to tailor a wide range of physical properties, such as Young's modulus, toughness, impact resistance, electrical and thermal conductivity [42,43]. In addition, by strategically combining conventional reinforcing fibers (~μm-scale) with CNTs (~nm-scale) to create a macro multiscale material system (~m-scale), structurally hierarchical composites can be enabled to further tailor the structural and functional properties by the selective reinforcement [44,45]. Specifically, CNTs are predominantly placed in two domains including either the entire matrix phase or the immediate vicinity of the fibers.

Dispersing CNTs throughout the fibrous composite matrix can toughen the matrix and consequently improve the out-of-plane stiffness, interlaminar strength and fracture toughness of the bulk composite which can ultimately enhance its resistance to matrix-dominated damage in the form of matrix microcracking and inter-ply delamination attributed to the crack bridging effect by CNTs [43,44,46]. This strategy is straightforward and simple but neglects the control to the load transfer mechanism in the interphase region (i.e., the fiber/matrix interface) and difficulties exist regarding achieving homogeneous and stable dispersion of CNTs in the polymer matrix. Large CNT agglomerates can lead to a self-filtering effect of CNTs during composite manufacturing and thereby significantly compromises the overall performance [45].

Processing approaches for developing such composite systems have been widely documented and include shear mixing (i.e., calendaring or three-roll milling) [44,47-49] and sonication [50,51] for low-viscosity thermosetting resins, melt processing [52-54] for thermoplastic matrices, and a latex-based approach for highly viscous matrices [55].

On the other hand, hybridizing CNTs onto the reinforcing fibers can significantly increase the fiber surface area providing a larger area for transferring load, which directly promotes the load transfer efficiency in the interphase [45,56]. Additionally, by grafting functionalized CNTs on fibers, the interfacial bond at the fiber/matrix interface can be modified as a result of the increased chemical interaction within this region [57,58]. Both enhancements can raise interfacial shear strength and energy absorbing capabilities attributed to the improvement to the interlaminar performance of the multiscale hybrid composites [56,59]. This scheme offers the potential to achieve high nanotube volume fractions and functionally upgraded local properties, but requires significant process development with respect to the CNT/fiber hybridization [43,45,59]. Several CNT deposition techniques have been reported and proven industrially scalable as well as cost-effective, such as dip-coating [60-65], electrophoretic deposition (EPD) [57,66-68], and spray coating [69,70].

1.3 Carbon Nanotube-Based Multifunctional Composites as Resistive Sensors

Apart from the classical application of CNTs as nanoscale reinforcing modifiers, new multifunctional applications of CNT-based composites for damage sensing and SHM sensors have been widely explored during recent years due to the fast-growing industrial applications of fiber-reinforced composites and the urgent demand to improve the in-service reliability of these materials [71]. In 2004, Fiedler *et*

al. [72] first introduced the concept of CNT-based strain and damage sensing in a glass-fiber composite with CNT-modified matrix by measuring electrical resistance during loading. It is now well accepted that due to their nanoscale size, CNTs are able to infiltrate into the matrix-rich regions around the fibers and between the plies of the composite resulting in an electrically percolating network where CNTs behave as a network of distributed nano-sensors throughout the entire matrix [73,74]. In this way, the propagation of micro-sized cracks in the composite can alter the configuration of the conductive network by breaking local percolating pathways (i.e., losing CNT-CNT contacts), thereby leading to an instant rise in the bulk electrical resistance and enabling the *in situ* damage sensing capability of the multiscale composites. Additionally, the real-time resistance changes reflect the transient reaction of the CNT network (i.e., changing tunneling gap distance between CNTs or/and CNT-CNT contacts) in responding to the deformation that the mechanically strained composite undergoes, proving additional information on structural integrity of the composite. This is the core of realizing SHM in multiscale composites and is indicative of their self-sensing functionality. Similarly, vapors [75], temperature, humidity, infrared radiation [76,77] and other physical [78] or chemical [79,80] loads that can give rise to variations in dimensions or intrinsic properties of CNT can directly induce resistance changes in CNT-based composites. Consequently, these stimuli can be detected suggesting a promising route for next-generation SHM systems with multimodal sensing capabilities based on CNT composites.

In particular, the strain sensing functionality of CNT-based nanocomposites has been studied experimentally [43,61,81-85] and with numerical simulations [82,86]. For instance, Barber *et al*. [87] among others first used CNTs as stress sensors

for the microscale characterization of the glass/polypropylene interface by Raman spectroscopy. Dharap *et al*. [84,85,88] performed several primary studies on the macroscale strain sensing by utilizing a CNT film (namely, buckypaper [89] or CNT sheet) as a resistive strain sensor and found a nearly linear correlation between strain and voltage change. Similarly, Kang *et al*. [90] systematically characterized the piezoresistive responses of buckypaper and CNT/poly methyl methacrylate (PMMA) composites under static and dynamic loading conditions and demonstrated linear piezoresistivity up to 0.05% and 0.13% strain, respectively; the reported CNT/PMMA sensors showed gage factors (GF) of 1.0 to 5.0 and they also produced a long continuous strain sensor and suggested potential SHM applications. Loh *et al*. [91] showed that CNT/polyelectrolyte thin films fabricated using a layer-by-layer process can be used for strain sensing with linearity up to 1% strain and gage factors from 0.1 to 1.8. Hu *et al*. [82,92] and Yin *et al*. [83] studied the piezoresistive response of a CNT/epoxy composite and reported high gage factors of 7.0 in compression and 22.4 in tension showing linear but unsymmetrical piezoresistivity. They also numerically confirmed the dominant role of the electrical tunneling effect for the electrical conduction in CNT/polymer nanocomposites simulated using a 3D statistical resistor network model [92,93]. This conclusion was in agreement with the numerical results obtained by Li *et al*. [94] and Gau *et al*. [95]. Many other piezoresistive nanocomposite strain sensors were developed by dispersing CNTs into different polymer matrices, such as PC [96], PU [97], PP [98], PSF [99], etc. With this unique piezoresistive sensing response, CNT-based composites can be utilized as *in situ* strain sensors when integrated directly into the structural material [13,100-103] or as *ex situ*

sensors that can be attached to a structure (i.e., strain sensors [61,85,88,90,97,104,105], or body motion sensors [106,107], etc.).

In addition, the damage sensing capability of self-sensing multiscale composites has been systematically characterized. The current state of research related to this topic has been comprehensively reviewed by Zhang *et al*. [71] around 2015. Particularly, Thostenson and Chou [74] first experimentally investigated glass fiber cross-ply laminates with CNTs dispersed in the matrix for sensing damage evolution during static tension. They found that the resistance moderately increases when the deformation is elastic but dramatically jumps as delamination is initiated. Later, Thostenson and Chou [73] performed real-time *in situ* sensing of damage evolution in the same multiscale composites during cyclic loading. They introduced the concept of damaged resistance change, which is equal to the sum of the crack re-opening resistance change and the permanent resistance increase change. A similar study was also performed by Boger *et al*. [108]. Subsequently, an engineering application of CNT-based SHM was examined on a mechanically fastened composite joint by Thostenson and Chou [109] and further investigated by Friedrich *et al*. [110]. In particular, Li and Chou [111] performed numerical modeling of damage detection in CNT-modified glass fiber composites, which supported the experimentally obtained results showing how the damage evolution affects the electrical resistance.

Furthermore, particular efforts have been made on sensing the onset failure as monitoring damage. Nofar *et al*. [112] implemented a multiplexing monitoring concept on CNT-glass multiscale composites by dividing the bulk composite into several zones with multiple intermediate electrodes and then collecting the resistance responses from all individual channels simultaneously. The failure location was

accordingly identified as the region with greater resistance increase compared to other regions on the part. Later, Naghashpour and Van Hou [113] deployed a grid of 80 distributed surface electrodes on an electrically conductive composite panel made of CNT/carbon fiber/epoxy and collected 4-point measurements through the grid points as impact damage was applied on the composite panel. The applied damage were quantitatively represented by the percentage change in electrical potential between grid points and approximately located to the affected grid points between measurements.

Recently, some experimental studies have investigated the CNT-based SHM sensors for use in concrete structures. Schumacher and Thostenson [13] applied an integrated structural sensing composite patch of CNT/glass fiber/epoxy on a 6 in × 6 in × 21 in concrete beam specimen that was tested to failure under quasi-static loads. The real-time resistive response of the nanocomposite patch displayed a close correlation with the mechanical response of the concrete specimen in terms of mid-span displacement and strain recorded from the point sensors. The damage evolution of beam cracking up to failure was represented by the resistance change of the self-sensing patch, which was also validated by the response of the mounted acoustic emission sensor. Additionally, Saafi [114] developed CNT-based cement sensors which were embedded into small concrete beams for SHM under monotonic and cyclic loadings. A wireless communication system was interfaced with these *in situ* sensors to wirelessly collect their resistive responses. The results clearly demonstrated the cracking initiation and propagation of the concrete beam during loading. Similarly, CNT-cement composites were also fabricated and tested as *ex situ* SHM sensors by Ubertini, *et al*. [115] who investigated their potential for dynamic strain monitoring. A

2 in × 1.5 in × 2 in CNT-cement sensor was deployed and prestressed on a 14 ft long concrete beam which was subjected to a harmonic load varying between 0.25 and 15 Hz. The resistive response of the CNT-cement sensor showed ideal linear dynamic behavior with constant frequency response curves. After processing the resistive data by means of the classic frequency domain decomposition method, the power spectral densities of the data displayed a strong relationship with the frequency of the fundamental vibration mode of the concrete beam as measured by the accelerometers.

1.4 Problem Statement, Research Goal and Dissertation Organization

In general, the existing sensing methods are insufficient for SHM and not ideally suited for damage sensing of large-scale concrete structures. The aforementioned literature search has shown the feasibility and strong potential for using CNT-based composites as SHM sensors in light of the instant piezoresistivity of the electrically-percolated nanotube networks established naturally in the nanocomposites. However, only a few experimental studies have been performed toward employing nanotube-based sensing networks for SHM of concrete structures. Among the existing work, most of them have investigated the sensing responses from the materials point of view based on coupon-level experiments. Furthermore, they have important limitations which lead to a significant hurdle to transfer this novel sensing methodology to practical applications, including (1) the fabrication methods of CNT-based sensors are non-scalable, complex; and expensive; (2) fundamental understanding and repeatability of the sensing responses of the CNT-based sensors are not fully demonstrated; (3) the spatial sensing capability of the CNT-based sensors is substantially limited by the implemented sensing scheme (i.e., the direct current (DC)

based point measurements) and not well investigated and (4) temperature effects on the resistive responses of the CNT-based sensors are overlooked.

The goal of this research focuses on the development of an innovative CNT-based nonwoven composite sensor and advanced sensing schemes that can be tailored for strain sensing properties, spatial damage detection and potentially offers a reliable, scalable, and cost-effective sensing option with distributed sensing capabilities for large-scale SHM systems. In order to achieve this goal, the dissertation is outlined herein as follows:

This chapter introduces the basics of SHM for civil infrastructures and the background knowledge about sensing techniques for SHM. A literature review of recent advances in CNT-based composites and the concepts and fundamentals of CNT-based composite sensors for SHM are provided. The problem statement and the general research goal are highlighted. The dissertation structure is also outlined.

Chapter 2 presents in detail the processing and characterization of the distributed strain sensor for SHM using CNT-based nonwoven composites. A simple two-step method to fabricate CNT-based composite sensors is introduced. The microstructure, mechanical properties, the sensing mechanisms and *in situ* piezoresistive responses of the as-fabricated nanocomposites are fully characterized. The tensile and compressive strain sensing capabilities of this nanocomposite for *ex situ* distributed SHM sensors are also demonstrated.

Chapter 3 introduces a novel methodology for two-dimensional damage detection and imaging using the distributed CNT-based composite sensor combined with electrical impedance tomography (EIT). The background and recent applications of EIT-based damage sensing are first reviewed. The theory and formulation of EIT

are then presented. A difference imaging-based EIT algorithm was implemented to the formerly developed CNT-based nonwoven composite sensors and the integrated sensing approach is investigated for two damage scenarios including well-defined damage and drop-weight impact damage. The resulting EIT reconstructions are evaluated in detail and compared to infrared thermography images.

Chapter 4 systemically characterizes the thermoresistive behavior in binary-phase nanocomposites and ternary-phase hierarchical hybrid composites using *in situ* electrical resistance measurements during thermal cycling between 25 to 145 °C. Four series of CNT-based composites (including the previously established CNT-based nonwoven composite) with different morphological states of CNTs were fabricated via three-roll-milling, dip-coating, and electrophoretic deposition processes. A thermomechanical analysis and finite element analysis were also performed to study the temperature-dependent materials properties. For SHM applications, a temperature compensation method is proposed and verified.

Chapter 5 presents the experimental implementations of a hybrid composite system for integrated structural rehabilitation and SHM of large scale concrete beams. The CNT-based nonwoven sensing sheet is used as the *ex situ* SHM sensor, integrated with the glass fiber reinforcement, and deployed on the concrete beam by means of the vacuum-assisted-resin-transfer-molding (VARTM) process. Two concrete beams with dimensions 12 in × 24 in × 16 ft were pre-cracked and retrofitted using the proposed composite system. Both beams were tested to failure and real-time resistance responses were measured during the entire loading protocol and compared with the member deformations. In particular, a sensing scheme of multiplexing was employed to spatially estimate the damage location.

Chapter 6 contains the major conclusions of this research, highlights the contributions of this research, and provides recommendations for future work.

REFERENCES

1. Biezma MV, Schanack F. Collapse of steel bridges. J Perform Constr Facil 2007;21(5):398-405.

2. Hao S. I-35W bridge collapse. J Bridge Eng 2009;15(5):608-614.

3. Stewart MG, Rosowsky DV. Structural safety and serviceability of concrete bridges subject to corrosion. J Infrastruct Syst 1998;4(4):146-155.

4. Peekema RM. Causes of natural gas pipeline explosive ruptures. Journal of Pipeline Systems Engineering and Practice 2013;4(1):74-80.

5. Ettouney MM, Alampalli S. Infrastructure health in civil engineering: Theory and components, vol. 1: CRC Press, 2016.

6. Huston D. Structural sensing, health monitoring, and performance evaluation: CRC Press, 2010.

7. American Society of Civil Engineering. 2017 Infrastructure Report Card. 2017.

8. Moore M, Phares BM, Graybeal B, Rolander D, Washer G. Reliability of Visual Inspection for Highway Bridges. U S Department of Transportation Federal Highway Administration 2001;FHWA-RD-01-020.

9. Rolander D, Phares B, Graybeal B, Moore M, Washer G. Highway bridge inspection: State-of-the-practice survey. Transportation Research Record: Journal of the Transportation Research Board 2001(1749):73-81.

10. Bažant ZP, Belytschko TB, Chang T. Continuum theory for strain-softening. J Eng Mech 1984;110(12):1666-1692.

11. Bažant ZP, Pijaudier-Cabot G. Measurement of characteristic length of nonlocal continuum. J Eng Mech 1989;115(4):755-767.

12. Bazant ZP, Planas J. Fracture and size effect in concrete and other quasibrittle materials, vol. 16: CRC press, 1997.

13. Schumacher T, Thostenson ET. Development of structural carbon nanotube–based sensing composites for concrete structures. J Intell Mater Syst Struct 2014;25(10):1331-1339.

14. Ansari F. Real-time condition monitoring of concrete structures by embedded optical fibers. Proceedings of Nondestructive Testing of Concrete Elements and Structures: Publ by ASCE, 1992.

15. Moyo P, Brownjohn J, Suresh R, Tjin S. Development of fiber Bragg grating sensors for monitoring civil infrastructure. Eng Struct 2005;27(12):1828-1834.

16. Majumder M, Gangopadhyay TK, Chakraborty AK, Dasgupta K, Bhattacharya DK. Fibre Bragg gratings in structural health monitoring—Present status and applications. Sensors and Actuators A: Physical 2008;147(1):150-164.

17. Kusaka T, Qing P. Characterization of loading effects on the performance of SMART layer embedded or surface-mounted on structures. Proceeding of the Fourth International Workshop on Structural Health Monitoring, Stanford University, 2003. p. 1539-1546.

18. Park J, Chang F. Built-in detection of impact damage in multi-layered thick composite structures. Proceedings of the Fourth International Workshop on Structural Health Monitoring, 2003. p. 1391-1398.

19. Yao Y, Glisic B. Detection of Steel Fatigue Cracks with Strain Sensing Sheets Based on Large Area Electronics. Sensors 2015;15(4):8088-8108.

20. Mehrabi AB, Ciolko AT. Health Monitoring of Aging Cable Structures. In: Anonymous Structures 2001: A Structural Engineering Odyssey, 2001.

21. Fuchs P, Washer G, Chase S, Moore M. Laser-based instrumentation for bridge load testing. J Perform Constr Facil 2004;18(4):213-219.

22. Ohtsu M, Uchida M, Okamoto T, Yuyama S. Damage assessment of reinforced concrete beams qualified by acoustic emission. ACI Struct J 2002;99(4):411-417.

23. Ridge AR, Ziehl PH. Evaluation of strengthened reinforced concrete beams: cyclic load test and acoustic emission methods. ACI Struct J 2006;103(6):832.

24. Nair A, Cai C. Acoustic emission monitoring of bridges: Review and case studies. Eng Struct 2010;32(6):1704-1714.

25. Behnia A, Chai HK, Shiotani T. Advanced structural health monitoring of concrete structures with the aid of acoustic emission. Constr Build Mater 2014;65:282-302.

26. Chan TH, Li Z, Ko JM. Fatigue analysis and life prediction of bridges with structural health monitoring data—Part II: Application. Int J Fatigue 2001;23(1):55-64.

27. Rumsey MA, Paquette JA. Structural health monitoring of wind turbine blades. Proc. SPIE, 2008. p. 69330E.

28. Ou J. Some recent advances of intelligent health monitoring systems for civil infrastructures in mainland China. Structural Health Monitoring and Intelligent Infrastructure, Edited by Wu ZS and Abe M 2003;1:131-144.

29. Chae M, Yoo H, Kim J, Cho M. Development of a wireless sensor network system for suspension bridge health monitoring. Autom Constr 2012;21:237-252.

30. Song G, Gu H, Mo Y, Hsu T, Dhonde H. Concrete structural health monitoring using embedded piezoceramic transducers. Smart Mater Struct 2007;16(4):959.

31. Wang X, Wang ML, Zhao Y, Chen H, Zhou LL. Smart health monitoring system for a prestressed concrete bridge. Smart Structures and Materials 2004:597-608.

32. Staszewski WJ. Structural health monitoring using guided ultrasonic waves. In: Anonymous Advances in smart technologies in structural engineering: Springer, 2004.

33. Rose JL. Ultrasonic guided waves in structural health monitoring. Key Engineering Materials: Trans Tech Publ, 2004. p. 14-21.

34. Raghavan A, Cesnik CE. Review of guided-wave structural health monitoring. Shock Vib Dig 2007;39(2):91-116.

35. Tennyson R, Mufti A, Rizkalla S, Tadros G, Benmokrane B. Structural health monitoring of innovative bridges in Canada with fiber optic sensors. Smart Mater Struct 2001;10(3):560.

36. Ko J, Ni Y. Technology developments in structural health monitoring of large-scale bridges. Eng Struct 2005;27(12):1715-1725.

37. Chan TH, Yu L, Tam H, Ni Y, Liu S, Chung W, Cheng L. Fiber Bragg grating sensors for structural health monitoring of Tsing Ma bridge: Background and experimental observation. Eng Struct 2006;28(5):648-659.

38. Li S, Wu Z. Development of distributed long-gage fiber optic sensing system for structural health monitoring. Structural Health Monitoring 2007;6(2):133-143.

39. Li C, Thostenson ET, Chou T. Sensors and actuators based on carbon nanotubes and their composites: A review. Composites Sci Technol 2008;68(6):1227-1249.

40. Thostenson ET, Ren Z, Chou T. Advances in the science and technology of carbon nanotubes and their composites: a review. Composites Sci Technol 2001;61(13):1899-1912.

41. De Volder MF, Tawfick SH, Baughman RH, Hart AJ. Carbon nanotubes: present and future commercial applications. Science 2013;339(6119):535-539.

42. Thostenson ET, Li C, Chou T. Nanocomposites in context. Composites Sci Technol 2005;65(3–4):491-516.

43. Pandey G, Thostenson ET. Carbon nanotube-based multifunctional polymer nanocomposites. Polymer Reviews 2012;52(3):355-416.

44. Godara A, Mezzo L, Luizi F, Warrier A, Lomov SV, Van Vuure A, Gorbatikh L, Moldenaers P, Verpoest I. Influence of carbon nanotube reinforcement on the processing and the mechanical behaviour of carbon fiber/epoxy composites. Carbon 2009;47(12):2914-2923.

45. Qian H, Greenhalgh ES, Shaffer MS, Bismarck A. Carbon nanotube-based hierarchical composites: a review. Journal of Materials Chemistry 2010;20(23):4751-4762.

46. Qiu J, Zhang C, Wang B, Liang R. Carbon nanotube integrated multifunctional multiscale composites. Nanotechnology 2007;18(27):275708.

47. Gojny F, Wichmann M, Köpke U, Fiedler B, Schulte K. Carbon nanotube-reinforced epoxy-composites: enhanced stiffness and fracture toughness at low nanotube content. Composites Sci Technol 2004;64(15):2363-2371.

48. Thostenson ET, Chou T. Processing-structure-multi-functional property relationship in carbon nanotube/epoxy composites. Carbon 2006;44(14):3022-3029.

49. Yourdkhani M, Hubert P. A systematic study on dispersion stability of carbon nanotube-modified epoxy resins. Carbon 2015;81:251-259.

50. Li J, Ma PC, Chow WS, To CK, Tang BZ, Kim J. Correlations between percolation threshold, dispersion state, and aspect ratio of carbon nanotubes. Advanced Functional Materials 2007;17(16):3207-3215.

51. Gojny FH, Schulte K. Functionalisation effect on the thermo-mechanical behaviour of multi-wall carbon nanotube/epoxy-composites. Composites Sci Technol 2004;64(15):2303-2308.

52. Pegel S, Pötschke P, Petzold G, Alig I, Dudkin SM, Lellinger D. Dispersion, agglomeration, and network formation of multiwalled carbon nanotubes in polycarbonate melts. Polymer 2008;49(4):974-984.

53. Alig I, Pötschke P, Lellinger D, Skipa T, Pegel S, Kasaliwal GR, Villmow T. Establishment, morphology and properties of carbon nanotube networks in polymer melts. Polymer 2012;53(1):4-28.

54. Mohiuddin M, Hoa S. Temperature dependent electrical conductivity of CNT–PEEK composites. Composites Sci Technol 2011;72(1):21-27.

55. Grossiord N, Loos J, Regev O, Koning CE. Toolbox for dispersing carbon nanotubes into polymers to get conductive nanocomposites. Chemistry of materials 2006;18(5):1089-1099.

56. Thostenson E, Li W, Wang D, Ren Z, Chou T. Carbon nanotube/carbon fiber hybrid multiscale composites. J Appl Phys 2002;91(9):6034-6037.

57. An Q, Rider AN, Thostenson ET. Electrophoretic deposition of carbon nanotubes onto carbon-fiber fabric for production of carbon/epoxy composites with improved mechanical properties. Carbon 2012;50(11):4130-4143.

58. Rider AN, An Q, Brack N, Thostenson ET. Polymer nanocomposite–fiber model interphases: Influence of processing and interface chemistry on mechanical performance. Chem Eng J 2015;269:121-134.

59. Garcia EJ, Wardle BL, Hart AJ, Yamamoto N. Fabrication and multifunctional properties of a hybrid laminate with aligned carbon nanotubes grown in situ. Composites Sci Technol 2008;68(9):2034-2041.

60. Dai H, Gallo GJ, Schumacher T, Thostenson ET. A Novel Methodology for Spatial Damage Detection and Imaging Using a Distributed Carbon Nanotube-

Based Composite Sensor Combined with Electrical Impedance Tomography. J Nondestr Eval 2016;35(2):1-15.

61. Dai H, Thostenson ET, Schumacher T. Processing and Characterization of a Novel Distributed Strain Sensor Using Carbon Nanotube-Based Nonwoven Composites. Sensors 2015;15(7):17728-17747.

62. Dai H, Schumacher T, Thostenson E. Carbon nanotube-based sensing composites for structural health monitoring of civil infrastructure using non-woven fabrics. *Safety, Reliability, Risk and Life-Cycle Performance of Structures and Infrastructures*, Proceedings of the 11th International Conference on Structural Safety and Reliability (ICOSSAR), New York, NY, USA: CRC Press, 2013. p. 299.

63. Warrier A, Godara A, Rochez O, Mezzo L, Luizi F, Gorbatikh L, Lomov SV, VanVuure AW, Verpoest I. The effect of adding carbon nanotubes to glass/epoxy composites in the fibre sizing and/or the matrix. Composites Part A: Applied Science and Manufacturing 2010;41(4):532-538.

64. Rausch J, Mäder E. Health monitoring in continuous glass fibre reinforced thermoplastics: Manufacturing and application of interphase sensors based on carbon nanotubes. Composites Sci Technol 2010;70(11):1589-1596.

65. Rausch J, Zhuang R, Mäder E. Surfactant assisted dispersion of functionalized multi-walled carbon nanotubes in aqueous media. Composites Part A: Applied Science and Manufacturing 2010;41(9):1038-1046.

66. An Q, Rider AN, Thostenson ET. Hierarchical composite structures prepared by electrophoretic deposition of carbon nanotubes onto glass fibers. ACS applied materials & interfaces 2013;5(6):2022-2032.

67. Bekyarova E, Thostenson E, Yu A, Kim H, Gao J, Tang J, Hahn H, Chou T, Itkis M, Haddon R. Multiscale carbon nanotube-carbon fiber reinforcement for advanced epoxy composites. Langmuir 2007;23(7):3970-3974.

68. Zhang J, Zhuang R, Liu J, Mäder E, Heinrich G, Gao S. Functional interphases with multi-walled carbon nanotubes in glass fibre/epoxy composites. Carbon 2010;48(8):2273-2281.

69. Gnidakouong JRN, Roh HD, Kim J, Park Y. In situ process monitoring of hierarchical micro-/nano-composites using percolated carbon nanotube networks. Composites Part A: Applied Science and Manufacturing 2016;84:281-291.

70. Zhang H, Liu Y, Kuwata M, Bilotti E, Peijs T. Improved fracture toughness and integrated damage sensing capability by spray coated CNTs on carbon fibre prepreg. Composites Part A: Applied Science and Manufacturing 2015;70:102-110.

71. Zhang H, Bilotti E, Peijs T. The use of carbon nanotubes for damage sensing and structural health monitoring in laminated composites: a review. Nanocomposites 2015;1(4):167-184.

72. Fiedler B, Gojny FH, Wichmann MH, Bauhofer W, Schulte K. Can carbon nanotubes be used to sense damage in composites? Ann Chim Sci Mat 2004;29(6):81-94.

73. Thostenson ET, Chou T. Real-time in situ sensing of damage evolution in advanced fiber composites using carbon nanotube networks. Nanotechnology 2008;19(21):215713.

74. Thostenson ET, Chou T. Carbon nanotube networks: sensing of distributed strain and damage for life prediction and self healing. Adv Mater 2006;18(21):2837-2841.

75. Zahab A, Spina L, Poncharal P, Marliere C. Water-vapor effect on the electrical conductivity of a single-walled carbon nanotube mat. Physical Review B 2000;62(15):10000.

76. Aliev AE. Bolometric detector on the basis of single-wall carbon nanotube/polymer composite. Infrared Phys Technol 2008;51(6):541-545.

77. Simmons TJ, Vera-Reveles G, González G, Gutiérrez-Hernández JM, Linhardt RJ, Navarro-Contreras H, González FJ. Bolometric properties of semiconducting and metallic single-walled carbon nanotube composite films. ACS Photonics 2015;2(3):334-340.

78. Hasan T, Sun Z, Wang F, Bonaccorso F, Tan PH, Rozhin AG, Ferrari AC. Nanotube–polymer composites for ultrafast photonics. Adv Mater 2009;21(38-39):3874-3899.

79. Collins PG, Bradley K, Ishigami M, Zettl A. Extreme oxygen sensitivity of electronic properties of carbon nanotubes. Science 2000;287(5459):1801-1804.

80. Valentini L, Mercuri F, Armentano I, Cantalini C, Picozzi S, Lozzi L, Santucci S, Sgamellotti A, Kenny J. Role of defects on the gas sensing properties of carbon

nanotubes thin films: experiment and theory. Chemical Physics Letters 2004;387(4):356-361.

81. Hu N, Fukunaga H, Atobe S, Liu Y, Li J. Piezoresistive strain sensors made from carbon nanotubes based polymer nanocomposites. Sensors 2011;11(11):10691-10723.

82. Hu N, Karube Y, Yan C, Masuda Z, Fukunaga H. Tunneling effect in a polymer/carbon nanotube nanocomposite strain sensor. Acta Materialia 2008;56(13):2929-2936.

83. Yin G, Hu N, Karube Y, Liu Y, Li Y, Fukunaga H. A carbon nanotube/polymer strain sensor with linear and anti-symmetric piezoresistivity. J Composite Mater 2011:0021998310393296.

84. Dharap P, Li Z, Nagarajaiah S, Barrera EV. Flexural strain sensing using carbon nanotube film. Sens Rev 2004;24(3):271-273.

85. Dharap P, Li Z, Nagarajaiah S, Barrera EV. Nanotube film based on single-wall carbon nanotubes for strain sensing. Nanotechnology 2004;15(3):379-382.

86. Hu N, Karube Y, Arai M, Watanabe T, Yan C, Li Y, Liu Y, Fukunaga H. Investigation on sensitivity of a polymer/carbon nanotube composite strain sensor. Carbon 2010;48(3):680-687.

87. Barber A, Zhao Q, Wagner H, Baillie C. Characterization of E-glass–polypropylene interfaces using carbon nanotubes as strain sensors. Composites Sci Technol 2004;64(13):1915-1919.

88. Li Z, Dharap P, Nagarajaiah S, Barrera EV, Kim JD. Carbon Nanotube Film Sensors. Adv Mater 2004;16(7):640-643.

89. Liu J, Rinzler AG, Dai H, Hafner JH, Bradley RK, Boul PJ, Lu A, Iverson T, Shelimov K, Huffman CB, Rodriguez-Macias F, Shon YS, Lee TR, Colbert DT, Smalley RE. Fullerene pipes. Science 1998;280(5367):1253-1256.

90. Kang I, Schulz MJ, Kim JH, Shanov V, Shi D. A carbon nanotube strain sensor for structural health monitoring. Smart Mater Struct 2006;15(3):737.

91. Loh KJ, Lynch JP, Shim B, Kotov N. Tailoring piezoresistive sensitivity of multilayer carbon nanotube composite strain sensors. J Intell Mater Syst Struct 2008;19(7):747-764.

92. Hu N, Karube Y, Arai M, Watanabe T, Yan C, Li Y, Liu Y, Fukunaga H. Investigation on sensitivity of a polymer/carbon nanotube composite strain sensor. Carbon 2010;48(3):680-687.

93. Alamusi, Liu Y, Hu N. Numerical simulations on piezoresistivity of CNT/polymer based nanocomposites. Computers Materials & Continua 2010;20:101-117.

94. Li C, Thostenson ET, Chou T. Dominant role of tunneling resistance in the electrical conductivity of carbon nanotube–based composites. Appl Phys Lett 2007;91(22):223114.

95. Gau C, Kuo C, Ko H. Electron tunneling in carbon nanotube composites. Nanotechnology 2009;20(39):395705.

96. Zhang W, Suhr J, Koratkar N. Carbon nanotube/polycarbonate composites as multifunctional strain sensors. Journal of nanoscience and nanotechnology 2006;6(4):960-964.

97. Chang F, Wang R, Yang H, Lin Y, Chen T, Huang S. Flexible strain sensors fabricated with carbon nano-tube and carbon nano-fiber composite thin films. Thin Solid Films 2010;518(24):7343-7347.

98. Paleo A, Van Hattum F, Pereira J, Rocha JG, Silva J, Sencadas V, Lanceros-Méndez S. The piezoresistive effect in polypropylene—carbon nanofibre composites obtained by shear extrusion. Smart Mater Struct 2010;19(6):065013.

99. Oliva-Avilés A, Avilés F, Sosa V. Electrical and piezoresistive properties of multi-walled carbon nanotube/polymer composite films aligned by an electric field. Carbon 2011;49(9):2989-2997.

100. Gao L, Thostenson ET, Zhang Z, Chou T. Sensing of Damage Mechanisms in Fiber-Reinforced Composites under Cyclic Loading using Carbon Nanotubes. Advanced Functional Materials 2009;19(1):123-130.

101. Gao L, Thostenson ET, Zhang Z, Byun J, Chou T. Damage monitoring in fiber-reinforced composites under fatigue loading using carbon nanotube networks. Philosophical Magazine 2010;90(31-32):4085-4099.

102. Thostenson ET, Chou T. Carbon nanotube-based health monitoring of mechanically fastened composite joints. Composites Sci Technol 2008;68(12):2557-2561.

103. Lim AS, Melrose ZR, Thostenson ET, Chou T. Damage sensing of adhesively-bonded hybrid composite/steel joints using carbon nanotubes. Composites Sci Technol 2011;71(9):1183-1189.

104. Park M, Kim H, Youngblood J,P. Strain-dependent electrical resistance of multi-walled carbon nanotube/polymer composite films. Nanotechnology 2008;19(5):055705.

105. Wichmann MHG, Buschhorn ST, Böger L, Adelung R, Schulte K. Direction sensitive bending sensors based on multi-wall carbon nanotube/epoxy nanocomposites. Nanotechnology 2008;19(47):475503.

106. Cai L, Song L, Luan P, Zhang Q, Zhang N, Gao Q, Zhao D, Zhang X, Tu M, Yang F. Super-stretchable, Transparent Carbon Nanotube-Based Capacitive Strain Sensors for Human Motion Detection. Scientific Reports 2013;3.

107. Yamada T, Hayamizu Y, Yamamoto Y, Yomogida Y, Izadi-Najafabadi A, Futaba DN, Hata K. A stretchable carbon nanotube strain sensor for human-motion detection. Nat Nano 2011;6(5):296-301.

108. Böger L, Wichmann MH, Meyer LO, Schulte K. Load and health monitoring in glass fibre reinforced composites with an electrically conductive nanocomposite epoxy matrix. Composites Sci Technol 2008;68(7):1886-1894.

109. Thostenson ET, Chou T. Carbon nanotube-based health monitoring of mechanically fastened composite joints. Composites Sci Technol 2008;68(12):2557-2561.

110. Friedrich SM, Wu AS, Thostenson ET, Chou T. Damage mode characterization of mechanically fastened composite joints using carbon nanotube networks. Composites Part A: Applied Science and Manufacturing 2011;42(12):2003-2009.

111. Li C, Chou T. Modeling of damage sensing in fiber composites using carbon nanotube networks. Composites Sci Technol 2008;68(15):3373-3379.

112. Nofar M, Hoa S, Pugh M. Failure detection and monitoring in polymer matrix composites subjected to static and dynamic loads using carbon nanotube networks. Composites Sci Technol 2009;69(10):1599-1606.

113. Naghashpour A, Van Hoa S. A technique for real-time detecting, locating, and quantifying damage in large polymer composite structures made of carbon fibers and carbon nanotube networks. Structural Health Monitoring 2015;14(1):35-45.

114. Saafi M. Wireless and embedded carbon nanotube networks for damage detection in concrete structures. Nanotechnology 2009;20(39):395502.

115. Ubertini F, Laflamme S, Ceylan H, Materazzi AL, Cerni G, Saleem H, D'Alessandro A, Corradini A. Novel nanocomposite technologies for dynamic monitoring of structures: a comparison between cement-based embeddable and soft elastomeric surface sensors. Smart Mater Struct 2014;23(4):045023.

Chapter 2

PROCESSING AND CHARACTERIZATION OF CARBON NANOTUBE-BASED NONWOVEN COMPOSITE SENSORS FOR STRAIN MONITORING

Significant portions of this chapter are already published in a peer-reviewed journal:

- *Ref.[45]: "Processing and characterization of a novel distributed strain sensor using carbon nanotube-based nonwoven composites". Sensors 15(7), 17728-17747 (2015).*

2.1 Introduction

This chapter introduces a simple two-step method to fabricate CNT-based nonwoven composite strain sensors where CNTs are deposited from an aqueous dispersion onto a selected nonwoven carrier fabric, followed by infusing an epoxy resin into the CNT-modified nonwoven fabric via the vacuum-assisted-resin transfer-molding (VARTM) process. This manufacturing approach can be readily scaled up for large-scale applications. In addition, the sensor utilizes a relatively small concentration of CNTs of approximately 1.0% by weight, making it cost-effective. The as-fabricated nanocomposite sensor is mechanically robust, strain sensitive, and customizable in shape, which is especially important for SHM of large-scale structural members.

Nonwoven fabrics are plane sheets composed of randomly oriented short chopped fibers as schematically illustrated in Figure 2.1a. After depositing CNTs onto the preselected fabric, each individual short fiber becomes conductive and the whole nonwoven sheet turns into a network of arbitrarily connected resistors. As a result, simply implementing end electrodes and injecting an electric current crossing the CNT-modified fabric, a web of randomly oriented conductive pathways can develop

following a random fiber architecture as illustrated in Figure 2.1b. The bulk electrical conductivity is governed by the local contacts between individual fibers. In other words, due to the nonwoven configuration, an in-plane isotropic conductivity can be established in this CNT-based nonwoven composite. The epoxy resin is then infused into the CNT-modified nonwoven fabric to hold the CNT network in place, to impart mechanical strength to the nonwoven substrate, and to protect the CNT-coating against environmental weathering.

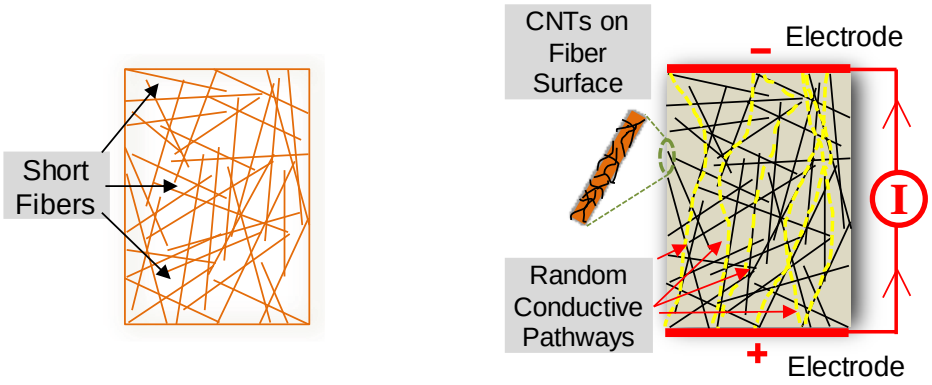

(a) (b)

Figure 2.1: Schematic illustrations of (a) nonwoven fabric and (b) random electrical pathways (idealized) formed in the CNT-modified nonwoven fabric.

This chapter first describes the fabrication process of CNT-based nonwoven composite sensors. Next, the strain sensing performance of the sensors produced with six types of nonwoven substrates was studied preliminarily for down-selecting the ideal substrates and processing conditions that yield a repeatable sensing behavior. Subsequently, a series of sensors with the optimal parameters were manufactured and

their microstructure and mechanical and electrical properties were experimentally characterized in detail. Notably, the self-sensing performance and strain sensitivity of the as-produced sensing composites were studied. The distributed sensing capability of the proposed CNT composite sensor for *ex situ* strain monitoring was finally investigated by bonding the sensor onto metal substrates of aluminum and steel, and subsequently testing it under quasi-static cyclic tensile and compressive loads.

2.2 Two-Step Manufacturing

In this study, CNT-based nonwoven composite sensors were fabricated following a simple two-step, named here as 'wetting-and-drying', manufacturing process. The 'wetting' procedure involves the formation of the nanotube network onto a carrier fabric through a solution casting process. The 'drying' process encompasses the infusion of epoxy resin into the CNT-modified nonwoven fabric via VARTM technique and resin cure. This approach enables application flexibility, since the fabric can be conformed to a variety of substrate configurations. By depositing nanotubes onto the porous nonwoven fabric, a macroscopic nanotube sensor can be produced with a relatively small concentration of CNTs. In addition, due to the high void content of the nonwoven fabric, a sufficient resin intake can be guaranteed as infusing, which finally results in the epoxy matrix dominated mechanical robustness of the CNT-based sensing composite after curing.

2.2.1 The 'Wetting' Process

The used CNT dispersion for solution casting is a commercially available fiber sizing agent consisting of nanotubes that are dispersed in an aqueous solution with some dispersant and film formers (SIZICYL^{TM} XC R2G, Nanocyl). The solid content

in the liquid sizing formulation is about 6%. The overall CNT concentration in the sizing agent was found to be approximately 1.5% by weight (wt.%) based on the thermogravimetric analysis of the solids after drying. Prior to coating the fabric, the sizing agent was diluted with ultra-pure distilled water at certain mass ratios (such as 1:1 and 1:2, i.e., sizing:distilled water by mass) to improve the workability of the sizing agent and to reduce the cost. For instance, based on the calculated concentration of nanotubes in the sizing and the mass change of the fabric after coating, it is estimated that the total concentration of nanotubes in the fabricated sensors are 1.0 wt.% and 0.75 wt.% for sizing dilution ratios of 1:1 and 1:2, respectively. To ensure uniformity in the CNT dispersions, the diluted sizing was first mixed using a centrifugal mixer (THINKY® ARM-310) at 2000 rpm for 120 s and then sonicated for 15 min in an ultrasonic bath (Branson® 1510). Figure 2.2a shows a small portion of the as-prepared CNT dispersion after standing for 5 days in room temperature, suggesting a stable and uniform dispersion without observing segregation and sediments. Finally, the selected fabric was impregnated for 20 min into the as-prepared CNT dispersion. Figure 2.2b shows a sample fabric saturated with the nanotube dispersion.

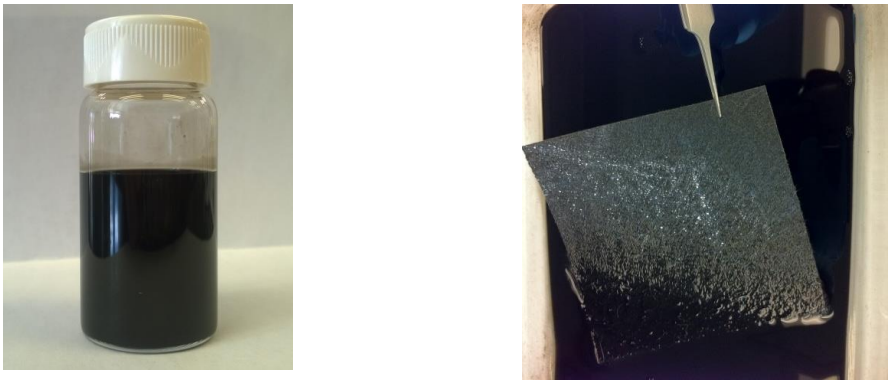

(a) (b)

Figure 2.2: Photographs showing (a) 30 mL sample of the as-prepared CNT dispersion after standing for 5 days in room temperature and (b) a sample of saturated nonwoven fabric with CNTs following bath impregnation (from Ref.[45]).

2.2.2 The 'Drying' Process

After drying the saturated fabric at 130 °C, the CNTs deposited onto the fabric form an electrically-conductive network on the fiber surface. An epoxy resin was infused into the fabric using VARTM to form a free-standing sensing composite where the nanotube network is protected by the polymer matrix. The epoxy resin (EPON® 862, Momentive Specialty Chemicals) was first mixed with an aromatic diamine curing agent (EPIKURE W, Momentive Specialty Chemicals) and degassed at 60°C for 20 min in a vacuum oven. The resin was then infused into the fabric using the VARTM setup as illustrated in Figure 2.3a. A snapshot of an operating VARTM setup is also shown in Figure 2.3b. After completing the resin infusion, the epoxy was cured in the oven at 130°C for 6 hours. Figure 2.3c displays an as-produced sensing composite layer. The final lamina thickness is approximately 470 μm. Figure 2.3c also demonstrates the flexibility of the composite sensor and its ability to conform to the

shape of structural members. An advantage of this manufacturing process is that it is industrially scalable. As shown in Figure 2.3d, a 1 × 4 ft composite sensing patch was fabricated permitting large-scale applications.

Furthermore, CNT composite sensors can be produced using a room temperature curing agent (EPIKURE 3223, Momentive Specialty Chemicals), which allows the sensing fabric to first conform to the surface of the structure and then integrally adhered to the structure on site while curing. In general, the as-fabricated sensing composites have very low fiber volume fraction, approximately 8%, owing to the high porosity (about 90%) of the nonwoven fabric.

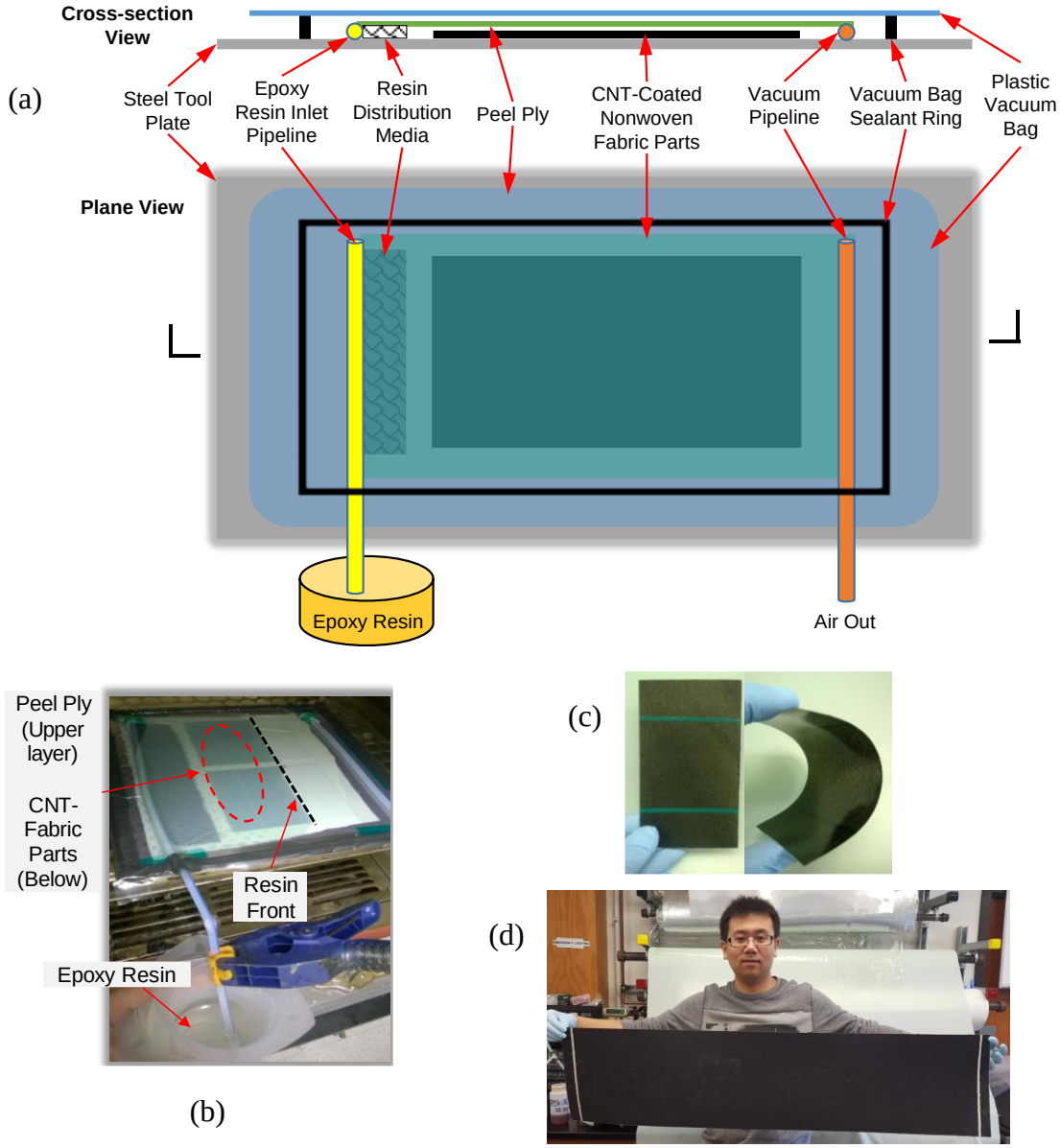

Figure 2.3: (a) Schematic diagram of the VARTM process utilized to infuse epoxy resin in the nonwoven fabric to form the CNT composite sensors (from Ref.[45]), (b) photograph showing an operating VARTM setup during manufacturing, and photographs showing (c) a 3 × 5 in free-standing CNT sensing composite layer after curing the epoxy, demonstrating its flexibility (from Ref.[45]) and (d) 1 × 4 ft CNT sensing composite patch with applied electrodes fabricated for large applications, indicating the excellent scalability of the proposed sensing approach.

2.3 Experimental Characterization of Self-Sensing Composites

The microstructure and mechanical and electrical properties of the as-manufactured CNT sensors were experimentally characterized at the Center for Composite Materials at University of Delaware. Prior to the systematic characterization, a preliminary study for screening the superior CNT carrier was conducted among six kinds of nonwoven fabrics. The preliminary results (showed in Section 2.3.2) suggested that the sensor with the aramid nonwoven fabric demonstrated a highly repeatable and stable strain sensing response. Consequently, CNT aramid nonwoven composite sensors were utilized for the comprehensive investigation presented in this chapter.

2.3.1 Experimental Details

2.3.1.1 Mechanical and Electrical Measurements

To fully characterize the self-sensing response of the CNT-based nonwoven composites, a series of simultaneous mechanical and electrical measurements were conducted under tensile loading conditions. Strain gages (350 Ω, 3.2 mm long gage length, Micro-Measurements®, Vishay Intertechnology Inc.) were used to measure strain on the specimens. The mechanical loading protocols for the various specimens are discussed in the following sections.

Prior to conducting electrical measurements, electrodes were applied using conductive silver paint (SPI Flash-Dry™, Structure Probe Inc.). Lead wires were anchored to the electrodes using conductive epoxy resin (EPOXIES® 40-3900, Epoxies, Etc) which was cured at 90 °C for 30 min. Electrical measurements of the specimens were conducted and synchronized with the applied loading protocols in real-time. A Keithley 6430 voltage-current meter was used to measure the electrical

resistance of the specimen by sourcing a constant voltage of 10 V and measuring the resulting current to calculate the electrical resistance (i.e., the two-point method). All measurements, including applied load, strain, and electrical resistance, were controlled and collected using a customized LabVIEW program (LabVIEW 8.5, National Instruments Corporation) at a sampling frequency of 10 Hz.

2.3.1.2 Preliminary Study

Several different areal weights and types of fibers were examined as candidate substrate materials (Technical Fiber Products). For the initial tests, the nonwoven fabrics studied and their areal weights include aramid (26 g/m^2), e-glass+carbon (20 g/m^2), polyester (12 g/m^2), copper-nickel coated carbon (34 g/m^2), carbon with polyvinyl alcohol binder (20 g/m^2), and carbon with styrene soluble binder (17 g/m^2). All short fibers have a length of 12 mm as reported by the manufacturer. Figure 2.4 shows optical micrographs of the as-received fabrics and their porosity.

Samples of these nonwoven fabrics were first trimmed to 13 × 80 mm size patches and processed with the 0.75 wt.% CNT dispersion as per Section 2.2.1. Next, the composite sensors were fabricated following the manufacturing process detailed in Section 2.2.2. After anchoring electrodes, the sensors were adhered on six aluminum tensile bars (178 × 25 × 1.5 mm, 6061-T6) using EPON 862 epoxy resin. Figure 2.5a illustrates the specimen configuration and Figure 2.5b shows a photograph of the prepared specimens. The baseline electrical resistances of these CNT-based nonwoven composite sensors were measured as 88.7 Ω, 6943.6 Ω, 1864.5 Ω, 7.2 Ω, 21.7 Ω, and 44.9 Ω, respectively.

All six specimens were subjected to a quasi-static load-unload protocol using an Instron 5567 universal testing machine. The loading protocol was displacement-

controlled and a displacement rate of 1.27 mm/min was maintained during the entire testing history for all six specimens. To introduce elastic deformation to the aluminum coupons, the loading protocol consisted of four incremental tensile load steps corresponding to 1.5 kN, 3.0 kN, 5.0 kN, and 7.5 kN as the designated peak amplitudes. Every loading step included four loading-unloading cycles with the same peak amplitude to ensure repeatability. The specimens were also held under constant load for 30 seconds in the third cycle of each loading step to examine any transient effects such as creep.

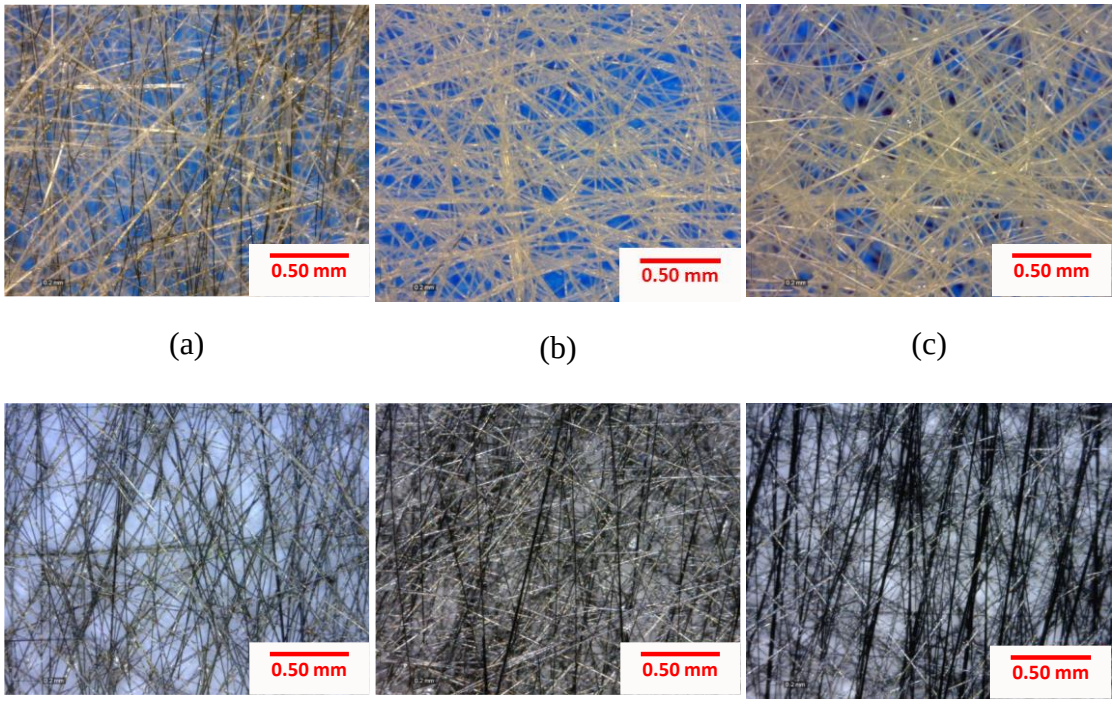

Figure 2.4: Optical micrographs showing the nonwoven structures of the different fabrics used in this study: (a) e-glass and carbon, (b) polyester, (c) aramid, (d) nickel-copper coated carbon, (e) carbon with poly (vinyl alcohol) binder, and (f) carbon with styrene soluble binder.

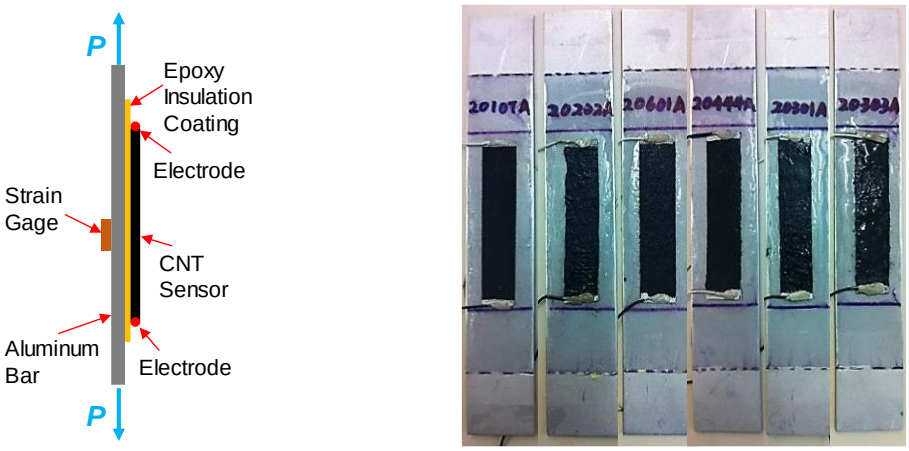

Figure 2.5: (a) Schematic diagram (cross-sectional view) of the test specimen for preliminary study and (b) photograph of the prepared specimens with CNT-based sensors consisting of six different nonwoven substrates.

2.3.1.3 Microscopic Study

To study the structure of the electrically-conductive nanotube network, scanning electron microscopy (SEM) was utilized to image the morphology of the CNT coating on the nonwoven fabric, as well as image fracture surfaces of the as-produced composite sensors. This experimental investigation was performed at the Keck Center for Advanced Microscopy and Microanalysis, at the University of Delaware. The specimens were imaged with an AURIGA™ 60 Crossbeam™ FIB-SEM with a 5-kV acceleration voltage. To minimize sample charging, all samples were coated with a thin conductive Pt/Au layer (~5 nm) in a vacuum sputter coater (Denton Desk IV, Denton Vacuum, LLC) prior to imaging. In particular, the CNT nonwoven composite specimens were first immersed in liquid nitrogen for approximately 5 min and then fractured in order to obtain a good surface for imaging.

2.3.1.4 Self-Sensing Characterization

First, to learn the electrical percolating behavior of the CNT nonwoven composites, eleven individual CNT-aramid nonwoven composite layers (102 × 127 mm) with CNT concentrations of 1.0 to 0.05 wt% were fabricated (that is, varying the sizing dilution ratios from 1:1 to 1:50 as dip coating nanotubes onto the aramid nonwoven fabric per Section 2.2.1). Each layer was cut into multiple 13 × 127 mm coupons to collect the in-plane baseline resistance measurements.

Second, the mechanical and resistive response of the proposed composite sensors were characterized in tension to determine their mechanical properties, the fundamental electromechanical response, and to validate the self-sensing capability of the sensors. Three sets of 80 × 127 mm composite layers were prepared. One composite was made using only the aramid nonwoven fabric and tested as a reference; the other two composites were composed of the CNT-coated aramid nonwoven fabrics with CNT concentrations of 1.0 wt.% and 0.75 wt.% per Section 2.2.1. All three composite layers were cut into 20 mm wide tensile specimens. For each coupon, a pair of 25.4 mm long nonconductive woven glass fiber/epoxy composite (G-10/FR4, Professional Plastic Inc.) end tabs were bonded at each end using high strength epoxy paste adhesive (Hysol® EA9309, Henkel). The electrodes were located at 3 mm from each edge of the end tab resulting in a gage length of 64 mm for all electrical measurements. Figure 2.6a illustrates the geometry of the self-sensing CNT composite specimen and an actual specimen is shown in Figure 2.6b.

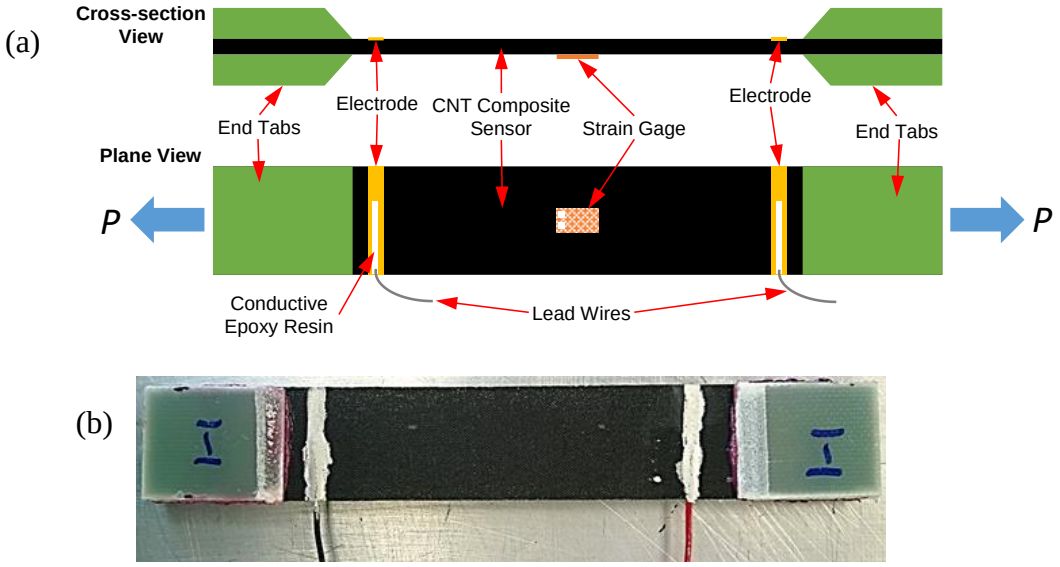

Figure 2.6: (a) Schematic diagram of the *in situ* CNT composite sensing specimens subjected to tension (from Ref.[45]) and (b) photograph of an actual specimen tested.

The mechanical characterization was then conducted while simultaneously measuring electrical property changes. All specimens were subjected to monotonic tensile loading and tested to failure at a constant displacement rate of 1.3 mm/min using a screw-driven universal testing machine (Instron 5567). An acoustic emission (AE) system (Physical Acoustic Corporation) was used to monitor damage initiation and propagation to validate the self-sensing results obtained using *in situ* resistance measurements. One AE sensor (R6α, Physical Acoustic Corporation) with 35–100 kHz operating frequency was mounted on the center of the specimens. A threshold of 35 dB was selected to eliminate AE events due to ambient noise not related to the formation of damage in the specimen. Figures 2.7a and b show the experimental setup for the mechanical characterization of the aramid nonwoven composite (the reference)

and the self-sensing characterization of the CNT-based nonwoven composite, respectively.

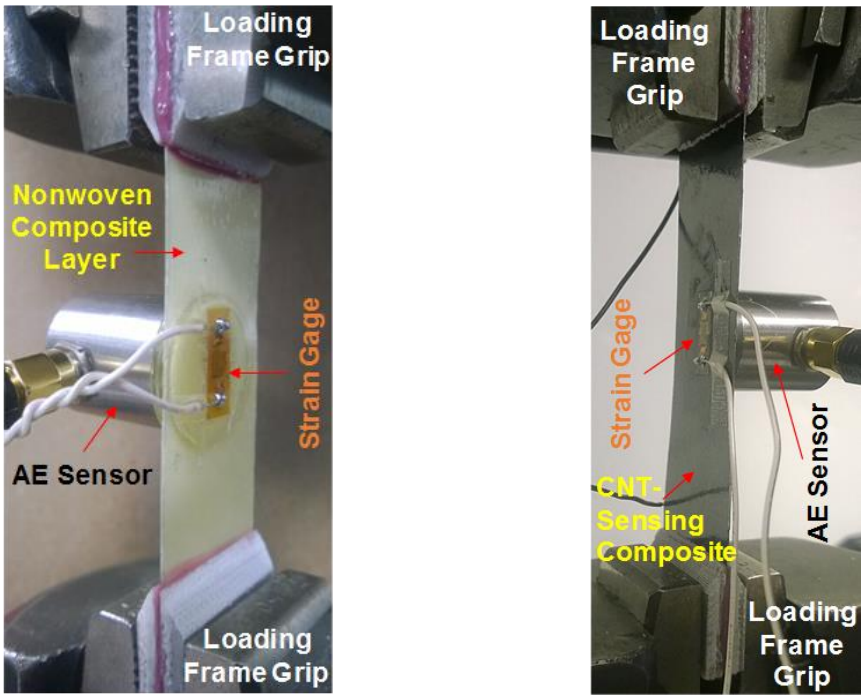

(a) (b)

Figure 2.7: Experimental setup for (a) the mechanical characterization of the aramid nonwoven composite (the reference specimen, no CNT) and (b) the self-sensing characterization of the CNT-based nonwoven composite.

2.3.2 Preliminary Strain Sensing Responses of the Composite Sensors with Different Nonwoven Substrates

A sensitive, repeatable and stable sensor is key to enable a successful strain sensing application for SHM. A group of six composite sensors with different nonwoven fabric substrates were tested preliminarily for strain monitoring of aluminum bars under a static tension load. Figure 2.8 summarizes the transient

responses of all tested specimens including the applied strain of the tension coupon and the simultaneously measured resistive responses of the CNT sensors. It can be observed from the bottom graph (= strain) that the aluminum member undergoes elastic deformation during the entire loading history without exhibiting any permanent strain change. The real-time electrical resistance responses of the six composite sensors are shown in the top six graphs as the normalized resistance change which is defined using Equation 2.1,

$$\textit{Normalized Electrical Resistance Change}\ (\%) = \frac{\Delta R}{R_0} = \frac{R - R_0}{R_0} \times 100\% \qquad (2.1)$$

where R_0 is the baseline resistance of the CNT composite measured before mechanical testing, R is the measured electrical resistance during testing, and ΔR is the electrical resistance change resulting from testing. In this preliminary study, R_0 for all six sensors is listed in Section 2.3.1.2.

It can be seen that as the attached sensor deforms with the aluminum member there is a clear and instant change in the bulk electrical resistive response for each specimen. The reference lines are shown at zero load (= solid line) and peak load (= dashed line). Overall, all six composite sensors showed a certain degree of sensitivity to applied strain. However, the composite sensors with the nonwoven substrates using a carbon with styrene soluble binder and copper-nickel coated carbon show significant baseline drifts over time. In addition, these two specimens show poor stability in the load holding periods and a corresponding mismatch at the peak loading amplitudes. Meanwhile, the sensor with a polyester substrate displays slight shifts at zero load. It is clear that three sensors with the nonwoven carriers including e-glass+carbon, carbon with polyvinyl alcohol binder, and aramid demonstrate the most robust real-time electrical responses from all.

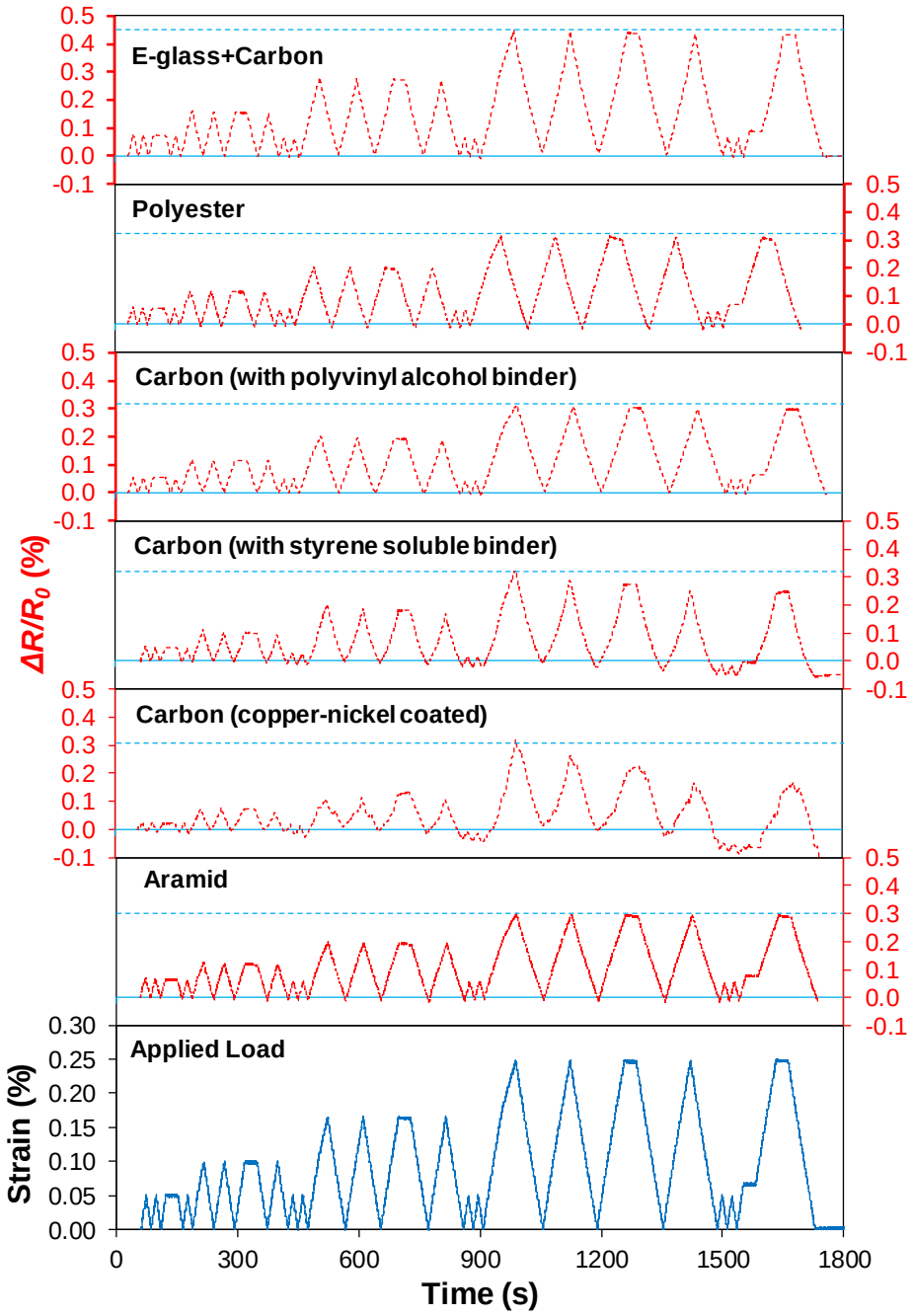

Figure 2.8: Preliminary results for monitoring tensile strains using CNT composite sensors fabricated with different nonwoven substrates.

As introduced in Section 1.3, the established conductive nanotube-based networks in CNT composites are inherently piezoresistive, which enables the strain sensitivity of CNT composites. The magnitude of the piezoresistive response is quantified by the gage factor (*G.F.*, also referred to as piezoresistivity) as defined in Equation 2.2,

$$G.F. = \frac{\Delta R}{R_0} / \Delta\varepsilon \tag{2.2}$$

where $\frac{\Delta R}{R_0}$ is the normalized resistance change (in %) calculated by Equation 2.1 and $\Delta\varepsilon$ is the strain change displayed by the CNT composite due to the applied loads.

The piezoresistive properties of the CNT composite sensors (with e-glass+carbon, carbon with polyvinyl alcohol binder, and aramid nonwoven substrates) during the uniaxial tensile tests are represented by the resistance change-strain responses shown in Figure 2.9. Linear least-squares curve fitting was applied to all experimental data shown in Figure 2.9 and expressed as Equation 2.3,

$$y = a\,x + b \tag{2.3}$$

where a and b are the fitting parameters; x and y are the strain and resistive data, respectively.

It was found that all three sensors demonstrate highly linear piezoresistive behavior with a linear correlation coefficient above 99% (R^2). The slope of the linear regression curve, a, that is, the normalized electrical resistance change due to the applied unit strain, can be interpreted as an estimate of the *G.F.* of the sensor. The y-intercept, b illustrates the sensor's electrical stability (electrical baseline resistance drift) during the entire loading sequence. By comparison, it is notable that the sensor with the aramid nonwoven substrate demonstrates the most linear strain sensitivity with the lowest baseline resistance drift and highest repeatability. Although the CNT-

aramid sensor shows lower sensitivity (the slope is lower) as compared to the CNT e-glass+carbon sensor, the higher linearity and repeatability of the CNT-aramid sensor made it the most suitable for strain monitoring. A comprehensive characterization of the CNT-aramid sensor is presented in the later sections.

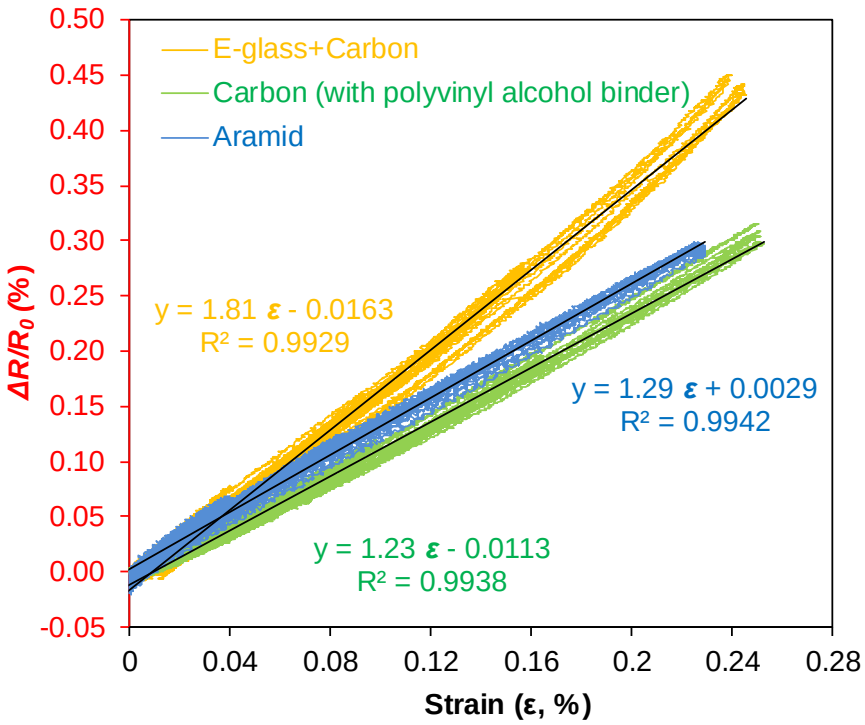

Figure 2.9: Piezoresistive responses to tensile strains of CNT composite sensors fabricated with different nonwoven substrates. Also shown are the linear curve fits, including fitted parameters.

2.3.3 Microstructure

The proposed CNT-based nonwoven composite sensors consist of a multiscale material system in which CNTs, nonwoven fibers, and the finished composites are in nanometer-, micrometer- and centimeter-to-meter-scale, respectively. A uniform

dispersion state of nanotubes is key to form a well-connected CNT sensing network in the composites. To better understand the bulk mechanical and electrical properties, knowledge about the microstructure of the as-fabricated CNT sensing composites are needed. The morphologies of the raw nonwoven fabric, CNT sizing agent, and the multiscale composite were herein qualitatively assessed under a SEM.

2.3.3.1 Constituent Materials

Figure 2.10 shows the randomly distributed fiber architecture of a nonwoven aramid fabric (26 g/m^2) in its as-received state. It can be seen that the existing binder has a point bonding structure due to the low weight content of binder agent used (12.5 wt.% as reported by the manufacturer), which creates a thin and slightly rough coating on the fiber surface. In addition, the binder accumulates in the fiber intersection points from the exterior to the interior of the fabric, forming the bonding sails [1] in the 100 to 200 μm range (highlighted in circle), which further results in the increase of the fabric surface area. As the high magnification SEM image shows in Figure 2.10b, the diameter of an aramid fiber is around 12 microns. Meanwhile, local fiber debonding and binder cracking are observed at a focused bonding point, which is most likely due to the handling of the sample. Based on the clean cracking surface of the binder, it can be deduced that the applied binder layer, also referred to as crosslinked polyester (as reported by the manufacturer), is much more brittle than the aramid fiber. Also, the smooth debonding surface indicates a relatively weak adhesion between fiber and binder, which however, is not stringently required for a nonstructural fabric.

(a)

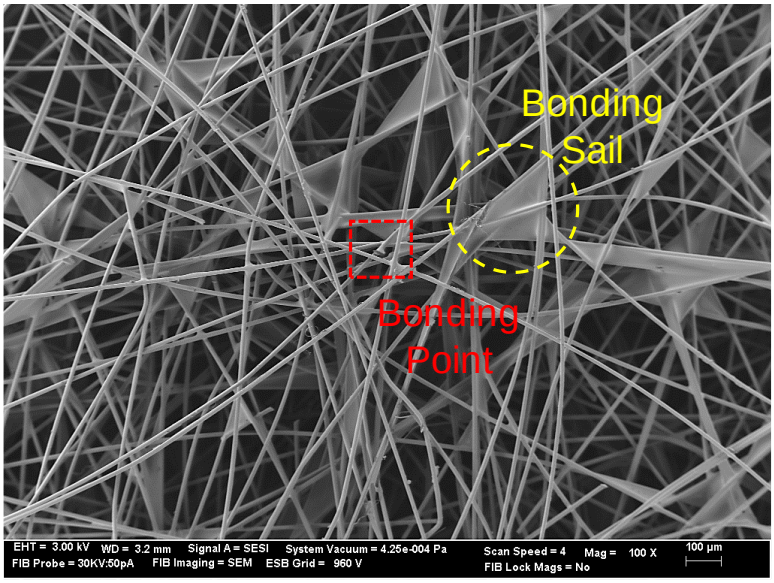

(b)

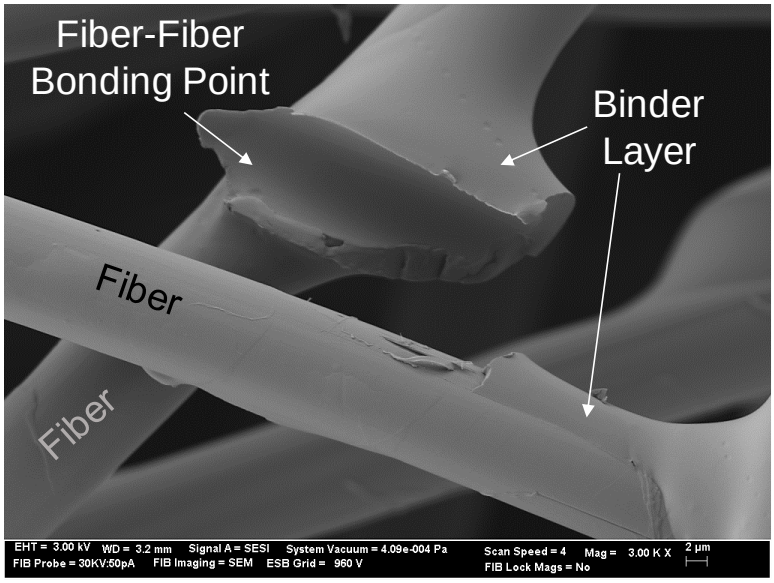

Figure 2.10: SEM micrographs showing (a) nonwoven aramid fabric in its as-received state and (b) individual aramid fiber with binder layer, magnified view of the dashed area in (a).

A few drops of raw aqueous CNT sizing agent were first placed onto a thin stainless-steel shim and then dried at 130 °C in order to acquire a solid CNT sizing film for SEM imaging. The morphology of the CNT sizing agent in its solid state is presented in Figure 2.11. The low magnification image shows a highly concentrated film of CNTs with random agglomerates of 1-2 microns in size, indicating a homogeneous in-plane distribution of CNTs. From the high magnification SEM image shown in Figure 2.11b, individual curvy CNTs in their free-standing state can be clearly observed. Interestingly, there seems to be a multi-layered structure in few hundreds nanometer-scale stacked by the interconnected CNT agglomerates in the through thickness direction of the film, which is presumably due to the fast volatilization of solvent content at 130 °C drying temperature. These loose and relatively porous CNT networks can create extra volume between CNTs and CNT agglomerates, rendering more surface areas for potential interactions between CNTs and their surrounding media such as the fiber and resin in a composite. As a result, this special morphological state reveals the potential enhancement to the stability of the CNT networks as long as the CNT sizing agent is integrated in the nonwoven composites.

(a)

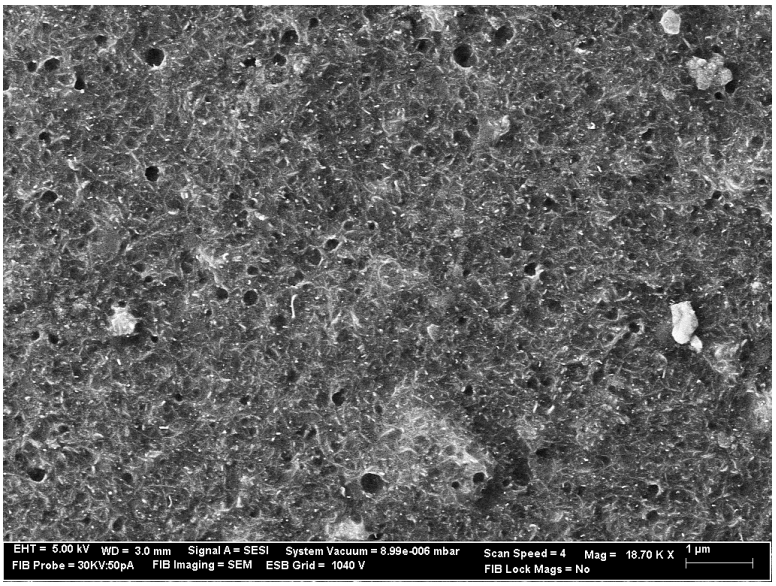

(b)

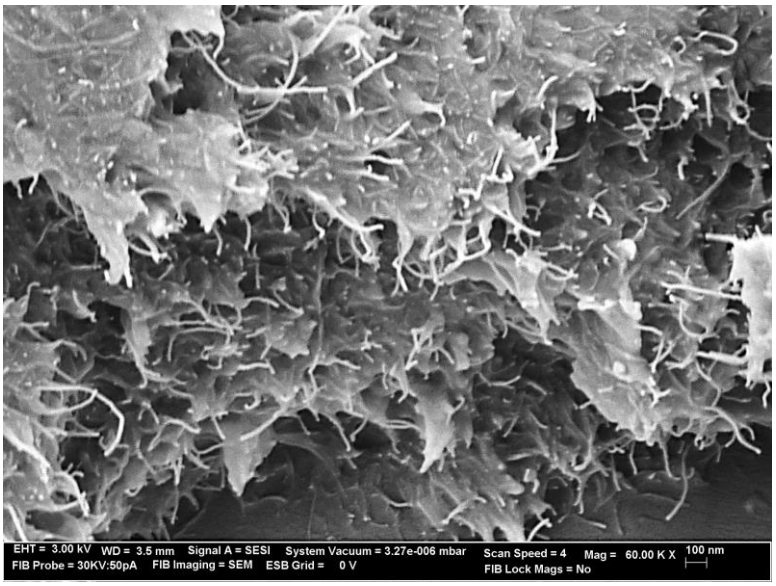

Figure 2.11: SEM images showing the morphology of CNT sizing film at (a) low magnification and (b) high magnification.

2.3.3.2 CNT-Modified Nonwoven Fabric

Figure 2.12 shows the aramid nonwoven fabric after the deposition of CNTs. There appears to be a film-like enclosure of the fiber network that CNTs are covering all fiber intersection points and bonding sails of raw fabric as shown in Figure 2.10a, indicating the good wettability between the nanotube sizing and the fibers. As the high magnification SEM image shows in Figure 2.12b, a uniform CNT coating layer has accumulated up to few microns in thickness. Additionally, the polymer solids in the sizing act to further bind together the fibers and form the electrically conductive network spanning the individual fibers. Locally there is some stripping of the nanotube coating, which is likely a consequence of handling the fabric during sample preparation for SEM imaging.

Figure 2.13a shows the nanotube coating that formed at a typical location of the fiber bonding sail. There is cracking observed in the fiber bonding point, also likely due to handling the fabric after drying, highlighting the need to further protect the fabric layer through infusion of an epoxy matrix. Figure 2.13b shows a high-magnification SEM image of the formation of a layer with a large concentration of CNTs. CNTs and CNT agglomerates are clearly visible. The large amount of nanotubes deposited on fiber surfaces effectively forms an electrically-conductive network over the entire fabric, imparting electrical conductivity onto the nonwoven fibers.

(a)

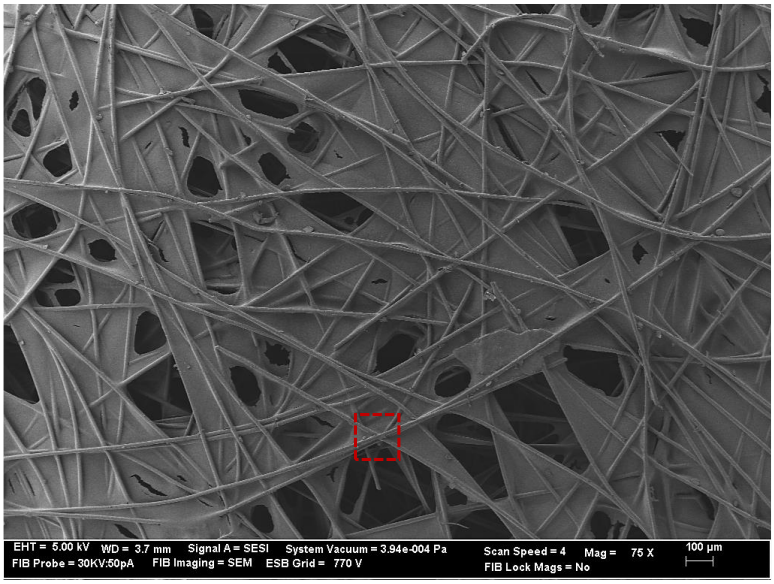

(b)

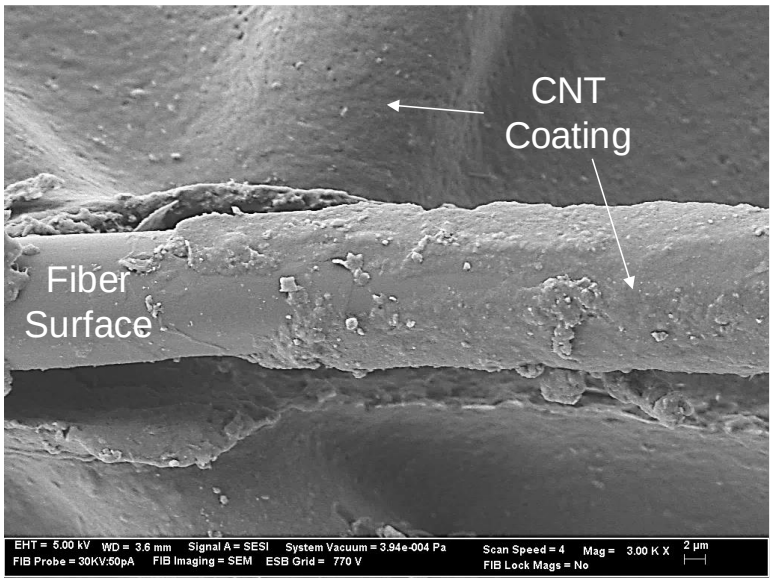

Figure 2.12: SEM images showing (a) aramid nonwoven fabric with CNTs deposited onto the fabric surface and (b) uniform CNT coating on fiber surface, the magnified view of the dashed area in (a) (from Ref.[45]).

(a)

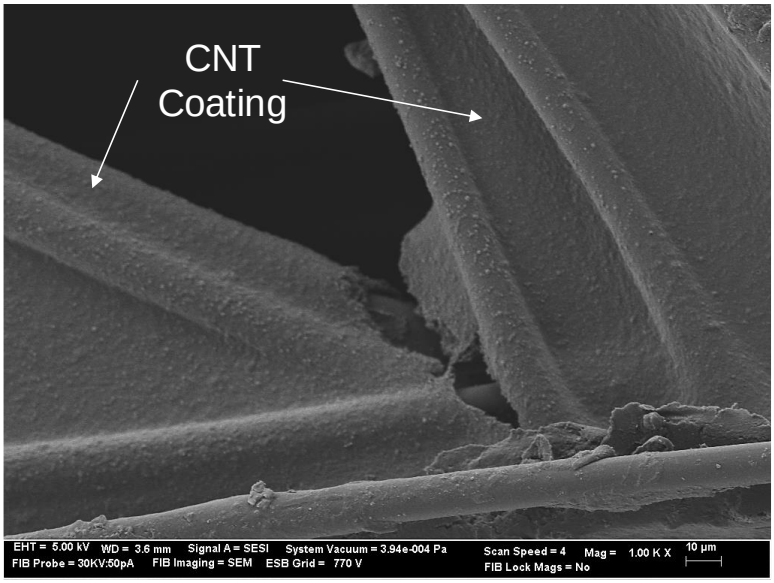

(b)

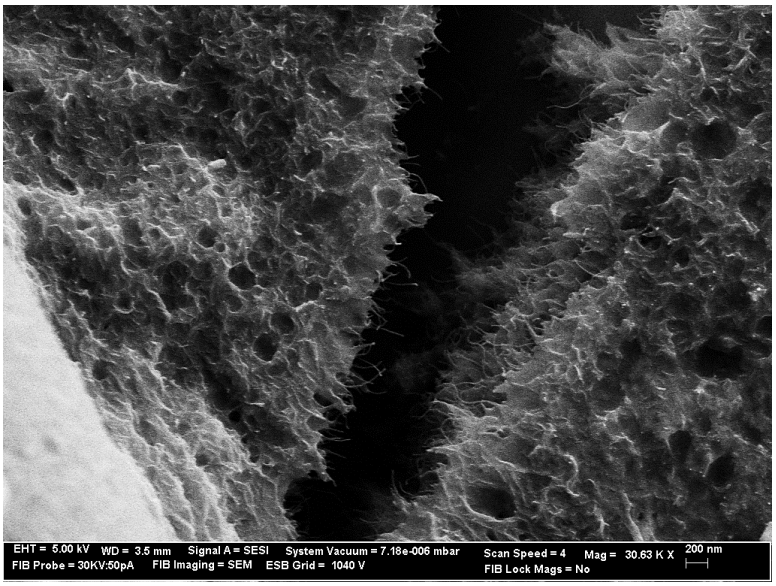

Figure 2.13: SEM micrographs showing (a) a typical fiber bonding sail area with the uniform nanotube coating and (b) a high-magnification image of CNT layer as formed on fiber surface (from Ref.[45]).

2.3.3.3 CNT-Based Multiscale Composites

The cryogenic fracture surface of the proposed CNT-based nonwoven sensing composites was imaged using a SEM. Figure 2.14a shows a typical fracture surface of the multiscale composite demonstrating the brittle cracking of the epoxy matrix and the ductile splitting of aramid fibers. Three fibers are seen protruding from the ruptured cross-section and their fractured ends have a brush-like appearance with extensive fiber splitting, indicating the fibrillation formation in the aramid fibers [2]. In addition, it can be seen that the nanotube-based sensor has a low fiber volume fraction overall. From the higher-magnification view in the region of the nanotube-modified fibers in Figure 2.14b, strong wetting between the coated fibers and the polymer matrix can be observed.

(a)

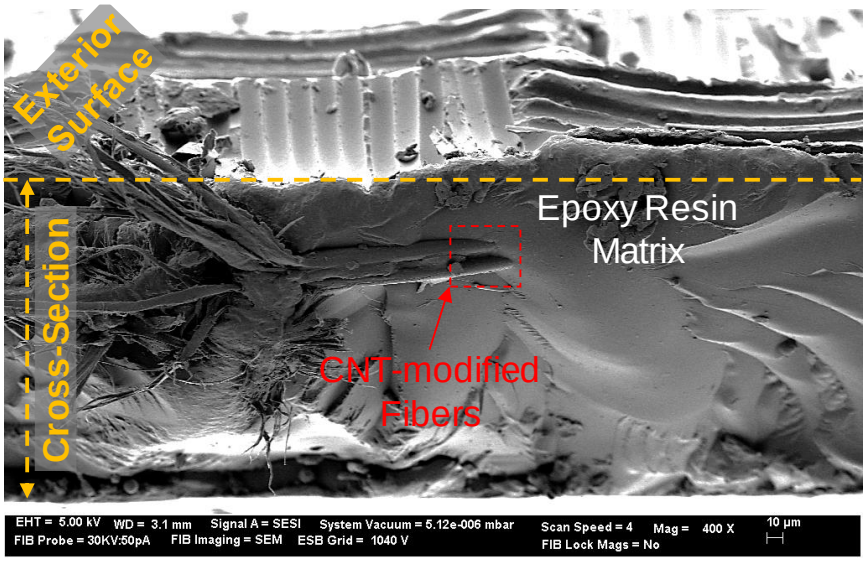

Figure 2.14: SEM images showing (a) fracture surface of the sensing composite proposed in this study and (b) the CNT-modified fibers in the composite, the magnified view of the dashed area in (a) (from Ref.[45]).

(b)

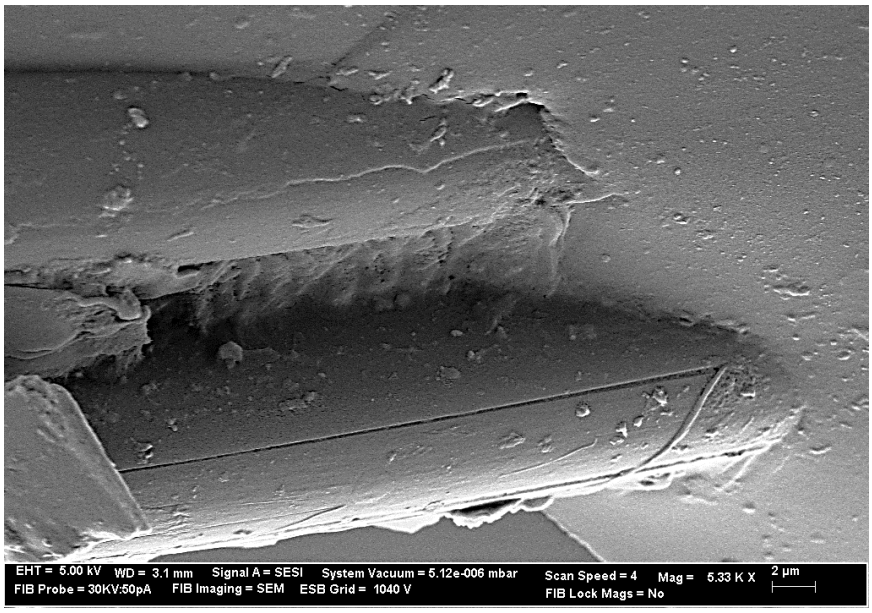

Figure 2.14: continued.

A more focused region in the CNT-based nonwoven composite is displayed in Figure 2.15, where the morphologies of the multiscale components including fiber, CNTs and epoxy matrix are clearly imaged. Similar to Figure 2.14, the fractured aramid fiber shows a serious split fibrillation and the epoxy matrix presents clean and distinctive river lines of cleavage for brittle cracking. Obviously, a few microns thick coating of nanotubes is uniformly formed outside of the fiber and spans between adjacent fibers. Due to the stress concentration, boundary cracking is found along the fiber-CNT and the CNT-epoxy interfaces, making the CNT coating a solid sensing layer capable of surviving during and after fracture damage. Additionally, the CNT coating shows a rough fracture surface most likely attributed to the loose arrangement of the CNT agglomerates as previously demonstrated in Figure 2.11b. It can be deduced that the locally integrated CNT layer behaves as an energy absorbing

medium, like a ‘cushion’ when the composite fractures. A high magnification view of the fractured CNT layer is shown Figure 2.15b, which reveals that the CNTs form a relatively porous structure, like a ‘sponge’, which is partially infused by the epoxy resin with small voids less than 500 nm heterogeneously distributed inside. To conclude, the globally distributed and locally well-connected CNT network forms bridges between aramid fibers. Being impregnated with surrounding epoxy matrix, the CNT coating layer ruptures whenever and wherever the composite fractures, thereby promoting an *in situ* damage sensing functionality of the multiscale composite.

(a)

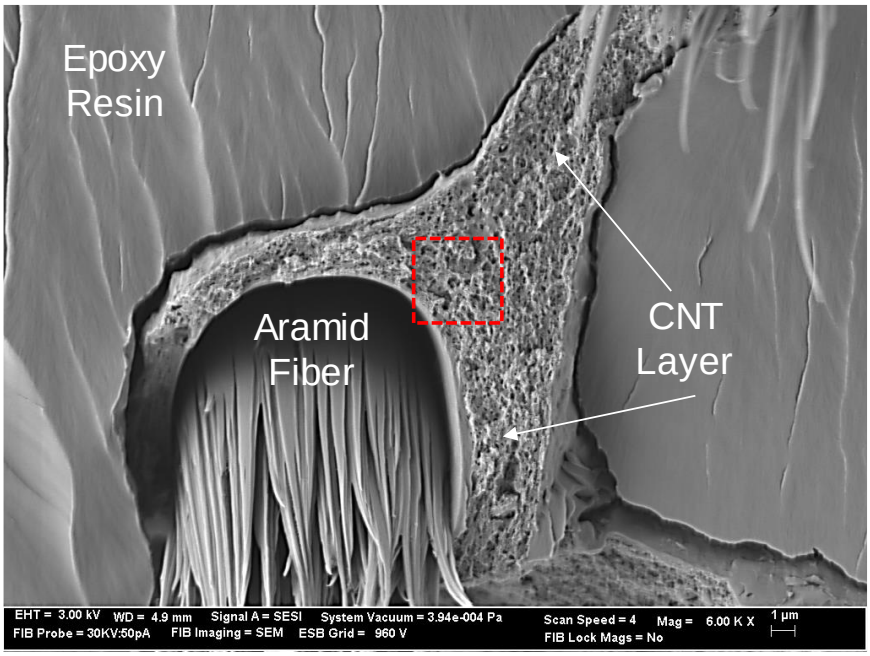

Figure 2.15: SEM cross-sectional images of the CNT nonwoven multiscale composite showing (a) the fractured aramid fiber, epoxy resin, and the locally integrated CNT layer and (b) the well-interconnected CNT networks, the high-magnification image of the dashed area in (a).

(b)

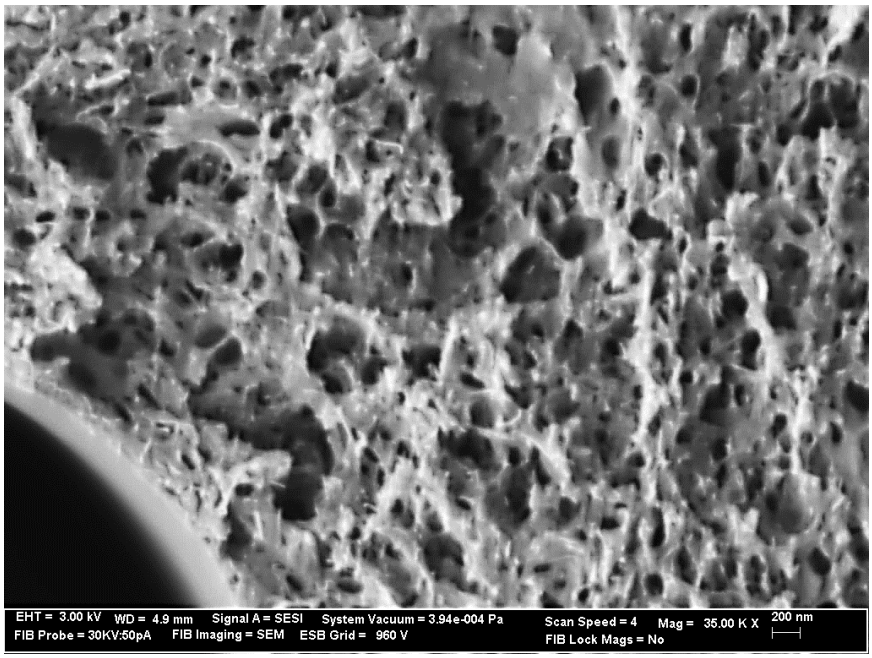

Figure 2.15: continued.

2.3.4 Mechanical Properties

The proposed CNT-based sensing composites are composed of a relatively low volume fraction of fibers, approximately 8%, which are also randomly oriented, resulting in mechanical properties dominated by the epoxy matrix. To fully understand the mechanical properties and failure mechanisms of the sensing composites, a series of tensile tests were performed on composite layer specimens per Section 2.3.1.4. Acoustic emission (AE) monitoring was applied to verify the damage initiation and evolution characteristics of the composites in order to establish their mechanical limits for sensing applications.

The composite specimens, which include the aramid without the nanotube coating (the reference), as well as the 1.0 wt.% and 0.75 wt.% CNT loadings, were all monotonically tested to failure in tension. The failed specimens are displayed in

Figure 2.16. All reference specimens and six CNT composite specimens clearly show even macroscopic fracture edges that are perpendicular to the tensile loading direction, i.e., indicating a brittle failure mode [3]. The two unusual specimens (No. 1-1 and 2-4) failed at the electrodes, which may be due to a stress concentration introduced by the electrodes. In addition, all specimens did not demonstrate any cracking pattern along the loading direction, suggesting that the nonwoven composites break catastrophically with an initial major crack. In short, the evolution of the initial transverse crack induces local fiber/matrix interfacial debonding, which propagates locally in the transverse direction and causes fracture of the entire system. A similar fracture mode was displayed by the nonwoven glass/epoxy composites with a fiber volume fraction of 13% according to Rios-Soberanis, *et al*. [4].

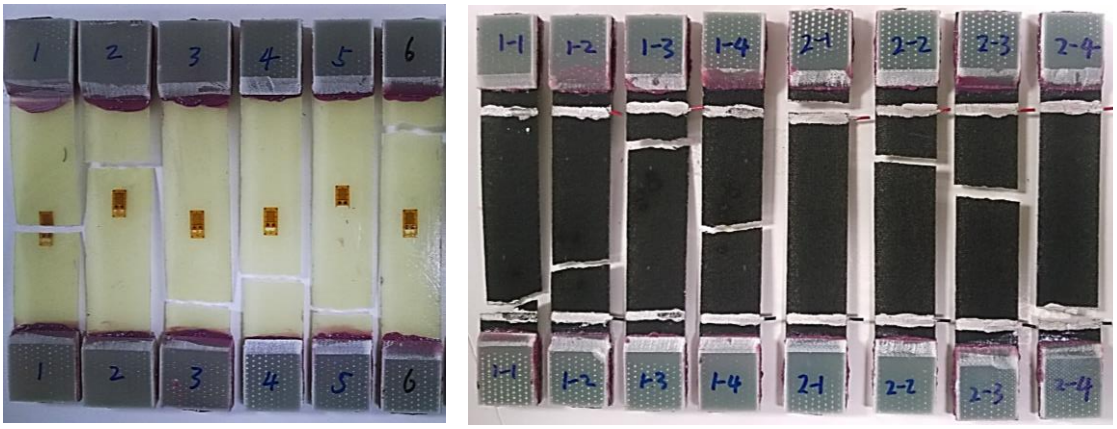

(a) (b)

Figure 2.16: Snapshots of the nonwoven composite specimens with (a) no CNTs (= reference) and (b) 1.0 wt.% and 0.75 wt.% CNTs. Also visible are the macroscopic fracture surfaces due to tensile failure.

The mechanical response of a typical reference specimen during the entire tension test is presented in Figure 2.17. It is clear that both the loading and strain responses are in a nearly linear fashion without showing any discontinuity that could correspond to the initiation of damage. Based on AE activity, it is notable that the entire damage progression of the aramid nonwoven composite includes two distinct stages (namely I and II shown in Figure 2.17) based on the concentration of AE hit rates. Evidently, Stage II is more severe than Stage I because of the significantly increased amount of AE hits, implying the initiation and evolution of severe damage in this stage. It is also noted that the first increase in AE activity of about 45 hits by count appears 21 seconds after loading, as the specimen is loaded to 4.6 MPa, i.e. reaching 0.12% strain, which is likely due to the initiation of microcracks in the epoxy matrix due to local stress concentrations [2,5,6]. Later, a couple of strong AE hit groups of more than 70 hits each, are recorded one after another as the composite is loaded to about 14.6 MPa (0.4% strain), making the accumulated AE hit curve first start to rise. This is likely caused by the saturation of microcracking in the matrix. In addition, due to the low fiber volume fraction, the extensively cumulated microcracks in the matrix lead the stress-strain curve of the composite to slightly deviate from its initial linear response. Stage I is then defined as the appearance of the initial major damage at this moment. As the load increases, AE events are continuously recorded, suggesting the propagation of microcracks. At 120 s, AE activity suddenly increases to about 250 hits in total, which reveals the initiation of macroscale damage and hence the beginning of Damage Stage II. This is likely due to fiber/matrix interface debonding as the local microcrack tips approach the fiber/matrix interface. After loading the specimen to 39 MPa (corresponding to 1.15% strain), the slope of the

stress-strain response obviously decreases corresponding to inelastic mechanical behavior and the accumulated AE counts sharply increase due to the growth of debonding cracks. Different from unidirectional and laminated composites [2,5,6], all fibers in the nonwoven composites are affected by the initial interfacial debonding because of the random fiber orientations. Once the first macro debonding crack has occurred, the growth of additional cracks along the tensile stress orientation terminates due to the lack of unidirectional reinforcement in this direction for effectively transferring the applied tension load. In addition, due to the crack-blunting mechanism [2], this major crack propagates along the fiber/matrix interface and interconnects with surrounding cracks near the crack plane under the increasing tensile stress, which then simply slices through the specimen, resulting in the final fracture along the transverse direction as shown in Figure 2.16a. This specimen finally failed at a tensile stress of 60 MPa at 1.9% strain.

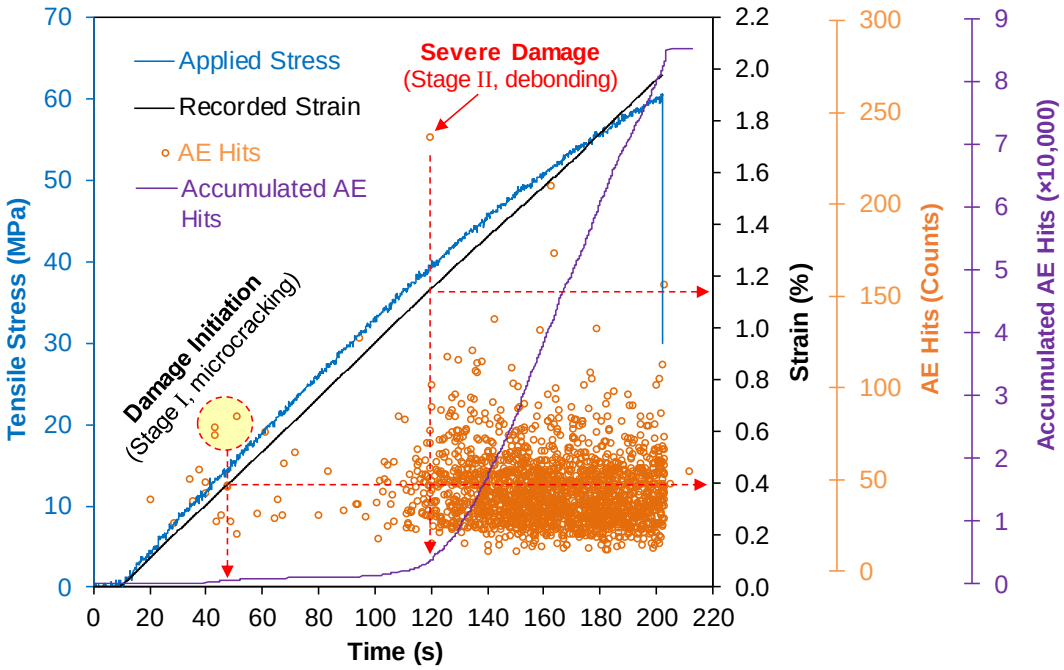

Figure 2.17: Typical mechanical responses of the nonwoven composite (with 0% CNT, the reference) during the uniaxial tension test.

Based on the aforementioned observations, the elastic strain limit of the proposed nonwoven composites is approximately 0.4%. It could be observed that damage progression of this composite involves the matrix microcracking and the fiber/matrix interfacial debonding. The fracture mechanism is dictated by the fiber/matrix interface failure, originally initiated as a debonding crack. This specific damage progression could be validated by the *in situ* resistive responses of the CNT-based nonwoven composite sensors, which are presented in Section 2.3.5.2.

Figure 2.18a through c represent the mechanical properties of the different aramid/epoxy composites in terms of elastic modulus, fracture strain and ultimate strength, respectively. A 12% increase in the elastic modulus of the CNT-coated specimens could be observed, indicating the structural enhancement of nanotubes to

the bulk stiffness of the composite, which is in agreement with other experimental research [7-10]. While there is an increase in stiffness, the coating makes the specimens more brittle, and the ultimate failure strain decreases with the addition of a CNT coating. This adverse effect agrees with the experimental study by Ci and Bai [11] and is speculated to be due to the poor CNT-epoxy adhesion caused by complete cross-linking of the epoxy matrix around the nanotubes. Although there is a decrease in the average failure strain there is a slight increase in the average strength for the sensing composite with 1.0 wt.% CNT loading, owing to its higher elastic modulus. The composite sensors with 0.75 wt.% CNT loading show a slight decrease in average strength.

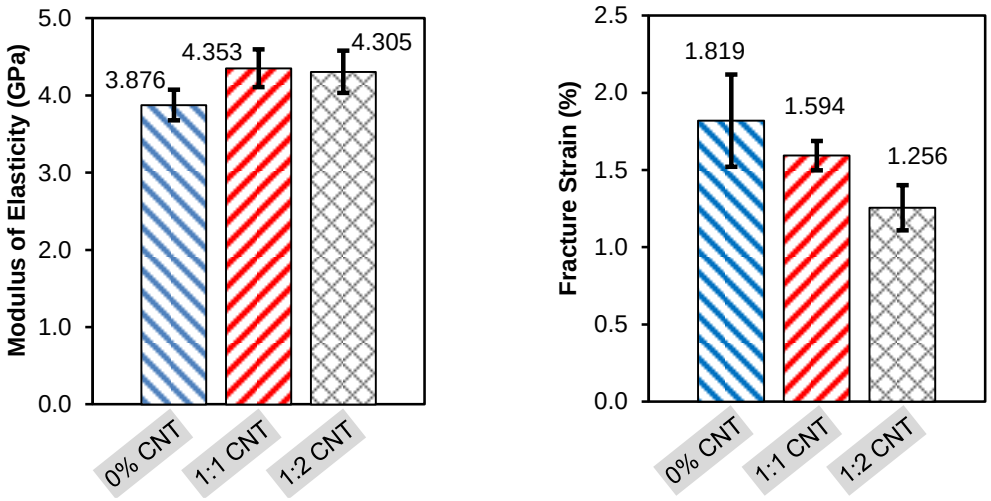

(a)

(b)

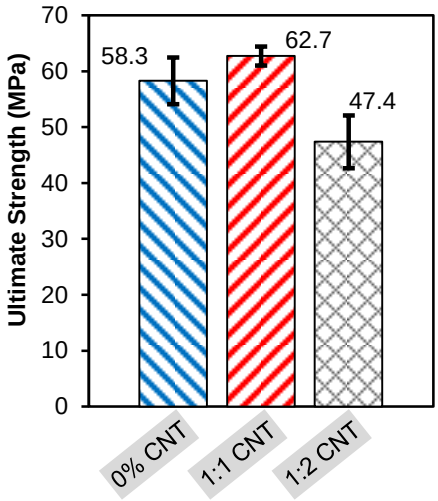

(c)

Figure 2.18: Mechanical properties of the aramid/epoxy composite (=0% CNT) and the CNT composite sensors (=1.0 and 0.75 wt.%) (error bars represent ± one standard deviation) (from Ref.[45]).

2.3.5 Electrical Properties

As reviewed in Section 1.3, CNT-based sensing techniques for SHM are typically using the in-plane electrical measurements from CNT-based sensing networks which largely depend on the electrical conductivity of the as-established nanotube networks. Many factors including categories, dispersion states, concentrations, etc. of nanotubes, can affect the electrical conductivity of the network. Percolation is the top priority to be accomplished in order to enable a well-connected, conductive CNT sensing network. In light of this, the percolating behavior of the proposed CNT nonwoven sensing composites is demonstrated first and then the resistive responses are characterized in the following sections.

2.3.5.1 Electrical Double Percolation

A series of CNT-aramid nonwoven composite specimens were prepared per Section 2.3.1.1 and the in-plane resistive measurements were acquired at room temperature, noted as the baseline resistance. The volume electrical conductivity of the composite specimen is calculated using Equation 2.4,

$$\sigma = \frac{1}{R} \cdot \frac{L}{A} \tag{2.4}$$

where σ is the conductivity (S/m), R is the resistance (Ω), L (m) is the distance between the applied electrodes along the current direction, and A (m^2) is the cross-section area perpendicular to L. In addition, the volume electrical resistivity ρ (Ω·m) is defined as the reciprocal of conductivity,

$$\rho = \frac{1}{\sigma} \tag{2.5}$$

Figure 2.19 shows the influence of nanotube concentration on the volume conductivity of the as-processed CNT composites. At a concentration of only 0.05 wt.% of nanotubes the volume conductivity decreases by 130 times in comparison

with 1.0 wt.% CNT. In general, the electrical conductivity of CNT-based nonwoven composites is depending on the CNT concentration by following the scaling function [12] of Equation 2.6,

$$\sigma \propto (P - P_0)^t \tag{2.6}$$

where P is the CNT concentration, P_0 is the percolation threshold and t is the exponent constant reflecting the system dimensionality with calculated values of ~1.33 in two and ~2 in three dimensions [12-14]. By taking into account statistical percolation theory [14], this dependence can be predicted by Equation 2.7,

$$\sigma = n \cdot (P - P_0)^t \text{ , for } P > P_0 \tag{2.7}$$

where n is a fitting parameter related to the intrinsic conductivity of CNTs.

Here, the best fit to the experimental data shown in Figure 2.19 produces values of n = 3625 S/m, t = 1.47, and P_0 = 0.015 wt.% which were found by the least-squares fitting of the data points until the best linear fit of Ln (σ/n) versus Ln (P-P_0) was obtained [14,15] as shown in Figure 2.19 inset graph. Compared with the experimental results of other 42 CNT-epoxy nanocomposites recently reviewed by Bauhofer and Kovacs [14], the proposed sensing composite shows enhanced percolating behavior with a low percolation threshold of 0.015% as well as a generally high volume conductivity, such as 0.04 S/m at 0.05 wt.% CNT.

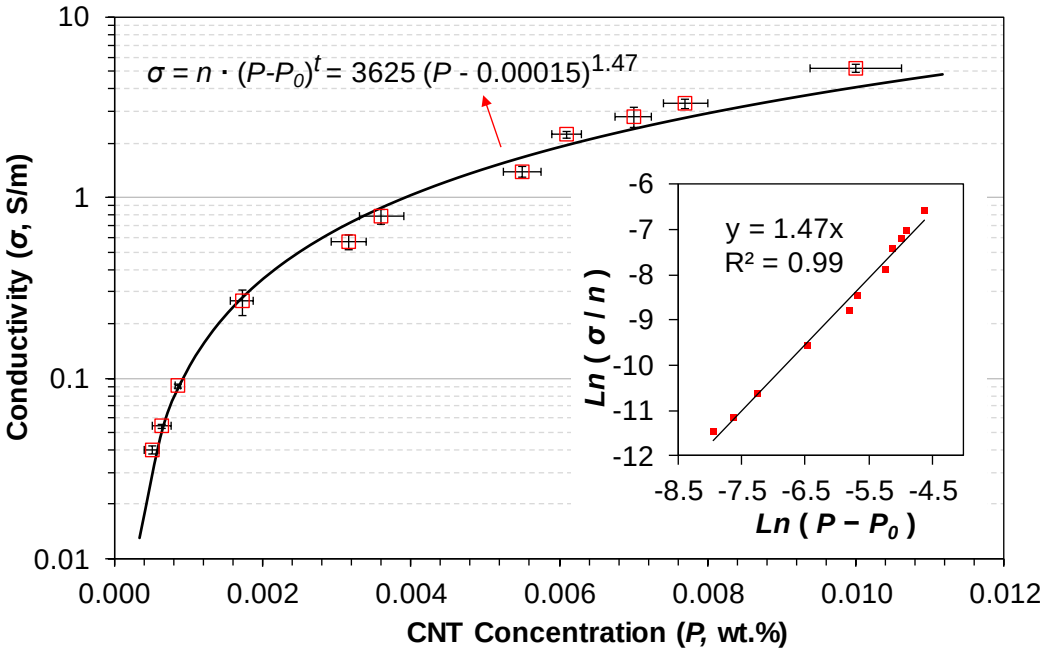

Figure 2.19: Dependence of the electrical conductivity on the CNTs weight fraction at room temperature. Inset: The percolation scaling law between *Ln* (σ/n) and *Ln* (P-P_0) where the solid line corresponds to the best fitted line, indicating an exponent of 1.47.

At first glance, it could be hypothesized that the electrical features might be a result from the kinetic percolation effect [16,17]. Nevertheless, all CNT-aramid nonwoven composites were fabricated in this research following a static process per Section 2.2.l. The CNTs coated on the fiber surface in the as-processed composites are in a stable solid state as demonstrated by SEM images shown in Section 2.3.3.3. As a result, these nanotubes are unable to move freely within the composite, thus rejecting this hypothesis. According to Connor *et al*. [18], tunneling between randomly distributed CNT separated by a thin isolating barrier should result in a linear proportional correlation between *Ln* σ and $P^{-1/3}$. In Figure 2.20, this relationship is

applied to the experimental data. It can be observed that it is following a bilinear trend showing an inflection point as $P^{-1/3}$ equals to 6.926, which corresponds to a CNT concentration of 0.30 wt.% (noted as the 'inflecting concentration'). This unique dependence is distinctive from the single linear trend as observed from similar investigations of using this correlation [15,19,20]. It is likely that there is a coexistence of two or mixed tunneling mechanisms separated by the inflecting concentration of nanotubes, i.e., double percolating behavior.

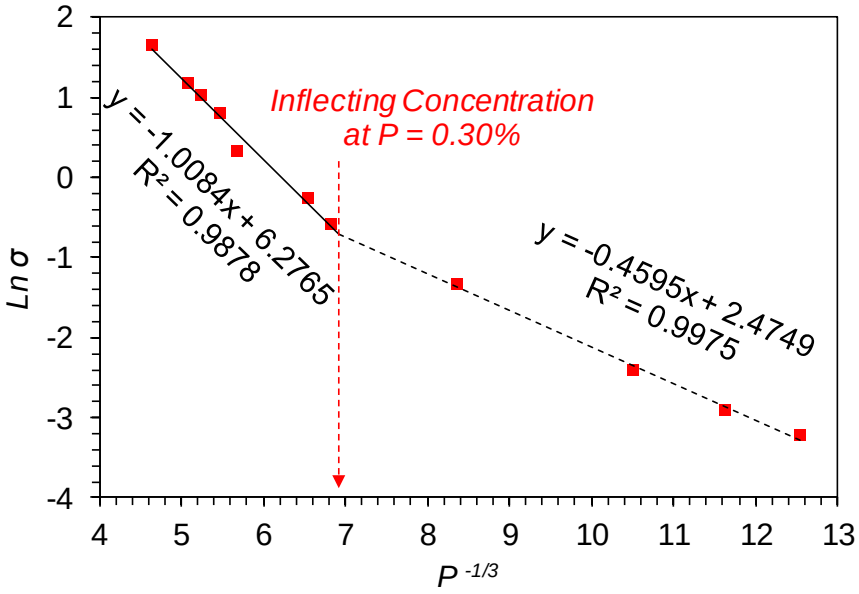

Figure 2.20: Plot of σ as a function of CNTs weight fraction $P^{-1/3}$ at room temperature, showing a bilinear correlation, indicative of the existence of electrical tunneling condition.

In this ternary composite system, the bulk percolating behavior can be attributed to the hierarchic micro/nano double-percolation [21-25]. As schematically

illustrated in Figure 2.21, the two percolating mechanisms involve structural percolation of the randomly distributed fibers in the epoxy matrix at the microscale and electrical percolation of the nanotubes on the fiber surfaces at the nanoscale, respectively. Additional noteworthy, substituting a conductivity value 455 S/m for the CNT sizing film (measured value) back to the previously fitted statistical percolation equation (shown in Figure 2.19), yields a CNT loading of 24.5 wt.%, which is almost equal to the measured CNT concentration of 25% in the raw CNT sizing solids. This is validating that the microscale percolation network formed by random aramid fibers does not influence the intrinsic properties of the CNTs and solely serves as the CNT carrier.

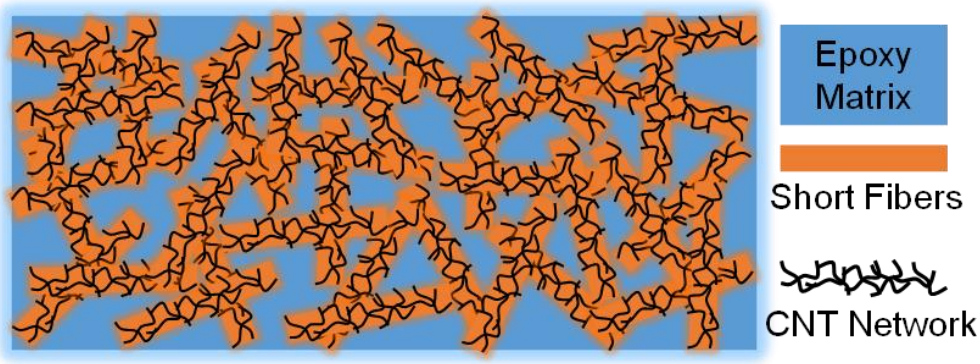

Figure 2.21: Schematic representation of the hierarchical micro/nano double-percolation phenomenon in the CNT-based nonwoven multiscale composites.

Based upon the excluded volume concept [26], the percolation threshold, P_0, in a three dimensional system of randomly oriented cylinders with high aspect ratio, is approximately calculated using Equation 2.8 [23,26],

$$P_0 = 2.8 \cdot (L/D)^{-1} \quad (2.8)$$

where L is the length and D is the diameter of the cylinder.

In the case of nonwoven composites without CNTs, an individual short fiber is 12 mm long and 12 μm in diameter as formerly noted, which yields P_0 of 0.28% by volume following the above equation. This volume fraction can be further converted to the weight concentration by multiplying the density of this composite, that is 1.22 g/m^3, which is calculated based on the material properties including a fiber volume fraction of 8% (measured per Section 2.2.2), a fiber density of 1.44 g/m^3 (reported by the manufacture), the EPON 862 epoxy density of 1.2 g/m^3 [27] following the rule of mixture [6], giving 0.34 wt.% as the structural percolation threshold for the neat nonwoven composite. Obviously, this threshold is very close to the inflecting concentration of nanotubes, 0.30 wt.% as previously determined for the CNT-based percolating network, suggesting that at low CNT concentrations of < 0.30 wt.% the observed tunneling dependence shown in Figure 2.20 is solely dominated by the nanotube network. In addition, selectively localized CNTs on the fiber surfaces only occupy 8% (i.e., the fiber volume fraction) of the total volume of the composite. A very low electrical percolation threshold of 0.015 wt.% is manifested to be existing, most likely by taking advantage of the significantly pre-percolated microscale fiber network (8 vs. 0.28 vol.%) that creates tremendous amount of continuous and homogeneously interconnected subdomains for carrying CNTs to form conductive pathways. Furthermore, at a high CNT loading, the complete coating of the fibrillary domains can be achieved, forming a superimposed micro/nano-scale percolating network that is uniform and homogeneous as shown in Figure 2.22a to d. On the other hand, partial non-uniform coating can occur with CNT concentration is lower than 0.3 wt%, leading to an inhomogeneous network as displayed in Figure 2.22e to f, which is

in agreement with the experimental work by Rausch and Mader [28,29]. Therefore, the micro- and nano-percolating mechanisms can coexist at different CNT concentrations due to the different percolating structures.

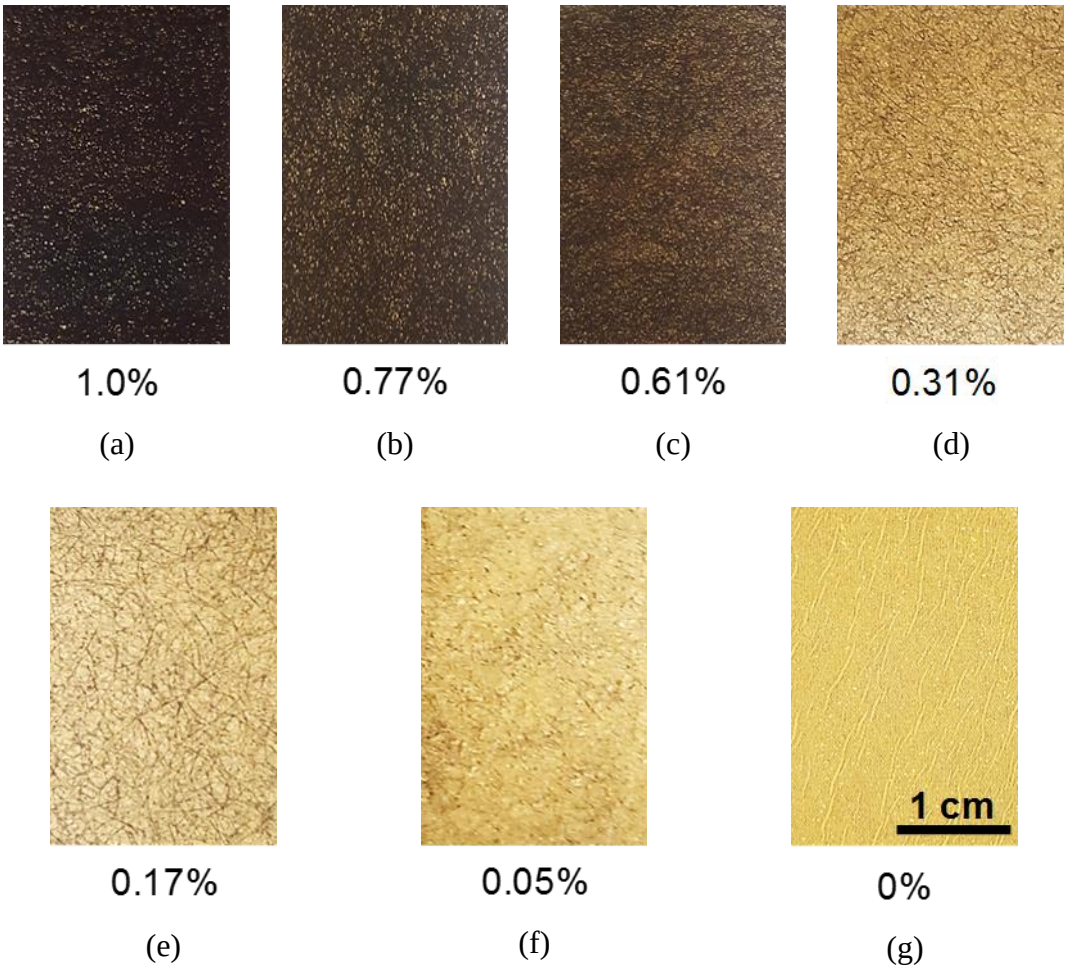

Figure 2.22: Optical photographs of the CNT-based aramid nonwoven multiscale composites with different CNT loadings including (a) 1.0 wt.%, (b) 0.77 wt.%, (c) 0.61 wt.%, (d) 0.31 wt.%, (e) 0.17 wt.%, (f) 0.05 wt.%, and (g) 0 wt.%, the reference, in which as CNT% > 0.3%, showing a stable and spatially uniform network in the macroscale composites; as CNT% < 0.3%, showing the inhomogeneous network with “flocs”.

To summarize, based on the synergy between the microscale and nanoscale percolating networks, using the approach of dip-coating CNTs onto nonwoven fabrics is an efficient way to improve the electrical percolation and conductivity of nonwoven composites and offers a new route to design conductive multiscale composites by simultaneously tuning the double percolation networks at the micron-/nano-scale. In comparison, recent numerical simulations conducted by Tallman [30] showed that the network with aligned nanofillers demonstrates a generally degraded percolation and conductivity transverse to the alignment direction, which is attributable to the decreased likelihood of nearly parallel sticks intersecting, which in turn reduces the number of tunneling junctions. Obviously, with the enhanced percolating and conductive properties, the proposed CNT-based nonwoven sensing composites require a small excitation voltage, maybe only several volts, making themselves a practical sensing material for SHM applications.

2.3.5.2 Self-Sensing Performance

As demonstrated in Section 2.3.4, under uniaxial tensile loading the as-processed nonwoven composites show two stages of damage progression including matrix microcracking and fiber/matrix interfacial debonding. To validate and further investigate this microscale damage mechanism, a distributed network of nanometer sized carbon nanotube sensors is extremely helpful to monitor the damage process. Therefore, a series of CNT-based nonwoven composites were tested following the same loading protocol with their resistive behaviors measured in real-time. Due to the selective localization of nanotubes in the fiber/matrix interphase region (see SEM image in Section 2.3.3.3), the formed CNT network is utilized as *in situ* sensing layer to detect interfacial damage, resulting in a smart self-sensing nonwoven composite.

Figure 2.23a shows the real-time response of electrical resistance change, stress, strain, and acoustic emission for a nonwoven composite specimen with 0.75 wt.% CNT. Both stress and strain follow a linear-elastic fashion, in which, however, no local features could be related to the damage progression but the sudden drop at 46 MPa (i.e., 1.2 % strain) due to final fracture. On the other hand, both resistance and AE responses display remarkably nonlinear trends with local sharp increments, seen as 'knees', during the applied load protocol, indicating the progressive evolution of damage. In particular, the AE behavior displays a similar pattern as those recorded from the reference specimen presented in Section 2.3.4, indicating the two-stage damage mechanism.

The first three AE activities (70 hits in total) are recorded simultaneously when the specimen is loaded up to 4.4 MPa (0.1% strain), suggesting the initiation of the microcracks in the matrix. Nevertheless, the resistive response does not reveal this onset of micro damage, because the nanotube sensing network in this composite system is only concentrated on the fiber surfaces and not uniformly distributed in the matrix phase, like in other performed research [5,31-35]. In addition, at this low stress level, the composite deforms elastically, so does the nanotube network. Later, a distinctive AE activity (about 113 hits) is detected as the specimen is loaded to 17.6 MPa that corresponds to 0.41% strain at 77.5 s. A closer look at the period from 75 s to 80 s when damage initiates is shown in Figure 2.23b and demonstrates that a sharp resistance change is observed coincidently with a sudden accumulation of AE hits. It can be envisioned that in a local transverse region of the composite microcracks propagate under the increasing load. As those microcracks first approach the CNT coating, the crack tips induce local stress concentrations to the nanotube network,

therefore, resulting in the immediate increase in resistance. As the load is increasing, microcracks are reaching near-saturation in the matrix, which results in the rise of resistance and AE activity.

Back to Figure 2.23a, after loading the specimen to 28.6 MPa (0.68% strain), two intense AE activities (about 110 hits each) are recorded, implying the start of damage Stage II. A magnified view of this critical moment is shown in Figure 2.23c. It is clear that the resistive response dramatically jumps as soon as spiking AE activities are detected, revealing the initiation of interfacial damage, i.e., debonding. Under increasing load, debonding cracks could grow, propagate through the CNT coating, and gather along a crack plane, forming macro cracks that sever the nanotube network. This damage progress in the CNT composite is inherently represented by the resistive response in real-time and further confirmed by observed AE response. In comparison, the strain data do not show any evidence regarding the evolution of damage, most likely due to the fact that the location of the strain gage is far from the initiated crack plane as shown in Figure 2.16b (sample No. 2-2).

Subsequently, as the interfacial cracks accumulate and interconnect from each other under further loading, a fracture plane initiates and the composite specimen then fails immediately. It can further be observed that the amount of accumulated AE hits during damage Stage II from the CNT-based nonwoven composite specimen are about seven times less than the reference specimen (as shown in Figure 2.17), which is mainly due to the different tensile stress levels these two specimens experienced in this damage state, that is, 28-46 MPa versus 40-60 MPa, respectively. Less stress in general causes less cracking in the same type of epoxy resin. In addition, this discrepancy may be partially attributing to the porous structure of the selectively

integrated CNT coating (as shown in Figure 2.15) that creates numerous nanosized voids and extensive boundaries possibly for attenuating elastic stress waves released as damage initiates, increasing wave attenuation [36-38].

Based on the aforementioned observations, the damage evolution of the as-established CNT-based nonwoven sensing composites under uniaxial tension is demonstrated explicitly by the *in situ* resistive response of the nanotube network, which is promising and further confirmed by the real-time AE recordings. Specifically, compared with the reference test, the elastic behavior of the nonwoven composites with and without CNTs are nearly identical, i.e., (1) the first AE events from these two composites were recorded at the same stress level, i.e., 4.4 MPa vs. 4.6 MPa; (2) the observed elastic limits are very close, i.e., 0.41% strain at 17.6 MPa vs. 0.40% strain at 14.3 MPa.

It was observed that the failure mechanism here is governed by a two-stage damage progression including (1) saturation of microcracks in the epoxy matrix (micro-level), and (2) propagation of fiber/matrix interfacial debonding cracks (macro-level). Additionally, due to the selective location of CNTs on the fiber surfaces, nanotube-based sensing networks demonstrate much higher electrical resistance sensitivity due to interfacial damage than microcracking, making this CNT-based nonwoven composite a useful smart self-sensing material.

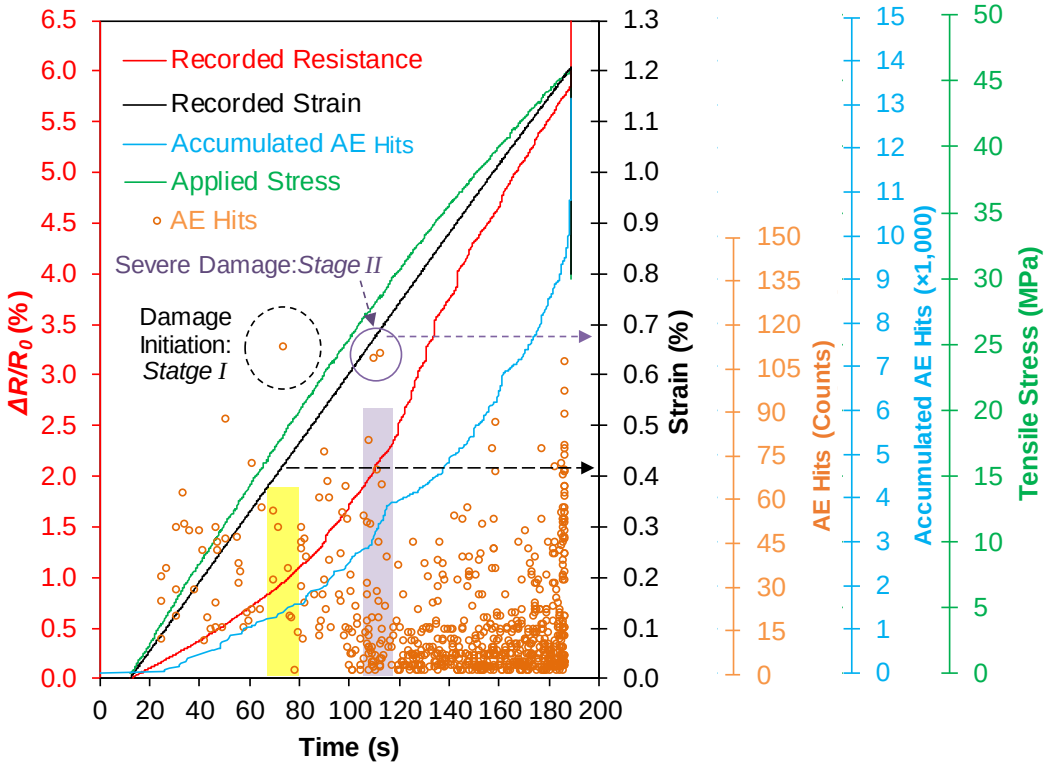

(a)

Figure 2.23: *In situ* electrical resistance, strain, and acoustic emission responses of the aramid nonwoven composite with 0.75 wt.% CNT under uniaxial tensile testing showing (a) entire loading protocol, and the initiation of damage (a) Stage I and (c) Stage II.

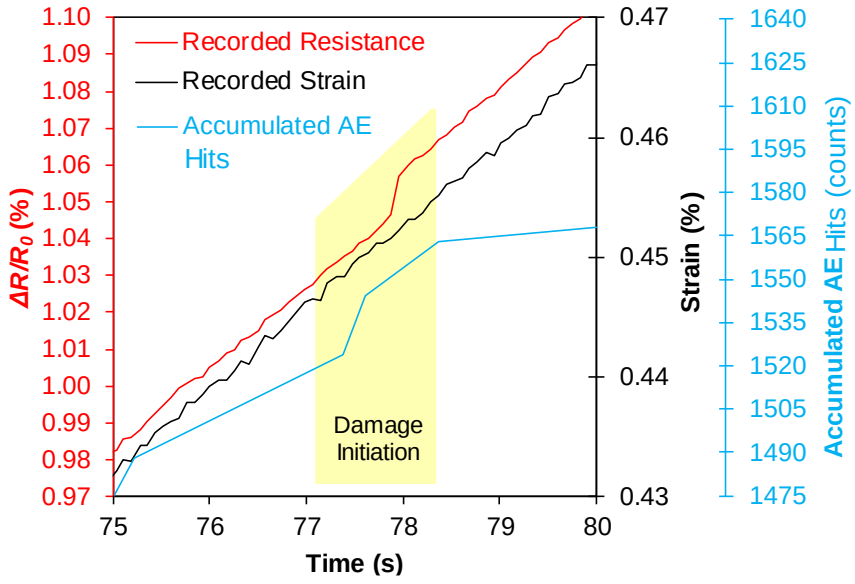

(b)

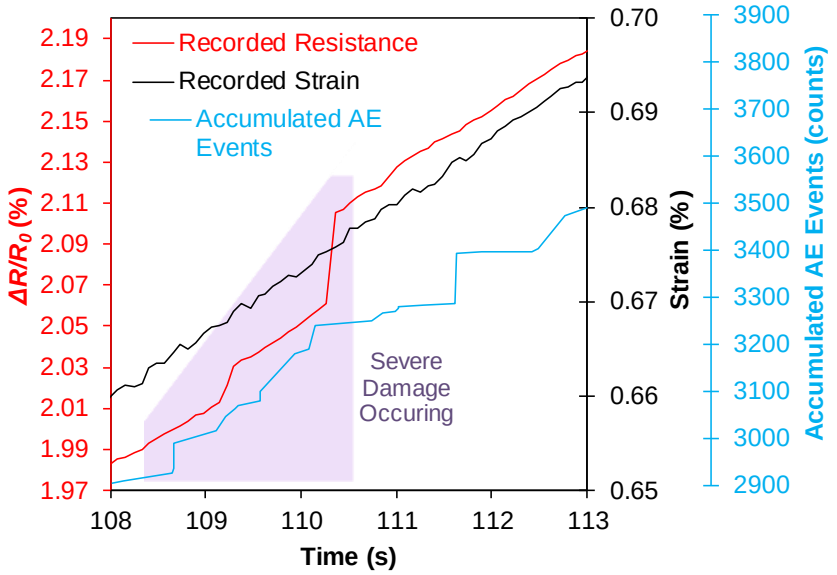

(c)

Figure 2.23: continued.

2.3.5.3 Piezoresistivity

To facilitate potential strain monitoring applications with the proposed CNT-based nonwoven composite sensors, the piezoresistive response of this type of sensing composite was characterized *in situ* under uniaxial tensile testing. Figure 2.24 shows the typical piezoresistive response and stress-strain behavior for a nonwoven composite sensor with 0.75 wt.% CNT. In the elastic zone, the piezoresistive response of the sensor shows an ideal linear trend similar to the transient resistance change as presented in Figure 2.23a. At strains beyond the elastic zone (i.e., >0.4%), the piezoresistive response begins to deviate from its initial linearity, which is represented as the red dashed line in the figure. In addition, more noise in the measurement is noted, which is attributed to the accumulation of microcracks in the matrix. After 0.68% strain (i.e., initiation of fiber/matrix debonding), there are some sharp knees observed in the piezoresistive response, which corresponds to the formation of debonding cracks that permanently sever portions of the electrically conductive network. This progressive increase in macrocracks results in a conspicuous change in the slope of the stress-strain curve and corresponds to the inelastic behavior of the sensor, revealing the reduction in stiffness. Later, when fracture occurs, the resistance change goes to infinity. In general, the slope change of the piezoresistive response in the inelastic zone is substantially nonlinear, demonstrating an increased sensitivity of resistance change to inelastic deformation.

The piezoresistive behavior of the nanotube sensors is quantified in terms of their gage factors, which have been defined in Section 2.3.2. For strain monitoring applications, gage factors are further categorized under two specific strain levels corresponding to the un-cracked elastic state (under 0.4% strain) and the matrix-

cracked inelastic state (above 0.4% strain) by performing a linear least-squares curve-fit on the experimental data.

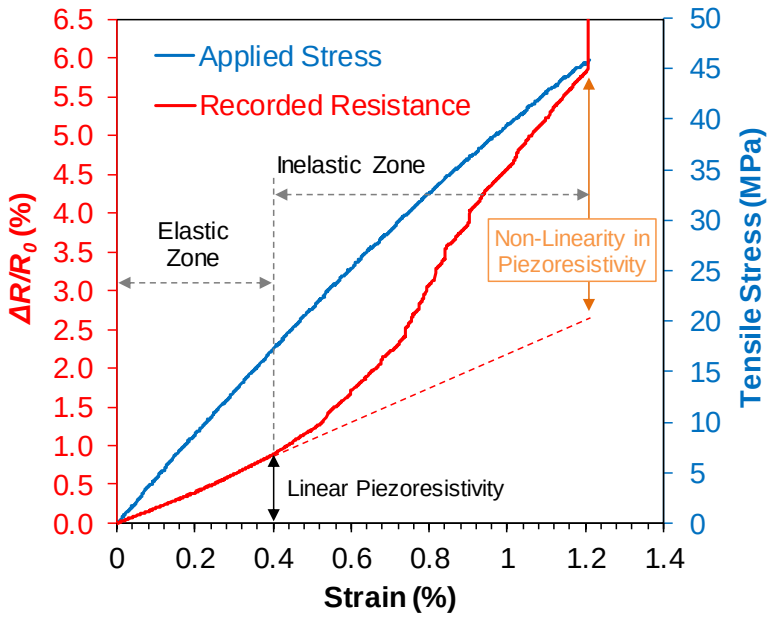

Figure 2.24: Typical piezoresistive response and stress-strain behavior of CNT composite sensors.

Two groups of CNT composite sensors with nanotube concentrations of 1.0 and 0.75 wt.% were tested. The piezoresistive response of these sensors for the elastic state and inelastic states are shown in Figure 2.25a and b, respectively. Figure 2.26 summarizes gage factors obtained for both groups of specimens in accordance to the elastic and inelastic strain levels. It can be seen that the group of four specimens with 0.75 wt.% CNT loading shows higher strain sensitivity than 1.0 wt.% CNT group. There have been a number of experimental studies on the piezoresistive behavior of nanocomposites based on CNTs. Experimental results [39-43] indicate that there is a

higher degree of sensitivity with reduced CNT concentration, and the general trend in gage factor is consistent with that reduction. However, the elastic gage factors are somewhat lower than expected as compared to nanocomposites with nanotubes dispersed throughout the polymer matrix developed by other researchers [42-44]. This lower gage factor is attributed to the formation of the conducting networks preferentially along the surfaces of the fibers. The high concentration of CNTs on the fiber surface results in a nanocomposite "interphase" that forms around the fiber. This interphase region effectively acts like an overall nanocomposite sensor that has a high volume fraction of nanotubes. In addition, it is likely that by providing excessive electrical conductive pathways the random fiber architecture also influences the piezoresistive response. Meanwhile, the inelastic gage factors are also higher than the elastic gage factors. The breaking up of the CNT network due to cracking and fiber-matrix debonding severs conducting pathways, resulting in a lower effective volume fraction of nanotubes conducting current in the sensor.

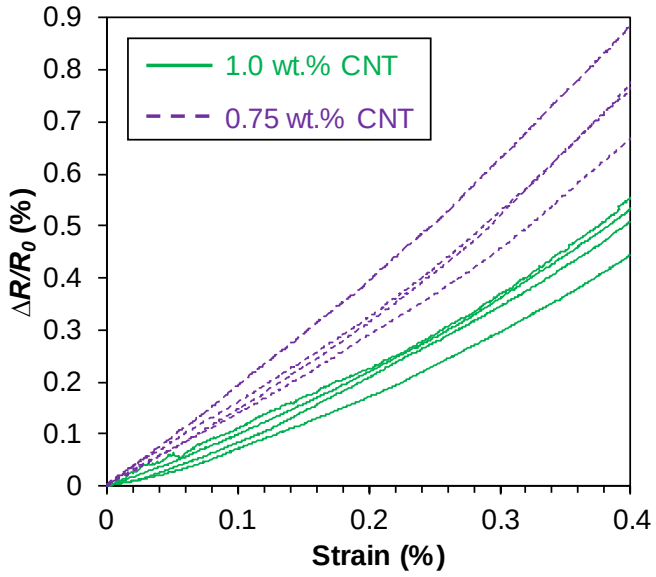

(a)

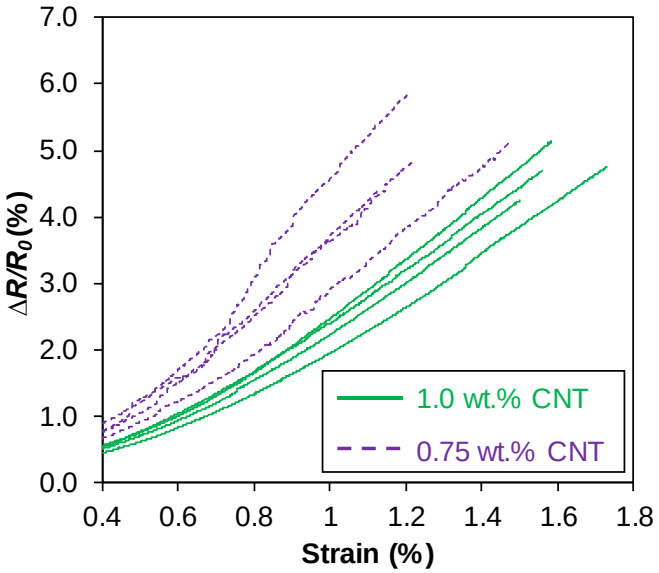

(b)

Figure 2.25: (a) Elastic and (b) inelastic piezoresistive responses from individual test coupons of the CNT-based nonwoven composite sensors fabricated in this research (from Ref.[45]).

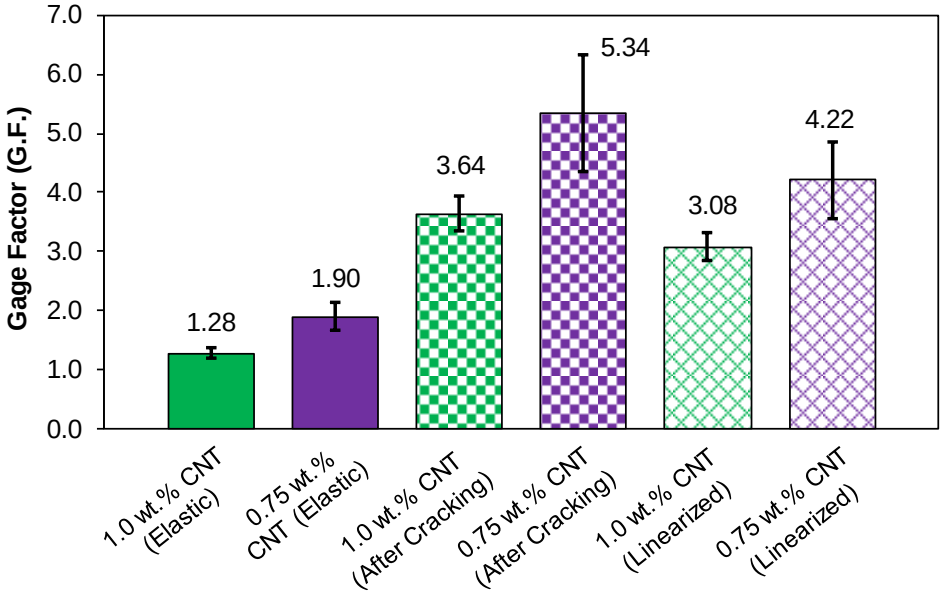

Figure 2.26: Gage factors for the CNT-based nonwoven composite sensors (error bars represent one standard deviation) (from Ref.[45]).

2.4 *Ex Situ* Strain Monitoring

The previously established CNT-based nonwoven composite sensors consist of a pervasive, well-connected nanotube network that conveys electrical conductivity to the nonwoven composites and behaves as an integrated nanoscale sensor network, representing extraordinary *in situ* perception of the mechanical state of the composite, i.e., the self-sensing capability. Under the applied stress, the configuration of the nanotube network changes as the composite deforms, which manifests as the quantitative variations of electrical resistance in the local CNT network. After characterizing the *in situ* strain sensitivity of the nonwoven sensing composite, the proposed sensors were then bonded onto metal substrates for *ex situ* strain monitoring, including aluminum and steel, and tested under quasi-static cyclic tensile and compressive loads. In addition, a distributed sensing network with four CNT sensors

was created and tested to show the CNT sensors' capability of monitoring distributed strains in both the longitudinal and transverse directions.

2.4.1 Experimental Setup

2.4.1.1 Case Study 1: Elastic and Plastic Strain Monitoring

To verify elastic and plastic strain monitoring capabilities of the proposed CNT-based strain sensors, a uniaxial strain monitoring specimen was further investigated on an aluminum substrate. A sensor size of 89 × 13 mm, composed of the aramid nonwoven fabric with a CNT concentration of 1.0 wt.%, was mounted at the center of a dogbone-shaped aluminum tensile bar (152 × 25 × 2 mm, 6061-T6). This specimen (Al-1.0%-CNT) was subjected to incremental tensile cyclic loadings performed using an Instron 5567 universal testing machine at a fixed displacement rate of 1.3 mm/min. The loading protocol consisted of six steps with resulting stress amplitudes of 23.5, 47.1, 70.6, 106, 141, and 188 MPa. A 47.1 MPa loading-unloading cycle was placed between the 106, 141, 188 MPa steps in order to validate the electrical stability of the sensing layer. The baseline electrical resistance of this specimen was measured as 7.38 kΩ. The test specimen geometry is illustrated in Figure 2.27.

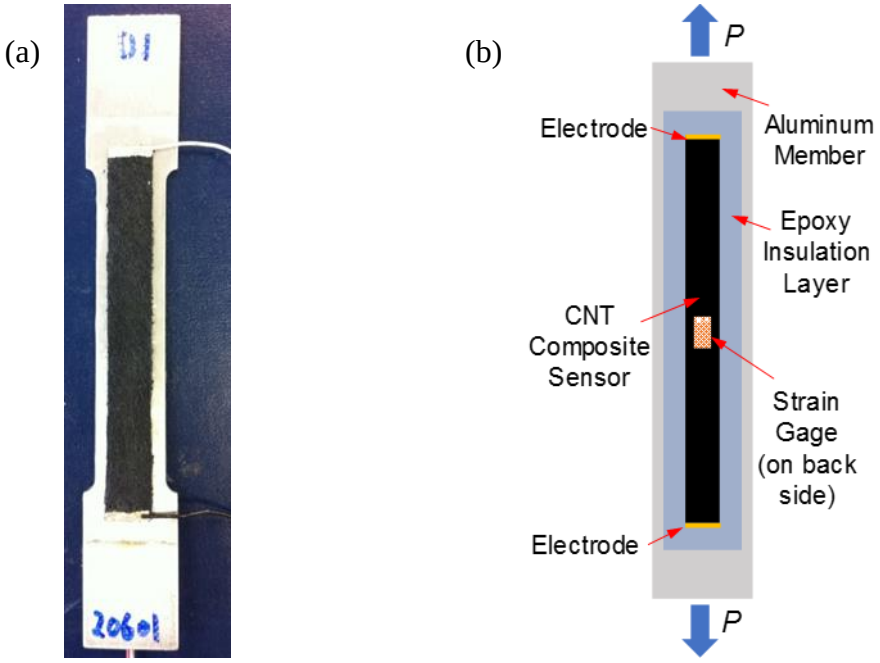

Figure 2.27: (a) Photograph of the test specimen (Al-1.0%-CNT) for elastic and plastic strain monitoring and (b) illustration of the specimen configuration (from Ref.[45]).

2.4.1.2 Case Study 2: Compressive and Tensile Strain Monitoring

To validate the monitoring capabilities of both compressive and tensile strains, a uniaxial compression and tension test was performed on an aluminum specimen with the composite sensor attached. This 64 × 10 mm sensor contains 0.75 wt.% CNT and was bonded on a 6.4 mm thick aluminum bar (152 × 25.4 mm, 6061-T6). This specimen (Al-0.75%-CNT) was subjected to a seven-step compression-tension cyclic loading at the same displacement rate as specimen Al-1.0%-CNT. The initial loading cycle resulted in a stress of ±24.8 MPa. Each loading step included two cycles with identical magnitude at the peak and a full compression-tension loading step with four individual cycles. The load steps increased from resulting stresses of 24.8 to 99.2 MPa

in tension at an even increment of 12.4 MPa and, due to the slenderness of this bar, the largest compressive load cycle resulted in a stress of 62.0 MPa after the fourth compression step. The baseline electrical resistance of this specimen was measured as 24.8 kΩ. Figure 2.28 shows the specimen configuration.

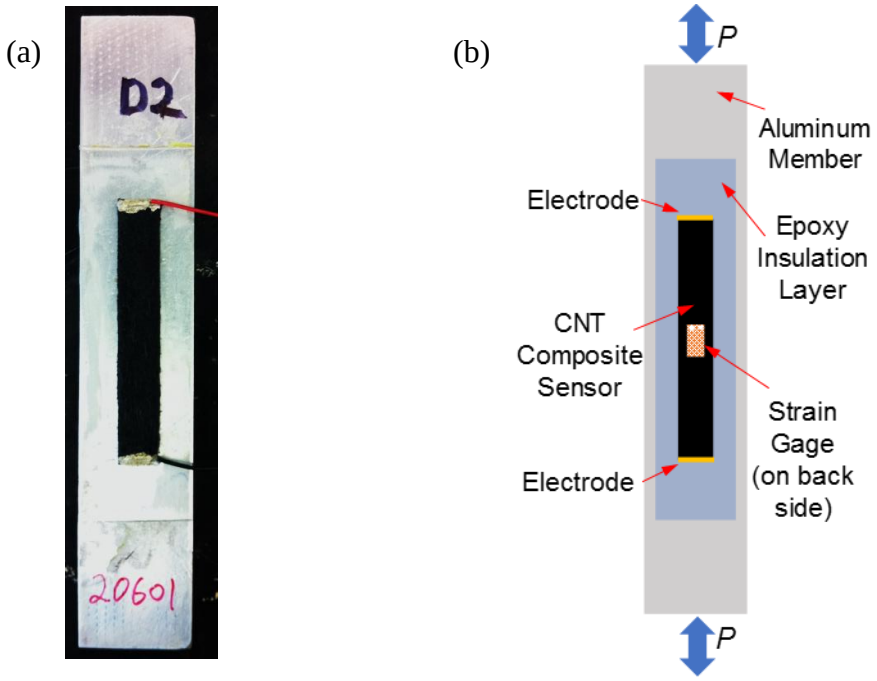

Figure 2.28: (a) Photograph of the test specimen (Al-0.75%-CNT) for tensile and compressive testing and (b) illustration of the specimen configuration (from Ref.[45]).

2.4.1.3 Case Study 3: Distributed Strain Monitoring

To investigate the sensing capability of the CNT composite sensors in the longitudinal and transverse directions, four sensors were distributed on a steel (ASTM A572 Grade 50) dogbone-shaped tensile bar (dimensions: 432 × 64 × 5 mm) with a neck area of 229 × 38 mm. The sensors are composed of the aramid nonwoven fabric

processed with 1.0 wt.% CNT loading and adhered along the longitudinal centerline of the steel bar using epoxy resin (EPON® 862) with a curing agent (EPIKURE 3223). In accordance with the sensor size as well as the electrical current sourcing direction between the electrodes, these sensors are referred to as Sensor 1-1-L, 1-1-T, 0.3-1-L and 1-0.3-T as shown in Figure 2.29. Specifically, Sensor 1-1-L and Sensor 1-1-T are 25 × 25 mm (i.e., aspect ratio = 1) and their electrical measurements are made in the longitudinal and transverse directions, respectively. Similarly, Sensor 0.3-1-L and Sensor 1-0.3-T are 32 mm in the *x*-direction and 10 mm in the *y*-direction; they are monitoring the axial strain in the longitudinal direction and the transverse strain due to Poisson's contraction, respectively. A 350 Ω bi-axial stain gage (0°/90° pattern, Micro-Measurements®) with a gage length of 6.4 mm was used to measure the strains in both principal directions. The steel specimen was then subjected to a quasi-static loading protocol using an Instron 8562 servo-hydraulic load frame. The displacement-controlled loading protocol included five continuous loading-unloading cycles: two to a stress level of 110 MPa and three to 248 MPa using a displacement rate of 0.5 mm/min and an unloading rate of 0.8 mm/min. During the second and fifth loading cycles, the stress was maintained for 30 s to examine any transient effects. The test was discontinued at a peak load corresponding to 300 MPa. In particular, when multiple sensors were measured simultaneously, the lead wires were connected to a terminal block, which is screwed on a multiplexer (Keithley 3706A system switch). This multiplexer is linked with Keithley 6430 source meter and rapidly switches channels between the four sensors to execute the electrical measurements.

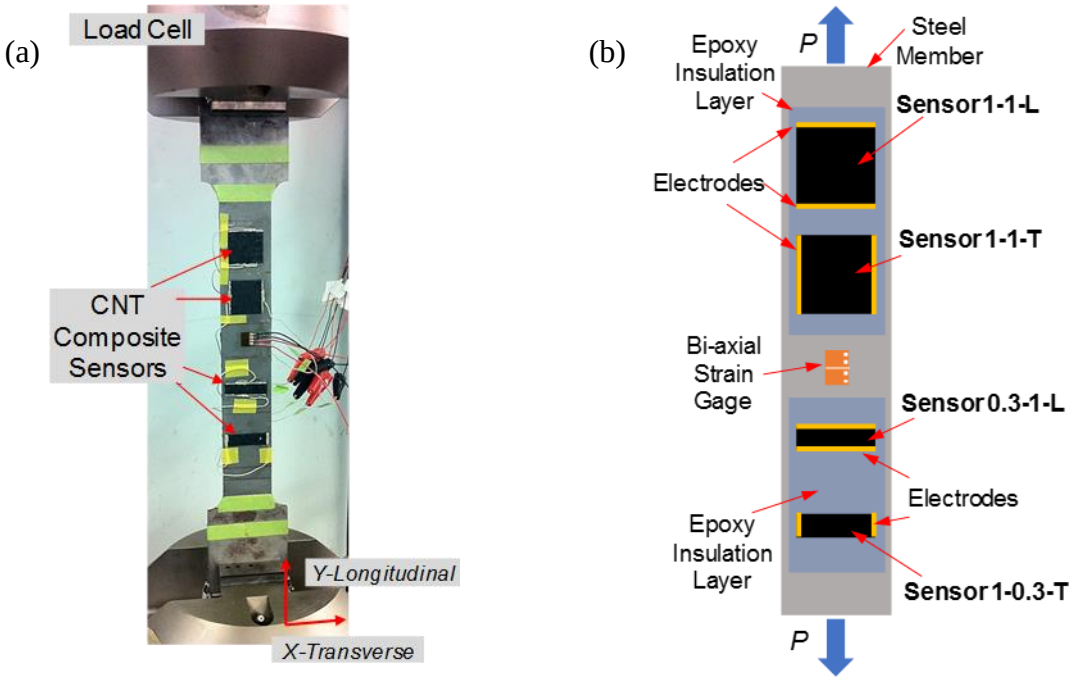

Figure 2.29: (a) Photograph of the experimental setup for distributed strain monitoring test and (b) illustration of the specimen configuration (from Ref.[45]).

2.4.2 Results

2.4.2.1 Monitoring of Elastic and Plastic Tensile Strains

Understanding the *ex situ* strain sensing response of the sensor in uniaxial tension, as well as its response while the substrate undergoes plastic deformation, is important for SHM applications. Figure 2.30a shows the transient response of the sensor (Al-1.0%-CNT) due to applied tensile deformation. This specimen undergoes elastic deformation in the first 12 applied load cycles without permanent strain change. The response of the sensor directly correlates to the elastic strain. Plastic deformation of the aluminum occurs beyond 0.3% strain, which is at 75% of the elastic limit of the sensor. There is a permanent deformation of 0.52% strain at the end of this cycle. In

addition to the plastic strain that occurs, this deformation is near the elastic limit of the CNT composite sensor, resulting in a larger sensitivity to the permanent deformation in the last cycle. Specifically, there is a permanent electrical resistance change of 1.2% (or 88 Ω in real resistance). It is clear that the trends in the resistance response of the attached composite sensor and strain measurements are very comparable and there are no resistance drifts observed in the electrical response of the sensor. Figure 2.30b shows the piezoresistive response of the CNT composite sensor during the full loading profile. As the aluminum bar begins to deform plastically, resistance increases nonlinearly with strain and a permanent resistance change was found at the end of the loading corresponding to a strain of 0.52%. The evolution of the plastic deformation of the specimen is comprehensively reflected by the trend of the electrical resistance response, which is desirable. The bottom inset of Figure 2.230b shows the linear elastic piezoresistive response corresponding to the first 12 applied elastic load cycles. It can be observed that under elastic loading, the piezoresistivity of the sensor (GF = 1.44) is quite constant compared to the strain gage measurement, which is promising.

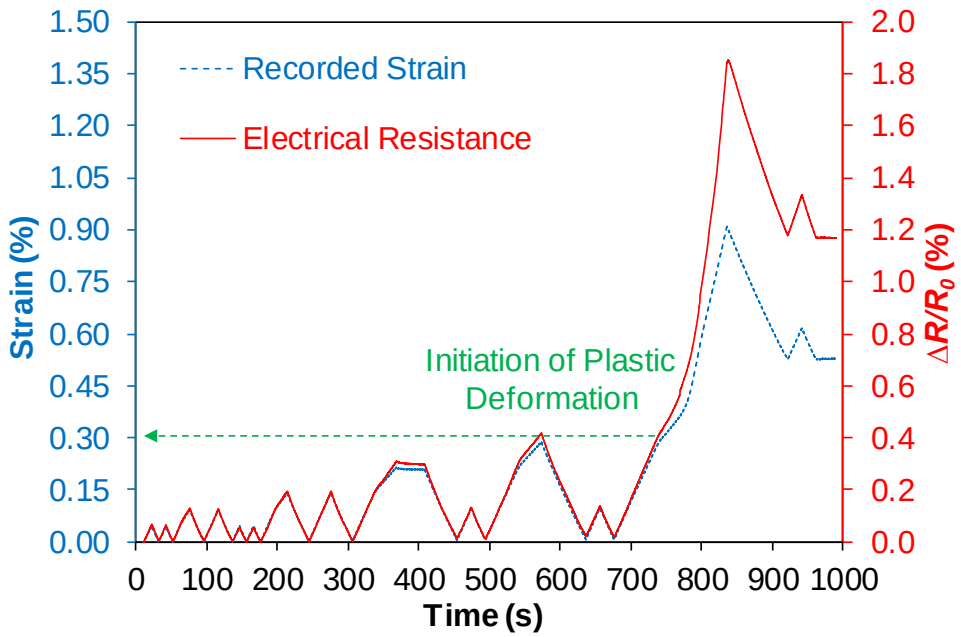

(a)

Figure 2.30: (a) Transient resistive response of Specimen Al-1.0%-CNT during a full cyclic loading test, showing the close correlation between strain and resistance up to plastic deformation of the specimen and (b) the resistance change-strain response of the sensor (Bottom inset: elastic piezoresistive response) (from Ref.[45]).

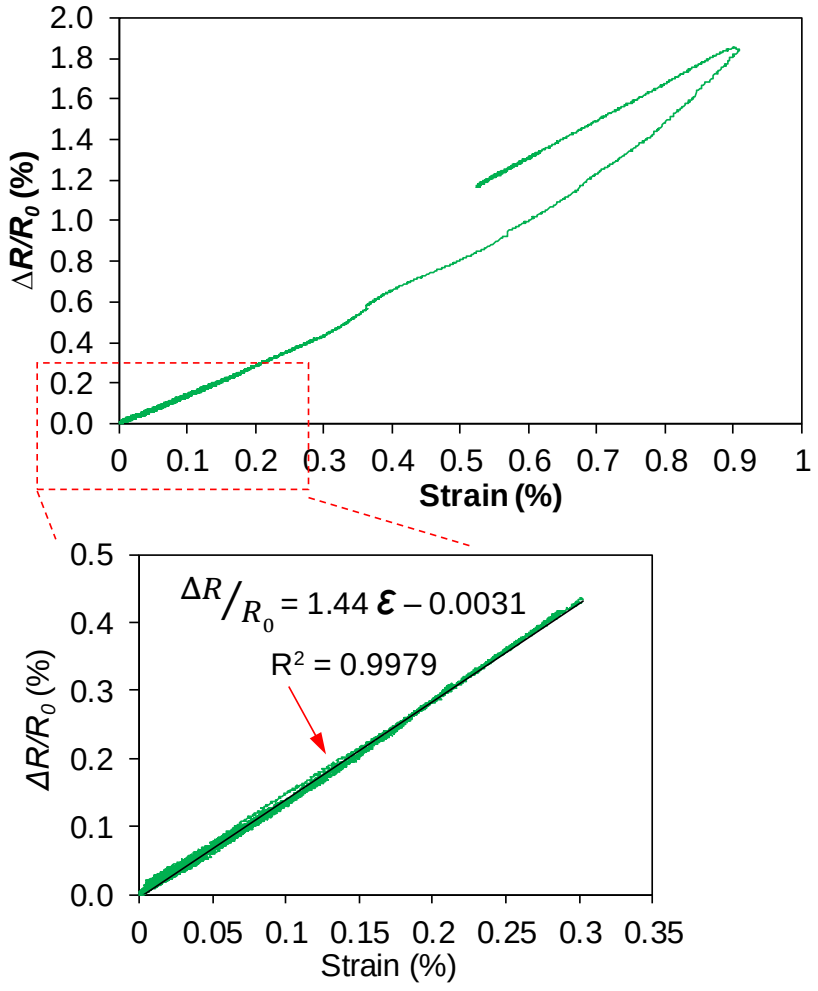

(b)

Figure 2.30: continued (from Ref.[45]).

2.4.2.2 Monitoring of Compressive and Tensile Strains

For specimen Al-0.75%-CNT, Figure 2.31a shows the tensile and compressive elastic resistive response of the sensor in real-time under the prescribed loading cycle. The peak tensile strains are +0.14% and minimum compressive strains are −0.08%, which are all in the elastic range of the aluminum member. Under compression, the

nanotube-nanotube tunneling gaps decrease resulting in more conductive pathways and then the reduced electrical resistance of the CNT composite sensor. It can be seen that under the compression-tension cyclic loading protocol, the recorded electrical resistance displays very close correlations to the member strains. The sensor shows strong electrical stability as well as negligible amount of baseline resistance change among all compression-tension loading steps in real-time.

From Figure 2.31b, it can also be seen that the piezoresistive response of the CNT composite sensor displays strong linearity for both compressive and tensile strains with a single gage factor, GF = 1.80 which is close to the gage factor (GF = 1.90) of the group of sensors with 0.75 wt.% CNT loading characterized in Section 2.3.5.3, indicating a high degree of repeatability. These results are desirable and facilitate applications of this fabricated composite sensors for future SHM.

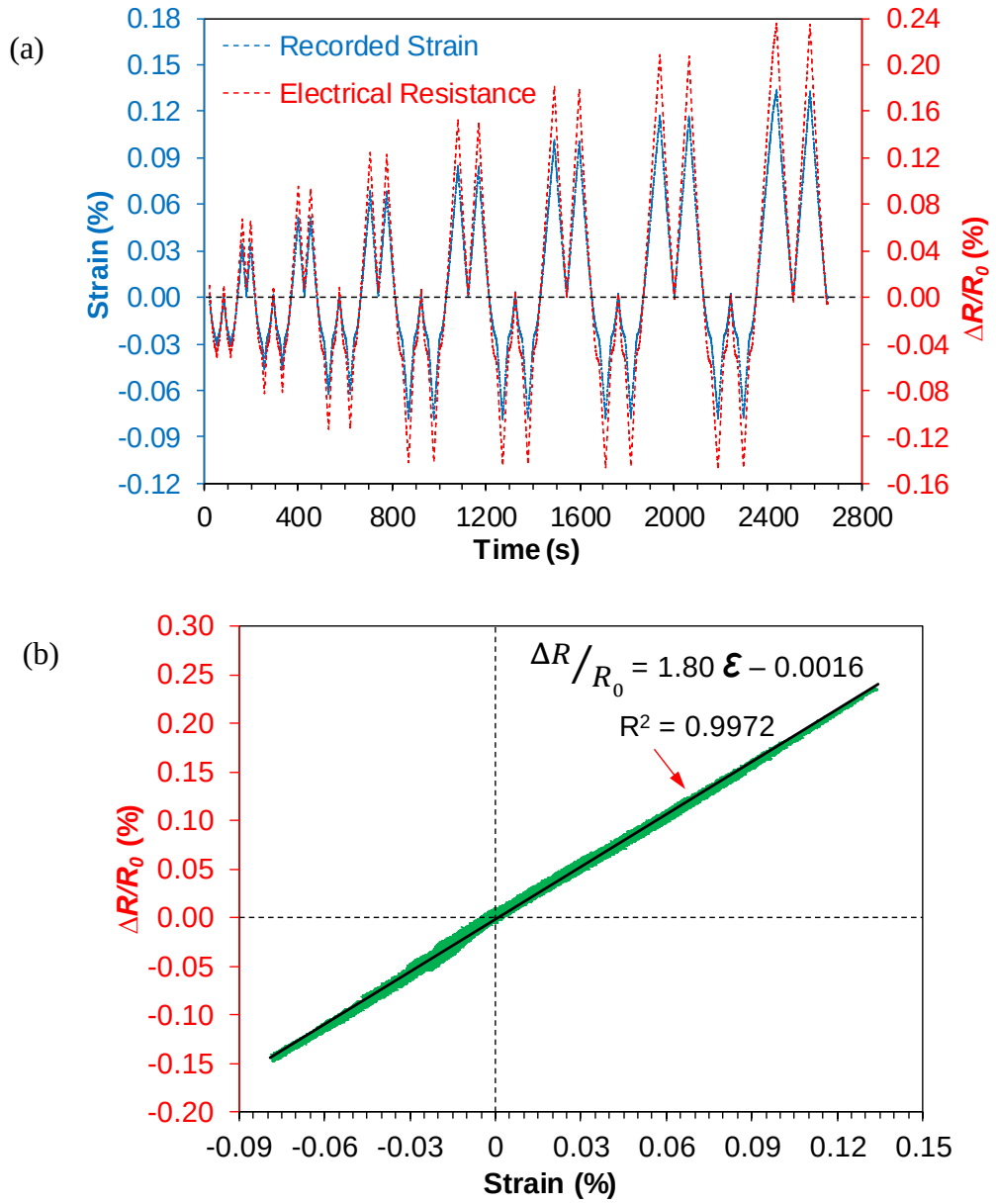

Figure 2.31: Linear-elastic resistive response of CNT composite sensor on Specimen Al-0.75%-CNT according to applied compression-tension cyclic loads: (a) real-time response under cyclic loading and (b) linear piezoresistive behavior under tension-compression loading (from Ref.[45]).

2.4.2.3 Monitoring of Distributed Longitudinal/Transverse Strains

With the *ex situ* uniaxial strain sensitivity of the sensor established previously, enabling the distributed sensing capability of the sensor for multidirectional strain monitoring, is of great importance for practical SHM applications. Figure 2.32a shows the mechanical response of the steel member subjected to a longitudinal tensile stress as well as its transverse strain response due to Poisson's contraction. It can be seen that this specimen deforms elastically under the applied loading. The corresponding sensing responses of the four distributed CNT composite sensors are displayed in Figure 2.32b. All show a strong linear response where the piezoresistivity of Sensors 1-1-T (GF = −3.95) and 1-0.3-T (GF = −2.76) in the transverse direction is higher compared to Sensors 1-1-L (GF = 1.41) and 0.3-1-L (GF = 1.21) in the longitudinal direction. Although the strain in the transverse direction is compressive, the resistance of the sensing increases, resulting in a negative gage factor. Unlike a traditional strain gage, the CNT network is random and shows sensitivity to both transverse and longitudinal strain. At the nanoscale there are changes in tunneling gaps associated with both transverse and tensile strains in the sensor. In this case the longitudinal strain is much higher than the transverse strain. As a consequence, the net increase in the electrical tunneling gaps is dominated by the strain in the longitudinal direction resulting in an increase in resistance in both directions. In addition, under the same strain field, longer conductive pathways along the longitudinal strain direction attract more changes in CNT-to-CNT tunneling gaps, which result in the higher strain sensitivity in Sensor 1-1-L than Sensor 0.3-1-L.

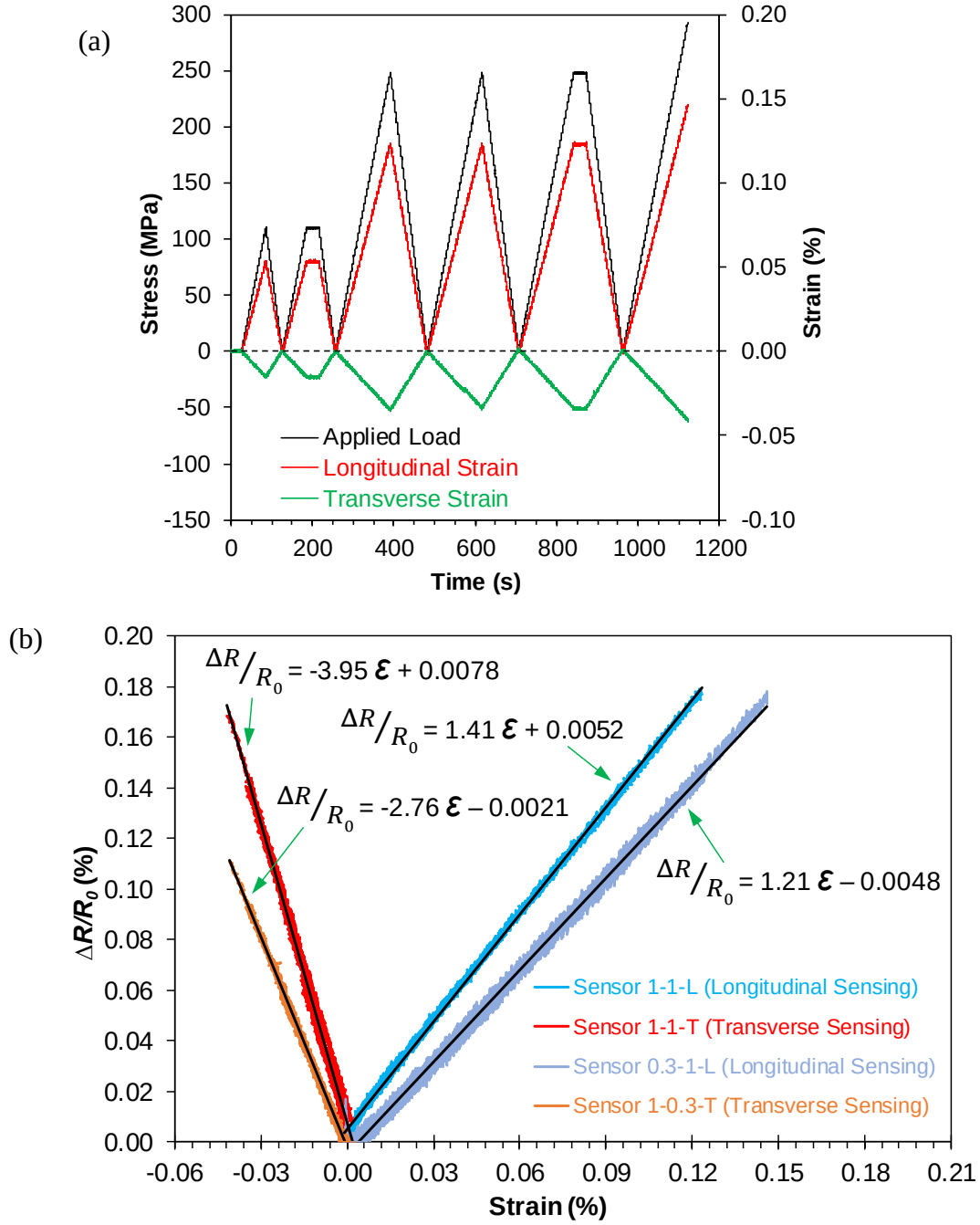

Figure 2.32: (a) Applied load and longitudinal and transverse strain of the steel member and (b) the strain sensing responses of the four sensors, showing the linearity and gage factors estimated using linear least squares curve fitting (from Ref.[45]).

2.5 Summary and Conclusions

Chapter 2 presents the processing and characterization of the proposed distributed strain sensor for SHM using CNT-based nonwoven composites. A simple two-step method to fabricate CNT-based composite strain sensors is introduced. The microstructure, mechanical properties, and the sensing mechanisms and *in situ* piezoresistive responses of the as-fabricated nanocomposite are fully characterized. The tensile and compressive strain sensing capabilities of this nanocomposite for *ex situ* distributed SHM sensors are also demonstrated.

This chapter has established a simple and cost-effective two-step approach for the manufacturing of novel carbon nanotube (CNT)-based piezoresistive composites that can be used as strain sensors for structural health monitoring (SHM) applications. This technique is readily scalable for field applications and has a high degree of application flexibility. The nanotube-based strain sensors have been successfully fabricated by, first, coating nanotubes onto an aramid nonwoven carrier fabric using a CNT-based fiber sizing agent (i.e., the 'wetting' process) followed by infusing epoxy resin into the fabric to hold the nanotube network in place (i.e., the 'drying' process). Comparing with nanotube-based films (i.e., buckypaper), the proposed nonwoven composite sensors in this study have a much lower concentration of CNTs, which will substantially reduce cost and facilitate engineering applications.

Next, a preliminary study for down-selecting the most suitable nonwoven carrier fabric was performed experimentally. The aramid fabric was selected and further studied due to the observed high sensitivity and stability. A microscopic investigation of the CNT-based nonwoven composite system was also conducted to understand the microstructure of the composite sensors. It was found that the selectively integrated CNT networks in the fiber/matrix interphase region can

effectively enhance the electrical conductivity of the composite at a very low percolating threshold of 0.015 wt.% nanotubes, attributed to a double percolating mechanism.

In addition, mechanical, *in situ* electrical and AE characterization of the CNT-based nonwoven sensing composites was performed under uniaxial tensile loadings. For the first time, the CNT networks were successfully used to study the failure mechanisms of nonwoven composites and clearly demonstrate a two-stage damage progression, validating the self-sensing capability of the CNT-based nonwoven composites. A series of coupon level characterizing tests were conducted and the results have proven that the proposed composite sensors are mechanically robust and have linear piezoresisitivity up to 0.4% strain. In specific, linear piezoresistive responses with an elastic gage factor (GF) of 1.90 and a nonlinear GF of 5.34 corresponding to the longitudinal strains, were obtained for these CNT composite sensors.

Lastly, three case studies that used the composite sensors for *ex situ* strain monitoring of metal members were performed. The sensors' resistive responses corresponding to elastic and plastic strains, compressive and tensile strains, as well as distributed strains were investigated. For the proposed CNT composite sensors, strong linearity in the piezoresistive response due to elastic tensile and compressive strains were observed and the permanent electrical resistance change corresponding to plastic deformation was also identified. The transverse sensitivity of the sensor was established and shows negative piezoresistivity (with an elastic gage factor, GF = −3.95) in the transverse direction. In addition, the real-time sensing capacity of these sensors was further verified.

REFERENCES

1. Lünenschloss J, Albrecht W. Non-woven bonded fabrics: Ellis Horwood, 1985.

2. Hull D, Clyne T. An introduction to composite materials: Cambridge university press, 1996.

3. Hull D. Fractography: observing, measuring and interpreting fracture surface topography: Cambridge University Press, 1999.

4. Rios-Soberanis CR, Cruz-Estrada RH, Rodriguez-Laviada J, Perez-Pacheco E. Study of mechanical behavior of textile reinforced composite materials. Dyna 2012;79(176):115-123.

5. Gao L, Thostenson ET, Zhang Z, Chou T. Sensing of Damage Mechanisms in Fiber-Reinforced Composites under Cyclic Loading using Carbon Nanotubes. Advanced Functional Materials 2009;19(1):123-130.

6. Chou T. Microstructural design of fiber composites: Cambridge University Press, 2005.

7. Thostenson ET, Chou T. Aligned multi-walled carbon nanotube-reinforced composites: processing and mechanical characterization. J Phys D 2002;35(16):L77.

8. Breton Y, Désarmot G, Salvetat JP, Delpeux S, Sinturel C, Béguin F, Bonnamy S. Mechanical properties of multiwall carbon nanotubes/epoxy composites: influence of network morphology. Carbon 2004;42(5–6):1027-1030.

9. Gojny FH, Wichmann MHG, Fiedler B, Schulte K. Influence of different carbon nanotubes on the mechanical properties of epoxy matrix composites – A comparative study. Composites Sci Technol 2005;65(15–16):2300-2313.

10. Yu N, Zhang ZH, He SY. Fracture toughness and fatigue life of MWCNT/epoxy composites. Materials Science and Engineering: A 2008;494(1–2):380-384.

11. Ci L, Bai J. The reinforcement role of carbon nanotubes in epoxy composites with different matrix stiffness. Composites Sci Technol 2006;66(3–4):599-603.

12. Stauffer D, Aharony A. Introduction to percolation theory: CRC press, 1994.

13. Li C, Thostenson ET, Chou T. Dominant role of tunneling resistance in the electrical conductivity of carbon nanotube–based composites. Appl Phys Lett 2007;91(22):223114.

14. Bauhofer W, Kovacs JZ. A review and analysis of electrical percolation in carbon nanotube polymer composites. Composites Sci Technol 2009;69(10):1486-1498.

15. Kilbride Be, Coleman J, Fraysse J, Fournet P, Cadek M, Drury A, Hutzler S, Roth S, Blau W. Experimental observation of scaling laws for alternating current and direct current conductivity in polymer-carbon nanotube composite thin films. J Appl Phys 2002;92(7):4024-4030.

16. Kovacs JZ, Velagala BS, Schulte K, Bauhofer W. Two percolation thresholds in carbon nanotube epoxy composites. Composites Sci Technol 2007;67(5):922-928.

17. Rosca ID, Hoa SV. Highly conductive multiwall carbon nanotube and epoxy composites produced by three-roll milling. Carbon 2009;47(8):1958-1968.

18. Connor MT, Roy S, Ezquerra TA, Calleja FJB. Broadband ac conductivity of conductor-polymer composites. Physical Review B 1998;57(4):2286.

19. Barrau S, Demont P, Peigney A, Laurent C, Lacabanne C. DC and AC conductivity of carbon nanotubes-polyepoxy composites. Macromolecules 2003;36(14):5187-5194.

20. Laredo E, Grimau M, Bello A, Wu D, Zhang Y, Lin D. AC conductivity of selectively located carbon nanotubes in poly (ε-caprolactone)/polylactide blend nanocomposites. Biomacromolecules 2010;11(5):1339-1347.

21. Pang H, Chen Q, Bao Y, Yan D, Zhang Y, Chen J, Li Z. Temperature resistivity behaviour in carbon nanotube/ultrahigh molecular weight polyethylene composites with segregated and double percolated structure. Plastics, Rubber and Composites 2013;42(2):59-65.

22. Mao C, Zhu Y, Jiang W. Design of electrical conductive composites: Tuning the morphology to improve the electrical properties of graphene filled immiscible polymer blends. ACS applied materials & interfaces 2012;4(10):5281-5286.

23. Maiti S, Shrivastava NK, Khatua B. Reduction of percolation threshold through double percolation in melt-blended polycarbonate/acrylonitrile butadiene styrene/multiwall carbon nanotubes elastomer nanocomposites. Polymer Composites 2013;34(4):570-579.

24. Xiu H, Zhou Y, Dai J, Huang C, Bai H, Zhang Q, Fu Q. Formation of new electric double percolation via carbon black induced co-continuous like morphology. RSC Advances 2014;4(70):37193-37196.

25. Thongruang W, Spontak RJ, Balik CM. Bridged double percolation in conductive polymer composites: an electrical conductivity, morphology and mechanical property study. Polymer 2002;43(13):3717-3725.

26. Balberg I, Anderson C, Alexander S, Wagner N. Excluded volume and its relation to the onset of percolation. Physical review B 1984;30(7):3933.

27. An Q. Electrophoretic deposition of ultrasonicated and functionalized nanomaterials for multifunctional composites. PhD, University of Delaware, 2016.

28. Rausch J, Zhuang R, Mäder E. Surfactant assisted dispersion of functionalized multi-walled carbon nanotubes in aqueous media. Composites Part A: Applied Science and Manufacturing 2010;41(9):1038-1046.

29. Rausch J, Mäder E. Health monitoring in continuous glass fibre reinforced thermoplastics: Manufacturing and application of interphase sensors based on carbon nanotubes. Composites Sci Technol 2010;70(11):1589-1596.

30. Tallman TN. Conductivity-Based Nanocomposite Structural Health Monitoring via Electrical Impedance Tomography. PhD, University of Michigan, 2015.

31. Thostenson ET, Chou T. Carbon nanotube networks: sensing of distributed strain and damage for life prediction and self healing. Adv Mater 2006;18(21):2837-2841.

32. Thostenson ET, Chou T. Real-time in situ sensing of damage evolution in advanced fiber composites using carbon nanotube networks. Nanotechnology 2008;19(21):215713.

33. Thostenson ET, Chou T. Carbon nanotube-based health monitoring of mechanically fastened composite joints. Composites Sci Technol 2008;68(12):2557-2561.

34. Nofar M, Hoa S, Pugh M. Failure detection and monitoring in polymer matrix composites subjected to static and dynamic loads using carbon nanotube networks. Composites Sci Technol 2009;69(10):1599-1606.

35. Gao L, Thostenson ET, Zhang Z, Chou T. Coupled carbon nanotube network and acoustic emission monitoring for sensing of damage development in composites. Carbon 2009;47(5):1381-1388.

36. Bandarian M, Shojaei A, Rashidi AM. Thermal, mechanical and acoustic damping properties of flexible open-cell polyurethane/multi-walled carbon nanotube foams: Effect of surface functionality of nanotubes. Polym Int 2011;60(3):475-482.

37. Basirjafari S, Malekfar R, Esmaielzadeh Khadem S. Low loading of carbon nanotubes to enhance acoustical properties of poly (ether) urethane foams. J Appl Phys 2012;112(10):104312.

38. Verdejo R, Stämpfli R, Alvarez-Lainez M, Mourad S, Rodriguez-Perez M, Brühwiler P, Shaffer M. Enhanced acoustic damping in flexible polyurethane foams filled with carbon nanotubes. Composites Sci Technol 2009;69(10):1564-1569.

39. Park M, Kim H, Youngblood J,P. Strain-dependent electrical resistance of multi-walled carbon nanotube/polymer composite films. Nanotechnology 2008;19(5):055705.

40. Chang F, Wang R, Yang H, Lin Y, Chen T, Huang S. Flexible strain sensors fabricated with carbon nano-tube and carbon nano-fiber composite thin films. Thin Solid Films 2010;518(24):7343-7347.

41. Wichmann MHG, Buschhorn ST, Böger L, Adelung R, Schulte K. Direction sensitive bending sensors based on multi-wall carbon nanotube/epoxy nanocomposites. Nanotechnology 2008;19(47):475503.

42. Hu N, Karube Y, Yan C, Masuda Z, Fukunaga H. Tunneling effect in a polymer/carbon nanotube nanocomposite strain sensor. Acta Materialia 2008;56(13):2929-2936.

43. Hu N, Karube Y, Arai M, Watanabe T, Yan C, Li Y, Liu Y, Fukunaga H. Investigation on sensitivity of a polymer/carbon nanotube composite strain sensor. Carbon 2010;48(3):680-687.

44. Zhang W, Suhr J, Koratkar N. Carbon nanotube/polycarbonate composites as multifunctional strain sensors. Journal of nanoscience and nanotechnology 2006;6(4):960-964.

45. Dai H, Thostenson ET, Schumacher T. Processing and characterization of a novel distributed strain sensor using carbon nanotube-based nonwoven composites. Sensors 2015; 15(7):17728-17747.

Chapter 3

SPATIAL DAMAGE DETECTION AND IMAGING USING A DISTRIBUTED CARBON NANOTUBE-BASED COMPOSITE SENSOR COMBINED WITH ELECTRICAL IMPEDANCE TOMOGRAPHY

Significant portions of this chapter are already published in a peer-reviewed journal:

- *Ref.[55]: "A novel methodology for spatial damage detection and imaging using a distributed carbon nanotube-based composite sensor combined with electrical impedance tomography". Journal of Nondestructive Evaluation 35(2):1-15 (2016).*

3.1 Introduction

As introduced in Section 1.1, the traditional nondestructive evaluation & testing (NDE&T) methods of the general structural health monitoring (SHM) systems that normally rely on point-type measurements, are coming to be deficient in providing useful information on structural damages and performance level of inspected structures due to lacking coverage, low robustness of sensors, impropriate operations of practitioners, application difficulties, complex data interpretations and indirect representation of results [1,2]. An innovative NDE technology with features of spatial detection, accurate and sensitive response, durable working life, fast data processing and visual outputs, is always demanded in the community of structural engineering to obtain instant information on health of in-service structures so as to ensure their long-term safety and reliability timely. To establish this ideal NDE methodology, both the sensors and the implemented sensing algorithms need to be optimized and well incorporated between each other.

Recent advances in composite materials have taken advantage of both nanotechnology and composite engineering and created a new era for developing novel and multifunctional composite sensors that possess high sensitivity and excellent mechanical response [3-6] which are suitable for NDE and SHM applications. As reviewed in Section 1.3 of Chapter 1, numerous researchers have investigated and characterized the electromechanical behaviors of CNT-based composites [5]. Experimental results have validated the feasibility and demonstrated great potential of employing CNT-based composites as distributed strain/damage sensors [7-13] in light of their extraordinary piezoresistivity [14], durability [15], and application versatility [16]. However, most of these experiments are able to only represent qualitative results that the location and magnitude of the strain/damage cannot be determined due to the implementation of limited sensing algorithm using two- or four-wire resistance measurements.

To optimize the performance of CNT-based nanocomposite sensors, a more advanced and powerful sensing scheme is needed. One approach to locate and image damage on a structure is by using a series of one-dimensional measurements collected from a two-dimensional (2-D) sensing area covered by densely-spaced strain gages [17] or from the quasi-distributed surface electrodes on an electrically conductive composite panel [18]. However, this quasi-2-D algorithm compromises the results by confining the possible damage locations to the grid points of the measurements and is also limited by the density of the grid array employed. That is, sparse arrays can only produce limited amount of interpolating points, resulting in very coarse estimation of locating damage. Meanwhile, dense arrays are prohibitively burdensome to be implemented for field applications.

Fortunately, electrical impedance tomography (EIT) is a noninvasive, and true 2-D imaging algorithm that is able to execute visually interpretative outputs of measurements and has been recently studied to perform spatial damage evaluation on fiber reinforced composite plates [19-23], nanocomposites [24-26] and concrete members [27-30]. Nevertheless, the results from these studies are influenced by the anisotropic conductivity of the sensors used such that relatively low resolution and high background noise are observed in the final EIT reconstructions [19-23,26]. Additionally, field applications may be considerably limited due to the low sensitivity of the sensor, vulnerability to environmental effects [24,28,29], and also fabrication challenges [19,21,22,24,25].

In this chapter, a 2-D CNT-based damage sensor was first fabricated following the previously established manufacturing process of CNT-based nonwoven composites. Due to the nanoscale size of CNTs combined with their large aspect ratio (length/diameter), an electrically conductive network can be established in the CNT-based composites by integrating small amounts of CNTs via coating the nonwoven carrier fabric [13]. This spatial, skin-like composite sensor can be adhered to virtually any shape to detect deformation and damage and is also mechanically robust and electrically isotropic due to the random, nonwoven structure. Then, a series of boundary electrodes were attached to the sensor to allow measurements of the resistance changes in the CNT network across the entire 2-D sensing area. By assuming that damage on the sensor directly affects its conductivity, a difference imaging-based EIT algorithm was implemented and tailored to offer two-dimensional maps of conductivity changes, from which damage location and size can be estimated. In particular, the reconstruction is based on a newly defined adjacent current-voltage

measurement scheme associated with 32 electrodes located along the boundary of the sensor. Subsequently, this spatial damage sensing methodology was first evaluated by introducing well-defined damage where sensing sections were either removed or narrow cuts were made on a series of sensor specimens. In addition, a more realistic damage scenario was investigated to show the capability of this methodology to detect impact damage on a composite laminate. The resulting EIT maps were also compared to visual inspection and thermograms taken with an infrared camera. Additional noteworthy this study demonstrates for the first time the feasibility of performing the difference imaging-based EIT on a CNT-based nonwoven composite sensor to estimate the location and severity of different types of damage.

3.2 Electrical Impedance Tomography (EIT)

Electrical impedance tomography has been extensively studied for medical and geological applications since the 1980s [31,32] but has been largely overlooked by the NDE and SHM communities until recently. By measuring boundary voltages EIT is able to map the internal conductivity distribution in an electrically conductive material [33-35]. In order to solve this non-linear and ill-posed inverse problem, regularization and linearization techniques as well as numerical solvers are employed to produce an approximate solution [33,34]. Until now, some pilot studies have been conducted on the applications of EIT for NDE/SHM purpose.

For instance, Baltopoulos, *et al*. [20] used a 20-electrode EIT scheme to assess damage in carbon fiber reinforced composite laminates that were subjected to indentation impacts. The reconstructed conductivity maps were produced using the least-squares method with Tikhonov regularization and showed the localized areas with reduced conductivity corresponding to impact damage. Following the same EIT

algorithm they also performed impact damage evaluation on a CNT-modified glass fiber-reinforced composite plate [19]. However, the resulting EIT reconstructions from both studies showed a significant amount of artifacts and low resolution.

Hou and co-workers [24] first employed the EIT technique on a nanocomposite (i.e., CNT-PSS/PVA thin film) for spatial damage sensing. They created a small (25 mm × 25 mm) planar sensor and used Gauss-Newton regularization algorithm for EIT imaging of etching damage. Loyola, *et al*. [21,22] used EIT for strain and impact damage monitoring of glass fiber composites by implementing a CNT-based polymer thin film as the spatial sensor. In these two experimental studies, a one-step linear reconstruction algorithm was employed and tuned to achieve normalized differential conductivity maps with optimal resolution. Additionally, Tallman and coworkers used the difference imaging algorithm and conducted 16-electrode-based EIT on a 95 mm × 95 mm carbon nanofiber epoxy plate for detecting simple through-hole damage [26] and on a 101 mm × 152 mm carbon black filled glass fiber/epoxy laminates for imaging impact damage [23]. They also performed the same EIT algorithm on a 25.4 mm × 25.4 mm flexible carbon nanofiber/polyurethane composite for imaging tactile contacts and distributed strains [36] and reported a detectability limit of 3.18 mm by EIT [37].

Some experimental studies have shown the potential of using EIT for quantitative NDE. For example, Loh, and co-workers [25] quantitatively correlated the reconstructed EIT maps with the applied strain. They monitored the surface strains of a PVC coupon axially loaded from -0.2% to 0.2% strain using a 25 mm × 25 mm CNT-based sensing film. A standard regularized Gauss-Newton algorithm was employed to solve the reconstruction of conductivity. They found a linear relationship

between the contrast of the reconstructed conductivity maps and strain. Similarly, Hou and Lynch [27] used EIT to detect the flexural strain on a conductive fiber-reinforced cementitious composite beam subjected under three-point bending. The reconstructed conductivity maps were executed at multiple strain levels and coupled to the stress-strain response of the beam in accordance with the maps' contrast.

Furthermore, some EIT applications have also been conducted to image surface cracking of concrete members [28] and to detect internal anomalies [30]. Recently, Hallaji, *et al*. [29] performed EIT on a 45.7 cm × 10.2 cm silver painted sensing area using an absolute imaging scheme to detect cracking of a concrete beam under three-point bending obtaining high-resolution quantitative reconstruction maps, which accurately show the complex and evolving crack pattern.

3.3 EIT Methodology

In order to reconstruct conductivity variation using EIT method, a forward and inverse problem are required to be solved. Figure 1 illustrates the reconstruction approach for mapping the sensor's internal distribution of conductivity change. The inputs and variables shown in the figure are defined in the following sections detailing the theoretical basis for the EIT methodology.

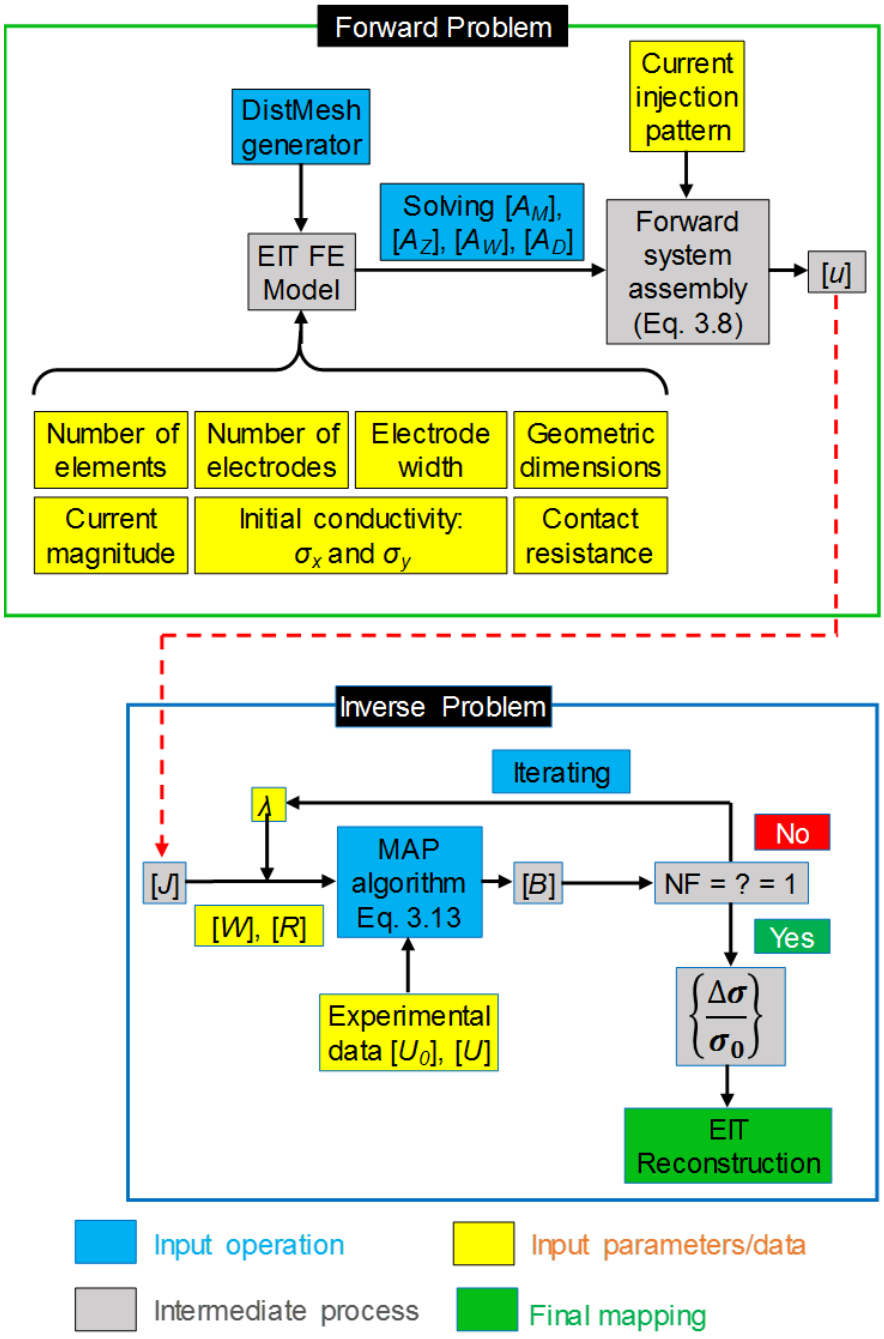

Figure 3.1: Flowchart visualizing EIT methodology implemented in this study (from Ref.[55]).

3.3.1 Forward Problem

The forward problem solves the physical model for simulating the boundary voltages due to the applied electrical current in the 2-D sensor (see Figure 3.2a, b). The geometry and boundary conditions are given and the initial conductivity distribution of the sensing medium is pre-selected. Mathematically, the relationship between the conductivity distribution (σ) inside a linear isotropic material (Ω) and the voltages (u) is governed by the following partial differential equation [34], assuming the absence of an interior current source [33]:

$$\nabla \cdot (\sigma \nabla u) = 0, \text{ in (2-D } \Omega) \tag{3.1}$$

In this study, the boundary conditions of Equation 3.1 follows the so-called complete electrode model (CEM) [36,37,40,41] which is expressed as:

$$u + z_l \, \sigma \frac{\partial u}{\partial \boldsymbol{n}} = U_l \text{ on } e_l, \text{ with } l = 1, 2, \dots, L \tag{3.2}$$

$$\int_{e_l} \sigma \frac{\partial u}{\partial \boldsymbol{n}} \, dS = I_l \text{ , on } e_l, \text{ with } l = 1, 2, \dots, L \tag{3.3}$$

$$\sigma \frac{\partial u}{\partial \boldsymbol{n}} = 0, \text{ on } \partial\Omega \setminus \bigcup_{l=1}^{L} e_l, \text{ with } l = 1, 2, \dots, L \tag{3.4}$$

$$\sum_{l=1}^{L} I_l = 0 \text{ and} \tag{3.5}$$

$$\sum_{l=1}^{L} U_l = 0 \tag{3.6}$$

where z_l is the effective contact impedance between the electrode and the object, U_l is the voltage on the electrode e_l, $\boldsymbol{n}$ is the outward unit normal and L is the number of electrodes. Specifically, Equations 3.2-3.4 define the total amount of current and voltage at boundary electrodes and for the rest of the domain by considering both the shunting effect and the contact impedance for each of the electrodes [33,34,38]. In addition, Equation 3.5 and 3.6 ensure the existence and uniqueness of the solution, respectively [33,34,38].

As extensively detailed in literature [19-22,28,30,33,34,38], finite element (FE) method is employed to numerically solve for the discrete approximation of Equation 3.1 with CEM boundary conditions. The domain (Ω) is divided into a finite number of small triangular elements as illustrated in Figure 3.2c with N_n nodes. The conductivity within each element is assumed to be constant. The weak solution (u_{FEM}) is then estimated as:

$$u \approx u_{FEM} = \sum_{i=1}^{N_n} u_i \varphi_i \tag{3.7}$$

where u_i denotes the nodal voltage of the i-th element and φ_i are the piecewise linear basis functions.

Details about the FE model used in this study are further explained in Section 3.3.3. For a finite set of injecting current, the FE system for the forward problem is commonly formulated as a system of linear equations [34,38]:

$$\begin{bmatrix} A_M + A_Z & A_W \\ A_W^T & A_D \end{bmatrix} \begin{bmatrix} u \\ U \end{bmatrix} = \begin{bmatrix} 0 \\ I \end{bmatrix} \tag{3.8}$$

where

$$[A_M]_{ij} = \int_\Omega \sigma \nabla \varphi_i \cdot \nabla \varphi_j \, dxdy \tag{3.9}$$

$$[A_Z]_{ij} = \sum_{l=1}^{L} \frac{1}{z_l} \int_{e_l} \varphi_i \, \varphi_j dS \tag{3.10}$$

$$[A_W]_i = -\frac{1}{z_l} \int_{e_l} \varphi_i \, dS \tag{3.11}$$

$$[A_D] = \text{diag}\left(\frac{|e_l|}{z_l}\right) \tag{3.12}$$

with $i, j = 1, 2, \ldots, N_n$, and $|e_l|$ is the length of the electrode e_l (in 2-D). The unknown nodal voltages [u] and boundary voltages [U] at electrodes are then solved with the known injecting current [I] at the electrodes. These calculated voltages are used to

construct the Jacobian matrix in the inverse problem as explained in the following section.

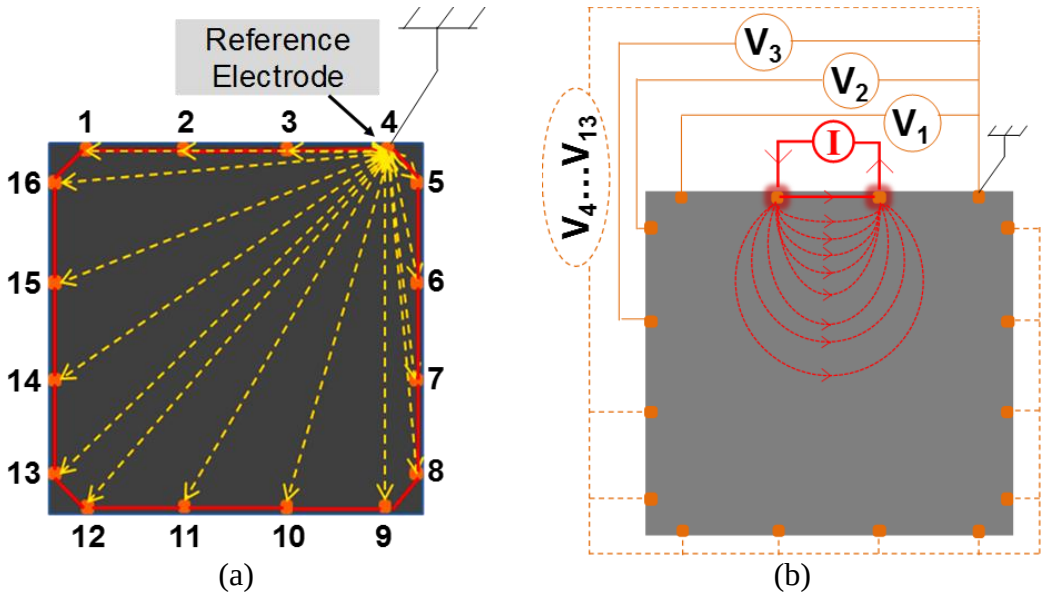

Figure 3.2: Illustration of EIT methodology adapted for the proposed CNT composite sensor: (a) current injection route (solid red line) along the boundary and voltage measurement protocol (dashed yellow lines) for a 16-electrode (boundary dots) sensor, (b) detailed illustration of the series of voltage measurements (i.e., V_1 to V_{13}) corresponding to a selected current injection electrode pair (for simplicity, only 16 electrodes are shown in (a) and (b)), and (c) FE mesh with 2336 triangular elements used in modeling of the actual 32-electrode CNT composite sensor (from Ref.[55]).

(c)

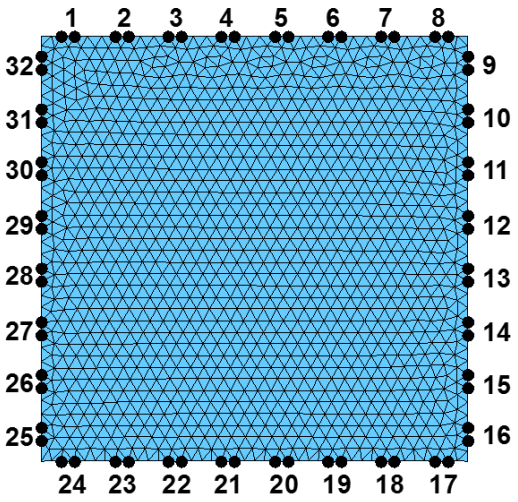

Figure 3.2: continued.

3.3.2 Inverse Problem

The inverse problem reconstructs the sensor's internal distribution of conductivity variation in accordance with the voltage measurements at all electrodes resulting from the adjacent current injection scheme (Figure 3.2a, b). This represents an ill-posed non-linear problem and the result is sensitive to modeling errors and measurement noise [33,34,38]. In this study, for solving the inverse problem a maximum a posteriori (MAP) reconstruction approach developed by Adler and Guardo [39] was employed. This MAP algorithm makes the Gaussian assumptions for the '*a posteriori*' distribution and is a one-step linearization solver. This algorithm reconstructs the normalized variation in electrical conductivity between the intact and damaged condition of the sensor. This probabilistic method yields the estimate ($[\Delta\sigma/\sigma_0]$) following the regularized inverse as [21,22,39]:

$$\left\{\frac{\Delta\boldsymbol{\sigma}}{\boldsymbol{\sigma_0}}\right\} = [(\boldsymbol{J^T W J} + \lambda \boldsymbol{R})^{-1}\boldsymbol{J^T W}]\left\{\frac{\Delta \boldsymbol{U}}{\boldsymbol{U_0}}\right\} = \boldsymbol{B}\left\{\frac{\Delta \boldsymbol{U}}{\boldsymbol{U_0}}\right\} \tag{3.13}$$

where

$$[J]_{ij} = -\int \sum_{i=1}^{2} (\nabla u)_i (\nabla u^*)_j dxdy \quad (3.14)$$

for isotropic 2-D medium [33], [*W*] is the covariance matrix containing the inverse variance of noise for every voltage measurement, [*R*] is the regularization matrix imposing conditions of smoothing and stabilization by using a spatially invariant Gaussian high-pass filter to treat the measurement noise, λ is the regularization parameter controlling the amplification of noise in the reconstructed images [21,22,39], [*B*] is the image reconstruction matrix corresponding to a given λ, [U_0] represents baseline voltage measurements from the undamaged state of the sensor, [*U*] includes the voltage measurements taken after damage has occurred, [ΔU] = [*U*]−[U_0], and [*J*] is the Jacobian matrix.

In this study, we implemented two kinds of noise models by setting [*W*] be a sparse or an identity matrix. For the sparse matrix, it is assumed that Gaussian noise exists. The identity matrix on the other hand assumes the zero-mean Gaussian white noise, ignoring the physical errors within the specimen. The regularization parameter λ is determined according to the resulted noise figure (*NF*) of MAP algorithm, in which *NF* is defined as the signal-to-noise-ratio (*SNR*) of the voltage measurements (SNR_U) divided by the *SNR* of the reconstructed conductivity (SNR_σ) according to [39]:

$$NF = \frac{SNR_U}{SNR_\sigma} = \frac{(\mathbf{1^t Z})\sqrt{N \cdot trace(\mathbf{ABW^{-1}B^tA})}}{(\mathbf{1^t ABZ})\sqrt{M \cdot trace(\mathbf{W^{-1}})}} \quad (3.15)$$

where *N*, *M*, and [*A*] are the number of elements, number of voltage measurements and the diagonal matrix composing of the areas of the elements, respectively. [*Z*] = ([*U*] - [U_0])/[U_0] and [*B*] is defined in Equation 3.13. In order not to under- or over-smooth the reconstruction, an optimal regularization parameter, $\lambda_{optimal}$, was determined when the reconstructed image results in *NF* = 1 [21,22,39].

3.3.3 Numerical Modeling

The finite element method is employed along with partial calculation routines selected from the electrical impedance tomography and diffuse optical tomography reconstruction software (EIDORS) [38,40,41] through MATLAB (R2012a, MathWorks®). The geometry and mesh generation of the FE models for the CNT-based composite sensors were developed using a MATLAB-based mesh generator, DistMesh [42]. The final mesh of the FE models consists of 1238 nodes and 2336 2-D triangular elements as shown in Figure 3.2c where each electrode was modeled as two adjoining nodes represented by black dots. By applying the MAP algorithm, the difference in voltage measurements between the undamaged and damaged states is immediately calculated and used for the EIT reconstruction. In this way, the experimental errors associated with the contact impedance, poor electrode contact and electrode mismatches do not change in the EIT measurements for both states, then by subtracting the initial measurements it's avoiding these errors influencing the reconstruction of the damaged specimens [26,39]. Here, the complete electrode model (CEM, [43]) was employed and a unit contact impedance value was assumed for all 32 electrodes. For the forward problem, the initial electrical conductivity of the FE model was considered isotropic. The final EIT reconstruction map for each specimen was achieved in correspondence to $\lambda_{optimal}$ (defined in Equation 3.15). Specifically, MATLAB was used to handle the EIT calculations based on a customized script to perform the direct inversion of the system matrix. This large sparse matrix is in the size of 1270 by 1270 (with conditioning numbers of $3 \sim 6\times10^{17}$ for the FEMs) and stored in the MATLAB program. The solution to the forward problem takes about 4 minutes of computational time on a 2.40 GHz desktop computer with 8 GB RAM and 2-3 minutes of computational time to solve the inverse problem.

3.4 Experimental Details

3.4.1 Sensor Fabrication Process

The CNT-based nonwoven composite sensors were fabricated following the previously established two-step manufacturing process as represented in Section 2.2. The 34 g/m^2 nonwoven aramid veil was employed as the non-conductive carrier fabric of CNTs. This 0.5 mm thick fabric consists of 12 mm long randomly oriented short fibers. The bulk fabric was first trimmed in to 102 mm × 102 mm square patches as shown in Figure 3.3a and then coated with nanotubes through the CNT solution casting process per Section 2.2.1. In particular, the used CNT aqueous dispersion was prepared by diluting CNT sizing agent with distilled water at the weight ratio of 1:2 (i.e., CNT sizing : water) and following with a 15-minute bath sonication session. The CNT-modified fabric was then dried at 130°C and infused with epoxy resin to form the final CNT-based composite sensor via VARTM process. The composite manufacturing setup is demonstrated in Figure 3.3b and the details are presented in Section 2.2.2. After finishing the resin infusion, the composite sensor was cured in the oven at 130°C for 6 hours. The resulting final CNT-based composite sensor has a uniform thickness of 0.47 mm across the entire area with the CNT loading of 0.75 wt.%. Through this process, each individual short fiber becomes conductive and the whole nonwoven fabric turns into a dense network of randomly connected resistors. As formerly discussed, this manufacturing process using a prepared low CNT concentration dispersion significantly reduces the material and labor cost comparing with other EIT studies using CNT-based sensors [21,22,24,25]. In addition, solely coating the nonwoven fabric significantly improves the efficiency of CNTs as forming conductive networks within the nanocomposites by concentrating the limited amount

of CNTs onto a small amount of fibers. Therefore, this approach is low cost, simple to setup and operate, and able to be easily scaled up. Specifically, the CNT layer uniformly coats the individual fibers and is supported by the nonwoven fiber architecture, forming a global random network of nanotubes and therefore attributing to an isotropic 2-D conductivity.

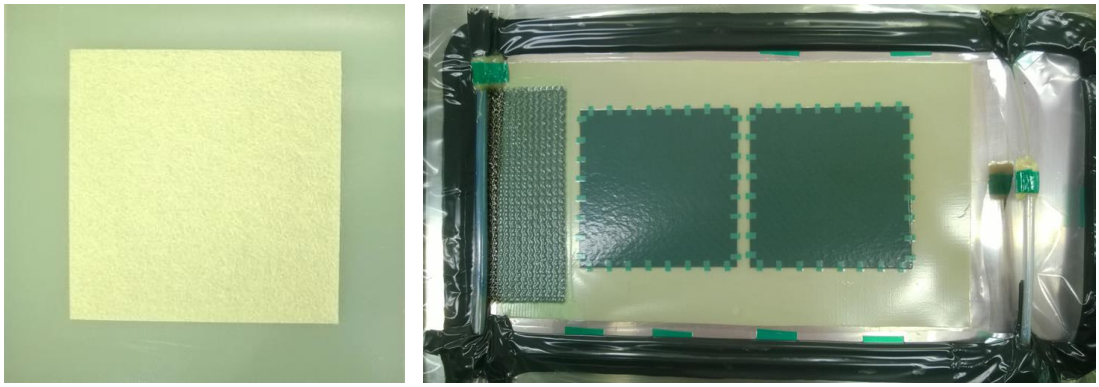

(a) (b)

Figure 3.3: Photographs showing (a) a 34 g/m^2 nonwoven aramid fabric in size of 102 mm × 102 mm for fabricating a CNT-based sensing patch, and (b) the vacuum-assisted resin transfer molding (VARTM) setup for manufacturing two square CNT-based composite sensors.

3.4.2 Preparation of Test Specimens

Boundary electrodes were applied to the sensor in order to conduct the EIT measurements (described in Section 3.3.1). A 32-electrode arrangement with eight electrodes equally spaced along each boundary was selected for this study, as shown in Figure 3.4a. For each electrode location, an area of 3.2 mm × 3.2 mm was coated with a conductive silver paint (SPI Supplies®, Structure Probe, Inc.). Two lead wires

were then attached to each electrode using a conductive epoxy (EPOXIES® 40-3900, Epoxies, Etc.). According to the manufacturer the electrical resistivity of the conductive epoxy is 0.0001 Ω-cm. The conductive epoxy was cured at 90°C for 30 minutes. Finally, the sensor was attached to a 178 mm × 114 mm × 3.2 mm glass fiber composite (G-10/FR4, Professional Plastics, Inc.) using a 5-minute epoxy (Loctite® E-00CL Hysol®, Henkel) to form the final test specimen. The non-conductive composite has an elastic modulus of 18.6 GPa and flexural strength of 379 MPa, as reported by the manufacturer. A total of three test specimens were prepared for this study with reference conductivities for Specimen 1, 2, and 3 of 3.0, 3.5 and, 3.4 S/m, respectively. Figure 3.4b shows an example of the three specimens.

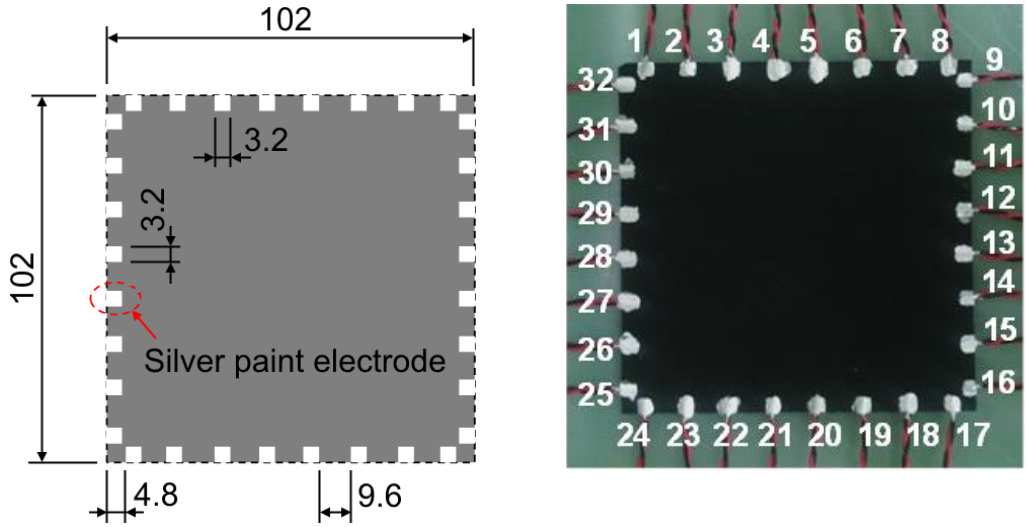

(a) (b)

Figure 3.4: (a) Illustration of the electrode array for a 32-electrode CNT composite sensor made and (b) photograph showing the final EIT specimen used in this study where CNT composite sensor is attached on a nonconductive composite. Dimensions in (mm) (from Ref.[55]).

3.4.2.1 Specimen 1: Square Holes

Three identical holes each with a size of 12.7 mm × 12.7 mm were introduced to Specimen 1 by successively removing the sensing area at three random locations. These holes introduce an infinite resistance increase in the electrical field at those locations and correspond to 1.6%, 3.1%, and 4.7% of the total sensing area. This test aimed at validating the feasibility and sensitivity of our methodology to localized damage occurring at different locations simultaneously.

3.4.2.2 Specimen 2: Simulated Crack

A 25.4 mm long narrow notch was cut using a razor-blade on Specimen 2 to introduce a local discontinuity in the sensor, simulating a crack. Figure 3.10a shows the sensor with a 0.4 mm wide cut (i.e., aspect ratio = 64). This localized damage represents 0.1% of the total sensing area. The goal of this test was to evaluate the sensitivity of this proposed methodology to detect damage with a large aspect ratio, similar to an actual crack.

3.4.2.3 Specimen 3: Impact Damage

Impact damage is a common problem for composites because of their relatively low out-of-plane strength [44]. The objective of this specimen is to examine the sensitivity of the proposed methodology to the damage severity. After specifying an impact energy level of 6.7 J/mm in accordance with ASTM-D7136 [45], Specimen 3 was impacted multiple times with 21-J nominal energy impacts using an Instron Dynatup 9200 drop weight tester with a 12.7 mm blunt hemispherical tup hitting the center of this specimen. Figure 3.5 shows the impact test setup where the specimen was clamped on along its long edge with screw bolts. The specimen was impacted six

times. After the sixth impact the tup completely perforated the composite laminate. Snapshots of the impacted specimen are shown and discussed further in Section 3.5.4.

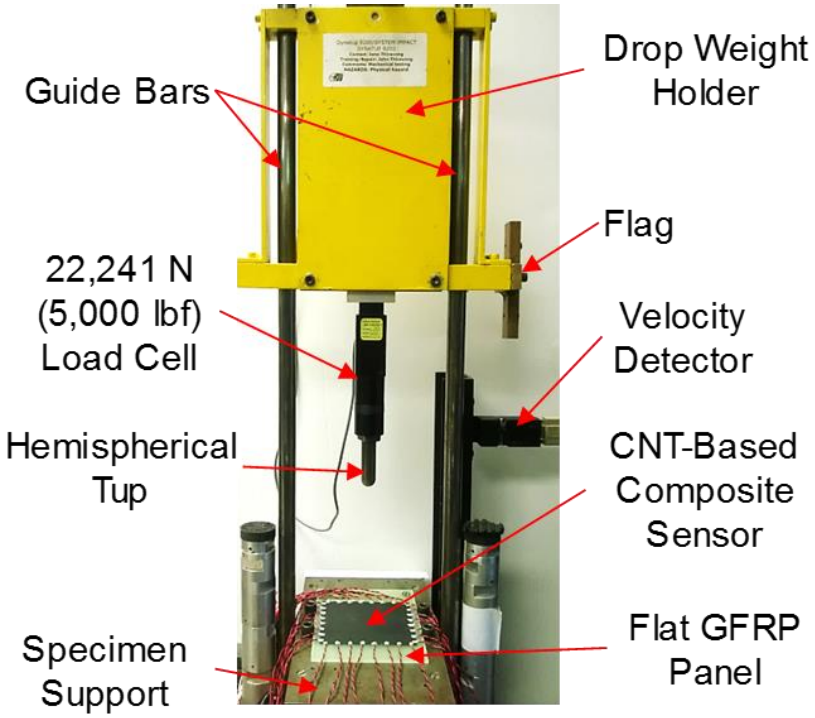

Figure 3.5: Photo of impact test apparatus with Specimen 3 (from Ref.[55]).

3.4.3 Non-Destructive Characterization

For each specimen, visual inspection, EIT measurements, and infrared (IR) thermography were performed after each impact. Prior to the initial impact boundary voltage measurements were obtained and used as the undamaged reference measurement.

3.4.3.1 EIT Measurements

For EIT measurements current was sourced using the adjacent (neighboring) pattern [31]. Compared to the traditional adjacent current-voltage schemes, we measured the voltage differences from all other remaining pairs of electrodes with respect to a reference electrode as illustrated in Figures 3.2a and 3.2b to increase the number of independent measurements and the overall sensitivity at the center of the sensor. The domain used in the EIT inversion has exactly the same dimensions as the specimen. As highlighted in Figure 3.2a the simplified sample is a 2-D square sensor with 16 electrodes, where all 16 current injection pairs are located successively along the boundary (i.e., clockwise from the first pair of electrodes #1 and #2, the second pair of electrodes #2 and #3…, to the 16th pair of electrodes #16 and #1) and the resulting voltage differences are measured from electrode #1 to #16 between the grounded reference electrode #4 shown as the yellow-dashed lines. To minimize errors caused by the contact impedance at current-carrying electrodes, only the voltage measurements taken from the pairs of electrodes not overlapping the current injecting electrodes are used in the EIT reconstruction algorithm. For example, when the current is applied between electrodes #2 and #3, as shown in Figure 3.2 (b), 13 voltage measurements are acquired and saved. In this way, total of 13 × 14 = 182 voltage measurements are obtained. Correspondingly, a complete measurement set of 29 × 30 = 870 differential voltages are acquired for the CNT-based composite sensor with 32 electrodes (shown in Figure 3.4b). Following the commonly accepted minimal contrast of the EIT approach defined in accordance with the number (N_{ivol}) of independent differential voltage measurements as [46]:

$$\text{Nominal resolution} = \frac{1}{\sqrt{N_{ivol}}} \times 100\% \tag{3.16}$$

Therefore, the proposed EIT methodology is believed to hold the minimal planar contrast of $^{1}/_{\sqrt{870}}$ = 3.4%. The data acquisition system used to perform the current-voltage measurements consists of three components: a current source meter, a voltmeter, and an electrical multiplexer as shown in Figure 3.6. These were integrated and controlled by a customized National Instruments LabVIEW program. All 64 connection wires from the test specimens (shown in Figure 3.4b) were connected into a Keithley 3750-ST terminal block attached to a Keithley 3706A multiplexer. By following the prescribed current injection pattern, a DC current was applied using a Keithley 6430 source meter via an electrode pair consisting of a current source and current sink. In order to avoid Joule heating while providing an accurate measurement with minimal noise, 10 mA was selected for all EIT experiments in accordance with the conductivity of the fabricated sensor. The resulting voltage measurements were collected using a Keithley 2182A nano-voltmeter. Electrode #8 per Figure 3.4b was assigned as the fixed ground electrode. A full set of EIT data was obtained until the current as injected to all pairs of adjacent electrodes excluding the two pairs involving the ground electrode. The initial (reference) conductivity of the specimens was determined in accordance with the average resistance measured in its horizontal (i.e., electrodes of #32 and #9, electrodes #31 and #10…, electrodes #25 and #16) and vertical directions (i.e., electrodes of #1 and #24, electrodes of #2 and #23…, electrodes #8 and #17). The conductivity of each sensor was calculated using Equation 2.4 that is defined in Section 2.3.5.1 of this dissertation.

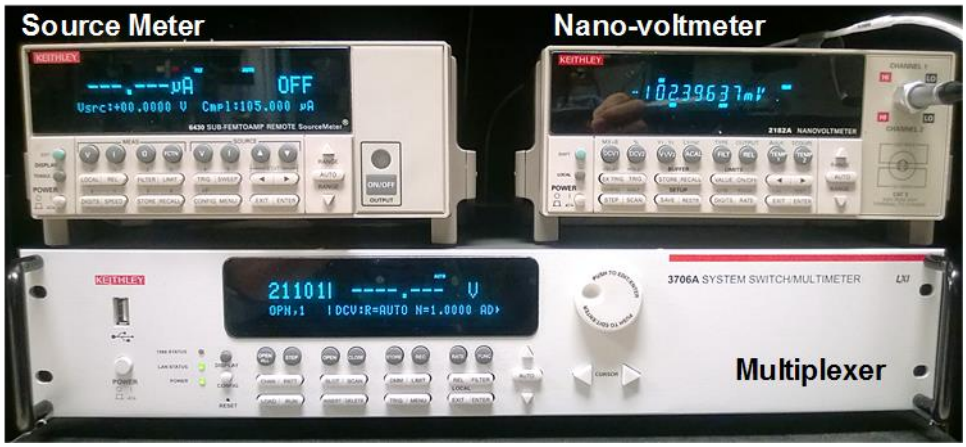

Figure 3.6: Photograph showing the data acquisition system for EIT experiments including the Keithley 6430 source meter, the Keithley 3706A multiplexer, and the Keithley 2182A nano-voltmeter.

3.4.3.2 Infrared Thermography

Infrared thermography (IRT) is a non-contact non-destructive evaluation (NDE) technique frequently used for the inspection of civil structures [47,48], electronics [49], machinery [50], and composites [51,52]. IRT utilizes an infrared detector to capture the infrared radiation emitted by an object [53]. For this study, active IRT was used to perform the post-damage inspection with the handheld IR camera (i7, FLIR® Systems, Inc.). Active IRT uses a heat source to produce thermal contrast between the damage and damage-free regions in an object. The entire specimen was heated up to a temperature of 125ºC in the oven to maintain a consistent thermal reference for all IRT images, followed by cooling outside the oven. Due to the different thermal conductivities between the composite, the adhesive layer, and the damaged and undamaged regions within the sensor, the heat energy dissipates from the specimen at different rates which results in temperature differentials in different

areas. For each specimen, multiple thermograms were taken at different temperatures and the one with the best resolution of showing the damage is reported.

3.5 Results and Discussion

3.5.1 Baseline Measurements

Prior to damaging the specimen, EIT measurements were conducted to obtain the baseline reconstruction maps and quantify the background noise level. As detailed in Section 3.3.2, two kinds of covariance matrices including the sparse and identity matrix were employed in this study. Figure 3.7a shows a photo of the undamaged sensor used for the three damage cases. As displayed in Figure 3.7b, the sparse covariance matrix leads to scattered background noise and corresponds to a $\lambda_{optimal}$ = 4.1289×10^{-7} (defined in Section 3.3.2). The identity covariance matrix produces concentrated background noise only along the boundary as presented in Figure 3.7c and the corresponding $\lambda_{optimal}$ = 0.0519. It can be seen that both approaches cause minimal background noise (< -0.5% conductivity change).

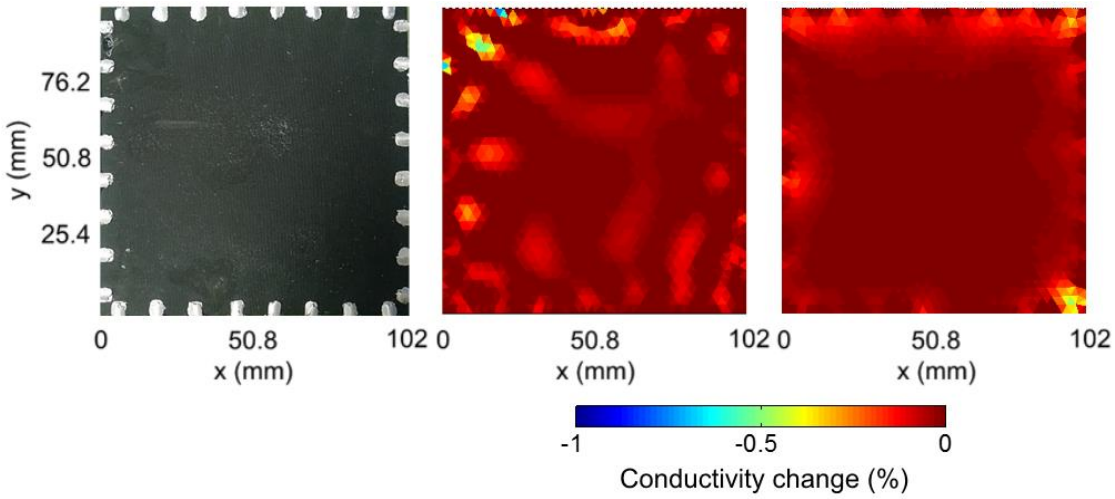

(a) (b) (c)

Figure 3.7: Baseline reconstruction results: (a) photo of undamaged sensor, and EIT reconstructions of normalized conductivity change for (b) Specimens 1 and 2 using sparse covariance matrix and for (c) Specimen 3 using identity covariance matrix (from Ref.[55]).

3.5.2 Specimen 1: Square Holes

The executed EIT reconstructions for Specimen 1 corresponding to the three-step damage test described in Section 3.4.2.1 were obtained by using a unit *NF* with $\lambda_{optimal} = 6.3939 \times 10^{-7}$ (per Section 3.3.2) and are shown in Figures 3.8a-2 through 3.8c-2. Photos of Specimen 1 for the different damage stages are shown in Figures 3.8a-1 through c-1. The dashed squares represent the holes removed from the CNT-based composite sensor. While our EIT methodology accurately maps the location of all three holes, the damage severity and shape are slightly overestimated and shown as round-shaped areas with a negative conductivity change. A possible reason may be that the sensor is treated as an electrically homogeneous object where, in reality, it likely contains some local anisotropy due to the fibrous structure. Quantitatively, the predicted damage areas are 2.87, 5.91, and 10.3% of the total sensing area, which

results in an 84, 89, and 119% overestimation compared to the actual damage size, respectively.

As damage is added to the sensor more background noise is evident in the EIT reconstructions. Figure 3.8c-3 shows an IRT temperature map for Specimen 1 for the case where all three square holes are present. The shape of the holes is distinctly represented by the darker (hot) lines indicating non-uniform heat flux occurring along the sharp edges of the discontinuities. The electrodes are also clearly observed as yellow-green dots corresponding to a much lower temperature because the thermal conductivity of the silver-filled epoxy electrodes is much higher than the rest of the specimen. In short, it is feasible to detect and map damage at multiple locations simultaneously using the proposed EIT methodology.

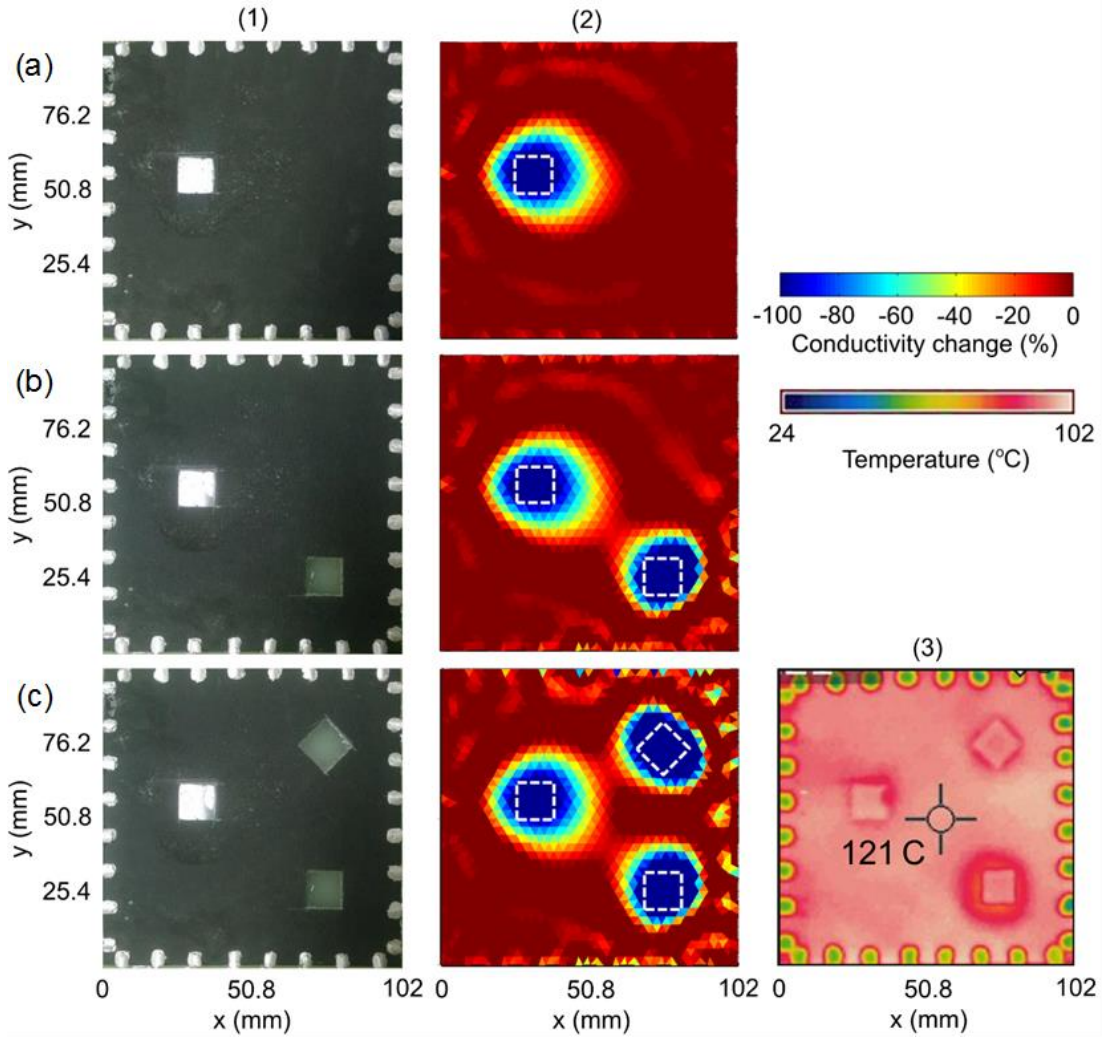

Figure 3.8: Experimental results: Columns show (1) Photo of CNT composite sensor on Specimen 1, (2) EIT reconstructions of normalized conductivity change, and (3c) temperature map from IR thermography. Rows (a) through (c) correspond to the number of square holes (from Ref.[55]).

A histogram of the elementary results from the EIT reconstruction is shown in Figure 3.9. It can be observed that the number of elements with $\geqslant$ -100% change in

conductivity are 67, 138 and 240 corresponding to one, two and three square holes, respectively. At the same time, the number of elements with no conductivity change decreases. Both trends follow a linear fashion, which validates the use of the linear reconstruction algorithm of MAP. These observations are in line with the experimental study conducted by Loyola *et al*. [21,22].

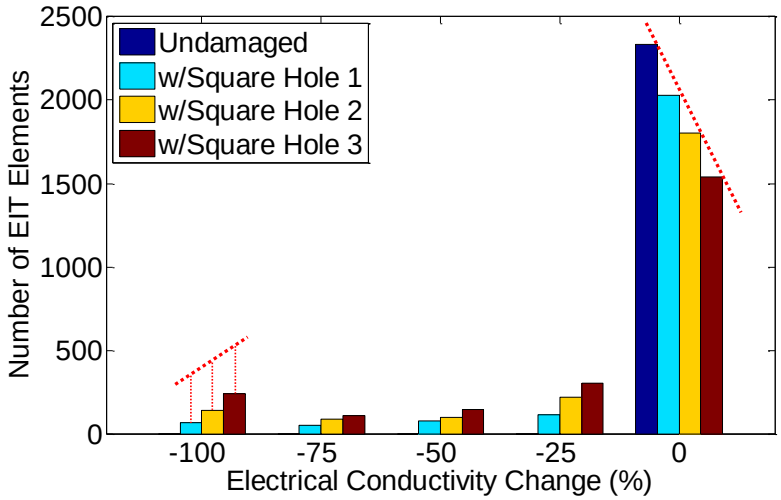

Figure 3.9: Distribution of the obtained 2336 EIT element results of Specimen 1 from each damage case (from Ref.[55]).

3.5.3 Specimen 2: Simulated Crack

A photo of Specimen 2 is shown in Figure 3.10a, and the obtained EIT reconstruction of Specimen 2, as described in Section 3.4.2.2, is shown in Figure 3.10b. Similar to the previous case, the reconstruction was executed using the sparse covariance matrix when solving the inverse problem. The $\lambda_{optimal}$ corresponding to a unit *NF* (described in Section 3.3.2) was found to be 2.0842×10^{-7}. As a result, these maps of normalized conductivity change for Specimens 1 and 2 show similar levels of

noise and types of artifacts. It can be observed that the area with ⩾ -100% conductivity change fully covers the simulated crack. In addition, the EIT reconstructed area with localized conductivity change is stretched along the diagonal direction. Figure 3.10c shows an IRT thermogram for Specimen 2. The shape of the simulated crack is shown by a darker (hot) area indicating the non-uniform heat flux caused by the discontinuity. The electrodes are also visible, similar to Specimen 1. Both EIT and IRT images are able to locate the simulated crack. Although the exact shape is not resolved there is a clear aspect ratio to the damaged area, indicating an elongated area of damage. Nevertheless, it is feasible to detect and map a discontinuity with a large aspect ratio (i.e., 64 in this case) using the proposed EIT methodology.

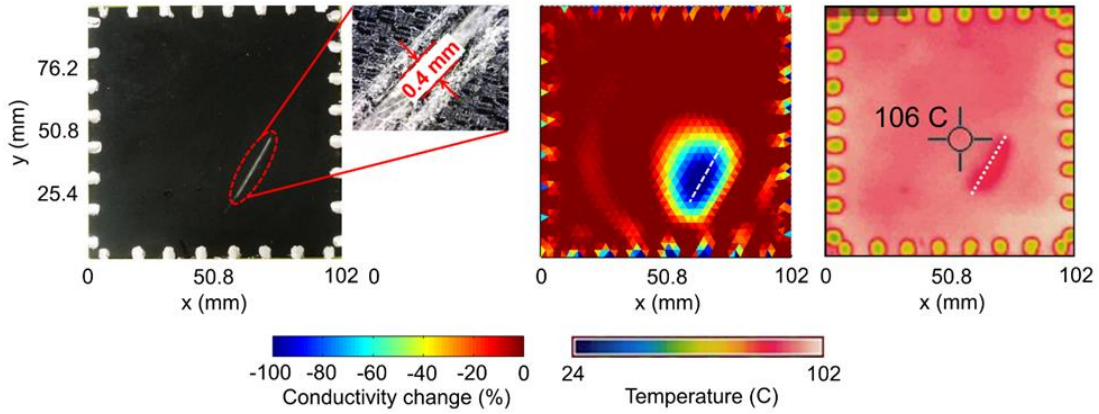

(a) (b) (c)

Figure 3.10: Experimental results: (a) Photo of CNT composite sensor on Specimen 2 with insert of artificial crack, (b) EIT reconstructions of normalized conductivity change, and (c) temperature map from IR thermography (from Ref.[55]).

A histogram of elementary results from the EIT reconstruction is plotted in Figure 3.11, in which 82% of the elements maintain unchanged in conductivity and 2.7% of them represent ⩾100% decrease in conduction due to the applied damage on the sensing skin. This is consistent with the minimal planar contrast of 3.4% defined in Section 3.4.3.1.

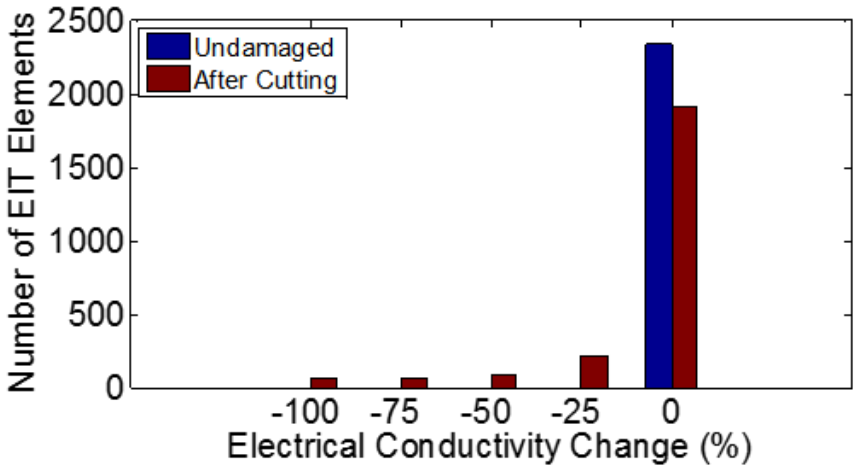

Figure 3.11: Distribution of the obtained 2336 EIT element results of Specimen 2 after applying the crack damage (from Ref.[55]).

3.5.4 Specimen 3: Impact Damage

For Specimen 3 the identity matrix was used for [*W*] to further reduce background noise. This implies that all boundary voltage measurements have uncorrelated noise (i.e., equal noise). Figures 3.12a-3 through 3.12f-3 present the resolved EIT reconstructions of Specimen 3, which show minimized boundary noise and a clean background. The $\lambda_{optimal}$ corresponding to the unit *NF* (described in Section 3.3.2) is found to be 0.0464, which is much bigger than that for the previous two

specimens. Similar to the previous two cases, the location of the impact damage is accurately predicted, although the size is slightly overestimated. Nevertheless, the proposed EIT methodology is able to capture the evolution of the accumulated damage. The color gradient of the EIT identified damage areas is consistent with the severity of the imposed damage, revealing in general a good sensitivity to damage severity. After each impact, the specimen was visually inspected. Photos of the impacted top face (sensor) and the back face (composite laminate) taken during the six-step impact test are shown in Figures 3.12a-1 through 3.12f-1 and Figures 3.12a-2 through 3.12f-2, respectively. It is evident that damage in Specimen 3 accumulates with each impact. A comprehensive description of the visual observations from the test is presented in Table 3.1 and 3.2.

The IRT temperature maps for Specimen 3 are shown in Figures 3.12a-4 through 3.12f-4. It can be observed that the temperature images for the first three impacts (Figures 3.12a-4 to 3.12c-4) do not indicate any signs of impact damage. This is likely due to the fact that heat dissipation from the hot specimen to the cold ambient air can still be accomplished by the bridging fibers within the matrix-cracked zone. After the third impact, thermal images show the impact damage (Figures 3.12d-4 to 3.12f-4), and match the location of the boundaries of the real damaged areas on the test specimen. For this test, the EIT reconstructions were able to detect damage that was barely visible. IRT, on the other hand, required severe damage (i.e., surface cracking or fiber fracture) before the damage was detectable.

Table 3.1: Visual Observations of the Impacted Face of the Specimen 3 from the Six-Step 21-J Impact Test (from Ref.[55]).

Impact No.	Impacted Face: Sensor Figure 11a-1 through f-1		
	Figure	Observations	Damage mode
1	(a-1)	3 mm-diam. dot, no sign of surface cracking	Barely visible damage
2	(b-1)	7 mm-diam. spot, no sign of surface cracking	Slightly visible damage
3	(c-1)	Barely visible ring-shaped surface cracking with 10 mm-quatrefoil-shaped central dent	Minor surface cracking
4	(d-1)	22 mm-diam. ring-shaped cracking with 12 mm-quatrefoil-shaped central dent	Surface cracking
5	(e-1)	22 mm-diam. ring cracking with 12 mm-quatrefoil-shaped central dent and cross cracking	Sever surface cracking
6	(f-1)	hole penetrated through the panel	Puncture

Table 3.2: Visual Observations of the Back Face of the Specimen 3 from the Six-Step 21-J Impact Test (from Ref.[55]).

Impact No.	Back Face: Composite Laminate Figure 11a-2 through f-2		
	Figure	Observations	Damage mode
1	(a-2)	10 mm-square spot with surface cracking	Matrix cracking
2	(b-2)	20 mm- cross-shaped spot with surface cracking	Matrix cracking
3	(c-2)	31 mm-cross-shaped spot with partial bulging, surface cracking	Delamination / Fiber fracture
4	(d-2)	41 mm-cross-shaped bulge with broken fiber at the corner	Fiber fracture
5	(e-2)	47 mm-cross-shaped bulge with broken fiber along the edge	Fiber fracture
6	(f-2)	41 mm-cross-shaped opening with broken lamina	Lamina fracture and penetration

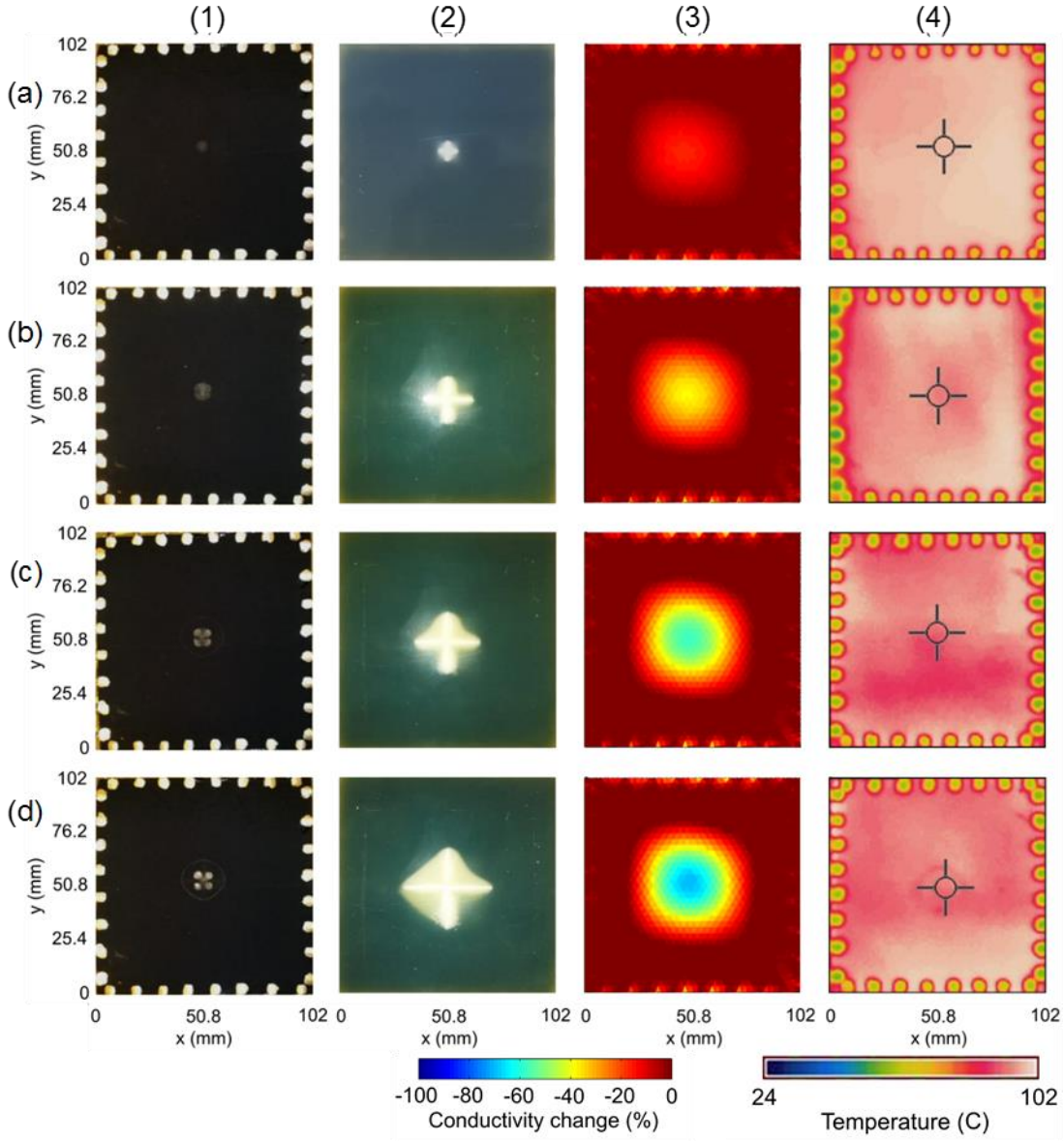

Figure 3.12: Experimental results: Columns show (1) Photo of CNT composite sensor on Specimen 3, (2) Photo of GFRP panel (backside), (3) EIT reconstructions, and (4) thermograms from IR thermography. Rows (a) through (f) correspond to the 1st to 6th 21-J impact, respectively (from Ref.[55]).

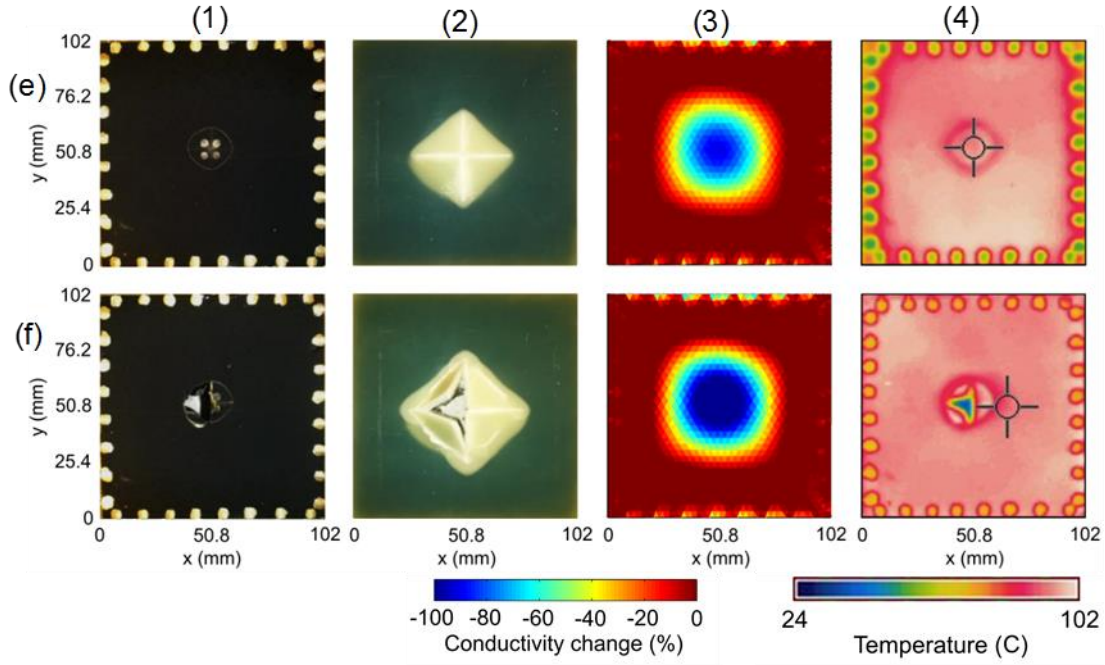

Figure 3.12: continued (from Ref.[55]).

A histogram of the elementary conductivity changes for Specimen 3 is plotted in Figure 3.13. It can be observed that the number of elements with no conductivity change in the EIT reconstructions correlate well to the six successive impacts in a bi-linear fashion, which is explained by visual observations included in Table 3.1 and 3.2. Since the first impact only causes minor damage in the specimen without permanently cracking the CNT composite sensor, the conductivity change is small at the impacted areas and a large number of conductive pathways around this area exist. Once the surface cracking is initiated after the 3rd impact, a large and direct reduction in local conductivity due to the damage on the CNT composite sensor is introduced. Next, the local change in conductivity continues declining with each successive

impact and finally reaches the infinitesimal level due to the loss of sensing area after full penetration. From these results, we demonstrate that our damage detection methodology is capable of detecting, locating, and estimating the severity of accumulating damage due to impact.

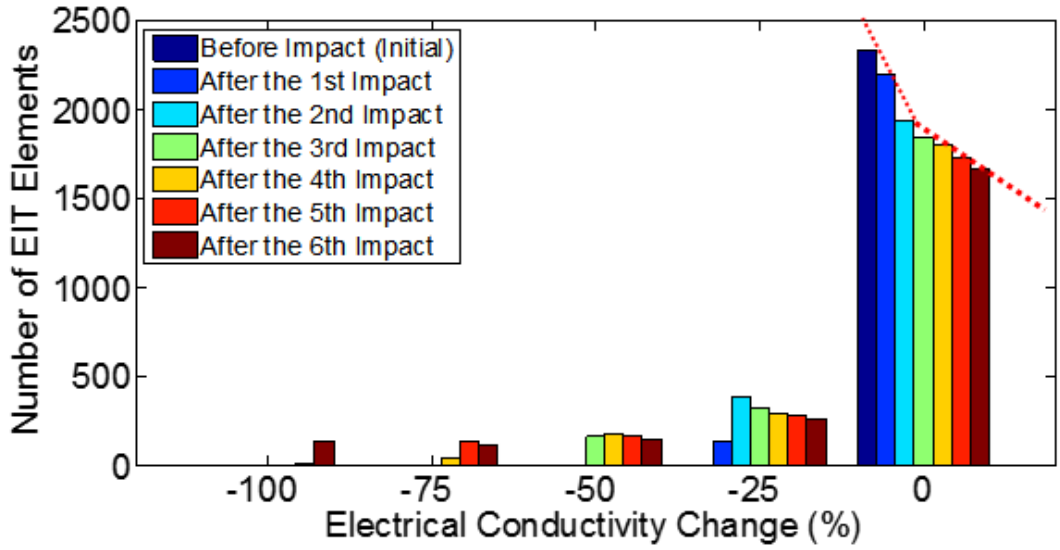

Figure 3.13: Distribution of the obtained 2336 EIT element results of Specimen 3 from each impact damage case (from Ref.[55]).

3.6 Discussion

In general it can be observed that the resolved EIT reconstructions are able to predict the location and size of damage. However, the shape is not predicted well and for the damage having a large aspect ratio, such as a crack, the area of damage is significantly overestimated. This relatively low spatial resolution is a common issue existing in all EIT applications [19-21,23,25,26,35] due to the inherent difficulties of this problem: (1) EIT is a diffusion problem where the injected electrical current propagates within the entire material [34,38], (2) solving the severely ill-posed inverse

problem continuously depends on the boundary voltage measurements, which are not always stable and accurately measurable [34], and (3) the smoothing regularization used in the inverse problem usually exaggerates the area with decreased conductivity [28].

It can also be seen from the EIT reconstructions that artifacts appear at the electrodes and are rippling around the vicinity of conductivity-changed regions in Figures 3.8 and 3.10. Obviously, these artifacts are intensified as more conductivity discontinuities are introduced as for Specimen 1. Possible reasons for this could be the anisotropic conductivity around areas under the electrodes that violates the assumption of isotropic conductivity in the FE model and results in an inappropriate interpolation of the voltage measurements or the small electrode contact impedance leads the voltage measurements at the electrode depending on the neighboring mesh's conductivity in the FE model [54]. In addition, the use of a sparse [W] (described in Section 3.3.2) in the MAP algorithm, assumes that the noise in the voltage measurements is correlated and causes relatively low measurement accuracy simulated in the inverse problem [31]. Meanwhile, the level of this correlated noise is amplified as more differential voltage measurements are associated with the enlarged regions with conductivity change (i.e., more holes on the sensor).

Additionally, $\lambda_{optimal}$ (described in Section 3.3.2) values for Specimens 1 and 2 are very small, suggesting that these specific inverse problems are close to where linear approximation is valid. After employing an identity [W] for Specimen 3, a comparatively large $\lambda_{optimal}$ is obtained. As discussed by others [20,39], large $\lambda_{optimal}$ leads the regularization to amplify large singular value decomposition (SVD) components of the calculated voltage change corresponding to the conductivity change

but to restrain the smaller SVD components. Since the large SVD components are associated with the voltage changes closer to the electrodes, therefore amplifying the large SVD components increases the contrast in the area around the electrode and results in the reduction of noise near the electrodes as shown in Figures 12a-3 through 12f-3. On the other hand, the small SVD component controls the reconstruction of conductivity at the interior of the object and to restrain them reduces the background noise and the resolution at the areas away from the electrodes in the EIT reconstruction map.

3.7 Summary and Conclusions

This chapter has presented the methodology implementing a novel carbon nanotube-based composite sensor in conjunction with electrical impedance tomography (EIT) for detection and imaging of a variety types of damage. The novel sensor is based on a CNT-modified nonwoven aramid fabric and possesses isotropic electrical conductivity, mechanical robustness, and the ability to be adhered to complex surfaces. Additionally, the manufacturing process is cost efficient and allows the sensor to be scaled up for large engineering applications. A difference imaging-based EIT algorithm was implemented and adapted to enable 2-D spatial damage sensing capability of the sensor.

A series of tests were conducted to evaluate our methodology with a newly defined adjacent current-voltage measurement scheme. Damage included: (1) square holes cut into the sensor, (2) a narrow cut simulating a crack, and (3) progressive impacts on a composite laminate. The results demonstrate that the proposed EIT-based methodology is possible to adeptly detect and locate damage as well as capture the severity of the accumulated damage. However, the size is typically overestimated and

the shape not well represented. This is a particular problem for cracks, which have a large aspect ratio. Infrared thermography (IRT) images were also taken for comparison and produced comparable results. In some cases, however, the EIT-based methodology was able to detect the initiation of damage well before it was visible with IRT. Based on these results, it is believed that the presented sensing methodology of CNT-based sensors integrated with EIT has considerable potential for SHM and NDE of civil, aerospace, and mechanical structures. In addition, the presented methodology has advanced a considerable improvement over the commonly implemented point-to-point resistance sensing methods for the conductive composite-based SHM and NDE, by enabling the spatial sensing capability.

REFERENCES

1. Huston D. Structural sensing, health monitoring, and performance evaluation: CRC Press, 2010.

2. Ettouney MM, Alampalli S. Infrastructure health in civil engineering: Theory and components, vol. 1: CRC Press, 2016.

3. Thostenson ET, Li C, Chou T. Nanocomposites in context. Composites Sci Technol 2005;65(3–4):491-516.

4. Pandey G, Thostenson ET. Carbon nanotube-based multifunctional polymer nanocomposites. Polymer Reviews 2012;52(3):355-416.

5. Zhang H, Bilotti E, Peijs T. The use of carbon nanotubes for damage sensing and structural health monitoring in laminated composites: a review. Nanocomposites 2015;1(4):167-184.

6. Ryu D. Multi-Modal, Self-Sensing, and Photoactive Structural Coatings For Sustainable Infrastructures. PhD, University of California, Davis, 2014.

7. Hu N, Fukunaga H, Atobe S, Liu Y, Li J. Piezoresistive strain sensors made from carbon nanotubes based polymer nanocomposites. Sensors 2011;11(11):10691-10723.

8. Gao L, Thostenson ET, Zhang Z, Chou T. Coupled carbon nanotube network and acoustic emission monitoring for sensing of damage development in composites. Carbon 2009;47(5):1381-1388.

9. Kang I, Schulz MJ, Kim JH, Shanov V, Shi D. A carbon nanotube strain sensor for structural health monitoring. Smart Mater Struct 2006;15(3):737.

10. Gao L, Thostenson ET, Zhang Z, Chou T. Sensing of Damage Mechanisms in Fiber-Reinforced Composites under Cyclic Loading using Carbon Nanotubes. Advanced Functional Materials 2009;19(1):123-130.

11. Thostenson ET, Chou T. Carbon nanotube-based health monitoring of mechanically fastened composite joints. Composites Sci Technol 2008;68(12):2557-2561.

12. Lim AS, Melrose ZR, Thostenson ET, Chou T. Damage sensing of adhesively-bonded hybrid composite/steel joints using carbon nanotubes. Composites Sci Technol 2011;71(9):1183-1189.

13. Dai H, Thostenson ET, Schumacher T. Processing and Characterization of a Novel Distributed Strain Sensor Using Carbon Nanotube-Based Nonwoven Composites. Sensors 2015;15(7):17728-17747.

14. Hu N, Karube Y, Arai M, Watanabe T, Yan C, Li Y, Liu Y, Fukunaga H. Investigation on sensitivity of a polymer/carbon nanotube composite strain sensor. Carbon 2010;48(3):680-687.

15. Yu N, Zhang Z, He S. Fracture toughness and fatigue life of MWCNT/epoxy composites. Materials Science and Engineering: A 2008;494(1):380-384.

16. Li C, Thostenson ET, Chou T. Sensors and actuators based on carbon nanotubes and their composites: A review. Composites Sci Technol 2008;68(6):1227-1249.

17. Yao Y, Glisic B. Detection of Steel Fatigue Cracks with Strain Sensing Sheets Based on Large Area Electronics. Sensors 2015;15(4):8088-8108.

18. Naghashpour A, Van Hoa S. A technique for real-time detecting, locating, and quantifying damage in large polymer composite structures made of carbon fibers and carbon nanotube networks. Structural Health Monitoring 2015;14(1):35-45.

19. Baltopoulos A, Polydorides N, Pambaguian L, Vavouliotis A, Kostopoulos V. Exploiting carbon nanotube networks for damage assessment of fiber reinforced composites. Composites Part B: Engineering 2015;76:149-158.

20. Baltopoulos A, Polydorides N, Pambaguian L, Vavouliotis A, Kostopoulos V. Damage identification in carbon fiber reinforced polymer plates using electrical resistance tomography mapping. J Composite Mater 2013;47(26):3285-3301.

21. Loyola BR, Briggs TM, Arronche L, Loh KJ, La Saponara V, O'Bryan G, Skinner JL. Detection of spatially distributed damage in fiber-reinforced polymer composites. Structural Health Monitoring 2013;12(3):225-239.

22. Loyola BR, Saponara V, Loh KJ, Briggs TM, O'Bryan G, Skinner JL. Spatial sensing using electrical impedance tomography. Sensors Journal, IEEE 2013;13(6):2357-2367.

23. Tallman TN, Gungor S, Wang K, Bakis CE. Damage detection via electrical impedance tomography in glass fiber/epoxy laminates with carbon black filler. Structural Health Monitoring 2015;14(1):100-109.

24. Hou T, Loh KJ, Lynch JP. Spatial conductivity mapping of carbon nanotube composite thin films by electrical impedance tomography for sensing applications. Nanotechnology 2007;18(31):315501.

25. Loh KJ, Hou T, Lynch JP, Kotov NA. Carbon nanotube sensing skins for spatial strain and impact damage identification. J Nondestr Eval 2009;28(1):9-25.

26. Tallman TN, Gungor S, Wang K, Bakis C. Damage detection and conductivity evolution in carbon nanofiber epoxy via electrical impedance tomography. Smart Mater Struct 2014;23(4):045034.

27. Hou T, Lynch JP. Electrical impedance tomographic methods for sensing strain fields and crack damage in cementitious structures. J Intell Mater Syst Struct 2008.

28. Hallaji M, Pour-Ghaz M. A new sensing skin for qualitative damage detection in concrete elements: Rapid difference imaging with electrical resistance tomography. NDT E Int 2014;68:13-21.

29. Hallaji M, Seppänen A, Pour-Ghaz M. Electrical impedance tomography-based sensing skin for quantitative imaging of damage in concrete. Smart Mater Struct 2014;23(8):085001.

30. Karhunen K, Seppänen A, Lehikoinen A, Monteiro PJ, Kaipio JP. Electrical resistance tomography imaging of concrete. Cem Concr Res 2010;40(1):137-145.

31. Harikumar R, Prabu R, Raghavan S. Electrical Impedance Tomography (EIT) and Its Medical Applications: A Review. International Journal of Soft Computing Engineering 2013;3(4):2231-2307.

32. Brown B. Electrical impedance tomography (EIT): a review. J Med Eng Technol 2003;27(3):97-108.

33. Vauhkonen M. Electrical impedance tomography and prior information. Ph.D, Univeristy of Kuopio, Finland, 1997.

34. Holder DS. Electrical impedance tomography: methods, history and applications: CRC Press, 2004.

35. Silvera-Tawil D, Rye D, Soleimani M, Velonaki M. Electrical Impedance Tomography for Artificial Sensitive Robotic Skin: A Review. Sensors Journal, IEEE 2015;15(4):2001-2016.

36. Tallman TN, Gungor S, Wang K, Bakis C. Tactile imaging and distributed strain sensing in highly flexible carbon nanofiber/polyurethane nanocomposites. Carbon 2015;95:485-493.

37. Tallman TN. Conductivity-Based Nanocomposite Structural Health Monitoring via Electrical Impedance Tomography. PhD, University of Michigan, 2015.

38. Polydorides N. Image reconstruction algorithms for soft-field tomography. PhD, University of Manchester Institute of Science and Technology, United Kingdom, 2002.

39. Adler A, Guardo R. Electrical impedance tomography: regularized imaging and contrast detection. Medical Imaging, IEEE Transactions on 1996;15(2):170-179.

40. Bera TK, Nagaraju J. A MATLAB-based boundary data simulator for studying the resistivity reconstruction using neighbouring current pattern. Journal of Medical Engineering 2013;2013.

41. Polydorides N, Lionheart WR. A Matlab toolkit for three-dimensional electrical impedance tomography: a contribution to the Electrical Impedance and Diffuse Optical Reconstruction Software project. Measurement Science and Technology 2002;13(12):1871.

42. Persson P, Strang G. A simple mesh generator in MATLAB. SIAM Rev 2004;46(2):329-345.

43. Vauhkonen PJ, Vauhkonen M, Savolainen T, Kaipio JP. Three-dimensional electrical impedance tomography based on the complete electrode model. Biomedical Engineering, IEEE Transactions on 1999;46(9):1150-1160.

44. Richardson M, Wisheart M. Review of low-velocity impact properties of composite materials. Composites Part A: Applied Science and Manufacturing 1996;27(12):1123-1131.

45. ASTM Standard. D7136/D7136M–05, Standard test method for measuring the damage resistance of a fiberreinforced polymer matrix composite to a drop-weight impact event. West Conshohocken (PA): ASTM International 2005.

46. Graham B, Adler A. Objective selection of hyperparameter for EIT. Physiol Meas 2006;27(5):S65.

47. Titman D. Applications of thermography in non-destructive testing of structures. NDT E Int 2001;34(2):149-154.

48. Grinzato E. State of the art and perspective of infrared thermography applied to building science. In: C. Meola, editor. Infrared Thermography Recent Advances and Future Trends, vol. 9: Bentham eBooks, 2012.

49. Breitenstein O, Langenkamp M, Altmann F, Katzer D, Lindner A, Eggers H. Microscopic lock-in thermography investigation of leakage sites in integrated circuits. Rev Sci Instrum 2000;71(11):4155-4160.

50. Ge Z, Du X, Yang L, Yang Y, Li Y, Jin Y. Performance monitoring of direct air-cooled power generating unit with infrared thermography. Appl Therm Eng 2011;31(4):418-424.

51. Meola C, Carlomagno GM, Squillace A, Vitiello A. Non-destructive evaluation of aerospace materials with lock-in thermography. Eng Failure Anal 2006;13(3):380-388.

52. Menaka M, Bagavathiappan S, Venkatraman B, Jayakumar T, Raj B. Characterisation of adhesively bonded laminates using radiography and infrared thermal imaging techniques. Insight-Non-Destructive Testing and Condition Monitoring 2006;48(10):606-612.

53. Bagavathiappan S, Lahiri B, Saravanan T, Philip J, Jayakumar T. Infrared thermography for condition monitoring–a review. Infrared Phys Technol 2013;60:35-55.

54. Boyle A, Adler A. The impact of electrode area, contact impedance and boundary shape on EIT images. Physiol Meas 2011;32(7):745.

55. Dai H, Gallo G, Schumacher T, Thostenson ET. A novel methodology for spatial damage detection and imaging using a distributed carbon nanotube-based composite sensor combined with electrical impedance tomography. Journal of Nondestructive Evaluation 2016;35(2):1-15.

Chapter 4

SYSTEMATIC INVESTIGATION OF THERMORESISTIVE BEHAVIORS IN CARBON NANOTUBE-BASED NANOCOMPOSITES AND MULTISCALE COMPOSITES

4.1 Introduction

Chapter 2 established a 1-D sensing approach for strain monitoring using self-sensing CNT-based nonwoven composites, and Chapter 3 considerably expanded the sensing capability of these composite sensors for 2-D damage sensing and imaging by effectively integrating EIT into the sensing approach. For future field implementation it is important to understand the sensor response under a variety of environmental conditions. This chapter presents a systematic characterization of the thermoresistive behaviors of binary-phase (i.e., CNT/epoxy) nanocomposites and ternary-phase hierarchical (i.e., CNT/fiber/epoxy) hybrid composites using *in situ* electrical measurements during thermal cycling between 25 to 145 ºC.

Four sets of composite sensors were manufactured with controlled carbon nanotube morphologies (via three-roll-milling, dip-coating and electrophoretic deposition methods. After characterizing the thermoresistive responses, a temperature compensation approach using a Wheatstone bridge circuit is proposed for the CNT-based composite sensors.

4.1.1 Temperature Dependence of Resistance in Carbon Nanotubes

It is known that individual CNTs (SWCNT or MWCNT), entangled CNT networks (in form of ropes, bundles, mats, films and agglomerations) as well as CNT-

based nanocomposites and multiscale composites are distinctly different in many aspects, such as the atomic structures of tubes, the morphology of tube-based networks and the interfacial interactions between CNTs and the surrounding matrix. Consequently, different CNT-based piezoresistive sensors may demonstrate unique thermoresistive behavior due to the various physical and chemical interactions.

Individual SWCNT can be either metallic where the electrical resistance increases as temperature raises, i.e., a positive temperature correlation (PTC) or semiconducting where the resistance decreases as temperature increases, i.e., a negative temperature correlation (NTC) depending on the tube diameter and chirality [1-3] and shows ballistic conduction [4,5]. Since only the outermost tube contributes to its conduction [6,7], a large-diameter MWCNT mostly shows a metallic character with the weak inter-tube coupling [8] and its conductance is commonly described by the Luttinger liquid model [9]; on the other hand, a small-diameter MWCNT behaves similar to an SWCNT as the interaction between adjacent shells is too strong to be neglected [10]. For an individual MWCNT, the individual walls that are metallic have relatively low electrical resistance compared to the semiconducting ones [11]. At the nanoscale, the electrical properties of tubes are also significantly influenced by structural defects and impurities, and therefore the measured response can be entirely different than theoretical expectations [2].

Additionally, Fischer *et al*. [12,13], Hone *et al*. [14], Bae *et tal*. [15] and Skakalova *et al*. [8] have studied the electrical transport phenomena in SWCNT-thin films and -thick mats. They found that both macroscopic networks of SWCNTs are semiconducting in low temperature but metallic above the room temperature and the data can be fit to the model of interrupted metallic conduction [16]. This response is

independent of the aligned tube directions and dominated by the Schottky contacts between metallic and semiconducting tubes [8,17], and the metal-metal crossed junctions between metallic tubes for the thin- and thick-networks of SWCNTs [8,15,18], respectively. As an outlier, Barnes *et al*. [19] did not observe the crossover phenomenon but a monotonous semiconducting behavior shown by their SWCNT films, which can be caused by the doping from atmospheric impurities [20]. In comparison, MWCNT films almost always show a monotonously semiconducting behavior in a wide temperature ranges as tested from -272 to 27 ºC by Baumgartner *et al*. [21] and Pohls *et al*. [22], -150 to 300 ºC by Koratkar *et al*. [23], -48 to 147 ºC by Di Bartolomeo *et al*. [24], 20 to 150 ºC by Lu *et al*. [25] and 27 to 1627 ºC by Barberio *et al*. [26]. Particularly noteworthy, the conduction mechanism is dominated by the defects in tubes and intertube contacts at low temperatures and the intertube tunneling at higher temperatures [22].

4.1.2 Temperature Dependence of Resistance in CNT-Based Composites

Inevitably, the complexity of electrical conduction mechanisms is further complicated when CNTs are dispersed into polymers, and there is wide variation in the scientific literature on the thermoresistive behavior of CNT-based nanocomposites. For example, Barrau *et al*. [27] studied the DC conductivity of the MWCNT-epoxy composites with 0.4 to 2.5 wt.% CNT in the temperature range 20-110 ºC; they found that all specimens show a monotonous NTC, which is not necessarily due to nature of the polymer but is dominated by the tunneling effect in the CNT network. However, a monotonous PTC in the MWCNT (1-5 wt.%)-epoxy nanocomposite from 60 to 100 ºC was reported by Alamusi *et al*. [28]. They also found that the temperature coefficient of resistance (*TCR*) increases with increasing temperature and MWCNT content, and

they identified the temperature-dependent tunneling effect to be the primary conduction mechanism. In particular, a PTC-to-NTC crossover phenomenon in the MWCNT (2-3 wt.%)-epoxy composites from -20 to 110 ºC was recently published by Njuguna *et al*. [29] that as the temperature increases, the resistance first rises to a local peak around 50 ºC, then suddenly drops to a local minimum near 80 ºC, and finally increases again. By combining the polymer properties examined from DSC and Raman spectroscopy analyses with the thermoresistive behavior of the nanocomposites, they concluded that this phenomenon is attributed to physical aging of the epoxy matrix and the rearrangement of the CNT network.

Similarly, it has been reported that MWCNT-HDPE (high-density-polyethylene) composites show both the monotonous PTC [30] and the crossover of PTC to NTC [31,32], which in general are considered to be dominated by the CNT network and the polymer properties of matrix. Moreover, the temperature dependence of resistance has been investigated among a wide range of nanocomposites including SWCNT-polycarbonate [33], MWCNT-PEEK [34],-SEBS [35],-polyamide-6 [36] and -polyurethane [37] show the resistive responses with monotonous NTC. Additionally, MWCNT-vinyl ester [38] and -PVDF [39] demonstrate a PTC-to-NTC crossover in their resistance while, on the other hand, the low-polymer-content/CNT films of the SWCNT/PDDA+PSS [40] and the MWCNT/PSS+PVA [41] exhibit a NTC-to-PTC crossover in a manner similar to SWCNT mats [8].

To date, investigation of the temperature dependence of resistance for the CNT-hybridized multiscale composites has been quite limited. Only very few studies have performed on the micron-scale composite specimens. Gao *et al*. [42] introduced MWCNTs onto a single glass fiber through a dip-coating procedure and then

embedded into an epoxy to form a multiscale composite. The resistance of the specimens were measured in real-time as it was heated from -150 to 180 ºC in a hot-stage, showing a monotonous NTC, which was regarded as the results of the semiconducting characteristics of the used MWCNTs. Later, Zhang *et al*. [43] repeated the same experiment with fiber samples having CNTs coated via EPD and found their resistance showing a strong PTC-NTC crossover phenomenon, which was firmly correlated with local changes of polymer properties. However, a systematic investigation of the thermoresistive behaviors of macro-level CNT-based hierarchical composites has not been found in the scientific literature.

4.1.3 Experimental Approach and Significance

Carefully comparing the results presented above highlights the need to better understand the dominant mechanism for the thermoresistive behavior of CNT-based nanocomposites. In addition, there is little published information on the thermoresistive behavior of multiscale composites. Several key parameters that contribute to the bulk resistive responses include the morphological structures of nanotubes and tube-based networks, the interfacial interactions between CNTs and the surrounding polymer, internal residual stresses in the composites, and the polymer thermomechanical properties. To address these key parameters, four types of CNT-based composites with the different morphological states of CNTs are created including (1) randomly dispersed CNTs in epoxy, i.e., the nanocomposite, (2) loosely- and (3) densely-concentrated CNTs, and (4) randomly dispersed CNTs in fibrous composites, as illustrated in Figure 4.1.

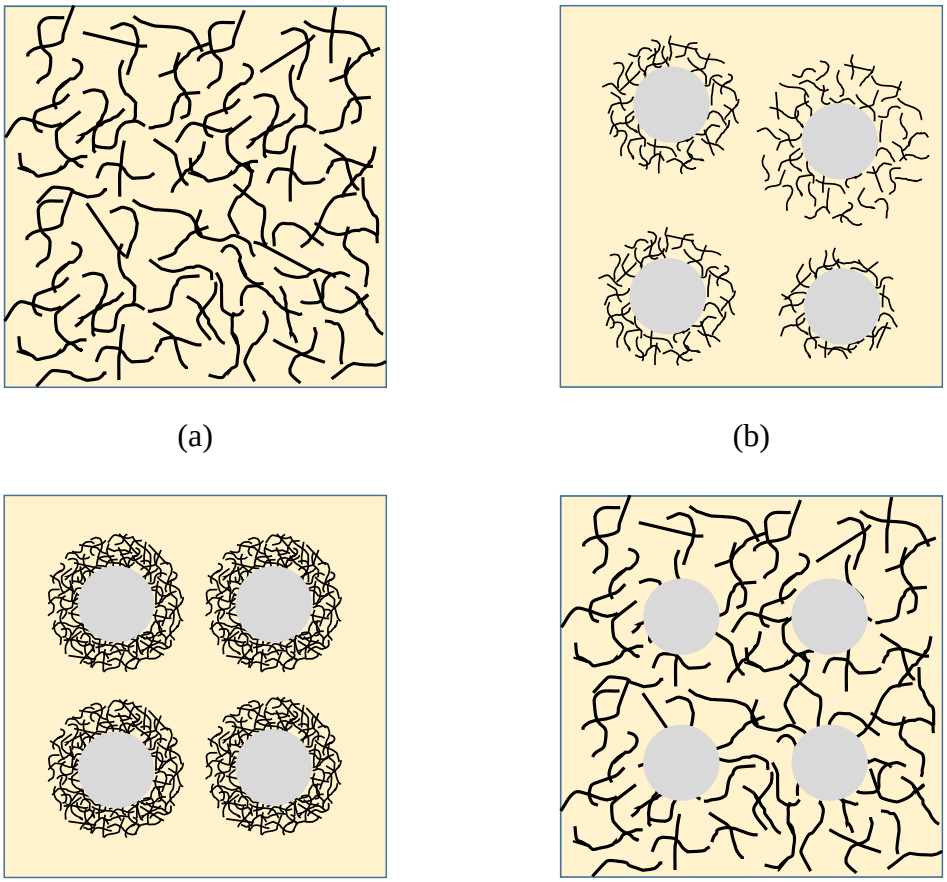

Figure 4.1: Schematic illustrations of the four common morphological states of CNTs evaluated in this study including (a) randomly dispersed CNTs in epoxy, (b) loosely-concentrated (inhomogeneous) CNTs as the fiber coating in multiscale composites, (c) densely-localized (homogeneous) CNTs as coated on the fiber surfaces in multiscale composites and (d) randomly dispersed CNTs in the matrix of multiscale composites.

In this chapter, a comprehensive study of the thermoresistive response of the different sensor systems has been conducted and the structure and morphology of the as-manufactured sensors characterized. A thermomechanical analyzer was used to study the temperature-dependent material properties and a finite element analysis was

performed to better understand the residual thermal stresses developed in fiber/epoxy composites. Through combining knowledge of thermomechanical properties with the modeling and sensor characterization research a fundamental understanding of the interrelationship between the processing-structure-response of these sensors is described. Finally, this specific investigation promotes a comprehensive understanding on thermoresistive behaviors of CNT-based composites and highlights the multifunctional potentials of using CNT-based multiscale composites. Besides serving as SHM sensors, these novel composites can be utilized for *in situ* fast-sensing and monitoring temperature, thermal transitions, and curing process, which could be transferred to real applications.

From this specific study, it has been observed that except the two-phase nanocomposite (with randomly dispersed nanotubes) showing a monotonous PTC, the bulk resistance changes in all multiscale composites demonstrate a reversible double-crossover-phenomenon as thermally cycled from 25 to 145 ºC, indicating that a dynamic dominance responsible for the thermoresistive behaviors is existing and based on the competition between the polymer thermo-mechanical/dynamic-motion driven and the thermal stresses-induced changes to the CNT networks. Additionally, this striking thermoresistive behavior is strongly depending on the CNT arrangement/rearrangement, CNT concentration, thermal expansion, fiber properties, interfacial interactions, and the polymer properties (before and after glass transition temperature).

4.2 Experimental Details

4.2.1 Materials, Composite Manufacture and Specimen Preparation

To manufacture the sensors in different morphologies (CNTs in forms of raw powder, aqueous sizing agent, and thin bulk sheet) three processing techniques (three roll milling, dip-coating and electrophoretic deposition) were utilized to experimentally manufacture the CNT-based composite sensors with the specific morphologies (Figure 4.1). Epoxy and nonwoven fabrics were used in common among all composite specimens:

(1) An epoxy system in this study was a bisphenol-f epichlorohydrin epoxy cured with an aromatic diamine curing agent (EPON 862 epoxy, Epi-Kure W curing agent; Momentive Specialty Chemicals Inc.) at a ratio of 100:26.4 (862:W by weight) at 130ºC for 6 hours.

(2) Nonwoven fabrics (Technical Fiber Products, Inc.) were chosen as the carrier for being coated with nanotubes and representing the microscale fiber phase in the multiscale composites. Its in-plane random fiber orientation results in an isotropic surface electrical conductivity in the bulk composites [44,45]. Two different non-conductive fibers were chosen for their different coefficient of thermal expansion and mechanical properties resulting in different thermally-induced stresses. The two nonwoven fabrics include a 27 g/m^2 Aramid (12 mm fiber length, with 12.5 wt.% cross-linked polyester binder) and the 50 g/m^2 E-glass (12 mm fiber length, with 12.5 wt.% polyvinyl alcohol (PVA) binder). The two nonwoven fabrics have similar porosity (about 90%).

4.2.1.1 Nanocomposites with CNTs Dispersed via Three-Roll Milling Technique

Bulk multi-walled carbon nanotubes (CM-95, 95 wt.% purity, Hanwha Nanotech, Korea) in their as-received state are highly entangled and have diameters between 10 and 20 nm were dispersed into the epoxy resin using a three-roll-mill (EXAKT 80E, EXAKT Technologies, Inc.), where the mixture was repeatedly passed through the adjacent rollers at gradually smaller gap settings down to the minimum setting to 5 μm following previously established processing protocols [46]. After milling, the mixture was degassed in a vacuum oven for 20 min and the curing agent was added to the dispersion by hand mixing. Two batches of carbon nanotube-epoxy matrix material with 0.25 and 0.5 wt.% CNT loading were prepared following the same procedures. The part of the prepared resin mix was poured into aluminum molds in order to be cast into nanocomposite specimens after curing.

4.2.1.2 Multiscale Composites with CNT-Hybridized Fibers via Dip-Coating Approach

As established in Section 2.2, the dip-coating approach is used where a commercially available fiber sizing agent with approximately 1.5 wt.% CNTs are dispersed in an aqueous solution with about 3.0 wt.% sodium dodecyl benzene sulfonate (SDBS) surfactant and 1.5 wt.% film former, resulting in about 6 wt.% solids after drying. It is notable that the dispersion of nanotubes is stabilized by the electrostatic repulsion between the micelles [47], and further enhanced by the formation of a strong aromatic stacking between the phenyl rings in SDBS and CNT within the micelle [48]. Two batches of CNT dispersions were prepared by diluting the sizing with ultra-pure distilled water at the mass ratios of 1:1 and 1:2. To ensure a uniform CNT dispersion, the diluted sizing was pre-mixed using a centrifugal mixer for 120 s and then sonicated for 15 min (see Section 2.2.1). Finally, the fabric was

immersed in the CNT aqueous dispersions for 20 min. After drying, the epoxy system was infused into the CNT-modified fabrics via VARTM process (see Section 2.2.2) to form a 0.4 to 0.5 mm thick, free-stranding composite sensing layers with 0.75 and 1.0 wt.% CNT. Particularly, one CNT-E-glass nonwoven composite layer with 1.0 wt.% CNT was made as the comparative sample group.

4.2.1.3 Multiscale Composites with CNT-Hybridized Fibers via Electrophoretic Deposition (EPD)

The multi-walled carbon nanotubes (the same nanotubes used in Section 4.2.1.1) were first oxidized using an ultrasonicated-ozonolysis (USO) method [49,50] by bubbling ozone gas into a mixture of nanotubes and ultra-pure water while continuously sonicating the dispersion. Next, the USO treated CNTs were functionalized with polyethylenimine (PEI, $H(NHCH_2CH_2)_{58}NH_2$, M_w=25000, Sigma-Aldrich, USA) in a high power sonicator (Sonicator 3000, Misonix, USA) as described in the previous work [49,50] in order to create a stable dispersion of CNTs. The pH of the PEI-functionalized CNTs was adjusted using the glacial-acetic acid (Sigma-Aldrich, USA) to a pH around 6 in order to protonate the PEI, which resulted in a zeta potential of the positively-charged CNTs of around +40 mV. Aqueous dispersion was prepared for EPD with the CNT concentration of 1.0 g/L.

EPD of the ozone and PEI-treated CNTs onto a single sheet of aramid-nonwoven fabric was performed at room temperature in a self-assembled apparatus with two parallel steel electrodes as discussed in [49,50]. The fabric was placed firmly on the cathode and fully immersed in the CNT dispersion. Cathodic deposition was conducted under the constant DC field of 37.5 V/cm and deposition times of 5 and 10 min for two pieces of fabric. After the deposition, the fabric layers were removed from

the CNT dispersion and allowed to dry at room temperature for 24 h. Finally, the epoxy system was infused into the as-prepared CNT-coated fabrics via VARTM approach. Two multiscale composite layers were obtained with the CNT concentrations of 1.8 and 3.4 wt.%, respectively.

4.2.1.4 Multiscale Composites with CNT-Modified Matrix

A portion of the carbon nanotube-epoxy mixture prepared in Section 4.2.1.1 was infused into the single-ply preforms of the aramid and E-glass nonwoven fabrics using the previously established VARTM technique to fabricate the multiscale composites with the dispersed carbon nanotubes in the epoxy matrix phase.

4.2.1.5 Control Samples

Three groups of control samples were manufactured for this study to serve as a reference material in the thermomechanical and the thermoresistive characterizations:

(1) *Plain nonwoven fabric composites* (no CNTs): two single sheets of each aramid and E-glass nonwoven fabric were infused with the epoxy using the VARTM technique. After curing, two plain nonwoven composite layers were obtained and then characterized using a thermomechanical analyzer.

(2) *Carbon nanotube sizing film on glass slide* (no epoxy): a small batch of CNT sizing dispersion with a dilution ratio of 1:0.5 was prepared first. Borosilicate glass slides (75 mm × 25 mm × 1 mm, Fisher Scientific, USA) were rinsed with water and thoroughly cleaned with acetone. Next, the as-prepared aqueous dispersion was filled in a 10-mL syringe to carefully spread 2 mL on one face of the glass slide and then completely dried out at 130ºC for 30 min. This procedure was repeated four times to obtain a visually uniform CNT coating on the glass slide. The resulting 0.1 mm

thick CNT sizing films on the glass slides were finally trimmed to the size of 15 mm × 40 mm, shown in Figure 4.2.

(a) (b)

Figure 4.2: Photographs showing (a) the control specimens of CNT sizing film on glass and (b) the cross-section of an individual specimen.

(3) *Carbon nanotube sheet/epoxy composites* (no fibers): Commercially available multiwall carbon nanotube sheet (25 μm thick, Miralon^{TM} Sheets, Nanocomp Technologies, Inc.) as shown in Figure 4.3a was infiltrated with the epoxy via VARTM approach. After curing, the composite layer was 0.2 mm thick and finally cut into 13 mm × 64 mm specimens as presented in Figure 4.3b and 4.3c.

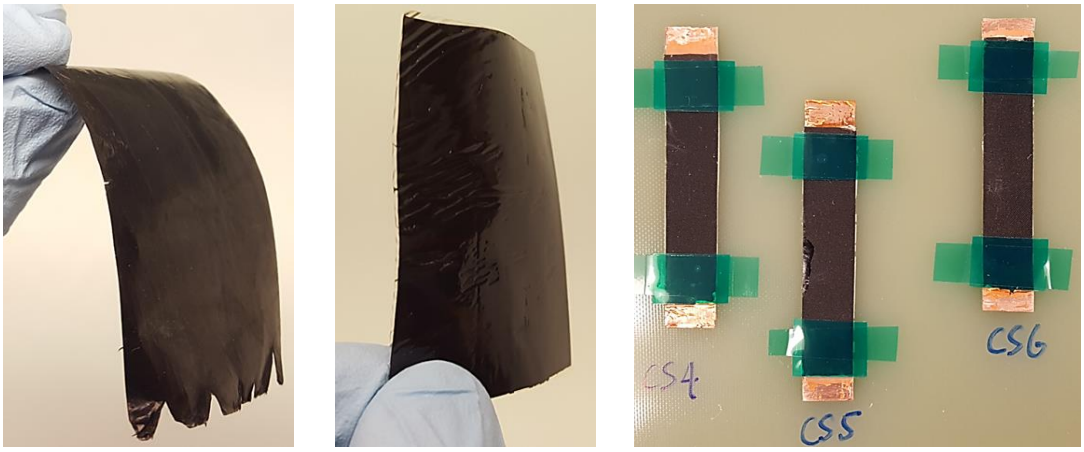

(a) (b) (c)

Figure 4.3: Photographs showing (a) the as-received thin CNT sheet, (b) CNT-sheet/epoxy composite layer and (c) the control specimens of CNT-sheet/epoxy composite.

4.2.1.6 Specimen Preparation

The different composites were trimmed into the same size and the specific sample dimensions were selected in accordance to the experimental limitations and requirements. For instance, the batch samples of composite layers fabricated in Sections 4.2.1.2 to 4.2.1.4 as shown in Figure 4.4a were in the same size of 102 mm × 127 mm, which finally were cut into 102 mm × 13 mm specimens for testing as shown in Figure 4.4b. As for the CNT-nanocomposites made in Section 4.2.1.1, the specimens were trimmed into the dimensions of 5 mm×3 mm×15 mm using a diamond saw as shown in Figure 4.4c. In addition, for thermoresistive characterization, electrodes and lead wires were attached to the specimens. To erase thermal histories resulting from the fabrication processes and to avoid the effects of humidity and the absorbed moisture, all specimens were annealed at 130ºC for 15 min

and then cooled in a desiccator cabinet (Fisherbrand™, Thermo Fisher Scientific Inc.) for 48 h before testing.

(a) (b)

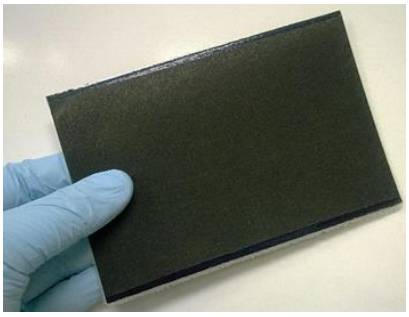

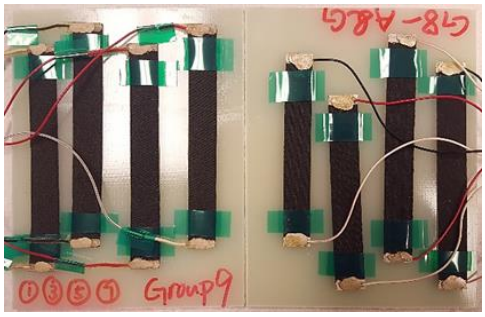

(c)

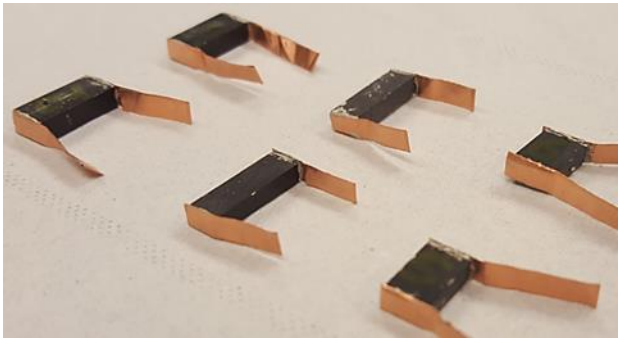

Figure 4.4: Photographs showing (a) one fabricated CNT-based multiscale composite layer and (b) several prepared multiscale composite specimens, and (c) a group of six CNT-based nanocomposite specimens.

4.2.2 Methods and Testing

4.2.2.1 Scanning Electron Microscopy

The dispersion state of carbon nanotubes, the microscopic morphologies of CNT coatings on fiber surfaces, and the fracture surfaces of the as-fabricated CNT-based composites were studied using an AURIGA™ 60 Crossbeam™ FIB-SEM with 3~5kV acceleration voltages. The composite specimens were fractured after freezing

in liquid nitrogen for 15 min. To minimize sample charging, all fracture surfaces were coated with a thin conductive Pt/Au layer (~5 nm) in a vacuum sputter coater prior to imaging.

4.2.2.2 Thermomechanical Analysis

The thermomechanical analysis was conducted using a thermomechanical analyzer (TMA) (Hyperion® TMA 402 F1, Netzsch). The samples were heated to 180ºC from room temperature at a ramp rate of 2ºC/min in an inert gas environment where pure nitrogen was purged into the chamber at 20 mL/min. Based on the dimensions of the samples, neat epoxy and CNT nanocomposites were tested under the expansion mode in TMA with an expansion probe, as shown in Figure 4.5a. The thin composite layers were characterized under the tension with a double-clamp tension probe with a gage length of 10 mm as shown in Figure 4.5b. A static normal force of 100 mN was applied by the TMA probe to all specimens while testing. The coefficient of linear thermal expansion (*CTE*) given by the normalized change of specimen height with temperature is calculated by the operating software and reported in this chapter.

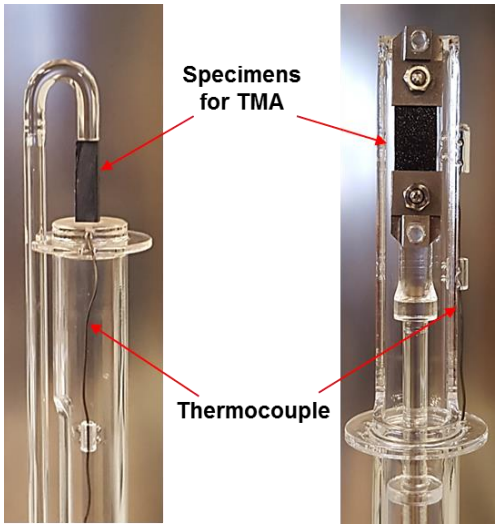

Figure 4.5: Snapshots showing the TMA setup with (a) the expansion mode sample stage for neat epoxy and nanocomposite specimens, and (b) the tension mode sample stage for thin layer specimens.

4.2.2.3 Finite Element Analysis

Thermal stresses are developed in the composite due to the mismatch in thermal expansion between the fiber and the matrix. The thermal stresses were investigated using finite element analysis (FEA). A microscale thermal stress simulation of the local constituents in terms of fiber and matrix is performed using COMSOL Multiphysics software (4.3b, COMSOL Inc., USA). The three-dimensional solid model comprising a quarter of two concentric cylinders in the height of 10-µm is created in the cylindrical coordinates. The FEA model (Figure 4.6a) has two domains including the fiber and the epoxy which are discretized into the tetrahedral elements with eight layers of finer boundary layer meshes between the fiber and the epoxy (Figure 4.6b). The boundaries are traction-free and assigned to be symmetric. The continuity of dependent variables across the internal boundaries between the two

domains is enforced automatically by the software. A specific temperature boundary was designated at the exterior surface of the matrix shown as highlighted in blue in Figure 4.6a. The initial and final temperature used during the simulation was set as 120 ºC (i.e., the glass transition temperature of epoxy) and 25 ºC, respectively. At glass transition the composite is in a stress-free state and the thermal stresses develop upon cooling.

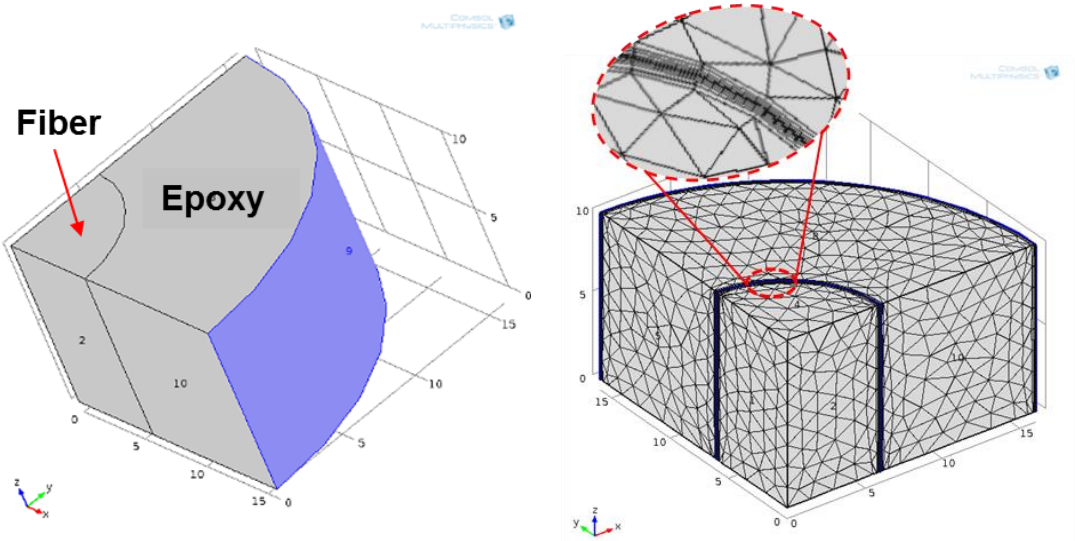

(a) (b)

Figure 4.6: Illustrations of the microscale quarter cylinder model of the single aramid fiber/epoxy composite built by COMSOL Multiphysics software including (a) the 3D model with two domains (i.e., the fiber and the epoxy) with the assigned symmetric boundary conditions (shown in Gray) and the fixed temperature boundary condition on the outermost side of the epoxy (shown in Blue) and (b) the FE model with tetrahedral elements and the refined boundary layer meshes (the inset) between the fiber and epoxy.

In this FEA model, the aramid and E-glass fibers are modeled as the orthotropic (transversely isotropic) and isotropic linear elastic materials, respectively. Without considering mechanical loadings and large deformations, a simplification was imposed in the modeling of the epoxy matrix by considering it as the linear elastic material. In real multiscale composites, carbon nanotubes are concentrated on the fiber surfaces and entirely immersed into the epoxy. This fiber-CNT-resin interphase region was not modeled due to the lack of its mechanical properties, but simply assumed to be the same as the epoxy. In addition, a perfect interfacial bonding was assumed to be existing between the fiber and epoxy matrix. As a result, a 10 μm thick epoxy zone was preselected to cover around the fiber and the resulted thermal stresses due to temperature changes within the domain of the epoxy were extracted and used to represent the thermal stress level afforded by the CNT coating. In particular, the material properties were input from experimental measurements or material property data from the manufacturer (Table 4.1).

Table 4.1: Material Properties for Finite Element Models.

Material	Radius (μm)	Young's Modulus (GPa)	Poisson's Ratio	CTE (α) (10^{-6}/°C)	Thermal Conductivity (W/(m*K))	Heat Capacity (J/(kg*K))	Density (kg/m^3)
Epoxy Resin (*isotropic*)	10 μm thick	2.58	0.35	72	0.202	1060	1110
E-Glass (*isotropic*)	10	75.0	0.22	5	1.275	802	2575
Aramid Fiber (*orthotropic*)	6	E_{rr} = 2.3 $E_{\theta\theta}$ = 2.3 E_{zz} = 80.0	$\nu_{r\theta}$ = 0.25 ν_{zr} = 0.60	α_{rr} = 78 $\alpha_{\theta\theta}$ = 78 α_{zz} = -5.4	0.040	1420	1440

4.2.2.4 *In Situ* Thermoresistive Characterization

Specimens were first moved into an environmental chamber (CSZ Z8-plus, Cincinnati Sub-Zero Products LLC.) and subjected to a total of three temperature cycles between 25 and 145 ºC at a ramping rate of 2 ºC/min. A 30-second isothermal segment was programmed for 25 and 165 ºC to enable the specimen reaching thermal equilibrium. The real-time thermoresistive behaviors of the carbon nanotube-based composites were measured with a multifunctional data acquisition system that was controlled by a customized LabVIEW program (National Instruments, NI). This integrated system consists of five devices including the Keithley 3706A System Switch/Multimeter, Keithley 3750-ST terminal block, NI-SC-2345 signal conditioner, NI-SCC-TC02 thermocouple input module, and a Type-K thermocouple. A two-probe current-voltage measurement scheme was used for collecting resistances of the specimens. Based on the resistance of the connected specimen, the input direct current provided by the 3706A meter varied from 10 mA to 10 μA. A minimum of four specimens of each composite group were tested in order to ensure repeatability of the observed response. To maintain the consistency with Chapters 2 and 3, electrical resistance measurements are represented in normalized form as defined by Equation 2.1 in Section 2.3.2. The measured average baseline resistances/resistivities of all composite groups investigated in this study at room temperature are summarized in Table 4.2 as follows.

Table 4.2: Baseline Electrical Resistances and Resistivities of CNT-Based Composites at Room Temperature.

Composite Group	R_0* (kΩ)	ρ_{v0} (Ω·m)
3-Roll-Mill CNT (0.5 wt.%)-Epoxy	34.3±3.7	33.4±3.5
3-Roll-Mill CNT (0.25 wt.%)-Epoxy	112.5±23.4	105.2±21.4
Aramid/3-Roll-Mill CNT(0.5 wt.%)-Epoxy	607.4±83.6	38.0±5.2
Aramid/3-Roll-Mill CNT(0.25 wt.%)-Epoxy	2811.0±644	175.7±40.3
E-Glass/3-Roll-Mill CNT(0.5 wt.%)-Epoxy	1099.3±283.7	68.7±17.7
E-Glass/3-Roll-Mill CNT(0.25 wt.%)-Epoxy	5792.5±1348	362.0±84.3
Aramid-Sizing (1.0 wt.%CNT)/Epoxy	3.1±0.1	0.19±0.01
Aramid-Sizing (1.0 wt.%CNT)/Epoxy (After Post-Cure)	2.9±0.04	0.18±0.004
Aramid-Sizing (0.77 wt.%CNT)/Epoxy	4.7±0.5	0.30±0.03
Aramid-Sizing (0.61 wt.%CNT)/Epoxy	7.3±0.7	0.45±0.04
Aramid-Sizing (0.17 wt.%CNT)/Epoxy	66.1±3.5	3.8±0.22
Aramid-Sizing (0.05 wt.%CNT)/Epoxy	402.3±28	25.0±1.7
E-Glass-Sizing (1.0 wt.%CNT)/Epoxy	2.6±0.3	0.16±0.02
Aramid-EPD CNT (3.4 wt.%CNT)/Epoxy	442.4±83.4	27.2±5.1
Aramid-EPD CNT (1.8 wt.%CNT)/Epoxy	3125±534	226.8±38.8
CNT Sizing Film on Glass Slide (Control Sample)	$(60.7\pm4) \times 10^{-3}$	$(2.2\pm0.15) \times 10^{-3}$
CNT Sheet/Epoxy (Control Sample)	$(2.7\pm0.2) \times 10^{-3}$	$(0.11\pm0.008) \times 10^{-3}$

* All data are shown in the format of average value ± ½ difference between the highest and lowest value.

In addition, the temperature coefficient of resistance (*TCR*) is defined as the resistance change with respect to the unit change of temperature and calculated using Equation 4.1 as follows.

$$TCR = \frac{R-R_0}{R_0} / (T\text{-}T_0) \quad (4.1)$$

where R_0 is the baseline resistance of the specimen at room temperature (T_0) and R is the transient resistance at temperature (T).

4.3 Results and Discussion

4.3.1 Morphological States of Carbon Nanotubes

4.3.1.1 Dispersed Carbon Nanotubes in Nanocomposites

Figures 4.7a and 4.7b show the cryogenic fracture surface of the neat epoxy. Obviously, there is no any microscale roughness, but smooth and uniformly distributed cracks, representing a typical brittle fracture feature. On the other hand, Figures 4.7c through f show the fracture surfaces of the CNT-based nanocomposites (Section 4.2.1.1). At low magnification, the fracture surface shown in Figure 4.7c shows substantial surface roughness due to the addition of 0.5 wt.% CNT where a great deal of short and highly curved structural features in the micron-level are randomly distributed, hindering the crack propagation, indicating that the failure was accompanied with localized plastic deformation [46,51]. The higher magnification image shown in Figure 4.7d shows a localized CNT-agglomerate near crack tip region where CNTs are either pulled out or fractured, demonstrating a strong interaction between CNTs and the epoxy. It can be also seen that as the fracture energy is dissipated while interacting with CNTs, the crack tips in the form of tail-like structures

are forced to frequently change its propagation direction, which gives rise to a disordered crack pattern.

Similarly, as demonstrated in Figure 4.7e and 4.7f the nanocomposite with 0.25 wt.% CNT show relatively reduced surface roughness with less, smaller and even more scattered CNT agglomerates, exhibiting a less interactive bonding with neighboring epoxy.

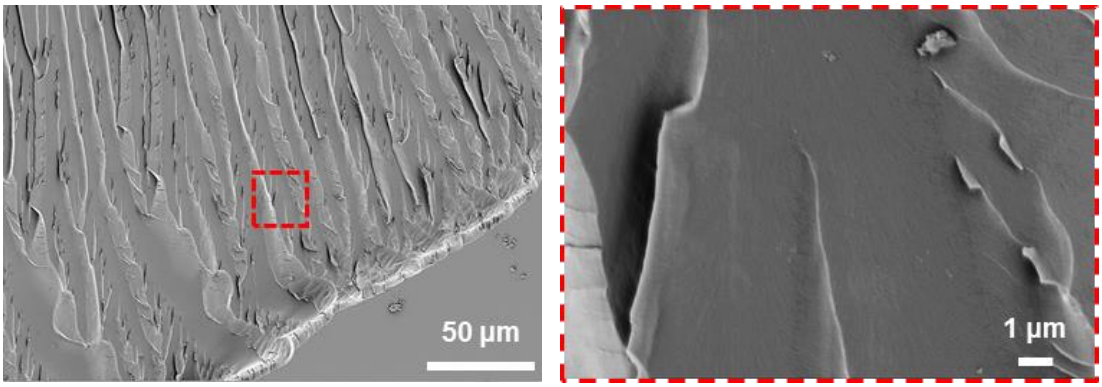

(a) (b)

Figure 4.7: SEM images showing typical fracture surfaces of (a) the neat epoxy and (b) the circled area on (a) at the high magnification, (c) the nanocomposites with 0.5 wt.% CNT, (d) a high magnification image of (c) near the region of crack initiation, and (e) the nanocomposites with 0.25 wt.% CNT, (f) a high magnification image of (e) evidencing a well-dispersed CNT morphology with submicron-level CNT agglomerates.

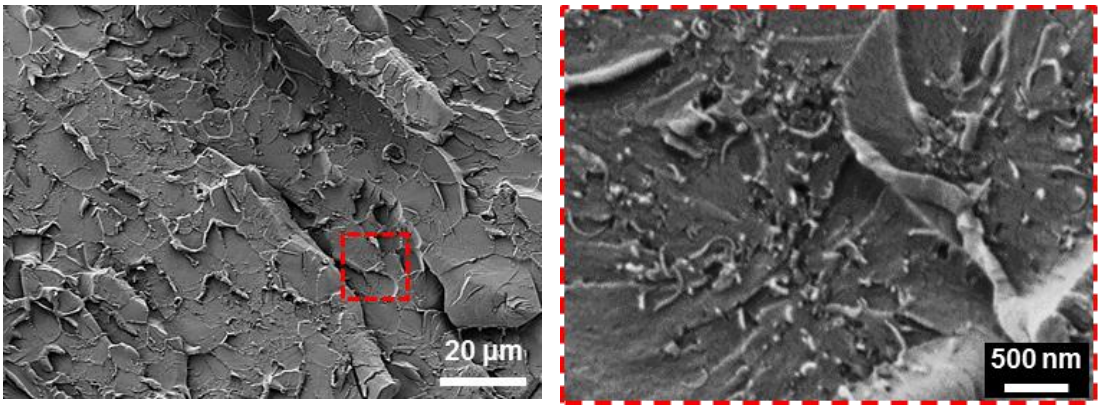

(c) (d)

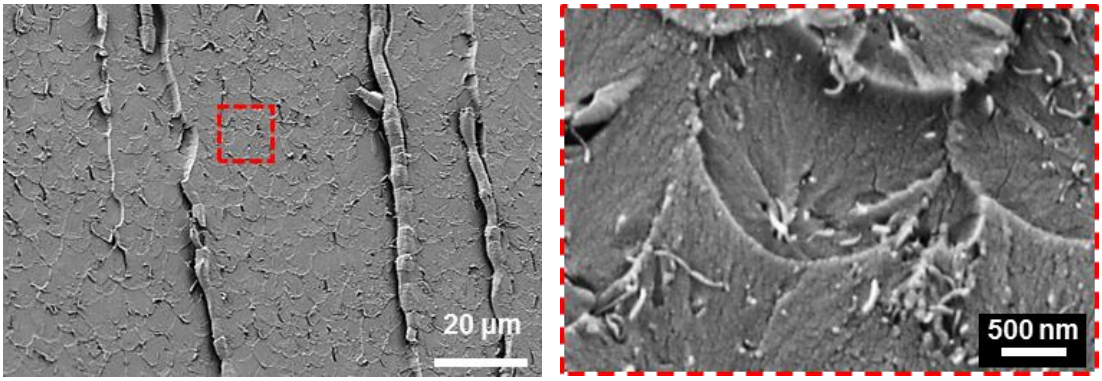

(e) (f)

Figure 4.7: continued.

4.3.1.2 Dispersed Carbon Nanotubes in Multiscale Composites

Figure 4.8 represents the fracture surfaces of the multiscale composites consisting of aramid fibers and 0.5 wt.% CNT randomly dispersed in the epoxy matrix. A clean and smooth fiber pullout hole was observed in this composite system, which demonstrates the weak wettability and interfacial bonding between the matrix and fiber. Compared with the nanocomposite, the micro-level surface roughness (seen in Figure 4.8a) of the matrix phase is reduced, although CNTs are well dispersed through the epoxy matrix. Additionally, as shown in Figure 4.8b, instead of causing

CNT ruptures, a lot of CNTs are just pulled out which are consistent to the experimental results found by Schadler *et al*. [52], indicating a relatively low-level stress transfer between CNT and epoxy. This could attribute to that most of the fracture energy was dissipated through fiber debonding rather than transferred to the matrix.

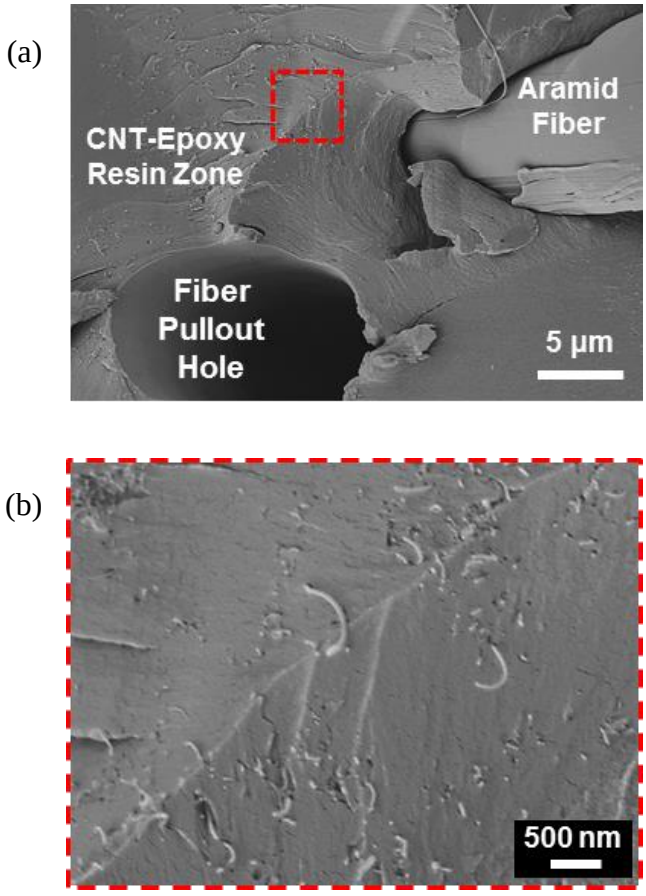

Figure 4.8: SEM images showing (a) the fracture surface of multiscale composite with random aramid fibers and CNT (0.5 wt.%)-dispersed epoxy matrix and (b) the high magnification image of the circled area in (a).

In short, being consistent with the experimental results found by Wong *et al*. [53], Gou *et al*. [54] and Watts and Hsu [55], it is obvious that as the non-functionalized CNTs randomly dispersed in epoxy, the interaction between CNTs and the surrounding epoxy is moderately strong and able to maintain a stable mechanism of energy dissipation such as the CNT pullout, although this interfacial action is most likely dominated by the physical interactions and the mechanical interlocking at the molecular level [52,53,56,57].

4.3.1.3 Loosely Concentrated Carbon Nanotubes in Multiscale Composites

Figure 4.9a shows the typical morphology of the dehydrated raw CNT sizing agent in form of a thin film, which shows the same solid surface characteristics as the CNT coating on the fiber surfaces (as shown in Figure 2.13 in Section 2.3.3.2). In this image, the free surface of the film is a very thin, smooth layer likely due to residual surfactant and film formers [58]. On the other hand, the core of the film shows a porous packing structure of highly agglomerated CNTs. During the drying process, the particle wettability of the CNT dispersion prompts capillary effects as water evaporates [59,60], which induces attractive interactions between SDBS wrapped CNTs and consequently reorganize the CNT network into a solid cellular structure with numerous micro-level voids that are originally filled with solvent before drying. As shown in Figure 4.9b, the charge-contrast image at high magnification shows a loosely packed CNT network where the networks of CNTs are mixed with the voids created by solvent evaporation.

In addition, to make a comparative analysis, a CNT sheet was selected to specifically replicate the locally porous network architecture of concentrated CNTs. Figure 4.9c depicts the surface morphology of the raw CNT sheet where all pristine

CNTs are randomly oriented and exhibiting a random microstructure. After the CNT sheet was infiltrated with epoxy, a thin sandwich-like composite layer was formed as shown in Figure 4.9d, in which both the top and bottom faces are covered with the epoxy resin and the core of CNT sheet is fully saturated with epoxy, indicating good wetting of the nanotubes with the epoxy resin.

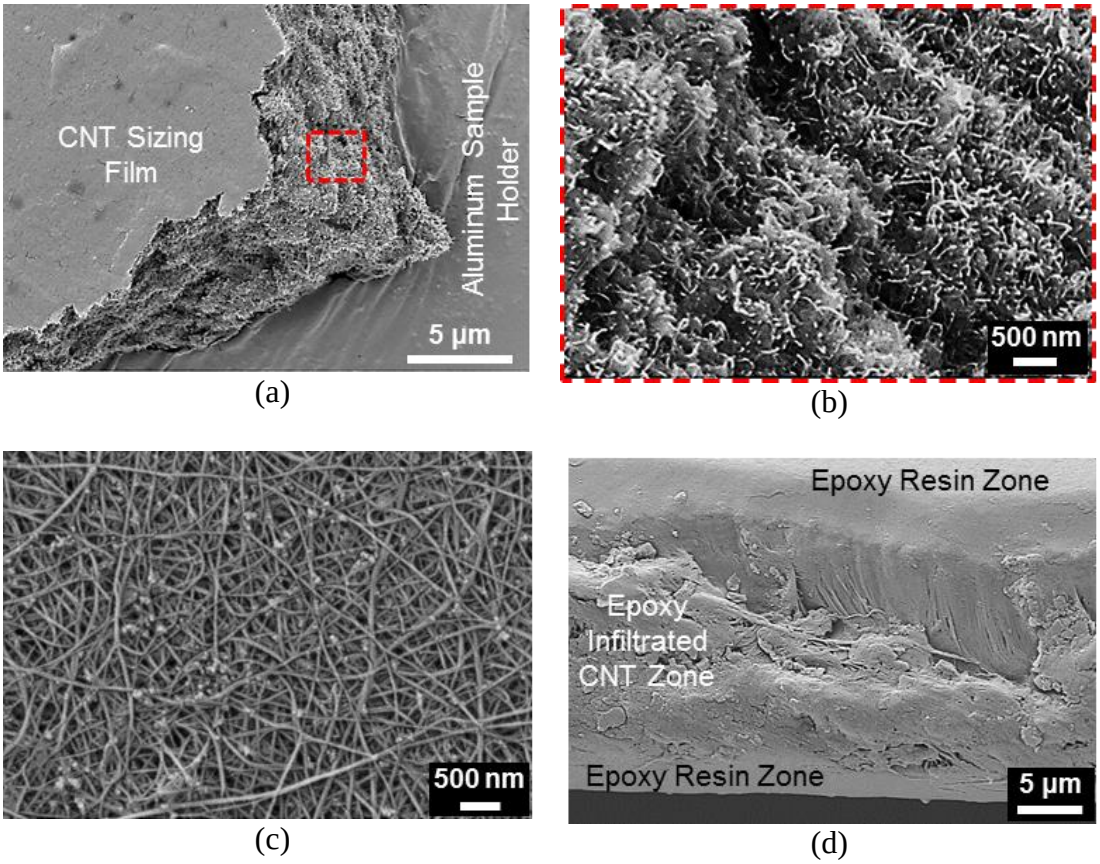

Figure 4.9: SEM images of the CNT-based materials including (a) the dehydrated CNT sizing agent in form of a thin film (i.e., the control sample without epoxy), (b) a high magnification charge contrast SEM image of the film core in (a), (c) the as-received CNT sheet (in-plane view) and (d) the CNT sheet-epoxy composite.

Figure 4.10 shows a typical fracture surface of the as-fabricated multiscale composite consisting of CNT-coated aramid fibers and epoxy matrix. It is apparent that the most parts of the epoxy resin zone are smooth and absent of any structural features, showing brittle fracture. In the areas where fibers are protruding micron-level surface roughness is formed due to the appearance of CNT-coating. Additionally, the aramid fibers demonstrate three failure modes including fiber pullout, splitting and fracture. Like all oriented synthetic fibers, aramid fibers have different moduli in the longitudinal and transverse directions due to the inherent asymmetry of the consisting organic molecules [61,62]. Therefore, aramid fiber fracture is always accompanied with the fiber splitting (i.e., fibrillation). In general, the nonwoven fabric/epoxy composite has a low fiber volume fraction, below 10%.

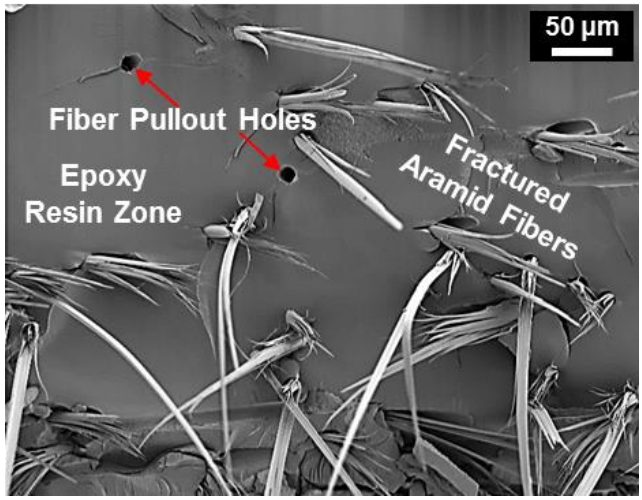

Figure 4.10: SEM image showing the typical fracture surface of the multiscale composite consisting of CNT-deposited aramid fibers (dip-coated) and epoxy matrix.

In this study, two types of CNT-grafted nonwoven fabrics were developed using the CNT-sizing-based dip-coating approach and the ozone-PEI-functionalized-CNT-based electrophoretic deposition (EPD) method. Figure 4.11 shows the resulting morphologies of the loosely-concentrated CNTs developed in the multiscale composites. Specifically, Figure 4.11a and 4.11c show the mixed fracture surfaces of nonwoven aramid composites with 0.75 and 1.0 wt.% CNT, respectively. It is clear that a non-uniform CNT sizing zone is confined by matrix-rich regions between adjacent aramid fibers in the composites. Similar to previous observations, the epoxy and aramid fiber exhibit a brittle and ductile failure mode, respectively. Interestingly, it can be seen that CNTs tends to accumulate in the narrow space (~5 μm wide and ~20 μm long) between neighboring fibers rather than entirely wrap around the fiber surface, which is like due to the capillary action while drying.

Figure 4.11b and 4.11d show the morphologies of the interfacial regions of epoxy-CNT coating and CNT coating-fiber at a high magnification. It is apparent that the cellular structure of the CNT coating is fully infiltrated with the resin matrix, indicating a high degree of epoxy wetting and infusion. Meanwhile, a good adhesion at the interface of CNT-epoxy is further ensured by forming the hydrogen bonding between the hydrophilic segment of SDBS and the epoxy [63,64]. In addition, the thickness of the locally concentrated CNT zone varies sharply and the alignment of CNTs is randomly oriented, evidencing a locally inhomogeneous CNT coating on the fiber surface, which is consistent with the experimental results found by Gao *et al*. [42] and Rausch and Mader [65,66] who implemented a similar dip-coating approach to coat MWCNTs onto single glass fiber and the fiberglass yarn bundles, respectively. However, the aramid fiber is completely debonded throughout the CNT coating,

indicating a poor adhesion at the fiber-coating interface. This is likely due to the poor compatibility between the epoxy infiltrated CNT coating and the existing cross-linked polyester binder layer on the aramid fibers.

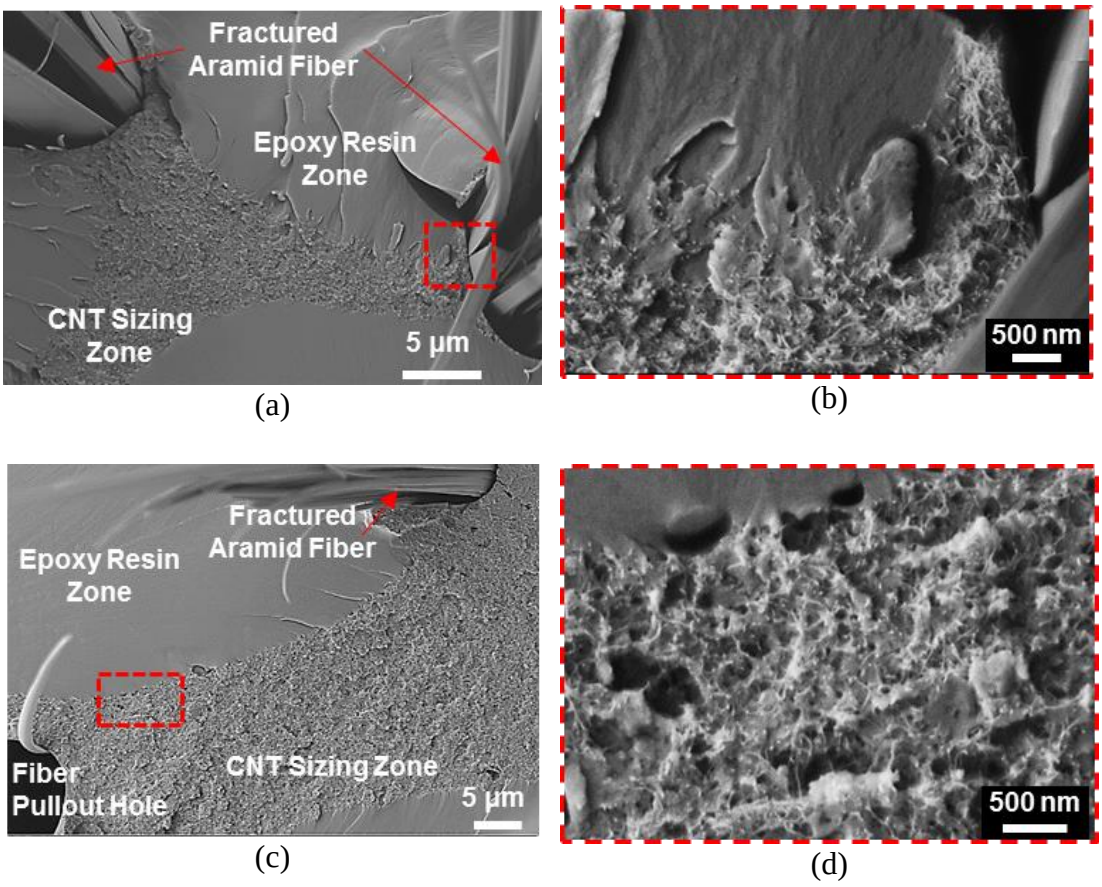

Figure 4.11: SEM images showing the fracture surfaces of the multiscale aramid composites with (a) 0.75 and (c) 1.0 wt.% CNT (dip-coated); (b) and (d) the high magnification images of interfacial regions in (a) and (c), respectively.

The fracture surface of the multiscale E-glass composite with 1.0 wt.% CNT is shown in Figure 4.12a, and reveals a distinctly different fracture morphology as compared with aramid composites. It can be seen that all E-glass fibers fracture in a brittle manner due to their isotropic nature of mechanical properties [61]. A clear view of the typical E-glass fiber crack plane with steep ridges can be seen in Figure 4.12c. In addition, in the higher magnification image shown in Figure 4.12b, the protruding fibers show micron-level surface roughness where a thin layer of highly agglomerated CNTs stays on the fiber surface indicating fracture through the CNT coating. Coincidentally, the fiber debonding trace remained in the matrix phase as shown in Figure 4.12d possesses a similar level of texture, indicating that there is likely a strong interaction at the interface between the fiber and CNT coating. This can be a result of the polymer-surfactant complexation between PVA (the binder layer on E-glass fabric) and anionic SDBS (the surfactant in CNT-sizing dispersion) that the alkyl chain polymerizing capacity of SDBS enables the co-operative hydrogen bonding with the amphiphilic chain of PVA [67]. Meanwhile, it may also partially due to that PVA is able to be more effectively adhering with the epoxy within the CNT coating since the hydroxyl groups in PVA can react with the epoxy resin [68].

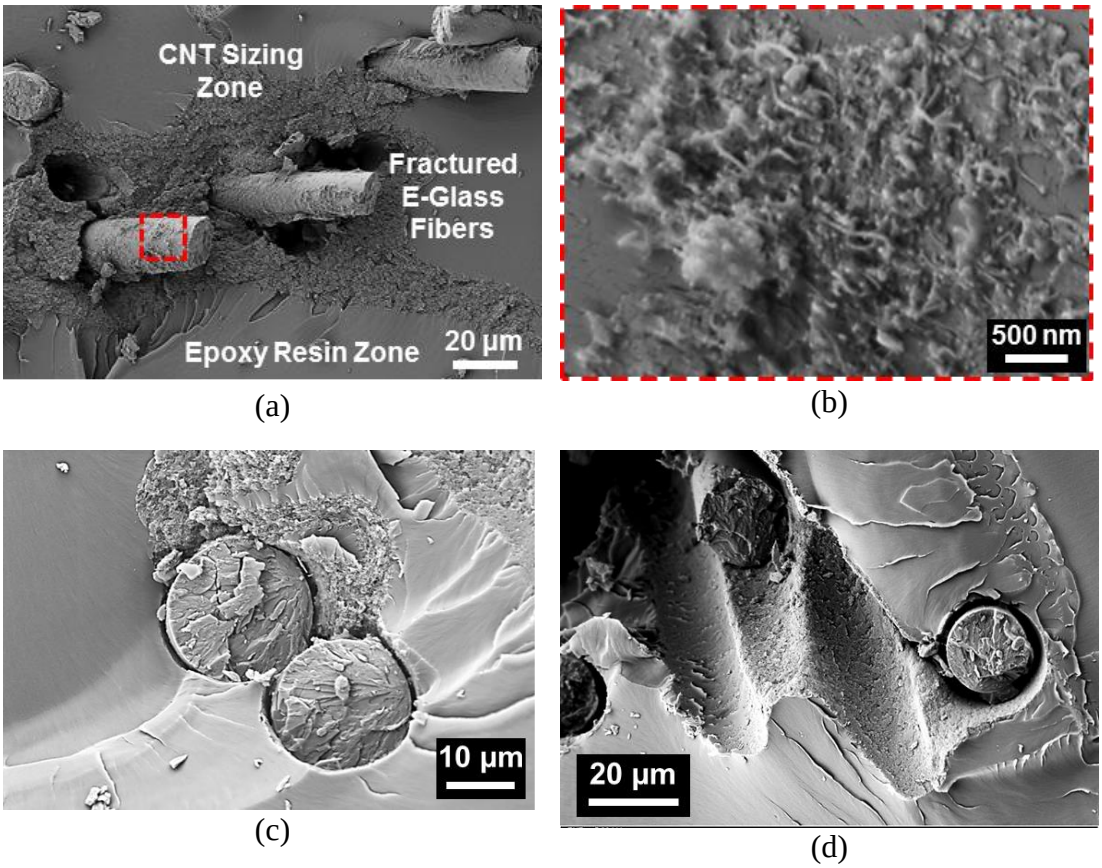

Figure 4.12: SEM images showing the fracture surfaces of the multiscale E-glass composites with 1.0 wt.% CNT (dip-coated) including (a) a low magnification image, (b) a high magnification image showing the residual CNT coating on the fiber surface of the fractured E-glass fiber, (c) the cross-sections of the fractured E-glass fibers and (d) the fiber debonding trace remained in the matrix phase, evidencing visible surface roughness.

4.3.1.4 Densely Concentrated Carbon Nanotubes in Multiscale composites

As shown in Figure 4.13, the morphologies of the multiscale composites with EPD-hybridized CNTs demonstrate a uniform and homogeneous CNT coating around the fiber, which is in general much denser than the solution-based CNT coating. This is mainly attributed to the EPD mechanism that CNT-deposition occurs through the

electrical double layer distortion and thinning, followed by coagulation of the electrically-charged CNTs on the nonwoven fabric-covered electrode [69,70], in which electrohydrodynamics or electroosmosis effects consolidate CNTs into densely-packed arrays [70,71]. Specifically, the distinguishable morphological characteristics illustrated in Figures 4.13a through f confirm that the EPD method creates a locally uniform CNT network onto the fiber surface with a consistent thickness along both the circumferential and longitudinal directions of the fiber. It is worth mentioning that the existing thickness of the CNT coating (~2 μm, in Figures 4.13a and b) is significantly lower than those obtained from dip-coating method (Figure 4.11), although the actual concentration of CNTs (1.8 wt.%) in the EPD-processed composites is much higher than those composites (0.75 and 1.0 wt.%). This reveals that EPD method deposited extraordinarily dense networks of CNTs onto the fiber surfaces, which is further validated by the higher magnification images shown Figure 4.13b and 4.13d. In these SEM micrographs, the localized coating appears to be compact with the PEI-wrapped CNTs randomly embedded in the diffused epoxy resin. Particularly, the amine functional groups in the PEI can react with both ozone-treated CNTs and epoxide group of the epoxy resin [49,50]. As a result, a strong wettability and adhesion are realized between the CNT coating and the resin matrix as observed in Figure 4.13b.

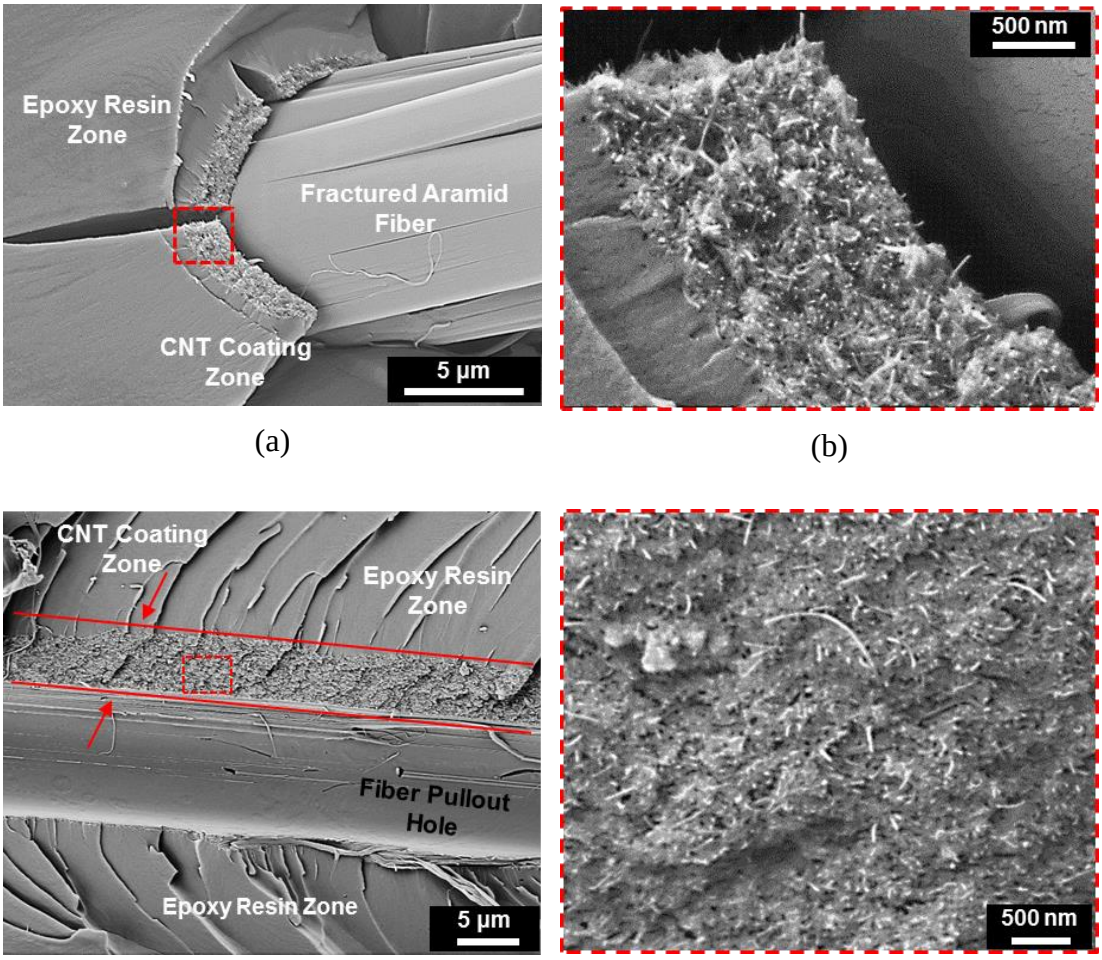

Figure 4.13: SEM images showing the fracture surfaces of the multiscale composites with EPD-hybridized CNTs (1.8 wt.%) including (a) a cross-sectional view, (c) a longitudinal view, and (d) and (b) high magnification images of the CNT coating highlighted in (a) and (c), respectively.

4.3.2 Thermomechanical Responses

The measurements of changes in volumetric dimension as function of temperature are shown in Figure 4.14 for a selected group of specimens. Coefficient of thermal expansion (*CTE*) before glass transition temperature (T_g) were measured from the slope of curves. Here, T_g appears as the onset of the abrupt change in slope in the linear thermal expansion curve, that is referred to as T_g^{onset}. Table 4.3 lists the *CTE* and T_g^{onset} measurements of 12 different composites characterized in this study. It can be seen that the dimensional change in all composite systems increases as temperature goes up until T_g^{onset}; however, after T_g the multiscale composites show a reduced *CTE* as compared with the nanocomposites with an elevated *CTE*. Generally, the overall molecular structure of a cured epoxy is amorphous and there exists significant free volume mixed with the rigid crosslinked network [72]. As an epoxy is heated up, its specific volume expands linearly due to the local vibration of the pendant phenyl group controlled by the steric hindrance of neighboring elements of chains [73]. As the temperature reaches T_g^{onset}, the long chain backbone becomes mobile and undergoes the segmental motion within the available free volume, causing a significant drop in the modulus and a dramatic change in volume expansion due to the greater separation between individual polymer chains [73].

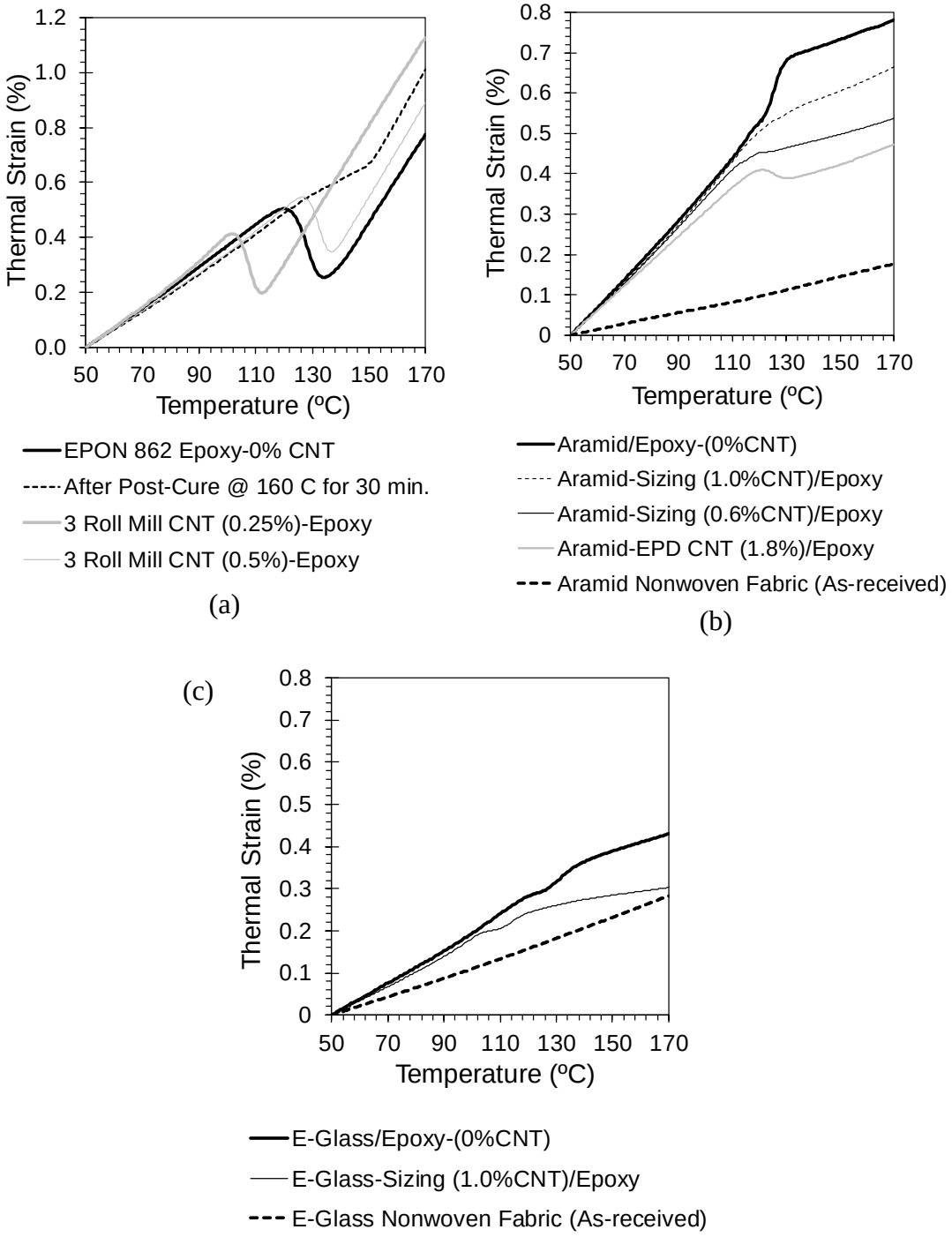

Figure 4.14: Thermomechanical responses showing dimensional changes as function of temperature of (a) CNT-based nanocomposites, (b) CNT-aramid nonwoven multiscale composites, and (c) CNT-E-glass nonwoven multiscale composites (CNT loadings shown in wt.%).

Table 4.3: Summary of *CTE* and T_g^{onset} of a Selected Group of CNT-Based Composites Measured Using Thermomechanical and Thermoresistive Methods.

Sample Group	*CTE*- (10^{-6}/ºC) ($T < T_g$)*	T_g (ºC)- from *TMA*	T_g (ºC)- from *TCR* Analysis
Aramid nonwoven fabric (raw)	15±3	N.A. (no resin)	N.A. (not conductive)
E-Glass nonwoven fabric (raw)	23±2		
EPON862 Epoxy-0 wt.% CNT	74±4	121±3	
EPON862 Epoxy-0 wt.% CNT (post-cured at 160ºC)	64±2	148±2	
3 roll mill CNT(0.25 wt.%)-Epoxy	81±3	105±3	104±2
3 roll mill CNT(0.50 wt.%)-Epoxy	68±2	125±4	122±4
Aramid/Epoxy-(0 wt.% CNT)	68±3	119±3	N.A.
Aramid-Sizing (1.0 wt.%CNT)/Epoxy	65±4	114±5	114±3
Aramid-Sizing (0.6 wt.%CNT)/Epoxy	64±5	115±4	113±3
Aramid-EPD CNT (1.8 wt.%CNT)/Epoxy	61±3	120±3	119±2
E-Glass/Epoxy-(0 wt.% CNT)	38±2	121±2	N.A.
E-Glass-Sizing (1.0 wt.%CNT)/Epoxy	36±3	110±2	109±2

* Note: all all T_g values shown in this table are equivalent to T_g^{onset} and showing the average of four specimens. *TCR* analysis is explained in Section 4.3.4.

It is clear that the neat epoxy in Figure 4.14a shows T_g^{onset} at 121ºC and then following a crossover phase transition to its rubbery state after 130ºC in which the *CTE* becomes two to three times higher than its value below the T_g^{onset}, resulting from the substantial changes in physical properties. Since post-curing results in a considerable increase in the crosslink density, the neat epoxy post-cured at 160ºC shows 22% increase in T_g^{onset} with a sharp transition as shown Figure 4.14a. In specific, the EPON 862 molecules are in the size of 2.3×0.9×0.6 nm [74] which is comparable to the dimension of individual carbon nanotubes. Therefore, the presence of CNTs in epoxy can significantly influence the molecular motions and interfere with the formation of the crosslinked network of the resin matrix during curing. Compared with the neat epoxy, the nanocomposite with 0.25 wt.% CNT displays 9% increase in *CTE* and 15% decrease in T_g^{onset}, which can mainly arise from the fact that the residual catalyst impurities attached on the raw CNT material and the physisorption of the curing agent surrounding CNTs can accelerate curing rate, leading to a reduced degree of cure and a low crosslink density [57,75-77]. It may also partially result from the well dispersed CNTs (as demonstrated in SEM images of Figure 4.7c-d) that can increase the intermolecular distance of the epoxy, resulting in decreased intermolecular forces and then a further reduced T_g^{onset} [76]. On the contrary, for the nanocomposite with 0.5 wt.% CNT (a significant CNT loading much greater than the percolation threshold of 0.1 wt.% [46], these negative effects to T_g^{onset} are counterbalanced by the restricted mobility of the polymer chains [51] due to the well-established CNT network (as evidenced in SEM images of Figure 4.7a-b) and interfacial interactions over a huge interfacial area between the CNTs and the polymer matrix [78], showing a slightly increased T_g^{onset} and 8% reduction in *CTE*.

Figures 4.14b and 4.14c show the thermomechanical behaviors of the fibrous composite systems. The plain aramid and E-glass composite have the identical T_g^{onset} as the neat epoxy but with a reduced *CTE* due to the strengthening effect of the fibers. As discussed previously in Section 4.3.1.3, the interfacial adhesion between the E-glass fiber and epoxy resin is much stronger than that in aramid fiber composites, which consequently results that the *CTE* of the aramid composite is close to the *CTE* of the neat epoxy (i.e., a matrix dominated response), whereas the *CTE* of the E-glass composite approaches the *CTE* of the raw aramid fabric (i.e., a fiber dominated response). Coincidentally, the CNT-based multiscale composites with the localized CNTs in the vicinity of the fibers follow the similar trend. In particular, some quantitative differences in T_g^{onset} are apparent that the CNT sizing-based composites exhibit a slightly reduced T_g^{onset} (~6%) in comparison with the plain composites, which can be attributed to the local perturbation effect of the inhomogeneously concentrated CNTs that the thin or thick and the partial or complete CNT coating at the fiber-scale may unevenly decelerate or accelerate the curing rate of nearby epoxy resin and diminish the heat curing reaction locally, leading to a non-uniformly crosslinked polymer network with reduced crosslink density [79].

In contrast, the multiscale composite with EPD-hybridized CNTs displays an unchanged T_g^{onset} of 120ºC and about 9% reduction in *CTE*. This can result from that the uniform and dense CNT coating as well as the enhanced interfacial bonding at the epoxy-CNT interface (as demonstrated in Section 4.3.1.4) allow CNTs to act as effective reinforcement which can hinder the mobility of epoxy chains within the local interphase, ensuring an undisturbed bulk thermomechanical response. For comparison,

the T_g^{onset} obtained from the thermal coefficient of resistance (*TCR*) analysis are also included in Table 4.3 and will be discussed in Section 4.3.4.

4.3.3 Simulated Thermal Stresses in Multiscale Composites

In fiber composites, thermal stresses are induced resulting from the mismatch in *CTE* and Young's moduli of the fibers and the matrix [80-86]. Additionally, changes in these thermal stresses can cause the embedded CNT network within the multiscale composites to display different electrical resistive outcomes. Thus, a micromechanical analysis is needed to study the effects of residual stresses in micro-level. In this context, a 10-μm high cylinder representative volume element (RVE) can be considered to describe the composite structure of the proposed CNT-based multiscale composites as shown in Figure 4.15, in which the localized CNT-coating is fully immersed within the epoxy resin and directly contacting the fiber surface in accordance with the findings of the electron microscopic analysis per Section 4.3.1.3. The thermal stresses exerted on the fiber/resin system can induce a stress field on the CNT-coating that can be resolved into three normal stresses including the radial (σ_{rr}), hoop ($\sigma_{\theta\theta}$) and axial (σ_{zz}) stress as shown in Figure 4.15. Particularly, increasing σ_{zz} and $\sigma_{\theta\theta}$ will extend the CNT network, enlarge the tunneling gaps between CNTs, and consequently give a rise to the increase of the bulk resistance. While the growth in σ_{rr} will compress the CNT network in its through-thickness direction, create CNT junctions, shorten CNT-tunneling gaps, and therefore reduce the resistance.

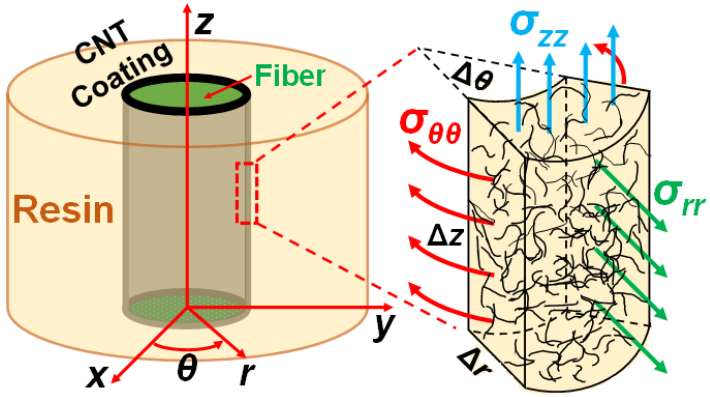

Figure 4.15: Schematic model of a cylinder representative volume element from the proposed CNT-based multiscale composites, and the detailed illustration showing the resolved normal stresses exerted on a typical volume element of the epoxy resin infiltrated CNT-coating on fiber surfaces.

Here, the finite element analysis of thermal stresses was performed on a quarter of the RVE (as illustrated in Figure 4.6) from T_g^{onset} to room temperature (i.e., the cooling process). The T_g^{onset} was selected as the initiate reference temperature because during the glass transition state of the epoxy resin, the molecular motion of the polymer and the amplitude of this motion are very high and the macromolecule is not practically in contact with each other [51,78], resulting in a stress-free state without physical interactions between fiber and matrix [85]. Figure 4.16a and 4.16b plot σ_{rr}, $\sigma_{\theta\theta}$ and σ_{zz} in the aramid/resin and E-glass/resin system, respectively. It is apparent that as temperature decreases, these stresses increase linearly in the matrix of both composite systems that $\sigma_{\theta\theta}$ and σ_{zz} are tensile and σ_{rr} is compressive. In specific, σ_{zz} ultimately reaches about 18 MPa in both systems, which is comparable to the residual axial tension of 45.5 MPa in matrix of the unidirectional Kevlar®29/epoxy composite experimentally studied using laser Raman microscopy by Anagnostopoulos

et al. [87]. Whereas, σ_{rr} and $\sigma_{\theta\theta}$ are respectively 17 MPa and -12 MPa in the E-glass/resin composite which are about five time higher than those in the aramid/resin system. Compared with their ultimate strength of about 55 MPa as reported in Section 2.3.4, these residual stresses are not negligible and can induce a significant resistive effect to the CNT network. Obviously, the CNT coating in both multiscale composites are substantially pre-tensioned around the fiber surface as ramping down to the room temperature. Due the thin thickness of the CNT coating, the compacting effect to the CNT network caused by σ_{rr} may not be as dominant as the combined expansion induced by $\sigma_{\theta\theta}$ and σ_{zz}.

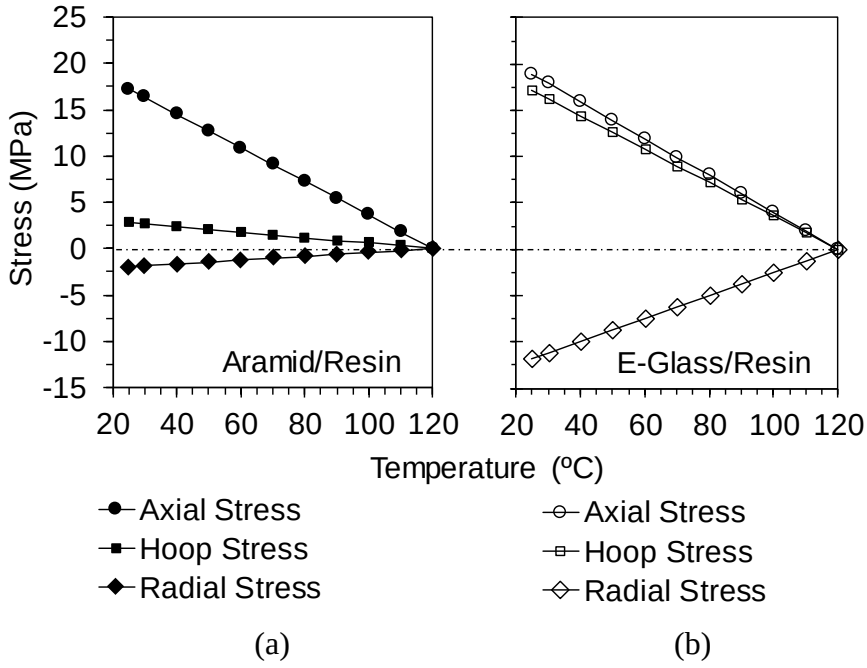

Figure 4.16: FEA results of thermal residual stresses in the close vicinity of the fiber-resin interface in (a) aramid/resin and (b) E-glass/resin composite system as cooling from T_g^{onset} to 25ºC.

Figure 4.17a and 4.17b show the stress distributions along the radial direction of the matrix phase with respect to the distance from the fiber-resin interface at room temperature. It is clear that a constant σ_{zz} is sustained throughout the whole resin matrix in the both aramid and E-glass composite systems. On the other hand, σ_{rr} and $\sigma_{\theta\theta}$ decrease as being away from the interface, exhibiting trends similar to those reported elsewhere [80,81,84]. Especially, these two stresses in the aramid/resin composite are found to be less than 1 MPa in magnitude after moving 5 μm against the interface within the matrix. Likewise, at the same relative location in the E-glass/resin composite $\sigma_{\theta\theta}$ and σ_{rr} are 10 MPa and -2 MPa, respectively. Consequently, it is believed that a minimal 5μm-wide influencing zone dominated by the residual tensile stresses is existing around the fiber surface in the aramid and E-glass composites. Furthermore, this zone of influence is large enough to impact the entire CNT-coating which are about few microns thick around fiber surfaces as shown in Sections 4.3.1.3 and 4.3.1.4, leading to considerably prestressed CNT networks at room temperature.

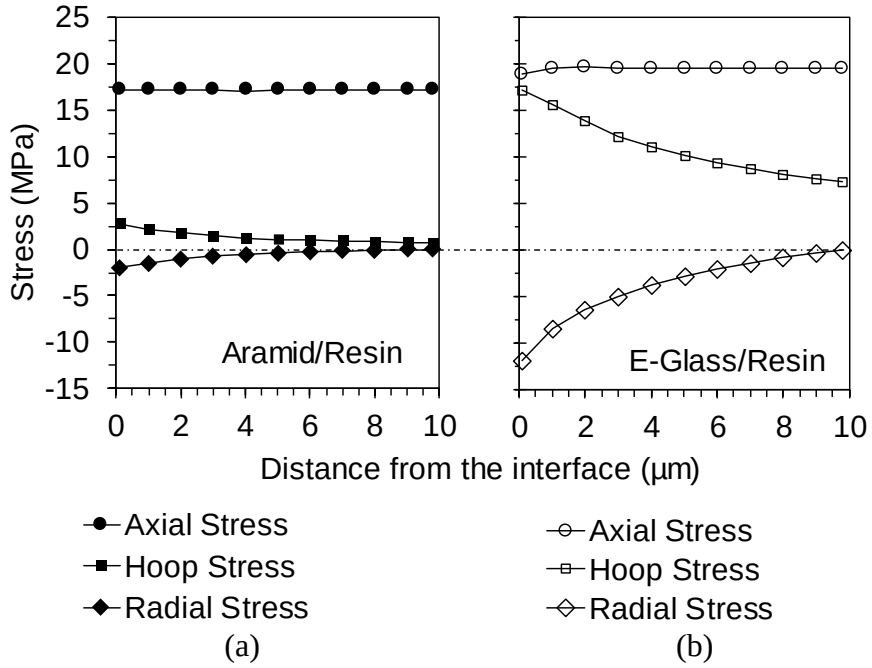

Figure 4.17: FEA results of the residual stress distributions in the radial direction of the matrix from the fiber-resin interface in (a) aramid/resin and (b) E-glass/resin composite system at room temperature.

4.3.4 Thermoresistive Behaviors

4.3.4.1 Nanocomposites with Randomly Dispersed Carbon Nanotubes

The previous experimental study by Thostenson and Chou [46] demonstrated that the formation of a conductive percolating network in a CNT-epoxy nanocomposite can be achieved at the CNT concentration below 0.1 wt.% by using the three-roll milling approach. In the current research, two nanocomposites with CNT loadings of 0.25 and 0.5 wt.% were fabricated and selected to investigate the thermoresistive behaviors as thermally cycled. Figure 4.18(a) and (b) show the typical electrical responses with respect to temperature (T). It is apparent that both nanocomposites display a monotonic growth in resistance as T increases and a

continuous reduction in resistance upon cooling during two thermal cycles from 25 to 145 ºC, evidencing a nonerasable but reversible thermoresistive behavior.

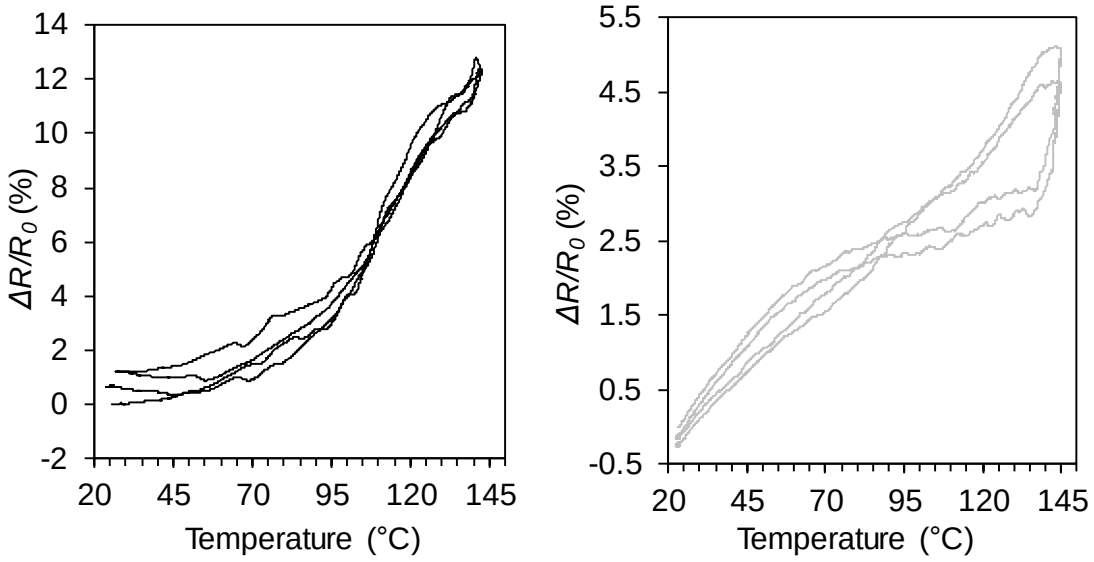

(a) (b)

Figure 4.18: Thermoresistive responses of CNT-epoxy nanocomposites with (a) 0.25 wt.% and (b) 0.50 wt.% CNTs during thermal cycling between 25 and 145 ºC, showing a PTC in general.

In particular, at the low CNT concentration of 0.25 wt.%, the electrical conduction of the nanocomposite is mainly dominated by the electrical tunneling effect [88] between the well dispersed CNTs as previously shown in Figure 4.7c. Additionally, the tunneling gap formed by the insulating polymer between CNTs determines the bulk resistive behavior. As *T* increases, thermal expansion of the polymer results in the extension of the gap, leading to the growth of resistance (i.e., the temperature-dependent tunneling effect [28]). As *T* further rises, the

macromolecule chain of the polymer starts to vibrate in place at an increasing rate, which therefore induces a faster increase in resistance. As *T* finally passes T_g^{onset}, those dispersed CNTs are significantly separated from each other due to the segmental motion of the large polymer chains, consequently giving rise to a dramatic jump in resistance. Thus, the curve of this nanocomposite shown in Figure 4.18a is in the concave-upward shape with the local peck corresponding to the highest temperature.

On the other hand, the CNT network in the nanocomposite with 0.5 wt.% CNTs contains both the dispersed CNTs and the interconnected CNT clusters (i.e., CNT agglomerates in microscale) as shown in Figure 4.7a, resulting in a combined dominance of the temperature-dependent tunneling and the tube-tube contacts to the bulk electrical response. Since the tunneling gap between CNTs on average is reduced in the network with a relatively high CNT loading, the linear thermal expansion from 25 to 70 ºC can induce more pronounced increases in resistance due to thermally-activated hopping of electrons [38,89]; whereas in the same temperature range the large CNT agglomerates are constrained by the crosslinked polymer network without altering the intertube contacts, leading to an inaction of the resistance change. As *T* approaches T_g^{onset}, polymer chains become mobile, but the mobility is hindered by the presence of CNT agglomerates due to the increased thermodynamic interactions [51,77,78], as a result the resistance increases at a reduced rate. After glass transition, the intense movement of large polymer chains further dissociates both CNTs and CNT agglomerates, which can break down the conductive network, resulting in a sharp ascending resistance change. Consequently, the shape of the thermoresistive curve shown in Figure 4.18b is concave-downward with a dramatic transition to the local summit at the great temperatures. As cooling below T_g^{onset}, the rearranged CNT

agglomerates are frozen in the glassy state by the crosslinked network, therefore a linear thermoresistive behavior can be observed as ramping down to the room temperature.

It is clear that during the same thermal cycles the 0.25 wt.%- and 0.5 wt.%-CNT nanocomposites correspondingly show 14% and 5% overall resistance change, evidencing the CNT concentration dependence of thermoresistive sensitivity. In order to better visualize the effect of temperature, the electrical responses of these two nanocomposites during the first ramp-up segment are shown in Figure 4.19a and 4.19b, respectively. Compared with the curve of 0.5 wt.%-CNT, a distinctive infection point appears at 104 ºC on the 0.25 wt.%-CNT curve, which matches the T_g^{onset} of this specific nanocomposite (i.e., 105 ºC in Table 4.3), indicating a strong correlation between the local distinction of the thermoresistive response and the TMA-measured T_g^{onset}. However, this correlation is ambiguous in the curve of 0.5 wt.%-CNT.

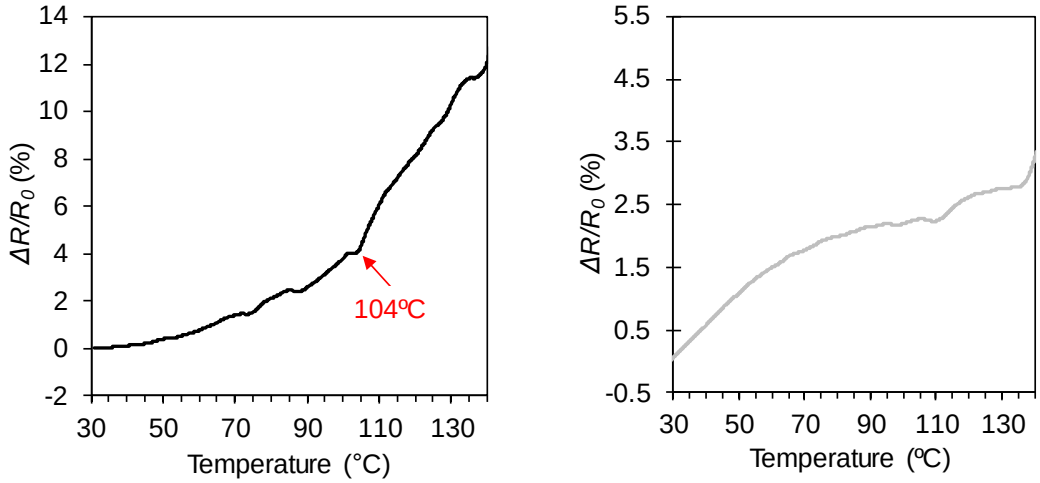

Figure 4.19: The first ramp-up segments of the thermoresistive responses of (a) 0.25 wt.% CNT and (b) 0.50 wt.% CNT nanocomposites during 25-145 ºC thermal cycles.

The temperature coefficient of resistance (*TCR*, as defined in Section 4.2.2.4) is widely used to evaluate the thermoresistive sensitivity of nanocomposites including CNT-vinyl ester [38], CNT-epoxy [28], CNT-HDPE [30], CNT-PC [33], CNT-SEBS [35], etc. Here, the *TCR* response of these two nanocomposites during the heating ramp are shown in Figure 4.20a and 4.20b with respect to temperature. It is obvious that both relationships are wavy in shape with multiple local minima and maxima corresponding to different temperatures. In general, the *TCR* curve of the nanocomposite with 0.25 wt.% CNT shows more sharp changes with higher amplitudes than the one with 0.5 wt.% CNT, demonstrating a network structure with the elevated thermoresistive sensitivity. Similar kinds of *TCR* correlations have been reported elsewhere [28-31,35,36].

In addition, the observed *TCR* behavior is analogous to piezoresistivity [44,90] in CNT nanocomposites where CNT networks with less nanotubes have relatively fewer conductive pathways, leading to more pronounced resistance changes in reaction to the thermally induced physical effects, which can shed light on the influence of CNT concentration to the system sensitivity. As explained previously, the CNT network with 0.25 wt.%-CNT is subjected to a dramatic structural change right after glass transition, therefore an increased *TCR* is expected when $T \geq T_g$. On the other hand, the network of 0.5 wt.%-CNT at elevated temperatures is allowed to become more interconnected and less resistive due to CNT-re-agglomeration, consequently showing less sensitivity towards temperature variations, i.e., a reduced *TCR* is predictable when $T \geq T_g$. Following this logic, the local minimum of 104 ºC and the local maximum 122 ºC as shown in Figure 4.20a and 4.20b are filtered out of the *TCR* responses and designated as the local *TCR* correspondence to T_g^{onset}, which

indeed follows the TMA results listed in Table 4.3. Lastly, these observations confirm the sensitivity and feasibility of using the percolating CNT networks distributed within the polymer matrix for sensing the polymer transitions.

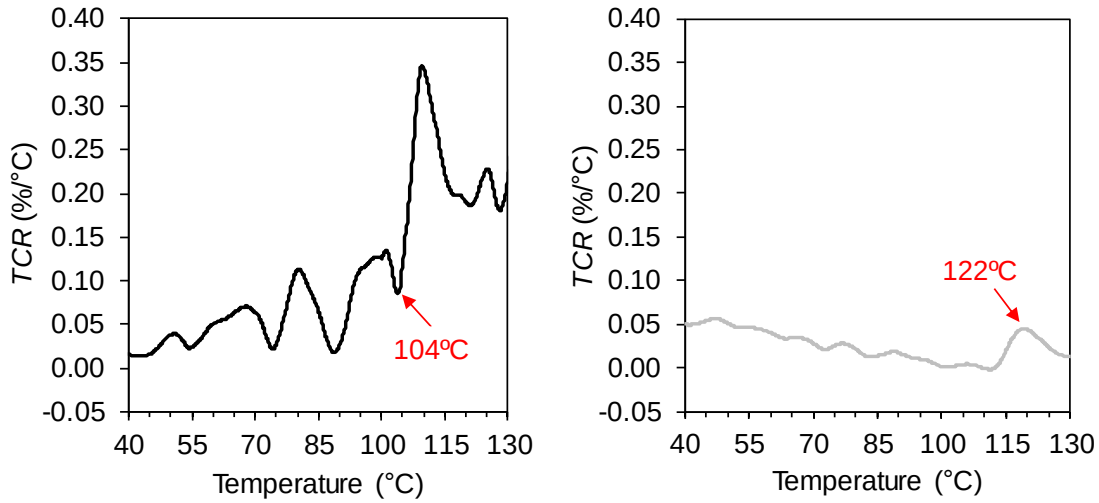

(a) (b)

Figure 4.20: Corresponding *TCR* relationships of (a) 0.25 wt.% CNT and (b) 0.50 wt.% CNT nanocomposites with the identified local inflection points as the T_g^{onset}.

4.3.4.2 Multiscale Composites with Loosely Concentrated Carbon Nanotubes

As well explained by the electron microscopic analysis in Section 4.3.1.3, the multiscale composites with CNT-modified fibers using the dip-coating approach show the unique morphology of loosely concentrated CNTs, following closely as proposed in Figure 4.1b. As listed in Table 4.2, six groups of aramid-sizing/epoxy samples for *in situ* thermoresistive characterization show a relatively low resistivity ranging from 0.18 to 25 Ω·m at room temperature and minor intra-/inter-batch variations of about 7% in average, which are primarily ascribed to the double-percolating effect originated from the exceptional structure of the composite system per Section 2.3.5.1 and the simple and robust two-step manufacture process per Section 2.2.

Figure 4.21 represents the typically observed thermoresistive responses during two thermal cycles for the selected samples from these multiscale composites with 1.0, 0.6, 0.17 and 0.05 wt.% CNT. The 1.0 and 0.6 wt.% specimens shown in Figure 4.21a and 4.21d that are well above the percolation threshold, present fewer fluctuations than the specimens with 0.17 and 0.05 wt.% CNT as shown in Figure 4.21c and 4.21d during the heating and cooling cycles. It is clear that the observed trends are following a negative temperature correlation (NTC) in overall with double crossover transitions as increasing temperature and with dual concave shifting upon cooling, showing a unique reversible temperature dependence of resistivity that has not yet been reported in scientific literature.

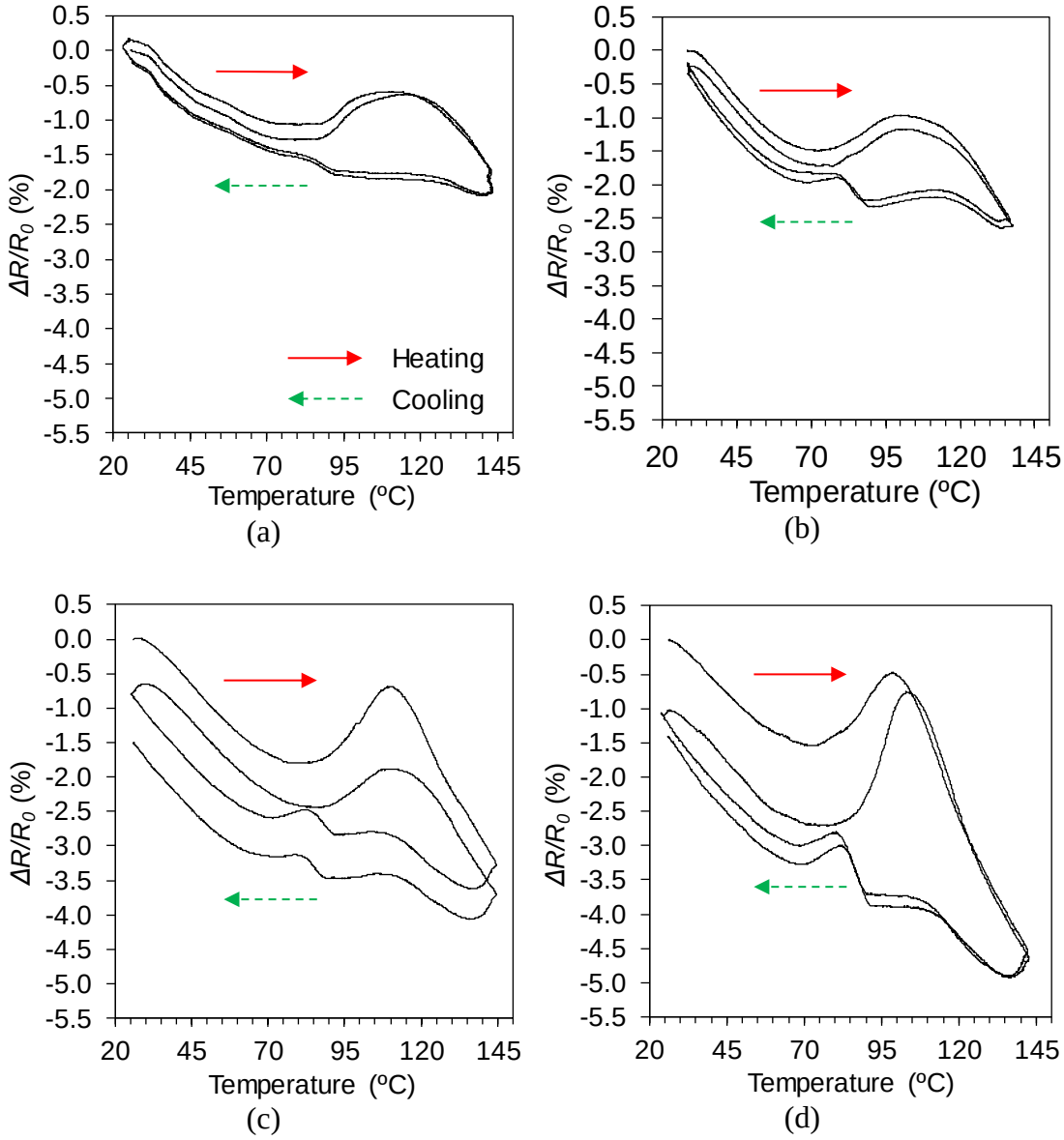

Figure 4.21: Thermoresistive responses of aramid-sizing/epoxy multiscale composites with CNT loadings of (a) 1.0 wt.%, (b) 0.61 wt.%, (c) 0.17 wt.%, and (d) 0.05 wt.% during 25 to 145 ºC thermal cycles.

As explained in Section 4.3.3, the CNT network in the multiscale composites is significantly pre-tensioned at the room temperature due to the residual thermal

stresses. Nonetheless, during heating segment, this pre-tensioning stress can be released gradually and then the CNT network contracts back to its original shape, leading to persistent decreases in bulk resistance as previously shown in Figure 4.21. It is clear that this stress-relieving induced volumetric shrinkage completely surpasses the local thermal expansion of the entire epoxy phase at the initial heating stage, therefore resulting in a strong NTC up until 70 ºC. Afterwards, the first crossover transition appears as the local minimum around 75 ºC for all aramid-sizing/epoxy specimens. Following closely, the thermoresistive curve shows a sharp catch-up rally as a result of the larger thermal expansion of polymer matrix (especially, the locally infiltrated epoxy in the CNT network) that balances out the contraction caused by releasing the residual stresses, extending the CNT network outright. Next, the second crossover transition shows up at the local peak around 105 ºC and immediately switches to a more dramatic NTC to 145 ºC. At the elevated temperature lower than T_g^{onset}, the charge carriers in epoxy originating from un-polymerized monomer can become substantially excited due to the increased mobility of small polymer chains, then facilitating the overall electrical conduction [43,91].

Meanwhile, for the locally concentrated CNT network, nanotubes appear in form of large agglomerates (as shown in Figures 4.11 and 4.12) that the number of tube-tube contacts is extremely large, leading to an electronic-movement dominated conductive network [34]. Therefore, the resistance is reduced due to the increased electron mobility at the raised temperature. As $T \geq T_g^{onset}$, the violent thermodynamic interactions driven by the macromolecules of the polymer allows CNT agglomerates to be rearranged [29,34,35,39,92] in a relatively reduced free volume [72], creating compacted CNT re-agglomerates and then giving rise to a more conductive network.

During the cooling segment, a mild resistive relaxation is first observed from 145 to 140 ºC on all thermoresistive curves shown in Figure 4.21, which is presumably due to the thermal hysteresis of epoxy in its rubbery state. Next, a clear NTC is found in the temperature range of 140 ºC > T > T_g^{onset}, in which the volume of the polymer slightly shrinks but the long chain molecules in the rubbery state still vibrate intensely, may break down the conductive network of the secondary CNT agglomerates and thereby resulting in the increasing resistance. At about 115 ºC (~T_g^{onset}), the first concave-downward shift is presenting due to the phase transition of the polymer. As cooling right below T_g^{onset}, the thermal stresses in tension starts to build up in the CNT interphase, and in the same time the crosslinked polymer chains initiate the restraint to the CNT network, leading to a combined consequence that makes the thermoresistive response reach a plateau near 110-85 ºC.

Later, in the glassy state, continuous reducing the temperature introduces a sharp rebound in resistance from 85 to 74 ºC which is mainly attributing to the resultant structural changes of the CNT network from the competition between the linear thermal contraction and the residual stress accumulation, evidencing the dominant role of the residual tensile stresses in electrical conduction of the composite system. Apparently, the second concave-downward shift shows at around 74 ºC which is in a good match with the first crossover temperature in the heating ramp. In particular, the multiscale composites with 0.17 and 0.05 wt.% CNT as shown in Figures 4.21c and 4.21d present a local reduction of resistance in 74-65 ºC, since the thermal contraction can cause more pronounced effects to the considerably thin CNT coatings than the 1.0 and 0.7 wt.%-CNT networks. It is obvious that below 65 ºC, all thermoresistive curves demonstrate a consistent NTC following the same trend as it in

the heating segment, which further confirms the dominance of the residual tensile stress to the thermoresistive behaviors at low temperatures.

In contrast, as shown in Figure 4.22a, the thermoresistive response of the post-cured specimen (with 1.0 wt.% CNT, same in Figure 4.21a) displays a single crossover transition during heating and cooling ramps, which is nearly constant and free of hysteresis. In general, the post-cure cycle enhances the degree of cure, increases the crosslink density, and reduces the free volume of the epoxy matrix. Compared with its original response shown in Figure 4.21a, the crossover temperature is delayed until 85 ºC, which is attributed to the increased residual thermal stresses at room temperature that accumulated over an extended temperature range from the increased $\boldsymbol{T_g^{onset}}$ as well as the enhanced stiffness of epoxy after post-curing.

Under the glassy state, the entire CNT network is significantly constrained by the densified crosslinked polymer network and then displays a plateau of slow growth in resistance during 85-145 ºC, due to the dominance of thermal expansion surpassing the residual stresses. In addition, the thermoresistive behavior of the E-glass-sizing-1.0wt.%-CNT specimen is represented in Figure 4.22b that the resistance changes with temperature is free of crossover transition and follows a monotonous NTC in a nearly linear fashion. It is obvious that two cyclic responses are overlapping from each other, indicating a high degree of reversibility. It is believed that this corrected thermoresistive behavior is primarily ascribed to first, the intensified residual tensile stress field on the CNT interphase by utilizing the isotropic fibers as explained in Section 4.3.3 that can result in a long-acting stress-relieving process (i.e., sustaining a linear NTC until 110 ºC); second, the improved interfacial bonding between the CNT network and the PVA coated E-glass fiber surface as demonstrated in Section 4.3.1.3

which can minimize the structural change of CNT network driven by the thermodynamic motions of the polymer during the rubbery state.

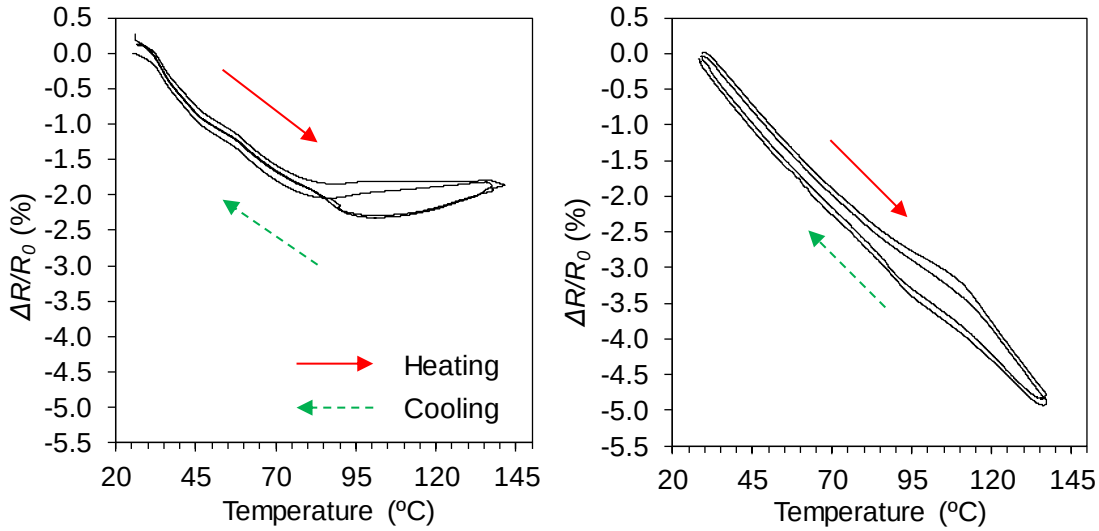

Figure 4.22: Thermoresistive responses of (a) aramid-sizing-1.0 wt.% CNT/epoxy composite after post-curing at 160 ºC for 30 minutes and (b) E-glass-sizing-1.0 wt.% CNT/epoxy composite, during 25-145 ºC thermal cycles.

In order to better visualize the effect of CNT concentration, the thermoresistive responses of five aramid-sizing/epoxy composite specimens during the first ramp-up segment are shown in Figure 4.23a. These specimens have CNT loadings of 1.0, 0.77, 0.61, 0.17 and 0.05 wt.%, and respectively show -1.5, -1.8, -2.4, -3.5 and -4.5% overall resistance change, indicating an inverse-proportional trend consistent to the CNT nanocomposites as discussed in previous section. The corresponding *TCR* responses are summarized in Figures 4.23b through 4.23f. It is clear that the curves of

1.0, 0.77 and 0.61 wt.% CNT are in the same shape that the local inflection point appears after 105 ºC (i.e., the second crossover temperature in average) can be observed distinctively and obeys T_g^{onset}, that is 114, 117, and 114 ºC, respectively. After glass transition, these three specimens show the reduced changing rate of *TCR*, which is expected for a CNT network with high CNT loading such that tube-tube contacts dominate the electrical conduction, resulting in relatively low system sensitivity to the polymer thermodynamic effects. On the other hand, the 0.17 and 0.05 wt.% curves display increased changing rate of *TCR* after the local minima of 118 ºC, which is reasonable for the conductive network with low CNT concentration in which electrical tunneling is the dominant conduction mechanism. These observed results are in agreement with the thermoresistive experiments on CNT-vinyl ester nanocomposites by Lasater and Thostenson [38]. Shortly, the thermoresistive measurements of the CNT-nonwoven multiscale composites are sensitive to local polymer motions and the system sensitivity is adjustable by altering CNT concentrations.

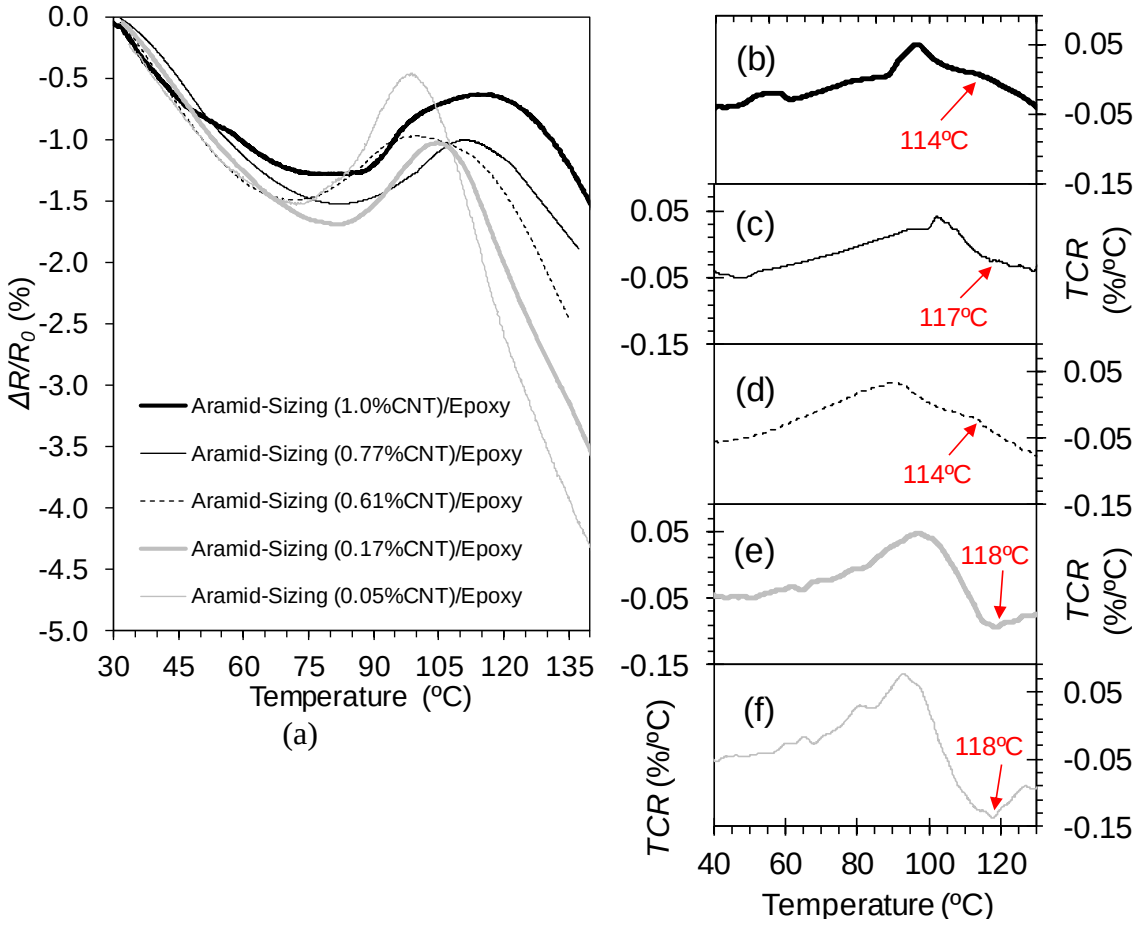

Figure 4.23: (a) Thermoresistive responses of aramid-sizing multiscale composites with 1.0, 0.77, 0.61, 0.17 and 0.05 wt. % CNT during the first ramp-up segment. (b) through (f) Corresponding *TCR* relationships with the identified local inflection points as the T_g^{onset} .

The properties of the polymer matrix can be improved through post-curing process. In order to better understand the individual role of CNT morphology, fiber and epoxy playing in thermoresistive behaviors of the multiscale composites, a quantitative comparative study among the untreated, the post-cured and the non-fibrous control specimens is presented in Figure 4.24. In particular, the control group

is made of CNT sheet/epoxy composites without fibers (as introduced in Figure 4.9) and intended to replicate the local morphological state of CNTs in the proposed multiscale composites that a relatively large amount of CNTs are concentrated within a narrow local interphase and infiltrated with epoxy as demonstrated in SEM images of Figure 4.11. As shown in Figure 4.24a, the thermoresistive responses of the three specimens during the first heating ramp present a comparatively similar trend of NTC before the first crossover temperature, indicating that the initial NTC shown by the multiscale composites cannot only be attributed to residual stresses but can be partially due to the unique intrinsic feature associated to the morphology of the macro CNT networks similar to those reported elsewhere [19,34,35,40,93]. Therefore, this strong NTC is not dominated by the residual thermal histories in polymer and then cannot be treated by annealing.

In addition, as shown in the inset of Figure 4.24a, the thermal cyclic response of the control specimen displays a U-shaped trend in general, which, however, is not fully reversible. This can result from the peak test temperature of 145 °C is higher than the epoxy cure temperature of 130 ºC, that is every heating ramp can induce slight permanent change (i.e., post-curing) to the polymer network above 130 ºC, therefore leading to the cycle-to-cycle resistance changes shown at 25 and 145 ºC. However, this irreversible feature is not observed in the aramid-sizing/epoxy specimens with CNT loadings of 1.0 and 0.61 wt.% as presented in Figure 4.21a and 4.21b, which reveals that fibers in the CNT-multiscale composites can improve the structural stability of the composite system, share the electrical dominance of the CNT network, and therefore can be beneficial for overcoming instable resistance changes induced by thermal relaxation of polymer matrix. Furthermore, it is clear that the non-fibrous,

fibrous and post-cured fibrous CNT composites show the overall resistance changes of 1.0, -1.5 and -2.0 %, and the crossover temperatures of 60, 75 and 85 ºC, respectively, which confirms that combining fibers and polymer matrix can induce a synergistic effect for sustaining an extended NTC and leading to a less resistive CNT network.

The corresponding *TCR* responses are shown in Figures 4.24b through 4.24d. Obviously, the untreated and post-cured specimens display a nearly identical *TCR* before the crossover temperature, which results from that within the thermoelastic range the thermoresistive sensitivity is dominated by the intrinsic features of the concentrated CNT network such as the morphology and CNT loading and is not governed by polymer matrix. Particularly, both the untreated and control specimens demonstrate the decreasing *TCR* after the local peak (that is, 109 and 114 ºC, respectively), which obey the previously observed trend that for a CNT-based composite with high CNT loading, the thermal sensitivity decreases after T_g^{onset}. Nevertheless, due to the excellent thermal stability, the post-cured specimen shows a constant *TCR* of 50×10^{-6}/ºC in 100-130 ºC, which is considerably smaller in magnitude than the reported *TCR* of -0.005/ºC for CNT/SEBS [35], 0.021/ºC for CNT/epoxy [28], -0.003/ºC for CNT/polycarbonate [33] and -0.046/ºC for buckypaper/epoxy [25] nanocomposites.

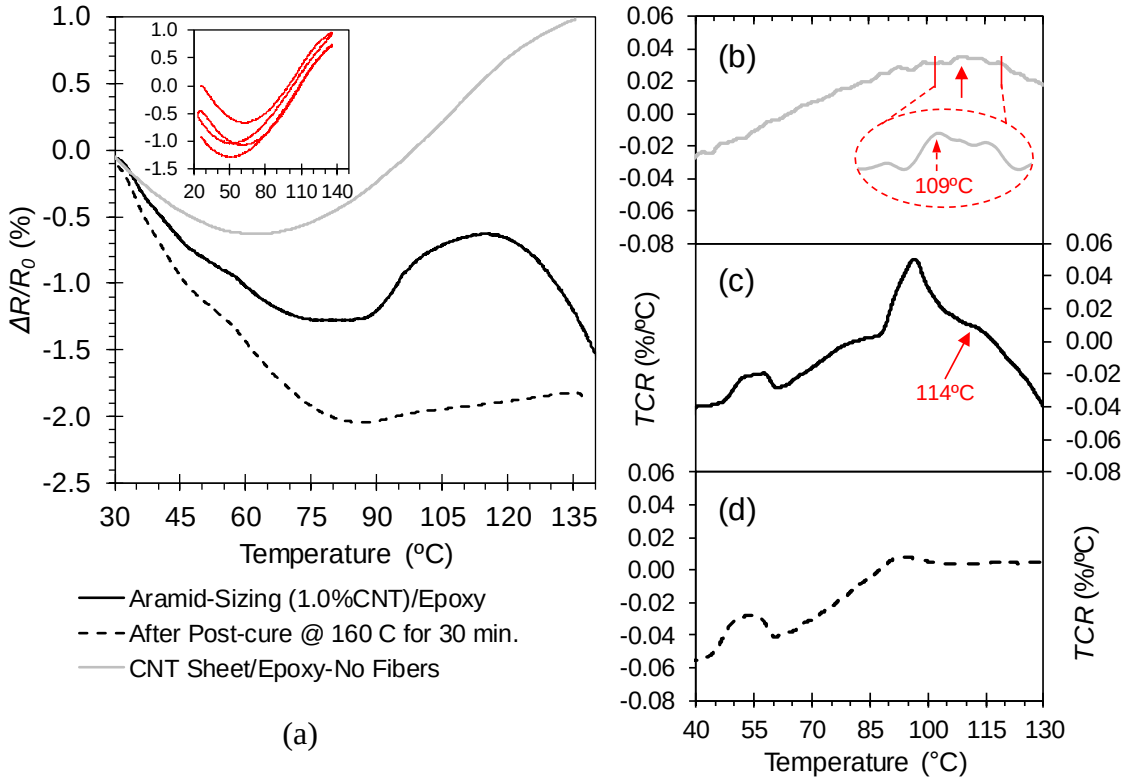

Figure 4.24: (a) Comparison with thermoresistive responses of CNT sheet/epoxy composite (control specimen) and aramid-sizing multiscale composites with 1.0 wt.% CNT before and after post-curing. Inset: thermoresistive behavior of the control specimen as thermally cycled. (b) through (d) Corresponding *TCR* relationships with the identified T_g^{onset}. The magnifier shows the enlarged local *TCR* response.

As previously shown in Figure 4.22, the E-glass-sizing multiscale composite shows different thermoresistive behavior as compared with the aramid-sizing specimens. In order to gain a better understanding on the observed responses, the micron-level interface between the CNT and E-glass fiber was replicated on planar glass substrates in a macroscale to learn the influence of fiber properties and interfacial adhesion on the bulk thermoresistive responses of multiscale composites. As shown in the inset of Figure 4.25a, this control specimen shows a fully reversible

temperature dependence of resistance as thermally cycled, indicating a high degree of thermal stability and bonding between the CNT-sizing coating and the glass substrate.

In addition, Figure 4.25a compares the thermoresistive responses of three composite systems including the E-glass-sizing/epoxy, the control specimen and the aramid-sizing/epoxy. It is clear that the NTC shown by the E-glass-sizing composite nearly follows the linear trend of the control specimen, indicating an overall fiber dominated thermoresistive behavior supported by the strong interfacial adhesion between the CNT network and the fiber. In specific, from 70 to 105 ºC, the E-glass-sizing composite shows a slight deviation from the linear correlation, evidencing the local effect due to the thermal expansion of the epoxy, which coincides with the electrical dominance transition between the first and second crossover temperature shown by the aramid-sizing composite (dashed line). In the rubbery state, the resistance change of the E-glass-sizing composite shows a linear temperature dependence parallel to the resistive response of the control specimen, which confirms the common character of the CNT-fiber and the modeled interfaces that the CNT network is confined by the glass fiber/substrate through a strong interfacial adhesion, leading to a synchronized dimensional change corresponding to temperature variations.

Figures 4.25b to 4.25d present the *TCR* responses of the three composite specimens. It is obvious that the local minima are determined as the representative T_g^{onset} of the E-glass-sizing composite and the control specimen which also show a nearly constant *TCR* of -550 and -650×10^{-6}/ºC as $T < 70$ºC and $T >$ their local T_g^{onset}. This identical behavior is expected in accordance to their uniform thermoresistive responses, since the CNT network in both composite systems is formed with the same

dehydrated CNT sizing agent, a solid compound of CNTs, SDBS and film former, showing a porous structure in micron-scale as imaged in Figures 4.9 and 4.12. In addition, the E-glass- and aramid-sizing composites display a comparable T_g^{onset} of 115 and 114 ºC, respectively, evidencing a good repeatability of *TCR* among the CNT-sizing-based multiscale composites.

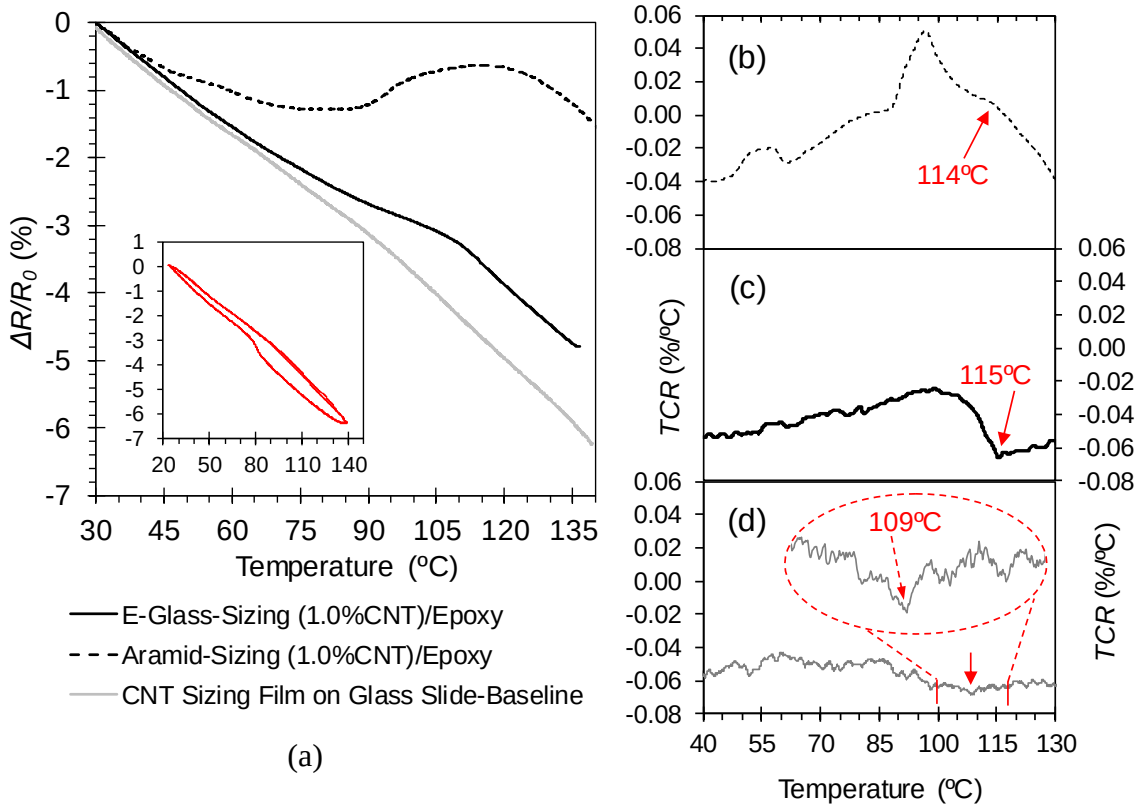

Figure 4.25: (a) Comparison with thermoresistive responses of CNT-sizing coated glass slide (control specimen) and the E-glass- and aramid-sizing multiscale composites with 1.0 wt.% CNT during the first ramp-up segment. Inset: thermoresistive behavior of the control specimen as thermally cycled. (b) through (d) Corresponding *TCR* relationships with the identified T_g^{onset}. The magnifier shows the enlarged local *TCR* response.

4.3.4.3 Multiscale Composites with Densely Concentrated Carbon Nanotubes

As demonstrated by the electron micrographs in Section 4.3.1.4, the multiscale composites with CNT-modified fibers using the electrophoretic deposition (EPD) approach show a morphology where the nanotubes are densely concentrated and uniformly distributed at the fiber interface. Two groups of specimens with CNT concentrations of 1.8 and 3.4 wt.% were fabricated using the aramid nonwoven fabric as the CNT carrier. As shown in Table 4.2, these two group of aramid-EPD CNT/epoxy specimens show considerably high room temperature resistivity of 226.8 and 27.2 Ω·m, respectively in comparison with other CNT composites, which are primarily ascribed to the ozone-PEI functionalization of CNTs (as detailed in Section 4.2.1.3). The ozone oxidation process can destroy the π-conjugated system of the CNT sidewalls [94], leading to a significantly increased intrinsic resistance of nanotubes. Meanwhile, the PEI functionalization process can create a thin insulating polymer layer on the surface of CNTs [50], giving rise to a high tube-tube contact resistance.

Figure 4.26 shows the typically observed thermoresistive responses of the EPD processed multiscale composites as thermally cycled from 25 to 145 ºC. It is clear that the two cyclic responses shown in Figure 4.26a and 4.26b are comparably similar in shape, demonstrating an overall monotonous NTC with a short intermediate transition plateau and slight hysteresis between each cycle. Undoubtedly, the first portion of the thermoresistive curve within 25-80ºC is a residual stress dominated behavior which is in an identical trend to the aramid- and E-glass-sizing multiscale composites as illustrated in the previous section. Due to the superior thermomechanical stability as per TMA in Section 4.3.2, a short plateau appears on the curve from 85 to 102 ºC, representing the smooth transition to a polymer dynamics-dominated thermoresistive response. This plateau period also resembles the transition interval between the first

and second crossover temperature (that is, 70-105 ºC) of the dip-coating-based CNT composites, indicating a good inter-batch repeatability.

In particular, the “hilly” crossover phenomenon as shown in Figure 4.21 is completely flattened-out, which can be attributed to the uniform and dense morphology of CNTs as previously detailed in Section 4.3.1.4. This localized network of highly packed nanotubes can only enable partial infiltration of epoxy resin during composite fabrication process, which results in an ultralow resin volume fraction in the CNT coating, consequently diminishing the overall effect of polymer dynamic motion to a large extent on the thermoresistive response of the CNT network. Furthermore, as suggested previously, the applied cure cycle (i.e., 130ºC for 6 hours) can cause an incomplete curing reaction. In this way, every thermal cycle can induce slight increase in crosslink density of the epoxy as ramping from 130 to 145 ºC, therefore leading to the cycle-to-cycle variations of decreasing resistance. Similar behavior has been also observed with the CNT sheet/epoxy composite as shown in Figure 4.24.

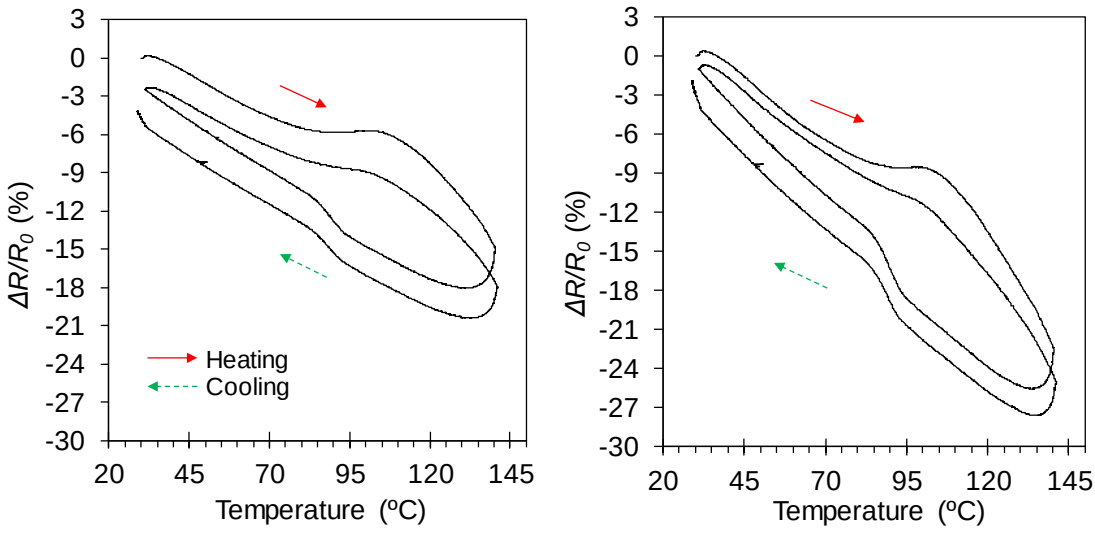

Figure 4.26: Thermoresistive responses of aramid-EPD/epoxy multiscale composites with CNT loadings of (a) 3.4 wt.% and (b) 1.8 wt.% during 25 to 145 ºC thermal cycles.

Based on the results shown in Figure 4.27a, the 1.8 wt.%-CNT specimen displays 7% more overall resistance change than that of the 3.4 wt.% one which further verifies the trend that the less CNTs are loaded in the network, the more resistance change is induced due to the network change, that is the CNT concentration dependence of thermoresistive behavior as discussed in the previous sections. However, although the dip-coated based CNT composite contains much less nanotubes than the EPD processed composites (i.e., 0.05 wt.% vs. 1.8 wt.%), the presented total resistance change is five time less than those EPD ones (i.e., -4.5% vs. -22%) which is mainly due to the distinctive morphological states and physical structures of CNTs in these two composite systems. For the EPD-based composites, the ozone-PEI functionalized nanotubes are densely packed and touch each other through the PEI molecular coating in which the hyperbranched PEI can induce a

relatively high activation barrier for electrons, therefore leading to an increased resistance change corresponding to temperature variations, just as implied by the thermal fluctuation induced tunneling model [89]. In contrast, the dip-coating approach is based on the dispersion of the SDBS surfactant-treated CNTs in which the SDBS particles on the CNTs promote the capability of charge movement and facilitate the wall-to-wall electrical conduction through CNTs [95], thereby resulting in a considerably less resistive CNT network. In particular, the *TCR* correlations shown in Figures 4.27b through 4.27d further confirms that the overall thermoresistive sensitivity of the tunneling-dominated CNT network in the EPD-based composites is higher in magnitude than the tube-tube contact dominated CNT network in the dip-coating-based composites.

In addition, the *TCR* curves of the EPD-based specimens show a local inflection point at 119 ºC, which conforms the T_g^{onset} of the epoxy (i.e., 121 ºC in Table 4.3), indicating a high degree of accuracy and repeatability for sensing the polymer segmental motion. Particularly, compared with the CNT nanocomposites and the dip-coating-based multiscale composites (as discussed in previous sections), the EPD-based composites are not likely to enable the CNT re-agglomeration during the rubbery state, which is attributed to the low volume fraction of infiltrated epoxy in the extraordinarily dense CNT network. Therefore, a relatively reduced rate of resistance change is expected and represented as the gradually decreasing *TCR* after T_g^{onset} as shown in Figure 4.27c and 4.27d.

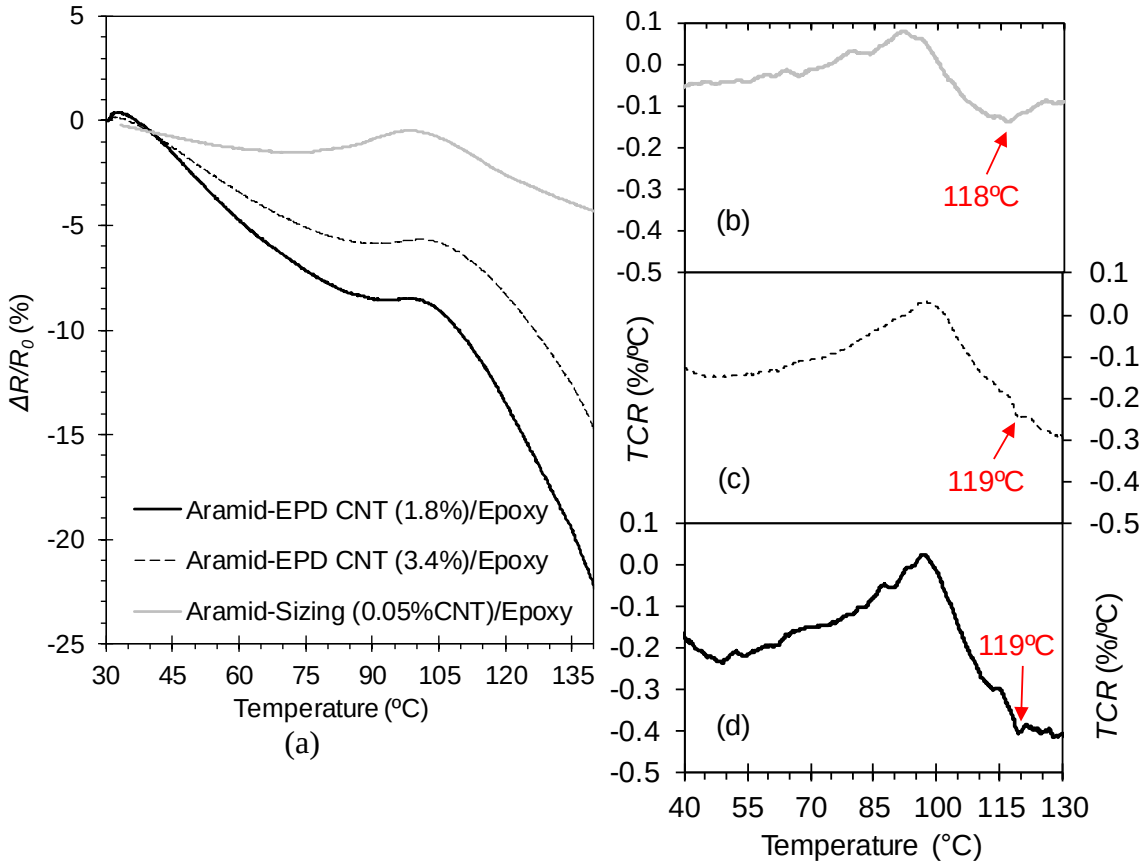

Figure 4.27: (a) Thermoresistive responses of EPD-based and dip-coating-based composites during the first ramp-up segment. (b) through (d) Corresponding *TCR* relationships with the identified T_g^{onset}.

4.3.4.4 Multiscale Composites with Randomly Dispersed Carbon Nanotubes

This study finally investigates the thermoresistive responses of the multiscale composites with randomly dispersed CNTs in the polymer matrix. The 0.5 and 0.25 wt.%-CNT-modified epoxy processed via three-roll mill technique was infused into the aramid and E-glass nonwoven fabrics respectively in order to obtain four sets of multiscale composite specimens for the *in situ* thermoresistive characterization. Figures 4.28a through 4.28d show the typical responses during two 25-145 ºC thermal cycles. At the first glance, the curves are quite diverse in shape from each other that the 0.5 wt.%-CNT specimens (in Figure 4.28a and c) present reversible temperature correlations with negligible hysteresis. Nevertheless, the 0.25 wt.%-CNT specimens (in Figure 4.28b and d) demonstrate irreversible behavior with a double-crossover transition and certain amount of resistive hysteresis cumulated between each cycle. Meanwhile, with the same CNT loading of 0.5 wt.%, the E-glass specimen presents a complete NTC as shown in Figure 4.28c, whereas the aramid specimens show a clear transition from NTC to PTC as shown in Figure 4.28a.

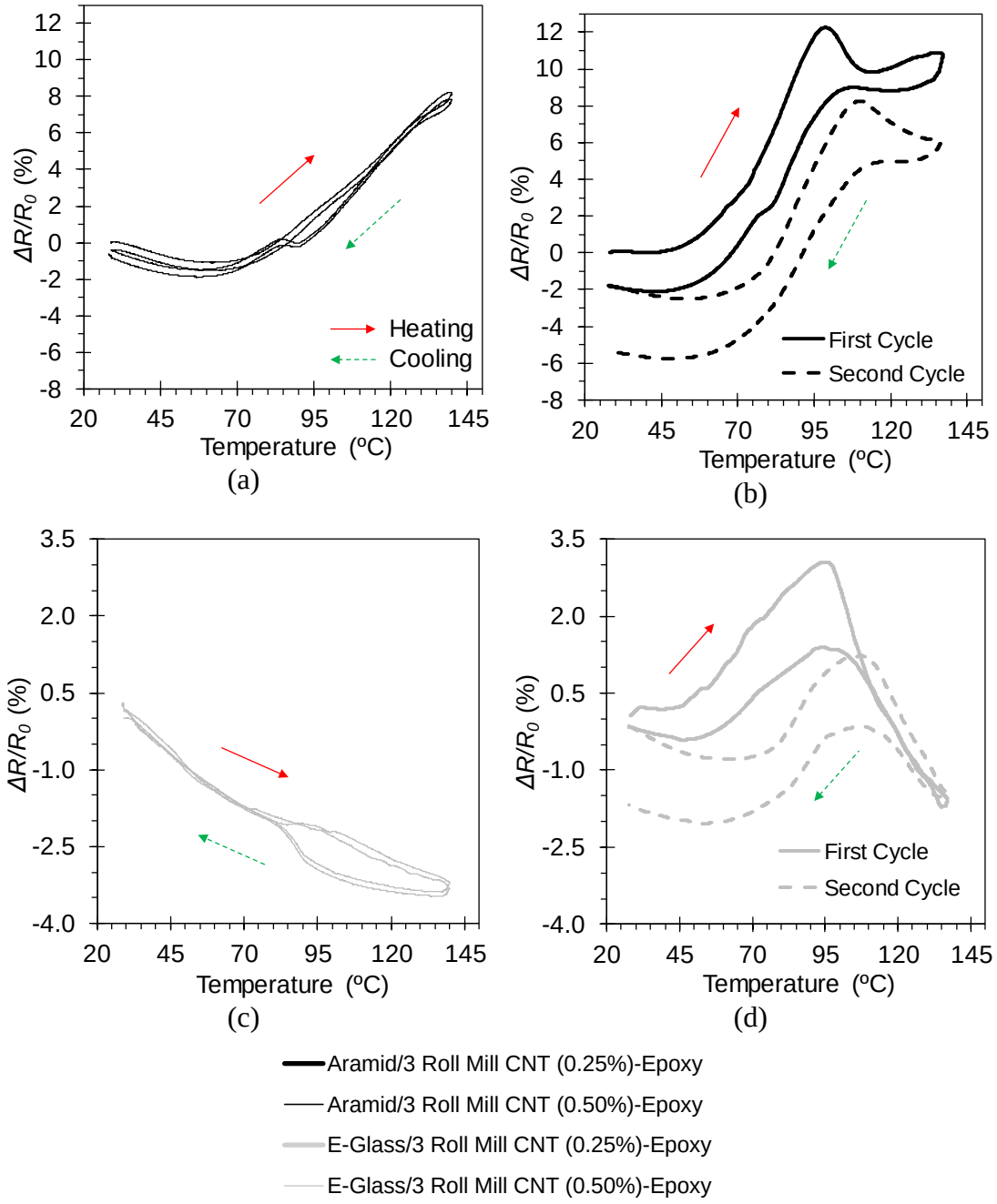

Figure 4.28: Thermoresistive responses of the multiscale composites with CNTs randomly dispersed in matrix including (a) aramid/3 roll mill CNT (0.5 wt.%)-epoxy composite; (b) aramid/3 roll mill CNT (0.25 wt.%)-epoxy composite; (c) E-glass/3 roll mill CNT (0.5 wt.%)-epoxy composite and (d) E-glass/3 roll mill CNT (0.25 wt.%)-epoxy composite during thermal cycling from 25 to 145 ºC.

In general, the thermal residual stresses can develop in this composite system following the same trends as explained in Section 4.3.3. To better envision their influences on the dispersed CNT network, the entire matrix phase can be separated into two domains including the close vicinity around the fiber, i.e., the residual-tensile-stress zone, and the region 10 μm away from the fiber surface, i.e., the residual-stress-free zone. For this particular category of fibrous composites, the CNT network is simultaneously influenced by these two distinctive zones such that as temperature starts increasing, the CNT network in the residual-tensile-stress zone contracts due to stress-relieving, leading to the decrease in resistance; meanwhile, the CNT network in the residual-stress-free-zone experiences the increasing resistance as result of the polymer thermal expansion. Therefore, the resultant effect dominates the bulk thermoresistive response.

As shown in Table 4.2, the aramid and E-glass composites with 0.5 wt.% CNT-dispersed epoxy matrix shows the average room temperature resistivity of 38 and 68.7 Ω·m, respectively, which is 14% and 106% more than that of the non-fibrous 0.5 wt.% CNT-epoxy nanocomposite (i.e., 33.4 Ω·m), confirming that the CNT network in the E-glass composite is considerably more pre-tensioned that that in the aramid composite. In particular, the non-fibrous 0.5 wt.%-CNT nanocomposite displays an overall resistance change of 5.0% as thermally cycled from 25 to 145 ºC (in Figure 4.18). Then, it is reasonable to find that the aramid composite presents the residual tensile stress dominated NTC in 25-62 ºC connecting with the thermal expansion dominated PTC till 145 ºC as shown in Figure 4.28a. Nevertheless, the relieving of the fairly high residual tensile stress in the E-glass composite results in dramatic decrease in resistance changes that balances out the thermal-expansion

induced increase in resistance, leading to a monotonous NTC as shown in Figure 4.28c.

Comparing with 0.5 wt.%-CNT composites, the effect of thermal expansion to the thermoresistive behavior becomes more pronounced as the CNT loading reduced to 0.25 wt.%. Particularly, the resistance change in the first thermal cycle of both aramid and E-glass composites represents an irreversible trend with lots of fluctuations as shown in Figure 4.28b and 4.28d, which is presumably due to the residual thermal histories built-up during the heating process. In contrast, the second thermal cycle of both composites are in a comparably similar shape that the first crossover temperature is shown as the local minimum around 65 ºC and the second crossover temperature peaks locally at 108 ºC, following the T_g^{onset} of the 0.25 wt.%-CNT nanocomposites (i.e., 105 ºC listed in Table 4.3). Obviously, the CNT network pre-stressed under the residual-tensile-stress zone contributes to the initial NPC in both composites.

Especially, the E-glass specimen presents a much steeper NPC, evidencing a more intensively pre-tensioned CNT network. As temperature increases, the well dispersed CNTs in the residual-stress-free zone starts dominating the resistance change as tunneling gaps greatly extend due to the polymer thermal expansion, therefore leading to a sharp increase in resistance following a similar trend displayed by the 0.25 wt.%-CNT nanocomposites as shown in Figure 4.18. Additionally, after glass transition, the thermomechanical responses of the fibrous composites as shown in Figure 4.14, are significantly reduced and limited to the fiber-level expansion. On the other hand, the epoxy matrix at the elevated temperatures can promote the curing reaction between uncured monomers, increase crosslinking of polymer chains and therefore can considerably reduce the free volume, leading to a compressed CNT

network overall that demonstrates a sharp reduction in resistance during 108-145 ºC as shown in Figure 4.28b and 4.28d.

Finally, Figure 4.29 shows the corresponding *TCR* relationships of the four multiscale composites during the first ramp-up segment. It is apparent that the 0.5 wt.%-CNT composites shown in Figure 4.29b and 4.29d display a less in magnitude but more stable thermoresistive sensitivity in overall as compared to the 0.25 wt.% ones. In particular, the E-glass composites with 0.5 wt.% CNT presents an average *TCR* of -350×10^{-6}/ºC from 40 to 115 ºC. Additionally, the *TCR* curves of the aramid and E-glass-0.25 wt.%-CNT composites respectively show local peak values of 0.002/ºC and 0.0012/ºC around 67 ºC (as pointed by blue arrows), evidencing a good sensitivity to the local transition of the electrical dominance in resistance change of the CNT network. It also can be found that the identified T_g^{onset} of the 0.25 and 0.5 wt.% composites correspond to the local minima and maxima of their *TCR* curves respectively, which is consistent to the CNT nanocomposites shown in Figure 4.20, indicating a high degree of repeatability. It is also noteworthy that the *TCR* after T_g^{onset} decreases in magnitude for all four specimens which is primarily ascribed to the fact that the promoted crosslinking of polymer chains significantly constrains the dispersed CNTs, leading to an overall reduced rate of the bulk change to the CNT network and therefore decreasing thermoresistive sensitivity.

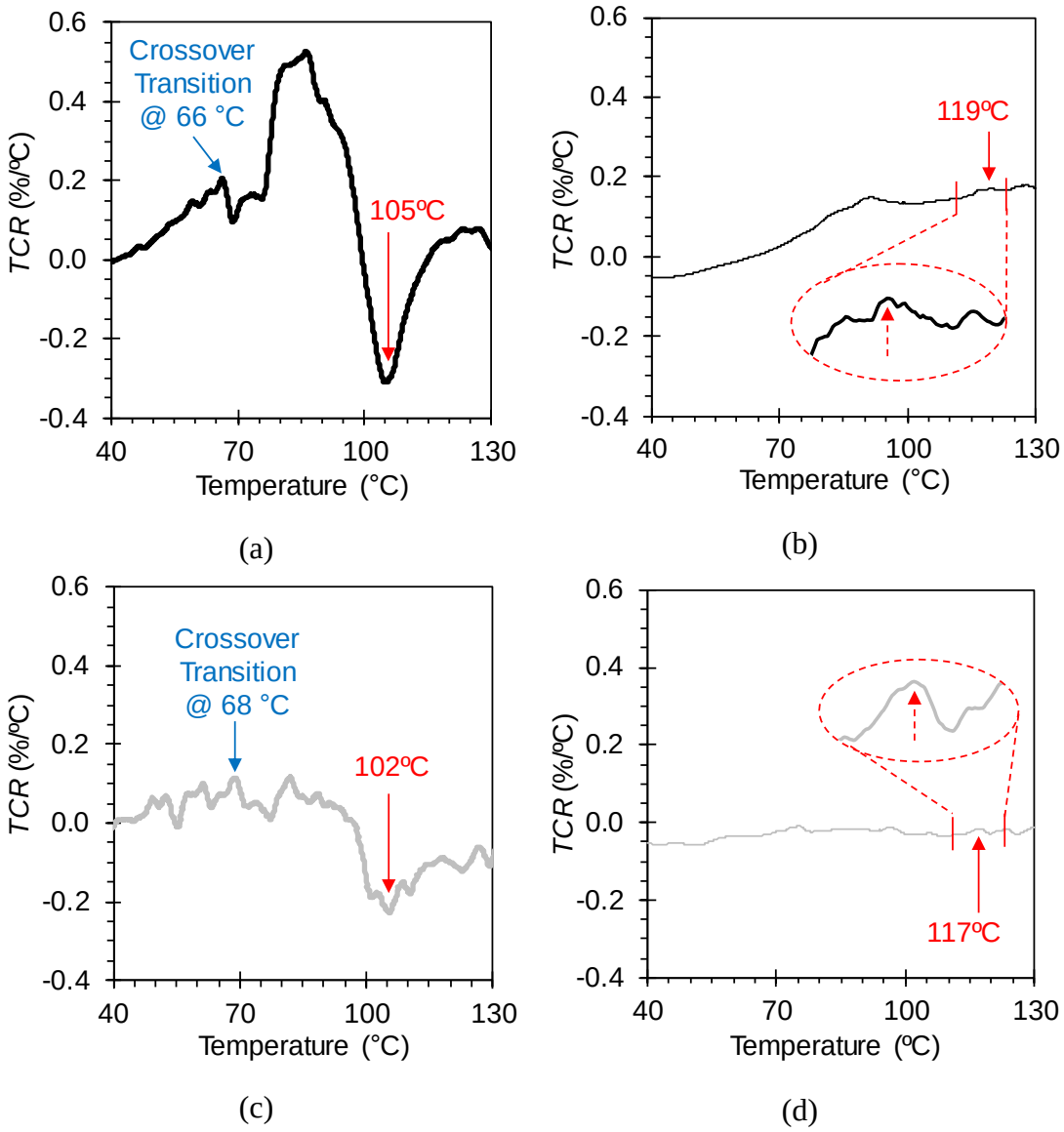

Figure 4.29: Corresponding *TCR* relationships of (a) aramid/3 roll mill CNT (0.25 wt.%)-epoxy composite, (b) aramid/3 roll mill CNT (0.5 wt.%)-epoxy composite, (c) E-glass/3 roll mill CNT (0.25 wt.%)-epoxy composite and (d) E-glass/3 roll mill CNT (0.5 wt.%)-epoxy composite with the identified local inflection points as the T_g^{onset}.

4.4 Temperature Compensation for CNT-Based Composite Sensors

As demonstrated in previous sections, the CNT-based nanocomposites and multiscale composites are showing considerable temperature dependence in their resistances. Therefore, to made use of these sensing composites as practical strain sensors for SHM, temperature compensation is necessary. For this purpose, a commonly applied electrical measurement method using Wheatstone bridge circuit [96] is customized in this study and integrated with the previously characterized aramid-sizing/epoxy composites as a pilot test to show the compensation of temperature effects. In particular, a full bridge circuit is experimentally developed and schematically illustrated in Figure 4.30. The four arms of the bridge are formed by the active sensors with baseline resistances R_1 to R_4. The known excitation voltage (V_E) is first subjected into the bridge through the excitation diagonal between node 2 and 4, and then the bridge output voltage (V_{out}) is acquired through the measurement diagonal between node 1 and 3.

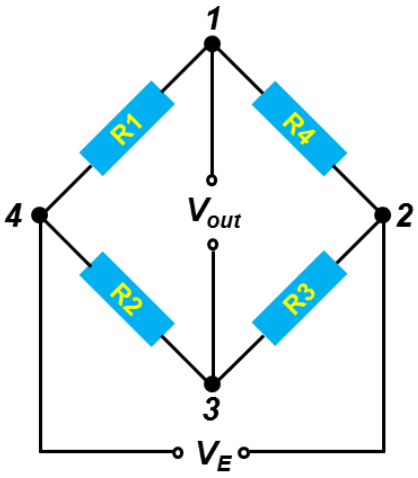

Figure 4.30: Schematic illustration of the implemented Wheatstone bridge circuit for temperature compensation, showing a full bridge with four active sensing elements.

In general, the value of V_{out} depends on the ratio of R_1 : R_4 and R_2 : R_3 following the Equation 4.2.

$$\frac{V_{out}}{V_E} = \frac{R_1 \cdot R_3 - R_2 \cdot R_4}{(R_1 + R_4)(R_3 + R_2)} \tag{4.2}$$

When $R_1 = R_4 = R_2 = R_3$, (4.3)

or $R_1 : R_4 = R_2 : R_3$, (4.4)

a so called 'balanced bridge' is resulted such that

$$\frac{V_{out}}{V_E} = 0 \tag{4.5}$$

where no bridge output voltage is detectable. However, as R_1 to R_4 of the sensing elements vary under interference effects such as temperature, the bridge is detuned and a V_{out} appears.

For compensating temperature effects, all four sensors are exposed to the same environment under the same temperature. When the baseline resistances and *TCR* of all four sensors are identical, the resistance changes (ΔR) corresponding to temperature variations have the same sign and magnitude, that is $\Delta R_1 = \Delta R_2 = \Delta R_3 = \Delta R_4$. In this ideal scenario, the state of the balanced bridge is maintained and the contribution of temperature change to the bridge output voltage is negligible. Consequently, the temperature effects are compensated. In addition, as demonstrated in Section 4.3.4.2, the inter-/intra-batch variations of the as-fabricated CNT-base nonwoven multiscale composites are relatively small such that the baseline resistances of the composites are similar and their thermoresistive behaviors are observed highly repeatable. As a result, four samples of aramid-sizing-1.0 wt.% CNT/epoxy composite sensors are integrated into the full bridge and assumed abiding by a single thermoresistive figure of merit (K) as thermally cycled, leading to an updated correlation as follows.

$$\frac{V_{out}}{V_E} = \frac{(R_1+R_1*K)(R_3+R_3*K)-(R_2+R_2*K)(R_4+R_4*K)}{(R_1+R_1*K+R_4+R_4*K)(R_3+R_3*K+R_2+R_2*K)} \quad (4.6)$$

where R_1 = 2830.4 Ω, R_2 = 3073.9 Ω, R_3 = 3047.4 Ω, R_4 = 3144.1 Ω, V_E = 5 volts, and V_{out} is measured in real-time during 25-145 °C thermal cycles. In particular, the excitation voltage was provided via Keithley 6430 source meter and the bridge output voltage was recorded by Keithley 2182A nanovoltmeter.

After expanding Equation 4.6, it obtains

$$[(R_1+R_4)(R_2+R_3)(V_{out}/V_E) + (R_1R_3 - R_2R_4)]\cdot K^2 +$$
$$2[(R_1+R_4)(R_2+R_3)(V_{out}/V_E) + (R_1R_3-R_2R_4)]\cdot K +$$
$$[(R_1+R_4)(R_2+R_3)(V_{out}/V_E) - (R_1R_3-R_2R_4)] = 0 \quad (4.7)$$

by setting

$$m = [(R_1+R_4)(R_2+R_3)(V_{out}/V_E) + (R_1R_3 - R_2R_4)], \quad (4.8)$$

$$n = 2[(R_1+R_4)(R_2+R_3)(V_{out}/V_E) + (R_1R_3-R_2R_4)], \quad (4.9)$$

$$\text{and } c = [(R_1+R_4)(R_2+R_3)(V_{out}/V_E) - (R_1R_3-R_2R_4)] \quad (4.10)$$

K is solved as

$$K = \frac{-n \pm \sqrt{n^2-4mc}}{2m} \quad (4.11)$$

which represents the temperature-compensated bridge response in real-time.

Figure 4.31 shows the transient response of the measured bridge output voltage during two 25-145 °C thermal cycles. As expected, the output voltage is nonzero but fairly small in magnitude (i.e., less than 0.006 volt of variations) due to the experimental errors mainly coming from the variations of fabrication process and the errors of electrical measurements. In addition, the overall trend of the output voltage is highly repeatable and closely follows the applied temperature profile, revealing a high

measurement uniformity acquired from thermoresistive response of the composite sensors.

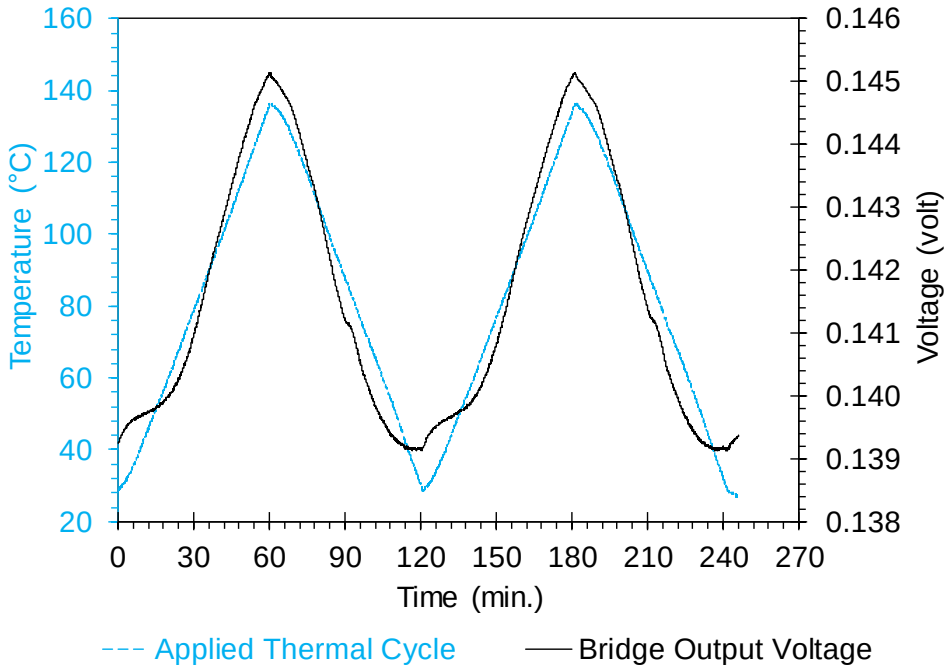

Figure 4.31: Transient response of the recorded bridge output voltage form the implemented Wheatstone bridge circuit consisting of four aramid-sizing-1.0 wt.% CNT/epoxy composite sensors.

Although all four composite sensors are responsible for the temperature compensation in the full bridge, the resulting resistive response for the Wheatstone bridge is presented by the normalized *K* which can be calculated using Equation 4.11. Figure 4.32a shows the measured real-time responses including the applied thermal profile, the compensated resistive response and the original resistive response of the bridge sensor #2. It is apparent that the compensated resistive response is nearly flat

and very close to zero during the entire temperature protocol, indicating a high degree of compensation. The enlarged view of the compensated response is shown in Figure 4.32b. It is notable that the resistance change of the proposed Wheatstone bridge is now less than 0.04%, which is about 50 times smaller than the original thermoresistive response of one composite sensor shown as the dashed line in Figure 4.32a. In particular, the compensated response demonstrates a monotonous PTC as shown in Figure 4.32c, which however, is not universal and not applicable to the other compensation testing. Depending on the resistance distribution of the active sensing elements in the full bridge, the temperature dependence can either have a positive or negative gradient, which is randomly distributed. It is believed that the higher is the uniformity of the composite sensors (with respect to the baseline resistance and *TCR*), the more considerable is then the degree of the temperature compensation. In addition, the current compensating methodology of the CNT-based nonwoven composite sensors shows much higher effectiveness than the similar approach performed by Dinh and Kanoun [97] on CNT-epoxy-based force sensors.

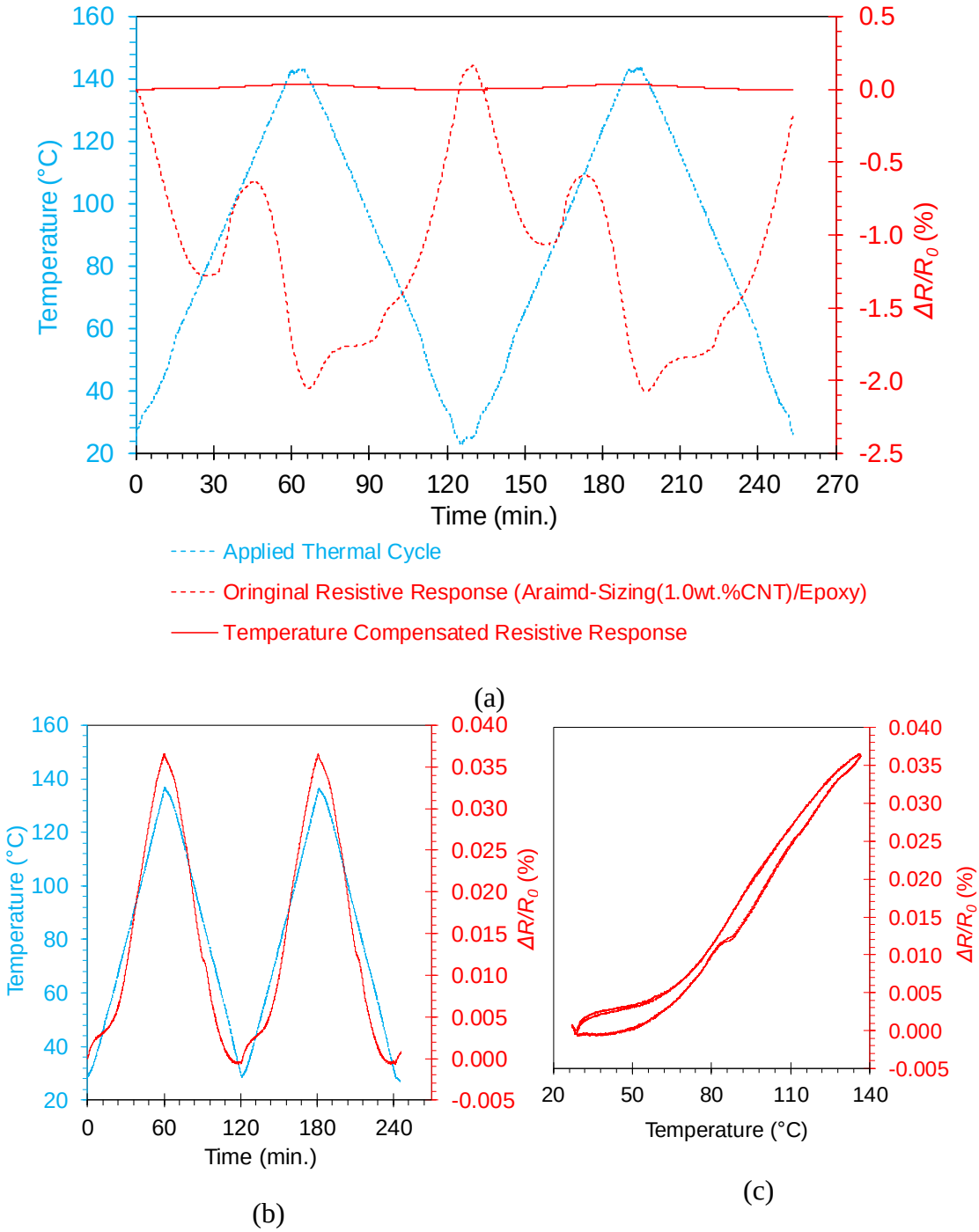

Figure 4.32: (a) Comparison between the original and compensated resistive response, indicating a high degree of compensation; (b) the enlarged view and (c) the temperature dependence of the compensated resistive response.

4.5 Summary and Conclusions

So far, a vast variety of CNT-based sensing composites have been developed and demonstrated attractive multi-functionalities including mechanical damage detection [45,98,99], structural health monitoring [44,100-102], chemical detection [103,104], process monitoring [25,105], bolometric sensing of infrared radiation [33,106,107], etc. However, the great majority of the published experimental studies on the CNT-based multifunctional composites were limited only to the room temperature characterizations in laboratory without considering the temperature-dependence of their electrical properties. This lack of knowledge significantly hinders the potential applications of these novel composites in real-world applications.

In this chapter, a systematic study on the thermoresistive behaviors of CNT-based nanocomposites and multiscale composites was presented. In the beginning of this study, four types of composites with the typically observed morphological states of CNTs were specifically created including (1) randomly dispersed CNTs in epoxy, (2) loosely- and (3) densely-concentrated CNTs as well as (4) randomly dispersed CNTs in fibrous composite, via three CNT dispersion techniques of three-roll-milling, dip-coating and electrophoretic deposition in dealing with the untreated, SDBS surfactant-modified, and the ozone-PEI functionalized CNTs, respectively. In addition, both aramid and E-glass nonwoven fabrics were used to fabricate the multiscale composites following the vacuum-assisted resin transfer molding (VARTM) approach.

In general, as the composite sensors are thermally cycled from 25 to 145ºC, the two-phase CNT nanocomposites showed the thermoresistive response with a monotonic positive temperature correlation due to thermal expansion; however, the multiscale composites demonstrated a reversible but crossover-shaped thermoresistive

behavior suggesting a dynamic dominance in their electrical resistance at different temperatures in accordance with the structural changes of the CNT network resulting from the competition between the thermal stresses and the polymer thermo-mechanical/dynamic-motion. It is worth nothing that the presence of fibers in multiscale composites generates thermal residual stresses during the curing process, leading to a pre-stressed CNT network at room temperature. Meanwhile, the fiber-induced confining effect can stabilize the CNT network at elevated temperatures.

In short, combining the various results from the scanning electron microscopy, the thermomechanical and the finite element based thermal stress analyses with the *in situ* thermoresistive behaviors of the CNT-based composites, the main conclusions with respect to the key parameters are drawn as follows:

(1) *CNT arrangement*: controls the structure of the CNT network, determines the electrical dominance of electrical conduction of the CNT-based composites, simply that the intertube tunneling governs the well dispersed CNT network and the tube-tube contacts dominate the concentrated CNT networks as well as the CNT agglomerates; in particular, compared with the densely concentrated CNTs in the EPD-based composites, the network of loosely concentrated CNTs in the dip-coating-based composites was locally infiltrated with more epoxy due to the highly porous structure at the submicron-level, leading to a more pronounced polymer thermal interactions at high temperatures shown as the significant fluctuations in their thermoresistive response.

(2) *CNT rearrangement*: may occur only among the large CNT agglomerates (i.e., in composites with high CNT concentration) promoted by the polymer segmental

motion in the rubbery state as cooling, leading to a more conductive but less sensitive CNT network via increasing tube-tube contacts, and causing more cyclic hysteresis;

(3) *CNT concentration*: for a CNT-based composites dominated by the electrical tunneling, the more CNTs are loaded, the less thermoresistive sensitivity can be resulted in; for a tube-tube contacts dominated CNT networks as seen as the fiber coating in the multiscale composites, higher CNT loading leads to a lower resistivity and may not influence the system sensitivity; particularly, the ozone-PEI functionalized CNTs always form the intertube tunneling-based network due to the PEI polymer wrapping effect, enabling a high thermoresistive sensitivity of a dense CNT network with high CNT loadings;

(4) *Fiber properties*: controls the bulk thermal expansion of the multiscale composites and determines the pre-stress level of the CNT network, therefore dominating the degree of negative temperature correlation shown by the multiscale composites; simply, the composites with isotropic E-glass fibers showed much less crossover phenomena in their thermoresistive responses than the ones with orthotropic aramid fibers due to the enhanced pre-tensioning of the CNT network at the room temperature.

(5) *Interfacial interactions*: high degree of interfacial bonding as shown in SEM images was achieved at the interfaces between the epoxy and respectively the untreated, ozone-PEI-functionalized and surfactant-modified CNTs; a strong chemical bonding between the CNT-sizing coating and the E-glass fibers was also observed and made the CNT coating resistant to the vigorous polymer thermodynamic motions, resulting in a linear negative temperature correlation in thermoresistive response at high temperatures;

(6) *Thermal expansion*: is the major momentum driving the positive temperature correlation in thermoresistive behavior of CNT-based composites in the glassy state, and causing the first crossover transition in the thermoresistive responses of multiscale composites, which however, can be balanced out from the thermoresistive responses as shown by the E-glass-sizing/epoxy composites;

(7) *Polymer thermal mobility*: changes in the free volume and mobility of the polymer above the glass transition causes structural changes to the CNT network, leading to the second crossover transition shown in the thermoresistive responses of the multiscale composites; particularly, post-curing process can increase the crosslink density of the polymer matrix and reduce the free volume, resulting in a relatively constrained CNT network with a high stability in the thermoresistive response at high temperatures;

(8) *Temperature coefficient of resistance (TCR)*: is a key parameter indicating the thermoresistive sensitivity of the CNT-based composites; its correlation with the *in situ* temperature was shown able to detect transition effects in the composites resulting from the thermodynamic motions, such as the onset of glass transition.

The knowledge obtained from this study promotes a comprehensive understanding about the temperature dependence of resistance in CNT-based composites and can serve as a good guide for developing CNT-based multifunctional composites such as the thermal sensors for *in situ* fast-sensing and monitoring temperature, thermal transitions and curing process in advanced fiber composites, which could be transferred to real applications.

Finally, the proposed Wheatstone bridge-based temperature compensation approach demonstrates a high degree of compensation for the highly repeatable

sensors, which therefore becomes a useful tool, facilitating the overall performance of the established CNT-based composite sensors in this study.

REFERENCES

1. Saito R, Fujita M, Dresselhaus G, Dresselhaus MS. Electronic structure of chiral graphene tubules. Appl Phys Lett 1992;60(18):2204-2206.

2. Ebbesen T, Lezec H, Hiura H, Bennett J, Ghaemi H, Thio T. Electrical-conductivity of individual carbon nanotubes. Nature 1996;382(6586):54-56.

3. Odom TW, Huang J, Kim P, Lieber CM. Structure and electronic properties of carbon nanotubes. The Journal of Physical Chemistry B 2000;104(13):2794-2809.

4. Javey A, Guo J, Wang Q, Lundstrom M, Dai H. Ballistic carbon nanotube field-effect transistors. Nature 2003;424(6949):654-657.

5. White CT, Todorov TN. Carbon nanotubes as long ballistic conductors. Nature 1998;393(6682):240-242.

6. Delaney P, Di Ventra M, Pantelides S. Quantized conductance of multiwalled carbon nanotubes. Appl Phys Lett 1999;75(24):3787-3789.

7. Frank S, Poncharal P, Wang ZL, Heer WA. Carbon nanotube quantum resistors. Science 1998;280(5370):1744-1746.

8. Skákalová V, Kaiser AB, Woo Y, Roth S. Electronic transport in carbon nanotubes: From individual nanotubes to thin and thick networks. Physical Review B 2006;74(8):085403.

9. Graugnard E, De Pablo P, Walsh B, Ghosh A, Datta S, Reifenberger R. Temperature dependence of the conductance of multiwalled carbon nanotubes. Physical Review B 2001;64(12):125407.

10. Bandaru PR. Electrical properties and applications of carbon nanotube structures. Journal of nanoscience and nanotechnology 2007;7(4-5):1239-1267.

11. Kaneto K, Tsuruta M, Sakai G, Cho W, Ando Y. Electrical conductivities of multi-wall carbon nano tubes. Synth Met 1999;103(1):2543-2546.

12. Fischer J, Dai H, Thess A, Lee R, Hanjani N, Dehaas D, Smalley R. Metallic resistivity in crystalline ropes of single-wall carbon nanotubes. Physical review B 1997;55(8):R4921.

13. Lee R, Kim H, Fischer J, Lefebvre J, Radosavljević M, Hone J, Johnson A. Transport properties of a potassium-doped single-wall carbon nanotube rope. Physical Review B 2000;61(7):4526.

14. Hone J, Llaguno M, Nemes N, Johnson A, Fischer J, Walters D, Casavant M, Schmidt J, Smalley R. Electrical and thermal transport properties of magnetically aligned single wall carbon nanotube films. Appl Phys Lett 2000;77(5):666-668.

15. Bae DJ, Kim KS, Park YS, Suh EK, An KH, Moon J, Lim SC, Park SH, Jeong YH, Lee YH. Transport phenomena in an anisotropically aligned single-wall carbon nanotube film. Physical Review B 2001;64(23):233401.

16. Rogers S, Kaiser A. Thermopower and resistivity of carbon nanotube networks and organic conducting polymers. Current Applied Physics 2004;4(2):407-410.

17. Hu L, Hecht D, Grüner G. Percolation in transparent and conducting carbon nanotube networks. Nano Letters 2004;4(12):2513-2517.

18. Cao C, Hu C, Xiong Y, Han X, Xi Y, Miao J. Temperature dependent piezoresistive effect of multi-walled carbon nanotube films. Diamond and Related materials 2007;16(2):388-392.

19. Barnes TM, Blackburn JL, van de Lagemaat J, Coutts TJ, Heben MJ. Reversibility, dopant desorption, and tunneling in the temperature-dependent conductivity of type-separated, conductive carbon nanotube networks. ACS Nano 2008;2(9):1968-1976.

20. Collins PG, Bradley K, Ishigami M, Zettl A. Extreme oxygen sensitivity of electronic properties of carbon nanotubes. Science 2000;287(5459):1801-1804.

21. Baumgartner G, Carrard M, Zuppiroli L, Bacsa W, de Heer WA, Forró L. Hall effect and magnetoresistance of carbon nanotube films. Physical Review B 1997;55(11):6704.

22. Pöhls J, Johnson MB, White MA, Malik R, Ruff B, Jayasinghe C, Schulz MJ, Shanov V. Physical properties of carbon nanotube sheets drawn from nanotube arrays. Carbon 2012;50(11):4175-4183.

23. Koratkar N, Modi A, Lass E, Ajayan P. Temperature effects on resistance of aligned multiwalled carbon nanotube films. Journal of nanoscience and nanotechnology 2004;4(7):744-748.

24. Di Bartolomeo A, Sarno M, Giubileo F, Altavilla C, Iemmo L, Piano S, Bobba F, Longobardi M, Scarfato A, Sannino D. Multiwalled carbon nanotube films as small-sized temperature sensors. J Appl Phys 2009;105(6):064518.

25. Lu S, Chen D, Wang X, Xiong X, Ma K, Zhang L, Meng Q. Monitoring the manufacturing process of glass fiber reinforced composites with carbon nanotube buckypaper sensor. Polym Test 2016;52:79-84.

26. Barberio M, Camarca M, Barone P, Bonanno A, Oliva A, Xu F. Electric resistivity of multi-walled carbon nanotubes at high temperatures. Surf Sci 2007;601(13):2814-2818.

27. Barrau S, Demont P, Peigney A, Laurent C, Lacabanne C. DC and AC conductivity of carbon nanotubes-polyepoxy composites. Macromolecules 2003;36(14):5187-5194.

28. Alamusi, Li Y, Hu N, Wu L, Yuan W, Peng X, Gu B, Chang C, Liu Y, Ning H, Li J. Temperature-dependent piezoresistivity in an MWCNT/epoxy nanocomposite temperature sensor with ultrahigh performance. Nanotechnology 2013;24(45):455501-455506.

29. Njuguna MK, Galpaya D, Yan C, Colwell JM, Will G, Hu N, Yarlagadda P, Bell JM. Investigation on Temperature-Dependent Electrical Conductivity of Carbon Nanotube/Epoxy Composites for Sustainable Energy Applications. Journal of nanoscience and nanotechnology 2015;15(9):6957-6964.

30. Zeng Y, Lu G, Wang H, Du J, Ying Z, Liu C. Positive temperature coefficient thermistors based on carbon nanotube/polymer composites. Sci Rep 2014;4:6684.

31. Pang H, Chen Q, Bao Y, Yan D, Zhang Y, Chen J, Li Z. Temperature resistivity behaviour in carbon nanotube/ultrahigh molecular weight polyethylene composites with segregated and double percolated structure. Plastics, Rubber and Composites 2013;42(2):59-65.

32. Gao J, Li Z, Peng S, Yan D. Temperature-resistivity behaviour of CNTs/UHMWPE composites with a two-dimensional conductive network. Polym Plast Technol Eng 2009;48(4):478-481.

33. Aliev AE. Bolometric detector on the basis of single-wall carbon nanotube/polymer composite. Infrared Phys Technol 2008;51(6):541-545.

34. Mohiuddin M, Hoa S. Temperature dependent electrical conductivity of CNT–PEEK composites. Composites Sci Technol 2011;72(1):21-27.

35. Matzeu G, Pucci A, Savi S, Romanelli M, Di Francesco F. A temperature sensor based on a MWCNT/SEBS nanocomposite. Sensors and Actuators A: Physical 2012;178:94-99.

36. Gau C, Kuo C, Ko H. Electron tunneling in carbon nanotube composites. Nanotechnology 2009;20(39):395705.

37. Xiang Z, Chen T, Li Z, Bian X. Negative temperature coefficient of resistivity in lightweight conductive carbon nanotube/polymer composites. Macromolecular Materials and Engineering 2009;294(2):91-95.

38. Lasater KL, Thostenson ET. In situ thermoresistive characterization of multifunctional composites of carbon nanotubes. Polymer 2012;53(23):5367-5374.

39. Li Q, Xue Q, Gao X, Zheng Q. Temperature dependence of the electrical properties of the carbon nanotube/polymer composites. Express Polym Lett 2009;3(12):769-777.

40. Xue W, Cui T. Characterization of layer-by-layer self-assembled carbon nanotube multilayer thin films. Nanotechnology 2007;18(14):145709.

41. Loyola BR, Zhao Y, Loh KJ, La Saponara V. The electrical response of carbon nanotube-based thin film sensors subjected to mechanical and environmental effects. Smart Mater Struct 2012;22(2):025010.

42. Gao S, Zhuang R, Zhang J, Liu J, Mäder E. Glass fibers with carbon nanotube networks as multifunctional sensors. Advanced Functional Materials 2010;20(12):1885-1893.

43. Zhang J, Zhuang R, Liu J, Scheffler C, Mäder E, Heinrich G, Gao S. A single glass fiber with ultrathin layer of carbon nanotube networks beneficial to in-situ monitoring of polymer properties in composite interphases. Soft Materials 2014;12(sup1):S115-S120.

44. Dai H, Thostenson ET, Schumacher T. Processing and Characterization of a Novel Distributed Strain Sensor Using Carbon Nanotube-Based Nonwoven Composites. Sensors 2015;15(7):17728-17747.

45. Dai H, Gallo GJ, Schumacher T, Thostenson ET. A Novel Methodology for Spatial Damage Detection and Imaging Using a Distributed Carbon Nanotube-Based Composite Sensor Combined with Electrical Impedance Tomography. J Nondestr Eval 2016;35(2):1-15.

46. Thostenson ET, Chou T. Processing-structure-multi-functional property relationship in carbon nanotube/epoxy composites. Carbon 2006;44(14):3022-3029.

47. Vaisman L, Wagner HD, Marom G. The role of surfactants in dispersion of carbon nanotubes. Adv Colloid Interface Sci 2006;128:37-46.

48. Britz DA, Khlobystov AN. Noncovalent interactions of molecules with single walled carbon nanotubes. Chem Soc Rev 2006;35(7):637-659.

49. An Q, Rider AN, Thostenson ET. Electrophoretic deposition of carbon nanotubes onto carbon-fiber fabric for production of carbon/epoxy composites with improved mechanical properties. Carbon 2012;50(11):4130-4143.

50. An Q, Rider AN, Thostenson ET. Hierarchical composite structures prepared by electrophoretic deposition of carbon nanotubes onto glass fibers. ACS applied materials & interfaces 2013;5(6):2022-2032.

51. Montazeri A, Khavandi A, Javadpour J, Tcharkhtchi A. Viscoelastic properties of multi-walled carbon nanotube/epoxy composites using two different curing cycles. Mater Des 2010;31(7):3383-3388.

52. Schadler L, Giannaris S, Ajayan P. Load transfer in carbon nanotube epoxy composites. Appl Phys Lett 1998;73(26):3842-3844.

53. Wong M, Paramsothy M, Xu X, Ren Y, Li S, Liao K. Physical interactions at carbon nanotube-polymer interface. Polymer 2003;44(25):7757-7764.

54. Gou J, Minaie B, Wang B, Liang Z, Zhang C. Computational and experimental study of interfacial bonding of single-walled nanotube reinforced composites. Computational Materials Science 2004;31(3):225-236.

55. Watts P, Hsu W. Behaviours of embedded carbon nanotubes during film cracking. Nanotechnology 2003;14(5):L7-L10.

56. Desai A, Haque M. Mechanics of the interface for carbon nanotube–polymer composites. Thin-walled structures 2005;43(11):1787-1803.

57. Ci L, Bai J. The reinforcement role of carbon nanotubes in epoxy composites with different matrix stiffness. Composites Sci Technol 2006;66(3–4):599-603.

58. Kiriya D, Chen K, Ota H, Lin Y, Zhao P, Yu Z, Ha T, Javey A. Design of surfactant–substrate interactions for roll-to-roll assembly of carbon nanotubes for thin-film transistors. J Am Chem Soc 2014;136(31):11188-11194.

59. Kralchevsky PA, Nagayama K. Capillary forces between colloidal particles. Langmuir 1994;10(1):23-36.

60. Dan B, Irvin GC, Pasquali M. Continuous and scalable fabrication of transparent conducting carbon nanotube films. ACS nano 2009;3(4):835-843.

61. Hull D, Clyne T. An introduction to composite materials: Cambridge university press, 1996.

62. Singletary J. Transverse compression of PPTA fibers. Mechanics of composite materials 2000;36(4):319-326.

63. Ma P, Siddiqui NA, Marom G, Kim J. Dispersion and functionalization of carbon nanotubes for polymer-based nanocomposites: a review. Composites Part A: Applied Science and Manufacturing 2010;41(10):1345-1367.

64. Geng Y, Liu MY, Li J, Shi XM, Kim JK. Effects of surfactant treatment on mechanical and electrical properties of CNT/epoxy nanocomposites. Composites Part A: Applied Science and Manufacturing 2008;39(12):1876-1883.

65. Rausch J, Zhuang R, Mäder E. Surfactant assisted dispersion of functionalized multi-walled carbon nanotubes in aqueous media. Composites Part A: Applied Science and Manufacturing 2010;41(9):1038-1046.

66. Rausch J, Mäder E. Health monitoring in continuous glass fibre reinforced thermoplastics: Manufacturing and application of interphase sensors based on carbon nanotubes. Composites Sci Technol 2010;70(11):1589-1596.

67. Geetha D, Thilagavathi T, Ramesh P, Rakkappan C. Influence of Synthetic Polymer on Aqueous Anionic Surfactant (SDBS) Micelle Investigated by FT-IR and Ultrasonic Study. Composite Interfaces 2010;17(2-3):247-256.

68. Chihani T, Flodin P, Hjertberg T. Modification of epoxy surfaces with different polyvinylalcohol polymers. J Appl Polym Sci 1993;50(8):1343-1350.

69. Sarkar P, Nicholson PS. Electrophoretic deposition (EPD): mechanisms, kinetics, and application to ceramics. J Am Ceram Soc 1996;79(8):1987-2002.

70. Ammam M. Electrophoretic deposition under modulated electric fields: a review. Rsc Advances 2012;2(20):7633-7646.

71. Zhang J, Zhuang R, Liu J, Mäder E, Heinrich G, Gao S. Functional interphases with multi-walled carbon nanotubes in glass fibre/epoxy composites. Carbon 2010;48(8):2273-2281.

72. Odegard G, Bandyopadhyay A. Physical aging of epoxy polymers and their composites. Journal of Polymer Science Part B: Polymer Physics 2011;49(24):1695-1716.

73. Dodiuk H, Goodman SH. Handbook of thermoset plastics: William Andrew, 2013.

74. Wang Z, Liang Z, Wang B, Zhang C, Kramer L. Processing and property investigation of single-walled carbon nanotube (SWNT) buckypaper/epoxy resin matrix nanocomposites. Composites Part A: Applied Science and Manufacturing 2004;35(10):1225-1232.

75. Shen J, Huang W, Wu L, Hu Y, Ye M. The reinforcement role of different amino-functionalized multi-walled carbon nanotubes in epoxy nanocomposites. Composites Sci Technol 2007;67(15):3041-3050.

76. Tao K, Yang S, Grunlan JC, Kim Y, Dang B, Deng Y, Thomas RL, Wilson BL, Wei X. Effects of carbon nanotube fillers on the curing processes of epoxy resin-based composites. J Appl Polym Sci 2006;102(6):5248-5254.

77. Allaoui A, El Bounia N. How carbon nanotubes affect the cure kinetics and glass transition temperature of their epoxy composites?–a review. Express Polymer Letters 2009;3(9):588-594.

78. Montazeri A. The effect of functionalization on the viscoelastic behavior of multi-wall carbon nanotube/epoxy composites. Mater Des 2013;45:510-517.

79. Cividanes LS, Simonetti EA, Moraes MB, Fernandes FW, Thim GP. Influence of carbon nanotubes on epoxy resin cure reaction using different techniques: a comprehensive review. Polymer Engineering & Science 2014;54(11):2461-2469.

80. Shokrieh M, Safarabadi M. Three-dimensional analysis of micro-residual stresses in fibrous composites based on the energy method: a study including interphase effects. J Composite Mater 2012;46(6):727-735.

81. Shokrieh M, Daneshvar A, Akbari S. Reduction of thermal residual stresses of laminated polymer composites by addition of carbon nanotubes. Mater Des 2014;53:209-216.

82. Anagnostopoulos G, Parthenios J, Galiotis C. Thermal stress development in fibrous composites. Mater Lett 2008;62(3):341-345.

83. Liao K, Tan Y. Influence of moisture-induced stress on in situ fiber strength degradation of unidirectional polymer composite. Composites Part B: Engineering 2001;32(4):365-370.

84. Quek M. Analysis of residual stresses in a single fibre–matrix composite. Int J Adhes Adhes 2004;24(5):379-388.

85. Detassis M, Pegoretti A, Migliaresi C, Wagner H. Experimental evaluation of residual stresses in single fibre composites by means of the fragmentation test. J Mater Sci 1996;31(9):2385-2392.

86. Wisnom M, Gigliotti M, Ersoy N, Campbell M, Potter K. Mechanisms generating residual stresses and distortion during manufacture of polymer–matrix composite structures. Composites Part A: Applied Science and Manufacturing 2006;37(4):522-529.

87. Anagnostopoulos G, Parthenios J, Andreopoulos A, Galiotis C. An experimental and theoretical study of the stress transfer problem in fibrous composites. Acta materialia 2005;53(15):4173-4183.

88. Li C, Thostenson ET, Chou T. Dominant role of tunneling resistance in the electrical conductivity of carbon nanotube–based composites. Appl Phys Lett 2007;91(22):223114.

89. Sheng P. Fluctuation-induced tunneling conduction in disordered materials. Physical Review B 1980;21(6):2180.

90. Böger L, Wichmann MH, Meyer LO, Schulte K. Load and health monitoring in glass fibre reinforced composites with an electrically conductive nanocomposite epoxy matrix. Composites Sci Technol 2008;68(7):1886-1894.

91. Learmonth GS, Pritchard G. Electrical resistivity and crosslinking in thermosetting resins. Industrial & Engineering Chemistry Product Research and Development 1969;8(2):124-127.

92. Alig I, Pötschke P, Lellinger D, Skipa T, Pegel S, Kasaliwal GR, Villmow T. Establishment, morphology and properties of carbon nanotube networks in polymer melts. Polymer 2012;53(1):4-28.

93. Babaev A, Khokhlachev P, Nikolaev YA, Terukov E, Freidin A, Filippov R, Filippov A, Manabaev N. Nanocomposite based on modified multiwalled carbon nanotubes: Fabrication by an oriented spinning process and electrical conductivity. Inorganic Materials 2012;48(10):997-1000.

94. Simmons J, Nichols B, Baker S, Marcus MS, Castellini O, Lee C, Hamers R, Eriksson M. Effect of ozone oxidation on single-walled carbon nanotubes. The journal of physical chemistry B 2006;110(14):7113-7118.

95. Tang Q, Shafiq I, Chan Y, Wong N, Cheung R. Study of the dispersion and electrical properties of carbon nanotubes treated by surfactants in dimethylacetamide. Journal of nanoscience and nanotechnology 2010;10(8):4967.

96. Holman JP, Gajda WJ. Experimental methods for engineers, vol. 7: McGraw-Hill New York, 2001.

97. Dinh NT, Kanoun O. Temperature-compensated force/pressure sensor based on multi-walled carbon nanotube epoxy composites. Sensors 2015;15(5):11133-11150.

98. Thostenson ET, Chou T. Carbon nanotube networks: sensing of distributed strain and damage for life prediction and self healing. Adv Mater 2006;18(21):2837-2841.

99. Nofar M, Hoa S, Pugh M. Failure detection and monitoring in polymer matrix composites subjected to static and dynamic loads using carbon nanotube networks. Composites Sci Technol 2009;69(10):1599-1606.

100. Zhang H, Bilotti E, Peijs T. The use of carbon nanotubes for damage sensing and structural health monitoring in laminated composites: a review. Nanocomposites 2015;1(4):167-184.

101. Schumacher T, Thostenson ET. Development of structural carbon nanotube–based sensing composites for concrete structures. J Intell Mater Syst Struct 2014;25(10):1331-1339.

102. Thostenson ET, Chou T. Carbon nanotube-based health monitoring of mechanically fastened composite joints. Composites Sci Technol 2008;68(12):2557-2561.

103. Salavagione HJ, Díez-Pascual AM, Lázaro E, Vera S, Gómez-Fatou MA. Chemical sensors based on polymer composites with carbon nanotubes and graphene: the role of the polymer. Journal of Materials Chemistry A 2014;2(35):14289-14328.

104. Li C, Thostenson ET, Chou T. Sensors and actuators based on carbon nanotubes and their composites: A review. Composites Sci Technol 2008;68(6):1227-1249.

105. Gnidakouong JRN, Roh HD, Kim J, Park Y. In situ process monitoring of hierarchical micro-/nano-composites using percolated carbon nanotube networks. Composites Part A: Applied Science and Manufacturing 2016;84:281-291.

106. Simmons TJ, Vera-Reveles G, González G, Gutiérrez-Hernández JM, Linhardt RJ, Navarro-Contreras H, González FJ. Bolometric properties of semiconducting and metallic single-walled carbon nanotube composite films. ACS Photonics 2015;2(3):334-340.

107. Hasan T, Sun Z, Wang F, Bonaccorso F, Tan PH, Rozhin AG, Ferrari AC. Nanotube–polymer composites for ultrafast photonics. Adv Mater 2009;21(38-39):3874-3899.

Chapter 5

A HYBRID SYSTEM FOR STRUCTURAL REHABILITAION AND HEALTH MONITORING OF CONCRETE STRUCTURES USING CARBON NANOTUBE-BASED SENSING COMPOSITES AND GLASS FIBER REINFORCED POLYMERS

5.1 Introduction

As the nation's infrastructure continues to deteriorate and design requirements become more stringent, structural repair, strengthening, and upgrading of the aging and substandard structures have been widely recognized and received considerable attention over the past three decades [1-6]. Due to the exceptional strength and stiffness-to-weight ratios, superior resistance to chemical corrosion and weathering, and excellent adaptability, fiber reinforced polymer (FRP) composites have become particularly attractive for civil infrastructure and offer great benefits for structural rehabilitation [2,7]. In FRP composites, fibers such as carbon, glass and aramid with high strength and high stiffness are embedded in and bonded together by the low-modulus and -strength polymeric matrix such as epoxy, polyester, and vinyl ester resins [7]. As a result, the reinforcing fibers constitute the backbone of the FRP composites and dominate the strength and stiffness of the composites in the direction of fibers [7]. Todays, the use of FRP composites in civil engineering structures covers a broad range of applications including strengthening structures vulnerable to earthquake hazards [8], bridge construction and repair [3], manufacturing and retrofitting of oil/gas pipes and tanks [9], as well as rehabilitation of timber [4], masonry [6], concrete [6,10] and steel [11] structures. FRP composites in forms of

plates, sheets, strips or jackets are commonly adhered to the exterior surfaces of structural members such as beams, girders and columns of the existing members of bridges and buildings to provide additional flexural, shear and axial strength [12,13]. Recent reviews by Rollins [14], Wu *et al*. [15] and Zaman *et al*. [16] represented numerous FRP-based structural rehabilitation applications performed since 1990s and highlighted a major concern of the long-term performance of this relatively recent technology, suggesting the crucial need for a fast, effective, and reliable structural health monitoring system for rehabilitated structures as well as the applied FRP composites.

As reviewed in Chapter 1, the introduction of carbon nanotubes into fiber composites has been successfully achieved and offers active and distributed sensing capabilities to the composites in responding to the external and internal stimuli, resulting in so-called smart composites. These materials have great potential to extend the performance of conventional FRP-based engineering systems well beyond FRP composites that are often used as the structural reinforcement during the past thirty years.

For example, Schumacher and Thostenson [17] developed a structural sensing strip using a CNT-integrated fiber composite for concrete structures. This 51-mm wide and 530-mm long sensing composite consisted of two-ply unidirectional glass fabrics. It was first applied to a 152 mm × 152 mm × 533 mm concrete beam specimen by impregnating the glass fibers with the 0.5 wt.% nanotube-dispersed epoxy resin with curing agent using a hand lay-up technique and then permanently integrated onto the beam surface after curing the composite under a vacuum bag. The final specimen was loaded monotonically in three-point bending with the structural sensing composite

representing the flexural tension reinforcement. The *in situ* electrical response of the sensing composite was measured during the entire loading process and found to exhibit a strong correlation with the specimen's mid-span deformation. Damage appearing along the tensile face of the concrete beam was also observed in the measurements, which validates the feasibility of using the CNT-based smart FRP composites as not only the structural reinforcement but also as an *in situ* strain/damage sensor for SHM purpose.

Similarly, Zhang *et al*. [18] developed a smart carbon fiber composite with enhanced fracture toughness and integrated damage sensing capabilities by spray-coating of CNTs on the carbon fiber prepreg. A 3.3 mm thick carbon fiber composite composed of 10 plies of twill prepreg of which coated with nanotubes by airbrushing was first cured using a vacuum bag molding and then cut in to 20 mm × 135 mm specimens for mechanical and electrical testing. They finally reported that the localization of nanotubes within inter-ply regions of the carbon fiber composite leads to the increase in interlaminar fracture toughness of 22% and 47%, respectively at low CNT loadings of 0.02 wt.% and 0.047 wt.%. In addition, the collected resistive response of this composite demonstrated good correlation with the crack propagation during the fracture Mode-1 loading condition.

In addition to structural sensing composites, Song *et al*. [19] established a self-sensing cross-ply carbon composite by embedding a network of CNT sensing threads. They first produced continuous 20-25 μm diameter CNT threads by pulling a web of a spinnable CNT array and simultaneously twisting, and then installed a 4 × 4 grid of CNT threads into a 200 mm × 200 mm × 2.4 mm eight-ply $[0/90]_2$ carbon fiber composite panel for impact testing. The real-time resistive responses were collected

from the 16 CNT thread sensors and displayed instant spikes as soon as the impact was applied. In addition, the location of the impact damage was roughly approximated at the grid point with the highest resistive peak locally. They finally concluded that the CNT thread sensor is a simple, reliable, accurate and practical technique for SHM.

With continuing advancements in both composite engineering and nanotechnology, it is most likely that high-performance smart composites with multiple activating physical mechanisms will be created and pursue large increases in new capabilities and usage for future civil infrastructure [20]. In particular, smart sensing composites need to be integrated to enable SHM of the entire structure or pre-selected critical locations. As experimentally characterized in Chapter 2 to 4, the CNT-based nonwoven sensing composites have electrically isotropic nanotube-based conductive networks and have demonstrated fast and effective sensing capabilities of mechanical strain, spatial damage, temperature, and polymer motion. The previously presented results are plausible and have confirmed the utilization of this established composite as a sensitive, promising, and cost-effective multifunctional sensor. Nevertheless, similar to the mainstream research of smart sensing composites, the focus has been limited to coupon-scale testing and simplified numerical modeling.

This chapter deals with the integration of smart composites and advanced sensing techniques for large-scale applications. Specifically, a novel hybrid composite system is developed for integrated structural rehabilitation and health monitoring of concrete structures. The central concept is that nanotubes are first coated onto a non-structural fabric following the ‘wetting’ approach as described in Chapter 2 to form an electrically conductive network that offers high strain sensitivity and distributed sensing capabilities. Next, the CNT-modified fabric is integrated with glass fiber

reinforcement using the on-site vacuum-assisted-resin-transfer-molding (VARTM) technique to create an integrated reinforcing and sensing solution. Strains and degradation in form of cracking are directly related to the overall resistance change measured between electrodes attached to the sensing layer. By employing a multiplexing approach, damage locations can be approximately quantified spatially within the sensing sheet. This approach provides the capability of real-time SHM of a structural concrete member and potentially ensure it to operate within its serviceability limits (i.e., elastic mechanical response without experiencing severe structural damage, yielding, and sudden failure of concrete).

In the following sections, the basic principles of the experimental approach are first discussed, and then the application on two full-size reinforced concrete laboratory beams (1 ft × 2 ft × 16 ft), which had been precracked to create typical service-level type cracking, prior to be retrofitted using the proposed strategy is presented. In particular, the first beam was rehabilitated with a 14 ft long and 1 ft wide composite patch at the tension side to increase its flexural strength; the second beam was intentionally designed with unsymmetrical transverse reinforcement and strengthened at its weaker side with three U-jackets. Both beams were tested to failure and the real-time resistance data were collected during the entire loading process and compared with member deformations (in form of strains and mid-span displacements) and the outputs of two acoustic emission sensors.

5.2 Experimental Details

The large-scale experiments were carried out in the Structures Laboratory at the University of Delaware (UD) in order to validate and study the potential and capabilities of the proposed sensing-retrofitting methodology under a nearly practical

scenario. The fabrication of the hybrid composite system was performed on-site with raw materials prepared in advance from the Center for Composite Materials at UD including nanotube dispersions, epoxy resin, fabric cloth, composite manufacturing supplies and tools, etc. In particular, large temperature variations were experienced during the experimental investigations in the wintertime due to the prolonged tests and the poor thermal insulation of the laboratory, where the average day and night temperature in those testing days was measured about 15 °C and 10 °C, respectively.

5.2.1 Large-Scale Concrete Beam Specimens

Two concrete beam specimens of identical dimensions, 1 ft × 2 ft × 16 ft were cast in-place with normal-weight concrete mix and steel reinforcement as detailed in Figure 5.1 and 5.2, respectively, which are referred as the flexure beam and the shear beam in the following sections. The two full-scale beam specimens were designed and used on previous work at UD [21], and tested under four-point bending conditions as described in Figure 5.1 and 5.2.

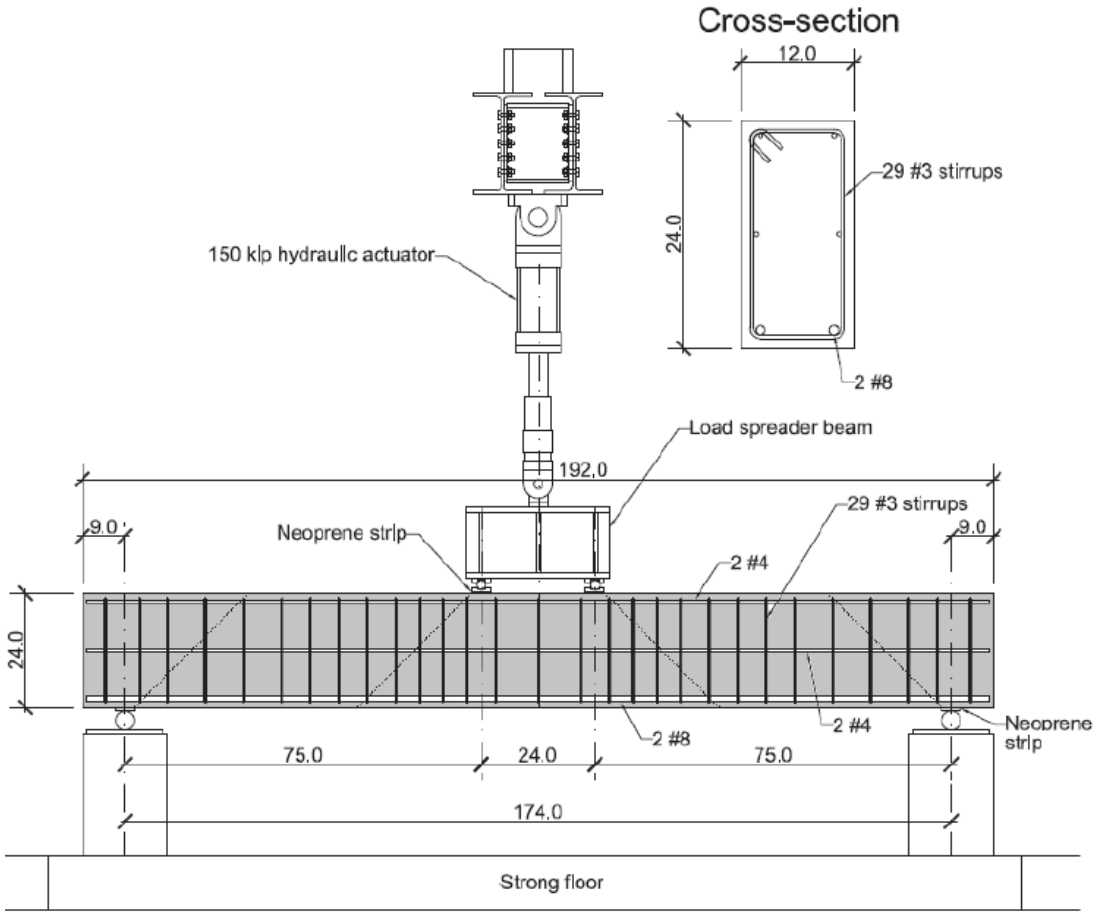

Figure 5.1: Flexure beam elevation view of reinforcing details, geometry, and the typical beam loading setup for four-point bending test. Courtesy by: Thomas Schumacher.

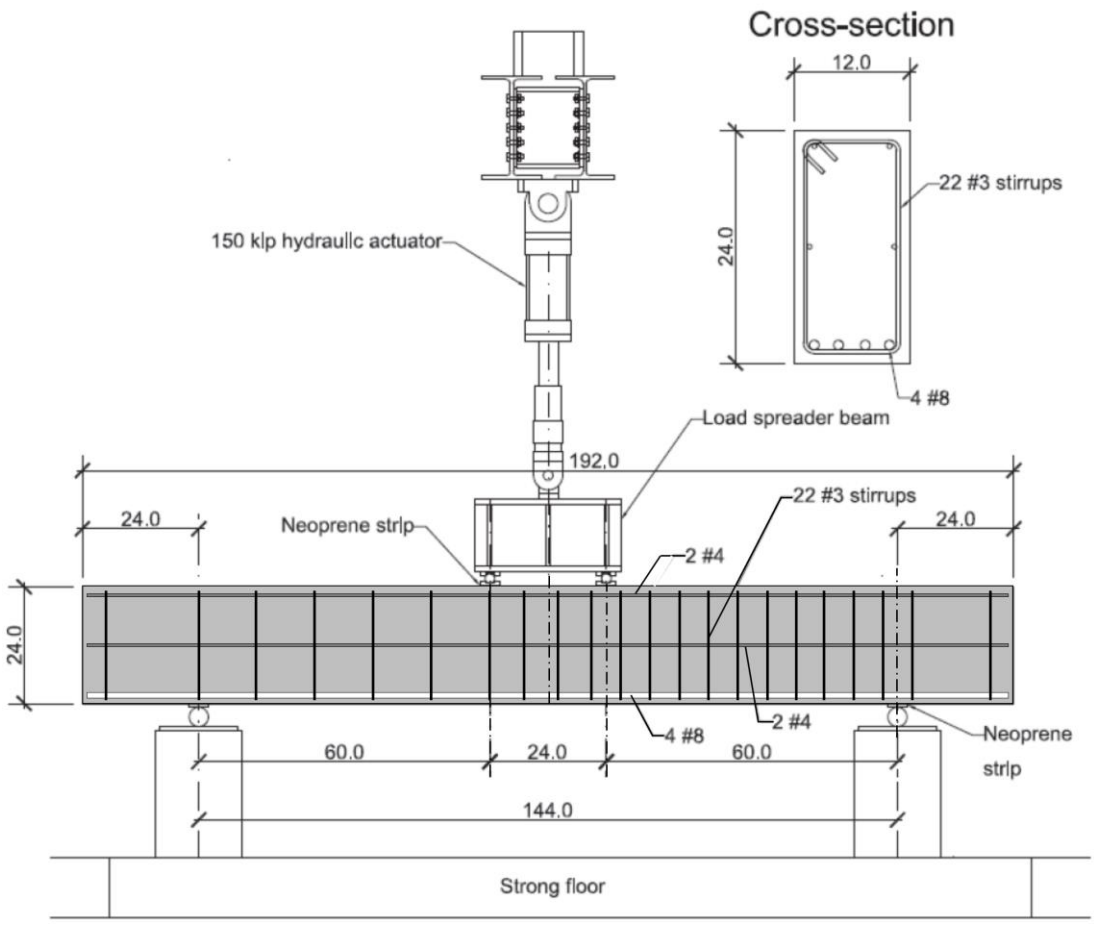

Figure 5.2: Shear beam elevation view of reinforcing details, geometry, and the typical beam loading setup for four-point bending test. Courtesy by: Thomas Schumacher.

5.2.1.1 The Flexure Beam

For the flexure beam, a total number of 29 #3 stirrups, 2 #8 and 4 #4 steel reinforcing bars were used to reinforce the concrete beam, which results in a section that fails in flexure in its ultimate state. Following the current U.S. code provision, *Building Code Requirements for Structural Concrete (ACI 318-11)* [22], the nominal flexural and shear capacity of the flexure beam section can be calculated using Articles 10.2-5 and 11.1-2, respectively. Table 5.1 lists the material and section

properties of the flexure beam and Table 5.2 shows the U.S. to metric conversion factors.

Table 5.1: Material and Section Properties of the Flexure Concrete Beam.

Symbol	Notation	Unit	Value
f_c'	Specified compressive strength of concrete	psi	4000
f_y	Specified yield strength of reinforcement	ksi	68
f_{yt}	Specified yield strength of shear reinforcement	ksi	60
E_s	Modulus of elasticity of reinforcement	ksi	29000
E_c	Modulus of elasticity of concrete	ksi	3606.5
A_s	Area of longitudinal tension reinforcement	in.^{2}	1.58
A_s'	Area of longitudinal compression reinforcement	in.^{2}	0.4
A_s''	Area of longitudinal reinforcement at the mid-plane	in.^{2}	0.4
A_v	Area of shear reinforcement	in.^{2}	0.22
ε_y	Yield strain of reinforcement	in./in.	0.00234
b	Width of compression face of member	in.	12
h	Overall height of member	in.	24
d	Distance from extreme compression fiber to centroid of longitudinal tension reinforcement	in.	21.625
d'	Distance from extreme compression fiber to centroid of longitudinal compression reinforcement	in.	2.125
s	Center-to-center spacing of shear reinforcement	in.	6.25

Table 5.2: Conversion Factors.

U.S.	Metric
1 in.	25.4 mm
1 in^2	645.16 mm^2
1 lb	4.45 N
1 psi	6.89 kPa
1 ksi	6894.7 kPa

Following the ACI 318-11 design code, the distance from the extreme compression fiber to neutral axis (c) is first obtained based on the force equilibrium when the concrete in compression reaches its assumed strain limit (ε_{cu}) of 0.003 per Article 10.3.3 and calculated as 3.6 in. after several iterations [23]. In particular, according to Article 10.2.7, the equivalent rectangular stress block of this beam section is used to calculate the concrete stress distribution and resultant forces, which is schematically illustrated in Figure 5.3. Here, ε_s = 0.0151 (> ε_y) as c = 3.6 in.

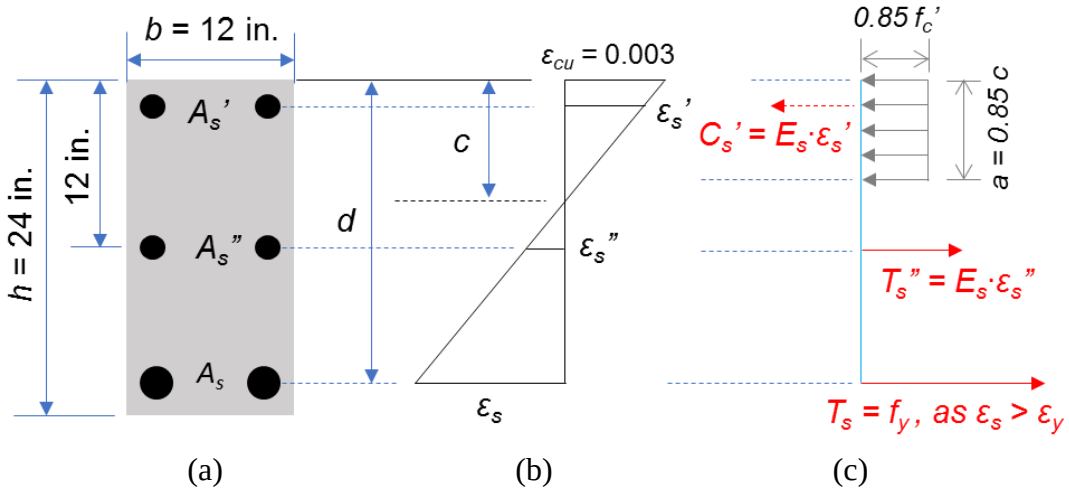

Figure 5.3: Schematic illustrations showing (a) the concrete section, and (b) strain and (c) stress distributions of the flexure beam at its nominal flexural capacity according to ACI 318-11 design code.

Next, the nominal moment capacity (M_n) of this beam section corresponding to its flexural strength is calculated as 250.6 kip-ft using Equation 5.1, that is the total resultant bending moment due to the tension forces from the tension reinforcement, and the compression forces from the compression reinforcement and concrete with respect to the plane of the bottom tension reinforcement.

$$M_n = (A_s'' \cdot E_s \cdot \varepsilon_s'') \cdot (d - 12)$$
$$+a \cdot (0.85 f_c') \cdot b \cdot \left(d - \frac{a}{2}\right)$$
$$+(A_s' \cdot E_s \cdot \varepsilon_s') \cdot (d - d') \qquad (5.1)$$

In addition, following ACI 318-11 Section 10.5, this beam section satisfies the requirement for the minimum tensile reinforcement ($A_{s,min}$) of flexural members denoted in Article 10.5.1 and given by Equation 5.2.

$$A_{s,min} = \frac{3\sqrt{f_c'}}{f_y} b_w d \geq 200\, b_w d / f_y \qquad \text{ACI 318-11 (10-3)} \qquad (5.2)$$

where b_w is equal to b for a rectangular section. The calculation yields $A_{s,min}$ = 0.763 in^2, which is less than the provided A_s of 1.58 in^2 in this concrete beam.

The shear capacity (V_n) of the beam section is determined following ACI 318-11 Chapter 11. Prior to calculation, ACI 318 requires a check to ensure minimum transverse steel area and spacing. Also, Article 11.1.2.1 limits the value of $\sqrt{f_c'}$ to 100 psi, unless the section of interest contains at least minimum reinforcement. Minimum shear reinforcement ($A_{v,min}$) is required as outlined in Article 11.4.6.1 when the factored shear force V_u exceeds 50% of the factored nominal concrete shear strength. Once met, the $A_{v,min}$ is determined in Article 11.4.6.3 using Equation 5.3.

$$A_{v,min} = 0.75\sqrt{f_c'}\frac{b_w s}{f_{yt}} \geq (50 b_w s)/f_{yt} \qquad \text{ACI 318-11 (11-13)} \qquad (5.3)$$

For this beam section, the $A_{v,min}$ is calculated as 0.0625 in^2 with the parameters listed in Table 5.1, which is less than the provided A_v of 0.22 in^2. In addition to minimum area requirements, Article 11.4.5 limits spacing of the shear reinforcement to the lesser of $d/2$, $0.75h$, or 24 in. for nonprestressed members, except when the shear strength provided by the shear reinforcement (V_s) is greater than $4\sqrt{f_c'}b_w d$, the above spacing limits must be reduced by 50%. Once minimum area and spacing requirements are satisfied, the nominal shear resistance resulting from the contribution of shear reinforcement (V_s) and concrete (V_c) can be determined as respectively outlined in Articles 11.2 and 11.4 using Equations 5.4, 5.5 and 5.6 as follows.

$$V_c = 2\sqrt{f_c'}b_w d \qquad \text{ACI 318-11 (11-3)} \tag{5.4}$$

or using the more detailed equation as:

$$V_c = \left(1.9\sqrt{f_c'} + 2500\rho_w \frac{V_u d}{M_u}\right) b_w d < 3.5\sqrt{f_c'}b_w d \qquad \text{ACI 318-11 (11-5)} \tag{5.5}$$

where $\rho_w = A_s/(b_w d)$ is the flexural reinforcement ratio; V_u (kips) and M_u (kip-ft) are the factored shear and moment at the section of interest and $V_u/M_u < 1.0$.

$$V_S = \frac{A_v f_{yt} d}{s} \qquad \text{ACI 318-11 (11-15)} \tag{5.6}$$

For this beam section, V_c = 32.8 kips and V_s = 45.7 kips. Then, the nominal shear strength is given as

$$V_n = V_c + V_s = 78.5 \text{ kips} \qquad \text{ACI 318-11 (11-2)} \tag{5.7}$$

and the factored shear force at the section considered must be limited to

$$V_u \leq \Phi\, V_n = 0.75\,(V_c + V_s) \qquad \text{ACI 318-11 (11-1)} \tag{5.8}$$

where Φ is the strength reduction factor per Article 9.3.1.

Under the predefined four-point loading condition as described in Figure 5.1, the moment capacity in accordance to V_n of the beam section is determined as 490.5

kip-ft corresponding to the bending moment diagram shown in Figure 5.4. This is greater than 250.6 kip-ft obtained using Equation 5.1 based on the flexural strength. Obviously, the overall moment capacity of the flexure beam is dominated by its flexural strength (that is, P = 80.2 kips) and a flexural failure mode is expected as it reaches its ultimate capacity. Additional noteworthy this beam was precracked under quasi-static loads of 30 kips and 35 kips prior to be structurally retrofitted. Figure 5.5 shows the traced cracking pattern after this preloading had occured.

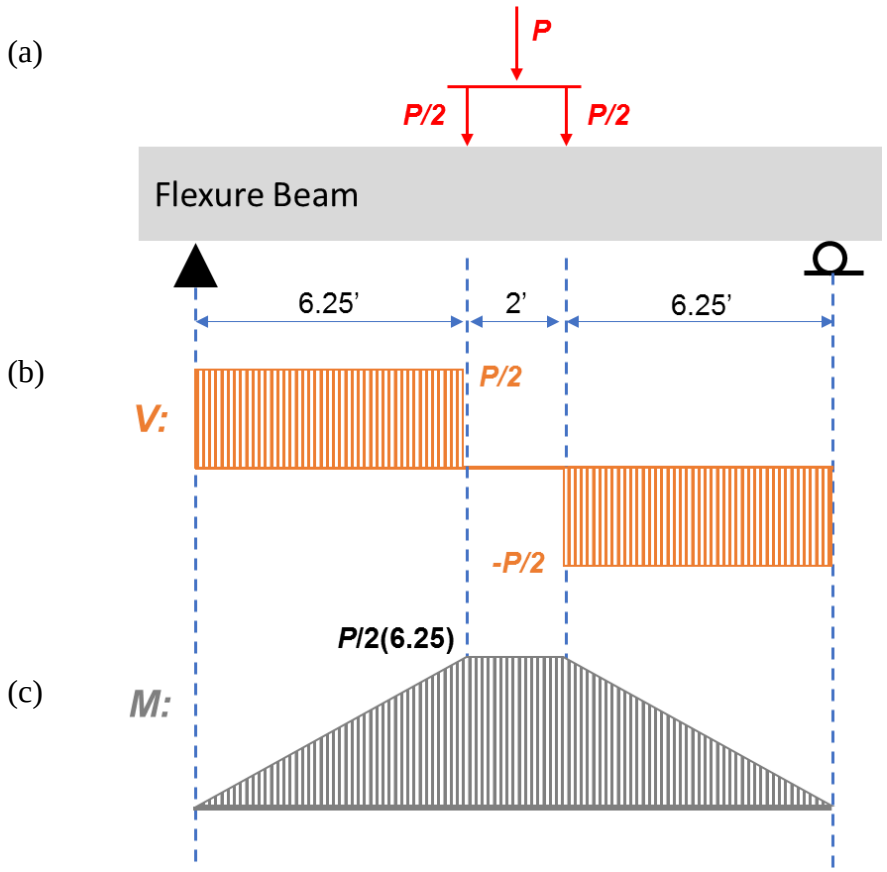

Figure 5.4: (a) The free-body, (b) shear force, and (c) bending moment diagrams of the flexure beam under the predefined four-point bending condition.

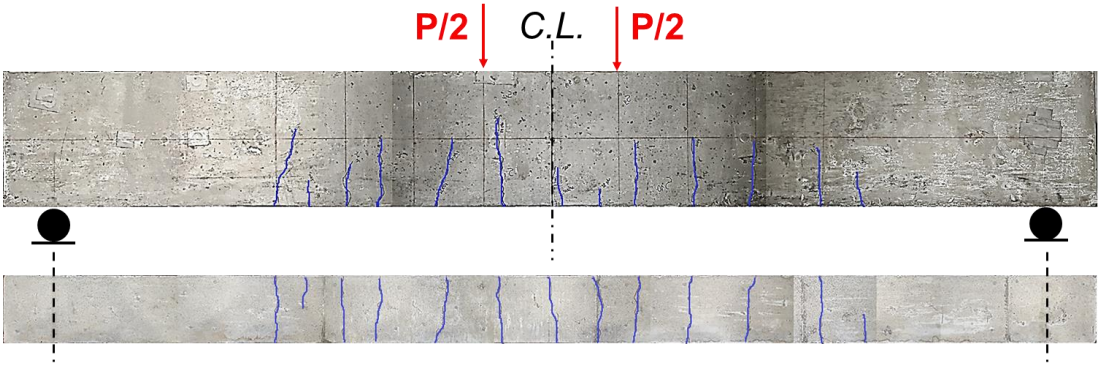

Figure 5.5: Photograph showing the elevation (top) and bottom (bottom) view of the traced cracking pattern observed on the flexure beam after 35-kip preloading (Note: crack width is exaggerated for clarity).

5.2.1.2 The Shear Beam

As illustrated in Figure 5.2, the shear beam has 4 #8 and 4 #4 reinforcing steel bars and the unsymmetrical transverse reinforcement (i.e., 8 #3 stirrups in the left portion with larger spacing and 14 #3 in the other side with smaller spacing), resulting in a weak and strong shear zone in its left and right portion, respectively. The aim of this special design is to produce shear cracks in a controlled manner and eventually force shear failure on the weak side as the beam is loaded to its ultimate capacity. Table 5.3 lists the material and section properties of the shear beam.

Table 5.3: Material and Section Properties of the Shear Concrete Beam.

Symbol*	Unit	Value	Symbol	Unit	Value
f_c'	psi	4000	A_v	in.^{2}	0.22
f_y	ksi	68	ε_y	in./in.	0.00234
f_{yt}	ksi	60	b	in.	12
E_s	ksi	29000	h	in.	24
E_c	ksi	3606.5	d	in.	21.625
A_s	in.^{2}	3.16	d'	in.	2.125
A_s'	in.^{2}	0.4	s in left side	in.	6
A_s''	in.^{2}	0.4	s in right side	in.	12

* Note: the notations of the symbols are presented in Table 5.1.

Following the same procedures for finding the load carrying capacity of the flexure beam described in Section 5.2.1.1, the neutral axis of the shear beam is first found at 6.4 in. from the top concrete cover, which results in ε_s of 0.0072 in accordance to ε_c=0.003 following strain compatibility per ACI 318-11 Article 10.3.3, and then the nominal flexural moment capacity of the beam section is calculated as 404.6 kip-ft. In other words, the shear beam can sustain a point load of 161.8 kips based on the force diagram of the beam presented in Figure 5.6 that corresponds to the four-point bending condition (see Figure 5.2).

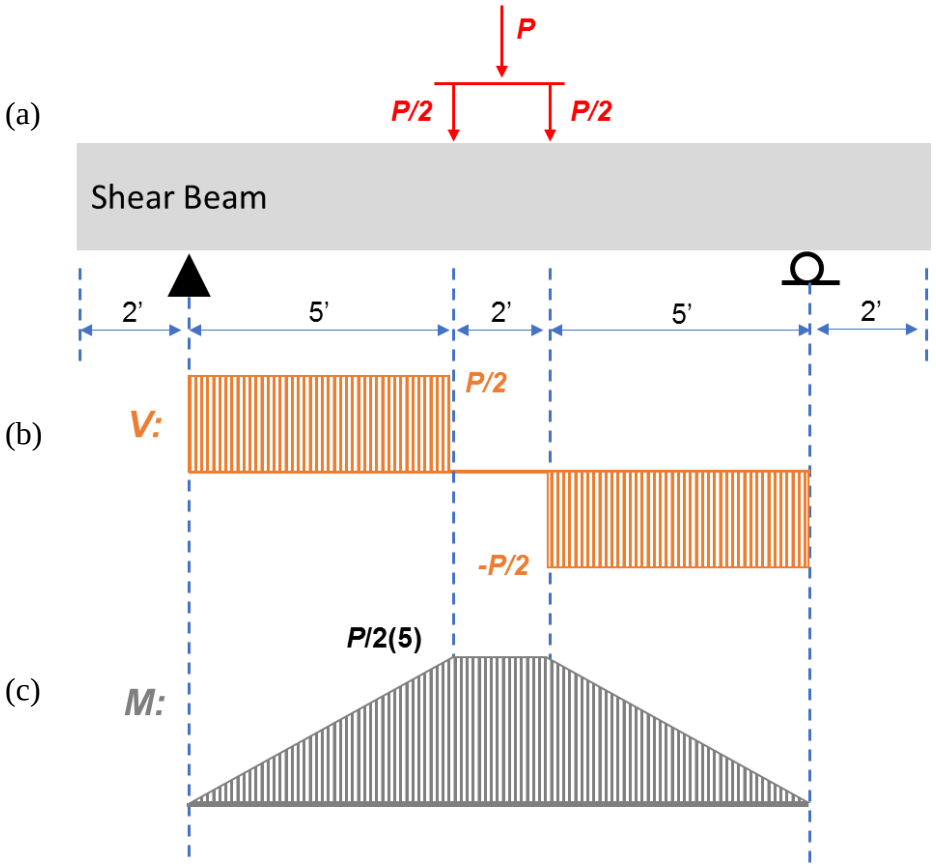

Figure 5.6: (a) The free-body, shear force, and bending moment diagrams of the shear beam under the predefined four-point bending condition.

In addition, the shear strength provided by concrete of this beam is identical to that of the flexure beam due to the same material and section size used, that is V_c = 32.8 kips as per ACI 318-11 Section 11.2. As previously shown, the shear strength provided by shear reinforcement depends on the spacing between the shear reinforcement. Therefore, according to Equation 5.6, the strong zone with s = 6 in. in the right side of the beam (see Figure 5.2) yields V_s^{right} = 47.6 kips, whereas the weak zone in the left side only gives V_s^{left} = 23.8 kips at s = 12 in., the maximum spacing for

shear reinforcement of this beam section as per ACI 318-11 Article 11.4.5. Based on Equation 5.7, the nominal shear capacity of this beam in its strong and weak portion is 80.4 kips and 56.6 kips, respectively, which can correspondingly sustain the bending moment of 402 kip-ft and 283 kip-ft in its left and right side as calculated according to the moment diagram shown in Figure 5.5.

As can be observed, the right portion of the shear beam is designed with the sufficient flexural and shear reinforcement and has comparable flexural and shear moment capacity (i.e., 404.6 kip-ft vs. 402 kip-ft), but the left portion is approximately 30% under-designed in shear strength compared to its nominal flexural strength (i.e., 283 kip-ft vs. 404.6 kip-ft). Thus, shear failure is most likely expected to occur on the left side before the beam reaches its ultimate flexural capacity. This beam was quasi-statically loaded-unloaded under four-point bending (see Figure 5.2) with eight cycles up to 95 kips in order to induce service-level shear cracking. The shear cracks started to appear at the 85 kip and 95 kip cycles. Figure 5.7 shows the traced cracking pattern after the preloading process.

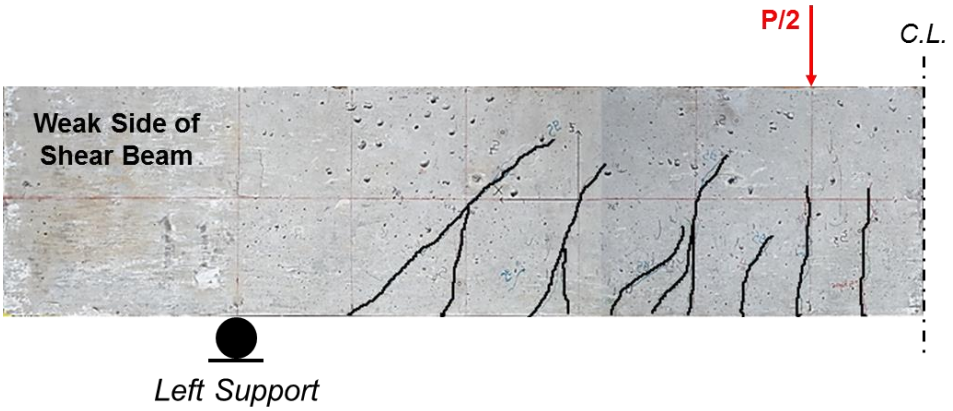

(a)

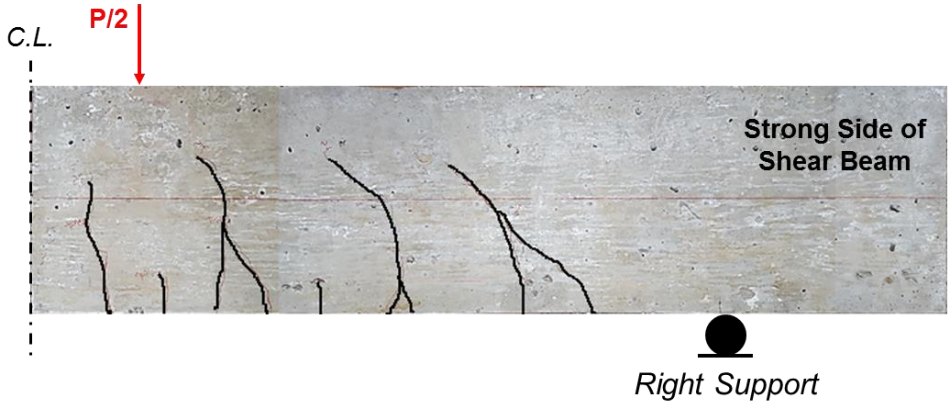

(b)

Figure 5.7: Photographs showing the traced cracking pattern observed on the shear beam on its (a) weak and (b) strong side after 95-kip preloading (Note: crack width is exaggerated for clarity).

5.2.2 Design of Externally Bonded Fiber Reinforced Polymer Composites for Structural Rehabilitation

As previously demonstrated, the special design of the reinforcement made the flexure beam most likely fail in flexure and the shear beam prone to exhibit shear failure on its left side. For both cases, strengthening using E-glass fiber reinforced

polymer (GFRP) composites is designed and implemented on these two concrete beams to increase their load-carrying capacities.

The 2015 American Concrete Institute (ACI) Manual of Concrete Practice [24] includes guidelines and specifications of Committee 440 regarding structural retrofitting of concrete structures with FRP systems including ACI 440.2R-08: *Guide for the Design and Construction of Externally Bonded FRP Systems for Strengthening Concrete Structures* [25], and ACI 440.8-13: *Specifications for Carbon and Glass Fiber-Reinforced Polymer (FRP) Materials Made by Wet Layup for External strengthening of Concrete and Masonry Structures* [26]. The design recommendations in ACI 440.2R-08 are based on the limit-states design principle to be compatible with the ACI 318 design code. Specifically, two limit states are considered for design, including the service limit state for controlling excessive deflections, cracking, vibration, etc., and the strength limit state for restraining failure of the member, stress rupture, and fatigue [27,28].

5.2.2.1 Flexural Strengthening with FRP Patch

Bonding FRP reinforcement to the tension face of the concrete flexural member with structural fibers oriented along the longitudinal axis of the member can provide additional flexural strength [25]. Therefore, a flexural strengthening approach using externally-bonded unidirectional GFRP patch was designed for the formerly analyzed flexure beam. The FRP design details are covered in Chapter 10 of ACI 440.2R-08. In addition to Table 5.1, Table 5.4 summarizes the GFRP properties needed for the flexural strengthening design calculations. In general, the additional strength gain from the GFRP repair is analogous to the flexural strength contribution from tension reinforcement and can be calculated based on the internal strain and

stress distribution diagrams ensuring strain compatibility and force equilibrium. At the ultimate capacity, concrete crushing is assumed to occur if the compressive strain in the concrete reaches ε_{cu} (=0.003). Figure 5.8 illustrates the strain and stress distributions of the FRP reinforced beam section under flexure at its ultimate limit state.

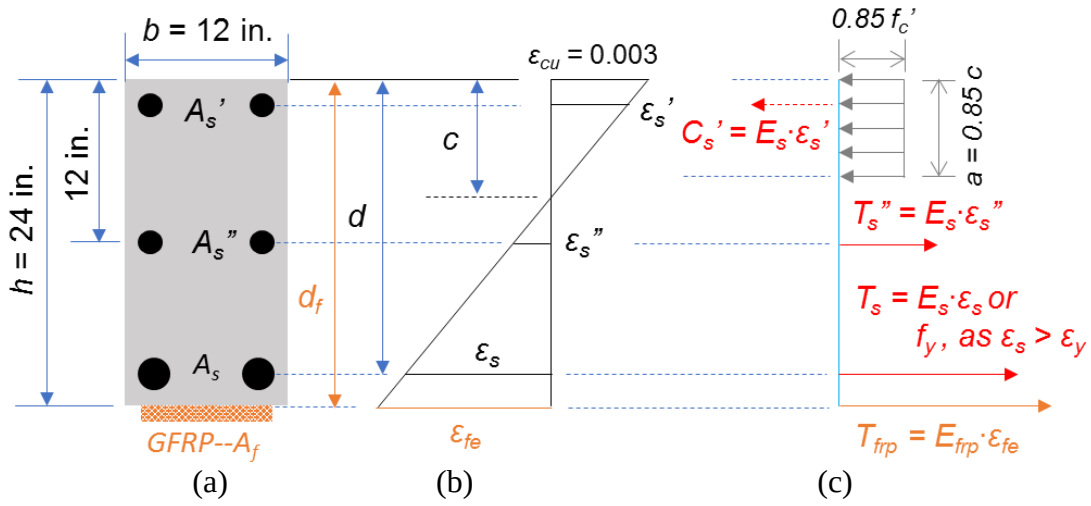

Figure 5.8: Illustration showing (a) the cross-section of the FRP-concrete section, and (b) strain and (c) stress distributions of the FRP reinforced flexure beam at the ultimate flexural limit state per ACI 440.2R-08.

Table 5.4: Material Properties of GFRP for Flexural Strengthening of Concrete Beam per ACI 440.2R-08 Specifications.

Symbol	Notation	Unit	Value*
E_f	Tensile modulus of elasticity of E-glass fiber	GPa	72.4
E_m	Tensile modulus of elasticity of EPON 862 epoxy resin	GPa	2.75
V_{fiber}	Fiber volume fraction in GFRP	None	60%
E_{frp}	Tensile modulus of elasticity of GFRP	GPa	44.54
σ_f	Tensile strength of E-glass fiber	MPa	2155
σ_m	Tensile strength of EPON 862 epoxy resin	MPa	58
ε_y^f	Yield strain of fiber	in./in.	0.0298
ε_y^m	Yield strain of matrix	in./in.	0.0211
ε_y^{frp}	Yield strain of GFRP	in./in.	0.0211
n	Number of plies of GFRP reinforcement	None	12
t_f	Nominal thickness of one ply of GFRP reinforcement	in.	0.0167
w_f	Width of FRP reinforcing plies	in.	12
A_f	$= n\ t_f w_f$, area of GFRP external reinforcement	$in.^2$	2.4
d_f	Effective depth of GFRP flexural reinforcement	in.	24
ε_{bi}	Strain level in concrete substrate at time of GFRP installation	in./in.	-0.000019 (*explained in the following section*)
ε_{fd}	Debonding strain of externally bonded GFRP reinforcement	in./in.	0.00462 (*explained in the following section*)
ε_{fe}	Effective strain level in GFRP reinforcement attained at failure	in./in.	0.00462 (*explained in the following section*)

* Note: values are found experimentally.

According to numerous experimental studies [2,6,25,29], the most common failure mode of the externally-bonded FRP-strengthened concrete member is FRP debonding in conjunction with the internal steel reinforcement in elastic or rather

yielding state. To prevent such an intermediate crack-induced debonding failure mode, ACI 440.2R-08 Article 10.1 requires the effective strain in FRP reinforcement to be lower than the debonding strain level (ε_{fd}) as calculated using Equation 5.9.

$$\varepsilon_{fd} = 0.083\sqrt{\frac{f_c'}{nt_f E_{frp}}} \leq 0.9\varepsilon_{fu} \qquad \text{ACI 440.2R-08 (10-2)} \qquad (5.9)$$

where $\varepsilon_{fu}$is the rupture strain of FRP.

It is clear that a thick FRP layer is more prone to debond from the concrete substrate than a thin ones. Here, a 0.1 in. and 0.2 in. thick GFRP layer corresponds to a debonding strain limit of 0.00653 and 0.00462, respectively. Next, following Article 10.2.3, the initial strain level on the bonded substrate (ε_{bi}) is determined from the elastic analysis of the existing member by considering all loads applied on the member during the installation of the FRP. For this laboratory experiment, the flexure beam was flipped over to deploy the FRP on its soffit. Thus, the beam self-weight was the only load contributing to the initial strain state, subsequently calculated as ε_{bi} = -0.000019, i.e., slightly in compression.

It is well known that FRP composites are linear elastic until failure [6,7]. As a result, the elastic strain level in the FRP dominates the stress level developed in the FRP. The attainable ultimate strain level in the FRP really depends on the flexural failure modes including concrete crushing, FRP debonding and rupture, which is a complex phenomenon in nature and impossible to be represented by simple equations. As for designing FRP, a lower bound of this strain level (i.e., the effective strain level, ε_{fe}) in FRP (as shown in Figure 5.8) is adopted by ACI 440.2R-08 guideline and calculated using Equation 5.10 according to Article 10.2.5:

$$\varepsilon_{fe} = \varepsilon_{cu}\left(\frac{d_f - c}{c}\right) - \varepsilon_{bi} \leq \varepsilon_{fd} \qquad \text{ACI 440.2R-08 (10-3)} \qquad (5.10)$$

which results in the stress level in the FRP (T_{frp}) as:

$$T_{frp} = E_{frp}\varepsilon_{fe} \quad \text{ACI 440.2R-08 (10-4)} \tag{5.11}$$

Afterwards, the strain level in the steel reinforcement can be obtained using strain compatibility (see Figure 5.8) as:

$$\varepsilon_s = (\varepsilon_{fe} + \varepsilon_{bi})(\frac{d-c}{d_f-c}) \quad \text{ACI 440.2R-08 (10-10)} \tag{5.12}$$

which consequently causes the stress level (T_s) in the steel following:

$$T_s = E_s\varepsilon_s \leq f_y \quad \text{ACI 440.2R-08 (10-11)} \tag{5.13}$$

It is notable that the determination of the neutral axis depth *c* is the key to fulfill the FRP design routine. Similar to ACI 318-12, *c* is calculated following a trial-and-error procedure [22,23]. That is, making an initial guess of *c* first, calculating strain levels the associated stress levels in all materials with the above equations, and then checking the internal force equilibrium. This process is repeated by revising *c* and finished when convergence is attained. In this study, a 12-in. wide, 0.2-in. thick GFRP layer was deployed on the flexure beam. After the iterative process, *c* was found to be 5.4 in. Finally, the nominal flexural strength of the FRP-reinforced concrete beam was computed by summing the resultant bending moments due to the internal forces from all contributions. Bonding this 12 in. × 0.2 in. GFRP to the beam produces an improved flexural moment capacity of 318 kip-ft, which is 27% greater than the original 250.6 kip-ft, as calculated in Section 5.2.1.1. This rehabilitated beam can sustain a point load of 102 kips under the predefined four-point bending configuration (see Figure 5.1), which is equivalent to a shear load at section (V_u) of 51 kips. Additionally, comparing with the shear strength of the section (i.e., V_n = 78.5 kips per Section 5.2.1.1), it is obvious that $V_u < V_n$ satisfying Equation 5.8, which means that

this GFRP-reinforced beam is capable of resisting the shear forces associated with the increased flexural strength, validating the design specifics of the GFRP.

To produce effective and strong structural strengthening action, FRP reinforcement details must be considered rigorously, so as to avoid bond-related failures, such as FRP debonding and FRP end peeling. Debonding has been observed to most likely initiate at flexural cracks, flexural/shear cracks, or both, near the region of maximum bending moment [25,30]. Under loading, these cracks can open and induce high interfacial shear stress resulting in FRP debonding that can propagate across the shear span in the direction of decreasing moment [28]. Meanwhile, the bond capacity of FRP is developed over a critical length l_{df}. To develop the effective FRP stress, a minimum anchorage length of the FRR layer deployed on the concrete member must exceed l_{df} past any cracks [25]. Article 13.1.3 in ACI 440.2R-08 guideline quantifies this length using Equation 5.14 as follows.

$$l_{df} = 0.057\sqrt{\frac{nt_f E_{frp}}{\sqrt{f_c'}}} \quad \text{ACI 440.2R-08 (13-2)} \qquad (5.14)$$

For the beam reinforced with a 0.2 in. thick GFRP patch in this study, l_{df} is determined as 8.2 in. Additionally, FRP end peeling (i.e., concrete cover delamination) can result from the normal stresses developed at the ends of externally bonded FRP reinforcement and can be partially controlled by the level of stress at the termination points of the FRP [25,31]. As per Article 13.1.2, each successive ply must be terminated extending not less than a 6-in. beyond the previous ply. Once the shear force is greater than 2/3 of V_c, the FRP patch must be extended further toward the supports.

Finally, the designed GFRP reinforcement for strengthening of the flexure beam is detailed in Figure 5.9. The existing flexural cracks observed in the bottom tension face (see Figure 5.5) are covered by this GFRP patch. Additional U-wraps to reinforce the flexure beam against cover delamination were not provided.

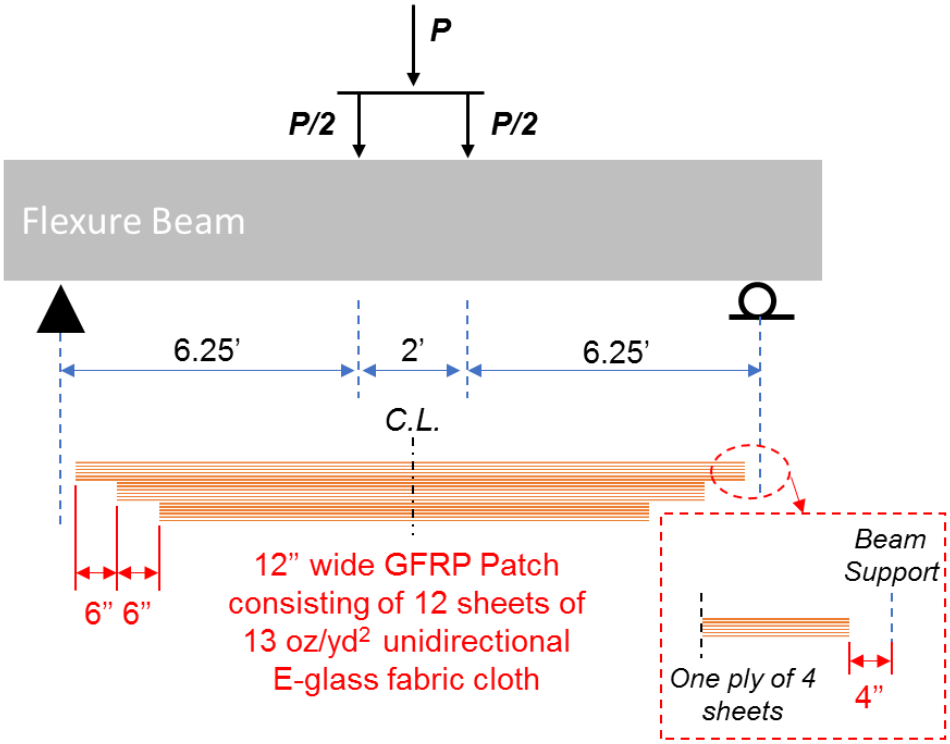

Figure 5.9: Graphical representation showing the GFRP reinforcement details for flexural strengthening of the flexure beam.

5.2.2.2 Shear Strengthening with FRP U-Wraps

According to Malvar *et al*. [32], Chajes *et al*. [33], Norris *et al*. [34], and Kachlakev and McCurry [35], the shear strength of existing concrete members can be increased by fully or partially wrapping members with FRP composites. To enable

effective shear strengthening action, the structural fibers in the FRP need to be distributed transverse to the axis of the member (i.e., aligning parallel to the steel stirrups) or perpendicular to shear cracks [36,37]. Strengthening for shear is encompassed in Chapter 11 of the ACI 440.2R-08 guideline. The three types of FRP wrapping schemes including complete wrap, three-sided U-wrap, and two-sided wrap, can be used to increase the shear strength. Evidently, completely wrapping around the concrete section is the most efficient wrapping scheme and is most commonly used in column applications where the entire member surface is accessible. For beam strengthening, it is impractical to completely wrap a member due to the geometric constraints of the integral slabs or superstructures between adjacent beams. Of the two remaining wrapping schemes, a U-wrap is more efficient than the two-sided wrap.

Similar to the FRP-based flexural strengthening presented in above, the added shear strength of the concrete member resulting from the addition of FRP shear reinforcement is analogous to the shear strength contribution of the concrete section from tension steel, stirrups and concrete. In this respect, the design equations for FRP shear strengthening are adapted from shear strength equations of the ACI 318 codes, giving the nominal shear strength of a FRP-strengthened concrete member as:

$$\phi V_n = \phi(V_c + V_s + \Psi_f V_{frp}) \qquad \text{ACI 440.2R-08 (11-2)} \qquad (5.15)$$

where ϕ is 0.75 for shear design. V_c is calculated using Equation 5.4 or 5.5, and V_s is calculated using Equation 5.6. The Ψ_f term is an additional reduction factor for the shear contribution from FRP and equal to 0.85 for U-wraps. V_{frp} is the nominal shear strength provided by FRP reinforcement corresponding to its effective stress level.

It is notable that once a repair scheme is selected, the FRP fiber orientation to the estimated failure crack is determined. According to Article 11.4, V_{frp} is calculated

as the force resulting from the tensile stress in the FRP across the failure crack, as presented in Equation 5.16.

$$V_{frp} = \frac{A_{fv} f_{fe} (sin\alpha + cos\alpha) d_{fv}}{s_f} \quad \text{ACI 440.2R-08 (11-3)} \tag{5.16}$$

where α is the inclination of the FRP fibers to the longitudinal axis of the member. d_{fv} is the depth of the FRP. s_f is the spacing between the discrete U-wraps. A_{fv} and f_{fe} are the effective cross-sectional area of U-wraps and the effective stress in FRP at failure that are correspondingly computed using Equation 5.17 and 5.18, respectively.

$$A_{fv} = 2nt_f w_f \quad \text{ACI 440.2R-08 (11-4)} \tag{5.17}$$

$$f_{fe} = \varepsilon_{fe} E_{frp} \quad \text{ACI 440.2R-08 (11-5)} \tag{5.18}$$

where ε_{fe} is the effective strain in the FRP at failure and calculated depending on the wrapping scheme as per ACI 440.2R-08 Article 11.4.1.

For the current investigation, as the shear beam has unsymmetric transverse reinforcement as demonstrated in former Section 5.2.1.2, three distributed GFRP U-wraps were deployed to provide the shear strength enhancement on the lightly reinforced side of the beam. Figure 5.10 represents the FRP strengthening details, where the associated shear deficiency of 23.8 kips is highlighted on the left side of the shear beam that the deployed strengthening scheme needs to account for. In addition, these planned U-wraps are able to cover more than 95% of the existing shear cracks on the weak portion of the beam (see Figure 5.7). To fulfill the calculations, in addition to Table 5.3 and 5.4, Table 5.5 shows the material properties of the GFRP U-wraps for shear strengthening of the concrete beam.

Table 5.5: Materials Properties of GFRP U-Wraps Designed for Shear Strengthening of the Concrete Beam per ACI 440.2R-08 Guideline.

Symbol	Unit	Value	Symbol	Unit	Value
n	None	6	V_f	None	60%
w_f	in.	15	ε_y^m	in./in.	0.0211
α	Degree	90°	ε_y^f	psi	0.0298
d_{fv}	in.	23	ε_y^{frp}	in./in.	0.0211
A_{fv}	in.^{2}	3	f_{fu}	ksi	129.5*
s_f	in.	18.5	ε_{fu}	in./in.	0.0200*

* Note: the design material properties have been applied with an environmental-reduction factor of 0.95 per ACI 440.2R-08 Article 9.4.

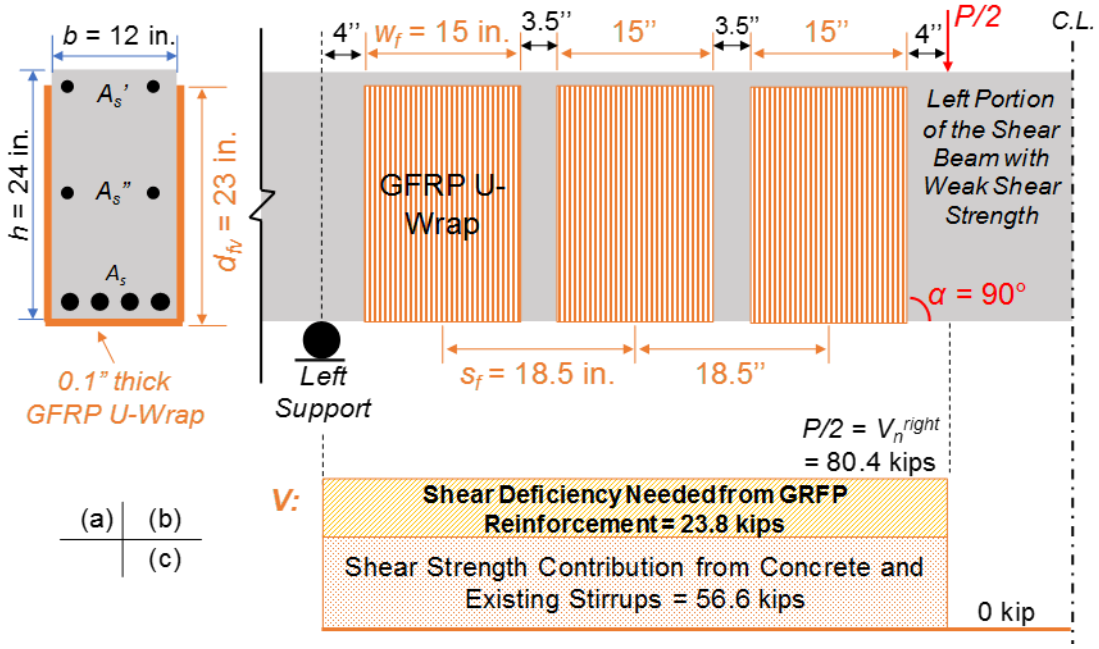

Figure 5.10: Illustration showing (a) the cross-sectional view of the FRP-reinforced shear beam, (b) configuration of the planned GFRP U-wraps, and (c) shear diagram presenting demand versus existing strength.

To quantify the added shear strength from GFRP and to further validate the effectiveness of the aforementioned strengthening scheme, the effective strain level in the GFRP layer needs to be estimated first using Equation 5.19. In correspondence with the 3-sided U-warp, the failure mode is dominated by the bond strength between FRP and concrete. Thus, a reduction coefficient (K_v) must be considered.

$$\varepsilon_{fe} = K_v \varepsilon_{fu} \leq 0.004 \quad \text{ACI 440.2R-08 (11-6b)} \tag{5.19}$$

where K_v is calculated based on the concrete strength, the wrapping scheme, and the stiffness of FRP, as denoted in Equation 5.20 below.

$$K_v = \frac{k_1 k_2 L_e}{468\varepsilon_{fu}} \leq 0.75 \quad \text{ACI 440.2R-08 (11-7)} \tag{5.20}$$

where k_1 and k_2 are the bond-reduction coefficients relating to the concrete strength and wrapping type, respectively. These two factors are computed using Equations 5.21 and 5.22.

$$k_1 = \left(\frac{f_c'}{4000}\right)^{2/3} \quad \text{ACI 440.2R-08 (11-9)} \tag{5.21}$$

$$k_2 = \frac{d_{fv} - L_e}{d_{fv}} \text{ for U-wraps} \quad \text{ACI 440.2R-08 (11-10)} \tag{5.22}$$

where L_e (in.) is the active bond length over which the majority of the bond is maintained per Article 11.4.1.2 and given as:

$$L_e = \frac{2500}{(nt_f E_{frp})^{0.58}} \quad \text{ACI 440.2R-08 (11-8)} \tag{5.23}$$

For the 0.1-in. thick GFRP U-Wraps shown in Figure 5.10, the calculations of the above Equations 5.23 through 5.18 produce L_e = 1.07 in., k_2 = 0.953, k_1 = 1, K_v = 0.109 (≤0.75), ε_{fe} = 0.0022 (≤0.004), and f_{fe} = 14.2 ksi, respectively. Finally, the shear strength contribution from the provided FRR is computed from Equation 5.16 as V_{frp} = 53 kips.

Therefore, the nominal shear strength of the GFRP U-wrap-based strengthening scheme for the left portion of the shear beam is obtained as 101.7 kips per Equation 5.15, which represents an approximately 80% enhancement in shear strength of the original shear beam (see Figure 5.2). Moreover, the strengthened side is now 26% stronger than the beam's right side (i.e., 80.4 kips). This improved shear strength can now sustain a point load of 203.4 kips under the four-point bending condition (see Figure 5.2), which is approximately 25% higher than the load capacity corresponding to its nominal flexural strength (i.e., 161.8 kips as determined in Section 5.2.1.2), most likely avoiding the occurrence of shear failure as originally expected. In short, the GFRP U-wrapping method detailed in Figure 5.8 is anticipated to rehabilitate the deficiency in shear strength of the weak side of the shear beam to make this beam section with nearly balanced shear load carrying capacity from its left to right side.

5.2.3 Manufacturing of Hybrid Composite Systems

As previously demonstrated, the flexure beam was strengthened with a 166 in. long, 12 in. wide, and 0.2 in. thick unidirectional GFRP patch (see Figure 5.9) for flexural enhancement; meanwhile, the weak portion of the shear beam was rehabilitated with three 0.1 in. thick and 15 in. wide GFRP U-wraps (see Figure 5.10) for strengthening its shear capacity. Particularly, nonstructural CNT-based nonwoven sensing sheets (established in Section 2.2.1 of Chapter 2) are integrated within the FRP strengthening composites at the bond interface for a comprehensive SHM of both the concrete beam and the deployed FRP composites. For the first time, this demonstrates a large-scale smart hybrid composite system for simultaneous structural rehabilitation and health monitoring of concrete structures. To experimentally

accomplish this novel idea, the vacuum-assisted resin transfer molding (VARTM) technique was implemented directly on the beams in this study to manufacture the hybrid composite systems.

5.2.3.1 Fabrication of the CNT-Based Sensing Sheets

Prior to applying the FRP strengthening scheme, the sensing strategy for SHM was developed. Owing to the excellent scalability and simplicity in process, the proposed CNT-based nonwoven sensing technique (as established in Section 2.2) allows mass fabrication of large area strain/damage sensors. For this study, the sensing sheets were customized individually and fabricated on-site for the two concrete beams.

The 34 g/m^2 aramid nonwoven fabric was selected as the nanotube carrier and trimmed into the appropriate size based on the dimensions of the used GFRP composites. Figure 5.11a and 5.11b present the raw nonwoven fabric carriers including the 11 in. wide and 160 in. long strip for the flexure beam and three 12 in. wide and 58 in. long strips for the shear beam, respectively. Next, nanotubes were coated onto the fabric following the solution casting method as presented in Section 2.2.1. In particular, two 500 mL masterbatches of CNT dispersions with nanotube loadings of 0.75 wt.% and 0.5 wt.% were prepared using a commercially available fiber sizing agent (See Section 2.2.1), in which the long and short nonwoven strips were first rolled up and correspondingly impregnated for 20 minutes in a plastic container as shown in Figure 5.11c. Later, the soaked fabric rolls were extended horizontally and dried in air for 24 hours. Figure 5.11d and 5.11e present the fabricated nonstructural large-scale sensing sheets. Finally, electrodes and lead wires were anchored on the sensing sheets to enable the electrical measurements. The multiplexing configuration is explained in Section 5.2.4.

(a)

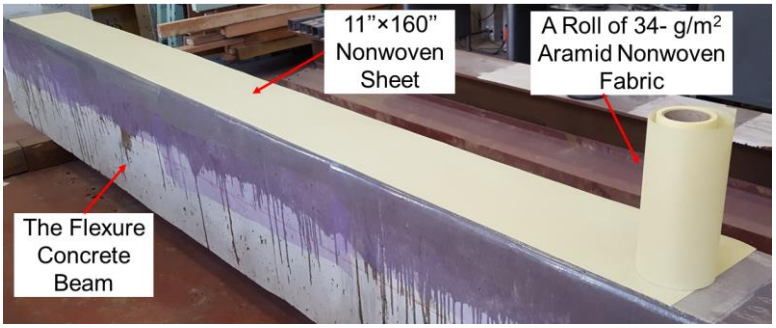

(b)

(c)

(d)

(e)

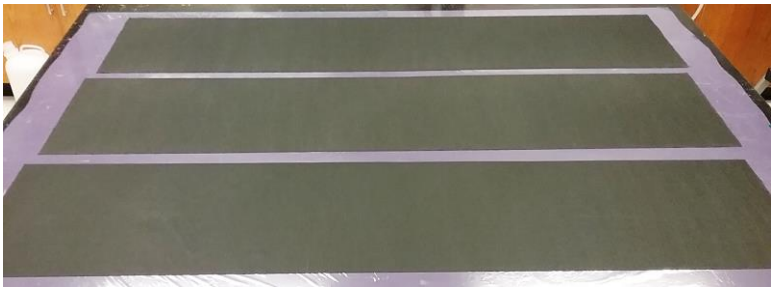

Figure 5.11: Photographs showing the fabrication process of CNT-based sensing sheets including the trimmed aramid nonwoven carrier fabrics for (a) flexure and (b) shear beam, (c) the dip-coating procedure, and (d-e) the fabricated sensing sheets for the current large-scale applications.

5.2.3.2 Manufacturing of Hybrid Composites

5.2.3.2.1 Preliminary Preparation

The application of the FRP repair scheme on the surface of the beams requires significant surface preparation and quality control of materials, plus attention to environmental factors such as temperature, humidity, and moisture. Prior to applying the composite retrofits, the concrete surface was prepared by mechanically abrading it with a high-speed electric grinder until the layer of 'milky-looking' laitance was removed [4], i.e., the coarse aggregates start to appear. Figure 5.12a and 5.12b show the appearance of the concrete beam surface before and after the mechanical grinding surface preparation. Additionally, the edges of the concrete beam were rounded and smoothed using the grinder. Next, high-pressure air-blasting was applied to the treated surface to remove any loose particles. In particular, inch-sized voids left on the side faces of the shear beam during concrete casting were filled with a high-strength putty material (BONDO® All Purpose Putty, 3M) and then sanded smoothly to create a uniform and solid surface for bonding FRP composites.

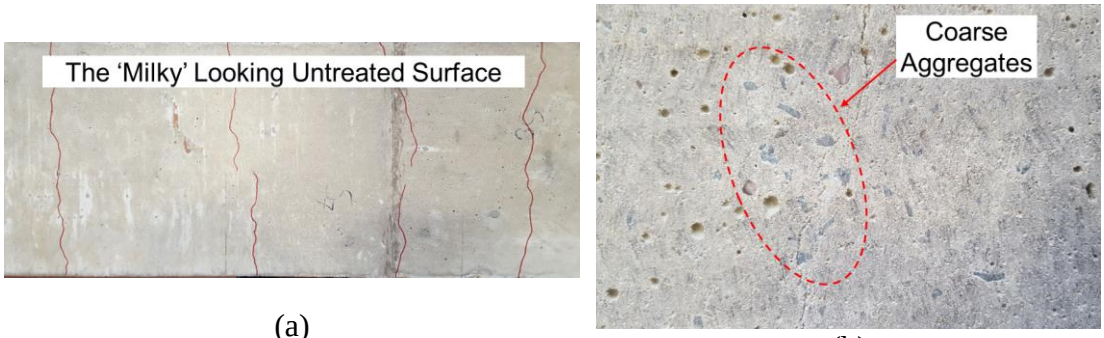

(a) (b)

Figure 5.12: Photographs showing the appearance of the concrete beam surface (a) before and (b) after mechanical grinding preparation.

A 100 ft-roll of 13 oz/yd^2 unidirectional fiberglass cloth supplied by Jamestown Distributors (Bristol, RI, USA) was used as the structural FRP fibers. The bulk cloth was trimmed into the proper fabric patches following the FRP design details as shown in Figures 5.9 and 5.10. Next, the CNT sensing sheets were placed on the concrete surface at the location of the FRP strengthening scheme. Subsequently, these fiberglass patches were laid up on top of the sensing sheets. 12 layers of fiberglass cloth were stacked on the flexure beam and three U-wraps formed with 6 layers of fabric were distributed along the longitudinal direction of the shear beam. Figure 5.13a and 5.13b illustrate the fabric preform finished on the flexure and shear beam, respectively. It can be observed that the CNT-based sensing sheets are fully covered by the structural fabric, which additionally offers the favorable protection to the sensing networks from environment.

It is also noted from Figure 5.13b that two supplemental layers of unidirectional fiberglass cloth were placed perpendicularly to the fiber direction of the U-wrap at the soffit (shown as the top in Figure 5.13b after flipping over during fabrication), to add additional stiffness to the soffit of the U-wrap in the longitudinal beam direction. In this way, the local transverse deformation (i.e., the matrix deformation perpendicular to the unidirectional fibers) developed over the bottom region of the U-warp under bending could be restrained, consequently reducing the occurrence of matrix splitting at high-level loads.

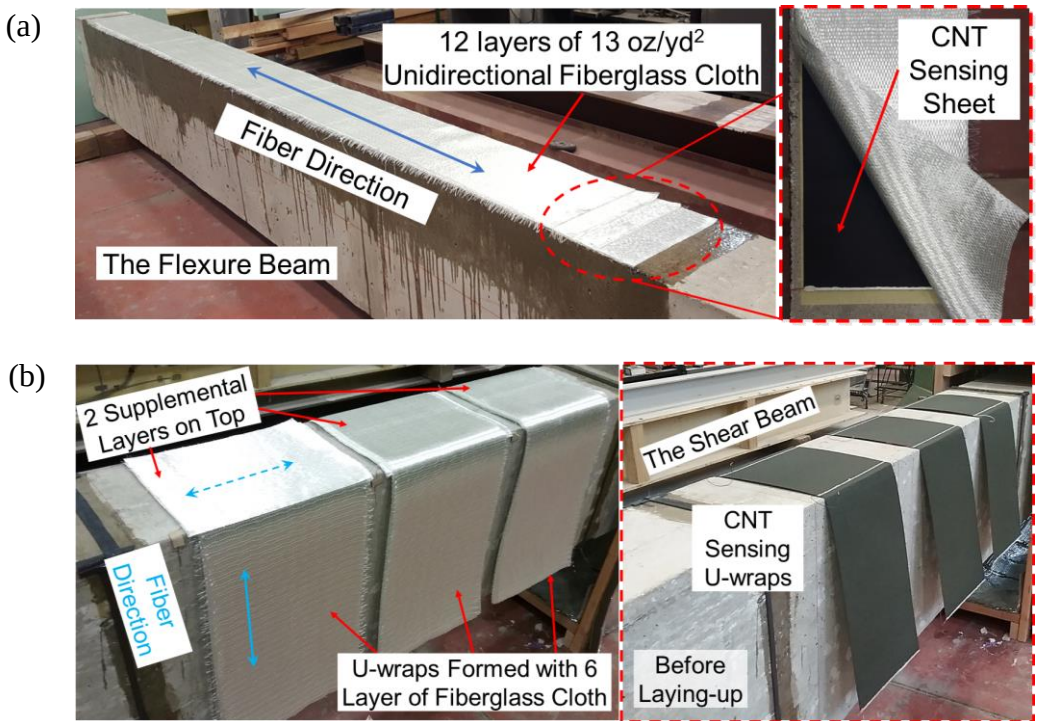

Figure 5.13: Photographs showing the unidirectional glass fabric preform on (a) the flexure as a continuous patch and (b) shear beam in form of three U-wraps. (Note: both concrete beam specimens were flipped over prior to laying up the glass fabrics.)

5.2.3.2.2 On-Site Manufacturing Process

To attain high quality hybrid composite parts, the vacuum-assisted resin transfer molding (VARTM) technique was utilized to infuse the epoxy resin into the glass fabric preforms directly onto the beam. Compared to the conventional wet layup approach, where dry fiber reinforcement is manually impregnated with a resin matrix layer by layer, VARTM utilizes vacuum pressure to draw the resin into the fiber preform and simultaneously impregnate numerous layers. When cured in-place on the beam the composite forms a bond on surfaces of the structure. Therefore, the VARTM process enables high efficiency of application, uniform distribution of resin to the fiber reinforcement, and intimate contact (i.e., the improved bond) between the FRP composites and the application surfaces.

In addition, common issues associated with a hand lay-up process including intensive labor, human application errors, and high waste factor [7,38,39], can be significantly minimized in the semi-automated VARTM process. Due to the vacuum pressure-based consolidation, the composite parts fabricated via VARTM normally possess relatively high fiber volumes of 55 to 65% and a low void content of less than 1% [40], whereas wet lay-up FRP composites have low fiber volumes of 25 to 40% per ACI 440.2R-08 guideline [25]. Therefore, from the perspective of design, less FRP fiber materials are needed to provide additional strength making this approach more cost-effective. Although the VARTM technique has been implemented to produce fiber composites in aerospace and automotive industries for decades, this approach has not been widely adopted in the field of civil engineering [5]. It is believed that with ongoing research and applications of FRP-based structural rehabilitation, applications of VARTM will increase compared to hand lay-up and eventually become a mainstream field technique.

Pilot studies of using VARTM for strengthening of concrete structures have been reported since 2004. Among others, Uddin *et al*. [41] first introduced VARTM process for concrete bridge girder strengthening. For laboratory demonstrations, they initially studied the bond strength between the carbon fiber composite coupons and concrete surface based on in-plane shear test. Particularly, the bonding interface developed using VARTM showed slightly higher interfacial strength than using hand lay-up. Next, they covered the entire soffit of a 6 in. × 12 in. × 72 in. concrete beam with a continuous U-wrap for both flexure and shear reinforcement. This U-wrap consisting of one single ply of carbon fiber/epoxy resin composite was fabricated and simultaneously attached on the concrete surface via on-site VARTM process. This beam showed end debonding at U-wrap bottom due to flexure failure. Both laboratory experiments demonstrated the feasibility of using VARTM approach for bonding and strengthening concrete members with FRP composites.

Finally, they implemented the VARTM process in the field for repairing a 63-in. tall pre-cracked reinforced concrete T-bulb bridge girder located on I-565 highway in Huntsville, Alabama. The strengthening scheme involved a three-sided wrap of four CRFP cross-plies in an area of 60 in. × 157 in. To conform the complex shape of the structure, multiple vacuum and infusion lines were placed in the VARTM setup and total filling time took about one hour. Notably, this entire project was completed within two days without causing any traffic interruption.

Recently, Ramos *et al*. [42] applied the VARTM process to fabricate FRR U-wraps on twelve 6 in. × 11 in. × 36 in. concrete beams. In particular, a series of vertically align 1/8 in. deep grooves in width of 1/8 in. and 1/4 in. were cut on the concrete surfaces of eight specimens to study the influence of grooving surface on

resin infusion time. For the 24 in. × 33 in. wrapping area, the resin infusion time on the grooved surface was significantly shortened to 22% of that on the smooth concrete surface, suggesting a useful method for further improving the efficiency of VARTM process for concrete strengthening applications.

In this research, the VARTM process was implemented to integrate the CNT-based sensing sheets with the structural glass reinforcement on the concrete member of interest within a single procedure to produce a hybrid composite with consistent mechanical properties and uniform bonding over the concrete surface. A typical VARTM configuration is shown in Figure 2.3a of Chapter 2. For these large-scale applications, VARTM was set up on-site by using two portable vacuum pumps and the essential materials as shown in Figure 5.14.

For the flexure beam, one continuous infusion line using the spiral tube was placed longitudinally along the centerline of the fabric preform and two vacuuming vents were located at the edges with two 3 in. wide strips of breather fabric bridging over to the part on the peel ply. Since this concrete beam was precracked, in order to prevent air leakage from the existing cracks, the two side faces of the beam were also fully bagged and vacuum applied with the second pump. Figure 5.15a shows the VARTM setup applied on the flexure beam at the state of full vacuum. The enlarged view of the secondary vacuum bag is shown in Figure 5.15b.

For the shear beam, the three U-wraps were infused within one process, then the entire left portion of the beam was bagged as shown in Figure 5.16. To create an effective vacuuming environment for all three U-wraps, a 4 in. wide breather fabric strip was placed over the spacing between them. The infusion line was located continuously along the centerline of the top face and two vacuuming outlets were

placed at the bottom (see Figure 5.16 inset). In both applications, a distribution mesh was used and placed on top of the peel ply. This distribution mesh only partially covers surface of the fabric preform, in order to promote resin infusion in the through-thickness direction, which however, extends the total infusion time.

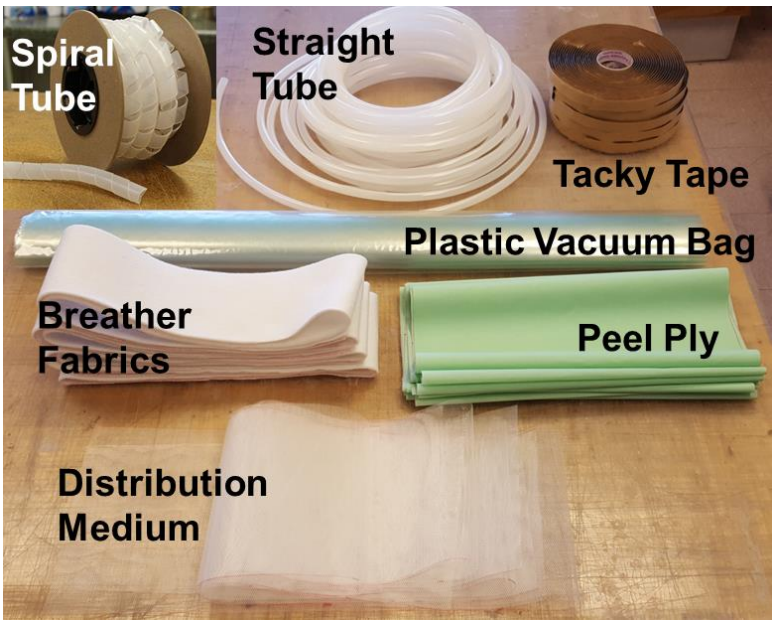

Figure 5.14: Photograph showing the essential materials for VARTM setup.

(a)

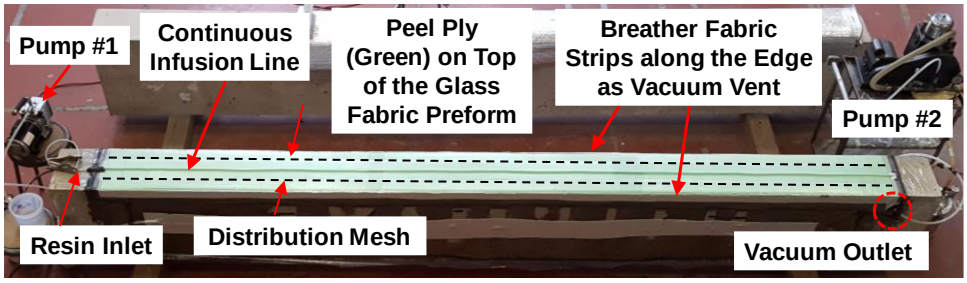

(b)

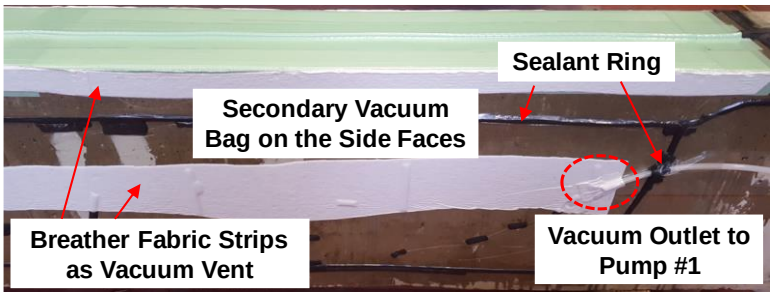

Figure 5.15: Photographs showing (a) the VARTM setup constructed on the flexure concrete beam at the state of full vacuum, and (b) an enlarged view of the secondary vacuum bag on the side face for preventing air leakage from the existing cracks.

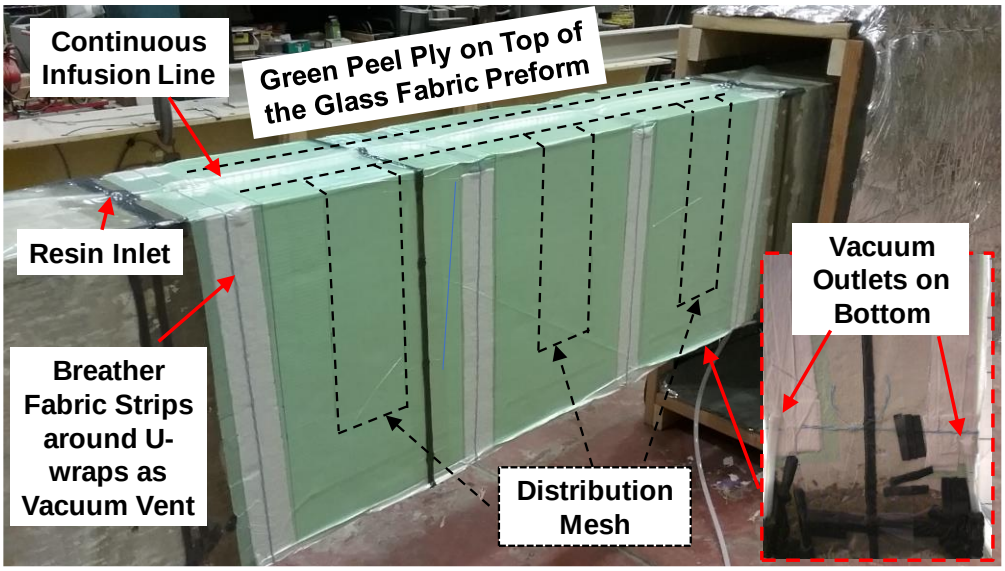

Figure 5.16: Photograph showing the VARTM setup built on the shear concrete beam. Inset image showing the bottom of the specimen.

After maintaining full vacuum (-30 inHg) in the whole VARTM arrangement for 30 minutes, a low viscosity epoxy resin (EPON 862) was mixed with EPIKURE 3230 curing agent at the mass ratio of 100 : 35.5 and infused into the mold. It took 10 minutes for the resin to fully fill the fabric preform on the flexure beam, which was indicated by saturation of the breather fabric strips along the edges (see Figure 5.17a). For the U-wraps on the shear beam, the infusion took about one hour due to its complex shape. Figure 5.17b shows the resin front appearing in the U-wrap fabric preform during the infusion process, which is in a symmetrical shape, indicating the consistent pressure in the mold.

After complete infusion was achieved, both parts were kept under vacuum during the cure cycle. Customized thermal tents were built on-site with aluminum foil insulation sheets in order to cover the wet parts and meet the required curing temperature of 75 °C with the assistance of using two heat guns and multiple heating lamps. Figure 5.18 shows the experimental setup during curing. After completing the two-hour 75 °C curing cycle, the specimens were debagged and followed with a one-hour post-curing cycle at 80 °C. Figure 5.19 shows the appearance of the final product. There are no dry spots or voids observed, indicating the high quality of the fabricated hybrid composite.

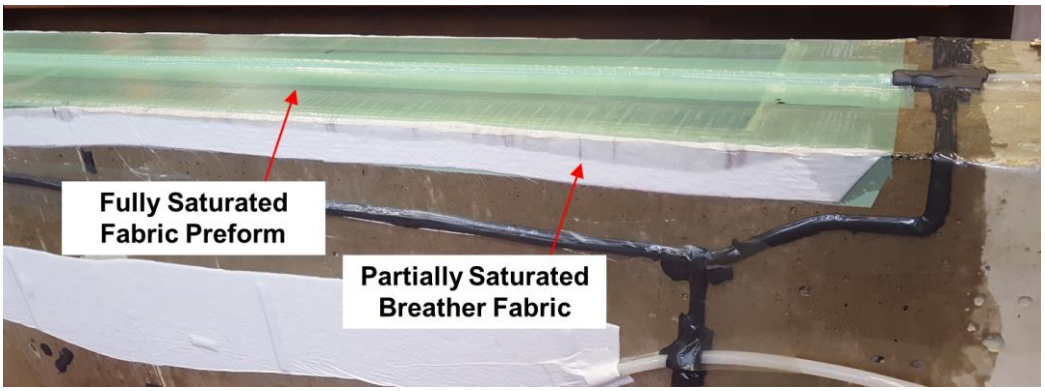

(a)

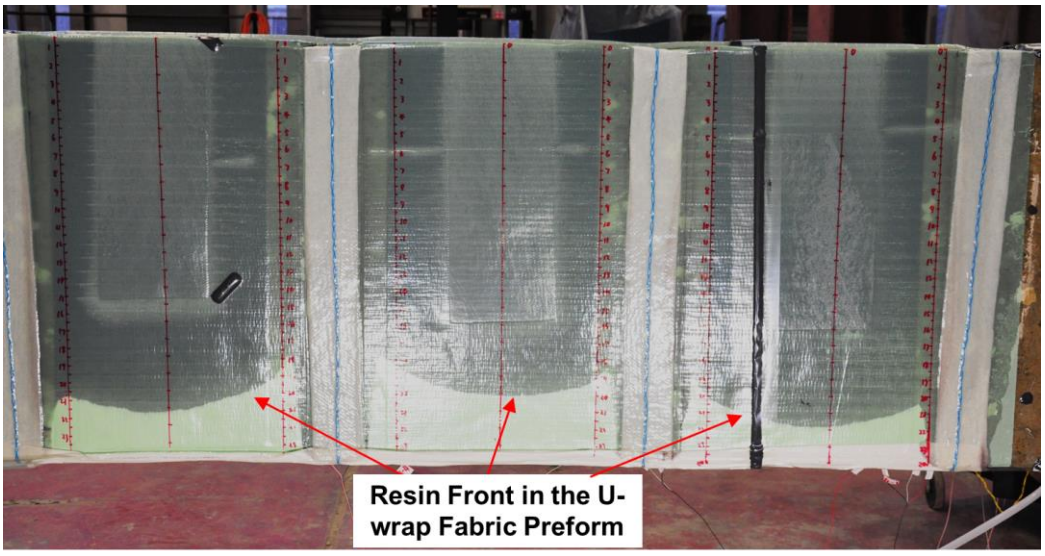

(b)

Figure 5.17: Snapshots showing the resin front in (a) the long part on the flexure beam and (b) the U-wraps on the shear beam during the infusion process.

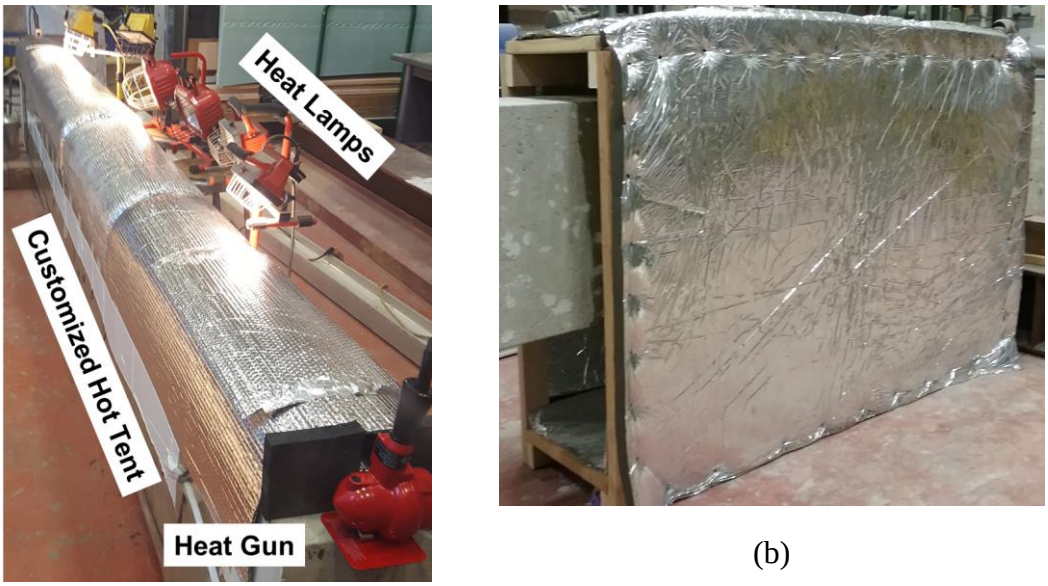

(a) (b)

Figure 5.18: Photographs showing (a) the experimental setup for curing the long composite part on the flexure beam and (b) the box hot tent built for curing the shear beam specimen.

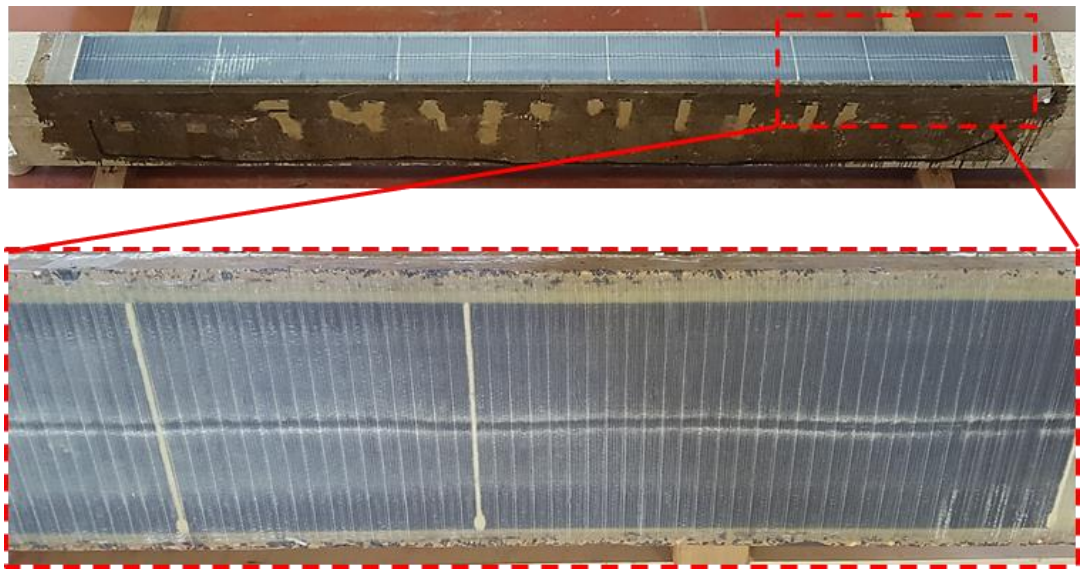

Figure 5.19: Photograph showing the finished hybrid composite specimen with a close-up view of the final composite, which is smooth and uniform in appearance, indicating the high quality.

Two supplemental 12 in. × 58 in. nonstructural CNT-based sensing sheets were added to the strong portion of the shear beam (i.e., the right side) in form of U-wraps to evaluate the sensing-only application. These two sensing U-wraps were placed at 16 in. and 37 in. from the beam centerline, respectively. Both were integrated on the concrete beam using the hand lay-up method. A room temperature curing epoxy resin (i.e., 100 parts of EPON 862 mixed with 12 parts of EPIKURE 3223 curing agent by weight) was used to saturate the sensing sheets. To remove excessive resin and air bubbles from the sensing sheets and to create a uniform and strong bond to the member, wet U-wraps were first covered with peel ply and breather fabric, then encapsulated with a vacuum bag, and cured under vacuum pressure for 24 hours. Figure 5.20 shows the finished specimen.

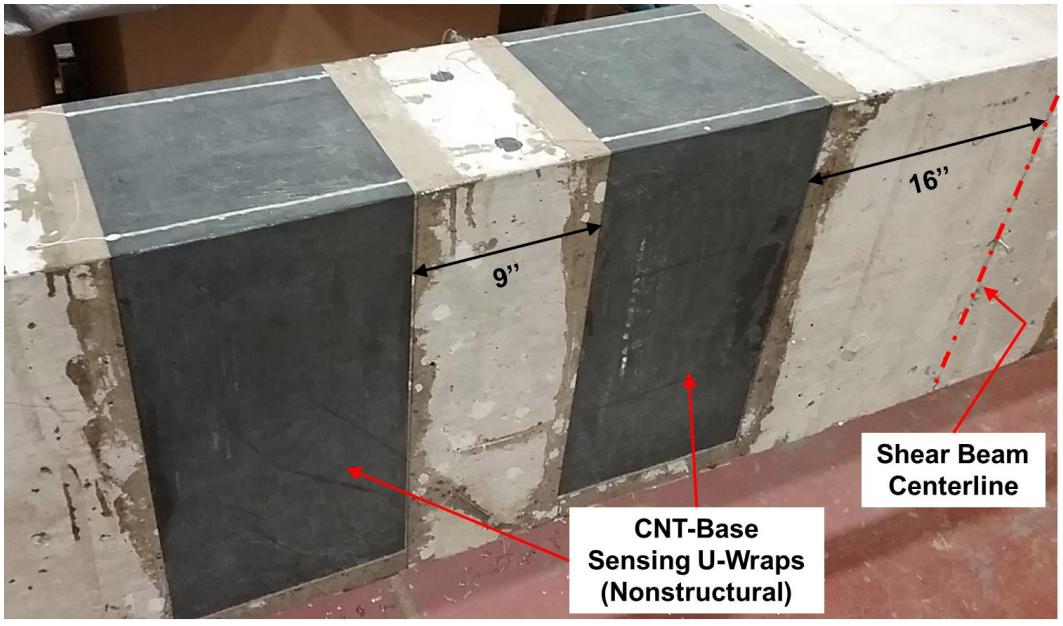

Figure 5.20: Photograph showing the nonstructural CNT-based sensing U-wraps attached in the strong side the shear beam for SHM.

5.2.4 Mechanical and Electrical Characterization

The aforementioned flexure and shear beam were tested under four-point bending conditions for mechanical characterization. The loads were applied using a 150-kip MTS hydraulic-driven actuator reacting against a 10 ft × 20 ft steel frame anchored to the laboratory strong floor. The concentrated load was distributed equally by a spreader beam to two points along the beams, generating a constant moment region at mid-span. The two-point loads were offset 12 in. from the mid-span of the beam. The simple span of the flexure and shear beam measured 174 in. and 144 in., respectively (see Figure 5.1 and 5.2). Two static loading scenarios including low frequency and low amplitude cyclic loading and a progressively increasing stepwise loading were applied to the beam specimens. The objectives were to demonstrate the structural enhancement of the hybrid composite system for the concrete beams as well as to evaluate the electrical behaviors of the integrated large-scale CNT-based sensors for SHM of both the concrete member and the strengthening FRP composites.

The cyclic loads were applied using a closed-loop system programmed to apply a sinusoidal load at a frequency of 0.2 Hz. Load stability with cycling was guaranteed by the servo valve controller. The load amplitude was varied for these two specimens based on their flexural capacities in order to generate representative deformations that are likely observed in an actual bridge due to normal daily traffic but at the same time are large enough to activate the embedded CNT-based sensors. The flexure and shear beams were subjected to 15,000 cycles of load oscillating from 15 to 5 kips and 35 to 15 kips, respectively.

After cyclic testing, both beams were slowly loaded and unloaded at the same rate of 5 kip/min. with progressively increasing peak loading until failure. Between each loading-unloading step, a short cyclic loading session, that is 500-cycle of the

previously defined cyclic loading protocol, was applied to both beams. In particular, before loading to failure, the flexure beam was loaded in a step-wise manner at 25, 30, 35, 45, 55, 65, 80, and 95 kips. Similarly, the shear beam was incrementally loaded with two 150-kip actuators to 45, 55, 65, 75, 85, 95, 115, and 140 kips.

Deflection measurements were taken at mid-span and both end supports (on both sides of the beam) using a total of six 0.5 in. linear potentiometers. The potentiometer measurements at the beam supports were used to subtract the deformation of the flexible bearing pads from the measurements at the mid-span to capture the actual deformation response of the beams. Additionally, a series of 350 Ω strain gages (Vishay Micro-Measurements) with 2-in. long gage lengths were bonded to the GFRP composites to determine their mechanical responses under the applied loads. Furthermore, a two-channel acoustic emission (AE) system (Physical Acoustics) was used to record acoustic events throughout the test. Two identical AE transducers (Physical Acoustics R6α, 100KHz) were mounted on the specimen (i.e., one on the GFRP composite surface, and the other one on the concrete surface) using a hot-melt adhesive. A threshold of 40 dB was set to filter-out low amplitude AE. The pencil lead break test was performed prior to applying load in order to confirm the reproducibility of the AE system. Three HD digital cameras were located around the concrete specimens to record from different angles during the entire loading protocols at a recording speed of 30 frames per second.

A multiplexing sensing scheme was used to collect the real-time SHM response of the hybrid composite systems. Specifically, the 160-in. long CNT-sensing sheet deployed on the flexure beam was divided into seven sensing sections by anchoring six intermediate electrodes over the sensing sheet between the two end

electrodes. Similarly, each sensing U-wrap applied on the shear beam was divided into three sensing sections including the front, back, and bottom, finally adding up to 15 sensing channels from the five sensing U-wraps. The *in-situ* resistive response of the embedded CNT-based sensing sheets were measured with the Keithley 3706A System Switch/Multimeter following a two-probe current-voltage measurement configuration, which was controlled by a customized LabVIEW program. Based on the resistance of the connected sensing channel, the input direct current provided by the 3706A meter varied from 10 mA to 10 µA and the resulting voltage was instantly measured and converted to resistance based on Ohm's law.

Figure 5.21 and 5.22 shows the experimental setup configured for the flexure beam and shear beam, respectively. Table 5.6 presents the baseline resistances and resistivities measured from each individual channel of the CNT based sensing sheets.

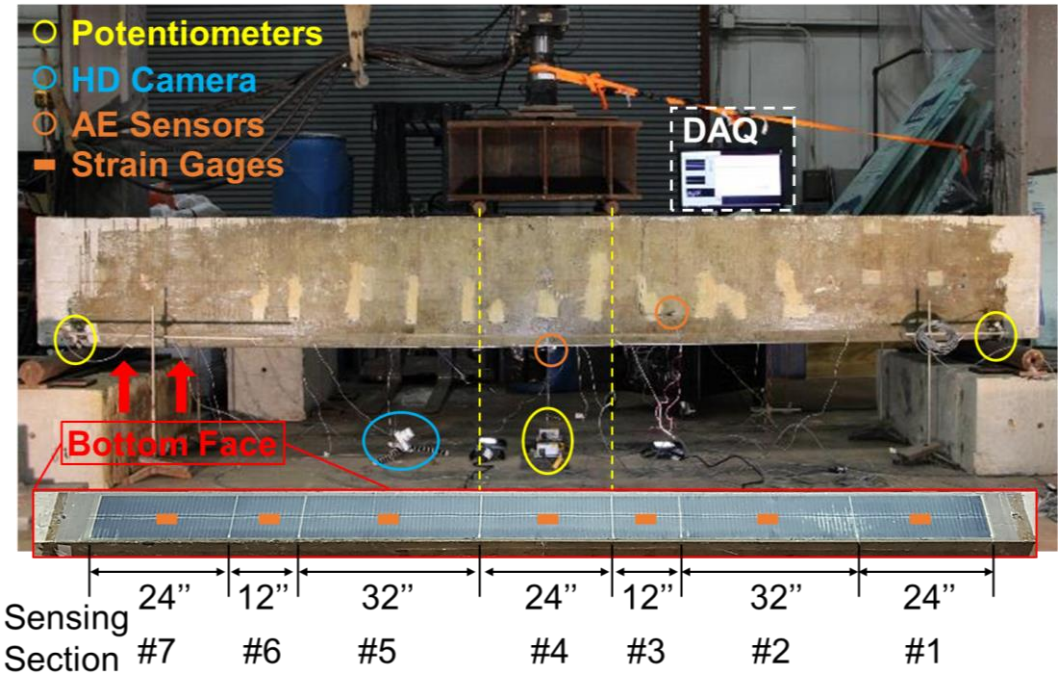

Figure 5.21: Instrumentation of the flexure beam specimen.

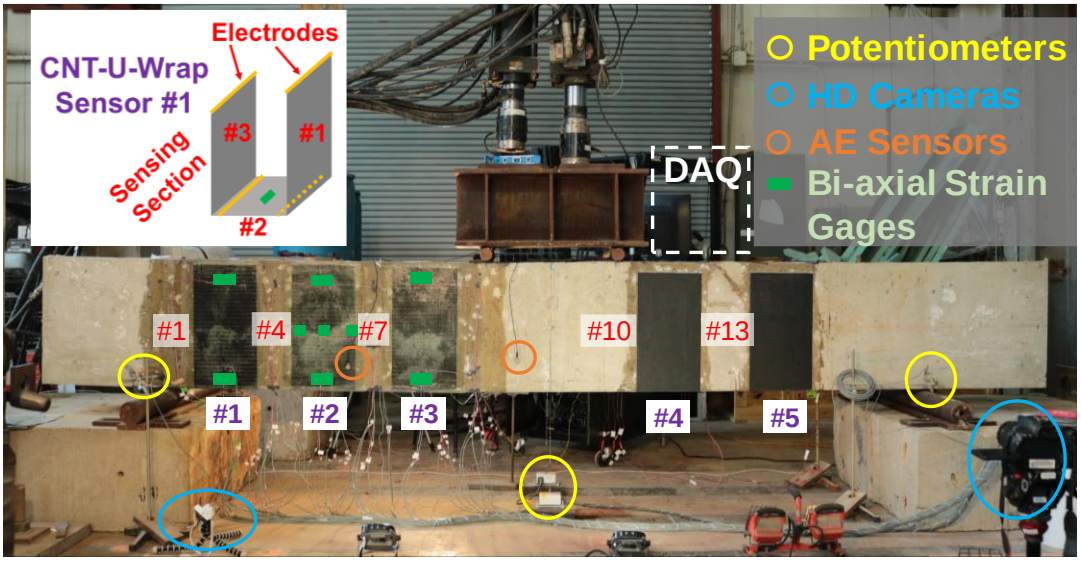

Figure 5.22: Instrumentation of the shear beam specimen. Note: (1) **U-wrap #4** and **#5** are nonstructural CNT-based sensors for SHM only; (2) **sensing sections #2**, **5**, **8**, **11**, and **#14** are on the soffit; (3) **sensing sections #3**, **6**, and **#9** are on the backside and 2 in. shorter than the front ones; (4) **strain gages** on the back face are symmetric to the arrangement of gages on the front face.

Table 5.6: Baseline Resistance (R_0), Resistivity (ρ_0) of the Multiplexed CNT-Based Sensing Sheets for SHM of the Flexure (F) and Shear (S) Concrete Beam.

Sensing Section	Processing Parameters	R_0 (Ω)	ρ_0 (Ω·m)	Sensing Section	Processing Parameters	R_0 (Ω)	ρ_0 (Ω·m)
F-#1	34 g/m^2-aramid-carriers, 1.0 wt.% CNT, VARTM, cured @ 75°C	2257	0.517	S-#5	*(continued)* VARTM, cured @ 75°C	3212	1.927
F-#2		3314	0.569	S-#6		8720	2.378
F-#3		1302	0.595	S-#7		10195	2.548
F-#4		2439	0.558	S-#8		3659	2.195
F-#5		3171	0.545	S-#9		9083	2.477
F-#6		1207	0.553	S-#10	50 g/m^2-aramid-carriers, 1.0 wt.% CNT, hand lay-up, cured @ 22°C	22699	5.675
F-#7		1868	0.428	S-#11		14236	8.542
S-#1	34 g/m^2-aramid-carriers, 0.75 wt.% CNT,	7894	1.973	S-#12		24658	6.164
S-#2		3217	1.930	S-#13		19530	4.882
S-#3		7047	1.922	S-#14		15364	9.218
S-#4		9152	2.288	S-#15		24532	6.133

5.3 Experimental Results

5.3.1 Mechanical Responses of GFRP Strengthened Concrete Beams

The mechanical effects of the low-amplitude repeated loading and the progressively increasing loading on the performance of the strengthened concrete beams were evaluated based on their force-displacement behaviors, crack growth, and measured strains during the applied loading protocols. The accumulation and extension of cracks observed in both GFRP composites and concrete beams during testing were monitored by visual inspection and acoustic emission sensors to characterize deterioration. The force-displacement responses of the strengthened beams following the stepwise increasing loading-unloading tests were compared with their original responses during the preloading tests (prior to the GFRP retrofit). These experimental observations and results on the GFRP-based flexural and shear strengthening of concrete beams are presented in the following sections.

5.3.1.1 Externally Bonded GFRP Patch for Flexural Strengthening

5.3.1.1.1 Service-Level Cyclic Loading

Figure 5.23a summarizes the overall transient response of the applied load and the recorded mid-span deflection of the flexure beam during the 15,000-cycle, 0.2 Hz cyclic testing. It is clear that a uniform and stable cyclic loading (5 to 15-kip in sinusoidal shape) was applied on the concrete beam and constantly maintained during the entire 22-hour protocol. On the other hand, the beam deflection showed a consistent trend with some variations observed during the first three-hour and last two-hour loading period. Figure 5.23b and 5.23c present the closer look at the beginning

and ending of the cyclic testing, respectively. As can be observed, the concrete beam responded linearly to the applied cyclic loading protocol.

A minor residual deflection of 0.008 in. was observed right after the beam was unloaded. The force-displacement relationship is illustrated in Figure 5.24. Overall, the concrete beam behaves linear-elastically under the applied cyclic loading without observing a loss of stiffness. The mid-span displacement responds uniformly between valley and peak loads at a constant difference of 0.035 in. It is also notable that a small amount of drifting deflection (about 0.012 in.) accumulates over the 15,000 loading cycles, which might be due to the gradual consolidation of the neoprene pads (see Figure 5.1) at the load supports. In addition, during the applied service-level cyclic loads, the flexure beam did not exhibit significant accumulation of damage, as indicated by the formation of new cracks or growth of existing cracks that are noticeable by visual inspection. In short, the flexure beam shows no significant structural change during the repeated loading, because of the improved performance of the applied GFRP patch.

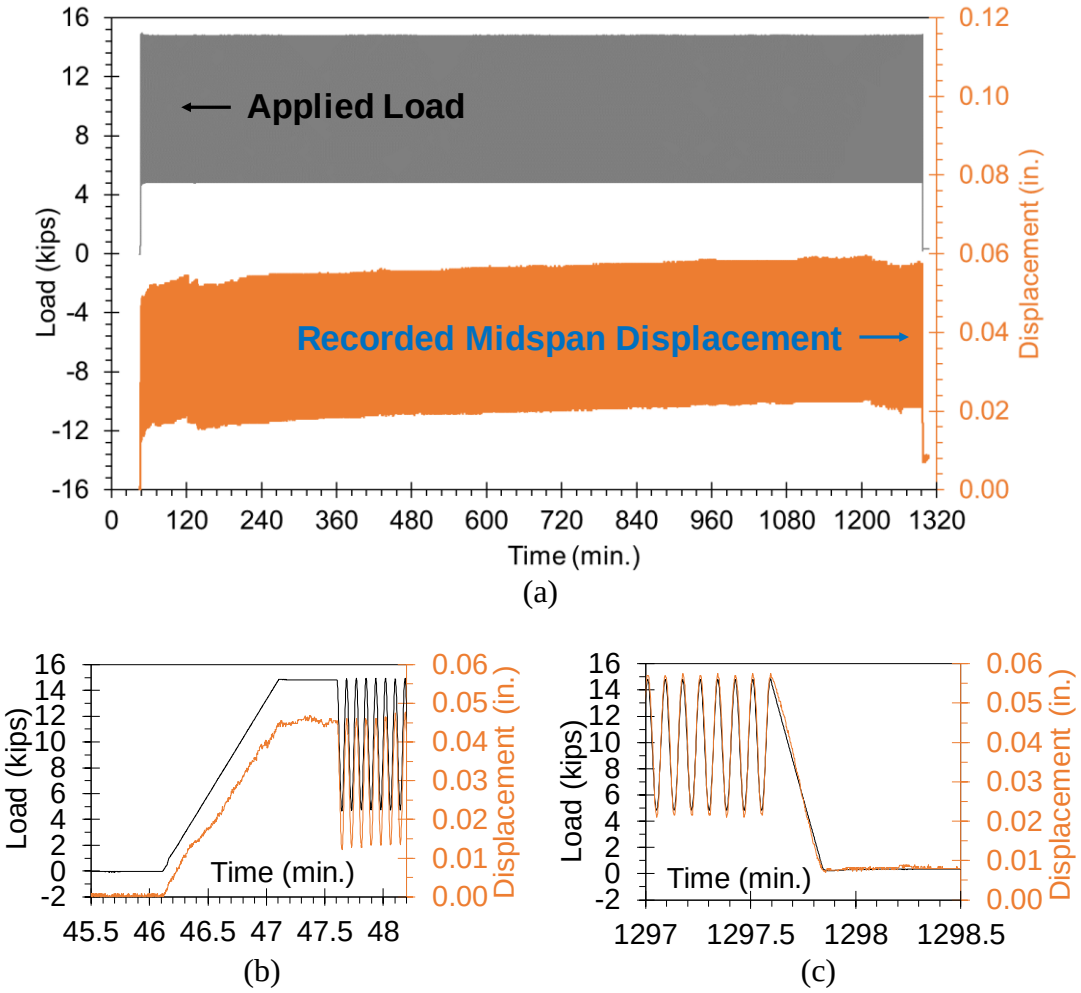

Figure 5.23: (a) Total responses of the applied load and the recorded mid-span displacement of the flexure beam during the 15,000-cycle, 0.2 Hz cyclic testing, and the close-up views showing the responses in (b) the first 5 cycles and (c) the last 5 cycles.

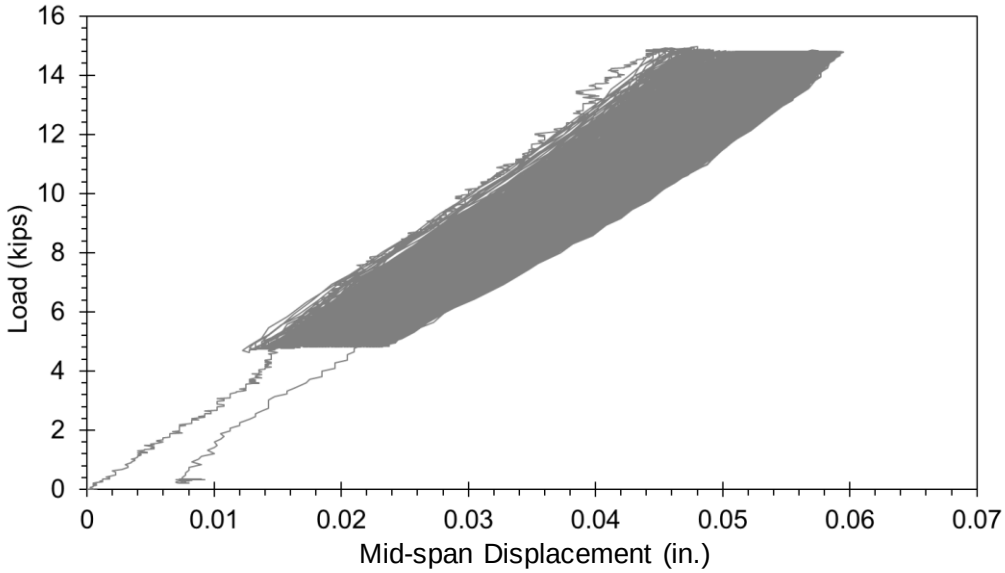

Figure 5.24: The load versus displacement response of the flexure beam during the cyclic testing phase (15,000 cycles).

The mechanical behavior of the attached GFRP patch during the repeated loading is represented by the strain responses from the seven distributed strain gages along the composite. Figure 5.25 shows the transient strains measured from three consecutive cycles at four time steps including Cycle-1-2-3, Cycle-5,000-5,001-5,002, Cycle-10,000-10,001-10,002, and Cycle-15,000-15,001-15,002. Similar to the beam deflection response (see Figure 5.23a), the strains on the composite patch became stabilized after approximately 2,000 cycles (that is, three hours after loading). For instance, the initial strains measured in the maximum moment region (i.e., the sensing section #4) reaches 240 and 85 microstrain (με) at the peak and valley loads, respectively. That is a 155- με difference between peaks. Afterwards, the range changes to the level of 355-155 με, corresponding to 200 με, for the rest of the cyclic testing. This reveals the evolution of large local strains in the GFRP composite

resulting from strain incompatibilities with the concrete substrate as the concrete develops cracks (see Figure 5.5). Similar strain relationships are also shown in sensing sections #3, #5 and #2 at reduced magnitudes. Additionally, in the low moment regions at a far distance from the loading points, such as sensing section #1 and #2, the highest strain is recorded as about 20 με.

The AE responses recorded from the two sensors are presented in Figure 5.26a and 5.26b. It is clear that a large number of AE hit counts are registered from both AE sensors during the initial stage of cyclic loading test, matching the three-hour variable period as previously mentioned. These phenomena correspond to the extension of the existing concrete cracks (see Figure 5.5) and are possibly exaggerated by the rapid growth and propagation of microcracks within the precracked concrete beam. This is shown by the high level of AE activity in Figure 5.26a. Afterwards, AE activity stabilized at a relatively low level, as the peak load remained unchanged at 15 kips. It can be observed that cumulative AE hits (solid lines) from the sensor located on the concrete are more than 35 times greater than that from the sensor located on the GFRP patch.

Additionally, the rate of AE activity shown as the slope of the cumulative AE hits curve remains nearly constant in the concrete beam shown in Figure 5.26a, but follows a ‘L-shape’ trend in GFRP composite presented in Figure 5.26b. In particular, the opening of an existing concrete crack can produce local debonding of the GFRP composite at the crack, causing the local strain incompatibilities and manifests itself with a large number of AE hits. Meanwhile, at the low service-level loading condition, local debonding is confined at a micro scale that is not noticeable by visual inspection and prevented from further propagation due to the strong interfacial bonding. Once the

nonvisible local debonding is fully stabilized under the repeated loads, opening of the existing crack under the same level of loading can avoid causing excessive AE hits, seen as the extremely low level of AE activity after 600 min. in Figure 5.26b. To conclude, the AE responses generally agree with the measured concrete beam deflection and the strain behavior of the GFRP composite patch and suggests a robust structural performance of the GFRP strengthened beam under the applied service-level cyclic loading.

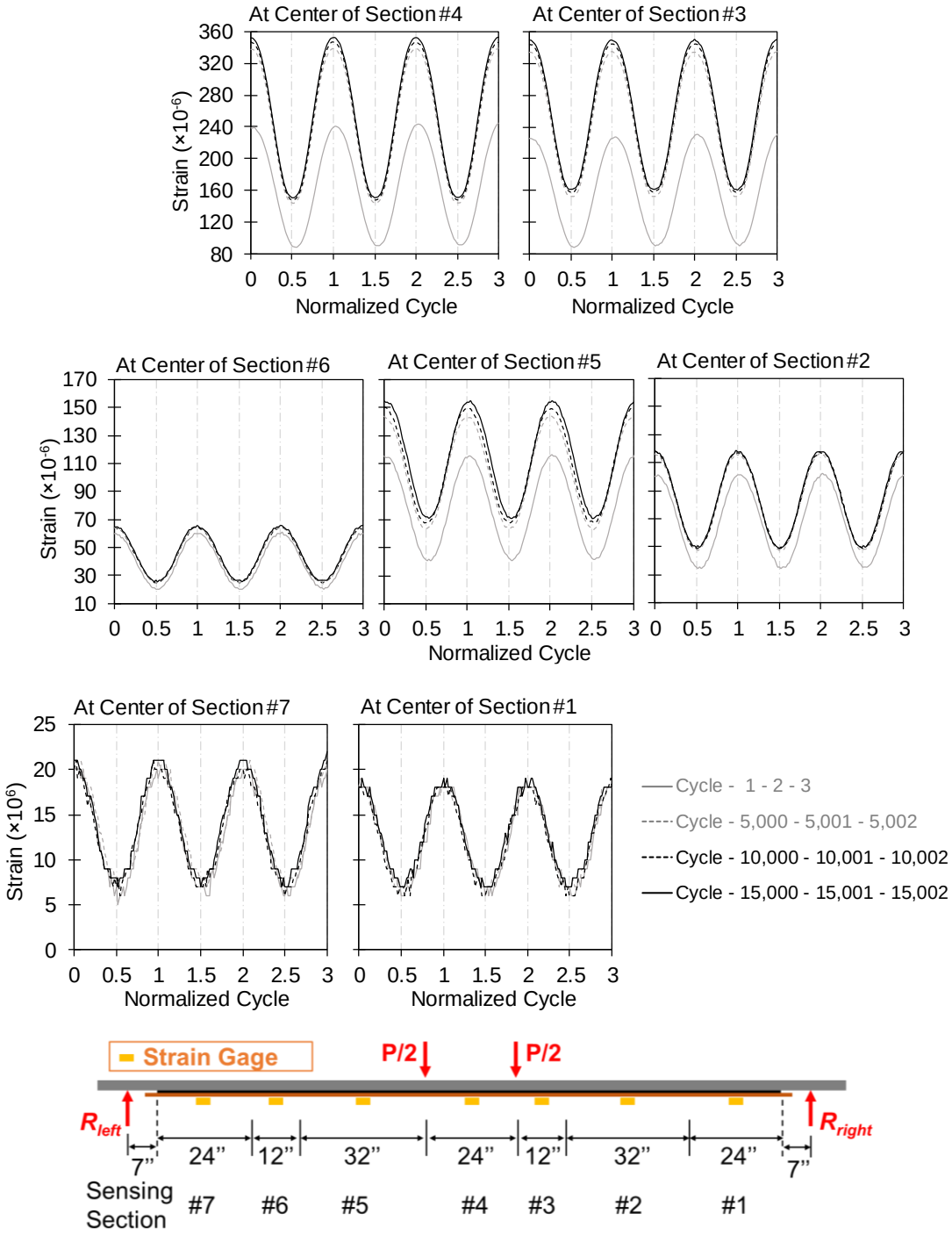

Figure 5.25: The distributed strain responses recorded along the GFRP composite (corresponding locations shown in the bottom inset) at the Cycle-1-2-3, Cycle-5,000-5,001-5,002, Cycle-10,000-10,001-10,002, and Cycle-15,000-15,001-15,002.

(a)

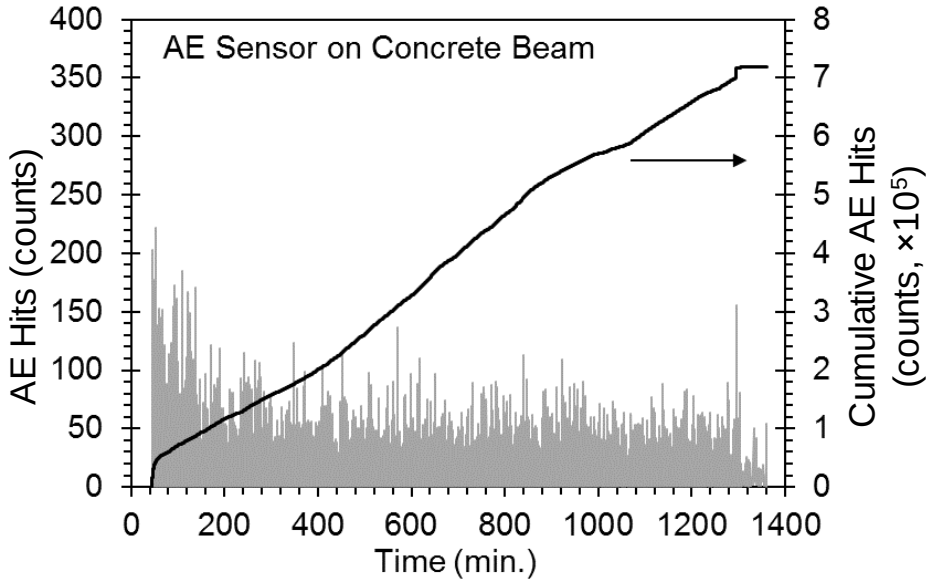

(b)

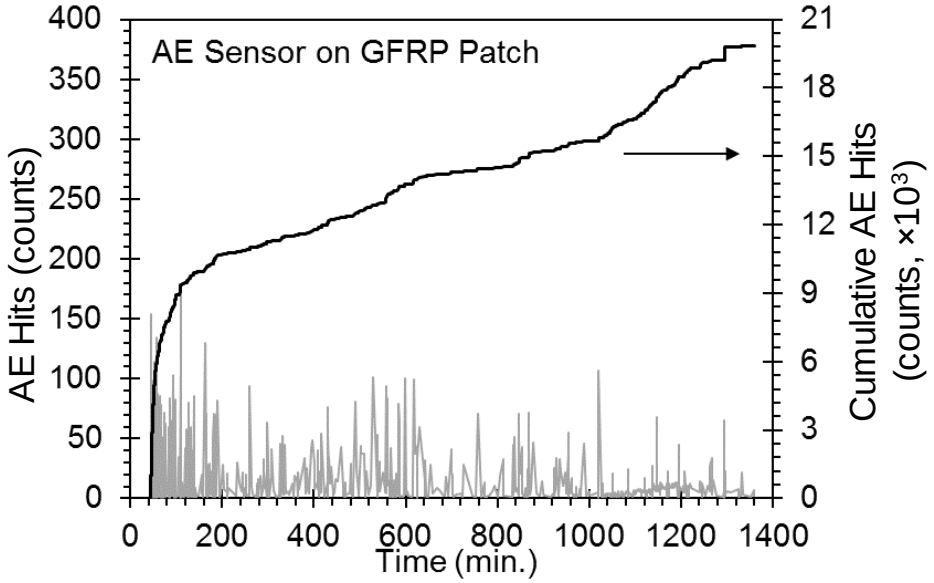

Figure 5.26: Real-time counts of AE hits and cumulative AE hits recorded from two sensors located at (a) the flexure concrete beam and (b) the GFRP patch during the 15,000-cycle repeated loading test.

5.3.1.1.2 Static Loading-Unloading Cycles up to Failure

The structural performance and flexural capacity of the GFRP strengthened concrete beam was evaluated under static loading conditions. A special loading protocol using a combination of stepwise and repeated loads was applied to the specimen in order to investigate its responses due to progressively accumulating damage at different levels of loading. Figure 5.27 shows the response of the flexure beam during the static eight-step loading-unloading cycles and the final failure cycle. Overall, the mid-span displacement closely follows the applied loading program. It can be observed that a residual deflection appears after the 65-kip cycle (Figure 5.27a), suggesting the initiation of the plastic deformation. This permanent change increases to 0.2 in. in the end of the 95-kip cycle, demonstrating the early stage of the ductile response.

In addition, seven 500-cycle repeated loadings were performed between the static loading steps. A general trend can be observed of an approximately 20% increase in the amplitude of deflection between the first session (before the step loading) and the last one (after the 95-kip cycle), indicating the reduced structural stiffness as the result of the accumulating loading history at high loads. Figure 5.27b shows the response of the beam in the last load cycle, where it was loaded to to failure. It can be found that the mid-span displacement shows an inflection point at 96 kips, after which the beam deforms in a faster rate, revealing yielding of the beam. The abrupt increase of mid-span displacement suggests the loss of member stiffness, indicating the failure of the strengthened concrete beam. Eventually, this specimen failed at the peak load of 115.2 kips at an ultimate mid-span deflection of 1.8 in.

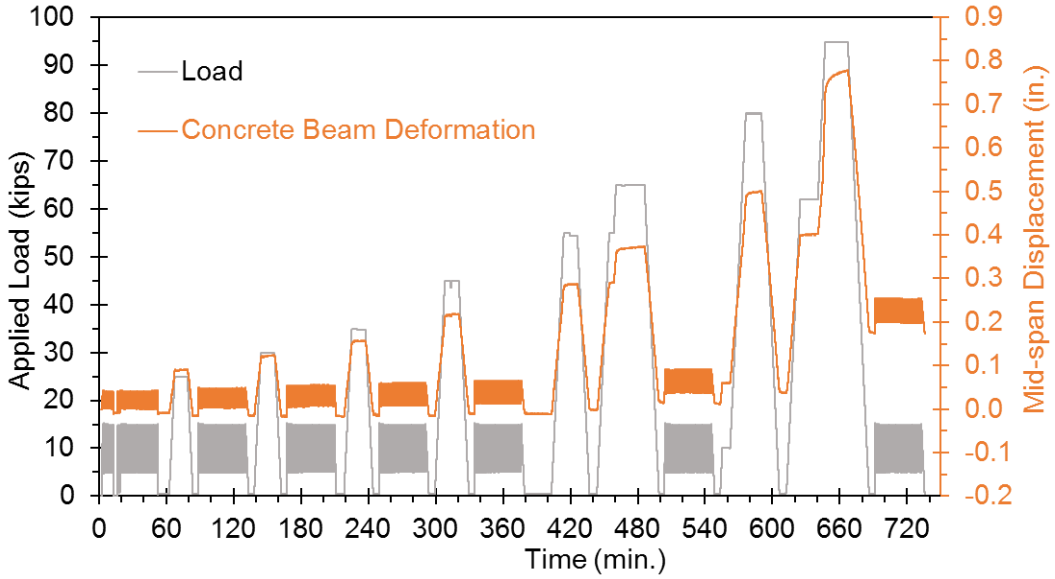

(a)

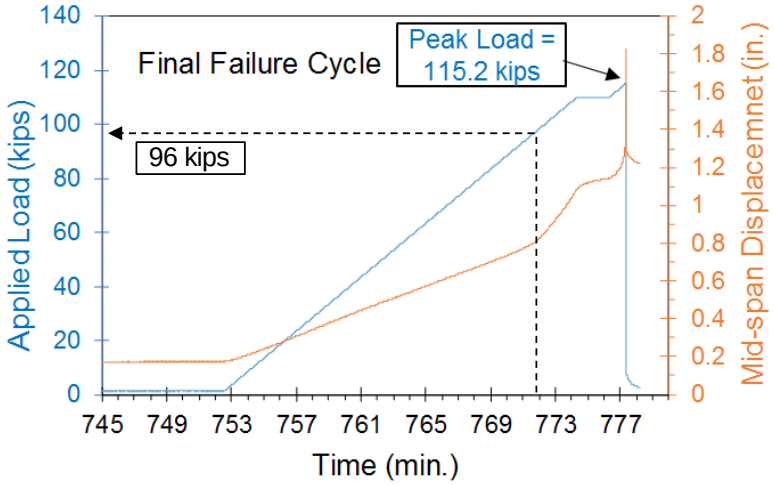

(b)

Figure 5.27: Applied load and the mid-span displacement of the flexure beam during (a) the static stepwise loading-unloading cycles and (b) the final load cycle.

Figure 5.28 illustrates the comparison on the force-displacement responses of the flexure beam before and after strengthening with the GFRP composite. It is obvious that the force-displacement relation of the strengthened beam is linear elastic and demonstrates a nearly 75% increase in member stiffness as compared to the original concrete beam, indicating the strong confining effect resulting from the GFRP retrofitting. It is also notable that the original beam exhibited a permanent residual deflection of about 0.03 in. and 0.05 in. after the 30-kip and 35-kip cycle, respectively. On the other hand, the strengthened beam does not show any accumulation of residual deflection in the end of 25-kip, 30-kip, and 35-kip cycle, revealing the improved serviceability of the beam due to GFRP retrofitting.

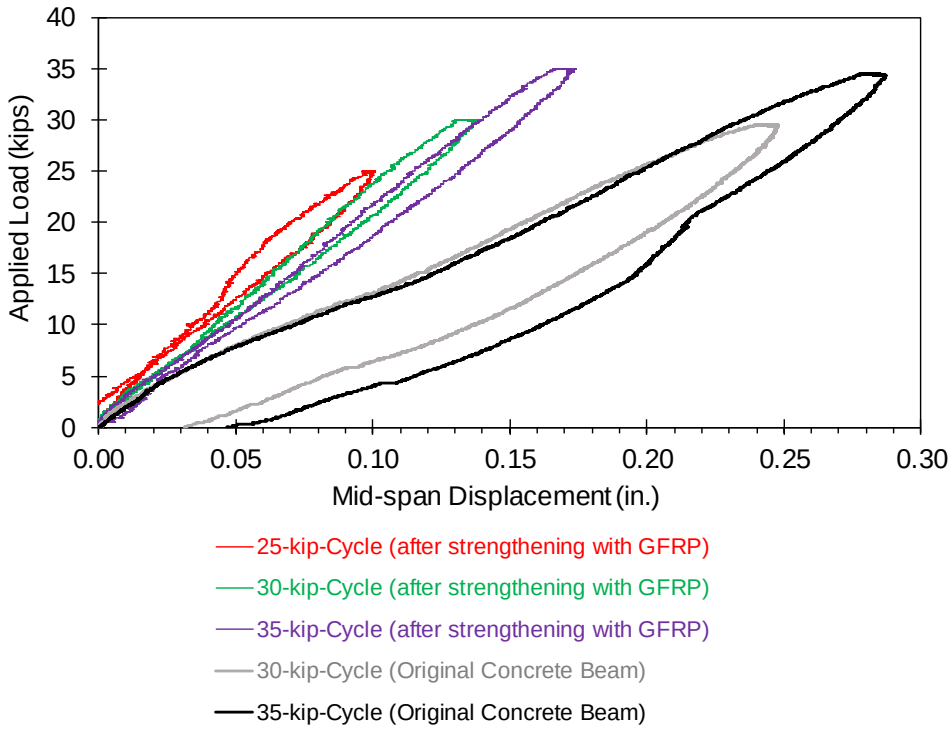

Figure 5.28: Load-displacement responses of the flexure beam before and after GFRP flexure strengthening.

Figure 5.29 summarizes the isolated force-displacement response of the strengthened flexure beam during the eight static load cycles and the final failure cycle, in which the noticeable loss in stiffness of the beam is first observed in the 65-kip cycle and then exaggerated in the 80-kip and 95-kip cycles. In particular, plastic deflection appears after loading above 85 kips, resulting in the pronounced increase of residual displacement of 0.14 in. after the 95-kip cycle. This behavior was likely caused by progressive accumulation of plastic strains in the steel reinforcement, extension of flexural cracks that opened during loading, local slippage of the reinforcing steel bars at the crack locations, and progressive debonding of the GFRP patch.

In the final cycle as the beam was loaded to failure, it displayed a tremendous amount of plastic deflection when the loading exceeded 96 kips, which then suddenly terminated at an extreme load of 115.2 kips when the beam failed. This ultimate load carrying capacity is approximately 44% greater than the nominal strength of the original beam (i.e., 80.2 kips, see Section 5.2.1.1) and 10% more than the ACI-440 design capacity of the GFRP strengthened beam (i.e., 102 kips, see Section 5.2.2.1), revealing the validity and effectiveness of the deployed flexural strengthening strategy for this beam. In addition, the linear elastic force-displacement response of the strengthened beam is maintained up to 85 kips, which is slightly higher than the flexural capacity of the original concrete beam (i.e., 80.2 kips, see Section 5.2.1.1), indicating the significantly improved serviceability after the structural rehabilitation.

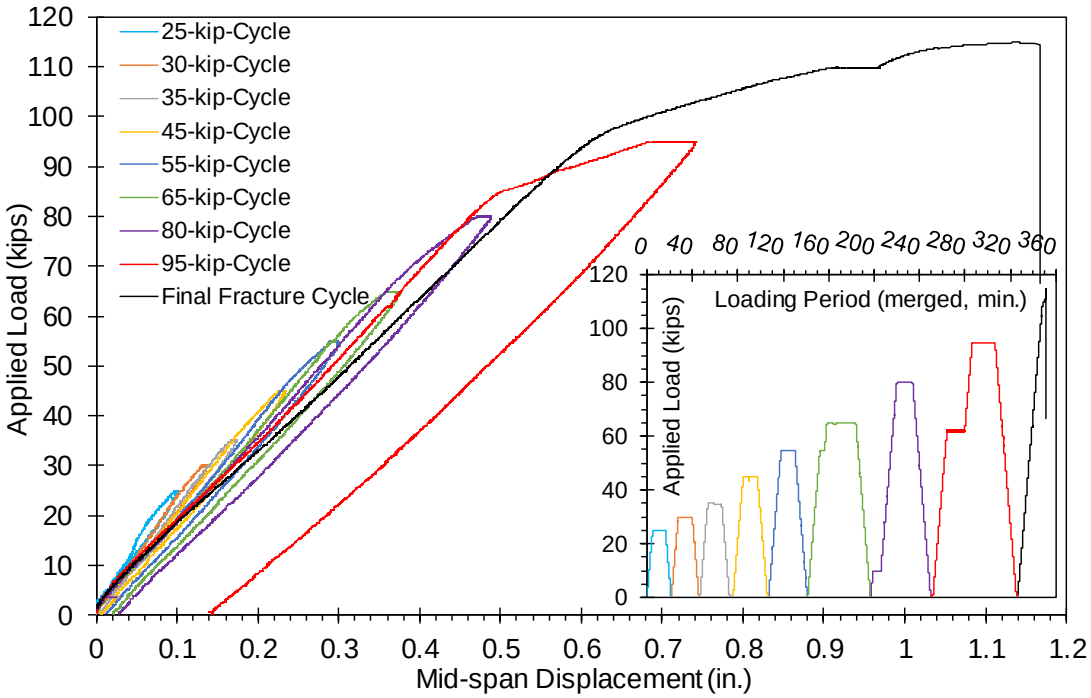

Figure 5.29: Total load-displacement responses of the GFRP patch strengthened flexure beam under the applied stepwise loading cycles (inset).

Figure 5.30 shows the strain distribution in the GFRP composite along the longitudinal axis at different levels of loading. It can be observed that the highest strain is always observed in the maximum moment region (i.e., in the central loading span) and the distribution of strains follows a quasi-parabolic fashion with strains to be nearly zero at the two ends of composite layer. In addition, the measured strains corresponding to the first six loading cycles (up to 65 kips) are less than 2000 με and their distributions are comparable in shape. Based on strain compatibility between the concrete substrate and the composite, it can be deduced that the strains in the reinforcing steel bars are also less than 2000 με, that is, lower than the yield strain limit of the used Grade 60 bars, enabling the elastic behavior as previously

demonstrated by the force-displacement responses. In addition, as the applied loads further increase, the strain distribution in the GFRP composite becomes irregular and shows large variations along the longitudinal axis, with strain values in the central region increasing significantly more rapidly than the rest of the beam. For instance, the 95-kip cycle causes a high strain level of 3600-4700 με in the central 4-ft-zone, which inevitably induce the accumulation of plastic strains in the steel bars, leading to the plastic response of the beam. At 114 kips, strains along the 80% test span are higher than the yield strain of the steel bars (i.e., 2100 με) and display a considerably higher strain level of 5500-7100 με in the central region, suggesting the imminent failure of the beam that promptly occurred at 115.2 kips. To conclude, the strain distribution in the GFRP composite clearly demonstrates the transition from elastic to plastic behavior of the beam as the applied load increases.

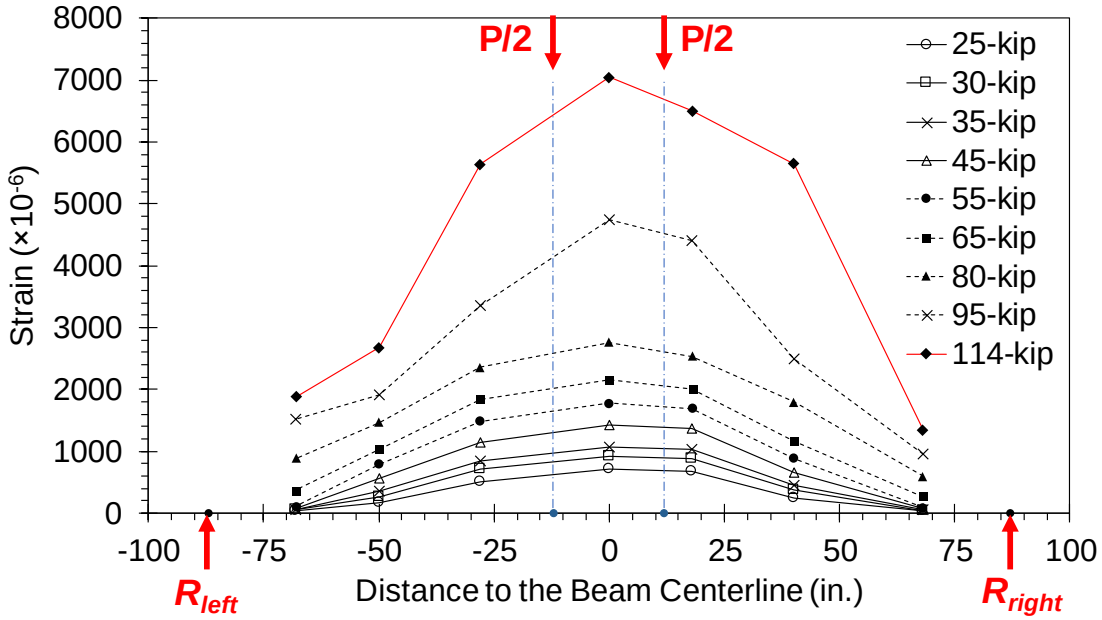

Figure 5.30: Strain distribution on GFRP patch along flexure beam longitudinal axis during the static loading test (the red arrows highlighting the locations of the loading and support points).

This strengthened flexure beam exhibited a brittle flexural failure mode evidenced by the exaggerative growth of the existing vertical flexural cracks at the tension face that had originated during the preloading test (see Figure 5.5). While loading to 110 kips, some cracking sounds were heard, but continuous visual inspection did not observe the formation of new cracks. After the specimen was further loaded above 110 kips, the abrupt opening of large cracks generated tremendous audible 'popping' noise, suggesting the imminent failure. Figure 5.31 shows the progressive debonding process of the GFRP patch during which rapid failure occurred. This figure shows five consecutive frames extracted from the video footage recorded with the HD camera in front of the beam.

As can be observed from Frame #1 and #2, the entire failure process simultaneously demonstrated two modes including the concrete cover delamination within the constant moment zone and the peeling of FRP from concrete substrate in the shear span. It is also noticed that the spalling of concrete cover was most likely caused by the insufficient lateral confinement (i.e., only the beam bottom face is restrained by the composite and the concrete is free to dilate transversely at the large moment.), displaying an explosive and catastrophic appearance. In nature, the concrete cover bridges the GFRP composite to the steel reinforcement. At extreme loading condition, the yielding of steel reinforcement can locally generate tremendous deformation, leading the bars to be splitting from the neighboring concrete, which suddenly induces the tension failure of the concrete cover without altering the bond between the composite and the concrete substrate.

Meanwhile, a significant flexural crack (see Frame #1) opened initiating ultimate debonding of FRP. This severe cracking damage induced considerably high interfacial shear stresses between the GFRP composite and the concrete substrate that consequently led to the sudden local debonding at this critical crack (see Frame #2), then promptly propagating along the longitudinal axis of the bond-line (see Frame #3 and #4), and resulting in the eventual fracture shown as the falling-off of the composite patch (see Frame #5). Additionally, in the shear span region, the shear-moment ratio is high, but the strain level is reduced (see Figure 5.30) and then the steel reinforcement can remain in the elastic range. Consequently, the ripping of concrete cover can be avoided in this region and the considerably opened debonding crack can only propagates through the relatively flexible epoxy bond-line (see Frame

#2 in Figure 5.31), resulting the peeling of GFRP patch along the direction of decreasing moment.

This observed failure process is in a good agreement with other similar experimental studies [29,43-47]. Additional noteworthy, as recommended by ACI 440 committee [25], the supplemental wrapping of this specific region using some anchoring FRP wraps can substantially mitigate the failure modes of concrete cover spalling and FRP debonding by providing additional lateral confinement [31,48,49].

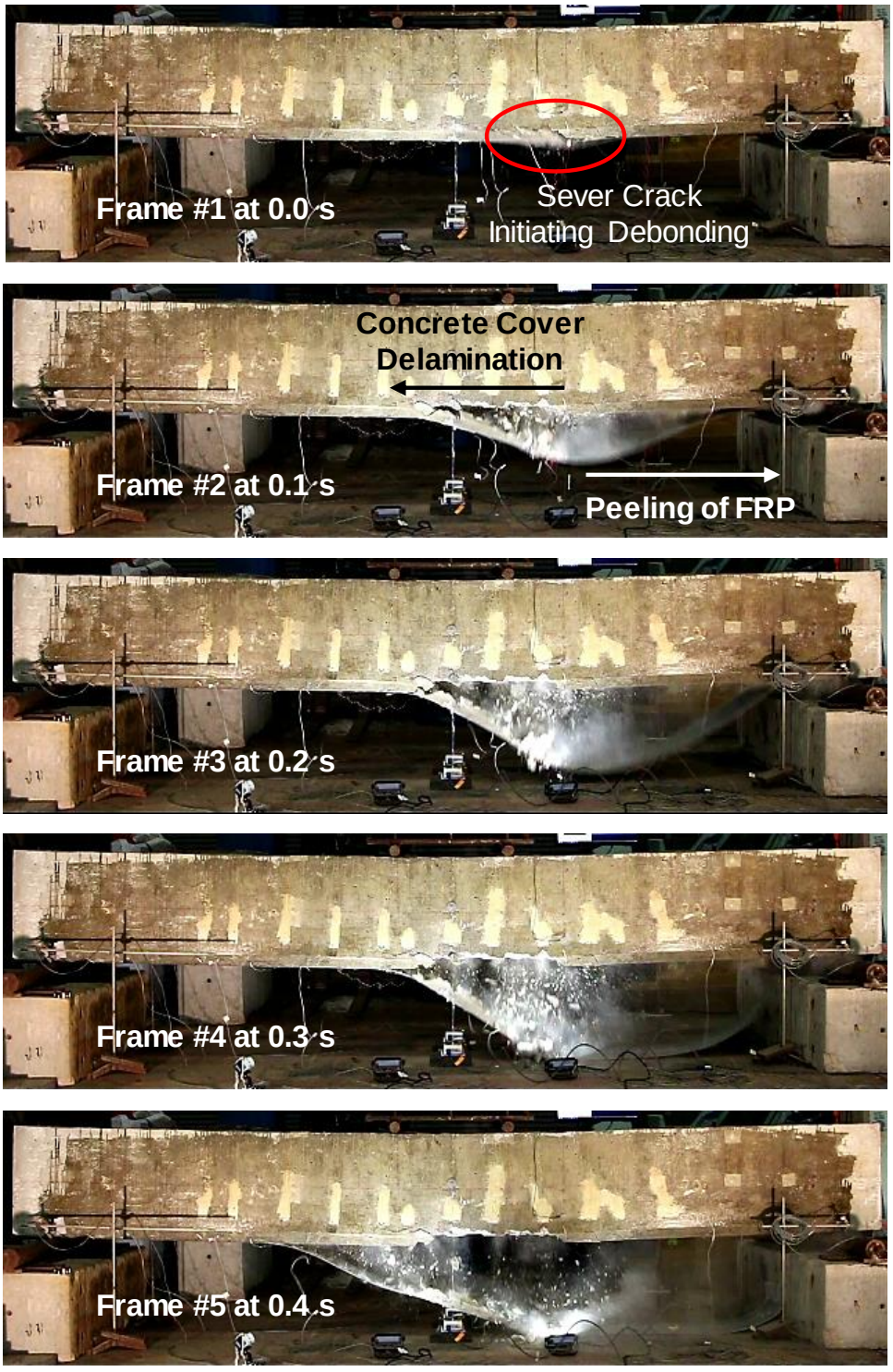

Figure 5.31: Snapshots showing the progressive debonding of the GFRP composite patch at the failure of the concrete beam specimen.

Figure 5.32 shows the post-failure appearance of GFRP strengthened beam. It can be found that the GFRP composite itself is overall intact and shows some longitudinal matrix cracking (see Figure 5.32a) as a result of the splitting of the resin-rich zone along the fiber bundles due to the Poisson effect. The fractured concrete surface shows a brittle 'teeth-like' pattern (see inset), revealing the action of the steel reinforcement as the bond breaker. The severe but common flexural cracking pattern in central loading span is captured in Figure 5.32b. Similar fracture surface and crack pattern have been also demonstrated in other experimental research on the FRP-based flexural strengthening of concrete beams [29,45,46,50-52].

Figure 5.33 depicts the left portion of the specimen after failure where about 3.5 ft long GFRP patch (from the left support) is survived during the catastrophic testing. It is clear that this part of the composite is in an excellent structural condition without showing any visual damage, like the matrix cracking observed in the peeled part (marked in red), indicating the good composite quality and bond formation due to the implemented GFRP manufacturing process used in this study.

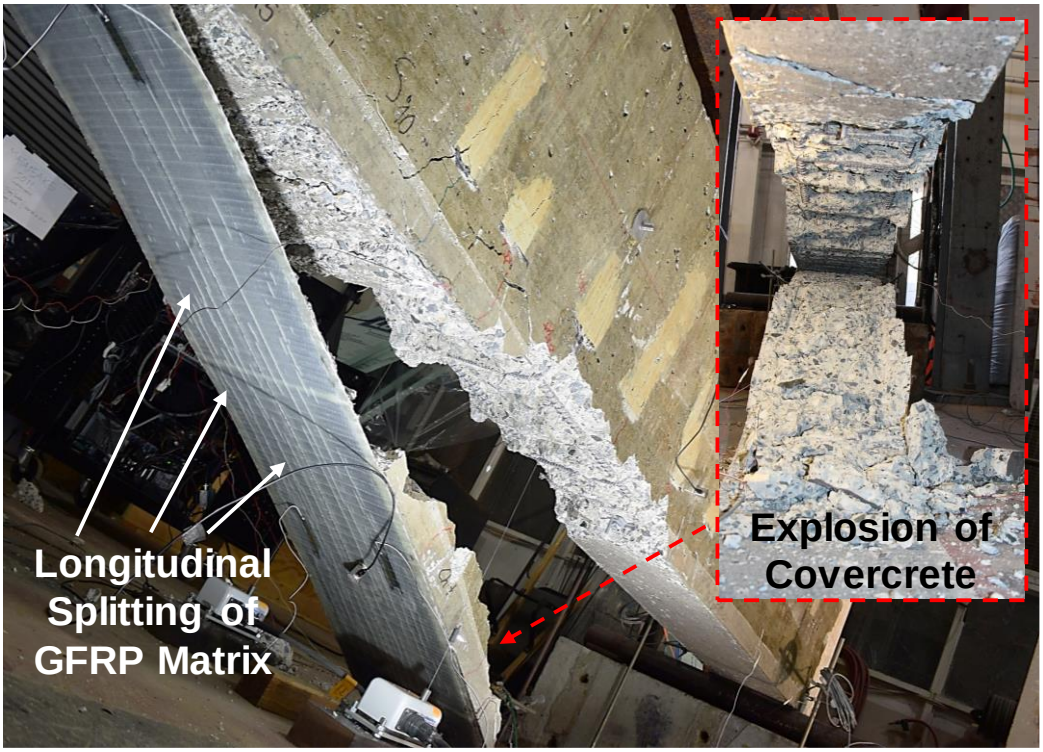

(a)

(b)

Figure 5.32: Photographs showing the close-up view of (a) the GFRP composite patch after debonding and (b) the concrete crack pattern in the central loading span of the beam after failure.

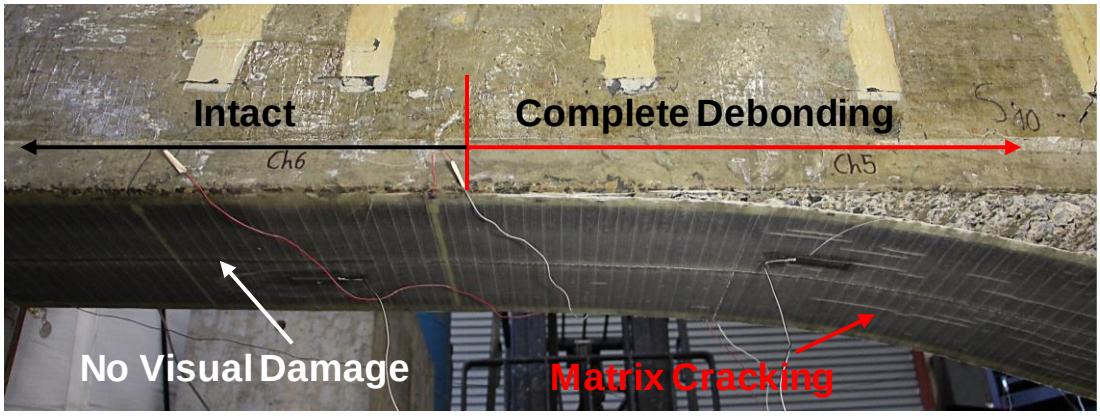

Figure 5.33: Photograph showing the distinctive appearance of the GFRP composite patch in the conjunctional area after failure.

5.3.1.2 Externally Bonded GFRP U-Wraps for Shear Strengthening

Being consistent with the testing scheme applied to the aforementioned flexure beam, the shear beam strengthened with the GFRP U-warps (see Figure 5.22) was subjected to a similar two-part loading protocol including the low amplitude service-level cyclic loads and the progressively increasing stepwise loads. Key experimental observations and results on the structural performance of the shear beam are presented in the following two sections.

5.3.1.2.1 Service-Level Cyclic Loading

Figure 5.34a shows the mid-span displacement of the shear beam during the 15,000 cycles of 15-35-kip repeated loads at 0.2 Hz (Figure 5.34b). It can be observed that both the loading history and the beam deflection are following a uniform and stable fashion over the entire 22 hours testing. The corresponding force-displacement response is shown in Figure 5.34c, which follows a linear elastic trend showing a constant change of 0.078 in. between peak and valley loads. Overall, a residual displacement of about 0.010 in. accumulated in the end of this cyclic test, which is

comparable to the previously tested flexure beam. In addition, the shear beam did not exhibit any visible accumulation of damage in the formation of new cracks or growth of existing cracks, indicating that the GFRP strengthened beam is performing adequately.

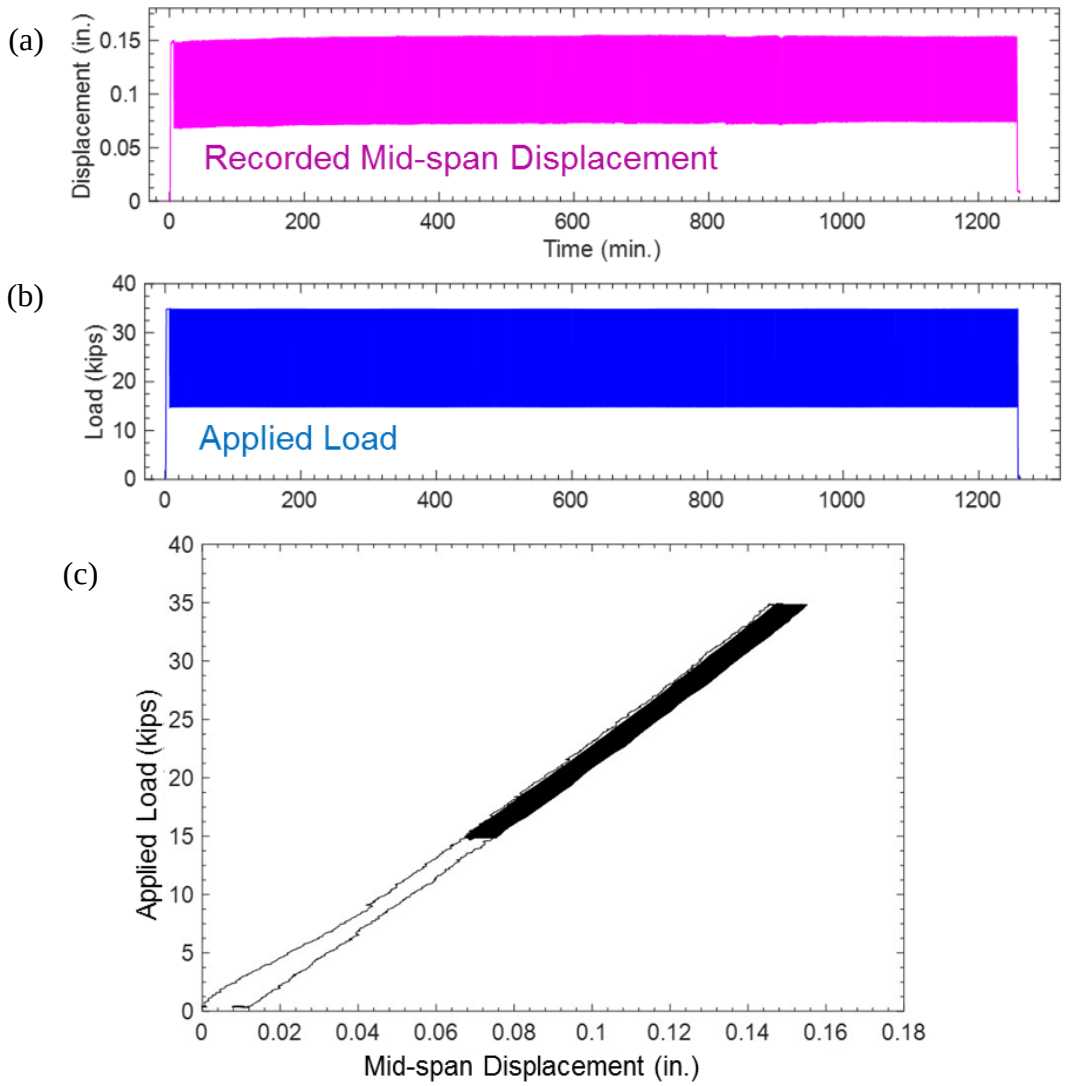

Figure 5.34: Total responses of (a) the mid-span displacement of the shear beam during (b) the applied repeated loads, and (c) the corresponding force-displacement relationship (15,000 cycles).

The structural response of the attached GFRP U-wraps under the repeated loading is shown by the strains measured on the composite. Figure 5.35 shows the typical longitudinal strain responses collected from the strain gages at the soffit center of these three U-wraps (see Figure 5.35 inset) at four points in time throughout the test. It can be seen that all strain responses closely follow the sinusoidal shape of the applied cyclic loads and are gradually decreasing in the direction of decreasing moment (i.e., from the loading point to the left support corresponding to Figure 5.35a though c) at an overall level of less than 100 με. It is also notable that the longitudinal strains at the bottom of U-wrap #3 shown in Figure 5.35a show a small drift of about 10 με after cyclically loading for several hours (i.e., Cycle-1-2-3 vs. Cycle-4,999-5,000-5,001), which is likely due to the stabilization of the existing cracks (see Figure 5.7) that can release the surface strains on the bottom, especially as the uncovered cracks in the vicinity of the U-wrap (see Figure 5.7a) are repetitively opening and closing under the cyclic loading.

The progression of invisible microcracks in concrete due to the repeated loads is detected and monitored using the AE sensor (see Figure 5.22). The total AE response is presented in Figure 5.36. It can be found that the bulk trend is comparable to the AE behavior observed in the flexure beam (see Figure 5.26) in which significant AE activity is recorded in the initial stage of the cyclic loading test as a result of the opening and further propagation of the existing cracks (especially in the right side of the beam that is not rehabilitated with composites), which then become stabilized at a relatively low level as the peak loads remain at 35 kips. Again, the accumulated AE counts (solid line) demonstrate a nearly linear trend similar to that of the flexure beam, indicating a constant rate of AE activity throughout the test. Notably, the total amount

of the accumulated AE counts is about 75% more than that observed from the flexure beam, which can most likely attributed to the evolution of cracks originating from the non-strengthened right portion of the shear beam.

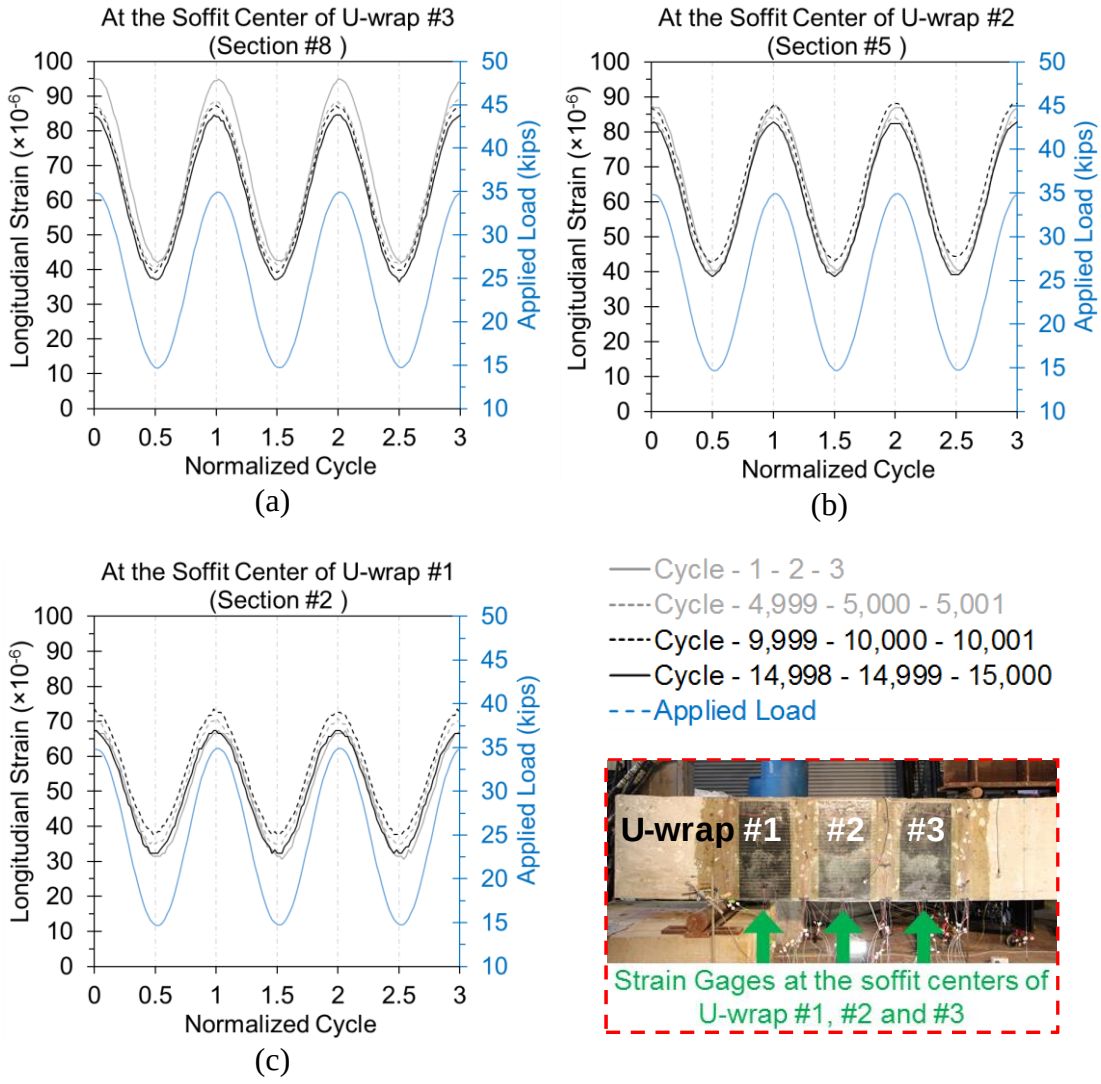

Figure 5.35: Typical strain responses at the soffit of the GFRP composite U-wrap (a) #3, (b) #2, and (c) #1. Inset shows the location of strain gages.

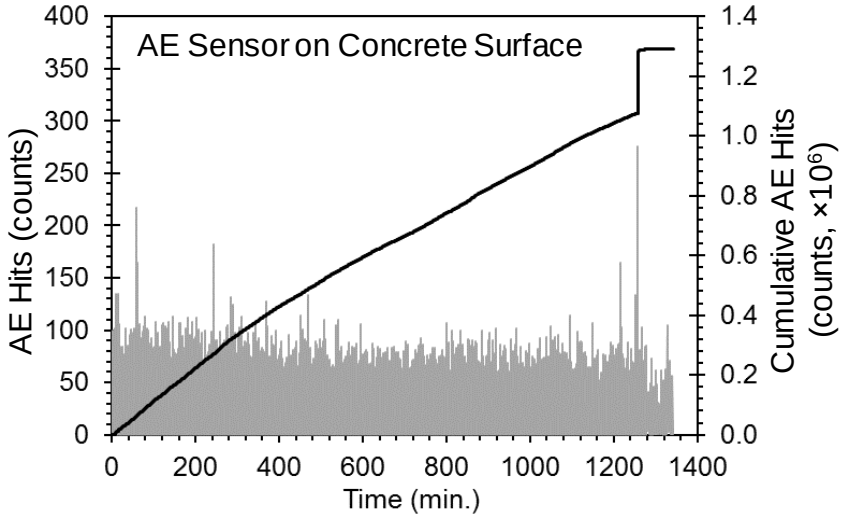

Figure 5.36: Real-time AE hits and cumulative AE counts recorded from the shear beam during the whole cyclic loading test.

5.3.1.2.2 Static Loading-Unloading Cycles up to Failure

Similar to the flexure beam, the GFRP U-wraps strengthened shear beam was first loaded following an eight-step loading-unloading protocol and then statically loaded to failure. The corresponding beam mid-span deflection is represented in Figure 5.37. It can be observed that the shear beam displayed noticeable residual deflections after the 75-kip cycle (Figure 5.37a), which accumulated to 0.05 in. in the end of the 140-kip cycle. In addition, the nine 500-cycle repeated loading sessions between the static loading cycles exhibited a comparable trend, where approximately 15% increase in the amplitude of deflection was observed between the first session (before the step loading) and the last one (after the 140-kip cycle), suggesting the lower stiffness as the result of the accumulated damage during high loads. Figure 5.37b presents the beam response during the final load step. As can be seen, the response of the mid-span displacement shows a distinctive inflection point at 157 kips, after which the beam deforms sharply, revealing the yielding of the beam. The sudden

increase of mid-span displacement indicates the loss of member stiffness. Eventually, this specimen failed at the peak load of 172.3 kips with the maximum mid-span deflection of 3.2 in.

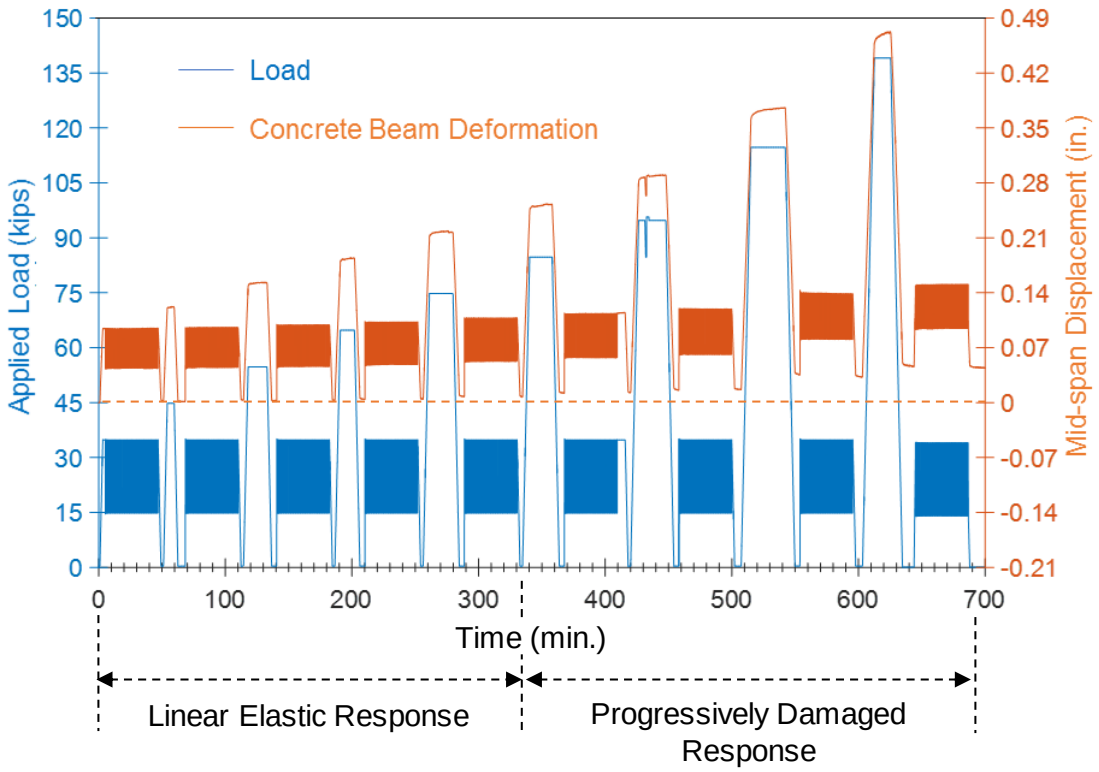

(a)

Figure 5.37: Applied load and mid-span deflection of the shear beam during (a) the static stepwise loading-unloading cycles and (b) the final failure cycle.

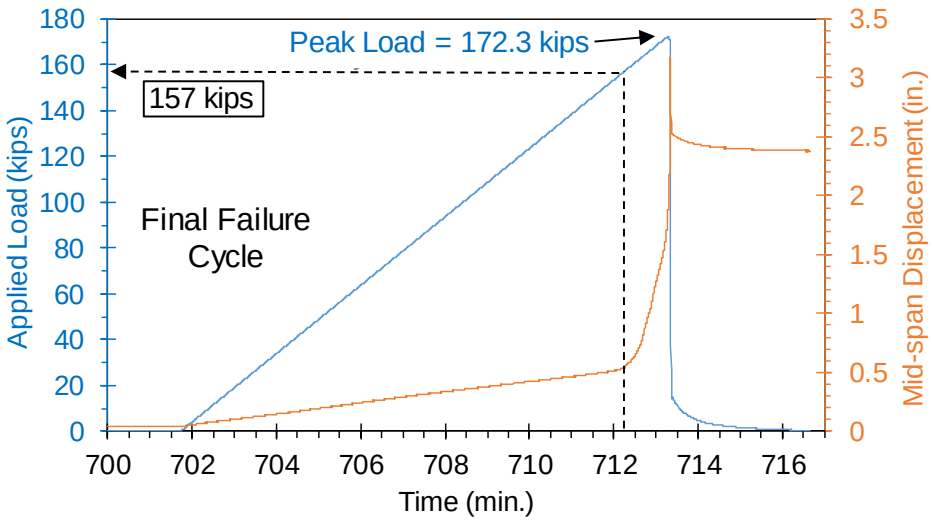

(b)

Figure 5.37: continued.

Figure 5.38 shows the force-displacement responses of the strengthened shear beam in comparison with its original responses up to 95 kips. For a clear presentation of the data, the six loading-unloading cycles are presented in two graphs, i.e., four cycles (45-55-65-75-kip) in Figure 5.38a and the rest two cycles (85-95-kip) in Figure 5.38b. It can be observed that the force-displacement relations of the strengthened beam (colored lines) are linear elastic under these cycles. Notably, significant hysteretic effects exist in the original responses (black and gray lines), which are completely corrected after the GFRP U-wrapping rehabilitation, revealing the enhanced serviceability control of the strengthened beam. In addition, it can be found that the initial member stiffness (before 15 kips, in Figure 5.38a) is comparably close before and after the FRP retrofitting, and only about 20% increase is demonstrated by the strengthened beam at high loads as the concrete beam softens (after 35 kips, in Figure 5.38a and b). This observation is expected because the design philosophy of the

GFRP U-wraps for this specific beam is only to compensate the deficiency in shear strength of the weak (left) portion of the concrete beam (see Section 5.2.2.2) and not to overly strengthen it. In this way, this beam is able to fail following a natural mode as the strong (right) portion of the beam remains in its original condition, free of any strengthening modification (see Figure 5.22).

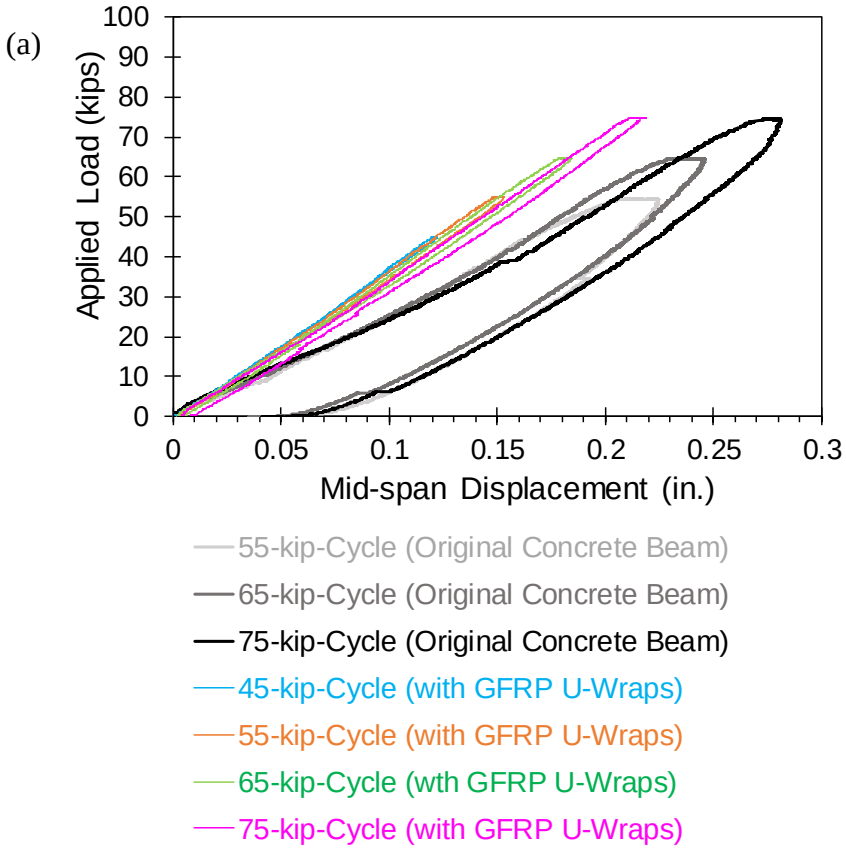

Figure 5.38: Force-displacement responses of the shear beam before and after GFRP flexure strengthening during (a) 45, 55, 65, 75-kip, and (b) 85, 95-kip loading-unloading cycles.

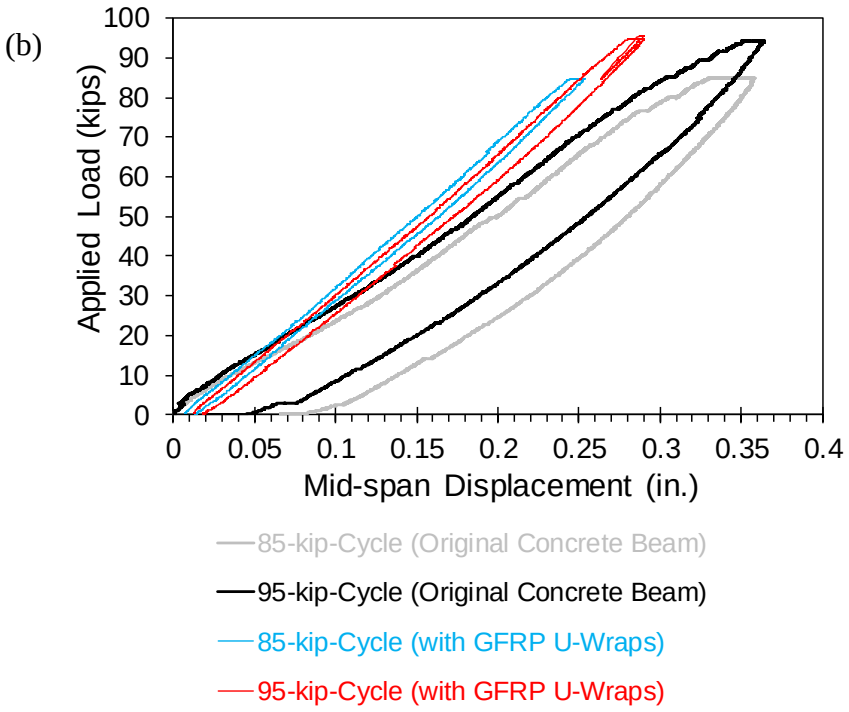

Figure 5.38: continued.

Figure 5.39 shows the force-displacement responses of the strengthened shear beam during the static loading test. To clearly present the data, the eight loading-unloading cycles are first highlighted in Figure 5.39a and the final failure cycle is shown in Figure 5.39b in comparison with the former loading cycles. It can be seen in Figure 5.39a that all force-displacement relationships are nearly linear elastic, however, the loss in member stiffness becomes exaggerated in the 115-kip and 140-kip cycles. It is also notable that the holding of peak loads at 115 and 140 kips (for about 20 minutes, see Figure 5.39b inset) causes a noticeable residual displacement of 0.02 in., suggesting the accumulation of permanent damage in the concrete beam at high loads. From Figure 5.39b, it is apparent that as testing to failure, this beam displays a significant amount of plastic deformation after first yielding at 157 kips

(also see Figure 5.37b). This is because the propagation of concrete cracks is not restrained on the right side of the beam, resulting in large deformations under high loads. Afterwards, the fracture process continues until reaching 3.2 in. displacement as evidenced by the rapid unloading of the beam, revealing the final failure.

It is worth mentioning that the ultimate load carrying capacity of this shear beam, i.e., 172.3 kips, is approximately 6% greater than its nominal flexural strength (i.e., 161.8 kips, see Section 5.2.1.2), which however, is about 15% less than the ACI-440 shear capacity (i.e., 203.4 kips, see Section 5.2.2.2) of the strengthened left side of the shear beam due to flexural failure at its ultimate. These results prove the FRP design philosophy of this specific task and validates the effectiveness of the deployed GFRP U-wraps for shear strengthening. In particular, the corrected force-displacement response of the strengthened beam maintains a linear elastic trend up to 150 kips, demonstrating the considerably improved serviceability after the structural rehabilitation.

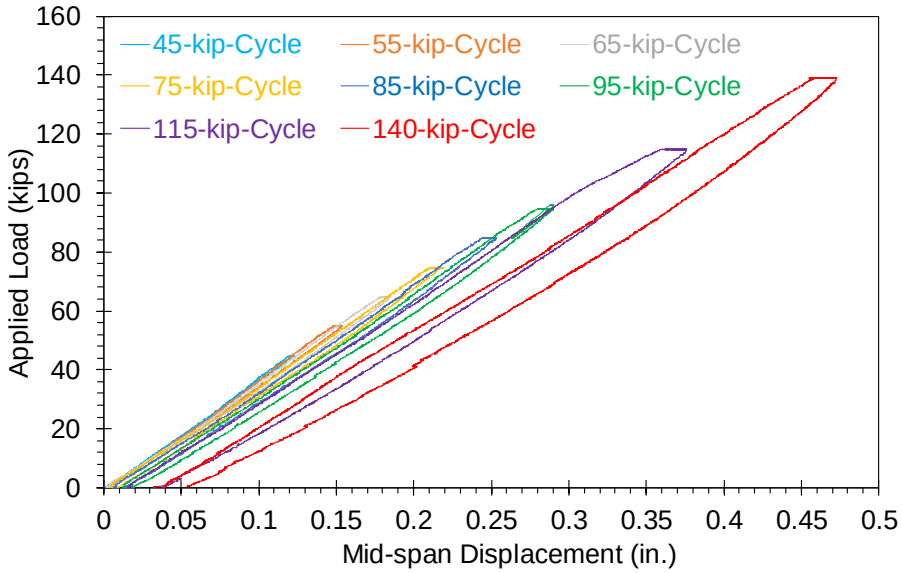

(a)

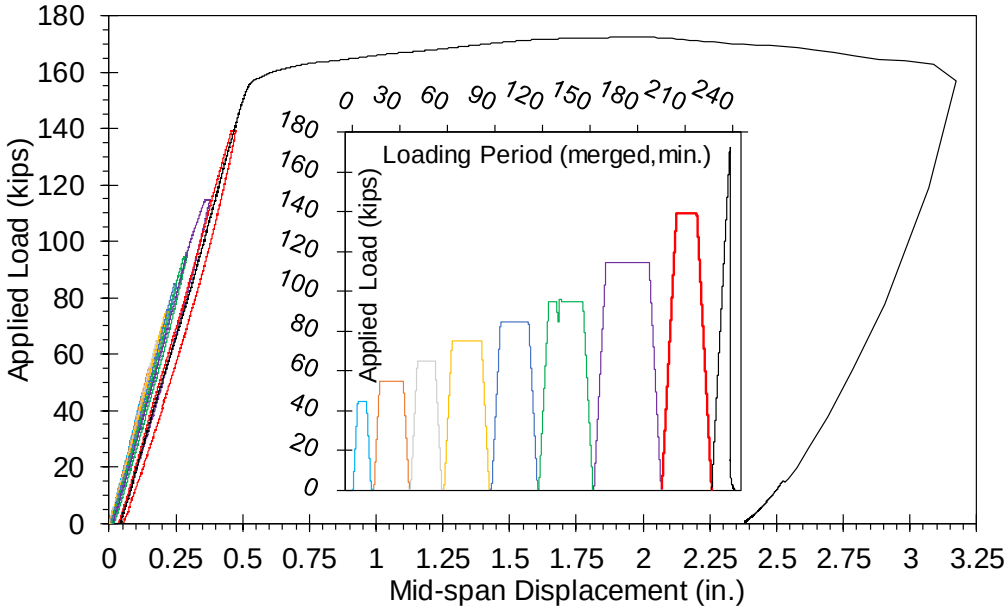

(b)

Figure 5.39: The total force-displacement responses of the strengthened shear beam (a) under the applied stepwise loading cycles and (b) up to failure; Inset shows the applied loading protocol.

To evaluate the effort of the deployed GFRP U-wraps, a series of strain gages were mounted on the composite surface to monitor their mechanical responses under the applied loading protocol. It is worth mentioning that at each selective location for strain measurement, strains were measured in both parallel and perpendicular direction with respect to the unidirectional fiber in the composite. In particular, since a 45-deg inclined shear crack formerly developed during preloading (see Figure 5.7a) is presently covered by the U-wrap #2, a denser arrangement of strain gages was implemented on the side face of this composite wrap.

Figure 5.40 shows the strain distributions on the side faces of the three GFRP U-wraps at their top and bottom regions under different levels of loading. Clearly, all distributed strains increase as loading level rises. In particular, all vertical strains (i.e., parallel to the fiber direction) are in tension, demonstrating the positive contribution to shear resistance. In the top region of the composite, as shown in Figure 5.40a the tensile strains increase along the direction of increasing moment, showing a low strain level of less than 210 με. On the other hand, in the bottom region (i.e., 3.25 in. from the lower edge) the maximum tensile strain of 515 με (Figure 5.40c) is represented at the central wrap (i.e., #2) that covers the critical shear crack. In comparison, at the height of 2.25 in. from the bottom edge, the maximum strain level is reduced to 230 με (Figure 5.40e) due the redirection of tensile loads near the corner zone. As expected, the horizontal strains (i.e., normal to the fiber direction) on the composite are compressive at top (Figure 5.40b) and tensile in the bottom (Figure 5.40d and f) due to the bending moment. Both the maximum compressive strain of 580 με and tensile strain of 1400 με appear on the U-wrap #3 next to the loading point. Apparently, the horizontal strains at the height of 3.25 in. from the bottom edge (Figure 5.40d) are

following a comparably trend as the vertical strains at the same location. However, near the corner zone, the horizontal strains (Figure 5.40f) increase in the direction of increasing bending moment. Just prior to failure of the concrete beam, strain measurements corresponding to the 170-kip load (red lines in Figure 5.40) show that all GFRP U-wraps are in the elastic range, far below their tensile capacity, indicating no local debonding at the critical cracks as a result of the extensive coverage and high quality of the provided composite U-wraps.

Figure 5.41 shows the strain distributions at the soffit of the GFRP U-wraps as statically loaded. The used bi-axial strain gages measured the strains in the transverse (i.e., normal to the beam axis) and longitudinal (i.e., parallel to the beam axis) direction as presented in Figure 5.41a and 5.41b, respectively. All strains are in tension at the soffit. Particularly, the transverse strains (Figure 5.41a) are at a relatively low level (less than 360 με) and display a similar trend as the horizontal strains in the bottom region of the composite side face (Figure 5.40f) that these strains are increasing along the direction of increasing bending moment. Meanwhile, the longitudinal strains (Figure 5.41b) are moderately large (less than 800 με) and follows a comparable fashion as the vertical strains in the lower region of the composite side face (Figure 5.40e). The phenomena indicate a smooth transition of the applied point load from the side face to the soffit over the corner zone. Additionally, at the high load of 170-kip, the measured longitudinal strain at the soffit of the U-wrap #3 (Figure 5.41b) drops suddenly, attributing to the extended opening of the flexural crack in very close proximity to this wrap (see Figures 5.7a and 5.44c) that releases the tensile strain and suggests imminent failure.

Figure 5.42 represents the strain distributions on the side face of the individual GFRP U-wrap #2 at its central line, which is also the location of the critical shear crack. Before loading to the ultimate capacity of the beam, strains in both vertical (Figure 5.42a) and horizontal (Figure 5.423b) direction show the similar decreasing trend as distancing from the crack path (but towards the loading point), at a low level of a few hundred με, suggesting a strong anchorage of the composite in arresting the shear crack. In particular, just prior to the failure of the beam, the horizontal strain sharply jumps under the load of 170 kips near the right edge of the composite wrap (red line in Figure 5.42b). This is because of the local bonding stress transfer zone between the composite and concrete where the mix-mode stress condition possibly exists and is dominated by the large deformation change at the sudden yielding of the beam (see Figures 5.37b and 5.39b).

To summarize, the strain distributions on the GFRP U-wraps are in a very low level of less than 1500 με, suggesting that all composite wraps are in their elastic range as the shear beam fails. Due to the extensive coverage of the critical shear crack using the narrowly-spaced wide U-wraps (i.e, both the lower and upper region of the shear crack are fully covered by the wraps.), local debonding at the crack is eliminated at high loading conditions. Therefore, the composite wraps were not fully utilized in resisting shear forces as failure occurred. In comparison, many experimental studies have shown that as the shear cracks are partially covered by the narrow U-strips, it is common to observe a rapid increase in strain of the composite due to the local debonding at the cracks, as demonstrated by Chajes *et al*. [33], Teng *et al*. [53], and Kim *et al*. [28]. For shear rehabilitation purposes, the deployed GFRP U-wrapping strategy appears effective.

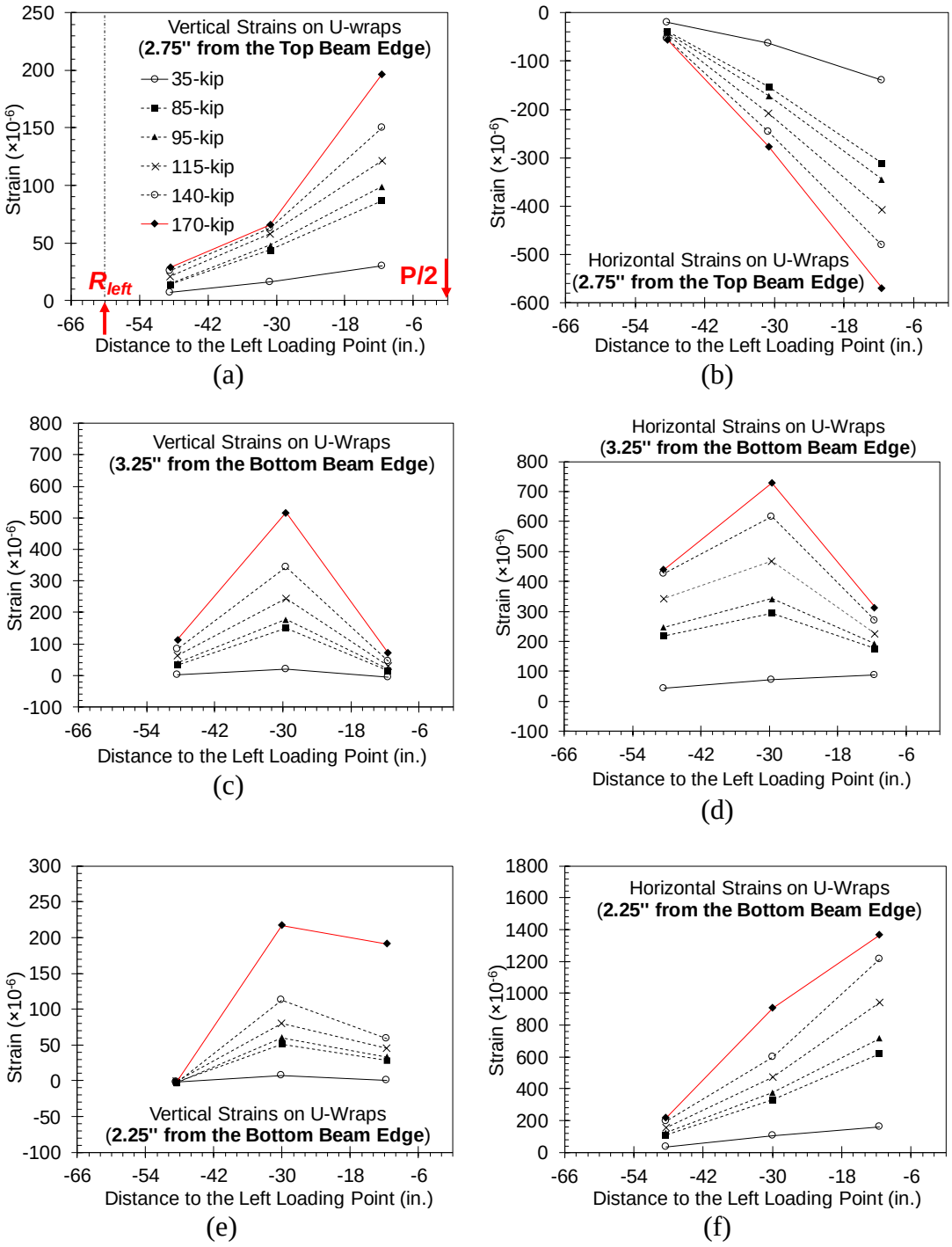

Figure 5.40: Strain distributions on the side faces of the GFRP U-wraps in vertical and horizontal direction at (a, b) 2.75 in. from the top beam edge, (c, d) 3.25 in., and (e, f) 2.25 in. from the bottom beam edge during the static loading test; (g) shows the relative locations of the strain gages.

(g)

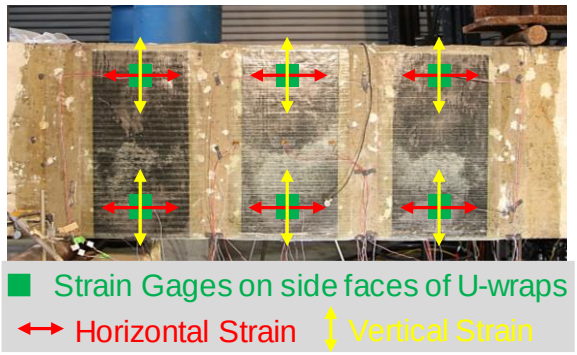

Figure 5.40: continued.

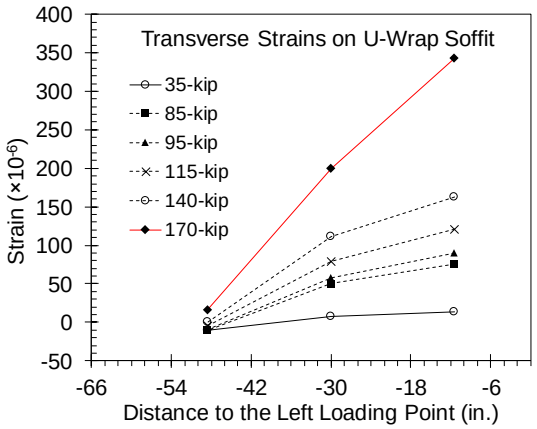

(a)

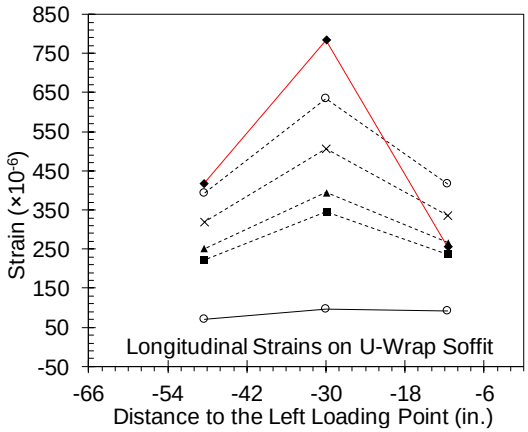

(b)

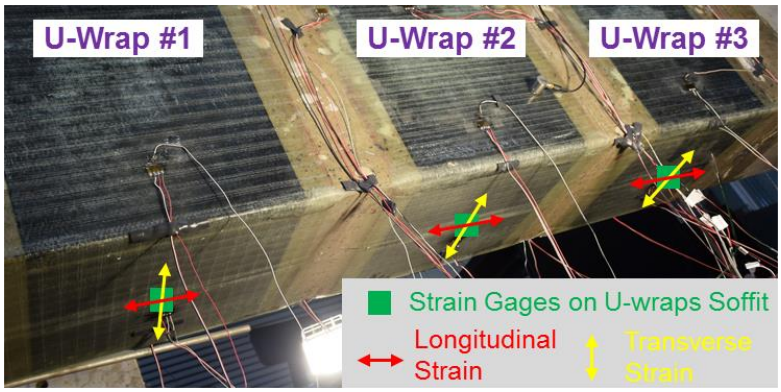

(c)

Figure 5.41: Strain distributions on the soffits of the GFRP U-wraps during the static loading test in (a) the transverse and (b) longitudinal direction; (c) shows the relative locations of the strain gages.

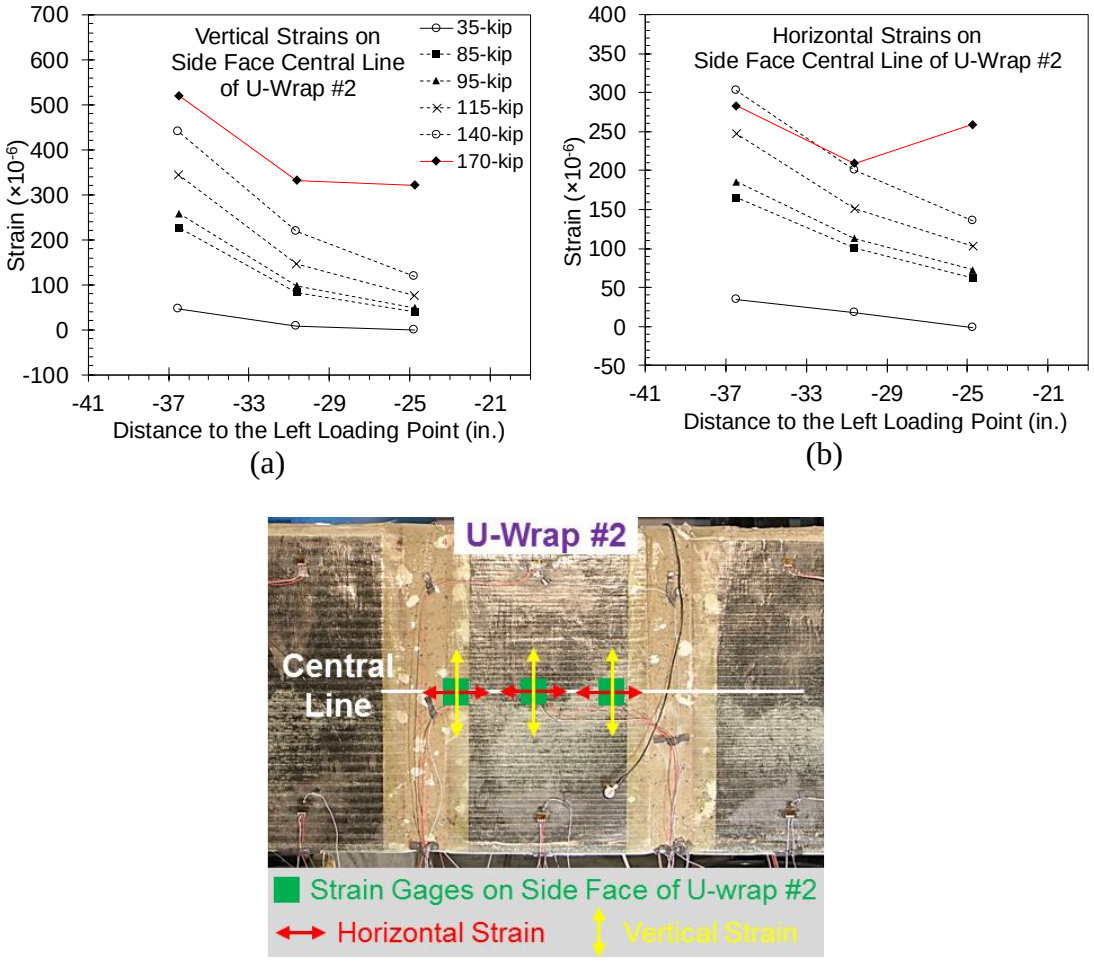

Figure 5.42: Strain distribution along the central line of the GFRP U-wrap #2 during the static loading test in (a) vertical and (b) horizontal direction; (c) shows the relative locations of the strain gages.

The progressive failure process of the strengthened shear beam was captured using the HD cameras. Four representative frames extracted from the recorded video footage are shown in Figure 5.43. It was found that this beam exhibited a brittle flexural failure mode evidenced as the crushing of the concrete in its compression zone (Frame #4). This is likely for two reasons: (1) the tensile reinforcement in this

shear beam section is overdesigned, and (2) substantial reserve capacity exists prior to steel yielding due to composite wrapping. Although concrete crushing in general is not favorable for traditional steel reinforced concrete (RC) members due to the suddenness and inadequate warning associated with crushing of concrete prior to member failure [22,23], this failure mode in the externally bonded FRP-strengthened RC members is more desirable than other brittle failure modes commonly seen as FRP debonding and rupture. Since FRP- strengthened RC members normally exhibit much less ductility than steel RC members [4,6], in comparison with FRP debonding and rupture, concrete crushing allows the FRP RC members to undergo certain plastic behavior prior to the final failure, enabling adequate deformability. This phenomenon has been confirmed in this study as well (i.e., Figure 5.39 vs. Figure 5.29) and also agrees with other experimental studies [10,29,37,45,47,51]. In addition, the failure process takes longer time as crushing of concrete in the compression zone than debonding or rupturing of FRP, just as demonstrated in present study that the failure process only took 0.4 second in the flexure beam test (see Figure 5.31), but 15.5 seconds in the shear beam test (see Figure 5.43). Simply, it is notable that the dominance of the failure mode of this concrete beam changed from shear in its original state to flexure in present study, indicating the effectiveness of shear strengthening using the deployed composite wrapping scheme.

Figure 5.44 shows the post-failure appearance of the central region of the GFRP U-wrap strengthened shear beam. It is clear that severe flexural concrete cracks originating from the bottom tension face are extensively propagating up to the compression zone within the loading span. Concrete in this compression zone is badly crushed and spalling off. The compression steel reinforcing bars are apparently

buckled at both front and back sides. Therefore, the previously observed large deformation at failure is most likely due to the extensive opening of significant flexural cracks as yielding of the compression zone that can locally introduce the plastic strains in the steel reinforcement and results in the local slippage of the reinforcing steel bars at the crack locations.

Figure 5.45a and 5.45b depicts the left and right portion of the specimen after failure, respectively. Obviously, the GFRP U-wraps are in the excellent structural condition without presenting any damage. In particular, the soffit of the composite wrap is free of any cracking (that is typically observed in GFRP patch on the flexure beam as shown in Figure 5.32a). On the other hand, the unstrengthened right portion is severely cracked that both vertical and inclined cracks are visible on concrete beam and the CNT-based sensing U-wraps.

It is worthy of mentioning that in this experiment, the shear beam with U-wraps has outperformed the GFRP bottom side bonded flexure beam with regards to debonding failure. Simply because each GFRP U-wrap is bent at two 90 degree corners and anchoring over the side faces, debonding potentially occurring at the boundary of the single side-bonded patch is effectively delayed due to the lateral confining effect, leading the composite to sustain a higher tensile load [28,30,54,55].

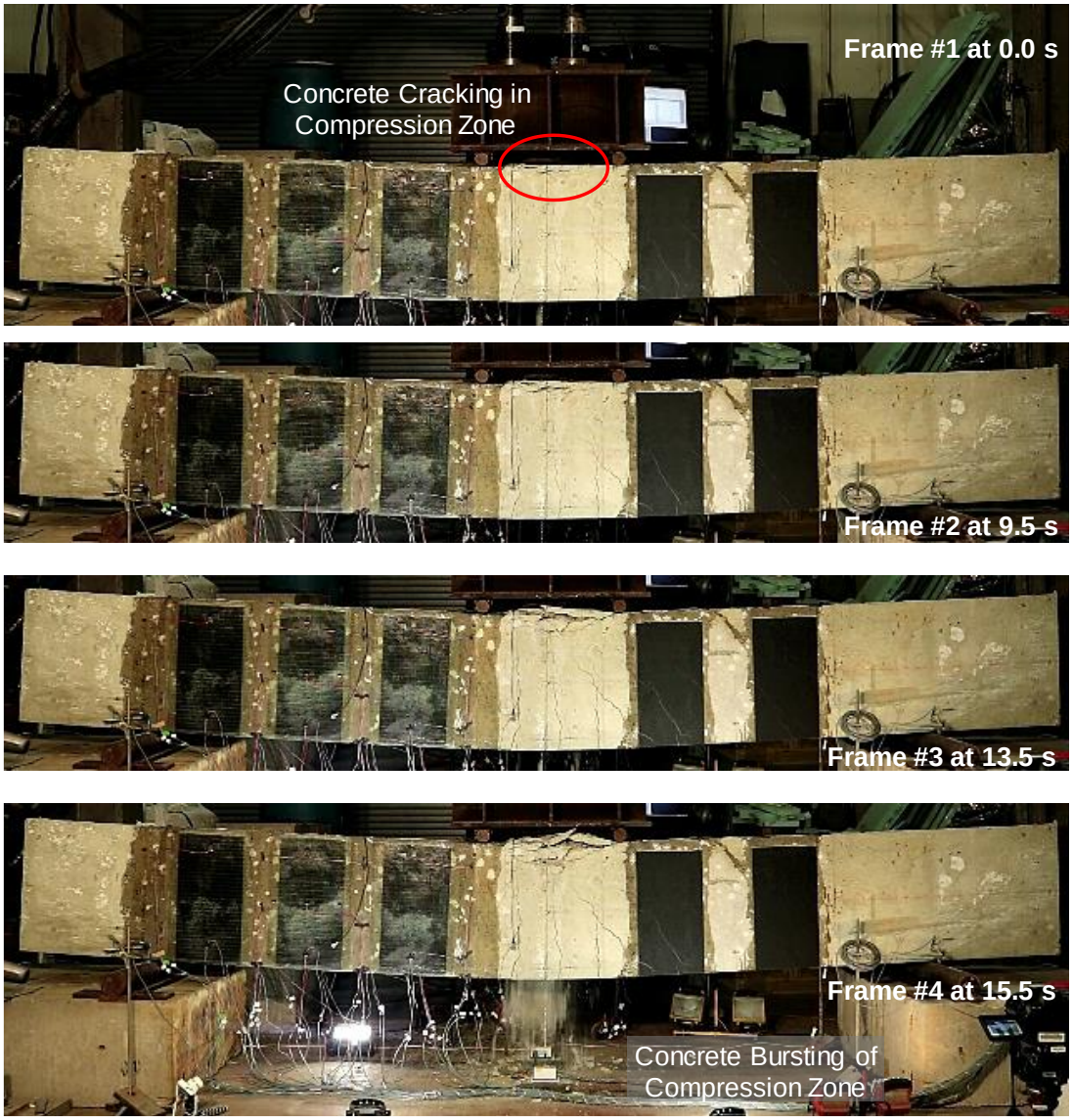

Figure 5.43: Snapshots showing the progressive failure process of the GFRP U-wrap strengthened shear beam evidenced as the concrete crushing in the compression zone.

(a)

(b)

(c)

Figure 5.44: Photographs showing the close-up view from (a) front side, (b) back side, and (c) bottom side of the central region of the shear beam after failure presenting a sever cracking pattern and buckling of the compression bars.

(a)

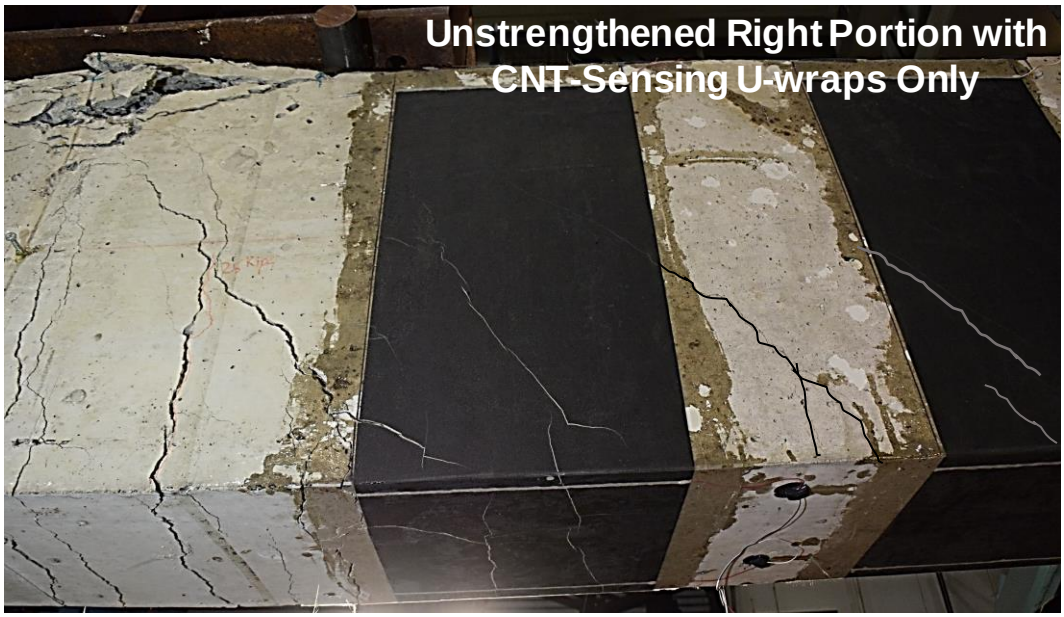

(b)

Figure 5.45: Photograph showing the appearance of (a) the GFRP U-wraps strengthened left portion and (b) the unstrengthened right portion of the shear beam after failure.

5.3.2 *In Situ* Resistive Responses for SHM

As introduced in the beginning of this chapter, the proposed hybrid composite system for concrete members simultaneously enables structural rehabilitation and health monitoring. Apparently, the validity and effectiveness of the developed GFRP schemes using the on-site VARTM-based fabrication approach for flexural and shear strengthening of concrete beams have been extensively demonstrated in the previous sections. During the mechanical characterization experiments of the flexure and shear beam, the real-time electrical measurements were collected from the large CNT-based area sensors that were specially integrated in the hybrid composites at the bonding interface (see Section 5.2.3). In the following sections, the *in situ* resistive responses will be presented and discussed with respect to the SHM of the GFRP-strengthened concrete beams. The interesting features of the CNT-based nonwoven sensors including the piezoresistivity, behaviors under cyclic and static loading, and the resistive reactions in responding to the temperature effects and damage progression, will be demonstrated.

5.3.2.1 SHM of the Flexure Beam

In order to ensure the viability of the measurement scheme for the electrical resistance of the CNT-based sensors. A voltage-current (V-I) sweep test was performed prior to the electrical characterization for SHM. All seven multiplexed sensing sections of the long sensor on the flexure beam (see Figure 5.21) were individually injected with the electric current ranging from 1 microamp to 10 milliamps (based on the baseline resistance of each channel) using the Keithley 6430 source meter and the resultant voltages were measured with the Keithley 2182A nano-voltmeter. Figure 5.46 shows the typical V-I characteristics of CNT-based nonwoven

sensor. It is clear that all V-I curves of the seven sensing channels are straight lines, indicating a great linearity fashion. Therefore, the unstrained CNT-based nonwoven sensor is demonstrating the constant electrical resistance (represented by the slope of the V-I curve) in the wide range of the supplied current, obeying the Ohm's law, which validates the implemented 2-wire measurement scheme as presented in Section 5.2.4.

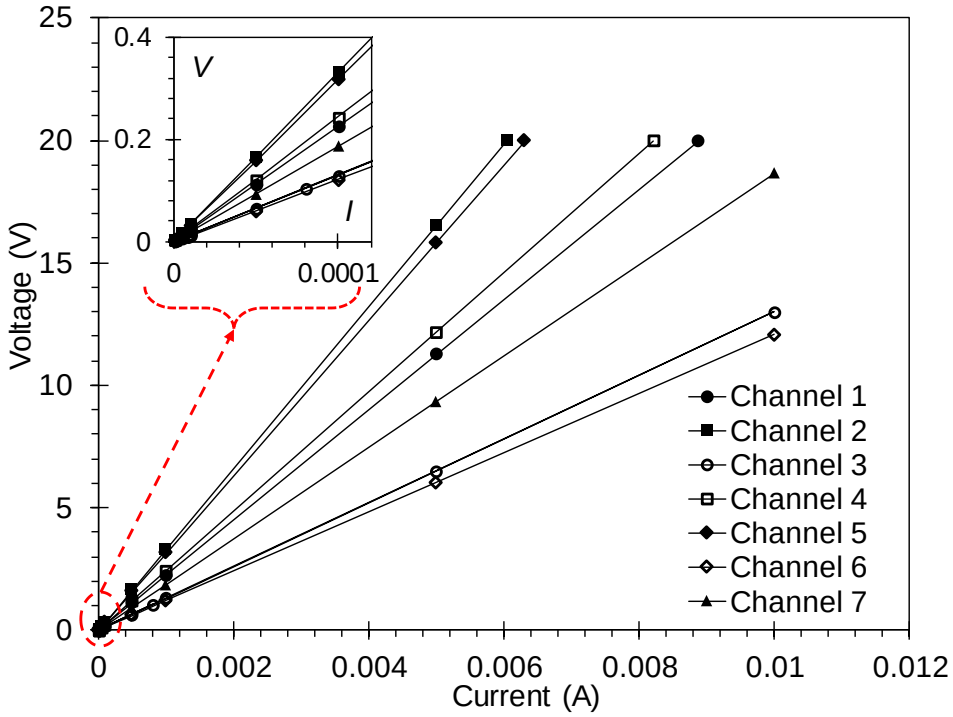

Figure 5.46: Typical V-I characteristics of the proposed CNT-based nonwoven sensor (R^2 = 1).

5.3.2.1.1 Cyclic Loading Condition

Figure 5.47a shows the typical real-time resistive response of one sensing section (#4, the central one, see Figure 5.21) from the continuous CNT-sensor under the 15,000-cycle repeated loads. Different with the measured beam deflection shown in Figure 5.23a, the bulk resistive response is not constant but in a fluctuant fashion that likely follows the variation of the temperature (green line) recorded during the 22-hour test. Two close-up views of the resistive data in the beginning and ending of the test are presented in Figure 5.47b and 5.47c, respectively. From these figures, it is clear that the CNT sensor is effectively responding to the applied cyclic loading protocol, showing a neat sinusoidal shape and strict matching to the peak and valley loads with a constant change of about 0.65 Ω as represented by this specific sensing section #4 located at the central region of the maximum moment.

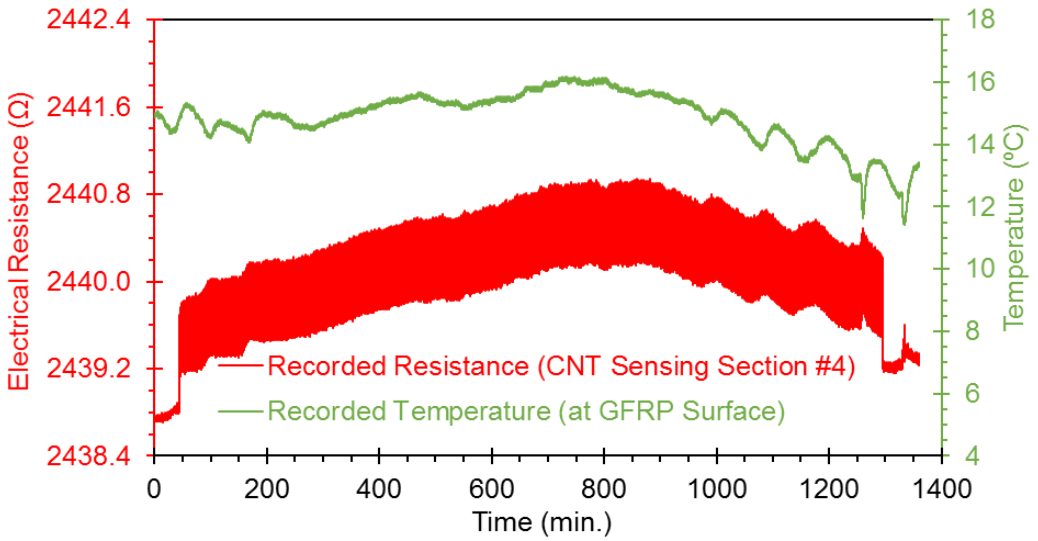

(a)

Figure 5.47: Typical transient resistive response of the CNT-based sensor on the flexure beam subjected to the 15,000-cycle repeated loads showing (a) the bulk response and the close-up view of few cycles in (b) the beginning and (c) the ending of the test.

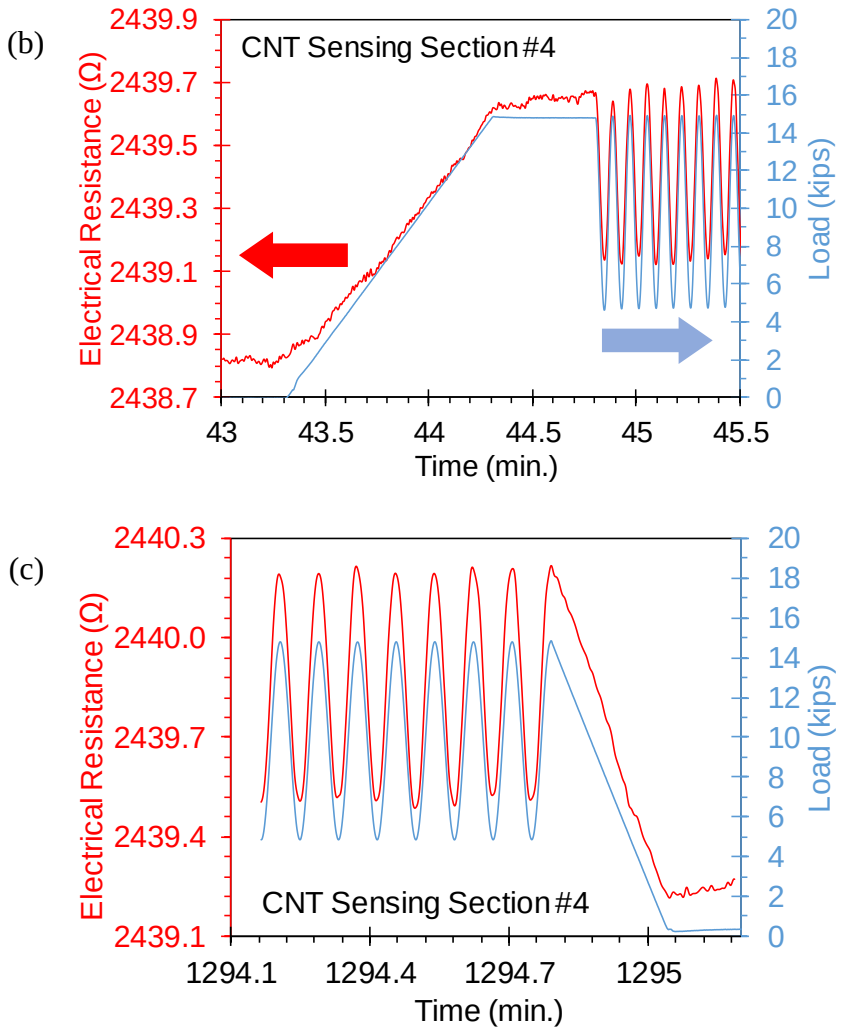

Figure 5.47: continued.

It was noted that due to the normal human activities, laboratory door was frequently opened and closed in the first three and last six hours of testing which caused abrupt temperature variations because of the large temperature difference between the inside and outside of the laboratory in the winter (green line in Figure 5.47a). Coincidently, the resistive behavior shows dramatic fluctuations in these durations (red line in Figure 5.47a). Therefore, prior to performing the further analysis

of the resistive data, the observed temperature effects need to be compensated for the bulk resistive responses. In particular, during 270-960 min., the variations of temperature are found to be relatively stable. As the first step, both the temperature and the baseline resistance of the sensing section measured in this specific period are fitted to the 2nd-order polynomials as shown in Figure 5.48a so as to obtain a simple analytical model of the transient variations of the both measurements. Afterwards, the fitted parabolic functions of the temperature and resistance change are normalized with respect to the time and plotted in Figure 5.48b, where the slope of the curve stands for the resistance change due to the temperature variation, i.e., the thermoresistivity. In particular, the sensing section #4 demonstrates a constant thermoresistivity of 0.019 %/°C as shown in Figure 5.48b.

With the understanding of the thermoresistive behavior, the temperature change induced resistive deviations can be calculated and subtracted from the bulk resistive responses, resulting in the temperature effect compensated resistive response of the CNT-based sensor. In this context, all resistive responses measured from the sensing sections of the CNT-based sensors were corrected following the aforementioned method.

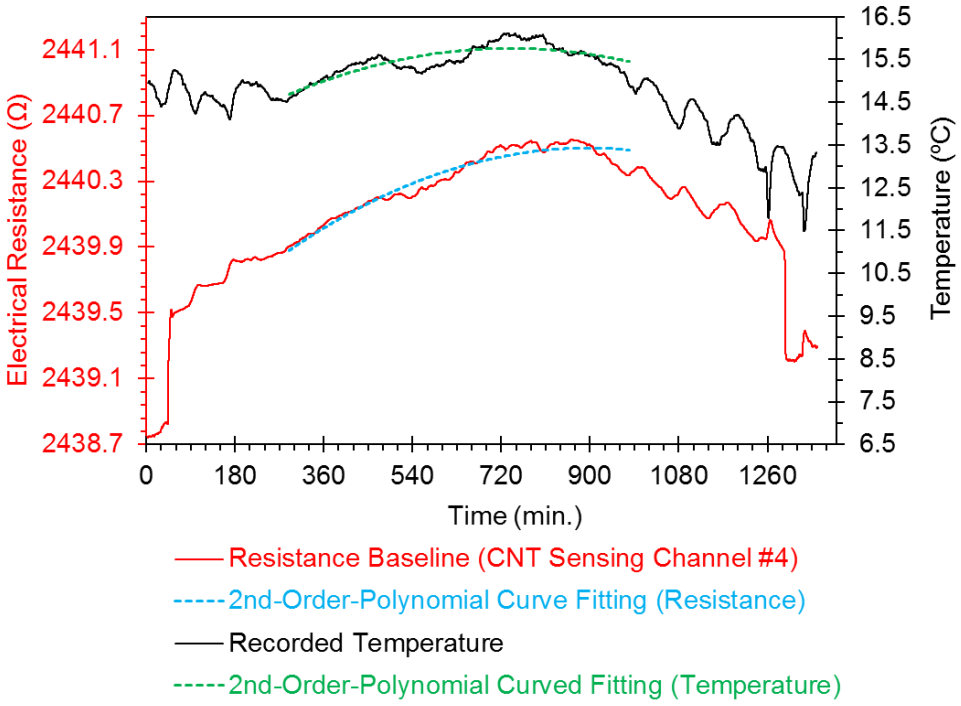

(a)

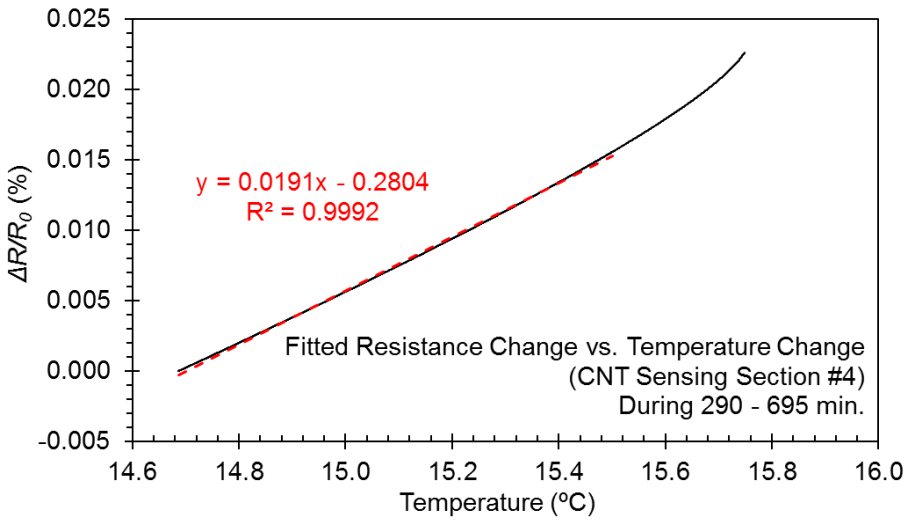

(b)

Figure 5.48: (a) Transient responses of the temperature and baseline resistance of the CNT sensor fitted to the 2nd order polynomial functions for temperature compensation procedure and (b) the thermoresistive relationship developed using the previously obtained functions of temperature and resistance change.

Figure 5.49 shows the typical transient resistive response of the long CNT-based sensor in all of its seven sensing sections at four time points of the cyclic test. It is apparent that the sensing sections including #4, #3 and #5 (shown in Figure 5.49a, b and c) are effectively responding to the applied loads and demonstrating the inerratic sinusoidal fashion as following the loading protocol. Notably, the resistance changes in corresponding to the peak and valley loads are found to be 0.029%, 0.025% and 0.014% respectively presented by the sensing section #4, #3 and #5, which are fairly small amplitudes due to the low strain levels of less than 350 με resulted in the GFRP patch (see Figure 5.25) under the 5-15-kip repeated loads. In addition, the sensing section #2 and #3 (Figure 5.49d and 5.49e) show the sinusoidal trend with some local dissimilarities attributing to the noise in resistance measurements observed at the further reduced strain levels of up to 110 με, which causes only about 0.01% resistance change in one full cycle. It is also found that the two sensing sections located next by the supports (i.e., #1 and #7 in Figure 5.49f and g) are barely showing the anticipated sinusoidal relationship, but resistance changes are less than 0.005%, which is nearly equal to the baseline resistance under the extremely low strain level around 20 με. It is worth mentioning that this small resistance change excites a fairly low resistive signal of less than 0.1 Ω in the system, leading to a reduced signal to noise ratio and consequently a resistive response with higher noise.

The baseline resistance of the CNT-based sensor during the 22-hour test exhibits an upward drift in the time domain. For instance, as shown in Figure 5.49a and b, a relatively large shift about 0.02%, between the first three cycles and Cycle-5,000-5,001-5,002 was observed, which mainly results from the self-stabilization of the concrete beam under the applied repeated loads, comparable to the observed

responses of the beam deflection (see Figure 5.23a) and strains on GFRP patch (see Figure 5.25). Afterwards, nearly 0.01% resistance change accordingly accumulated after Cycle-10,000 and Cycle-15,000, even though the mechanical state of the specimen under those loading periods was very stable as presented by the beam deflection and strains (Figures 5.23 and 5.23). This time-based drift is most likely due to the material polarization [56-63].

In this study, the established CNT-based nonwoven sensing composite is in nature a conductively heterogeneous material from a microscopic perspective. During the electrical measurement, the constantly applied DC electric field polarizes the dielectric epoxy in the vicinity of the nanotube networks (i.e., at the dielectric boundaries), resulting in the oriented dipole moments of molecules and consequently leading to a localized electric field near the nanotube/epoxy interface in the direction opposite to the applied electric field, i.e., the interface polarization (also called 'Maxwell-Wagner-Sillers polarization) [56,63]. This phenomenon has been observed and experimentally investigated in numerous nanocomposites including the CNT/epoxy [61], CNT/cement [56,57], CF/cement [64], CNT/polysulfone [62], CNT/PVDF [59], CNT/polystyrene [63] composites, and etc. In addition, since the degree of the interfacial polarization and charge density are originating from the conductivity difference between the nanotubes and the insulating polymer matrix, the higher resistivity of the composite material, the greater tendency of the composite is to polarize [56,57,63]. It is also notable that the changes of the dielectric constant of the constituent materials in the nanocomposites can attribute to the material polarization as presented by Saleem *et al*. [60] and Cao and Chung [64].

In particular, this time-dependent drift associated with the electrical behavior of carbon-based self-sensing materials can be effectively mitigated using a proper AC-based sensing scheme (that is, to continuously charge and discharge the composite as testing) as proposed by D'Alessandro *et al*. [57]. Moreover, this issue can also be eliminated using a biphasic DC measurement approach according to the recent study by Downey *et al.* [58].

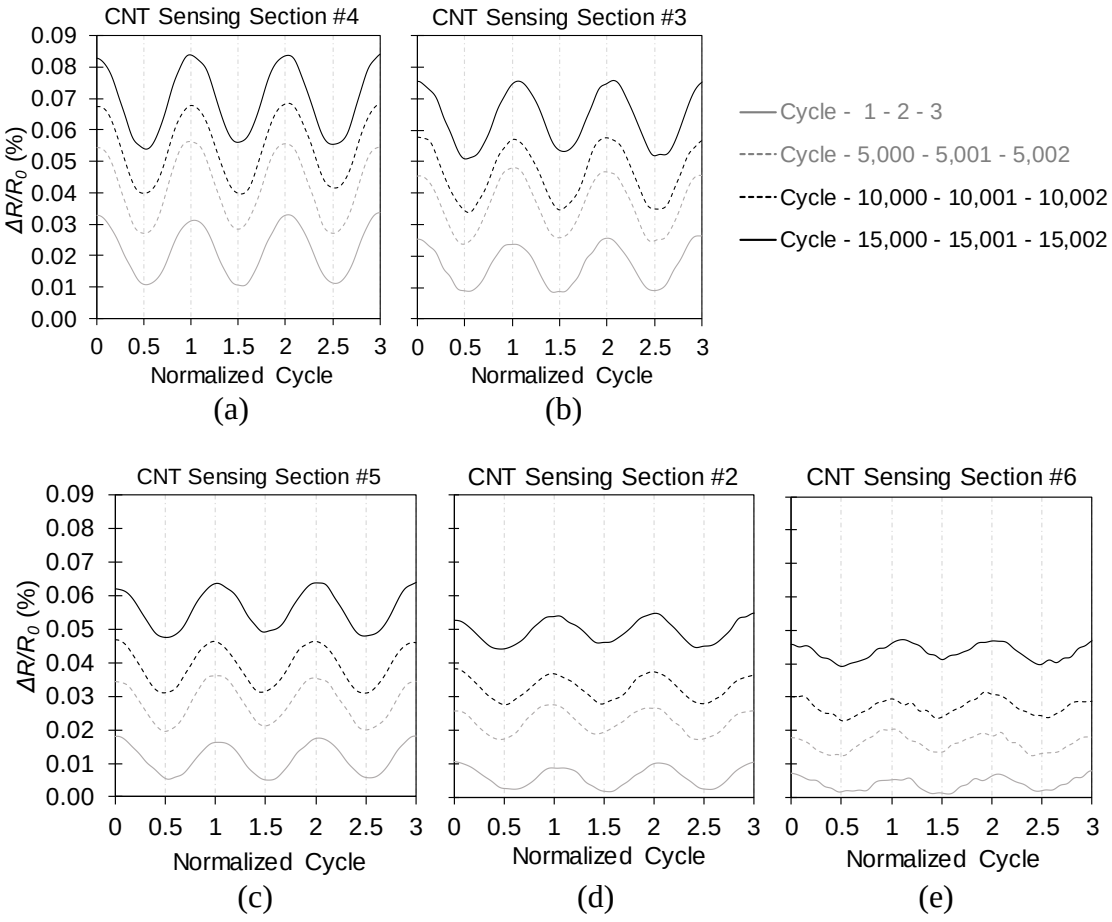

Figure 5.49: The comprehensive transient resistive responses (a – g) of the long CNT sensor on the flexure beam as illustrated in (h) under the repeated loads.

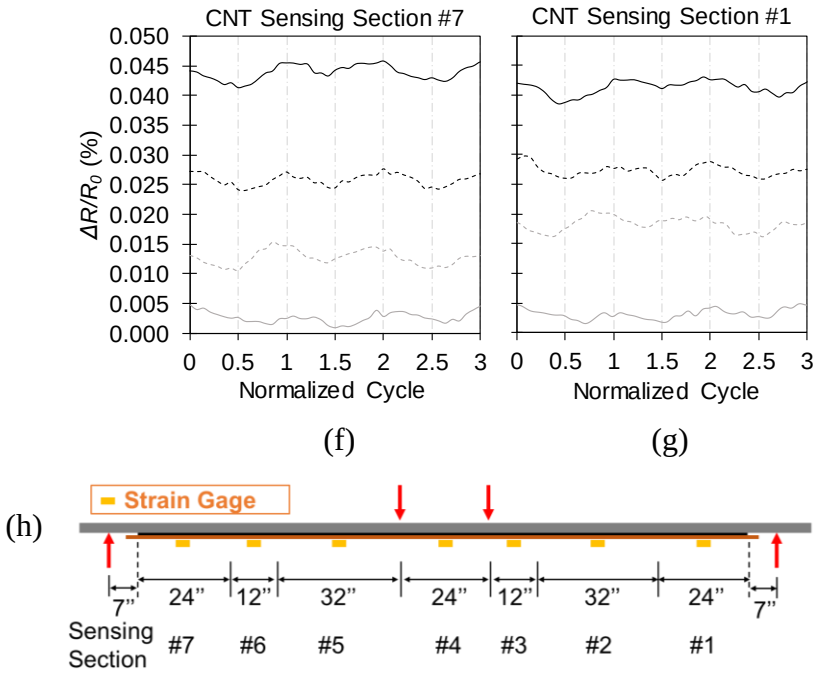

Figure 5.49: continued.

Figure 5.50 shows the typical piezoresistive responses in the CNT sensing sections #4, #3, #6, and #7 of the long CNT sensor deployed on the flexure beam during the 15,000-cycle repeated loads. It is apparent that section #4 shown in Figure 5.50a presents the most linear and stable pizoresistivity (as represented by the slope of the curve, i.e., the gage factor) among other sensing sections. This is mainly attributed to the relatively high and uniform strain field covered by the sensing section #4 within the central loading span of the constant moment. On the other hand, sensing sections #3, #6, and #7 covering the shear span of varying moment, show reduced linearity and some permanent changes in piezoresistivity over the 22-hour loading process. In particular, as observed in sensing sections #6 and #7, the nonlinearity in

piezoresistivity becomes exaggerated when the strain level on the monitored member diminishes in the direction of reducing moment.

Table 5.7 presents the thermal coefficient of resistivity (*TCR*) and gage factors demonstrated by the seven sensing sections of the long CNT sensor as monitoring the flexure beam under the cyclic loads. Clearly, the variations in *TCR*s are comparably small and likely following a decreasing trend as observed in resistivity (see Table 5.6) of the sensing sections #1 through #7, suggesting a desirable repeatability. As for gage factors, except sensing section #4, all other sensing sections display certain amount of permanent increments in the end of the test as comparing with the beginning, revealing slight structural change. This is most likely due to the progressive evolution of microcracks in concrete beam and at the bonding interface near the existing flexural cracks (due to local stress concentration) under the low service-level loading, as confirmed by the AE responses shown in Figure 5.26.

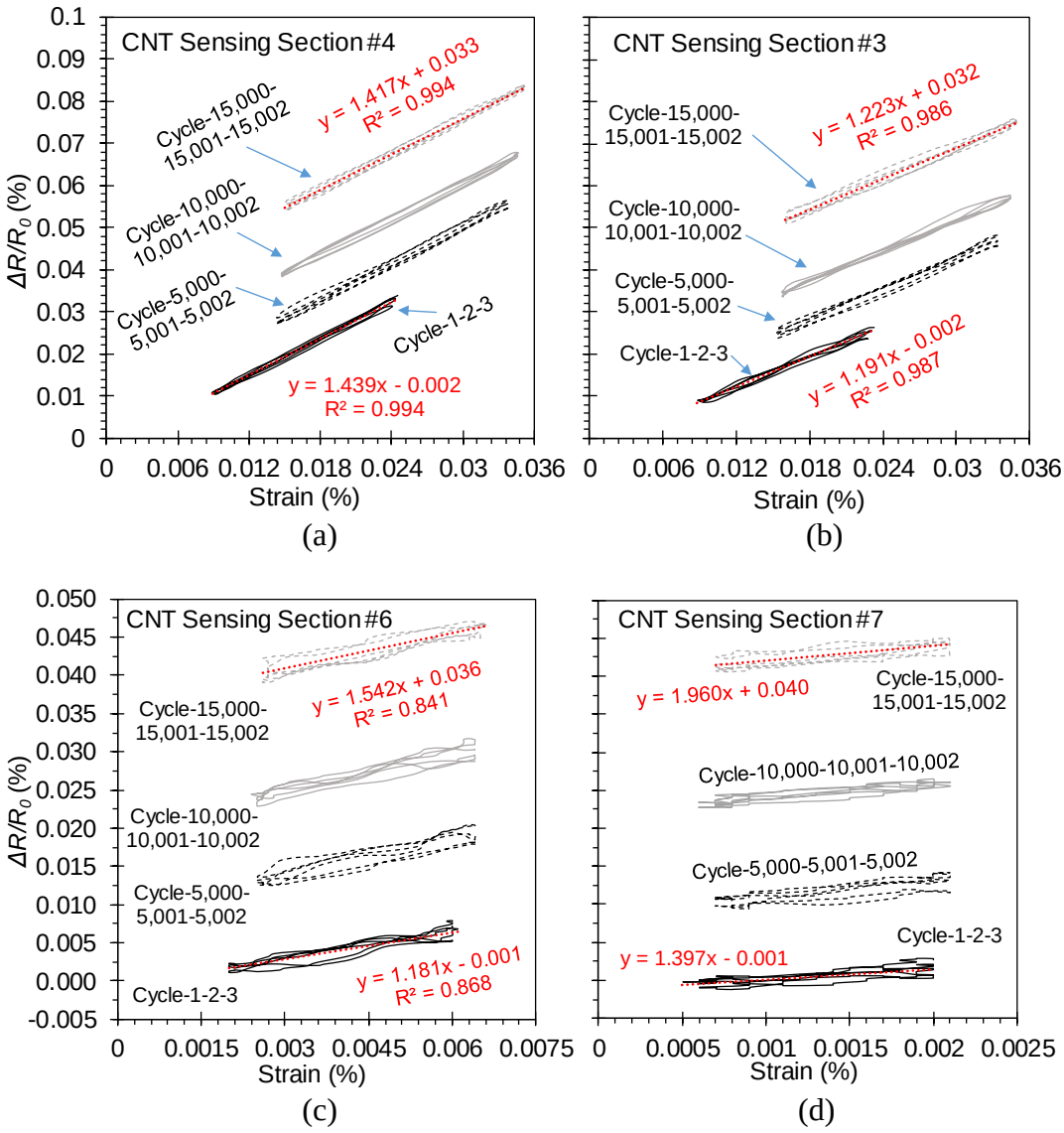

Figure 5.50: Typical piezoresistive responses of the long CNT-based sensor as monitoring the flexure beam under service-level cyclic loads; (a) though (d) showing the piezoresistive responses of sensing sections #4, #3, #6, and #7, respectively.

Table 5.7: Summary of *TCR* and Gage Factors Observed from the Seven Sensing Sections of the Deployed CNT-Based Sensor on the Flexure Beam.

CNT Sensing Section	*TCR* (%/°C)	Gage Factor (in 1st cycle)	Gage Factor (in 15,000th cycle)
#1	0.0204	1.325	2.034
#2	0.0206	1.185	1.327
#3	0.0193	1.191	1.223
#4	0.0191	1.439	1.417
#5	0.0189	1.653	1.842
#6	0.0167	1.181	1.542
#7	0.0162	1.397	1.960

5.3.2.1.2 Static Loading-Unloading Cycles up to Failure

During the mechanical characterization of the GFRP-strengthened flexure beam under the static loading condition, its structural performance was continuously monitored with the deployed long CNT-based composite senor on concrete surface of the beam soffit. Figure 5.51 shows the typical resistive response of the CNT sensor in real-time. In particular, the responses of the sensing section #4 and #1, covering the central region of maximum moment and the partial shear span next by the right support, and the corresponding strains measured at the centers of these sections are presented in Figure 5.51a and 5.51b, respectively. The applied quasi-static loading protocol and the measured temperature at the GFRP surface are shown in Figure 5.51c. Clearly, both sensing sections are effectively responding to the mechanical strains resulted from the applied loads. The sensing section #4 (Figure 5.51a) demonstrates the nearly identical variation trend as the measured strain. However, under a low strain level, section #1 (Figure 5.51b) displays obvious deviations in resistances during the first six hours of loading, which is mainly induced by the dramatic temperature change (green line in Figure 5.51c) in that period.

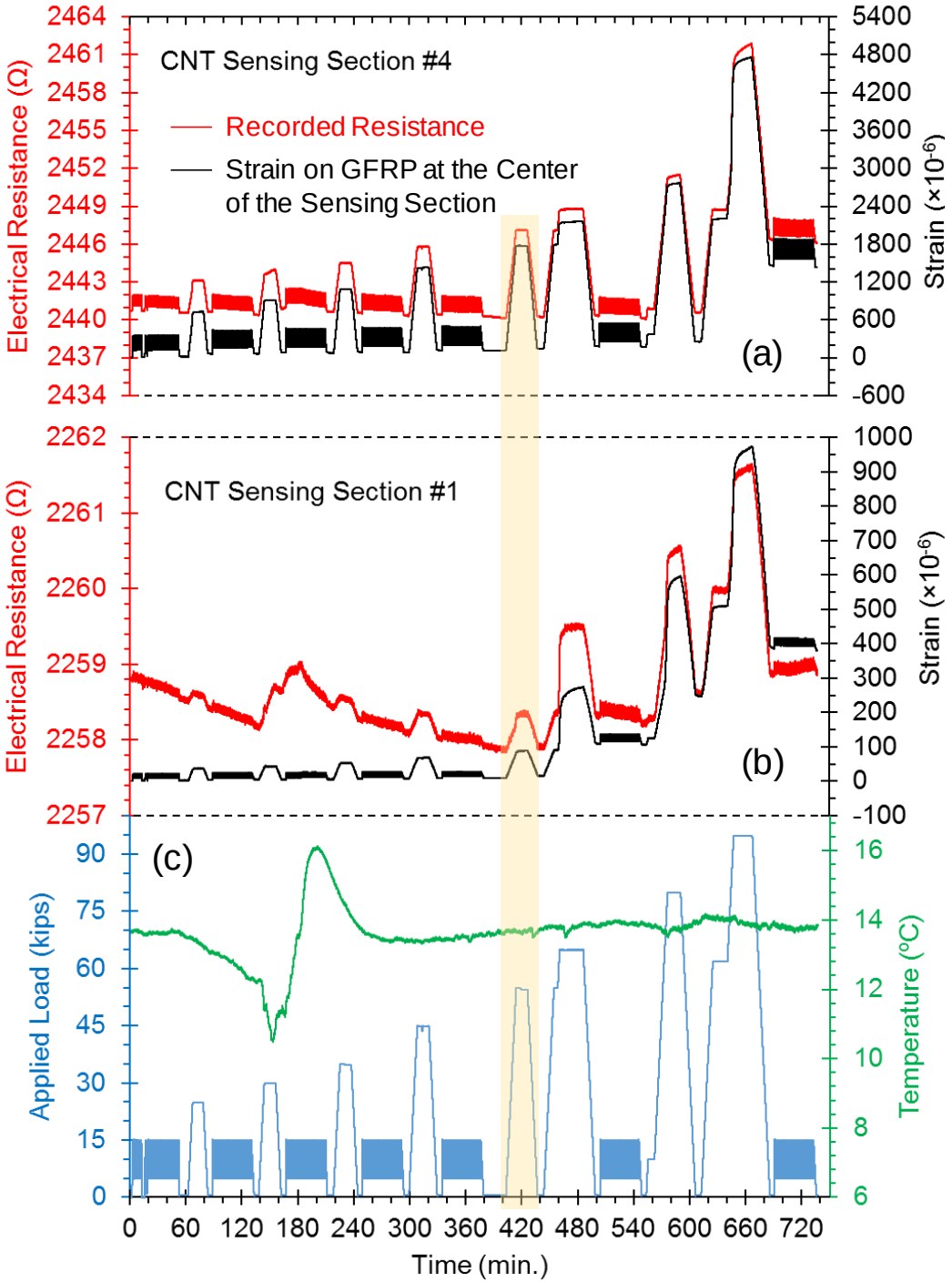

Figure 5.51: Typical transient resistive and strain responses of the selected sensing section (a) #4 and (b) #1 of the long CNT-based sensor as monitoring the flexure beam under the stepwise static loads (blue curve in (c)), and the measured temperature on the GFRP surface during the test (green curve in (c)).

From Figure 5.51, it is apparent that the nanotube networks in the CNT sensor are responding to both the strain and temperature variations simultaneously. Therefore, the bulk resistive behavior represents the resultant effects due to counteracting with different levels of strains and temperature changes. For instance, the sensing section #4 (see Figure 5.51a), under the high strain level, shows minor resistive deviations in the first six hours of loading, as compared to the slightly-strained section #1. Moreover, during the 55-kip cycle (highlighted yellow in Figure 5.51), temperature is relatively constant and then both sensing sections are able to correctly estimate the variation of strain without showing any deviation. It is also notable that sensing section #1 demonstrates the sudden increase in resistance when loading to 65 kips, indicating the incipient damage developed in that section. Similarly, sensing section #4 shows obvious residual resistive change after the 95-kip cycle, suggesting the permanent structural damage occurred in the central loading span. Overall, under the static loading-unloading cycles, sensing sections #4 and #1 show resistance changes of 21 Ω and 3.8 Ω, respectively.

Figure 5.52 shows the synchronous resistive responses of the sensing sections #4 and #1 as the specimen was statically tested to failure. Clearly, both sensing sections display sharp increases in resistance after loading above 96 kips, as the concrete beam starts to yield (see Figure 5.27). Afterwards, the two sensing sections present abrupt resistance changes out of the range of the DAQ due to the fracture of electrodes as the explosive debonding occurs at failure (see Figure 5.31). In total, 42 Ω and 8 Ω of resistance changes are respectively shown by the sensing section #4 and #1 during the final failure cycle. It should be noted that other sensing sections are

presenting the fairly similar trends as sections #4 and #1. Apparently, the proposed long CNT-sensor provides the comprehensive SHM of the flexure beam.

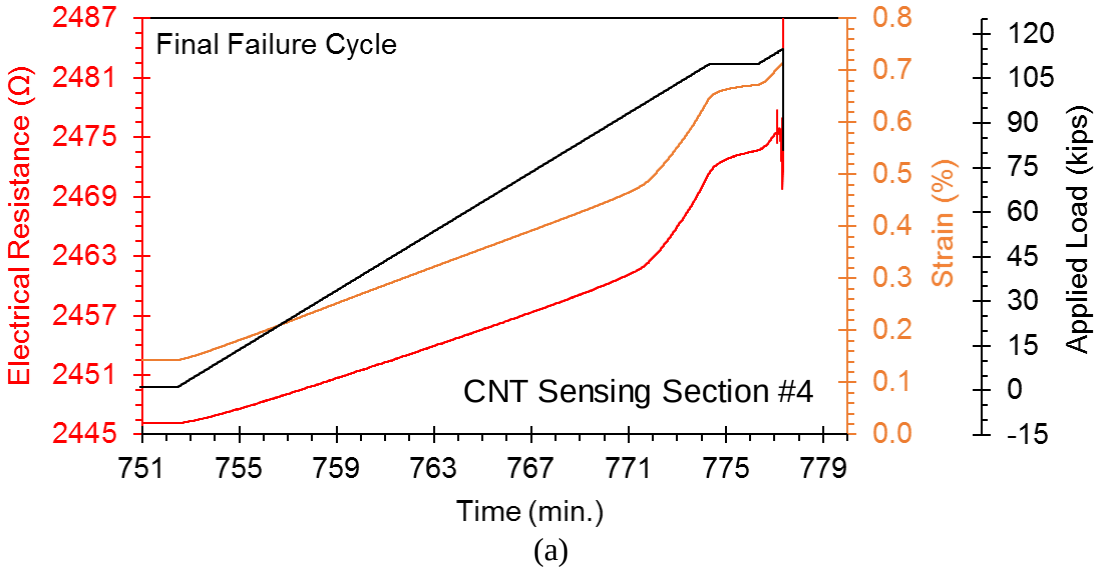

(a)

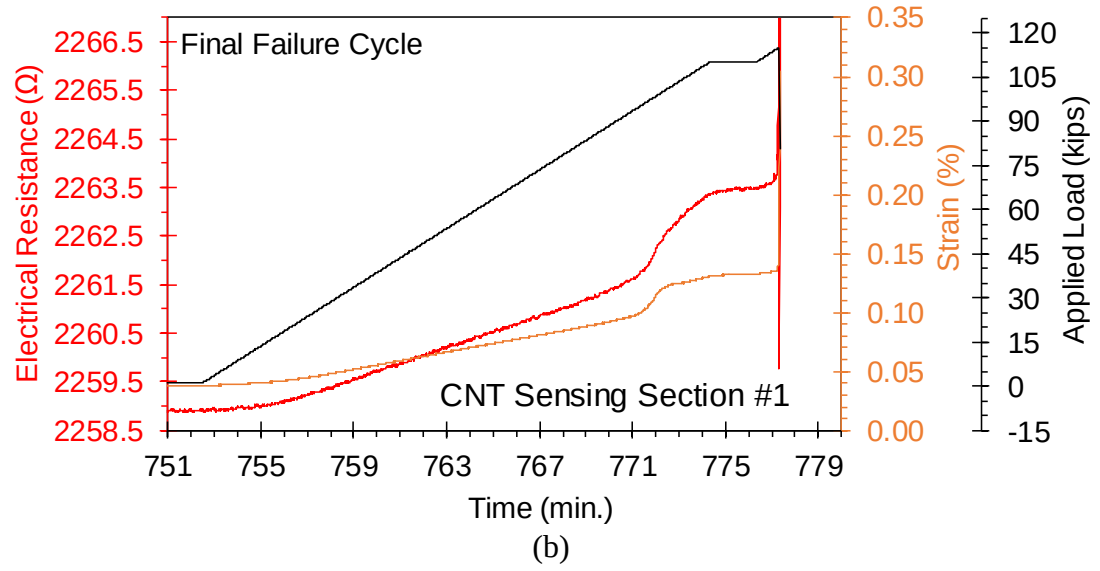

(b)

Figure 5.52: Typical transient responses of the CNT sensors in the selected sensing section (a) #4 and (b) #1 as the flexure beam statically tested to failure.

Figure 5.53 shows the typical piezoresistive response of long CNT sensor in its section #4 under the increasing stepwise loads. For clarity and accuracy in presentation of the experimental data, the total responses are presented in three Figures, 5.53a though c, in accordance to the first four cycles (i.e., 25-kip to 45-kip), the next four cycles (i.e., 55-kip to 95-kip), and the last failure cycle. This sensing section demonstrates the linear elastic piezoresistive behavior up to 0.38% strain and zero residual resistance changes as the flexure beam is loaded to 80 kips. Notably, the instantaneous non-linearity in piezoresistivity appears as the GFRP patch is strained above 0.3% when the beam is loading to 95 kips (see Figure 5.53b), revealing the structural damage developed in the specimen at high loads. In addition, about 0.22% resistance change is permanent at the end of the 95-kip cycle, further indicating the accumulation of damage. As shown in Figure 5.53d, to quantify the elastic piezoresistivity of the sensing section, the response corresponding to the 55-kip cycle is selected to apply the linear regression for data fitting due to the stable temperature observed during this cycle. The gage factor of sensing section #4 is then represented as the slope, i.e., 1.737.

Similarly, the 55-kip piezoresistive responses of the rest six sensing sections are shown in Figure 5.54. It is clear that the four sections including #3, #5, #2, and #6 (Figures 5.54a through d) present the linear elastic piezoresistivity that is quantitatively close to that of the sensing section #4 (i.e., 1.705, 1.683, 1.875, and 1.700), demonstrating the high repeatability in strain sensitivity for SHM. In particular, the sensing sections #1 and #7 (Figure 5.54e and f) display nonlinear piezoresistive behavior with relatively high noise during the loading ramp of the 55-kip cycle. Clearly, the inflection point in piezoresistivity is shown at the extremely low

strain of 0.008% that is even lower than the cracking strain limit of the concrete (i.e., 0.013% according to ACI318-11 with the moduli of rupture $f_r = 7.5\sqrt{f_c'}$ and elasticity $E_c = 57000\sqrt{f_c'}$, giving the concrete cracking strain $\varepsilon_{cr} = f_r/E_c$). Naturally, no structural damage is expected to occur in concrete beam at this low level of load. However, in the statically discontinuous region with the concentrated support reactions, localized effects exists and induces a complex strain field [23]. According to St. Venant's principle, the disturbance regions can extend one member-depth from the supports, which are exactly covered by the section sections #1 and #7 and consequently results in the abrupt piezoresistive nonlinearity as concrete cracks locally.

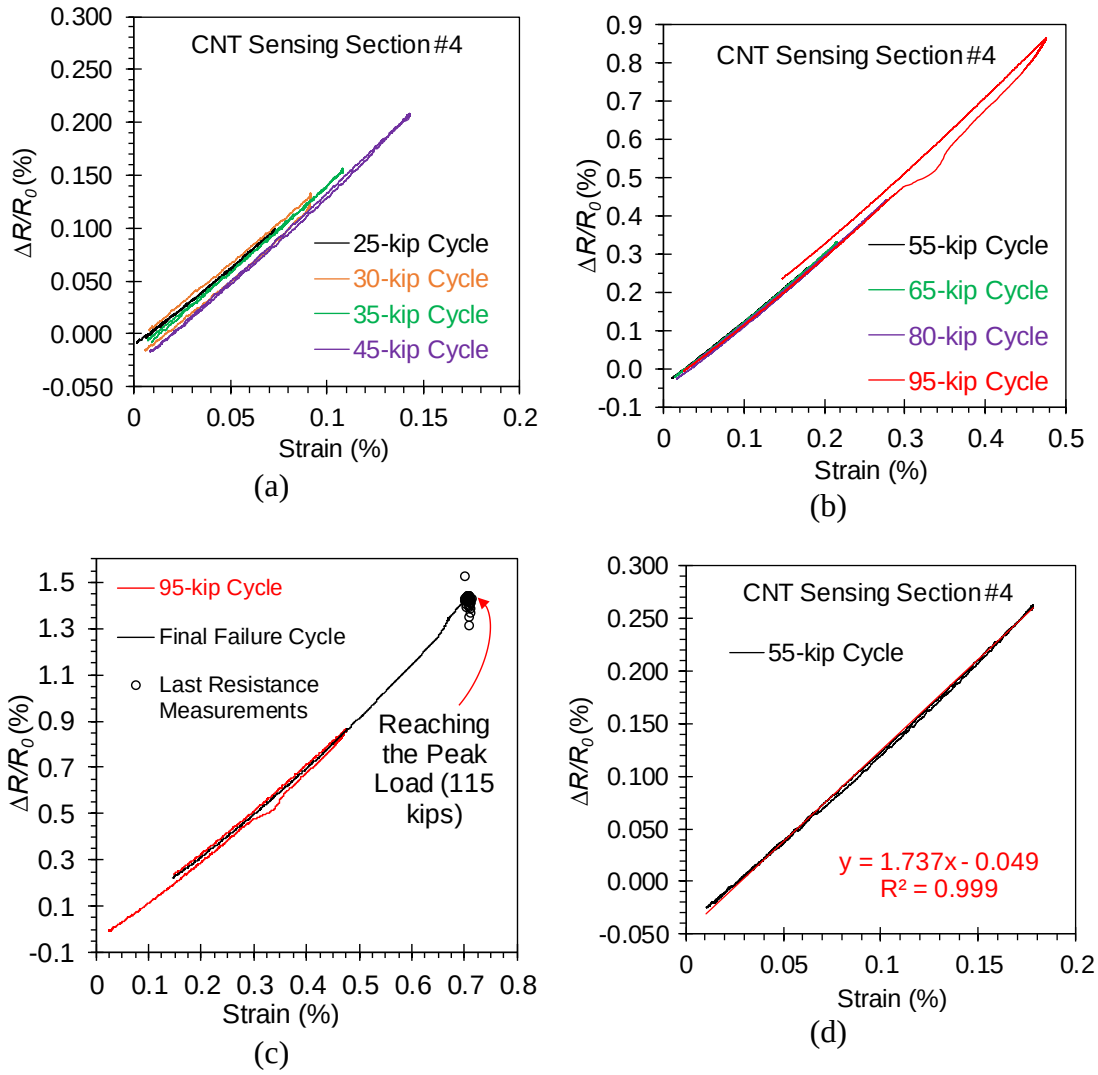

Figure 5.53: Typical piezoresistive response presented in sensing section #4 of the long CNT sensor as the flexure beam statically loaded during (a) 25-, 30-, 35-, and 45-kip cycles, (b) 55-, 65-, 80-, and 95-kip cycles, and (c) the failure cycle; (d) shows the linearized piezoresistivity.

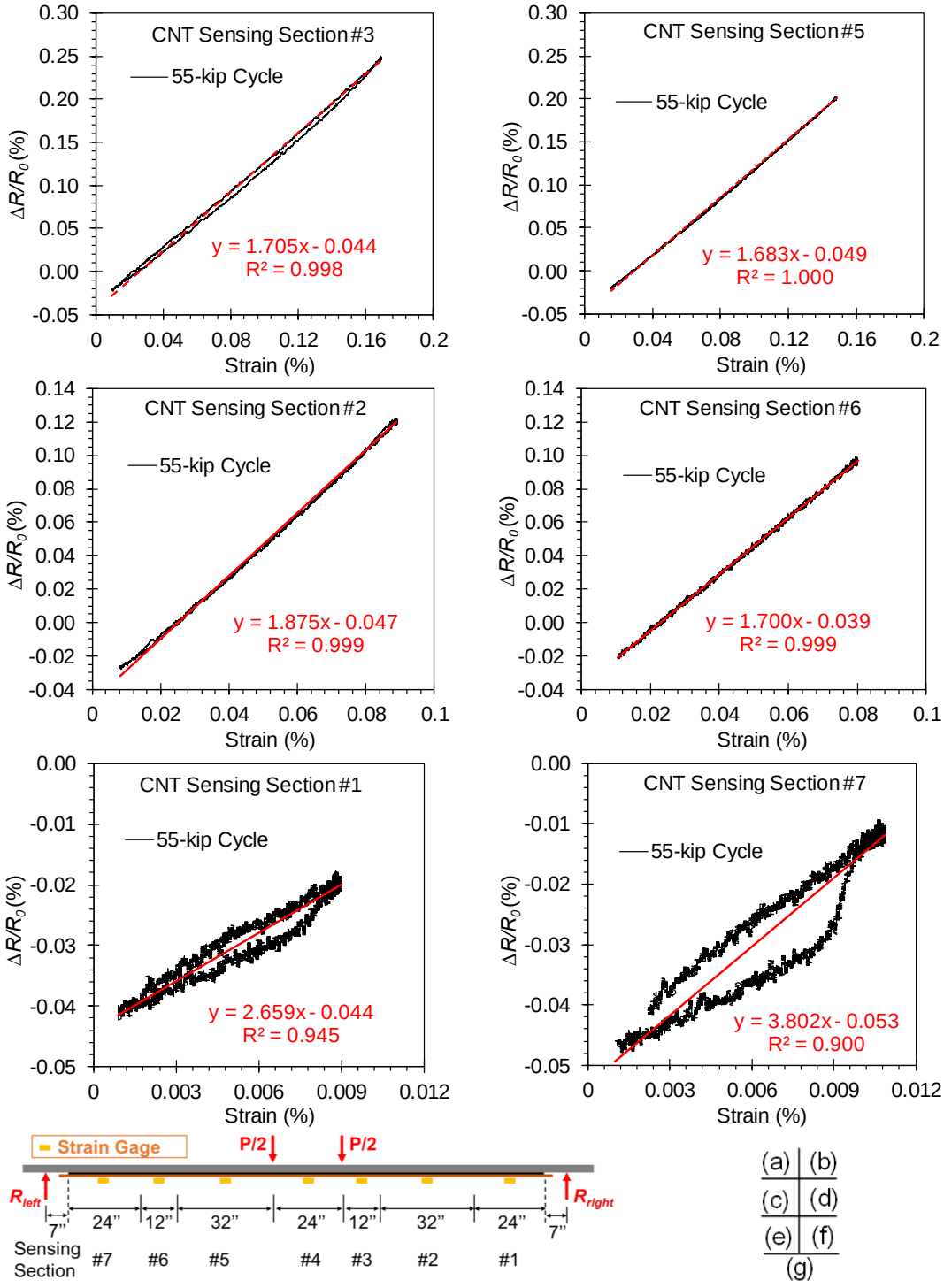

Figure 5.54: Typical piezoresistive responses presented in CNT sensing sections (a through f) covering the shear span (g) of the flexure beam under the 55-kip static loading cycle.

Figure 5.55 shows the piezoresistive responses of sensing section #4 in the CNT sensor as the flexure beam was cyclically loaded during the intervals between consecutive loading-unloading cycles (see Figure 5.51c for the loading protocol). In general, the entire piezoresistive responses are comparably similar, presenting the linear elastic trend with minor deviations in resistance change accumulated during 500 cycles of low service-level loads. In particular, relatively large resistive deviations (about 0.02%) are shown in the third cyclic loading session when temperature changes sharply as observed in Figure 5.51c. As shown in Figure 5.55b and c, the piezoresistivity is nearly constant during the individual cyclic sessions. Additionally, the permanent change in piezoresistivity is shown in the 7^{th} cyclic loading session as comparing with the initial session, which indicates the accumulated damage in the beam specimen. This interesting behavior is also demonstrated in sensing sections #2, #3, #5, and #6 as shown in Table 5.8, suggesting the promising action of the proposed CNT- based sensor for SHM under the low service-level loads.

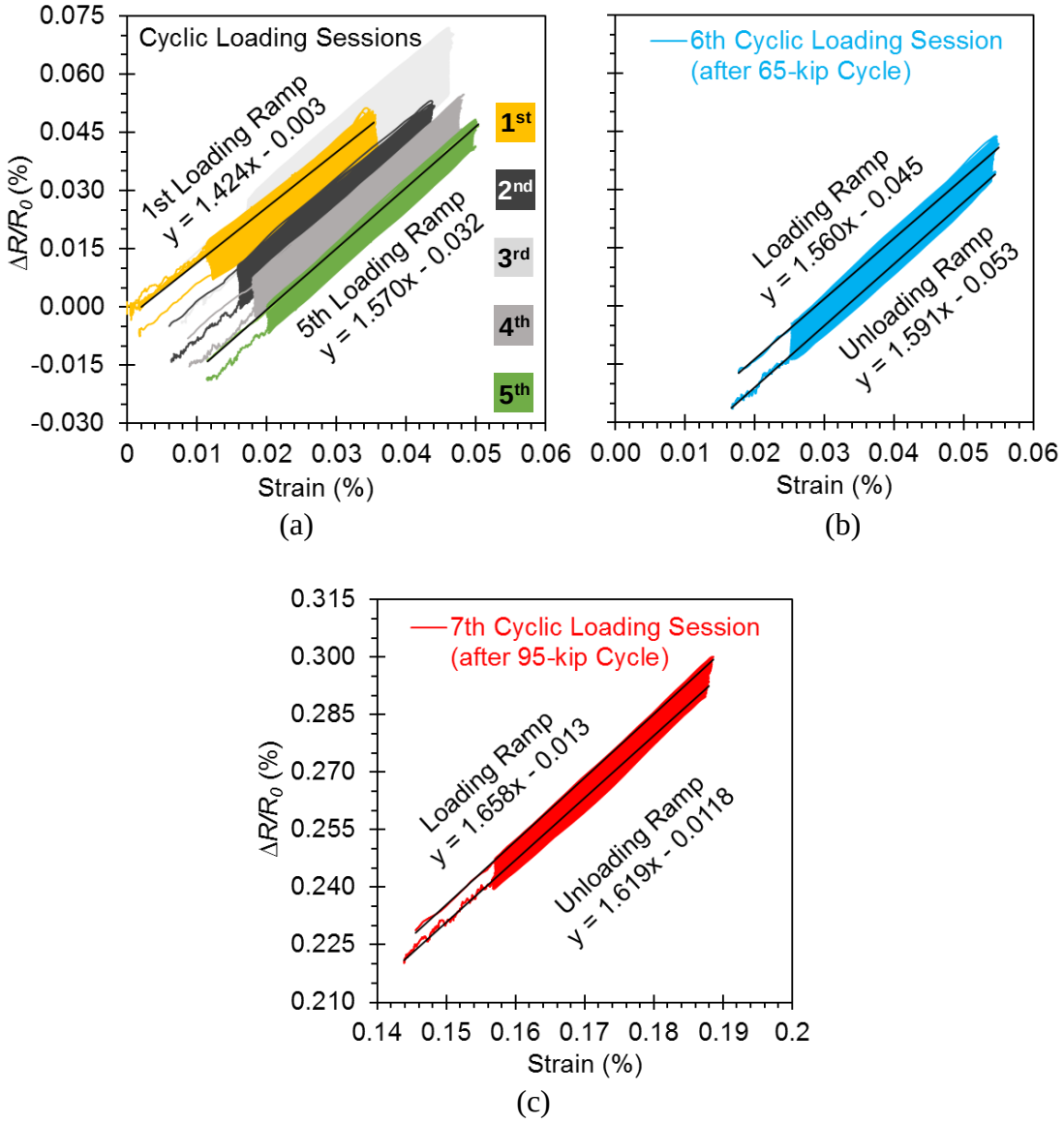

Figure 5.55: Typical piezoresistive responses presented in sensing section #4 of the long CNT sensor as the flexure beam cyclically loaded during (a) the first five, (b) the sixth, and (c) the seventh intervals between successive loading-unloading cycles.

Table 5.8: Linearized Gage Factors Demonstrated by the Sensing Sections of the Long CNT Sensor as the Flexure Beam Cyclically Loaded during the Intervals between Successive Loading-Unloading Cycles.

CNT Sensing Section	Linearized Gage Factors During Cyclic Loading Sessions					
	1st Loading Ramp	5th Loading Ramp	6th Loading Ramp	6th Unloading Ramp	7th Loading Ramp	7th Unloading Ramp
#2	1.347	1.584	1.492	1.559	1.709	1.709
#3	1.227	1.447	1.530	1.567	1.639	1.610
#4	1.424	1.570	1.560	1.591	1.658	1.619
#5	1.516	1.503	1.648	1.644	1.678	1.665
#6	1.547	1.460	1.456	1.701	1.661	1.661

In order to further demonstrate the damage sensing capability of the CNT sensor as the flexure beam statically loaded to failure, the resistive responses of the CNT sensing sections during the last 30 seconds of testing are extracted and reviewed in detail. Figure 5.56a shows the transient resistive response (red line) of the sensing section #4 at beam failure. It is clear that significant local nonlinearities in resistance change appears 15 seconds prior to the beam being rapidly unloaded due to the propagation of GFRP debonding, foreseeing the imminent failure. Nevertheless, the strain behavior (yellow line) does not show any useful reactions (other than two ignorable local pulse of less than 0.001% change in strain) for detecting the structural damage, mainly resulting from that the strain gage is at a discrete location where is far from the source of damage.

In particular, a closer look at the last 4 seconds of the ultimate failure process (Figure 5.56b) reveals that the resistance change sharply declines coincidently with sudden drop of load and abrupt increase in beam deflection. This shows the failure mechanism that as the GFRP patch debonding from the beam, the tensile stress on the

composite is instantaneously diminishing as the load is directly carried by the beam itself. At the meantime, the applied load is far greater than the flexural strength of this under-designed concrete beam (see Section 5.2.1.1), which consequently induces the sudden failure of the beam seen as the dramatic increase in mid-span displacement, suggesting the quick yielding of the steel reinforcing bars. Since the emergency brake was trigged when the concrete beam lost more than 80% member stiffness, the entire MTS hydraulic system was automatically shut down and suddenly unloaded to 65 kips, finally finishing the entire test.

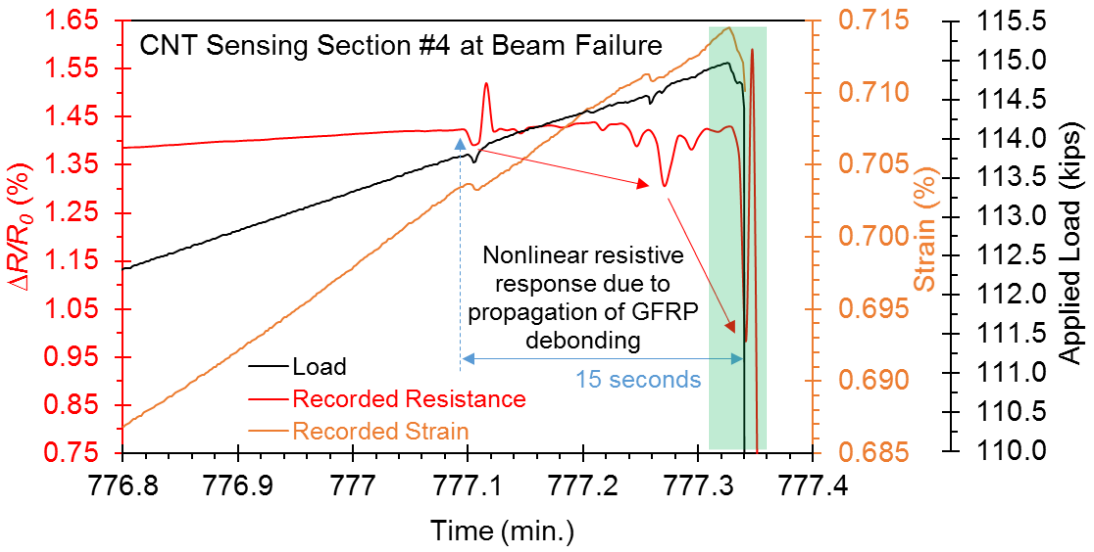

(a)

Figure 5.56: Transient resistive response of the CNT sensing section #4 (a) at beam failure, and showing (b) the enlarged view at the ultimate 4-second failure process, the highlighted zone in (a).

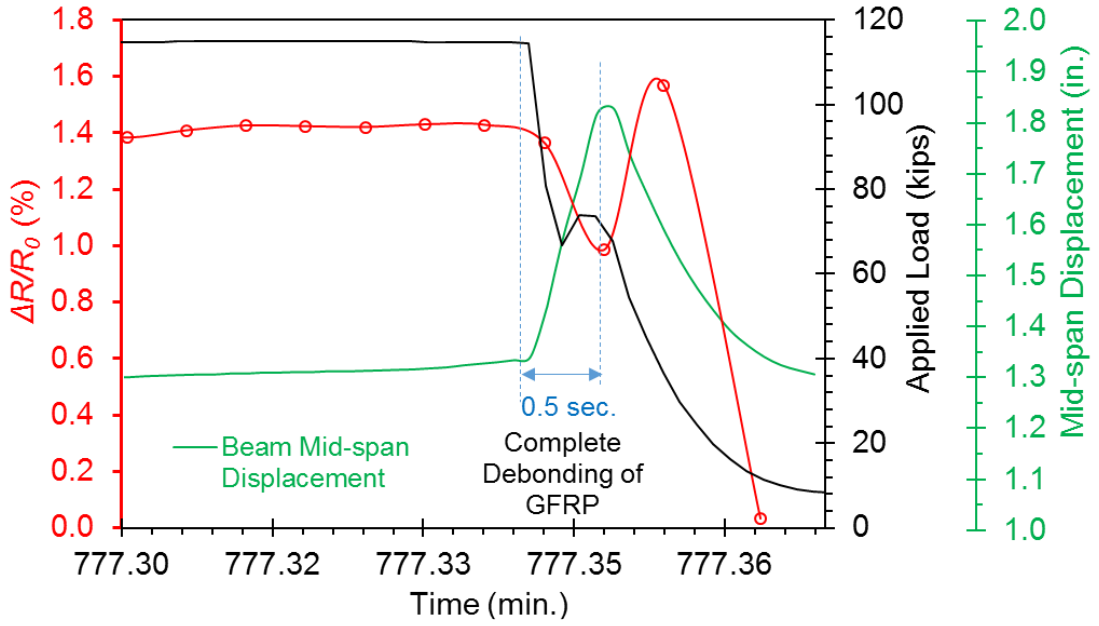

(b)

Figure 5.56: continued.

In addition, as highlighted in Figure 5.56b, the failure process evolves within a rapid period of about 0.5 second which is in good agreement with the real-time snapshots shown in Figure 5.31. It is also worth noting that after failure the resistance change of the sensing section #4 fluctuates intensively (that is most likely due to the post-debonding movement of the GFRP patch, i.e., being tensioned as colliding on the floor (see Frame #5 in Figure 5.31) and then being compressed as bouncing back from the ground) and eventually returns to zero at rest.

Other CNT sensing sections display the consistent resistive responses similar to that of the section #4 when the flexure beam fails. Typical responses from the sensing sections #2, #5, and #7 are presented in Figure 5.57a through c, with the enlarged views of the ultimate failure process shown in Figure 5.57d through f,

respectively. Based on Figure 5.31, it can be found that the debonding failure was initiated in the left shear span where is particularly within the coverage of the sensing section #2. As a result, the strain in this section shows the comparable nonlinearities as the resistance change of the CNT sensor (see Figure 5.57a) while GFRP debonding occurs. However, the strains in section #5 (Figure 5.57b) presents a smooth increasing trend to failure and only the resistive behavior of this sensing section is in responding to the structural damage, similar to the sensing section #4. Additionally, the enlarged views at the resistive responses of these two sensing sections during the ultimate failure process (Figure 5.57d and e) represent the comparable variations that the clearly visible 0.5-second zone shows the complete debonding of GFRP composite and the infinite resistance change after failure is due to the fracture of electrodes.

(a)

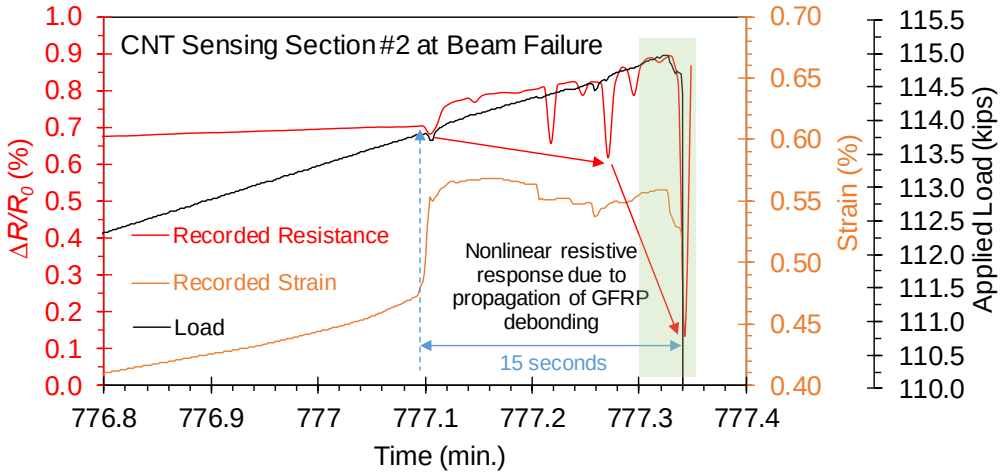

Figure 5.57: Transient resistive responses of the CNT sensing sections #2, #5, and #7 (a-c) at beam failure, and showing corresponding enlarged views (d-f) at the ultimate 4-second failure process, the highlighted zones in (a-c).

(b)

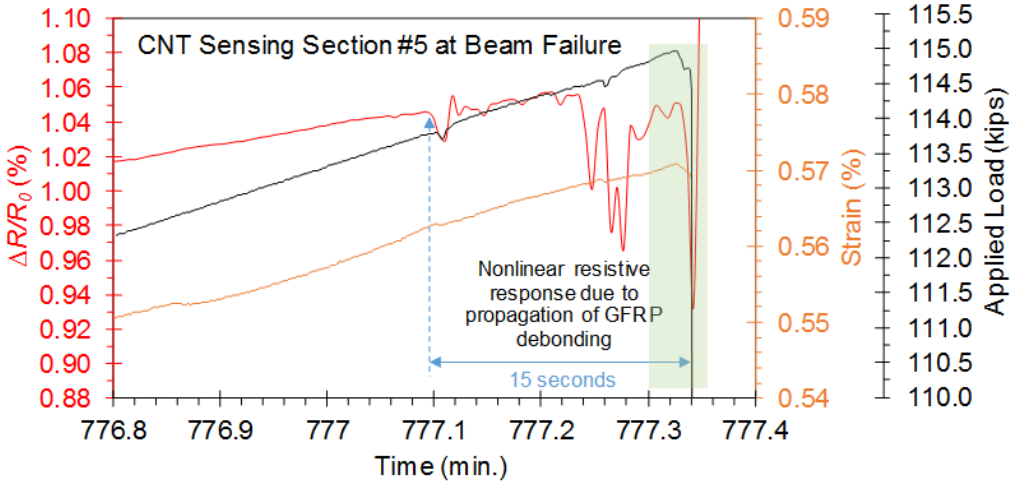

(c)

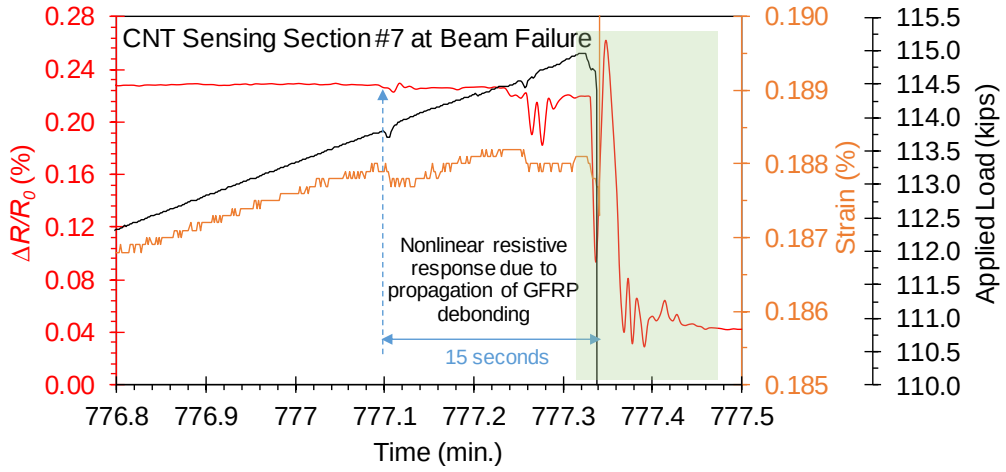

(d)

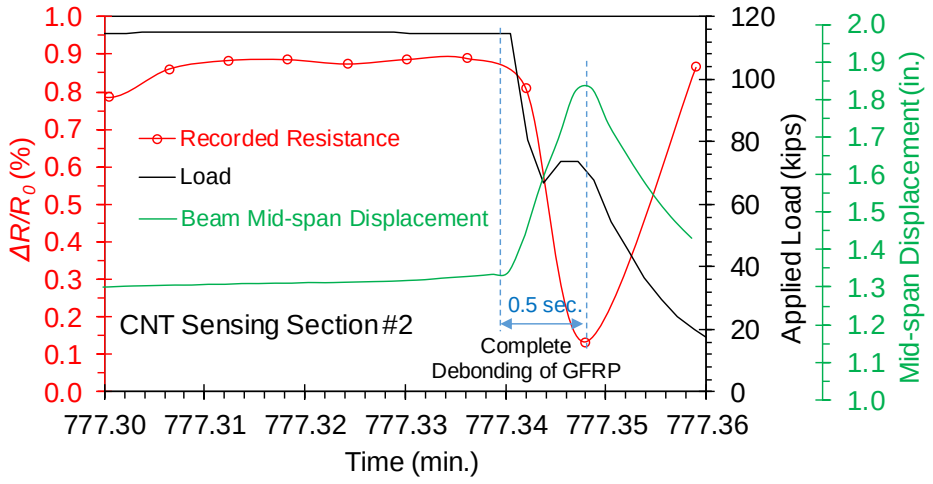

Figure 5.57: continued.

(e)

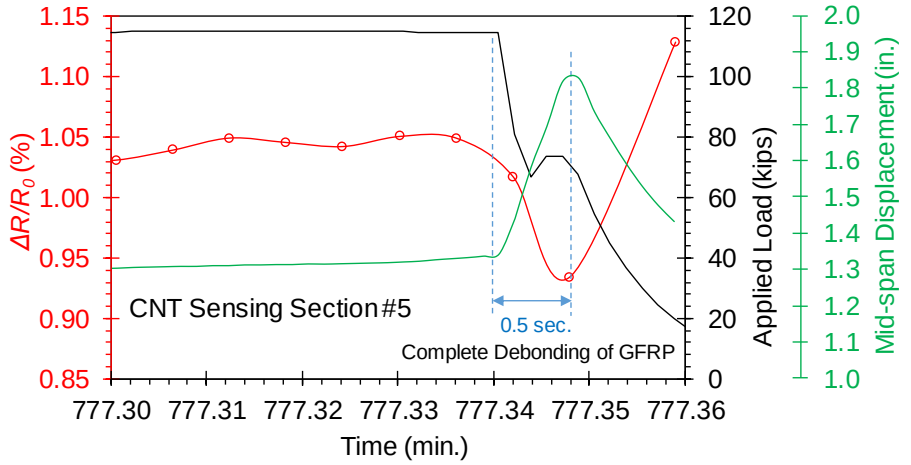

(f)

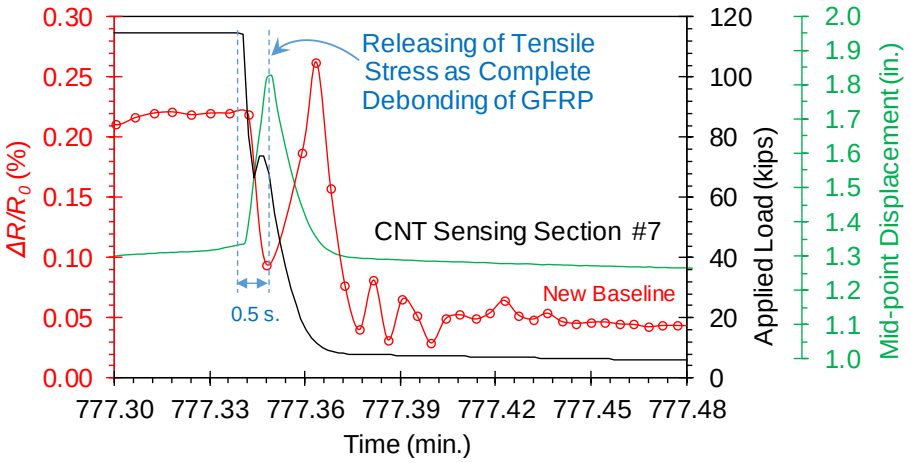

Figure 5.57: continued.

Figure 5.57c shows the resistive response of the sensing section #7 which survived after the beam failed. Noticeable nonlinearities of about 0.1% resistance change are observed during the propagation of GFRP debonding. Coincidently, very minor variations in strains (that is, less than 0.0005%) are also perceived locally. It is notable that after failure the sensing section shows extensive local fluctuations in resistance change (see Figure 5.57f) which are most likely due to the post-debonding movements of the GFRP composite, and then becomes stable at rest.

To conclude, the resistive response of the CNT sensor shows excellent correlations with the beam mid-span deflection and the applied load, validating its damage sensing and SHM capabilities for large-scale concrete members.

5.3.2.1.3 Comparison with Acoustic Emission Responses

The variations of cumulative AE hits versus time during the increasing stepwise loading cycles are shown in Figure 5.58 along with the mid-span displacement history for the flexure beam. In general, as the load increases, the emission count increases. In the first three loading-unloading cycles (i.e., 25, 30, and 35-kip cycles), the AE hits from the sensor on concrete (purple line) present a nearly constant rate of increase merely during the loading ramp and the intermediate service-level cyclic loading sessions, but stay constant as the beam unloaded, exhibiting the so-called Kaiser effect [6,65-67], i.e., the appearance of significant AE activities at a stress level above the previous maximum stress. Meanwhile, it is clear that the AE hits from the sensor on GFRP patch (green line) display the comparable trend as those from the concrete beam, but present a significantly reduced level of counts in essence, suggesting a damage-free state of the composite at the low-level of loading.

Obvious deviation in the AE response is observed as the beam was loaded beyond 65 kips that the AE hits from both concrete beam and GFRP patch are not only originating during the loading ramp, but also occurring as unloading, presenting the known Felicity effect [65,67]. At the meantime, the rate of increase of the AE counts rises considerably, revealing the initiation of permanent damage in both concrete beam and composite patch, such as the microcracking. It is also notable that very minor AE hits are observed from the sensor on GFRP patch (green line) during all intermediate cyclic loading sessions, suggesting a improved structural performance of the

strengthening composite under the service-level loading that is likely not influenced with the progression of damage in concrete.

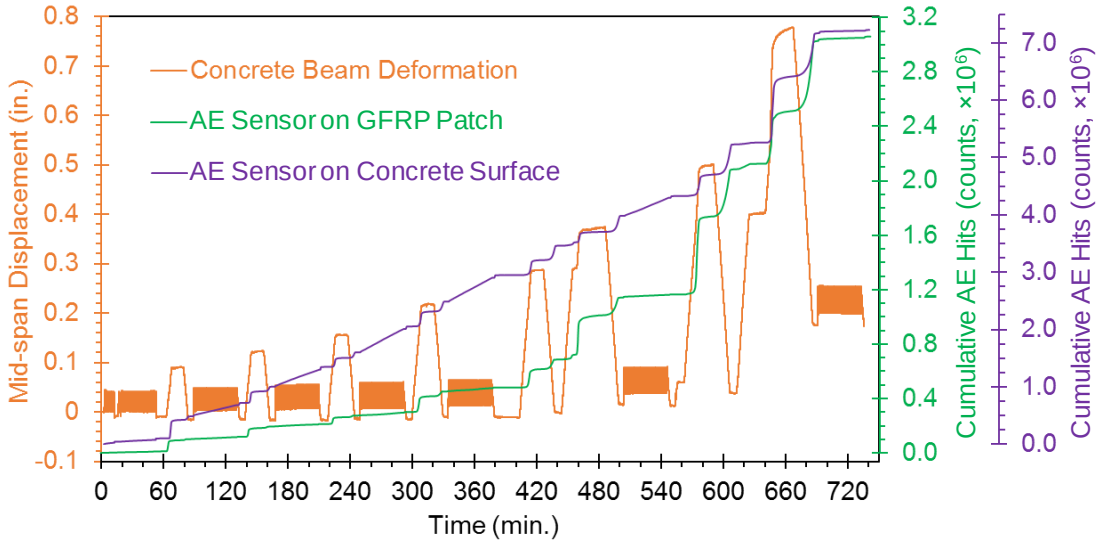

Figure 5.58: Observed cumulative AE hits as GFRP-strengthened flexure beam loaded-unloaded statically.

To highlight the correlations among the AE sensors, CNT-based sensor, and the mid-span displacement sensor for SHM of the flexure beam, typical transient responses from these sensors under the 80 and 95-kip loading-unloading cycles are presented in Figure 5.59. At the relatively high stress levels, the Felicity effect seen as the continuing emission during reloading dominates the AE responses from both the GFRP patch (gray dots in Figure 5.59a) and the concrete beam (orange dots in Figure 5.59b). During the 80-kip cycle, both resistive response (red line in Figure 5.59a) and beam deflection (black line in Figure 5.59b) are showing a smooth trend closely following the loading protocol (blue line). As shown in Figure 5.59c, no visual damage was observed on the composite patch at 80 kips and very minor opening of the existing flexural cracks were perceived several inches above the GFRP-concrete bonding layer (not visible in Figure 5.59c).

Before loading to 95 kips, the beam was held constant at 60 kips for 15 minutes, a lower stress level than the previous 80-kip loading cycle. Interestingly, AE activities were generated and registered at a moderate level from both sensors on GFRP composite and concrete surface (Figure 5.59a and b), most likely following the Dunegan corollary [65,68] and indicating the presence of structural damage. In particular, the CNT sensor display the sharp resistance change as the beam loaded above 82 kips, indicating the accumulation of the substantial damage, seen as the longitudinal matrix cracking in GFRP composite (see Figure 5.59d). At the same moment, a local peak of AE hits appears and the beam deflection increases nonlinearly that confirms the damaged state of the flexure beam, shown as the extensive opening of the vertical concrete cracks in the inset of Figure 5.59d. Therefore, the resistive

response of the CNT sensor is validated and proving to be effective for SHM of both the concrete beam and the strengthening GFRP composite.

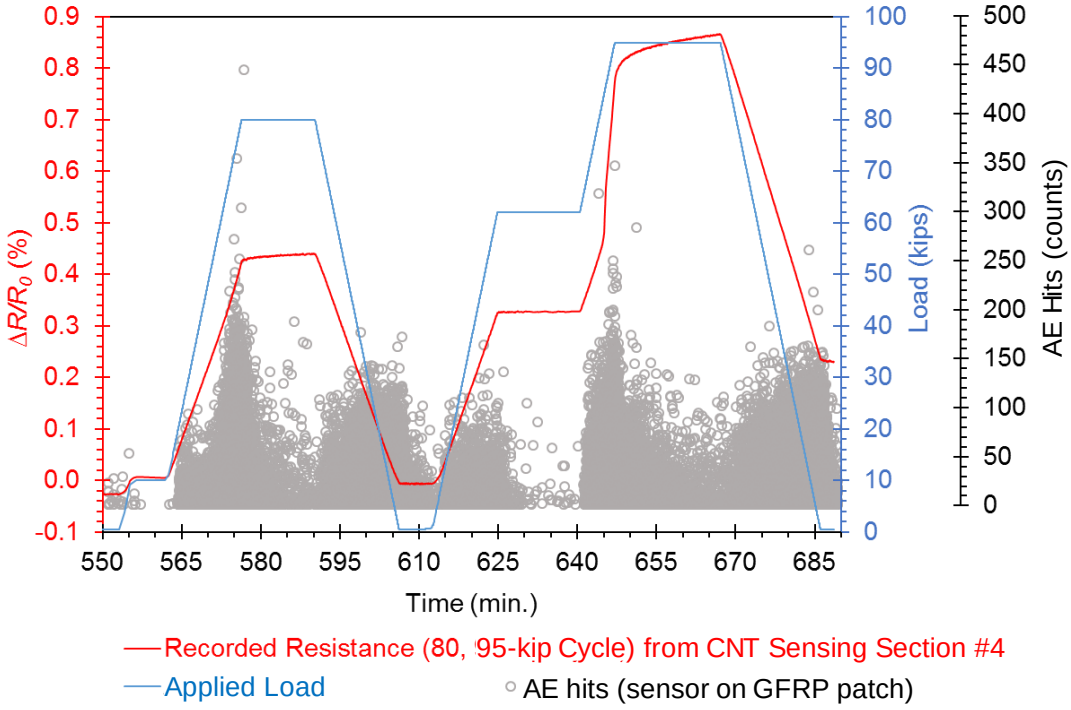

(a)

Figure 5.59: Transient responses of (a) resistance change and AE events from GFRP composite and (b) beam deflection and AE events from concrete beam during the 80, 95-kip loading-unloading cycles, and corresponding snapshots (c, d) showing the visual condition of the beam specimen.

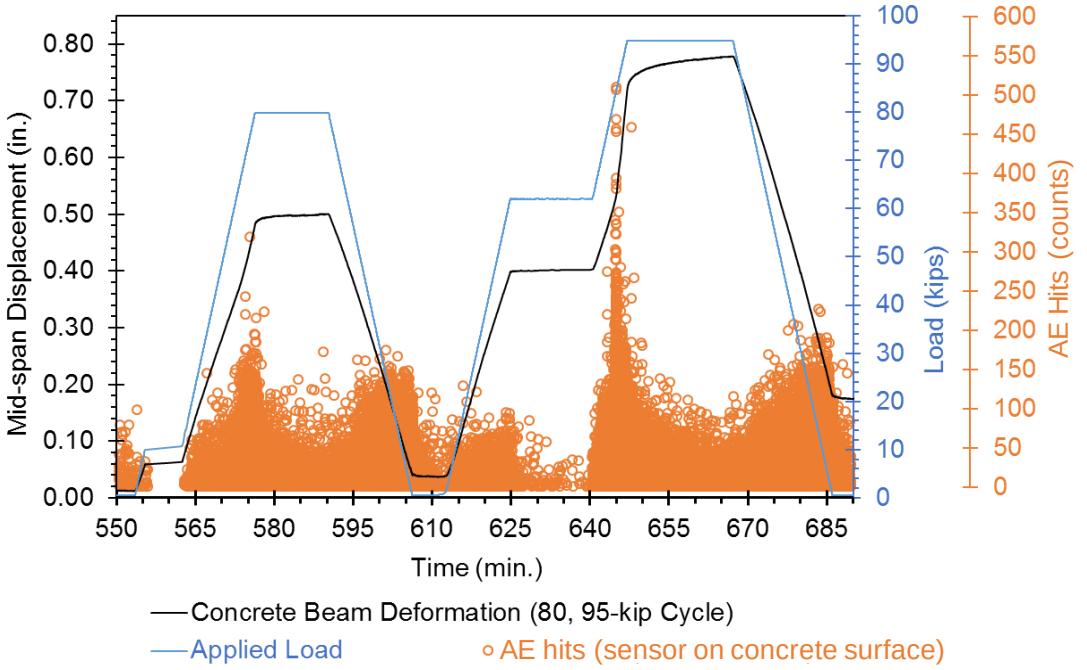

(b)

(c)

(d)

Figure 5.59: continued.

Figure 5.60a shows the cumulative AE hits collected from the sensor on GFRP composite patch and electrical resistance change of the CNT sensor as a function of strain during the incremental stepwise loading. Clearly, a strong correlation is

observed between the AE counts and resistance change at the peak strain of each loading cycle. The aforementioned Kaiser effect of AE counts is shown in the first six cycles that an obvious increment in AE counts is observed as the applied load is increased beyond the previous peak load. Meanwhile, the resistance-strain curve is nearly identical for each cycle, indicating the global elastic deformation of the GFRP composite. Therefore, it can be deduced that a good control on the structural performance of the strengthening composite is maintained, although microcracking damage might be developed inside as suggested by the increase of AE counts. Notably, substantial structural damage initiated during the 95-kip cycle results in the nonlinearities in both AE and resistive responses.

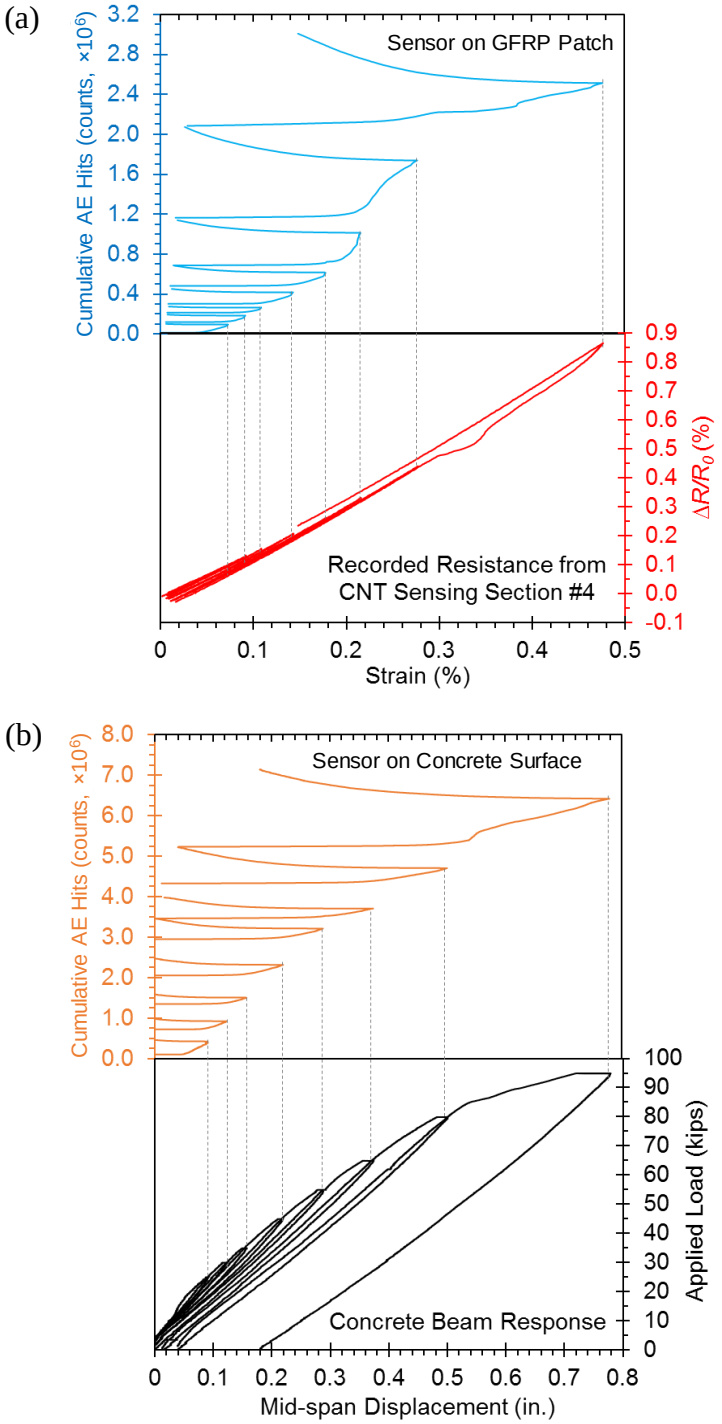

Figure 5.60: (a) Accumulated AE events from GFRP composite patch and electrical resistance change of the CNT sensor as a function of strain and (b) accumulated AE events from concrete beam and applied load as a function of beam deflection during the incremental stepwise loading.

For comparison, Figure 5.60b represents the cumulative AE hits from the other sensor on concrete surface and applied load as a function of mid-span displacement during the incremental loading-unloading cycles. As expected, a close correlation is observed between the AE counts and the structural performance of the GFRP-strengthened concrete beam. Clearly, the progression of concrete cracking due to increasing loading, shown as the growth of AE counts, most likely results in the gradual decrease in member stiffness that evidences as the declining of the slope of the force-displacement curve. The consistent presence of the Kaiser effect as loaded to 80 kips indicates that the concrete has experienced stress levels below 75%-85% of its ultimate strength [6]. In particular, the sharp increase of AE counts corresponding to the observed plastic deformation in the 95-kip cycle reveals the accumulation of severe damage in the concrete beam.

Figure 5.61 shows the cumulative AE hits collected from both sensors as the flexure beam statically tested to failure. It is apparent that the AE counts follow a strong correlation with the deformation of the concrete beam. The rate of increase of the AE counts is suddenly rising after the beam reaching 0.8 in. of mid-span displacement (i.e., loading beyond 97 kips), indicating severe damage to the concrete beam developed at the high stress levels. In addition, during the 3-min. load-hold at 110 kips, it is observed that substantial AE counts were registered from the sensor on concrete surface (purple line) which follows the previously mentioned Dunegan corollary (see Figure 5.59a and b), indicating the imminent failure. At the ultimate failure point, AE counts from both concrete beam and GFRP patch display the prompt and sharp increments.

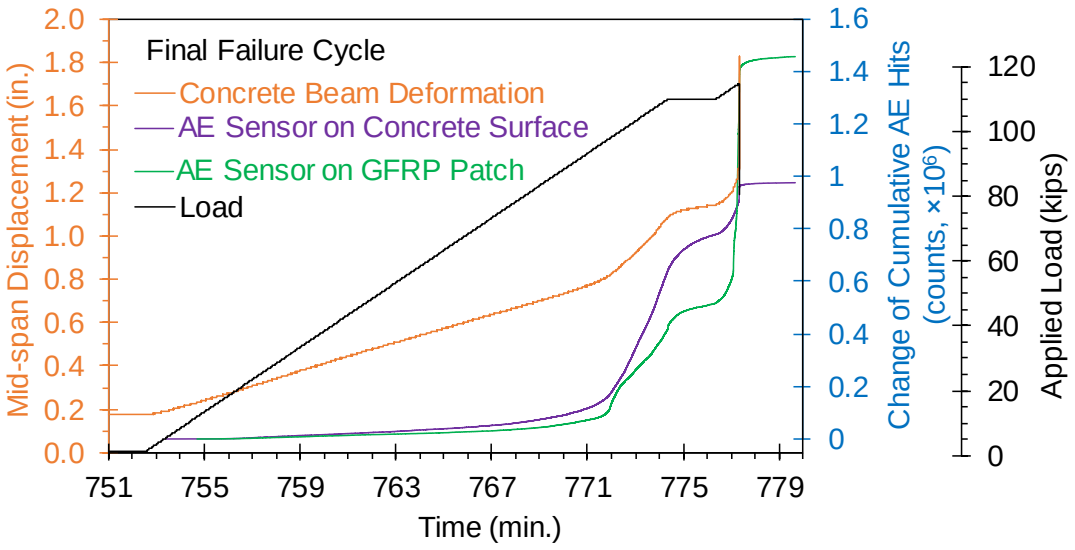

Figure 5.61: Cumulative AE counts as flexure beam statically tested to failure.

Figure 5.62a looks at the instantaneous relationship between acoustic emissions and resistance change at the failure of the flexure beam. Apparently, the resistive response of the CNT sensor is showing a close correlation with the registered AE activities that the local nonlinearities in resistance change appear as soon as the AE hits collected from the sensor on GFRP composite (green spikes), validating the formerly defined 15-second zone of GFRP debonding shown in Figures 5.56 and 5.57. Additionally, a closer view of the last 4-second failure process represented in Figure 5.62b reveals that tremendous amount of AE hits are observed from sensor on the concrete surface (purple dots) instantly as the GFRP patch completely debonded from the concrete beam, indicating the sudden fracture of concrete. Coincidently, in this 0.5-second fracture period, acoustic emissions recorded from the sensor on GFRP patch (green dots) present a moderate level of counts, most likely due to the rapid releasing of tensile stresses as the composite debonding from the concrete surface.

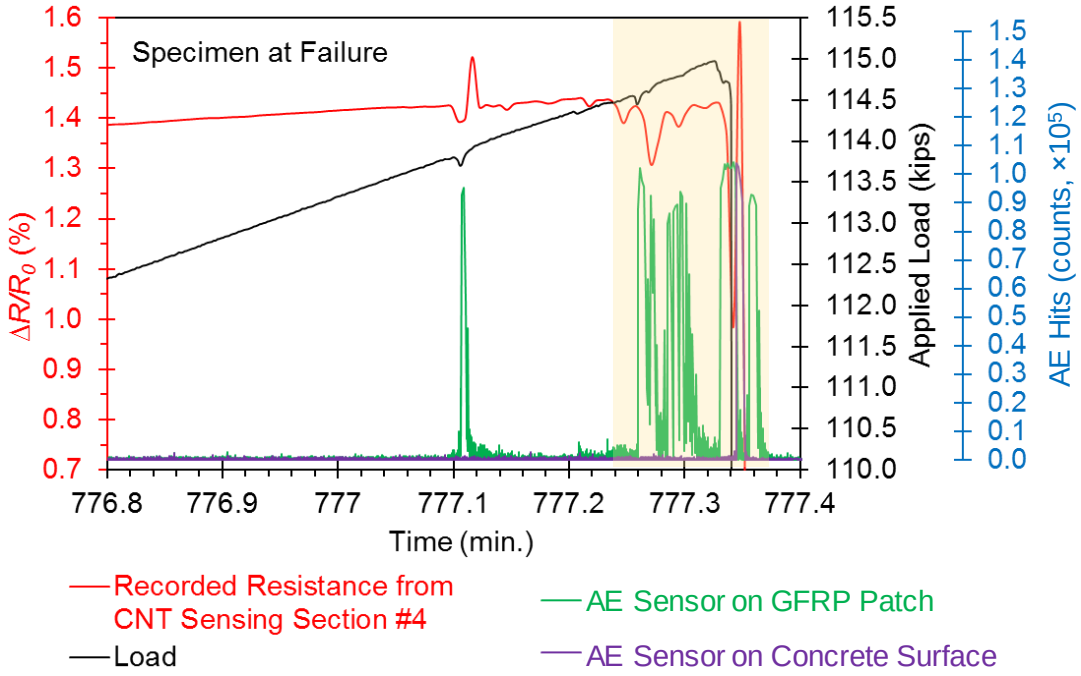

(a)

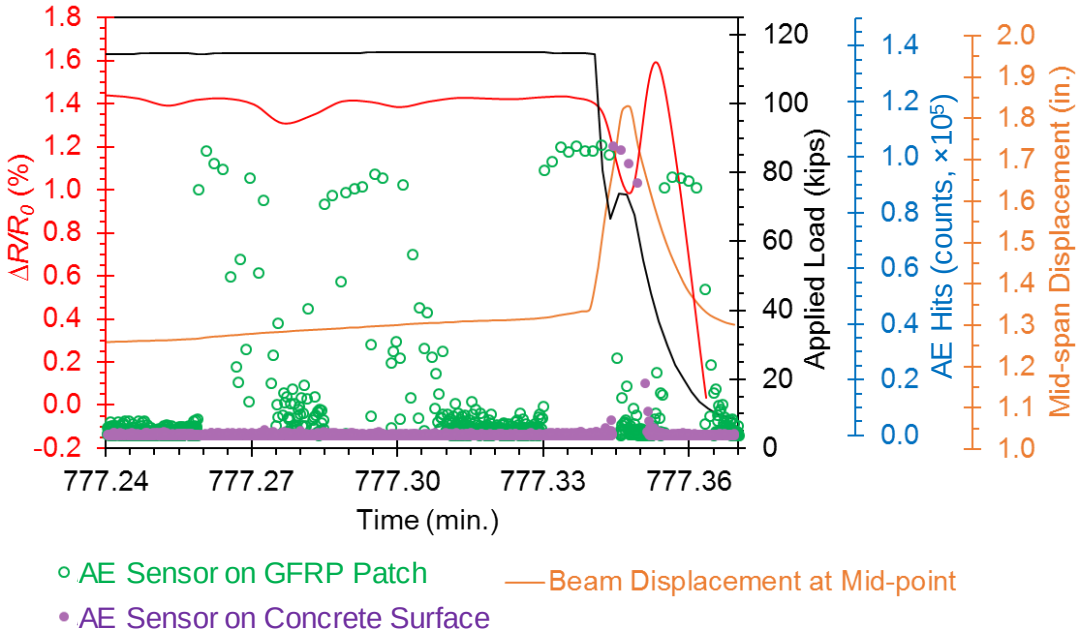

(b)

Figure 5.62: Instantaneous responses (a) of AE hits and resistance change with a closer view (b) of the ultimate 4-second failure process, the highlighted zone in (a).

Figure 5.63a shows the relationship between the resistance change and cumulative AE counts (collected from the sensor on GFRP composite) during the entire static loading test. Clearly, significant deviations on the bulk shape of the response are observed in the 95-kip cycle. As explained previously, this results from the damage (i.e., fiber bundle splitting, see Figure 5.59d) developed in the composite at the high stress levels. In particular, the relation corresponding to the final fracture (red) presents extensive local nonlinearities, most likely attributed to GFRP debonding, which is useful information for SHM of the local bonding interface between the GFRP and concrete.

Similar damage sensing features are also demonstrated in the relationship between the beam deflection and cumulative AE hits recorded from the sensor on concrete surface as shown in Figure 5.63b. It is observed that a certain amount of AE activities are generated during the intermediate cyclic sessions, indicating a relatively reduced structural performance of the concrete beam under the service-level loading, once cracking damage developed inside. Particularly, a smooth and sharp increasing trend is shown, revealing the brittle fracture of the concrete beam at failure.

To conclude, it can be seen that the proposed CNT-based sensor is able to detect structural damage initiated in both the strengthening composite and the concrete member, as well as the incipient/imminent failure of the entire structural system in real-time.

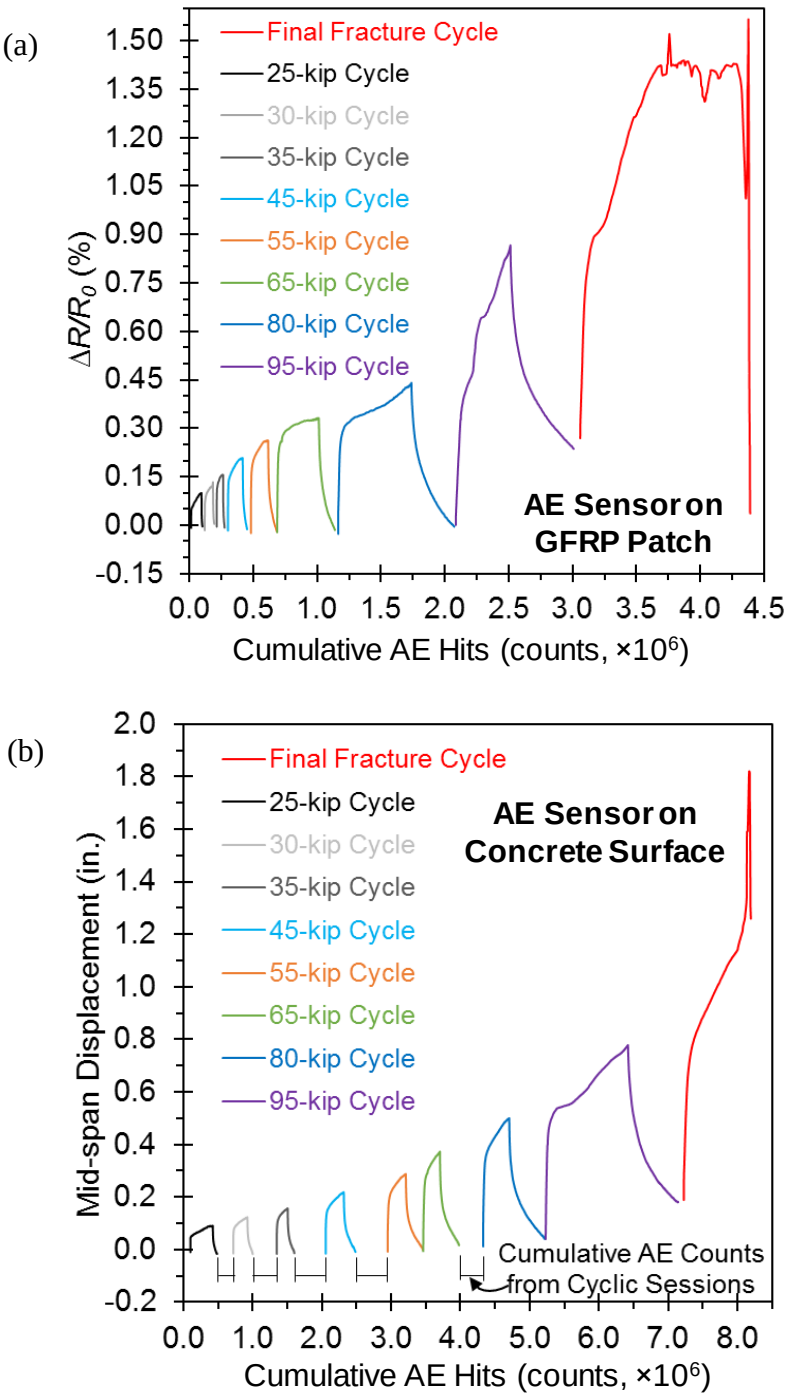

Figure 5.63: Relationships between (a) resistance change with respect to accumulated AE counts from GFRP composite patch and (b) beam deflection with respect to accumulated AE counts from concrete beam during the entire static loading test of the flexure beam up to failure.

5.3.2.2 SHM of the Shear Beam

5.3.2.2.1 Cyclic Loading Condition

Figure 5.64 shows the typical transient resistive response of the CNT sensors underneath the GFRP U-wraps on the shear beam as cyclically loaded from 15 to 35 kips at 0.2 Hz. In particular, the presented resistance data in Figure 5.64a are from the sensing section #8 which covers the soffit of U-wrap #3, the one next by the left loading point (see Figure 5.22 for the position). Clearly, the CNT sensing section is effectively responding to the 15,000 cycles of repeated loads. In general, this sensing section shows a constant change of 0.75 Ω, corresponding to the peak and valley loads. During the first 13 hours of testing, the temperature is relatively stable (Figure 5.64b), but minor drift is observed in the resistive behavior. This phenomenon is consistent with the resistive response of the long CNT sensor deployed on the flexure beam and most likely caused by the interfacial polarization of the CNT-based composite as explained in Section 5.3.2.1.1.

In contrary to the constantly stable loading protocol (Figure 5.64c) and beam deflection (see Figure 5.34a), a sudden jump in resistance appears as the temperature changes rapidly during 800-900 min., showing the inherent thermoresistivity of the CNT sensor that likely dominates the bulk resistive behavior at low strain levels (i.e., less than 50 με, see Figure 5.35 for strain distribution).

A closer view at the resistive response of sensing section #8 at several selected times during the cyclic testing is presented in Figure 5.64d. It is clear that the overall shape of the resistance change curves is barely sinusoidal following the applied load (see Figure 5.35) with the peak and valley resistance change appearing at the half-cycle points. Additionally, the fluctuations in resistance change are also visible and

likely caused by the local nonuniformity in the strain distribution under the low service-level loads. The corresponding piezoresistive behaviors are shown in Figure 5.64e. It can be observed that all curves follow a linear trend. The linearized gage factors of 1.08 and 1.12 observed in the beginning and ending of the cyclic testing are fairly close and therefore present a good repeatability of the deployed CNT sensor and indicates a great structural condition of the strengthening composite after withstanding the applied 15,000 repeated loads.

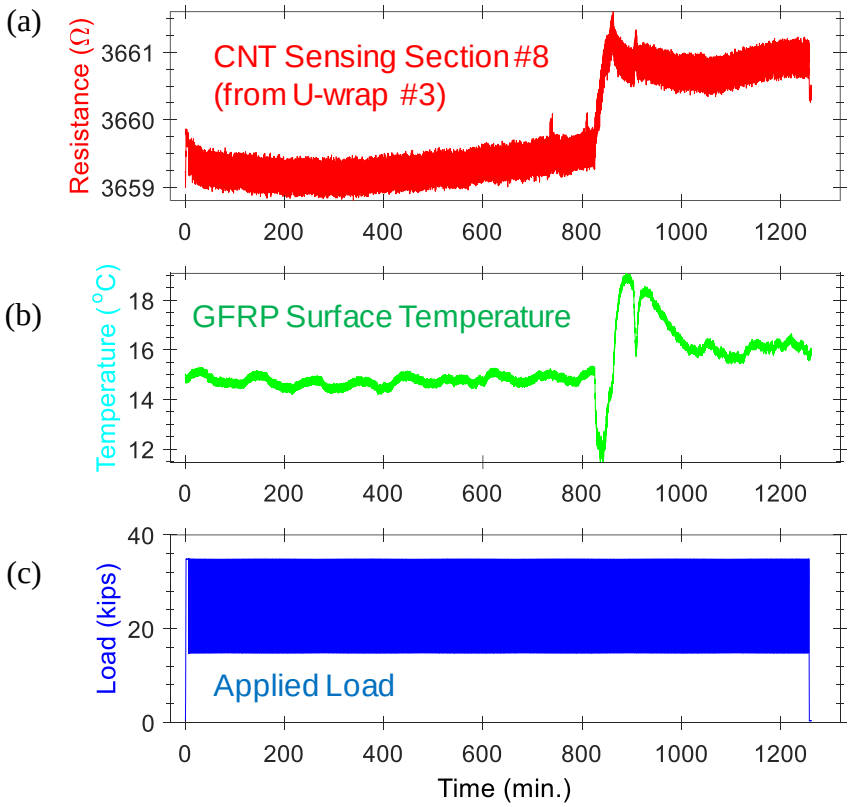

Figure 5.64: Typical resistive response of the CNT sensor underneath the GFRP U-wraps on the shear beam as cyclically loaded, including (a) the total resistive response of sensing section #8, (b) the measured temperature profile during the 22-hour test, (c) the applied load, (d) enlarged view of resistive response at four points of time, and (e) the corresponding piezoresistive behaviors of the sensing section #8 at selected cycles.

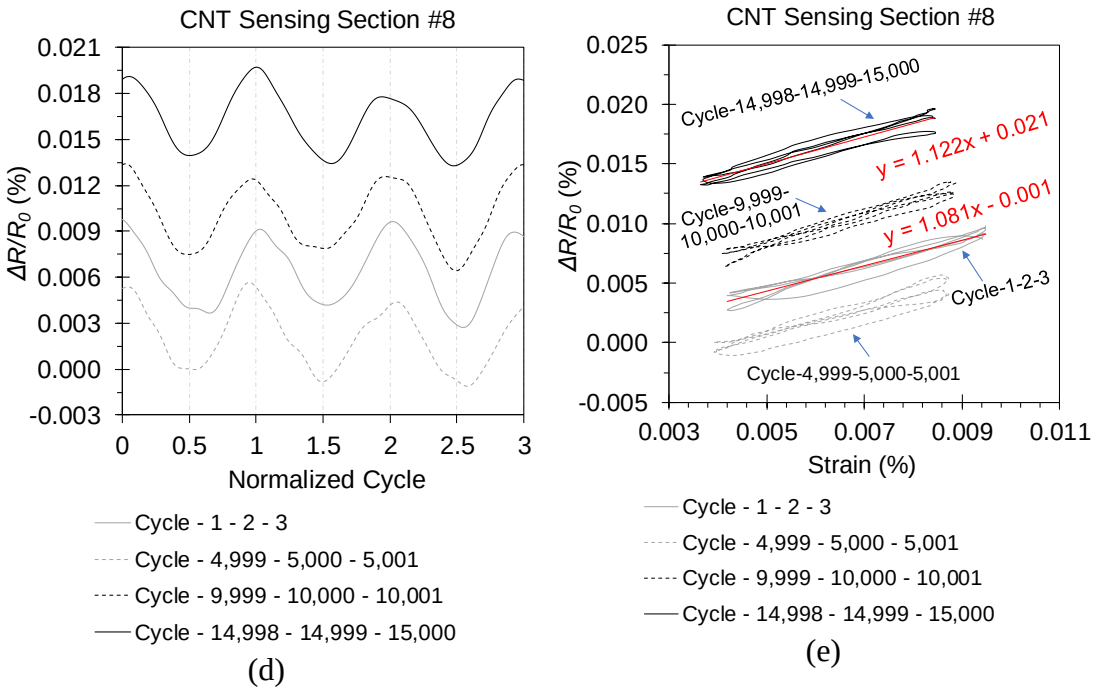

Figure 5.64: continued.

In addition to Figure 5.64, the resistive responses of the other two sensing sections (i.e., #5 and #2) covering the soffits of the U-wrap #2 and #1 are shown in Figure 5.65. Due to the lower strain levels in these two locations (see Figure 5.35), the bulk resistance change curves are all out of sinusoidal shape and presenting the local extremes barely corresponding to the peak and valley loads. Since the piezoresistivity of the CNT sensor is hardly activated at the extremely low strains. The piezoresistive responses shown in Figure 5.64b and d, display significant deviations to the linear trend of expectancy. As a result, the linearized gage factors of the sensing sections #5 and #2 are found to be quite diverse from each other.

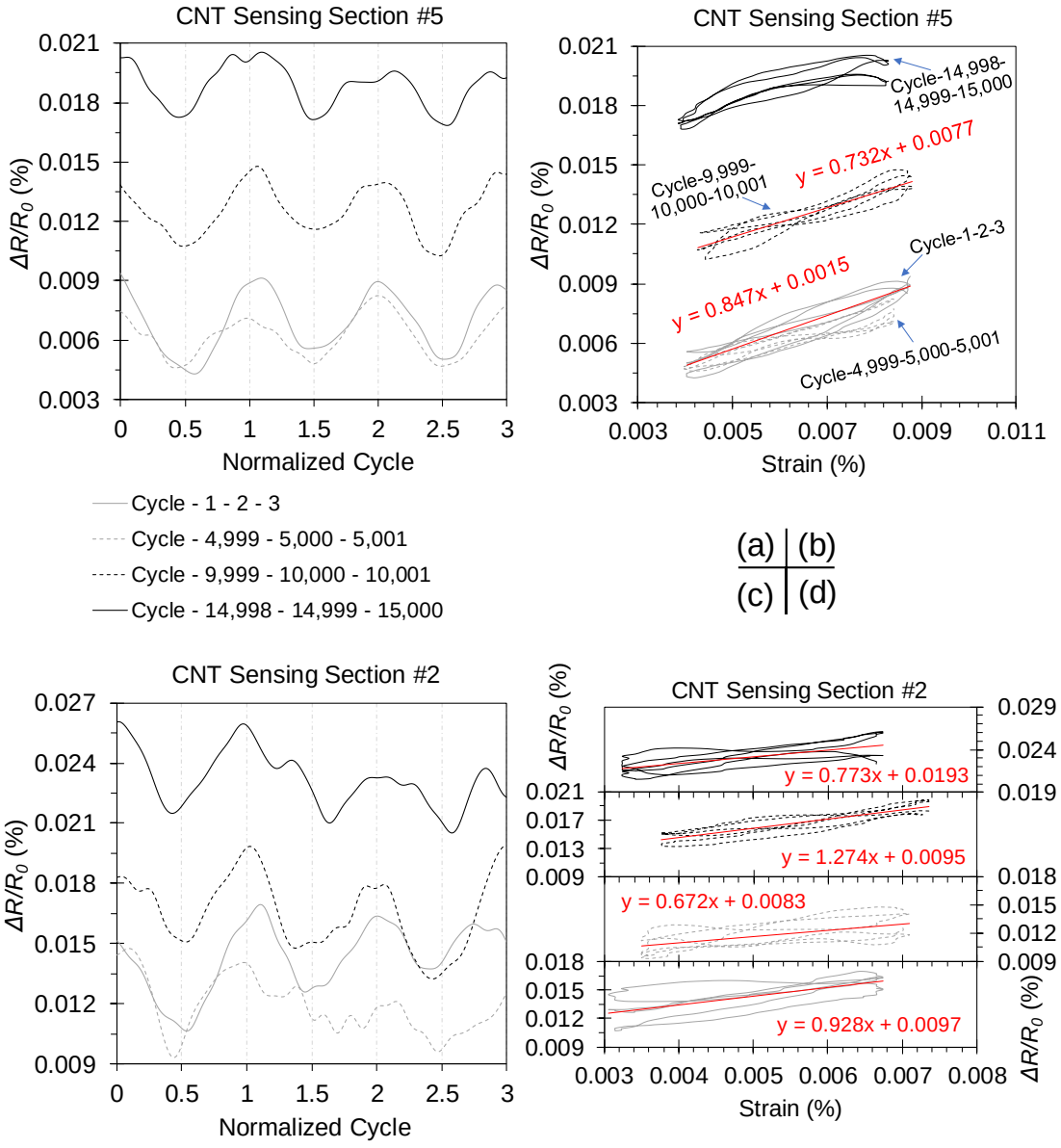

Figure 5.65: Transient resistive responses (a, c) and corresponding piezoresistive relationships (b, e) of selected sensing sections #5 and #2 at soffits of the CNT-based U-wrap sensors #2 and #1, respectively.

Figure 5.66 shows the resistive response of the CNT sensing sections that cover the side faces of the U-wraps during the cyclic testing of the shear beam. Based on the previously demonstrated strain distributions on the side faces of the GFRP wraps (see Figures 5.40 and 5.42), it is clear that only the horizontal strains in the top region are in compression, which likely leads to a tension-dominated surface strain field across the side faces. Consequently, the bulk resistive responses of the side sensing sections present the resultant resistance changes similar to those of the bottom sensing sections (shown in Figures 5.64 and 5.65), i.e., a tensile fashion with compressive effects balanced out. Again, the resistance change curves shown in Figures 5.66a through d, hardly follow the sinusoidal shape of the applied load, but show the local minima and maxima, matching the applied loads. It is also noted that the two side sensing sections in U-wrap #1 are likely inert under the extremely low strain levels, showing random fluctuations as shown in Figure 5.66e that are barely in correlation with the applied loads.

It has been shown that under the low service-level loads the deployed CNT sensors display consistent resistive responses with significantly small changes in electrical resistance, most likely resulting from that the piezoresisitivity of the nanotube networks are not fully stimulated at extremely low strain levels. Although the resistance changes are not quantitatively beneficial for estimating the stress levels the shear beam experienced, a qualitative evaluation of the overall structural condition of the strengthened member can be based on the lack of observed random sharp anomalies that both the concrete beam and the strengthening GFRP U-wraps are able to effectively resist the applied service-level cyclic loads without causing structural damage.

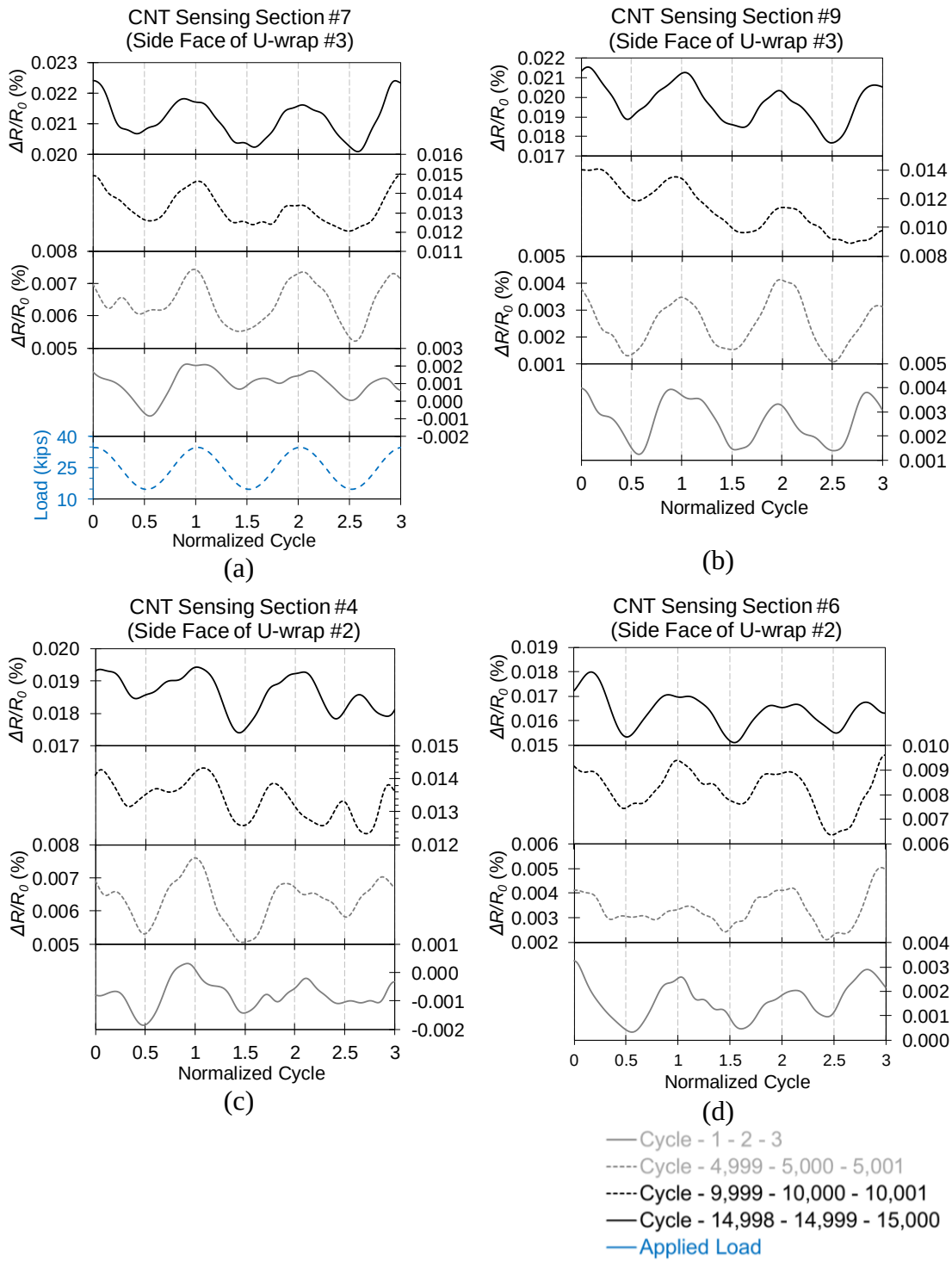

Figure 5.66: Transient resistive responses of the CNT sensing sections covering the side faces of (a, b) U-wrap #3, (c, d) U-wrap #2, and (e) U-wrap #1 at selected cycles during the cyclic testing of the shear beam.

(e)

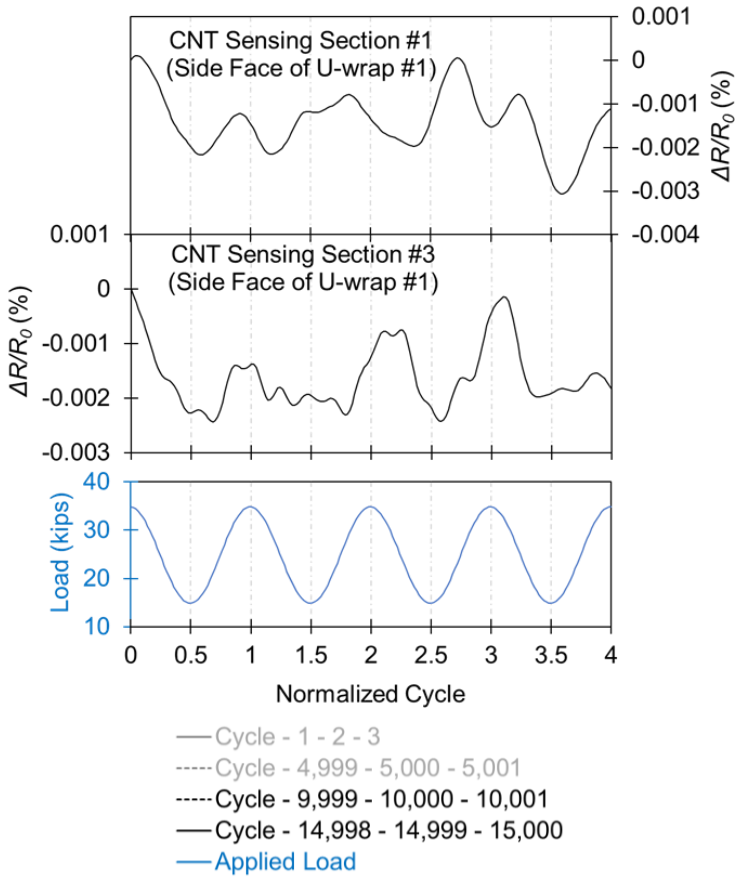

Figure 5.66: continued.

In particular, the typical thermoresistive response of the CNT sensors are presented in Figure 5.67. The sensing sections integrated with the GFRP composites (i.e., #1, #4 and #7) display the consistent thermoresistivity, similar to those of the long CNT sensor on the flexure beam (see Table 5.7), revealing a good repeatability of the hybrid composite system in this study. On the other hand, the nonstructural sensing U-wraps (i.e., #10 and #13) demonstrate a relatively divergent trend that is much more thermoresistive than those in the hybrid composites. This is mainly

because of the distinctive differences in CNT concentration, epoxy properties, and concrete-sensor insulation between these two types of CNT sensing U-wraps.

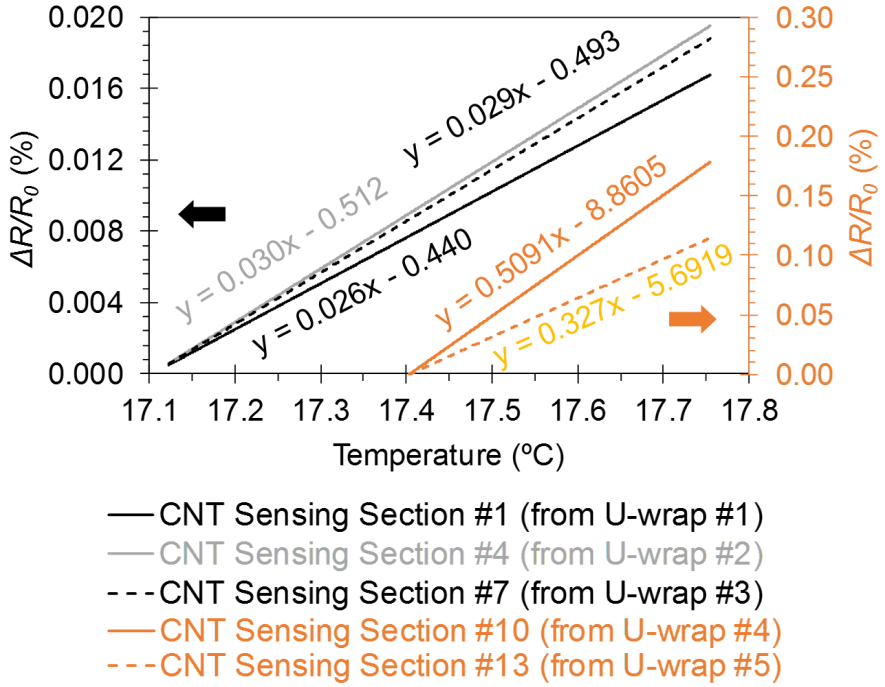

Figure 5.67: Typical thermoresistive responses of the CNT sensing U-wraps implemented on the shear beam.

5.3.2.2.2 Static Loading-Unloading Cycles up to Failure

For clarity and accuracy in presentation of the experimental data, the entire resistive responses of the CNT sensors on the shear beam are divided into two parts and presented separately in accordance to the flexural responses of the beam during the eight-step loading-unloading cycles (see Figure 5.37a). Figure 5.68 shows the resistive behaviors of the CNT sensing sections under the 45, 55, 65, and 75-kip cycles while the strengthened shear beam deforms elastically. It should be noted that transient resistive responses of the bottom (i.e., #2, #5, and #8 covering the U-wrap soffits) and the side (i.e., #3, #6, and #9 covering the side faces of the U-wraps) sensing sections are represented in Figures 5.68a-c and 5.68d-f, respectively.

All selected CNT sensing sections are effectively responding to the applied loads. The overall resistance changes observed depend on the strain levels the sensing section experienced and showing a decreasing trend in the direction of declining moment. For example, the sensing section #2 (Figure 5.68a) located in the low stress discontinuity region next by the left support shows a highly noisy resistive response that is only able to estimate the 65 and 75-kip cycles with less than 0.025% resistance change in overall. On the other hand, the resistive responses of the sensing section #5 (Figure 5.68b) and #8 (Figure 5.68c) are closely following the shape of the loading profile (Figure 5.68g) showing obvious resistance changes.

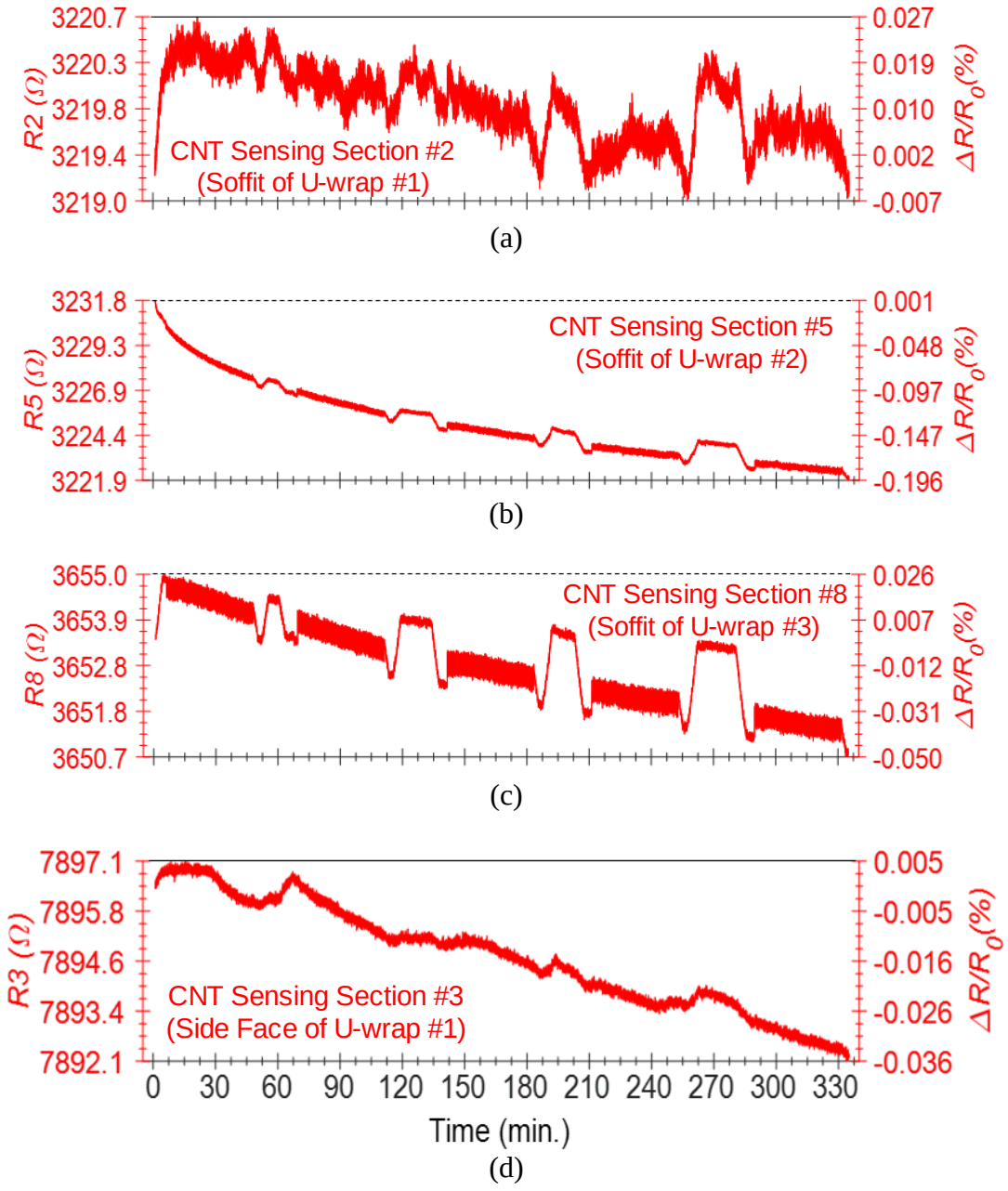

Figure 5.68: Typical transient resistive responses of the selected bottom sensing sections including (a) #2, (b) #5, (c) #8, and side sensing sections including (d) #3, (e) #6, and (f) #9 of the CNT-based U-wrap sensors as monitoring the shear beam under the stepwise static loads (g) up to 75 kips.

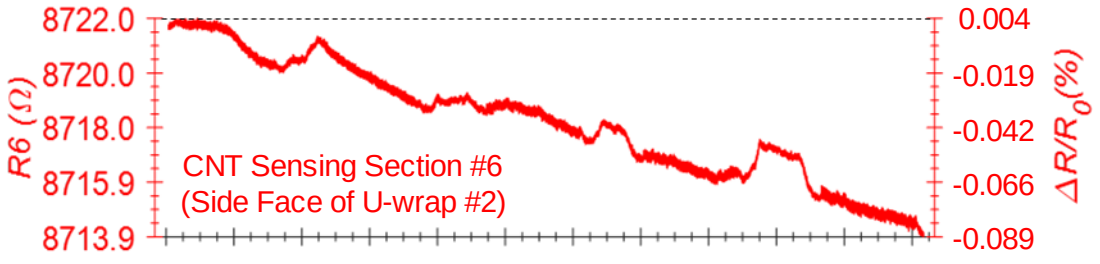

(e)

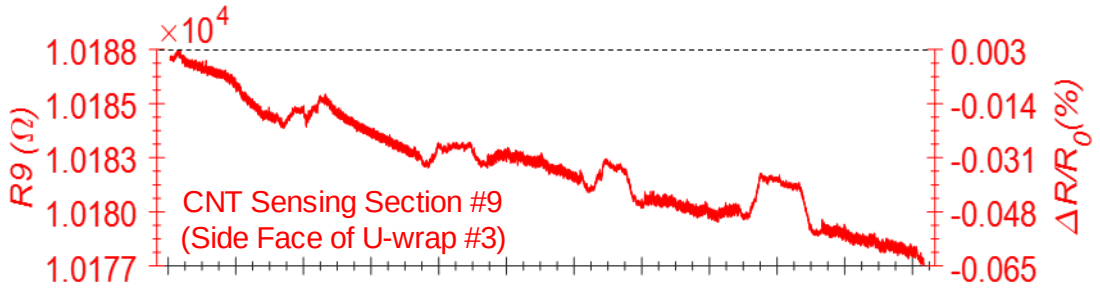

(f)

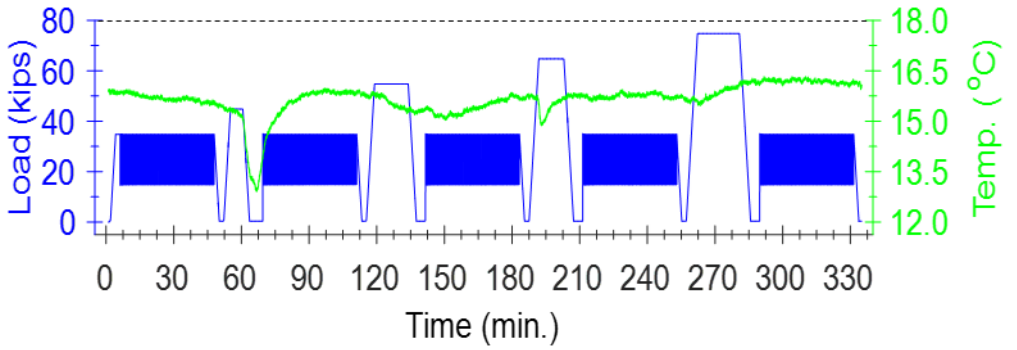

(g)

Figure 5.68: continued.

In addition, the side sensing sections (Figures 5.68d-f) show a less sensitive behavior in estimating the applied loads with even lower level of resistance changes than those of the bottom sensing sections. This is mainly resulting from the relatively complex strain distributions across the side faces of the U-wraps. In particular, sensing sections #6 and #9 (Figure 5.68e and f) show a clear correlation to the 65 and 75-kip

cycles. It is also notable that during the first 5.5-hour test, all presented CNT sensing sections display the slow time variations of electrical resistance, seen as the 'decreasing drift'. This is most likely induced by the different levels of electrical polarization. For instance, the uncured epoxy molecules inside of the CNT sensor can easily get polarized under the applied electrical field [61-63], therefore attributing to the electrical conductivity of the bulk sensing composite. In addition, the higher resistive networks in the side sensing sections (Figures 5.68d-f) can probably introduce more significant interfacial polarization that sometimes impedes the resistive responses in the 45 and 55-kip loading cycles, as compared with the bottom sensing sections #5 and #8.

Figure 5.69 shows the resistive responses of the CNT-based U-wrap sensors as the shear beam subjected to higher loads including the 85, 95, 115, and 140-kip loading-unloading cycles. It is clear that all bottom (i.e., #2, #5, and #8) and side (i.e., #1, #4, and #7) sensing sections (Figures 5.69 a through f) show consistent resistance responses that instantly respond to the variations in applied loads (Figure 5.69g), demonstrating an overall shape comparable to that of the loading protocol. The resistance changes are observed from 1.8 Ω (0.055%) in sensing section #2 (Figure 5.69a) up to 3.5 Ω (0.1%) in sensing section #8 (Figure 5.59c), which in general are small resistive variations, revealing the structural condition of the monitored areas. It is also noted that the side sensing sections (Figures 5.69d-f) show the activated piezoresistivity that promotes a strong correlation with the applied loading profile, indicating the likelihood of a tension-dominated strain field across the side faces of the U-wraps. Quantitatively, the resistance variations of 3.7 Ω (0.052%), 6.1 Ω (0.067%), and 5.9 Ω (0.065%) are observed in sensing sections #1, #4, and #7, respectively.

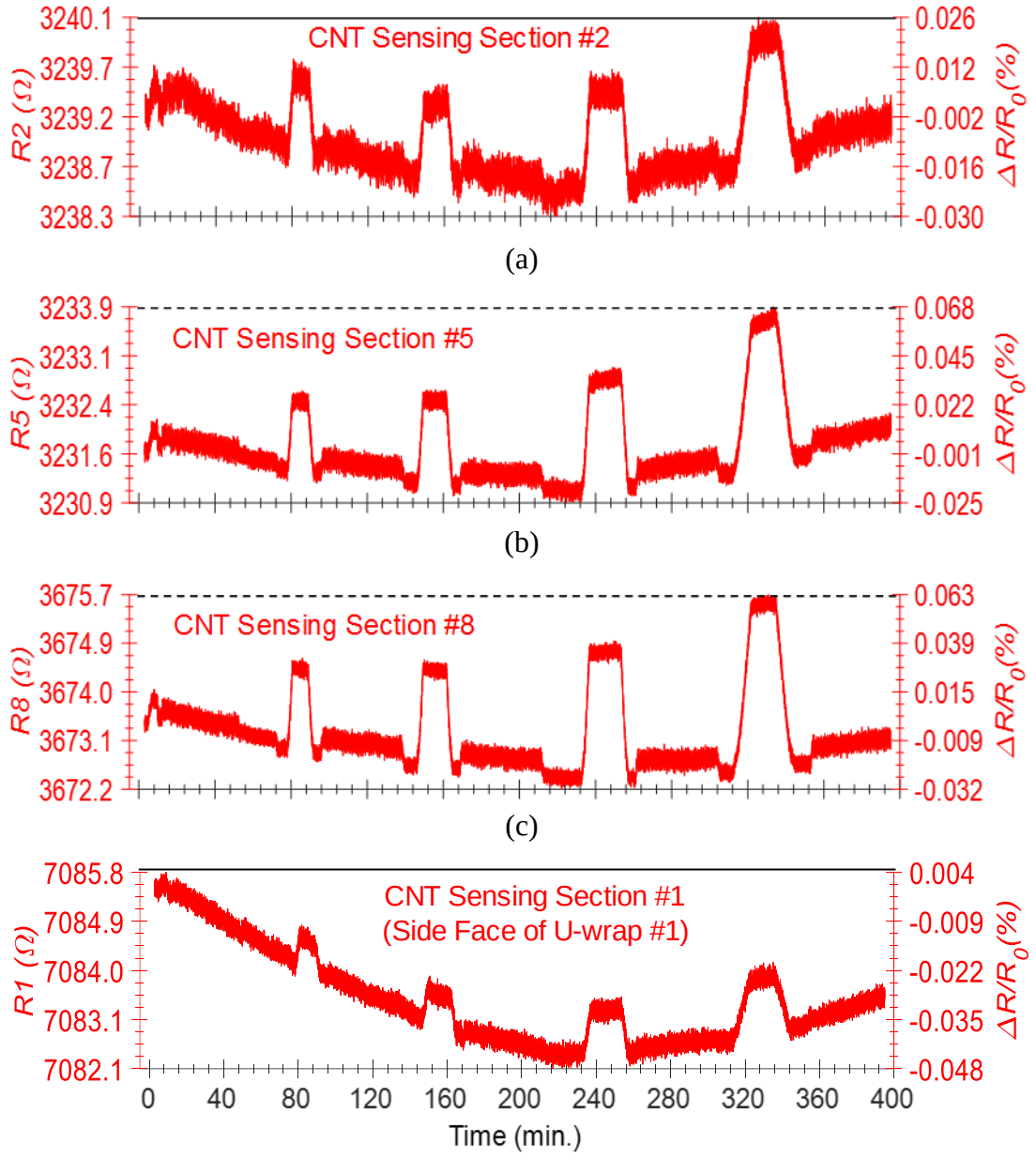

Figure 5.69: Typical transient resistive responses of the selected bottom sensing sections including (a) #2, (b) #5, (c) #8, and side sensing sections including (d) #1, (e) #4, and (f) #7 of the CNT-based U-wrap sensors as monitoring the shear beam under the stepwise static loads (g) from 85 to 140 kips.

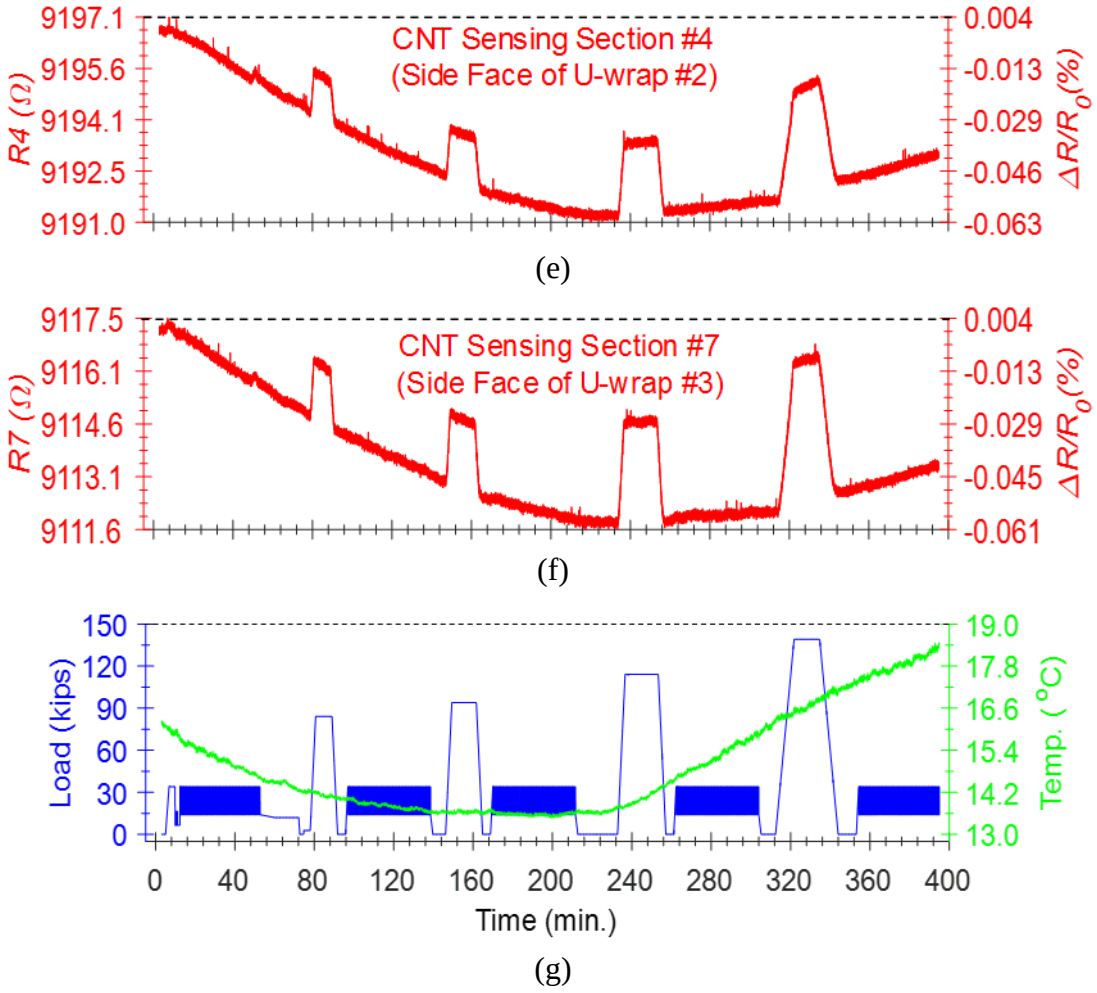

Figure 5.69: continued.

Obviously, under the relatively high loadings, these minor changes can infer an extremely low possibility of the opening of the existing shear cracks underneath the side sensing sections, suggesting a strong shear strengthening action of the deployed GFRP U-wraps to the weak side of the shear beam. In addition, the presented bulk resistive responses are showing a concave shape of the baseline resistance during the

7-hour test, which likely corresponds to the temperature variations shown in Figure 5.69g.

Compared with the side faces of the U-wraps, strain distributions on the soffits of the wraps are relatively uniform under the applied bending moment and then can be represented in two major directions, i.e., the longitudinal and transverse strains (see Figure 5.41). As a common practice [69], the resistance variations of the CNT sensing sections are correlated with these two principle strains to demonstrate the planar piezoresistivity of the CNT sensors in these two orientations. Here, the longitudinal direction refers to the beam axis direction that is perpendicular to the fiber direction of the composite U-wrap in soffit, and vice versa. Figure 5.70 shows the longitudinal piezoresistive responses of the sensing sections #8, #5, and #2 as the shear beam loaded to 75, 85, 95, 115, 140, and 160 kips (Figures 5.70 a though f). It is clear that all piezoresistive curves are linear elastic under the observed low strain levels, indicating a consistent piezoresistivity. It is also noted that the sensing section #8 (black lines) shows higher piezoresistivity than other two sensing sections during all six loading cycles, which is likely an amplified piezoresistivity due to the disturbed strain measurements at the discrete location. Besides the level of loading, the longitudinal strains on soffit are naturally dominated by the material properties of the epoxy matrix, which is much weaker than the concrete. Therefore, the opening of the existing flexural cracks in close proximity to the sensing section #8 (see Figures 5.44c and 5.7a) can cause tremendous variations in the surface strain field, leading to that the strain measurements at the center of the soffit may not be representative for the entire area covered by the sensing section #8.

In addition to Figure 5.70, the transverse piezoresistive responses are shown in Figure 5.71. It should be first noted that the response of section #2 are not included in this figure, because the measured transverse strains in this section are extremely low (less than 20 με) and noisy throughout the entire test. In general, the piezoresistive behavior (Figure 5.71a) appears due to the noisy electrical measurements when the strain level is less than 50 με. Notably, the transverse piezoresistive responses of the sensing sections #5 and #8 (Figure 5.71b through f) represent a stable and linear elastic fashion as the beam loaded beyond 85 kips. In addition, the discrepancy between the transverse piezoresistivity of the sensing section #8 and #5 is significantly reduced as compared with the longitudinal one (see Figure 5.70). This is because the transverse strains on soffit are controlled by the reinforcing glass fibers following a decreasing trend in the direction of declining bending moment.

As a useful figure of merit, the gage factor demonstrates the strain sensitivity of the CNT-based sensors. Table 5.8 lists the linearized gage factors of the bottom sensing sections at different levels of loading. As usual, they are calculated as the slopes of the piezoresistive responses shown in Figures 5.70 and 5.71. Apparently, every CNT sensing section presents comparable gage factors along the longitudinal direction that follows a slight increasing trend as the load increases, indicating a high repeatability of the deployed CNT sensors. It is also noted that the sensing section #5 and #8 represent consistent transverse gage factors that are nearly 2.5 and 6.5 times higher than the longitudinal ones, highlighting the planar strain sensitivity of the proposed CNT-based sensors. Similar results have been presented in Section 2.4.1.3 in Chapter 2.

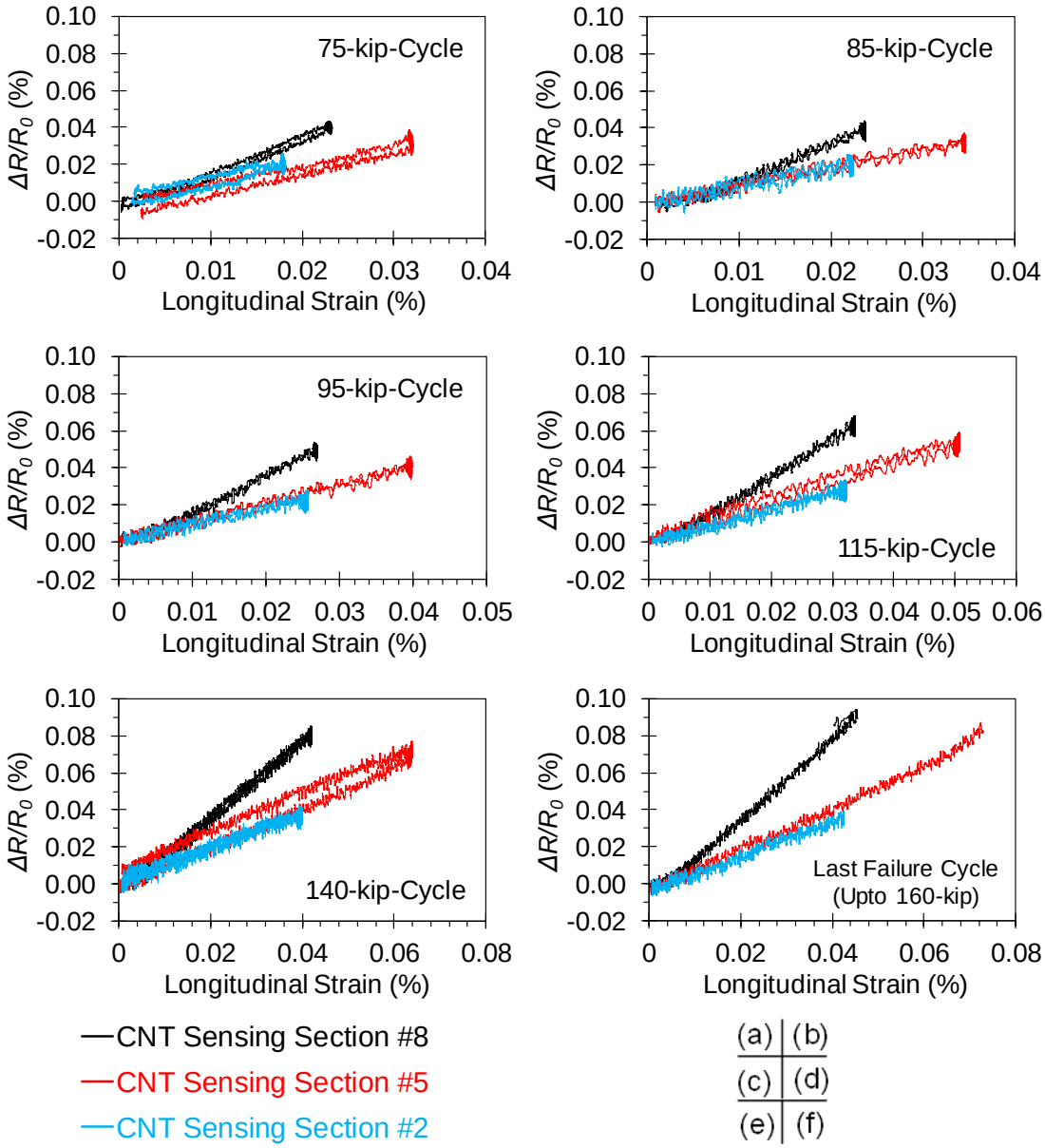

Figure 5.70: Piezoresistive responses of the bottom sensing sections #8, #5, and #2 in the longitudinal direction as the shear beam loaded to (a) 75, (b) 85, (c) 95, (d) 115, (e) 140, and (f) 160 kips.

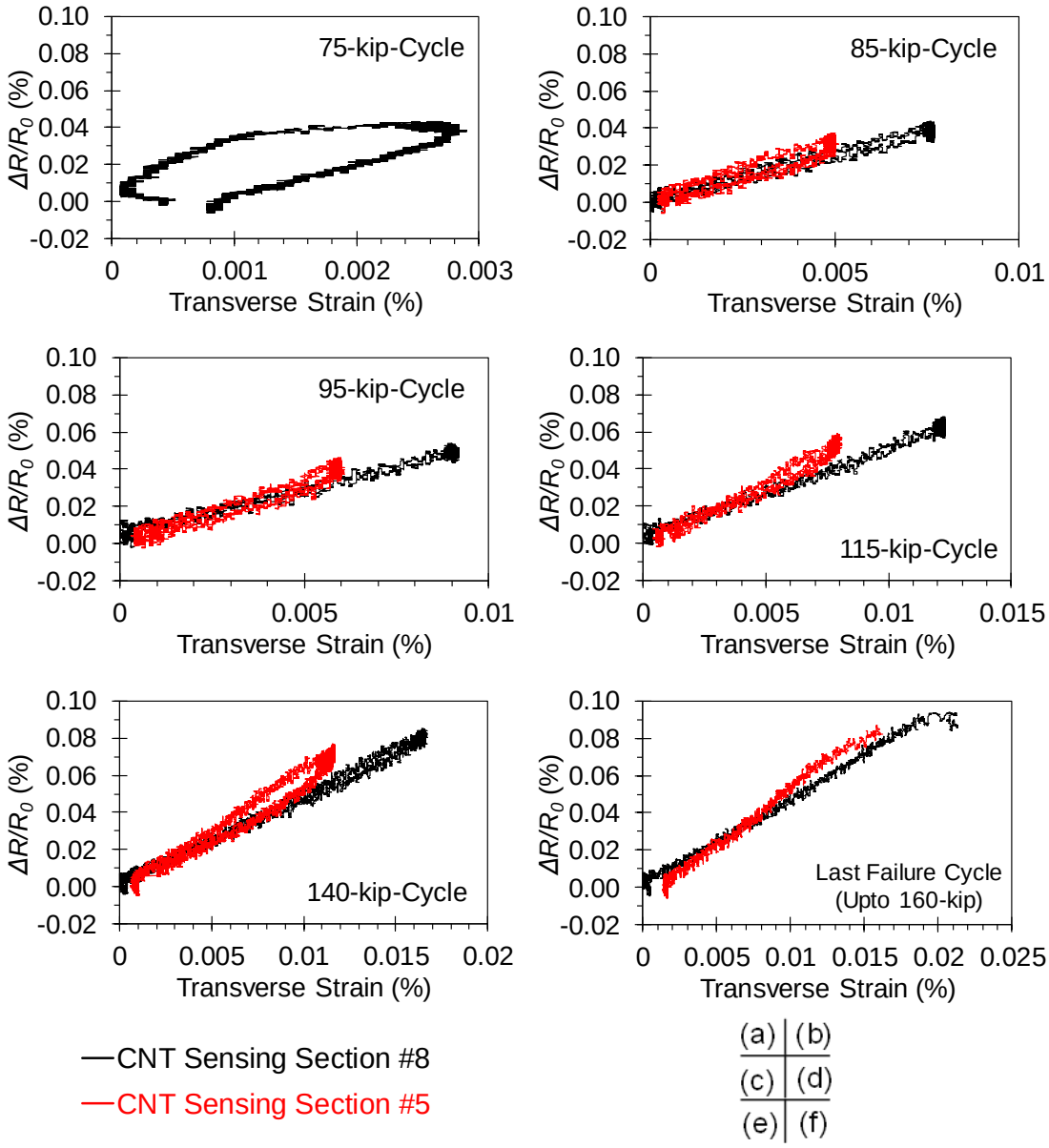

Figure 5.71: Piezoresistive responses of the bottom sensing sections #8 and #5 in the transverse direction as the shear beam loaded to (a) 75, (b) 85, (c) 95, (d) 115, (e) 140, and (f) 160 kips.

Table 5.9: Linearized Longitudinal and Transverse Gage Factors Demonstrated by the Bottom Sensing Sections of the CNT-Based U-Wrap Sensor as the Shear Beam Statically Loaded.

CNT Sensing Section	Linearized Longitudinal Gage Factors					
	75-kip Cycle	85-kip Cycle	95-kip Cycle	115-kip Cycle	140-kip Cycle	Failure Cycle (Upto 160 kips)
#2	1.00	0.94	0.82	0.87	0.90	0.93
#5	1.05	0.95	1.01	1.01	1.06	1.14
#8	1.93	1.96	1.96	2.00	2.06	2.15
CNT Sensing Section	Linearized Transverse Gage Factors					
	75-kip Cycle	85-kip Cycle	95-kip Cycle	115-kip Cycle	140-kip Cycle	Failure Cycle (Upto 160 kips)
#5	N.A.	6.66	7.04	7.04	6.41	6.04
#8		4.87	4.84	4.84	4.78	4.55

The non-rehabilitated portion of the shear beam (i.e., the right strong portion, see Figure 5.22) behaves as a conventional reinforced concrete member under the applied increasingly stepwise loading, presenting the progressively accumulated flexural and shear cracking damage (see Figures 5.43 and 5.45). The implemented nonstructural sensing U-wraps #4 and #5 aim at providing the continuous real-time health monitoring of this specific region. The transient resistive responses of the selected bottom and side sensing sections from these two CNT-based U-wrap sensors are shown in Figure 5.72 and 5.73, respectively. In general, both sensors are effectively responding to the applied loads and demonstrate distinctive variations in resistance (change) at different loading levels which consequently indicates different stages of damage progression occurred in the concrete beam.

In particular, the sensing section #11 (Figure 5.72a) shows a sharply increasing trend of resistance change over the entire loading protocol and a considerably large change of 44% in resistance is observed during the 140-kip cycle, indicating the

severe cracking damage accumulated at the soffit region close to the loading point. Similarly, the bottom sensing section #14 (Figure 5.72b), next to #11 in the zone of lower moment, represents a comparable trend of resistance variations as that of #11 but meanwhile shows a significantly reduced level of resistance change (i.e., < 5%) in overall, suggesting a relatively mild stage of damage developed in this region.

Notably, this sensing section presents an abrupt drift of resistance in the first two hours of testing, which is mostly likely caused by the interfacial polarization of the CNT-based composite. Additionally, due to the inherently high resistance of this CNT sensor as comparing with the low-resistive CNT sensors as shown in Figures 5.68 and 5.48, the polarization effect becomes aggravated and induces relatively large resistance change of ~3%. It is also noted that this slow time variations of electrical polarization are totally impeded by the piezoresistive response as the sensor experiences large strains (i.e., the cracking damage) as exemplified during the 95-kip cycle in Figure 5.72b.

The side sensing sections #10 and #13 of the CNT-based U-wrap sensors #4 and #5 (Figure 5.73a and b) demonstrate a strong correlation with the applied loads. As expected, a permeant resistance change is observed after each loading-unloading cycle, revealing the increasingly accumulated structural damage in the concrete beam. To facilitate the understanding of these resistive responses, the tracked pattern of concrete cracking progression in the un-retrofitted region of the beam is shown in Figure 5.74. Apparently, the previously observed resistance variations of the sensing sections #10 and #13 closely correspond to the evolutions of cracks accumulated on these two sensing sections, confirming that structural damage progression is accompanied with permeant resistance change.

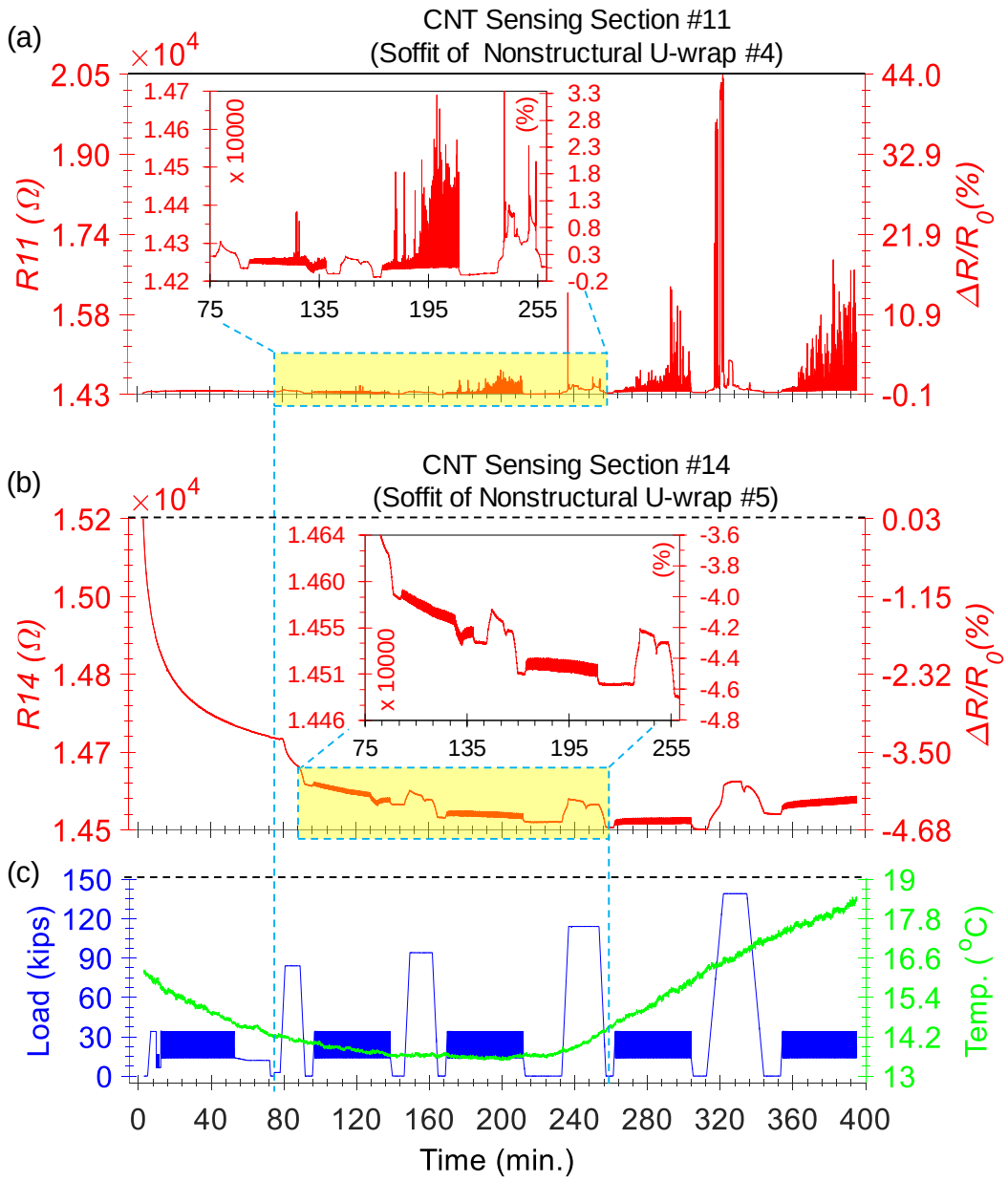

Figure 5.72: Transient resistive responses of the bottom sensing sections (a) #11 and (b) #14 of the nonstructural CNT-based sensing U-wraps #4 and #5 in the non-rehabilitated portion of the shear beam as statically loaded (c).

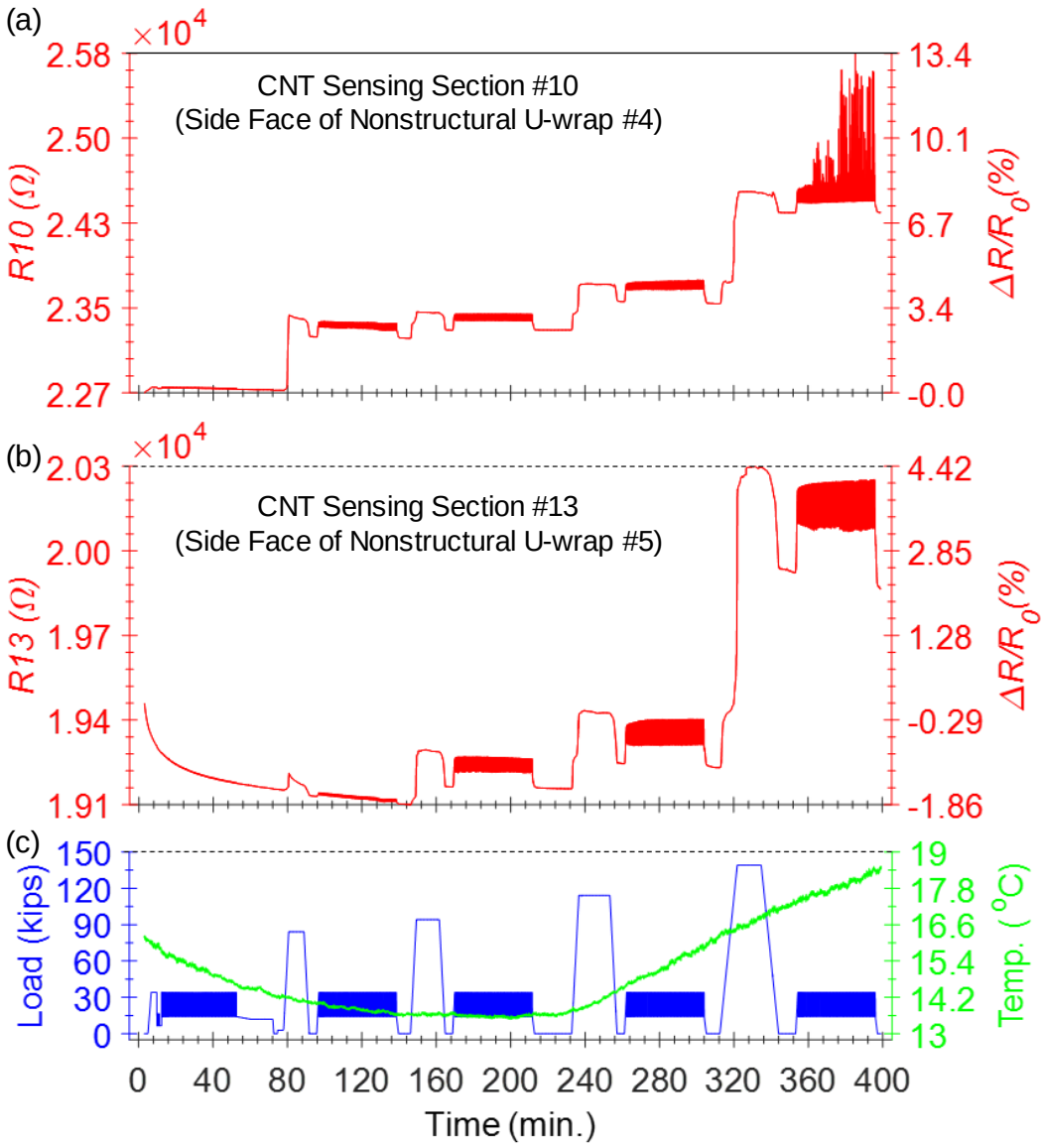

Figure 5.73: Transient resistive responses of the selected side sensing sections (a) #10 and (b) #13 of the nonstructural CNT-based sensing U-wraps #4 and #5 in the non-rehabilitated portion of the shear beam as statically loaded (c).

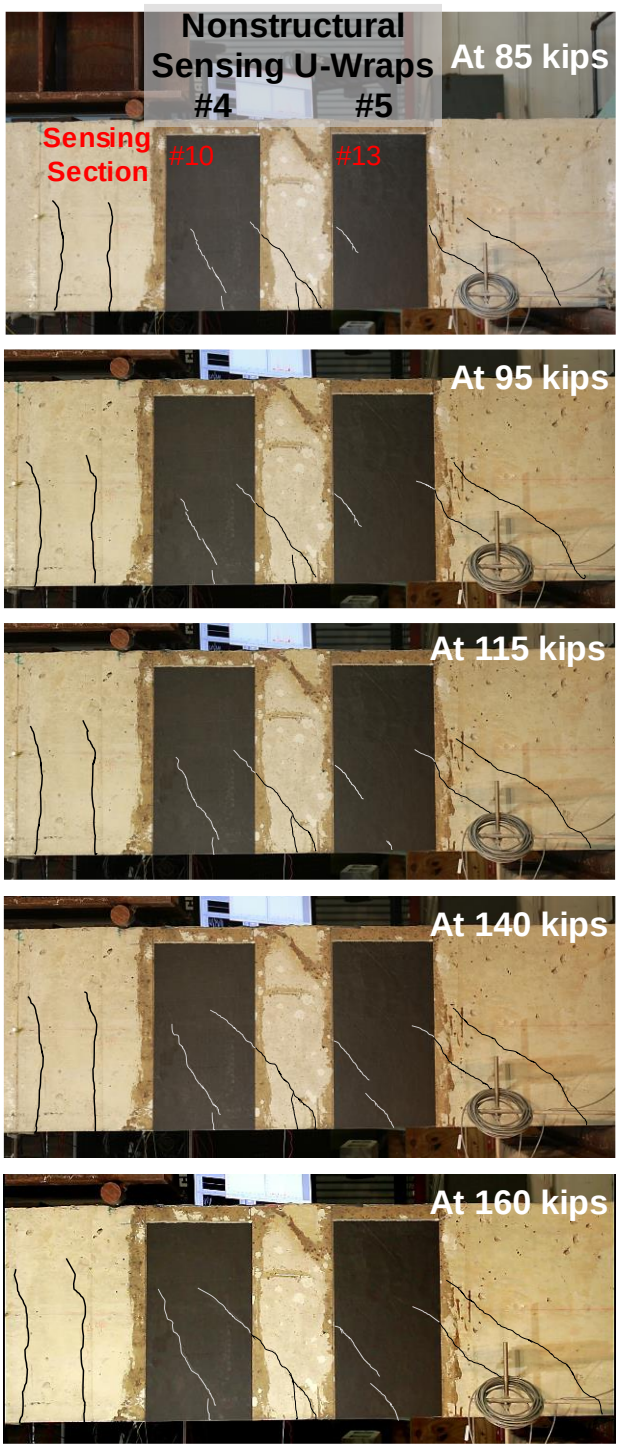

Figure 5.74: Photographs showing the traced cracking pattern observed from the shear beam in its strong side (un-retrofitted portion) after loading up to 85, 95, 115, 140, and 160 kips.

The nonstructural sensing U-wraps present considerably larger resistance variations than those of the hybrid U-wraps sensors, proving the strong and effective strengthening action provided by the GFRP-U-wraps to the weak portion of the beam that leads to a high structural performance of the retrofitted portion with the nearly damage-free state as the beam progressively loaded.

As planned initially, the goal of the intermediate cyclic loading sessions between the loading-unloading cycles (see Figure 5.37a) is to evaluate the structural performance of the partially strengthened shear beam under the low service-level loading condition after being increasingly loaded statically. Therefore, the outputs of the CNT-based sensing U-wraps during these cyclic loading sessions are useful and necessary to the continuous SHM of the shear beam. Figure 5.75 shows the typical transient resistive responses of CNT sensing sections in the GFRP-strengthened region of the beam at the half point of each session. Similarly, Figure 5.76 presents the typical responses of nonstructural sensing sections in the non-rehabilitated portion of the beam. Although some resistive fluctuations are observed locally, both sensing section #8 and #9 shown in Figure 5.75a and b represent nearly constant resistance changes of 0.006% and 0.004%, respectively as responding to the cyclic loads during the initial session and the rest four sessions correspondingly after the 85, 95, 115, and 140-kip cycle. Apparently, these responses are expected and showing the undamaged resistance change of the CNT sensing sections, which consequently indicates the stable and robust structural performance of the GFRP-strengthened region, i.e., maintaining a good serviceability in overall.

In contrast, significant variations in resistance change are observed in the resistance responses (Figure 5.76a-d) of the CNT sensors located in the un-retrofitted

region. For instance, as shown in Figure 5.76a the bottom sensing section #11 (next by the central span of maximum moment) displays 0.04% resistance change in the first cyclic session and then sharply increases to 0.16%, 1.0%, and 10% in the following sessions after 85, 95 and 140-kip loading cycles. Additionally, the side sensing section #10 of the same wrap #4 (Figure 5.76b) present the comparable trend of the increasing resistance change. Obviously, the U-wrap sensor #4 shows resistance change due to accumulated damage, revealing the damaged state and reduced serviceability of the un-retrofitted region of the shear beam. It is also noted that the bulk resistance responses of the U-wrap sensor #5 present a neat sinusoidal shape similar to that of the applied load. In addition, this sensor shows less accumulated resistance changes in the bottom (Figure 5.76c) and side (Figure 5.76d) sections, suggesting the reduced levels of damage in this lower moment region as comparing with the region near the loading point (i.e., covered by U-wrap sensor #4).

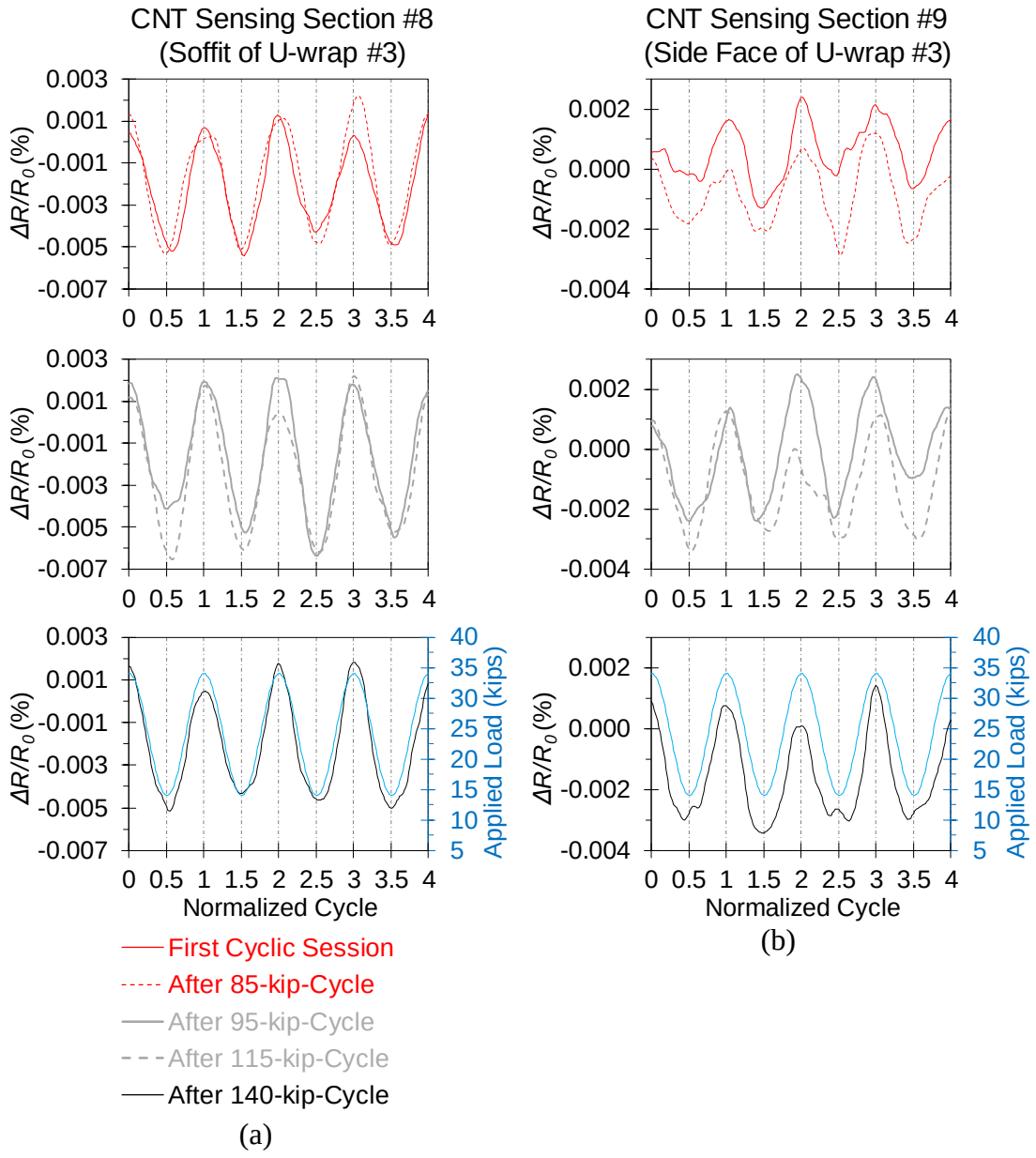

Figure 5.75: Transient resistive responses of the selected sensing sections (a) #8 and (b) #9 in the GFRP-strengthened region of the shear beam at the half time of five intermediate cyclic loading sessions including the initial one and the rest four after 85, 95, 115, and 140-kip static loading cycles.

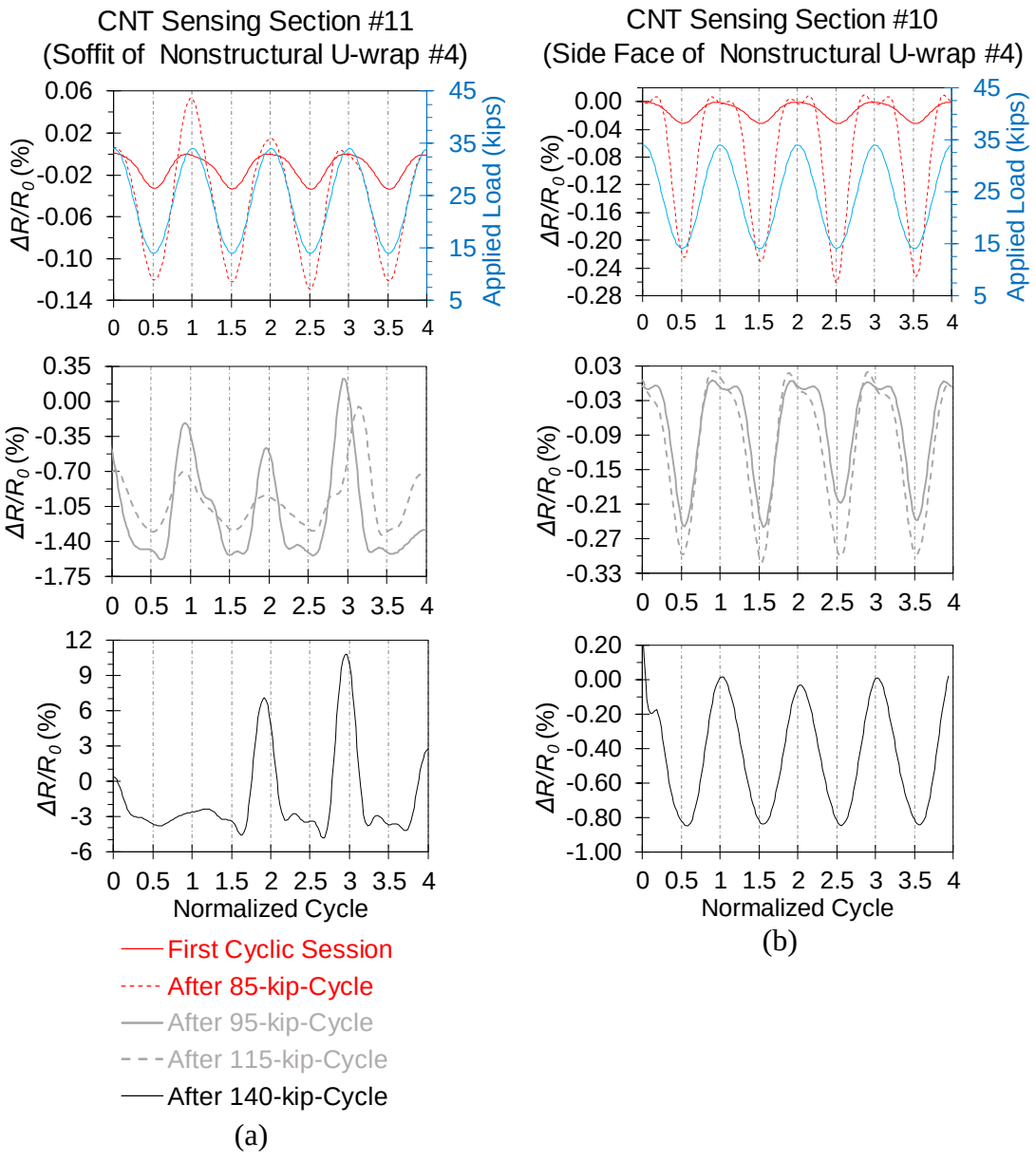

Figure 5.76: Transient resistive responses of the nonstructural sensing U-wraps #4 (a, b) and #5 (c, d) in the non-rehabilitated region of the shear beam at the half time of five intermediate cyclic loading sessions including the initial one and the rest four after 85, 95, 115, and 140-kip static loading cycles.

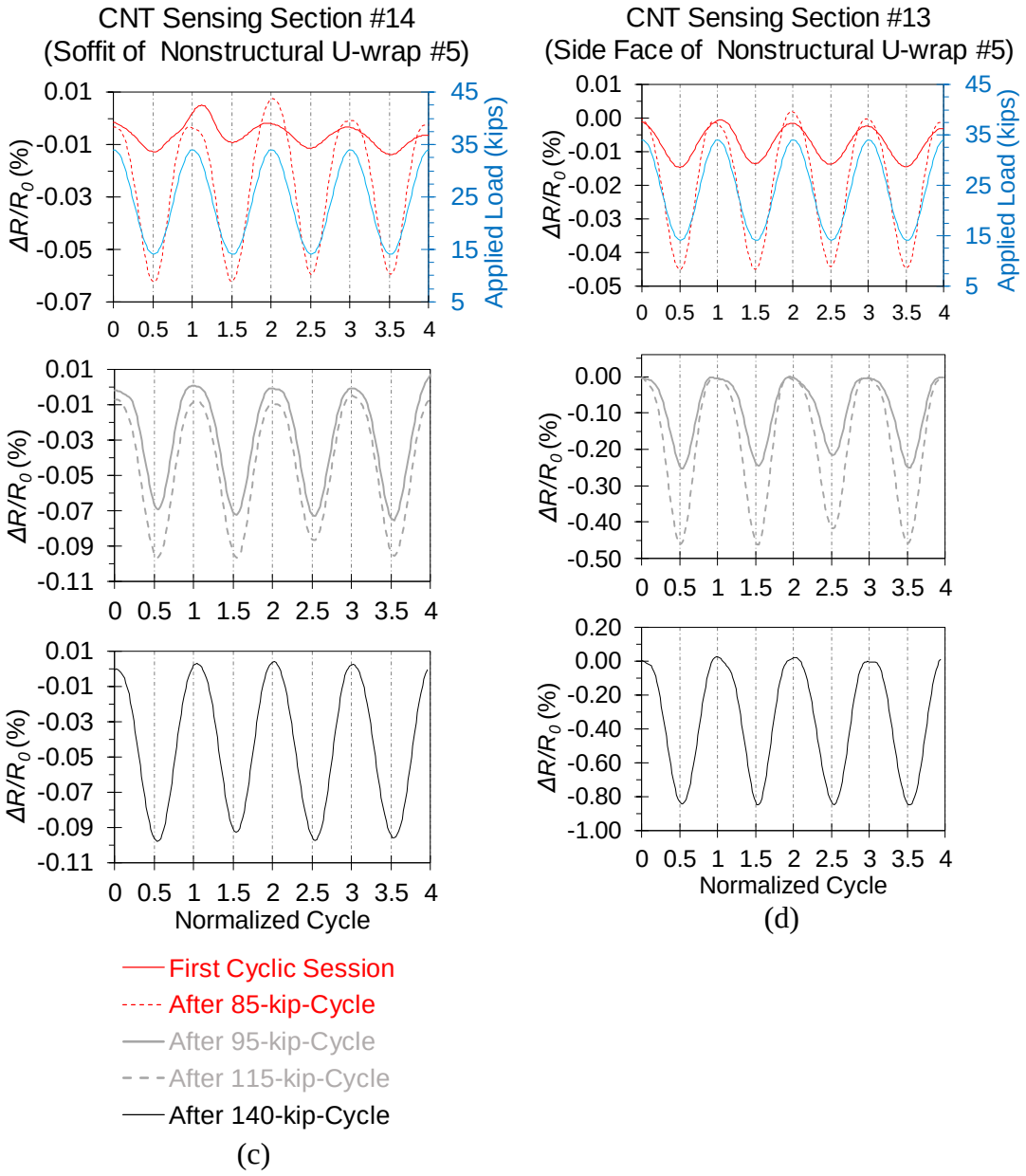

Figure 5.76: continued.

As the shear beam statically loaded to failure, the CNT-based U-wrap sensors distributed on the member are expected to present local information regarding the structural performance of the beam specimen in real-time. Figures 5.77 and 5.78 show the transient resistive response of the selected sensing sections from the CNT sensors located in the GFRP-strengthened and non-rehabilitated portions of the beam. All CNT U-wrap sensors display strong correlations with the loading protocol.

The bottom sensing sections #2, #5, and #8 (Figure 5.77a-c) show distinctive resistance variations closely following the trend of the measured longitudinal strains. Interestingly, a sharp resistance spike is observed in sensing section #8 (Figure 5.77c) as loading up to 157 kips, which exactly corresponds to the inflection point of the measured mid-span displacement of this beam shown in Figure 5.37a. Meanwhile, the longitudinal strain rapidly drops which is caused by the sudden releasing of surface strains as the extensive opening of the critical flexural crack in close proximity to this sensing section (see Figure 5.44c), when the beam deforms plastically. After failure, both sensing section #5 and #8 show some permeant resistance changes, but the resistance of sensing section #2 returns to its original value.

Similar resistance variations are also observed in the side section sections #1, #4, and #7 as showed in Figure 5.77d through f. Therefore, it can be concluded that the transient resistive responses of U-wrap sensor #3 (Figure 5.77c and f) show the instant feedback on the structural performance of the concrete beam, indicating imminent failure. In addition, the resistance changes of all three U-wrap sensors are amazingly small in magnitude, i.e., < 0.17%. There are also no any continuous nonlinearities observed in the resistive responses throughout the entire failure cycle. As a result, it can be deduced that (1) very minor structural damage may be

accumulated in the strengthened portion of the beam; (2) the deployed GFRP wrapping scheme is effectively providing the adequate rehabilitation to the shear beam, enabling the great structural integrity in overall and preserving the nanotube networks undamaged across the bonding layer.

In contrast, the resistive responses of the nonstructural sensing U-wraps #4 and #5 shown in Figure 5.78 demonstrate tremendous nonlinearities and sharp variations, as the shear beam tested to failure. Due to the close proximity to the central loading span, the bottom sensing section #11 is damaged by the progression of flexural cracks of concrete (see Figures 5.45b and 5.74). For example, about 3% resistance change (Figure 5.78a inset) is recorded as loading to 120 kips. Afterwards, the resistance changes of more than 250% are observed in this bottom sensing section (Figure 5.78a) at failure of the beam, and closely matches the severe cracking damage developed in this area (see Figure 5.45b). The other bottom sensing section #14 (Figure 5.78b) located in the region of less moment, displays a smooth increasing trend of resistance (i.e., only 1%) up to 157 kips and then presents nonlinear and sharp resistance variations (i.e., over 6%) as approaching the final failure.

As shown in Figure 5.79a and b, the side sensing sections #10 and #13 of the U-wrap sensors #4 and #5 show a comparable fashion of resistance variations as those observed in the bottom sensing sections, when the shear beam is tested to its failure. Before the beam starts to yield (i.e., loaded below 157 kips), the sensing sections #10 and #13 present about 2% (Figure 5.79a inset) and 4.5% (Figure 5.79b) resistance changes, respectively. Abrupt resistive spikes are observed in these two sensing sections as the shear beam reaching its load capacity. In total, about 50% and 22% resistance changes are displayed in the sensing section #10 and #13, respectively.

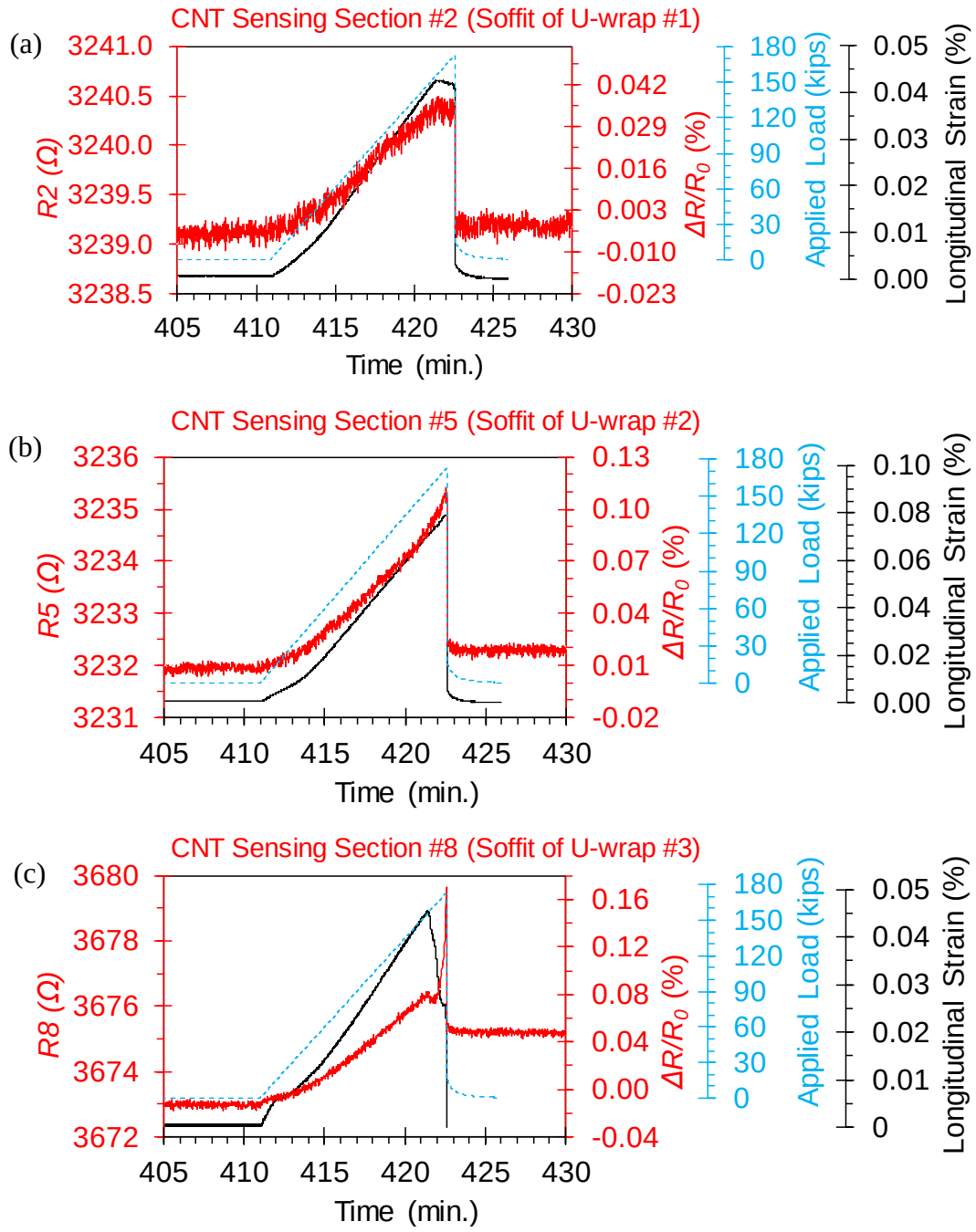

Figure 5.77: Transient resistive responses of the selected sensing sections (a) #2, (b) #5, (c) #8, (d) #1, (e) #4, and (f) #7 in the GFRP-strengthened region of the shear beam as statically tested to failure.

(d)

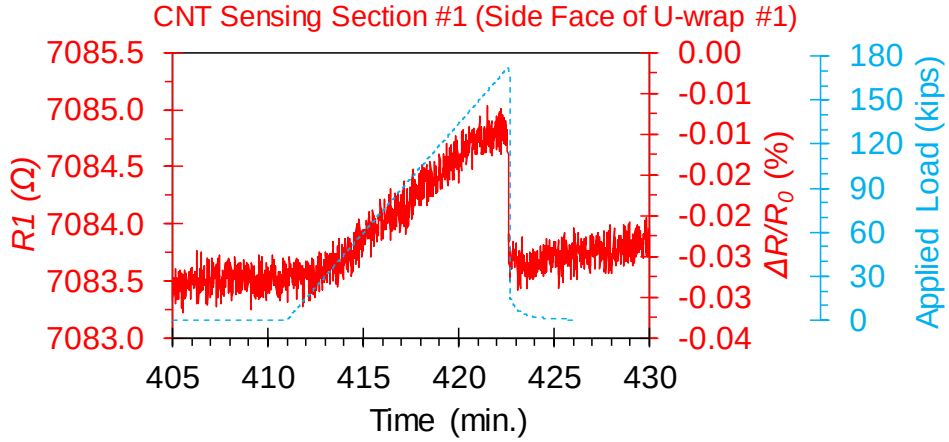

(e)

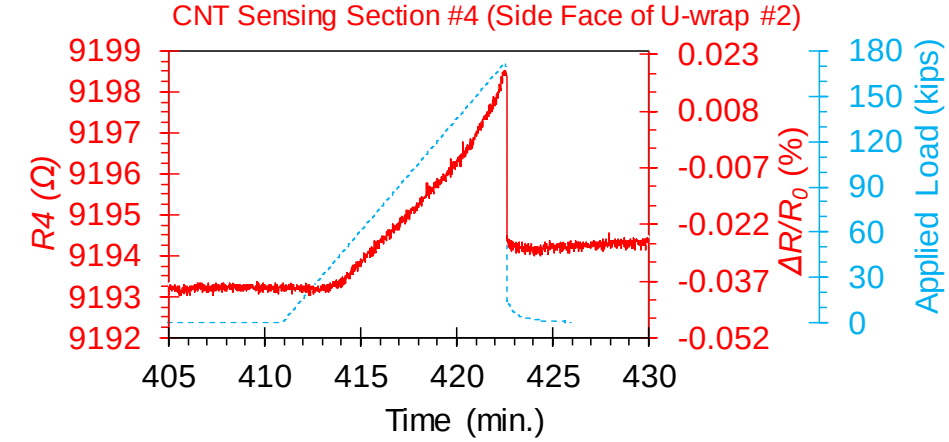

(f)

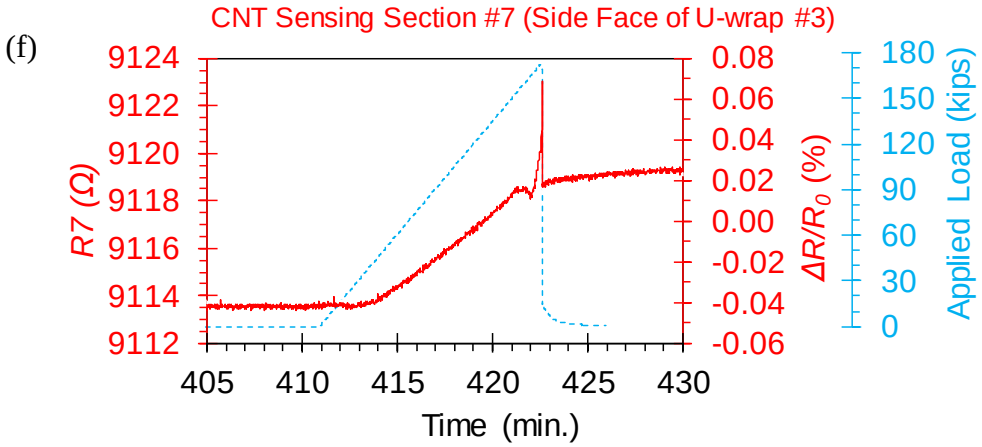

Figure 5.77: continued.

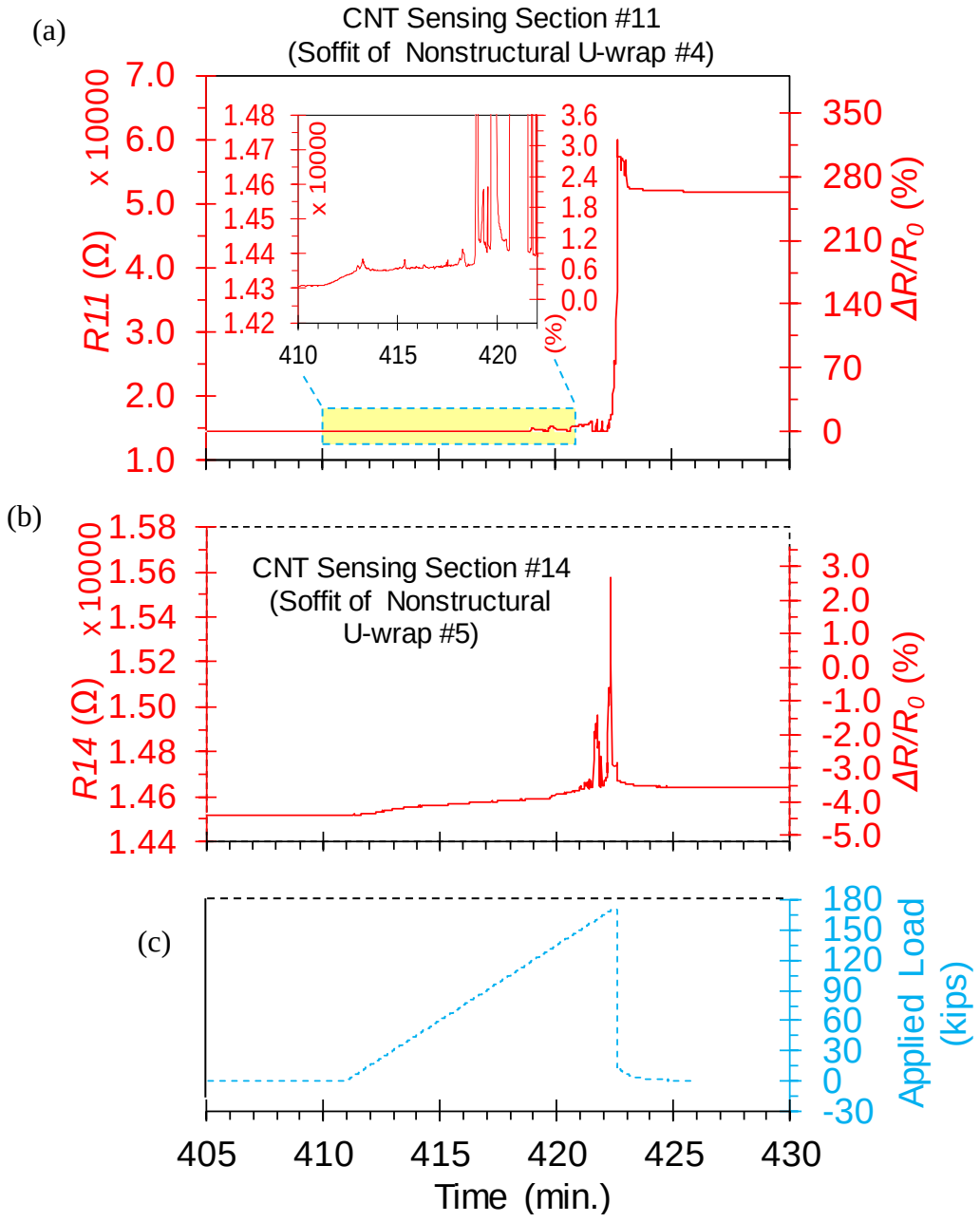

Figure 5.78: Transient resistive responses of the bottom sensing sections (a) #11 and (b) #14 in the nonstructural sensing U-wraps #4 and #5 on the non-rehabilitated region of the shear beam as statically tested to failure.

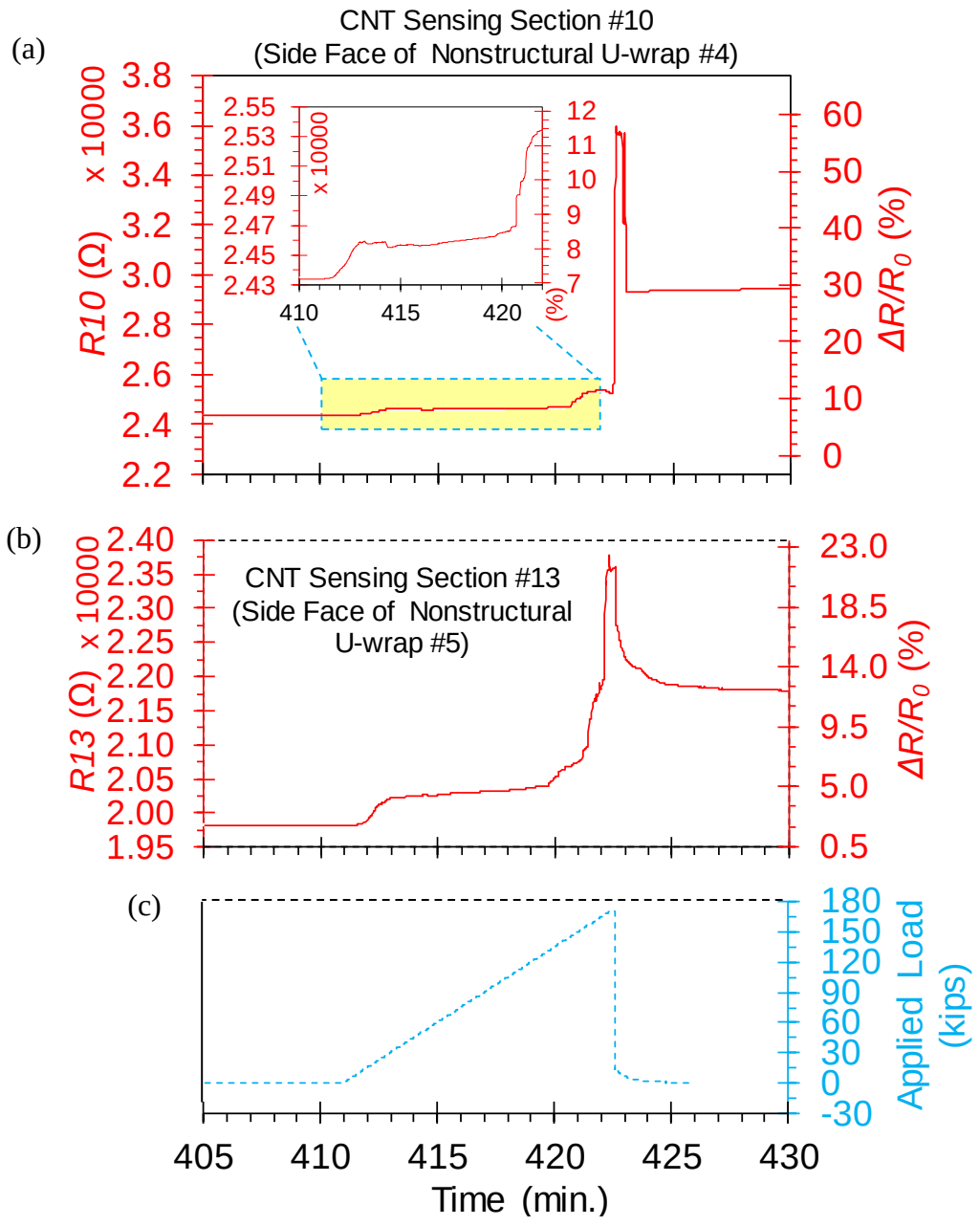

Figure 5.79: Transient resistive responses of the side face sensing sections (a) #10 and (b) #13 in the nonstructural sensing U-wraps #4 and #5 on the non-rehabilitated region of the shear beam as statically tested to failure.

Based on the experimental results, it can be concluded that the deployed nonstructural U-wrap sensors demonstrate a comprehensive monitoring of the un-retrofitted portion of the shear beam. Particularly, the transient resistive responses are able to track the stages of cracking damage progression in real-time. In addition, all sensors established new resistance baselines instantly after the failure of the beam. This is desirable and proves that the proposed CNT-based SHM method can achieve a comparably longer in-service life expectancy than that of the monitored concrete member, further enabling the in-field applicability of this method.

5.3.2.2.3 Comparison with Acoustic Emission Responses

In addition to Figure 5.36, the response of the AE sensor on the GFRP U-wrap #2 (see Figure 5.22 for location) during the 15,000-cycle repeated loading test is presented in Figure 5.80 and compared with the resistive responses of the CNT sensing sections #4, #5, and #9 that are right underneath or nearby this AE sensor. A nearly constant rate of increase of the AE count (Figure 5.80a) is maintained during the first 10 hours of testing, indicating an unchanged state of the structural performance of the structurally-rehabilitated beam system. The observed AE activities originate from two sources including the system vibration (of the fixture, load cell, hydraulic pump, etc.) during the cyclic testing as well as the releasing of concentrated strain energy at the fiber/matrix interface as the composite cyclically loaded.

Remarkably, an intensive AE hit of about 240 counts was registered around 730 min. (highlighted in the yellow box) and then the cumulative AE counts instantaneously increases (black line), suggesting the growth of damage of the structural system. In addition, closer views of the transient resistive responses of the CNT sensors (Figure 5.80b-d) located in the same region of the AE sensor show that a

series of abnormal resistance changes are observed in all three sensing sections during 735-740 min. This likely coincides with the sudden AE hit. After 760 min., AE hits reduce back to the initial level (i.e., about 75 counts/hit). Similarly, the resistance responses of the CNT sensing sections maintain a relatively stable baseline in the same level as before. Consequently, it can be deduced that the observed abrupt variations of acoustic emissions and resistance possibly result from either the microscale debonding at the critical existing shear cracks or the microscale separations of the fiber bundles in the composite. Nevertheless, single occurrences of these micro-level damage cannot influence the structural performance in overall.

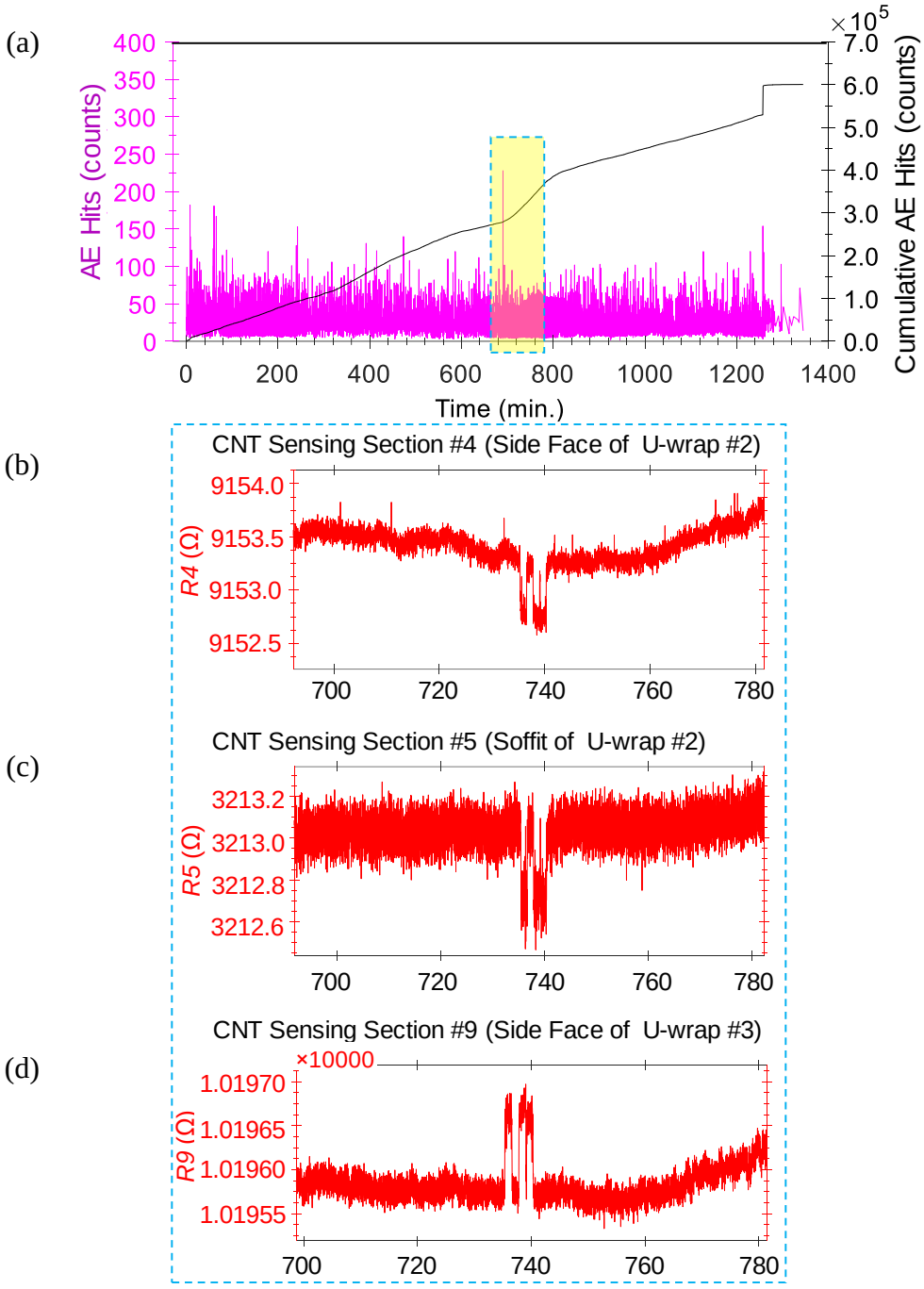

Figure 5.80: Total AE responses (a) collected from the AE sensor on the GFRP U-wrap #2 during the 15,000-cycle repeated loading test, in comparison with the resistive responses of the CNT sensing sections (b) #4, (c) #5, and (d) #9.

Figure 5.81a shows the cumulative AE counts recorded from the sensor on concrete surface and the applied static loading-unloading cycles as a function of the mid-span displacement of the shear beam. It can be seen that a strong correlation is presented between the AE counts and the peak load of each loading cycle. The cracking damage progression under the gradually increased loads is exhibited as the increments of AE counts.

It can also be seen that the presence of the Kaiser effect (that was noticed in the AE response of the flexure beam, see Section 5.3.2.1.3) is now observed in all loading cycles and the first two unloading cycles (i.e., 45 and 55-kip). Afterwards, the Felicity effect (shown as the continuous occurrence of emission during the unloading and reloading below the previous loading level) dominates the AE response during unloading, which is initiated at a much lower load level than that observed in the flexure beam. This is because that the shear beam was precracked at 95 kips prior to GFRP retrofitting. At this relatively high preloading level, considerable flexural and shear cracking damage can be easily generated within the concrete (see Figure 5.7). Although the deployed GFRP U-wraps in the left portion of the shear beam can substantially restrain the potential opening of these existing cracks in this region, the cracking progression in the non-rehabilitated portion of the beam (i.e., the right side) is not prevented and stopped during loading. In contrast, the flexure beam was only precracked at 35 kips and the GFRP patch was continuously deployed across the entire tension face of the beam. Therefore, a greater control on structural performance of the flexure beam was maintained by the provided composite than that of the shear beam.

In addition, the resistance-displacement curves (Figure 5.81b-d) show a nearly linear trend as the shear beam was loaded up to 85 kips. However, it can be observed

that these curves exhibit relatively high level of noise, which most likely caused by the unstable resistance measurements of the side CNT sensing sections, mainly attributing to (1) the extremely low strain levels and (2) the complex strain distributions across the side faces of the beam.

It can be also seen that the resistance-displacement relationship of the sensing section #4 (Figure 5.81c) begins to deviate from its initial linearity as loaded beyond 85 kips, revealing the onset of structural damage, presumably the micro-debonding at the critical shear crack underneath this section. During the 115-kip cycle, both the section #3 and #4 (Figure 5.81b and c) display a remarkable deviation in the trend of the resistance-displacement curves, suggesting the aggravation of the accumulated damage in the concrete beam at high loads. Clearly, structural damage results in the decrease in member stiffness shown by the declining slope of the force-displacement curve (Figure 5.81a). In particular, the disrupted stress field (i.e., the support disturbance) may also contribute to the observed nonlinearity in the response of the sensing section #3 due to the unique location of this section that covers the discontinuity region next to the left support.

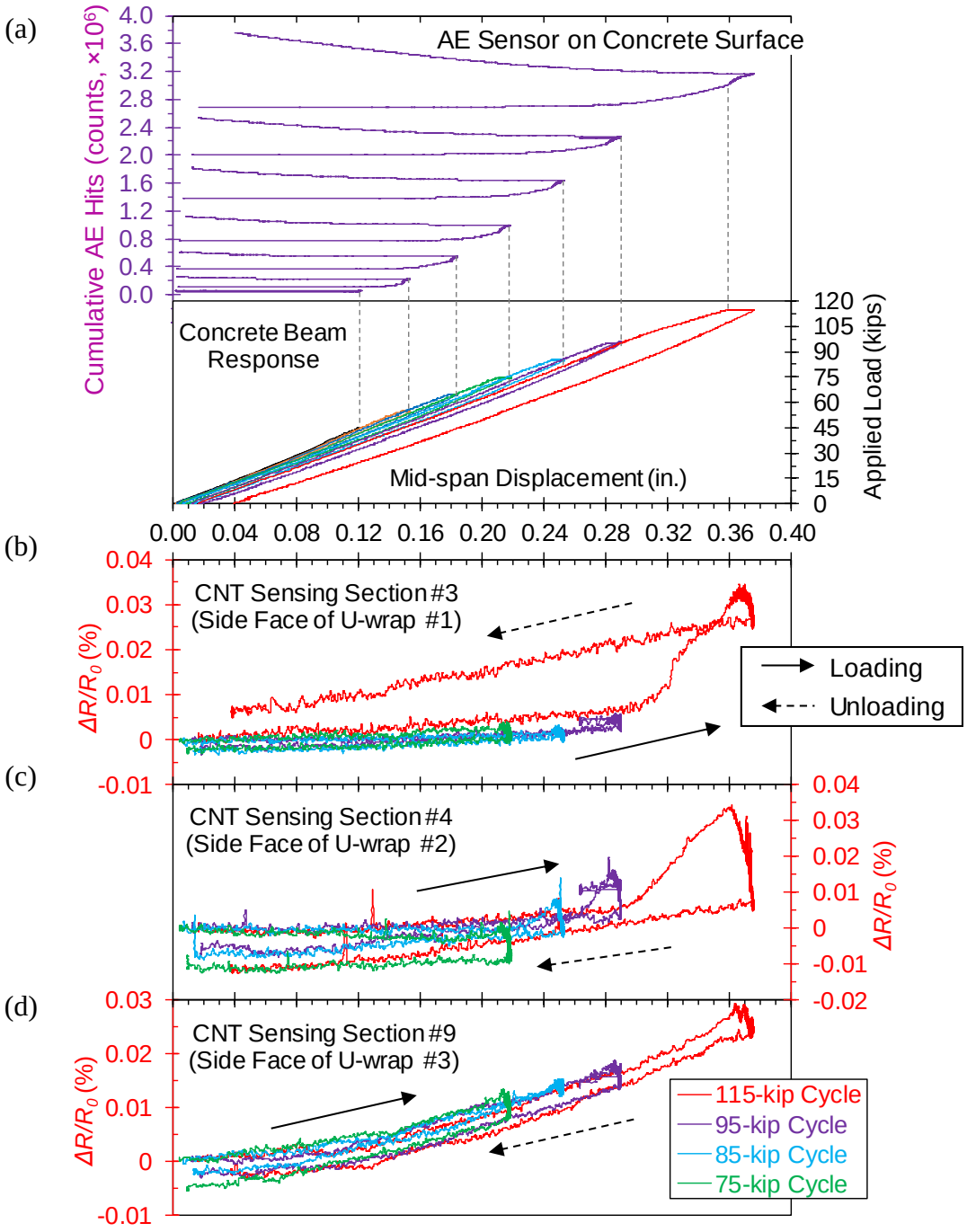

Figure 5.81: (a) Cumulative AE counts and the applied load as a function of beam deflection and (b-d) corresponding resistance-displacement relationships observed in side CNT sensing sections #3, #4, and #9 during the incremental stepwise loading.

In addition to Figure 5.81, the typical relationship between the resistance change and cumulative AE counts during the static loading-unloading cycles is shown in Figure 5.82. Particularly, the resistive response of the CNT sensing section #8 is selected to correlate with the observed AE response, since this sensing section has presented the most resistance changes (in %) among other sensing sections in the structural system and more importantly, this sensing section is close to the AE sensor. It can be seen that all curves display a comparable trend, showing three distinctive regions observed as the initial jump, the plateau (highlighted in yellow ellipses in Figure 5.82), and the final ramp.

In the initial jump region, the resistance of the CNT sensing section sharply increases due to the deformation of the shear beam. On the other hand, the AE counts remain nearly unchanged since the current loading level is less than the previous loading peak, i.e., the Kaiser effect. Nevertheless, this effect does not hold true during holding and unloading steps. For example, in the final ramp region, tremendous AE counts are displayed as the loading level falling below the previous level, highlighting the Felicity effect. It can be found that the observed Felicity effect initiates in the 65-kip cycle and gradually grows as loading level increases.

The most interesting results occur in the plateau region where the progressive increase in resistance is always accompanied with the instant accumulation of AE counts, confirming the correlation between the damage state of the GFRP-concrete structural system and the resistive response of the CNT sensor. The overall changes in the magnitude of the resistance are consistent with the variations in AE counts from the 55-kip to the 115-kip cycles, indicating the reduced structural performance of the rehabilitated beam due to the cracking damage propagated in the structural system.

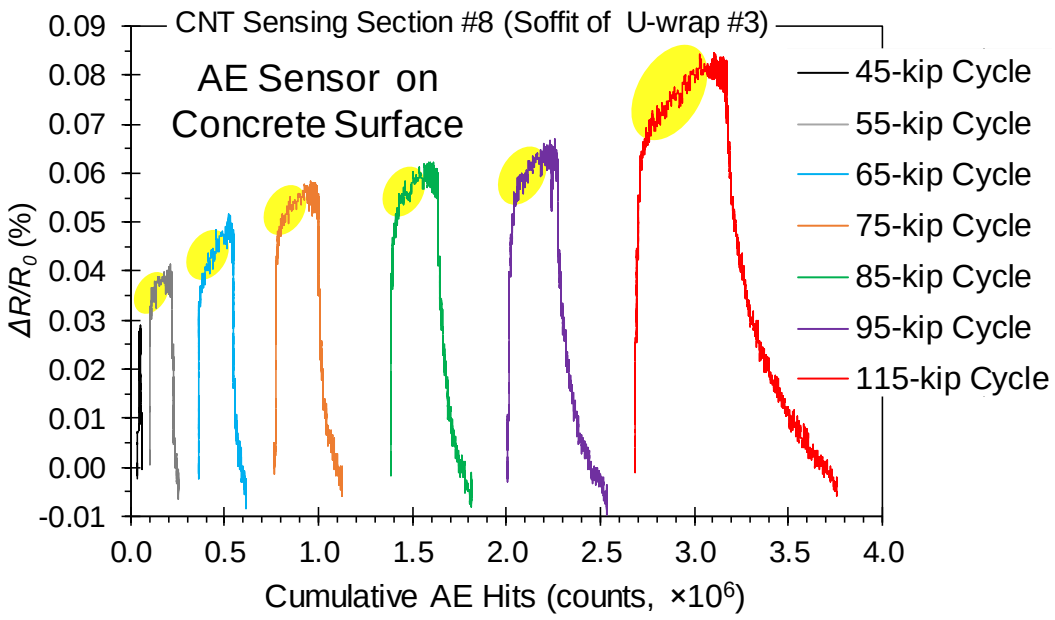

Figure 5.82: Typical relationship between the resistance change of the CNT sensor and the cumulative AE counts during the static cyclic test of the shear beam (Note: yellow ellipses highlight the plateau regions).

Figure 5.83 compares the acoustic emission data with the mechanical response of the shear beam (Figure 5.83a) and the resistive responses of the CNT-based U-wrap sensors (Figure 5.83b-e) as the shear beam was statically loaded to 140 kips and finally tested to failure. The cumulative AE counts demonstrate a close correlation with the deformation of the concrete beam. In particular, AE counts begin to dramatically increase at the onset of yielding of the shear beam, that is, at 157 kips as shown in Figure 5.83a. During the yielding of concrete beam, more than 250% changes in total AE counts are presented in comparison with those of the 140-kip cycle, revealing the severe damage developed in the structural system as approaching its imminent failure. It should be also noted that before the beam reached its ultimate strength, the AE sensor fell off the concrete surface due to the critically opening of

cracks (underneath the sensor, see Figure 5.44c) at high loads, which immediately terminated the task of monitoring acoustic emissions.

The resistance change-displacement relationships (Figure 5.83b-e) show two trends in general. The CNT-based U-wrap senor #2 (Figure 5.83b and c), compassed by the GFRP composite in the retrofitted region of the beam, shows a comparable fashion as the mid-span displacement (Figure 5.83a). It can be seen that during the 140-kip cycle, variations in resistance are steadily increasing and decreasing as loaded and unloaded, respectively. In the last loading cycle, low-amplitude nonlinearities in resistance change are observed constantly after the shear beam starts to yield, depicting the failure process of the beam.

In contrast, the nonstructural U-wrap sensor #4 (Figure 5.83d and e), located in the non-rehabilitated portion of shear beam, shows large resistance changes (plotted in logarithmic scale) during the 140-kip (black) and the failure (red) cycles. These observed sharp resistance changes reveal the severe damage state of the structural system, which agrees with the aforementioned AE response. Compared with the extremely small and relatively smooth variations in resistance of CNT-based sensors located in the strengthened portion of the beam, it can be concluded that the cracking damage progression is effectively prevented using the wide and narrowly-spaced GFRP U-wraps and the deployed CNT-based sensors are able to correctly estimate the structural behavior of the shear beam in real-time.

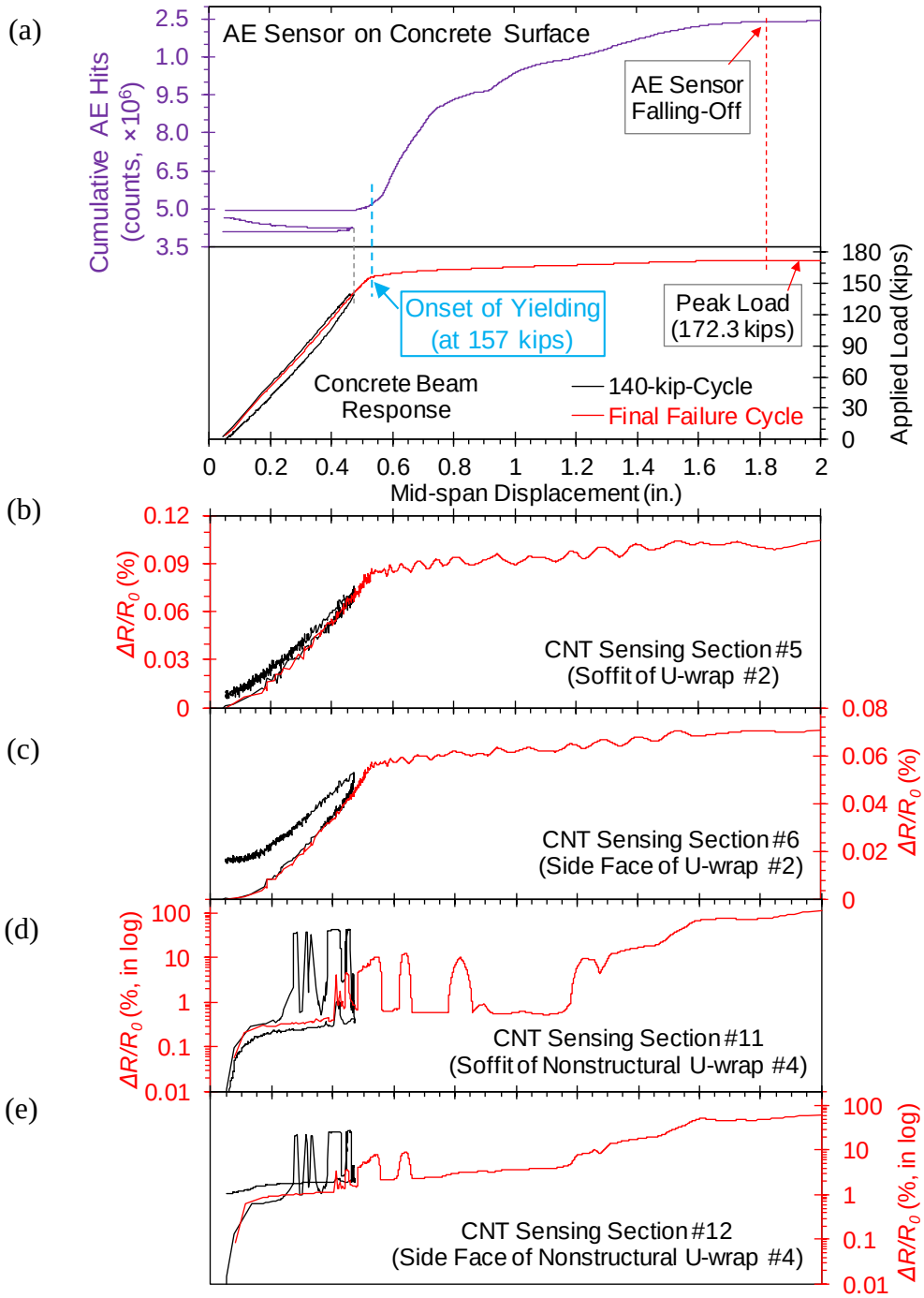

Figure 5.83: (a) Cumulative AE counts and the applied load as a function of beam deflection and (b-e) corresponding resistance-displacement relationships observed in CNT-based U-wrap sensors #2 and #4 as the shear beam statically loaded to 140 kips and tested to failure.

In addition to Figures 5.81-83, the AE response during the intermediate cyclic loading sessions (see Figure 5.37a) can be a useful figure of merit to evaluate the structural performance of the progressively damaged concrete beam, once subjected to the low service-level loadings. Figure 5.84 shows the real-time AE hits collected in the last three cyclic sessions (i.e., after the 95, 115, and 140-kip static loading cycles) and compares the acoustic emission data with the resistive responses of the nonstructural CNT-based U-wrap sensor #4 and the hybrid sensor #3 in the un-retrofitted and GFRP-rehabilitated portion of the shear beam, respectively.

From Figure 5.84a, it can be observed that the highest level of AE hits remains consistently below 180 counts/hit during all three cyclic sessions. However, more concentrated AE hits occur in the period of the 9^{th} cyclic session than those in the 7^{th} session. This most likely indicates that the overall structural performance of the structural system does degrade due to the cracking damage progressively accumulated inside as loaded at high levels (i.e., 95 vs. 140 kips). Particularly, this trend of damage progression is instantly demonstrated by spectacular variations in resistance of the nonstructural CNT-based U-wrap sensor as shown in Figure 5.84b and c. It can be observed that as soon as AE hit appears, a sharp spike of resistance change is observed and in general, the resistance change follows an increasing fashion, which further confirms the damage sensing capability of the installed CNT-based sensors.

On the other hand, the CNT sensor #3 (Figure 5.84d and e) located in the GFRP strengthened portion of the beam present a comparably unchanged trend of resistance changes at a very low level of magnitude during all three sessions. This most likely reveals that a robust structural performance of this beam portion is maintained due to the effective strengthening action of the depolyed GFRP U-wraps.

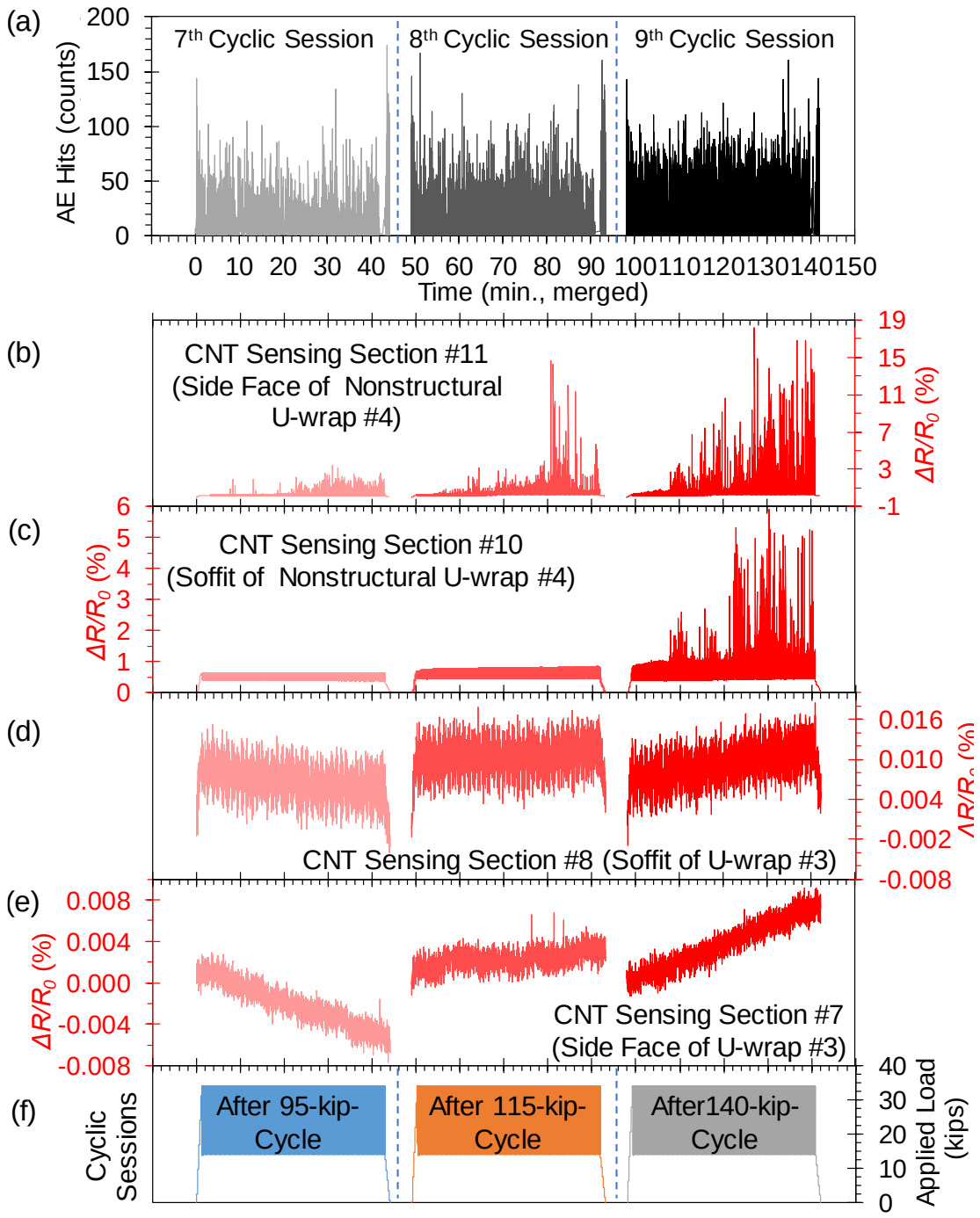

Figure 5.84: Comparisons between (a) AE hits and (b, c) the resistive responses of the nonstructural CNT-based U-wrap sensor #4 and (d, e) the structural sensor #3, during the 7th, 8th, and 9th cyclic loading sessions (f).

5.4 Summary and Conclusions

CNT-based smart sensing composites have been developed to offer multifunctional sensing capabilities of strain, damage, temperature, PH, gas, chemicals, etc. However, the overwhelming majority of the scientific literature on damage sensing/structural health monitoring have mainly focused on coupon-level experiments and involved complex manufacturing processes that are not suitable for large-scale applications. In particular, the applications of CNT-based sensing composites on concrete structures are rarely reported in scientific publications. For the first time, in this research, large-scale CNT-based hybrid composites have been designed and experimentally tested on two full-size concrete beams. The proposed hybrid composite simultaneously integrates the CNT-based sensing layer for structural health monitoring and the glass fiber reinforced polymer composite for structural strengthening. This novel composite system can be a strong candidate as a next-generation structural retrofitting methodology for concrete structures.

First, two reinforced concrete laboratory beams in size of 1 ft × 2 ft × 16 ft were designed with special steel reinforcement details such that the one beam could fail in flexure due to the insufficient tension bars and the other beam could fail in shear in its weak portion because of the unsymmetrical transverse reinforcement provided [21]. Both beams were cast in-place and preloaded under service-level loadings to generate moderate concrete cracks [21].

Second, the external GFRP composites were used to rehabilitate these pre-cracked beams. The design of the strengthening composites closely followed the procedures recommended by the ACI 440 Committee (2008) [25]. In particular, the first beam was rehabilitated with a continuous composite patch covering the entire

tension side to increase its flexural strength; the second beam was strengthened at its weaker side with three wide and narrowly-spaced composite U-jackets.

Next, nanotubes were coated onto nonstructural fabrics following the formerly developed 'wetting' approach (in Chapter 2) to establish the large planar sensors. These customized sensing sheets were first placed on the concrete surface, then covered with the glass fiber preforms, and finally integrated together onto the concrete beam through a one-step process, i.e., the on-site vacuum-assisted-resin-transfer-molding (VARTM) technique. After curing the part, the proposed hybrid composites were created. According to the existing literature, this 13.5 ft continuous sensing patch is the largest CNT-based sensing composite that has been created and tested.

Finally, both GFRP-strengthened beams were subjected to the low service-level cyclic loadings and the static incremental loading-unloading cycles, and ultimately tested to failure. Multiple kinds of sensors including strain gages, AE sensors, potentiometers, and cameras were used to monitor the mechanical responses of the beams and to verify and correlate with the real-time resistive responses of the deployed CNT sensors.

Based on the experimental results obtained in this study, the following general conclusions can be drawn:

(1) The implemented VARTM approach created high quality composite parts and ensured a smooth and uniform bonding layer between the composite and the concrete surface.

(2) The two strengthened concrete beams, each of which was originally designed to fail in a particular failure mode, behaved as expected. Their structural

performance and serviceability under the low service-level loads and high loads were substantially improved and properly maintained by the provided GFRP composites.

(3) The ultimate load carrying capacity of the strengthened flexure beams was found to be about 10% more than the design capacities according to ACI440.2R-8 recommendations, which is desirable and has validated the effectiveness of the VARTM-based GFRP strengthening approach. In particular, the wrapping scheme adopted in this study for the shear beam (i.e., the narrowly-spaced, wide unidirectional GFRP U-wraps) demonstrated a more superior shear-retrofitting action (i.e., no opening of shear cracks observed even at failure) than the discrete and narrow U-strips as commonly reported in literature.

(4) Large-scale CNT-based planar sensing sheets were successfully created and deployed at the bond interface between the concrete beam and GFRP via VARTM-based one-step process. Both local and integral behaviors of the beam were then monitored using these CNT sensors through the customized multiplexing approach.

(5) All CNT sensing sections were effectively responding to the mechanical responses of the concrete beam under difference loading scenarios. Particularly, the transient responses of the CNT sensors demonstrated great correlations with the responses of the applied loads, strains, deflections, and acoustic emission, validating the feasibility of using the integrated CNT sensors to perform continuous SHM of concrete structures.

(6) Based on the *in situ* AE responses and video monitoring, the observed nonlinearities in the resistive and piezoresistive responses of the CNT sensors have been confirmed to be an effective figure of merit presenting the local and integral damage propagations in both the concrete beam and the strengthening composite, such

as the onset of concrete cracking, fiber buddle splitting in GFRP, as well as the incipient and imminent failure of the beam member.

(7) In comparison with point sensors including strain gages, potentiometers and AE sensors, the large planar CNT sensors could enable the comprehensive and continuous SHM of the concrete members due to their extensive area of coverage, selective locations at the critical bonding interface, and the high sensitivities to damage. In particular, the nonstructural CNT-based U-wrap sensors demonstrated more than 250% resistance changes during the failure process of the concrete beam and their real-time resistive responses most likely depicted the entire damage progression in concrete.

(8) Under extremely low strain levels (i.e., $< 50\ \mu\varepsilon$), the piezoresistivity of the large CNT sensor could not be fully activated and the sensors likely become inert to the low loads and meanwhile are more affected by temperature variations.

(9) CNT sensors demonstrated the slow time variations of electrical resistance, seen as the baseline drifts, which are most likely associated with different levels of interfacial polarization in CNT-based composites. Sometimes, the electrical polarization effect could impede the piezoresistive responses of the CNT sensors at low levels of loadings.

REFERENCES

1. Bakis CE, Bank LC, Brown V, Cosenza E, Davalos J, Lesko J, Machida A, Rizkalla S, Triantafillou T. Fiber-reinforced polymer composites for construction—State-of-the-art review. J Composite Constr 2002;6(2):73-87.

2. Bai J. Advanced fibre-reinforced polymer (FRP) composites for structural applications: Elsevier, 2013.

3. Kim YJ. Advanced Composites in Bridge Construction and Repair: Elsevier, 2014.

4. Hollaway LC, Teng J. Strengthening and rehabilitation of civil infrastructures using fibre-reinforced polymer (FRP) composites: Elsevier, 2008.

5. Uddin N. Developments in fiber-reinforced polymer (FRP) composites for civil engineering: Elsevier, 2013.

6. Zoghi M. The international handbook of FRP composites in civil engineering: CRC Press, 2013.

7. Agarwal BD, Broutman LJ, Chandrashekhara K. Analysis and performance of fiber composites: John Wiley & Sons, 2006.

8. Sarker P, Begum M, Nasrin S. Fibre reinforced polymers for structural retrofitting: A review. J Civil Eng 2011;39(1):49-57.

9. Karbhari VM. Rehabilitation of pipelines using fiber-reinforced polymer (FRP) composites: Elsevier, 2015.

10. Teng J, Chen JF, Smith ST, Lam L. Behaviour and strength of FRP-strengthened RC structures: a state-of-the-art review. Proceedings of the institution of civil engineers-structures and buildings 2003;156(1):51-62.

11. Kamruzzaman M, Jumaat MZ, Sulong NH, Islam AB. A review on strengthening steel beams using FRP under fatigue. Scientific World Journal 2014;2014:702537.

12. Carse A, Spathonis MJ, Chandler ML, Gilbert MD, Johnson MB, UWS AJ, Pham L. Review of strengthening techniques using externally bonded fiber reinforced polymer composites. CRC for Construction Innovation, Brisbane 2002.

13. Mirmiran A, Shahawy M, Nanni A, Karbhari V. NCHRP Report 514: Bonded repair and retrofit of concrete structures using FRP composites: Recommended construction specifications and process control manual. Washington, D.C.: Transportation Research Board, 2004.

14. Rollins T. New and emerging methods of bridge strengthening and repair and development of a bridge rehabilitation website framework. M.S., University of Delaware, 2015.

15. Wu Z, Kim YJ, Diab H, Wang X. Recent developments in long-term performance of FRP composites and FRP-concrete interface. Adv Struct Eng 2010;13(5):891-903.

16. Zaman A, Gutub SA, Wafa MA. A review on FRP composites applications and durability concerns in the construction sector. J Reinf Plast Compos 2013;32(24):1966-1988.

17. Schumacher T, Thostenson ET. Integrated Strengthening and Monitoring of Structures using Structural Carbon Nanotubed-Based Composites. Patent 2014;61/941,686.

18. Zhang H, Liu Y, Kuwata M, Bilotti E, Peijs T. Improved fracture toughness and integrated damage sensing capability by spray coated CNTs on carbon fibre prepreg. Composites Part A: Applied Science and Manufacturing 2015;70:102-110.

19. Song Y, Hehr A, Shanov V, Alvarez N, Kienzle N, Cummins J, Koester D, Schulz M. Carbon nanotube sensor thread for distributed strain and damage monitoring on IM7/977-3 composites. Smart Mater Struct 2014;23(7):075008.

20. Elhajjar R, La Saponara V, Muliana A. Smart Composites: Mechanics and Design: CRC Press, 2013.

21. Mhamdi L. Seismology-based approaches for the quantitative acoustic emission monitoring of concrete structures. PhD, University of Delaware, 2015.

22. ACI Committee 318. Building code requirements for structural concrete (ACI 318-11) and commentary. Farmington Hills, MI: American Concrete Institute, 2012.

23. Wight JK, MacGregor JG. Reinforced Concrete Mechanics and Design (6th Edition). Upper Saddle River, NJ: PEARSON, 2012.

24. American Concrete Institute (ACI). ACI Manual of Concrete Practice. Farmington Hills, MI: American Concrete Institute, 2015.

25. ACI Committee 440. Guide for the Design and Construction of Externally Bonded FRP Systems for Strengthening Concrete Structures. Farmington Hills, MI: American Concrete Institute, 2008.

26. ACI Committee 440. Specifications for Carbon and Glass Fiber-Reinforced Polymer (FRP) Materials Made by Wet Layup for External strengthening of Concrete and Masonry Structures. Farmington Hills, MI: American Concrete Institute, 2013.

27. Higgins C, Howell DA, Smith MT, Senturk AE. Shear Repair Methods for Conventionally Reinforced Concrete Girders and Bent Caps. 2009;FHWA OR-RD-10-09.

28. Kim Y, Quinn K, Satrom N, Garcia J, Sun W, Ghannoum WM, Jirsa JO. Shear strengthening of reinforced and prestressed concrete beams using carbon fiber reinforced polymer (CFRP) sheets and anchors. 2012;FHWA/TX-12/0-6306-1.

29. Teng J, Smith ST, Yao J, Chen JF. Intermediate crack-induced debonding in RC beams and slabs. Constr Build Mater 2003;17(6):447-462.

30. Chen J, Teng J. Shear capacity of FRP-strengthened RC beams: FRP debonding. Constr Build Mater 2003;17(1):27-41.

31. Reed CE, Peterman RJ, Rasheed HA. Evaluating FRP repair method for cracked prestressed concrete bridge members subjected to repeated loadings (Phase 1). 2005;K-TRAN: KSU-01-2.

32. Malvar LJ, Warren GE, Inaba CM. Rehabilitation of Navy Pier Decks with Composite Sheets. The 2nd FRP International Symposium on Non-Metallic (FRP) Reinforcement for Concrete Structures, Ghent, Belgium, 1996.

33. Chajes MJ, Januszka TF, Mertz DR, Thomson TA, Finch WW. Shear strengthening of reinforced concrete beams using externally applied composite fabrics. ACI Struct J 1995;92(3):295-303.

34. Norris T, Saadatmanesh H, Ehsani MR. Shear and flexural strengthening of R/C beams with carbon fiber sheets. J Struct Eng 1997;123(7):903-911.

35. Kachlakev DI, McCurry Jr D. Testing of full-size reinforced concrete beams strengthened with FRP composites: Experimental results and design methods verification. 2000;FHWA-OR-00-19.

36. Sato Y, Ueda T, Kakuta Y, Tanaka T. Shear reinforcing effect of carbon fiber sheet attached to side of reinforced concrete beams. The 2nd International Conference on Advanced Composite Materials in Bridges and Structures, Montreal, Quebec, Canada, 1996.

37. Teng J, Lam L, Chen J. Shear strengthening of RC beams with FRP composites. Progress in Structural Engineering and Materials 2004;6(3):173-184.

38. Advani SG, Sozer EM. Process modeling in composites manufacturing: CRC Press, 2010.

39. Campbell Jr FC. Manufacturing processes for advanced composites: Elsevier, 2003.

40. Strong AB. Fundamentals of composites manufacturing: materials, methods and applications: Society of Manufacturing Engineers, 2008.

41. Uddin N, Vaidya U, Shohel M, Serrano-Perez J. Cost-effective bridge girder strengthening using vacuum-assisted resin transfer molding (VARTM). Advanced Composite Materials 2004;13(3-4):255-281.

42. Ramos L, Uddin N, Parrish M. Benefits of grooving on vacuum-assisted resin transfer molding FRP wet-out of RC beams. J Composite Constr 2013;17(5):636-640.

43. Reed MW, Barnes RW, Schindler AK, Lee H. Fiber-reinforced polymer strengthening of concrete bridges that remain open to traffic. ACI Struct J 2005;102(6):823.

44. Wang W, Li G. Experimental study and analysis of RC beams strengthened with CFRP laminates under sustaining load. Int J Solids Structures 2006;43(6):1372-1387.

45. Venkatesha K, Dinesh S, Balaji Rao K, Bharatkumar B, Balasubramanian S, Iyer NR. Experimental investigation of reinforced concrete beams with and without CFRP wrapping. Slovak Journal of Civil Engineering 2012;20(3):15-26.

46. Wang W, Dai J, Harries KA. Performance evaluation of RC beams strengthened with an externally bonded FRP system under simulated vehicle loads. J Bridge Eng 2011;18(1):76-82.

47. Thomsen H, Spacone E, Limkatanyu S, Camata G. Failure mode analyses of reinforced concrete beams strengthened in flexure with externally bonded fiber-reinforced polymers. J Composite Constr 2004;8(2):123-131.

48. Brena SF, Bramblett RM, Wood SL, Kreger ME. Increasing flexural capacity of reinforced concrete beams using carbon fiber-reinforced polymer composites. ACI Structural Journal 2003;100(1):36-46.

49. Brena SF, Benouaich MA, Kreger ME, Wood SL. Fatigue tests of reinforced concrete beams strengthened using carbon fiber-reinforced polymer composites. ACI Struct J 2005;102(2):305.

50. Dai J, Ueda T, Sato Y, Ito T. Flexural strengthening of RC beams using externally bonded FRP sheets through flexible adhesive bonding. International Symposium on Bond Behavior of FRP in Structures (BBFS 2005), Hong Kong, China, 2005. 205-213.

51. Duthinh D, Starnes M. Strength and ductility of concrete beams reinforced with carbon fiber-reinforced polymer plates and steel. J Composite Constr 2004;8(1):59-69.

52. Dong Y, Zhao M, Ansari F. Failure characteristics of reinforced concrete beams repaired with CFRP composites. The 3rd International Conference on Composites in Infrastructure, San Francisco, CA, 2002.

53. Teng J, Chen G, Chen J, Rosenboom O, Lam L. Behavior of RC beams shear strengthened with bonded or unbonded FRP wraps. J Composite Constr 2009;13(5):394-404.

54. Bousselham A, Chaallal O. Mechanisms of shear resistance of concrete beams strengthened in shear with externally bonded FRP. J Composite Constr 2008;12(5):499-512.

55. Bousselham A, Chaallal O. Behavior of reinforced concrete T-beams strengthened in shear with carbon fiber-reinforced polymer-an experimental study. ACI Struct J 2006;103(3):339.

56. Materazzi AL, Ubertini F, D'Alessandro A. Carbon nanotube cement-based transducers for dynamic sensing of strain. Cement and Concrete Composites 2013;37:2-11.

57. D'Alessandro A, Rallini M, Ubertini F, Materazzi AL, Kenny JM. Investigations on scalable fabrication procedures for self-sensing carbon nanotube cement-matrix composites for SHM applications. Cement and Concrete Composites 2016;65:200-213.

58. Downey A, Garcia-Macias E, D'Alessandro A, Laflamme S, Castro-Triguero R, Ubertini F. Continuous and embedded solutions for SHM of concrete structures using changing electrical potential in self-sensing cement-based composites. SPIE Smart Structures and Materials Nondestructive Evaluation and Health Monitoring, 2017. p. 101691G-101691G-13.

59. Baur C, DiMaio JR, McAllister E, Hossini R, Wagener E, Ballato J, Priya S, Ballato A, Smith Jr DW. Enhanced piezoelectric performance from carbon fluoropolymer nanocomposites. J Appl Phys 2012;112(12):124104.

60. Saleem H, Downey A, Laflamme S, Kollosche M, Ubertini F. Investigation of dynamic properties of a novel capacitive-based sensing skin for nondestructive testing. Mater Eval 2015;73(10):1384-1391.

61. Zhang M, Zhai Z, Li M, Cheng T, Wang C, Jiang D, Chen L, Wu Z, Guo Z. Epoxy nanocomposites with carbon nanotubes and montmorillonite: Mechanical properties and electrical insulation. J Composite Mater 2016;50(24):3363-3372.

62. Nayak L, Khastgir D, Chaki T. Study of alternating current impedance analysis and dielectric properties of carbon nanotube-based polysulfone nanocomposites. Polymer Composites 2012;33(1):85-91.

63. Shrivastava N, Maiti S, Suin S, Khatua B. Influence of selective dispersion of MWCNT on electrical percolation of in-situ polymerized high-impact polystyrene/MWCNT nanocomposites. Express Polymer Letters 2014;8(1).

64. Cao J, Chung D. Electric polarization and depolarization in cement-based materials, studied by apparent electrical resistance measurement. Cem Concr Res 2004;34(3):481-485.

65. Ettouney MM, Alampalli S. Infrastructure health in civil engineering: Theory and components, vol. 1: CRC Press, 2016.

66. Ettouney MM, Alampalli S. Sensors and Infrastructure Health. In: Anonymous Infrastructure Health in Civil Engineering: Theory and Components. Boca Raton, United States: CRC Press, 2012.

67. Huston D. Structural sensing, health monitoring, and performance evaluation: CRC Press, 2010.

68. Harris D, Dunegan H. Continuous monitoring of fatigue-crack growth by acoustic-emission techniques. Exp Mech 1974;14(2):71-81.

69. Dai H, Thostenson ET, Schumacher T. Processing and Characterization of a Novel Distributed Strain Sensor Using Carbon Nanotube-Based Nonwoven Composites. Sensors 2015;15(7):17728-17747.

Chapter 6

CONCLUSIONS, SCHOLARLY CONTRIBUTIONS, AND RECOMMENDATIONS FOR FUTURE RESEARCH

This doctoral research presented in this dissertation has drastically progressed and expanded the potential of utilizing carbon nanotube (CNT) -based sensing composites for structural health monitoring (SHM) of large concrete structures by solving four compelling problems including (1) fundamental development and characterization of the sensitive and scalable strain sensors using the novel CNT-based nonwoven composites, (2) establishment of spatial damage sensing capability of the CNT-based sensing composites using electrical impedance tomography (EIT), (3) systematic investigations on thermoresistive behaviors of the CNT-based nanocomposites and multiscale composites, and (4) large-scale experimental study on structural rehabilitation and health monitoring of concrete beams using the hybrid composites consisting of CNT-based nonwoven sensors and GFRP. These innovative insights and original work on the electrical conductive properties of the CNT-based composites and the 1D/2D sensing schemes are synergistically leveraged to develop a theoretical and practical framework to fundamentally enhance the CNT-based sensing composites for large-scale applications. The major conclusions and scholar contributions of each chapter are summarized as follows.

6.1 Scalable Strain Sensors Based on CNT-Nonwoven Composites

In Chapter 2, a simple and cost-effective two-step manufacturing approach for fabricating CNT-based nonwoven composites was first introduced. This technique is

scalable and customizable for field applications and has a high degree of application flexibility. Then, the proposed nanotube-based strain sensors were successfully developed in use of the CNT-based fiber sizing agent as the source of nanotubes, the nonwoven fabrics as the scalable carrier for nanotubes, the epoxy resin as the nonconductive substrate, and the VARTM approach for composite manufacturing.

Afterwards, a series of coupon-level experiments including scanning electron microscopy, mechanical and electrical tests were performed to characterize the as-established CNT-based nonwoven composites. Different properties including the morphological states, modulus of elasticity, elastic and ultimate strength and strain limits, double percolating behavior, electrical conductivity, and piezoresistivity (i.e., gage factor) were determined and proved that the CNT-based nonwoven composites are mechanically-robust and sensitive to strains.

In the last part of Chapter 2, three coupon-level case studies of using the proposed CNT sensors for *ex situ* strain monitoring of metal members were conducted under a static loading environment. The results demonstrated that (1) this newly developed sensors are effectively responding to the elastic and plastic, compressive and tensile strains, as well as the distributed strains; (2) strong linearity in the piezoresistive responses due to elastic tensile and compressive strains have been observed; (3) the permanent electrical resistance change corresponding to plastic deformation has also been identified; (4) the planar sensitivity including the major longitudinal and transverse piezoresistivities of the sensor has also been established and shows negative piezoresistivity (with an elastic gage factor, GF = −3.95) in the transverse direction; (5) the real-time strain sensing capacity of the CNT-based nonwoven composite sensors has been further verified.

6.2 Spatial Damage Detection and Imaging via EIT

The traditional nondestructive evaluation and testing (NDE&T) methods and general SHM systems are dominated by point-type sensors which normally possess limited area of coverage and deficient capability of evaluating the spatial damage in a structural member. In contrary, EIT is a noninvasive and true 2-D medical imaging approach that is capable of producing visual contours of electrical measurements. However, this powerful tool has been largely overlooked by the NDE and SHM communities until recently. Chapter 3 has explored the integration of EIT with the proposed CNT-based nonwoven sensing composites to construct a novel and unique spatial damage sensor that is capable of detecting, locating, and sizing the damage, and even determining the severity of the damage.

In this chapter, a series of square CNT-based sensing composites were first fabricated following the two-step manufacturing method as developed in Chapter 2. The inherent isotropy of the sensors' global conductivity serves as the cornerstone of integrating EIT approach. In particular, a difference imaging-based EIT algorithm was implemented and properly tuned to offer the 2D maps of conductivity changes, from which the spatial damage can be estimated. Both the forward and inverse problem associated with this EIT task were mathematically solved using a finite element model developed under MATLAB software. Specifically, a maximum a posteriori (MAP) reconstruction approach was used to reconstruct the normalized conductivity changes of the senor between its intact and damaged condition. All electrical measurements were collected from the 32 electrodes located along the boundary of the sensor by following a newly defined adjacent current-voltage scheme.

Afterwards, the established spatial damage sensing methodology was evaluated rigorously under three damage scenarios including (1) randomly distributed holes cut

into the sensor, (2) a narrow cut simulating a crack, and (3) progressive impacts on a GFRP laminate. For comparison, a commonly used NDE method, the infrared thermography (IRT) was also performed to evaluate the posed damage cases.

The obtained results have demonstrated that the proposed EIT-based methodology is possible to accurately detect and locate damage as well as capture the severity of the accumulated damage. Meanwhile, this innovative sensing approach displayed certain degree of overestimation and distortion in estimating the shape of the damage, which is also a common issue in all EIT applications as show in literature. Comparing with the IRT results, the proposed EIT approach presents better performance in assessing the initiation of damage (i.e., the nearly-invisible damage) well before it was visible with IRT. However, this new method displays relatively reduced resolution in estimating the sharp damage (i.e., with a high aspect ratio), in particular, the crack damage. In short, it is believed that the presented sensing methodology of CNT-based sensors integrated with EIT has considerable potential for SHM and NDE of civil, aerospace, and mechanical structures. In addition, the presented methodology has advanced a considerable improvement over the commonly implemented point-to-point resistance sensing methods for the conductive composite-based SHM and NDE, by enabling the spatial sensing capability.

6.3 Thermoresistive Behaviors of CNT-based Nanocomposites and Multiscale Composites

To date, a huge amount of resistive CNT-based sensing composites has been developed as review in Chapter 1. However, temperature dependence of resistance (i.e., the thermoresistive response) of these novel materials are normally ignored and not throughout characterized. The relevant investigations of the temperature effects to

the resistance of CNT-based composites, especially for the CNT-hybridized multiscale composites, are quite limited and not well documented in scientific literature. As a result, deficient understanding of this critical property significantly hinders the potential applications of CNT-based sensing composites in real-world.

In the beginning of Chapter 4, a review on the current advances and understanding of the thermoresistive responses of carbon nanotubes and their composites were rigorously performed so as to find the key parameters contributing to the temperature dependence of resistance of these materials, including the morphological structures of nanotubes and tube-based networks, the interfacial interactions between CNTs and the surrounding polymer, as well as the polymer thermo-mechanical/dynamic properties. Due to the complex electrical conduction mechanisms in nanotubes and CNT-based composites, the reported experimental results of their thermoresistive behaviors are very diverse and sometimes contradictory. Therefore, to perform a systematic investigation on this topic, the aforementioned parameters have to be properly considered. In this specific study, four types of CNT-based composites with the typically observed morphological states of CNTs are deliberately created including one kind of CNT nanocomposite (i.e., biphasic composites), the randomly dispersed CNTs in epoxy, and three kinds of multiscale composites, such as the loosely- and densely-concentrated CNTs, and the randomly dispersed CNTs in fibrous composites. To fabricate these specific composites, different materials and processing methods utilized such as the raw multi-walled nanotubes, CNT-based sizing agent, dip-coating method, three-roll milling approach, and electrophoretic deposition technique.

First, the thermomechanical properties of these four major composites were studied using a thermomechanical analyzer to understand the temperature-dependent material properties, such as the coefficient of thermal expansion, the glass transition temperature, etc. Next, for the multiscale composites, a simplified finite element model was created using COMSOL software to perform the thermal analysis on a fiber/epoxy system to understand the thermal residual stresses initiated at the fiber-epoxy interface (i.e., the region concentrating the CNT coating). Third, all of the composite samples were thermally cycled from 25 to 145 °C repeatedly in an environmental chamber and the *in situ* resistances were measured to study the thermoresistive behaviors.

It has been found that the CNT nanocomposites display a monotonous positive temperature correlation due to the volumetric thermal expansion, while all multiphase composites demonstrate a reversible double-crossover-phenomenon in their thermoresistive responses. This indicates that a complex dynamic dominance is responsible for these thermoresistive behaviors and depending on the competitive changes to the CNT networks originating from the polymer thermo-mechanical-/-dynamic-motions and the thermal stresses. In addition, the factors including the CNT arrangement/rearrangement, CNT concentration, thermal expansion, fiber properties, interfacial interactions, and the polymer properties (before and after glass transition temperature), have demonstrated certain degree of influences to the bulk thermoresistive responses of the CNT-based multiscale composites.

The findings from this comprehensive investigation are important scholarly contributions to the fundamental understanding of the thermoresistive behaviors of CNT-based composites. Finally, a Wheatstone bridge-based temperature

compensation approach was proposed and experimentally examined, which demonstrated a high degree of compensation for the temperature effects, facilitating the overall performance of the established CNT-based composite sensors in this study.

6.4 Large-Scale Applications of Using CNT-Based Sensors for SHM of Concrete Beams

Nowadays, FRP composites have been increasingly used in civil infrastructure due to their excellent mechanical properties and high resistance to environmental corrosions. As a common application method, since 1990s the externally-bonded FRP systems have been widely utilized to strengthen the existing civil structures that are deficient in flexure/shear strength or damaged due to unexpected loads, hazards, etc. Although the critical structures are commonly inspected routinely, the implemented FRP composites are rarely monitored according to the literatures. Consequently, the continuing concern of the long-term performance of the FRP-strengthened structures leads to a critical need for a fast, effective, and reliable SHM system for monitoring both the structures and the FRP composites. Despite the potential of CNT-based sensing composites for SHM of structures, these novel materials have important limitations, especially for large-scale applications. Chapter 5 has advanced the state of the art by contributing insightful knowledge on the integration of CNT-based nonwoven sensing sheets with GFRP composites to enable a hybrid composite system that is capable of simultaneous structural rehabilitation and health monitoring of large-scale concrete beams.

First, two steel reinforced concrete beams in size of 1 1 ft × 2 ft × 16 ft were specially designed that the one with insufficient tension bars and the other one with unsymmetrical transverse reinforcement (i.e, left portion is weaker in shear than the

right portion). After preloading, moderate concrete cracks were developed in these two beams. Next, the GFRP composites were proposed to strengthen the pre-cracked and deficient beams. After closely following the ACI 440.2R-08 recommendations, a continuous GFRP patch and three narrowly-spaced wide GFRP U-wraps were planned to be implemented on the flexure and shear beam, respectively. Afterwards, the large planar CNT-based nonwoven sensing sheets were customized to fit the size of the designed GFRP composites and then spectacularly deployed at the selective interface between the concrete beam and the GFRP. In particular, a one-step process was performed to instantly integrate the CNT sensors with GFRP and bond the composite onto the beam through the on-site vacuum-assisted-resin-transfer-molding approach. After curing the epoxy resin in-place, the proposed high quality hybrid composite parts were fabricated. To enable the distributed sensing capability of the proposed CNT sensors, a multiplexing sensing scheme was adopted.

The strengthened concrete beams were tested under a series of loading protocols and statically tested to failure in the end. Besides the planar CNT sensors, different point sensors including strain gages, potentiometers, acoustic emission sensors, and cameras were utilized to capture the mechanical responses of the concrete beams. The continuous SHM of the retrofitted concrete beams has revealed that the implementation of the narrowly-spaced and wide GFRP U-wraps for shear strengthening leads to the superior structural performance in comparing with the discrete narrow composite U-strips as commonly reported in literature. More importantly, the experimental results have demonstrated that the *in situ* resistive responses of the CNT sensors are in a great correlation with mechanical responses of the beam specimens in terms of displacements, strains, and AE evets. In particular, the

onset of damage such as the concrete and epoxy matrix cracking, the incipient and imminent failure of the concrete and GFRP were presented as the nonlinearities in the resistive and piezoresistive responses of the CNT sensors. In addition, due to extensive area of coverage and the selective location of the deployed CNT sensing sheets, a comprehensive and instantaneous SHM has been accomplished for the concrete beam members and the strengthening GFRP composites.

Apparently, important scholarly contributions are made by addressing a gap in existing concerns on the long-term performance of the FRP-based rehabilitation methods and instantly making a broader impact by demonstrating the large-scale applicability of the CNT-based nonwoven sensing composites for SHM of concrete members.

6.5 Recommendations for Future Work

This doctoral research has convincingly demonstrated the potential of CNT-based nonwoven sensing composites for strain sensing, spatial damage detection and identification, temperature sensing, as well as the continuous SHM of large-scale structures. Meanwhile, a few uncertainties, challenges, and defects have been also observed in some experimental results due to the complex nature of the CNT-based composite materials. For instance, these novel composites are prone to present the slow time drifts of the electrical resistance associated with the electrical polarization. Therefore, before starting the full field deployment of these CNT-based sensors, the future work will be performed to address some challenging issues so as to enable the full potential of this proposed methodology.

First, it should be focused on characterizing the long-term performance and reliability of these CNT-based sensing composites. In Chapter 5, the continuous SHM

was performed for a period of less than 30 hours and the resistive responses of the CNT sensors had demonstrated highly promising results. However, in comparing with the life expectancy of the civil structures, i.e., at least 30 years, prolonged tests need to be scheduled and conducted in order to investigate the fatigue behaviors and long-term performance of these CNT sensors. In particular, the sensors' resistive responses under the influences of the hydrothermal effects, UV radiation, water immersion, thermal shock, and etc., should be also investigated to enhance the field reliability of these novel sensing materials. In addition to the simple two-probe DC sensing scheme, more advanced and robust measurement schemes (such as the AC-based or the biphasic DC approach) should be researched and developed so as to compensate the time-dependent variations in the sensors' resistance from the aspect of sensing devices.

The second area of future research can be the enhancement of the EIT algorithms in order to improve the resolution and stability of the proposed spatial damage sensing and imaging methodology. At present, the reconstruction algorithm as presented in Chapter 3 is based on the MAP approach which is a fast and simple one-step linearization solver for reconstructing the conductivity changes. Some literatures have shown that the particular implement of iterative absolute imaging algorithm leads to the enhanced reconstructions of electrical conductivities with high contrast and high resolution. These successful experiences have suggested multiple application-specific approaches for reconstructions, such as the Gauss-Newton-based line searching method with interior point under the Bayesian inversion scheme and the approximation error approach with a total variation prior model for the modeling errors. In addition to improving the quality of the conductivity reconstructions, increasing the speed of image reconstruction without adversely influencing the image

quality will be another future direction in developing EIT-based sensing methodologies. In this way, a real-time EIT-based dynamic monitoring system will be ultimately achieved. The D-bar-based algorithms, the split augmented Lagrangian shrinkage algorithm, and the sparse reconstruction by separable approximation algorithm are the potential methods that can enable an on-line reconstruction with the fast frame rate.

Future work will also include further exploring the multi-functionalities of the established CNT-based nonwoven sensing composites. As fully demonstrated in Chapter 4, these novel composites are inherently sensitive to temperature, polymer motions, and phase changes. Therefore, a distributed sensor for on-line, *in situ* process monitoring of manufacturing fiber composites can be developed with the thin, light weight, and highly porous CNT-modified nonwoven sensing sheet, which is noninvasive to the overall structural integrity of the composites to be monitored and can either be integrated directly in the composite or used as sacrificial process layer in form of sensing peel ply. In particular, with the addition of the intrinsic piezoresistivity of the CNT-based sensors, the vacuuming process can be also monitored in real-time. Consequently, this proposed sensing is offering a simple, effective, and economical method to monitor the overall manufacturing process (i.e., vacuuming, resin flow, and polymer cure) of composite that can be readily integrated into existing processes of composites manufacturing industry.

For preliminary demonstration, Figure 6.1 shows the results of an experiment to monitor the progression in one-dimensional flow under vacuum. Figure 6.1a illustrates the experimental setup (flow left to right) in which four discrete sensing sections (1-4) are used to examine the flow progression and regions 5-8 are duplicate

sensing sections from the supplemental sensor for further validation. In particular, over section 1 and part of section 2 (Figure 6.1b), a high permeability layer was intentionally added to allow resin to flow rapidly while the rest of the flow area had a much lower flow permeability. Figure 6.1c shows the transient sensing response and the snapshots taken at different stages of resin flow. Clearly, when the resin flows through the sensing sections, a distinct change in resistance is observed and the resistance change increases at nearly constant slope. The increase in slope in the filling section shows the distributed nature of the sensor, where the response changes as the flow front progresses.

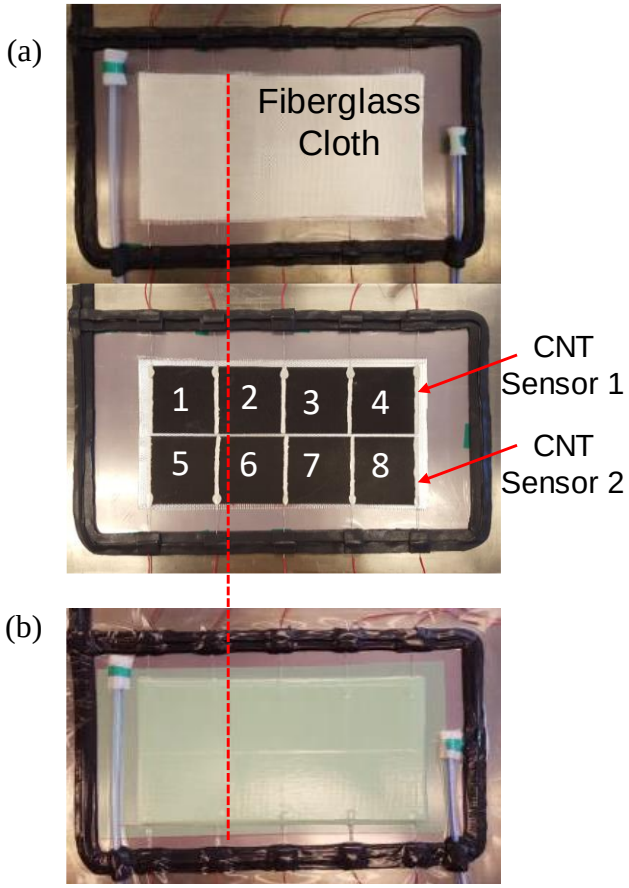

Figure 6.1: Photographs showing (a) the layout of two planar sensors for flow monitoring experiments with the flow regions monitored from left to right (sensor #1 covering sections 1-4, and sensor #2 covering sections 5-8 for duplicate validation) and (b) the VARTM setup under full vacuum with the high flow permeability area placed over region 1 and part of region 2 (dashed line marking the end of the high permeability region); (c) transient resistive responses showing the start and the end of 1D flow for sensing section 1 through 4.

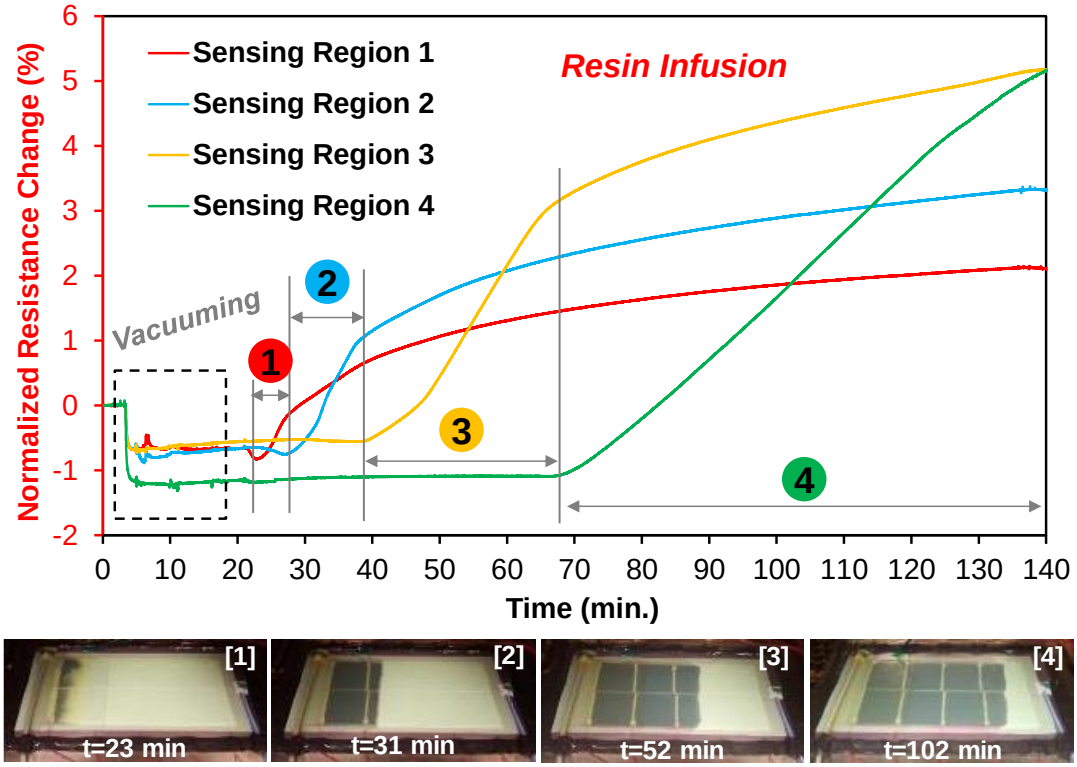

(c)

Figure 6.1: continued.

Appendix

PERMISSIONS

Sensors **2015**, *15*, 17728-17747; doi:10.3390/s150717728

OPEN ACCESS

sensors

ISSN 1424-8220

www.mdpi.com/journal/sensors

Article

Processing and Characterization of a Novel Distributed Strain Sensor Using Carbon Nanotube-Based Nonwoven Composites

Hongbo Dai [1,3], Erik T. Thostenson [2,3,†] and Thomas Schumacher [1,3,†,*]

[1] Civil and Environmental Engineering, University of Delaware, Newark, DE 19716, USA; E-Mails: hongbo@udel.edu

[2] Mechanical Engineering and Materials Science & Engineering, University of Delaware, Newark, DE 19716, USA; E-Mail: thosten@udel.edu

[3] Center for Composite Materials, University of Delaware, Newark, DE 19716, USA

[†] These authors contributed equally to this work.

[*] Author to whom correspondence should be addressed; E-Mail: schumact@udel.edu; Tel.: +1-302-831-4559; Fax: +1-302-831-3640.

Academic Editor: Bernhard Tittmann

Received: 2 June 2015 / Accepted: 16 July 2015 / Published: 21 July 2015

Abstract: This paper describes the development of an innovative carbon nanotube-based non-woven composite sensor that can be tailored for strain sensing properties and potentially offers a reliable and cost-effective sensing option for structural health monitoring (SHM). This novel strain sensor is fabricated using a readily scalable process of coating Carbon nanotubes (CNT) onto a nonwoven carrier fabric to form an electrically-isotropic conductive network. Epoxy is then infused into the CNT-modified fabric to form a free-standing nanocomposite strain sensor. By measuring the changes in the electrical properties of the sensing composite the deformation can be measured in real-time. The sensors are repeatable and linear up to 0.4% strain. Highest elastic strain gage factors of 1.9 and 4.0 have been achieved in the longitudinal and transverse direction, respectively. Although the longitudinal gage factor of the newly formed nanocomposite sensor is close to some metallic foil strain gages, the proposed sensing methodology offers spatial coverage, manufacturing customizability, distributed sensing capability as well as transverse sensitivity.

Keywords: Carbon nanotubes; distributed sensing; structural health monitoring; nanocomposites; strain sensors; longitudinal and transverse sensitivity; civil infrastructure

J Nondestruct Eval (2016) 35:26
DOI 10.1007/s10921-016-0341-0

A Novel Methodology for Spatial Damage Detection and Imaging Using a Distributed Carbon Nanotube-Based Composite Sensor Combined with Electrical Impedance Tomography

Hongbo Dai[1,5] · Gerard J. Gallo[2,5] · Thomas Schumacher[3] · Erik T. Thostenson[2,4,5]

Received: 1 October 2015 / Accepted: 22 February 2016 / Published online: 28 March 2016

Abstract This paper describes a novel non-destructive evaluation methodology for imaging of damage in composite materials using the electrical impedance tomography (EIT) technique applied to a distributed carbon nanotube-based sensor. The sensor consists of a nonwoven aramid fabric, which was first coated with nanotubes using a solution casting approach and then infused with epoxy resin through the vacuum assisted resin transfer molding technique. Finally, this composite sensor is cured to become a mechanically-robust, electromechanically-sensitive, and highly customizable distributed two-dimensional sensor which can be adhered to virtually any substrate. By assuming that damage on the sensor directly affects its conductivity, a difference imaging-based EIT algorithm was implemented and tailored to offer two-dimensional maps of conductivity changes, from which damage location and size can be estimated. The reconstruction is based on a newly defined adjacent current–voltage measurement scheme associated with 32 electrodes located along the boundary of the sensor. In this paper, we evaluate our methodology first by introducing well-defined damage where sections are either removed or narrow cuts are made on a series of sensor specimens. Finally, a more realistic damage scenario was investigated to show the capability of our methodology to detect impact damage on a composite laminate. The resulting EIT maps are compared to visual inspection and thermograms taken with an infrared camera.

Keywords Distributed sensing · Carbon nanotube · Composite materials · Nonwoven fabric · Electrical impedance tomography · Non-destructive evaluation · Damage detection · Difference imaging

Electronic supplementary material The online version of this article (doi:10.1007/s10921-016-0341-0) contains supplementary material, which is available to authorized users.

✉ Hongbo Dai
hongbo@udel.edu

[1] Civil and Environmental Engineering, University of Delaware, Newark, DE 19716, USA

[2] Mechanical Engineering, University of Delaware, Newark, DE 19716, USA

[3] Civil and Environmental Engineering, Portland State University, Portland, OR 97201, USA

[4] Materials Science & Engineering, University of Delaware, Newark, DE 19716, USA

[5] Center for Composite Materials, University of Delaware, Newark, DE 19716, USA

1 Introduction

1.1 Damage Sensing Approaches Using Resistive Sensors

Recent advances in composite materials have taken advantage of both nanotechnology and composite engineering and created a new era for developing novel and multifunctional composite sensors that possess high sensitivity and excellent mechanical response [1,2] which are suitable for non-destructive evaluation (NDE) and structural health monitoring (SHM) applications. A number of researchers have validated the feasibility and sensitivity of employing carbon nanotube (CNT)-based nanocomposites as strain/damage sensors [3–9]. One approach to locate and image damage on a structure is by using a series of one-dimensional measurements collected from a two-dimensional (2-D) sensing area covered by densely-spaced strain gages [10] or from the quasi-distributed surface electrodes on an electrically conductive composite panel [11]. However, this quasi-2-D algorithm compromises the results by confining the possi-